**Highlights in Theoretical Chemistry 8**
*Series Editors:* Christopher J. Cramer · Donald G. Truhlar

Hua Guo
Daiqian Xie
Weitao Yang *Editors*

# Guosen Yan

## A Festschrift from Theoretical Chemistry Accounts

Springer

Highlights in Theoretical Chemistry

Vol. 8
Series Editors: C. Cramer • D.G. Truhlar

More information about this series at http://www.springer.com/series/11166

Hua Guo • Daiqian Xie • Weitao Yang
Volume Editors

# Guosen Yan

## A Festschrift from Theoretical Chemistry Accounts

*With contributions from*

Benjamin Alday • Robert Balawender • Ting-Jun Bi • Zexing Cao • Xin Che
Jun Chen • Yun Chen • Wei-Hai Fang • Xuejun Feng • Bina Fu • Jun Gao
Xiumin Gao • Yi Qin Gao • Hua Geng • Xiaoli Gong • Jiande Gu
Pei-Jie Guan • Hua Guo • Andrzej Holas • Gao-Lei Hou • Xixi Hu • Jian Jin
Ryan Johnson • R. Bruce King • Jianyong Lei • Feng Li • Hui Li
Huiliang Li • Jun Li • Xiang-Yuan Li • Xin Li • Cheng-Wen Liu
Chengbu Liu • Lili Lin • Shu Liu • Yang Liu • Nai-Xia Lu • Yi Luo
Jian-Yi Ma • Ali Malek • Mei-Jun Ming • Degao Peng • Hai-Sheng Ren
Robert J. Le Roy • Pierre-Nicholas Roy • Mingsong Shi • Zhigang Shuai
Mingjun Sun • Huai Sun • Jing-Cong Tao • Guangjun Tian • Fan Wang
Lili Wang • Yan Wang • Zhifan Wang • Nan Xia • Changjian Xie
Daiqian Xie • Yani Xie • Yaoming Xie • Dingguo Xu • Pan Xu • Xin Xu
Ying Xue • Jinlong Yang • Jing Yang • Lan-Feng Yuan • Minghui Yang
Ting Yuan • Weitao Yang • Xin Yang • Zhong-Zhi Yang • Chunchun Zhang
Dong H. Zhang • Xiao-Long Zhang • Dong-Xia Zhao • Wei-Jun Zheng
Hua Zhu • Liyao Zhu

Springer

*Volume Editors*
Hua Guo
Department of Chemistry
and Chemical Biology
University of New Mexico
Albuquerque, NM, USA

Daiqian Xie
School of Chemistry
and Chemical Engineering
Nanjing University
Nanjing, China

Weitao Yang
Department of Chemistry
Duke University
Durham, NC, USA

Originally published in Theor Chem Acc, Volume 133 (2014)
© Springer-Verlag Berlin Heidelberg 2014

ISSN 2194-8666 ISSN 2194-8674 (electronic)
Highlights in Theoretical Chemistry
ISBN 978-3-662-47844-8 ISBN 978-3-662-47845-5 (eBook)
DOI 10.1007/978-3-662-47845-5

Library of Congress Control Number: 2015945574

Springer Heidelberg New York Dordrecht London
© Springer-Verlag Berlin Heidelberg 2015
This work is subject to copyright. All rights are reserved by the Publisher, whether the whole or part of the material is concerned, specifically the rights of translation, reprinting, reuse of illustrations, recitation, broadcasting, reproduction on microfilms or in any other physical way, and transmission or information storage and retrieval, electronic adaptation, computer software, or by similar or dissimilar methodology now known or hereafter developed.
The use of general descriptive names, registered names, trademarks, service marks, etc. in this publication does not imply, even in the absence of a specific statement, that such names are exempt from the relevant protective laws and regulations and therefore free for general use.
The publisher, the authors and the editors are safe to assume that the advice and information in this book are believed to be true and accurate at the date of publication. Neither the publisher nor the authors or the editors give a warranty, express or implied, with respect to the material contained herein or for any errors or omissions that may have been made.

Printed on acid-free paper

Springer-Verlag GmbH Berlin Heidelberg is part of Springer Science+Business Media (www.springer.com)

# Contents

Theor Chem Acc (2014) 133:1581
DOI 10.1007/s00214-014-1581-7

INTRODUCTION

# A tribute to Guosen Yan

**Hua Guo · Daiqian Xie · Weitao Yang**

Published online: 15 October 2014
© Springer-Verlag Berlin Heidelberg 2014

Professor Guosen Yan was born in 1930 in Nanchong, Sichuan Province, China. He graduated in 1951 from Chongqing University, majoring in Chemistry, and upon graduation joined the faculty in the same university. In 1953, he was transferred to Department of Chemistry in Sichuan University, rising through the ranks and became Associate Professor in 1962 and Full Professor in 1979. He served as the President of Sichuan University from 1984 to 1989. His leadership helped to secure Sichuan University as one of the top comprehensive universities in China. Professor Yan has also served as a director and executive director of the Chinese Chemical Society and in many other important posts in China, helping to lay a solid foundation for the ongoing expansion of the Chinese research enterprise.

Published as part of the special collection of articles celebrating the 85th birthday of Professor Guosen Yan.

H. Guo (✉)
Department of Chemistry and Chemical Biology, University of New Mexico, Albuquerque, NM 87131, USA
e-mail: hguo@unm.edu

D. Xie
Institute of Theoretical and Computational Chemistry, Key Laboratory of Mesoscopic Chemistry, School of Chemistry and Chemical Engineering, Nanjing University, Nanjing 210093, China

W. Yang
Department of Chemistry, Duke University, Durham, NC 27708, USA

W. Yang
Key Laboratory of Theoretical Chemistry of Environment, Ministry of Education, School of Chemistry and Environment, South China Normal University, Guangzhou 510006, China

Professor Yan is a pioneer in Theoretical Chemistry in China. He was one of eight original students of Professor Au-chin Tang, a Columbia-trained theoretical chemist, widely considered as the founding father of Theoretical Chemistry in China. Professor Yan's research interests spanned several areas, including crystal field theory, graph theory, quantum chemistry, and molecular spectroscopy. His major scientific contributions include (1) analysis of the symmetry and orthogonalization of the rotational group-point group coupling coefficients in ligand field theory, (2) graph theory for determinant expansions, (3) a vibrational self-consistent field/configuration interaction theory, and (4) molecular spectroscopy and potential energy surfaces. He has written three books and close to 200 journal articles.

Professor Yan has also been a great educator. His lectures were legendary. Whether it is quantum mechanics or group theory, he presented the materials in his characteristically meticulous fashion and filled the board with perfectly written derivations and equations, never miswriting or erasing anything. He has educated more than 20 graduate students (see list), many of whom have become accomplished scientists in China. His deep understanding of quantum mechanics and group theory greatly influenced his students.

In addition to being an accomplished scientist, Professor Yan also epitomizes a classical Confucius scholar. He read widely Chinese history, poetry, literature, and philosophy. Professor Yan is also an accomplished Chinese calligrapher. He has not only influenced many researchers through his scientific insights, but also helped many of us to shape our views of science, philosophy, and life.

On this occasion of Professor Yan's 85th birthday, we celebrate his accomplishments in science and education in this Special Collection. The breadth and depth of the work reported here are testaments of the vitality of theoretical

and computational chemistry in China, the fruits of the seeds sown by Professor Yan and his contemporaries.

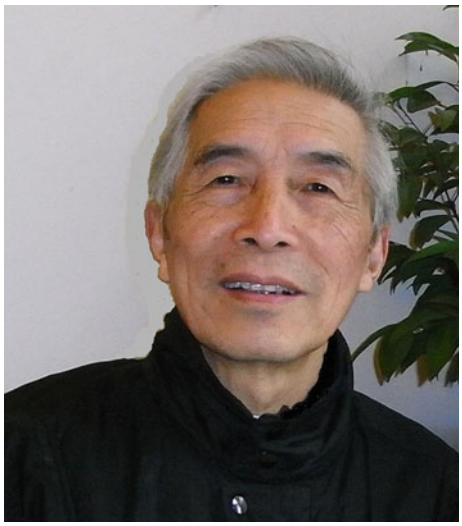

List of students of Professor Guosen Yan

| | Year | First name | Last name | 中文姓名 |
|---|---|---|---|---|
| M.S. | 1978 | Yaoming | Xie | 谢尧明 |
| | 1981 | Kaiqin | Lao | 劳开勤 |
| | | Huai | Sun | 孙 淮 |
| | 1982 | Daping | Cao | 曹大平 |
| | | Hua | Guo | 郭 华 |
| | | Zhi | He | 何 知 |
| | 1983 | Gaoqing | Yuan | 袁高清 |
| | | Chongde | Zheng | 郑重德 |
| | 1984 | Ruifeng | Liu | 刘瑞峰 |
| | | Kehe | Su | 苏克和 |
| | | Xingquan | Xiang | 向兴全 |
| | | Xuefeng | Zhou | 周学峰 |
| Ph.D. | 1987 | Jie | Yang | 杨 捷 |
| | 1988 | Changyuan | Tao | 陶长元 |
| | 1989 | Guoming | Liang | 梁国明 |
| | 1990 | Zexing | Cao | 曹泽星 |
| | | Huabei | Zhang | 张华北 |
| | 1991 | Junkai | Xie | 谢军楷 |
| | 1992 | Xiangyuan | Li | 李象远 |
| | | Jiande | Gu | 顾建德 |
| | 1993 | Hui | Xian | 先 晖 |
| | 1994 | Ying | Xue | 薛 英 |
| | | Minghui | Yang | 杨明晖 |
| | 1995 | Yi | Ren | 任 译 |
| | 1996 | Xuejun | Xu | 徐学军 |

## 1 Publications of Professor Guosen Yan


1. G. S. Yan and M. X. Карапетьянц, *J. Sichuan U.* **4**, 51–54 (1959).
2. M. X. Карапетьянц and G. S. Yan, *J. Sichuan U.* **6**, 65–70 (1959).
3. M. X. Карапетьянц and G. S. Yan, *J. Sichuan U.* **6**, 71–76 (1959).
4. M. X. Карапетьянц and G. S. Yan, *Zurnal. fiz. Chem.* (*russ*) **34**, 1647 (1960).
5. M. X. Карапетьянц and G. S. Yan, *J. High. Edu.* (*russ*) **4**, 99 (1960).
6. G. S. Yan and M. X. Карапетьянц, *J. Sichuan U.* **1**, 103–106 (1962). *Zurnal. fiz. Chem.* (*russ*) **34**, 1647 (1960).
7. M. X. Карапетьянц and G. S. Yan, *J. High. Edu.* (*russ*) **4**, 480 (1961).
8. G. S. Yan and M. X. Карапетьянц, *J. Sichuan U.* **1**, 93–103 (1962). *Zurnal. fiz. Chem.* (*russ*) **37**, 2041 (1963).
9. Academic discussion on structural chemistry, *Acta Sci. Nat. U. Jilin.* **3**, 79–100 (1964).
10. Academic discussion on structural chemistry, *Acta Sci. Nat. U. Jilin.* **1**, 59–70 (1965).
11. A. Q. Tang and G. S. Yan, Theoretical Method of the Ligand Field Theory, Science Press, Beijing (1979).
12. A. Q. Tang, Y. S. Jiang, G. S. Yan and S. S. Dai, Graph Theoretical Molecular Orbitals, Science Press, Beijing (1986).
13. G. S. Yan, *Int. J. Quantum. Chem.* **14**, 549–550 (1980).
14. G. S. Yan, Z. M. Sun, S. X. Xiao and X. F. Zhou, *J. Atom. Mol. Phys.* **2**, 68–83 (1985).
15. H. Sun, A. M. Tian and G. S. Yan, *Int. J. Quantum Chem.* **29**, 1303–1324 (1986).
16. W. G. Sun, Y. M. Xie, A. M. Tian and G. S. Yan, *Chem. J. Chinese U.* **7**, 448–452 (1986).
17. G. S. Yan, Z. M. Sun, S. X. Xiao and X. F. Zhou, *Chem. J. Chinese U.* **7**, 351–356 (1986).
18. G. S. Yan, Z. M. Sun, S. X. Xiao, X. F. Zhou and Y. Xue, *Acta Phys-Chim Sin.* **2**, 505–511 (1986).
19. K. Q. Lao, A. M. Tian and G. S. Yan, *J. Atom. Mol. Phys.* **3**, 189–196 (1986).
20. C. D. Zheng, G. S. Yan, Z. M. Sun, A. M. Tian and S. X. Xiao, *J. Atom. Mol. Phys.* **4**, 501–506 (1987).
21. H. Guo, A. M. Tian and G. S. Yan, *J. Mol. Sci.* (*Theochem*) **149**, 105–109 (1988).
22. A. M. Tian, R. F. Liu, Z. M. Sun and G. S. Yan, *Chem. J. Chinese U.* **8**, 836–837 (1988).

23. G. S. Yan, Z. M. Sun, S. X. Xiao and Y. Xue, *Chem. J. Chinese U.* **9**, 700–705 (1988).
24. G. Q. Yuan, A. M. Tian, Z. H. Tang and G. S. Yan, *J. Atom. Mol. Phys.* **5**, 803–810 (1988).
25. A. M. Tian, R. F. Liu, Z. M. Sun, X. F. Zhou and G. S. Yan, *Int. J. Quantum. Chem.* **36**, 765–771 (1989).
26. C. D. Zheng, G. S. Yan, Z. M. Sun and S. X. Xiao, *Acta Chim. Sinica* **47**, 603–608 (1989).
27. A. M. Tian, G. Q. Yuan, Z. H. Tang and G. S. Yan, *Chem. J. Chinese U.* **10**, 826–830 (1989).
28. Z. M. Sun, Z. X. Cao and G. S. Yan, *Chinese J. Chem. Phys.* **3**, 350–356 (1990).
29. S. X. Xiao, J. Ji, T. L. Chen, T. C. Cai and G. S. Yan, *J. Mol. Struct.* (*Theochem*) **204**, 33–40 (1990).
30. Z. R. Li, A. M. Tian and G. S. Yan, *J. Sichuan U.* (*Nat. Sci. Edit.*) **28**, 401–402 (1991).
31. Z. M. Sun, Z. X. Cao and G. S. Yan, *J. Atom. Mol. Phys.* **2**, 1859–1864 (1991).
32. M. Tian, G. M. Liang and G. S. Yan, Quantum Chemistry Computational Methods of Chemical Bonds, Sichuan University Press, Chengdu (1992).
33. Z. X. Cao, Z. M. Sun and G. S. Yan, *J. Sichuan U.* (*Nat. Sci. Edit.*) **29**, 246–253 (1992).
34. T. L. Chen, J. Ji, S. X. Xiao, T. Cai and G. S. Yan, *Int. J. Quantum. Chem.* **44**, 1015–1025 (1992).
35. G. S. Yan, Z. X. Cao, G. Liang and A. M. Tian, *J. Mol. Struct.* (*Theochem*) **282**, 283–286 (1993).
36. A. M. Tian, Z. X. Cao, J. L. Zhang and G. S. Yan, *J. Mol. Struct.* (*Theochem*) **285**, 293–296 (1993).
37. D. Q. Xie, G. S. Yan, J. K. Xie and A. M. Tian, *Chinese Chem. Lett.* **4**, 175–178 (1993).
38. J. Yang, G. S. Yan, A. M. Tian, A. Q. Tang and Q. S. Li, *Chinese Chem. Lett.* **4**, 93–94 (1993).
39. Z. X. Cao, A. M. Tian and G. S. Yan, *Chinese Sci. Bull.* **38**, 233–235 (1993).
40. Z. X. Cao, G. S. Yan and A. M. Tian, *Chem. J. Chinese U.* **14**, 711–713 (1993).
41. G. M. Liang, A. M. Tian and G. S. Yan, *Chem. J. Chinese U.* **14**, 1705–1709 (1993).
42. Z. M. Sun, J. S. Li and G. S. Yan, *Chem. J. Chinese U.* **14**, 1560–1564 (1993).
43. Z. X. Cao, G. M. Liang, A. M. Tian, G. S. Yan, A. Q. Tang and S. Q. Li, *Acta Phys-Chim Sin.* **9**, 770–775 (1993).
44. G. M. Liang, J. D. Gu, A. M. Tian and G. S. Yan, *J. Sichuan U.* (*Nat. Sci. Edit.*) **30**, 370–374 (1993).
45. Z. H. Tang, H. P. Zhou, G. S. Yan and A. M. Tian, *J. Sichuan U.* (*Nat. Sci. Edit.*) **30**, 375–379 (1993).
46. J. Yang, A. M. Tian, G. M. Liang and G. S. Yan, *J. Sichuan U.* (*Nat. Sci. Edit.*) **30**, 233–237 (1993).
47. Z. X. Cao, G. M. Liang, A. M. Tian, G. S. Yan, A. Q. Tang and S. Q. Li, *Chinese J. Chem. Phys.* **5**, 491–498 (1993).
48. Z. X. Cao, Z. M. Sun and G. S. Yan, *Chem. J. Chinese U.* **13**, 398–400 (1993).
49. G. S. Yan, D. Q. Xie and A. M. Tian, *J. Phys. Chem.* **98**, 8870–8875 (1994).
50. J. Yang, G. M. Liang, A. M. Tian, J. D. Gu and G. S. Yan, *Acta Chim. Sinica* **52**, 562–566 (1994).
51. Z. X. Cao, G. M. Liang, A. M. Tian and G. S. Yan, *Acta Chim. Sinica* **52**, 223–227 (1994).
52. X. Y. Li, F. C. He, A. M. Tian and G. S. Yan, *Chem. Onl.* **12**, 17–21 (1994).
53. J. Yang, A. M. Tian, G. M. Liang and G. S. Yan, *Chem. J. Chinese U.* **15**, 249–250 (1994).
54. D. Q. Xie, G. S. Yan and A. M. Tian, *Chem. J. Chinese U.* **15**, 1220–1221 (1994).
55. J. D. Gu, A. M. Tian and G. S. Yan, *Chem. J. Chinese U.* **15**, 886–890 (1994).
56. J. D. Gu, A. M. Tian and G. S. Yan, *Chem. J. Chinese U.* **15**, 1222–1224 (1994).
57. H. B. Zhang, G. M. Liang, A. M. Tian and G. S. Yan, *Acta Phys-Chim Sin.* **10**, 360–362 (1994).
58. Z. X. Cao, A. M. Tian and G. S. Yan, *Acta Phys-Chim Sin.* **10**, 387–390 (1994).
59. H. B. Zhang, A. M. Tian and G. S. Yan, *Acta Phys-Chim Sin.* **10**, 481–483 (1994).
60. J. Yang, G. M. Liang, A. M. Tian and G. S. Yan, *Acta Phys-Chim Sin.* **10**, 367–370 (1994).
61. J. L. Zhang, Z. X. Cao, J. D. Gu, A. M. Tian and G. S. Yan, *Acta Phys-Chim Sin.* **10**, 396–398 (1994).
62. J. Yang, G. M. Liang, A. M. Tian and G. S. Yan, *Chinese J. Chem. Phys.* **7**, 34–38 (1994).
63. Z. H. Tang, H. P. Zhou, Z. M. Sun, G. S. Yan and A. M. Tian, *Chinese J. Chem. Phys.* **7**, 221–226 (1994).
64. Z. X. Cao, A. M. Tian and G. S. Yan, *Chinese J. Chem. Phys.* **7**, 437–442 (1994).
65. Z. M. Sun, J. S. Li and G. S. Yan, *Chinese J. Chem. Phys.* **7**, 111–117 (1994).
66. Z. H. Tang, J. S. Chen, Z. M. Sun, Y. Xue, G. S. Yan and A. M. Tian, *J. Sichuan U.* (*Nat. Sci. Edit.*) **31**, 232–237 (1994).
67. Z. H. Tang, L. C. Li, Z. M. Sun and G. S. Yan, *J. Sichuan U.* (*Nat. Sci. Edit.*) **31**, 364–370 (1994).
68. G. M. Liang, A. M. Tian and G. S. Yan, *J. Sichuan U.* (*Nat. Sci. Edit.*) **31**, 238–245 (1994).
69. Z. H. Tang, J. S. Chen, Z. M. Sun, G. S. Yan and A. M. Tian, *J. Atom. Mol. Phys.* **11**, 232–237 (1994).
70. C. Y. Tao, J. L. Luo, Z. R. Li and G. S. Yan, *J. Atom. Mol. Phys.* **11**, 360–368 (1994).
71. X. Y. Li, F. C. He, A. M. Tian and G. S. Yan, *J. Mol. Struct.* (*Theochem*) **342,** 181–186 (1995).
72. Z. X. Cao, J. L. Zhang, A. M. Tian and G. S. Yan, *J. Mol. Struct.*(*Theochem*) **333,** 191–197 (1995).
73. L. X. Zhou, J. L. Zhang, A. M. Tian and G. S. Yan, *J. Mol. Struct.* (*Theochem*) **358,** 173–177 (1995).

74. X. Y. Li, A. M. Tian, F. C. He and G. S. Yan, *Chem. Phys. Lett*. **233,** 227–230 (1995).
75. J. D. Gu, A. M. Tian and G. S. Yan, *Chinese Sci. Bull.* **40,** 1972–1977 (1995).
76. G. S. Yan and D. Q. Xie, *Chinese Sci. Bull.* **40,** 1797–1800 (1995).
77. X. Y. Li, A. M. Tian, F. C. He and G. S. Yan, *Chinese Sci. Bull.* **40**, 1698–1702 (1995).
78. D. Q. Xie, G. S. Yan and A. M. Tian, *Chinese J. Chem.* **13**, 510–514 (1995).
79. G. P. Li, A. M. Tian and G. S. Yan, *Acta Chim. Sinica.* **53**, 332–335 (1995).
80. H. B. Zhang, A. M. Tian and G. S. Yan, *Chinese Chem. Lett.* **6**, 357–360 1995).
81. J. K. Xie, D. Q. Xie, G. S. Yan and A. M. Tian, *Chem. J. Chinese U.* **16**, 1940–1944 (1995).
82. H. B. Zhang, C. W. Hu, A. M. Tian and G. S. Yan, *Chem. J. Chinese U.* **16**, 626–628 (1995).
83. Z. H. Tang, J. S. Chen, Z. M. Sun, A. M. Tian and G. S. Yan, *Chem. J. Chinese U.* **16**, 761–764 (1995).
84. J. L. Zhang, J. D. Gu, A. M. Tian, G. S. Yan and Y. B. Wang, *Acta Chim. Sinica* **53**, 665–669 (1995).
85. X. Y. Li, A. M. Tian, F. C. He and G. S. Yan, *Acta Chim. Sinica* **53**, 933–936 (1995).
86. H. B. Zhang, A. M. Tian and G. S. Yan, *Acta Chim. Sinica* **53**, 538–542 (1995).
87. G. M. Liang, J. D. Gu, A. M. Tian and G. S. Yan, *Acta Chim. Sinica* **53**, 961–965 (1995).
88. G. P. Li, A. M. Tian and G. S. Yan, *Acta Chim. Sinica* **53**, 332–335 (1995).
89. G. P. Li, H. B. Zhang, A. M. Tian and G. S. Yan, *Acta Phys-Chim Sin.* **11**, 211–217 (1995).
90. H. B. Zhang, A. M. Tian and G. S. Yan, *Acta Phys-Chim Sin.* **11**, 142–146 (1995).
91. J. D. Gu, A. M. Tian and G. S. Yan, *Acta Phys-Chim Sin.* **11**, 719–723 (1995).
92. J. Yang, Z. H. Tang, D. Y. Wu, Z. R. Li, A. M. Tian and G. S. Yan, *Acta Phys-Chim Sin.* **11**, 1008–1013 (1995).
93. Z. R. Li, J. Yang, M. H. Yang, A. M. Tian and G. S. Yan, *J. Sichuan U.* (*Nat. Sci. Edit.*) **32**, 701–105 (1995).
94. Z. H. Tang, L. C. Li, Z. M. Sun, A. M. Tian and G. S. Yan, *J. Atom. Mol. Phys.* **12**, 190–201 (1995).
95. Z. H. Tang, Z. P. Huang, Z. M. Sun, A. M. Tian and G. S. Yan, *J. Atom. Mol. Phys.* **12**, 293–298 (1995).
96. Z. H. Tang, L. C. Li, Z. P. Huang, Z. M. Sun, A. M. Tian and G. S. Yan, *Chinese J. Syn. Chem.* **3**, 235–238 (1995).
97. D. Q. Xie and G. S. Yan, *Chem. Phys. Lett.* **248**, 409–413 (1996).
98. D. Q. Xie and G. S. Yan, *Mol. Phys.* **88,** 1349–1355 (1996).
99. Li X, A. M. Tian, F. C. He and G. S. Yan, *J. Comput. Chem.* **17,** 1108–1111 (1996).
100. J. D. Gu, J. L. Zhang, M. A, Tian and G. S. Yan, *Acta Chim. Sinica.* **54**, 320–324 (1996).
101. D. Q. Xie and G. S. Yan, *Sci. China* (*B*) **39,** 439–448 (1996).
102. J. D. Gu, A. M. Tian and G. S. Yan, *Sci. China* (*B*) **39,** 29–36 (1996).
103. Z. H. Tang, L. C. Li, Z. M. Sun, G. S. Yan and H. P. Zhou, *Sci. China* (*B*) **39,** 269–275 (1996).
104. L. X. Zhou, D. L. Zhang, A. M. Tian and G. S. Yan, *Chinese Chem. Lett.* **7**, 59–62 (1996).
105. J. K. Xie, D. Q. Xie, A. M. Tian and G. S. Yan, *Acta Chim. Sinica* **54,** 261–265 (1996).
106. J. K. Xie, D. Q. Xie and G. S. Yan, *Acta Chim. Sinica* **54,** 756–763 (1996).
107. J. D. Gu, J. L. Zhang, A. M. Tian and G. S. Yan, *Acta Chim. Sinica* **54,** 320–324 (1996).
108. J. D. Gu, A. M. Tian and G. S. Yan, *Acta Chim. Sinica* **54**, 331–337 (1996).
109. L. X. Zhou, A. M. Tian, J. C. Li, Y. Z. Chen and G. S. Yan, *Chem. J. Chinese U.* **17**, 117–120 (1996).
110. H. B. Zhang, J. L. Zhang, Z. R. Li, A. M. Tian and G. S. Yan, *J. Sichuan U.* (*Nat. Sci. Edit.*) **33,** 307–310 (1996).
111. H. B. Zhang, A. M. Tian and G. S. Yan, *J. Sichuan U.* (*Nat. Sci. Edit.*) **33,** 718–722 (1996).
112. J. Yang, D. Y. Wu, Z. H. Tang, Z. R. Li, A. M. Tian and G. S. Yan, *J. Sichuan U.* (*Nat. Sci. Edit*.) **33,** 723–727 (1996).
113. G. S. Yan, M. H. Yang and D. Q. Xie, *Chem. Phys. Lett.* **275,** 494–498 (1997).
114. G. S. Yan, H. Xian and D. Q. Xie, *Chem. Phys. Lett.* **271,** 157–162 (1997).
115. G. S. Yan, M. H. Yang and D. Q. Xie, *Sci. China* (*B*) **40,** 554–560 (1997).
116. G. S. Yan, H. Xian and D. Q. Xie, *Sci. China* (*B*) **40,** 342–347 (1997).
117. G. S. Yan, J. K. Xie and D. Q. Xie, *Chinese Sci. Bull.* **42,** 43–46 (1997).
118. J. K. Xie, G. S. Yan and D. Q. Xie, *Chinese Sci. Bull.* **42,** 268–272 (1997).
119. D. Q. Xie and G. S. Yan, *Chem. J. Chinese U.* **18,** 1136–1140 (1997).
120. H. Xian, D. Q. Xie and G. S. Yan, *Acta Phys-Chim Sin.* **13,** 865–867 (1997).
121. G. S. Yan, H. Xian and D. Q. Xie, *Sci. China* (*B*) **27,** 228–234 (1997).
122. G. S. Yan, M. H. Yang and D. Q. Xie, *Sci. China* (*B*) **27,** 527–533 (1997).
123. Z. M. Sun, B. Wang and G. S. Yan, *Acta Chim. Sinica* **55,** 9–12 (1997).

124. G. S. Yan, J. K. Xie and D. Q. Xie, *Acta Chim. Sinica* **55,** 1041–1046 (1997).
125. G. S. Yan, H. Xian, and D. Q. Xie, *Mol. Phys*. **93**, 867–872 (1998).
126. G. S. Yan, M. H. Yang, and D. Q. Xie, *Chem. Phys. Lett.* **287**, 162–168 (1998).
127. G. S. Yan, M. H. Yang, and D. Q. Xie, *J. Chem. Phys*. **109**, 10284–10292 (1998).
128. H. Xian, D. Q. Xie, and G. S. Yan, *Sci. China* (*B*) **41**, 320–324 (1998).
129. H. Xian, D. Q. Xie and G. S. Yan, *Sci. China* (*B*) **28**, 243–246 (1998).
130. G. S. Yan, Y. Xue, and D. Q. Xie, *Sci. China* (*B*) **41**, 91–96 (1998).
131. G. S. Yan, Y. Xue, and D. Q. Xie, *Int. J. Quant. Chem*. **72**, 53–60 (1999).
132. Y. Xue, X. J. Xu, D. Q. Xie and G. S. Yan, *J. Mol. Struc*. **469**, 151–165 (1999).
133. M. L. Yang, Z. M. Sun, and G. S. Yan, *Sci. China* (*B*) **42**, 70–76 (1999).
134. M. L. Yang, Z. M. Sun and G. S. Yan, *Sci. China* (*B*) **29**, 206–211 (1999).
135. H. Zhu, D. Q. Xie and G. S. Yan, *Chem. J. Chinese U.* **20**, 1910–1915 (1999).
136. Y. Xue, D. Q. Xie and G. S. Yan, *Chem. J. Chinese U.* **20**, 1102–1105 (1999).
137. M. L. Yang, Z. M. Sun and G. S. Yan, *Chem. J. Chinese U.* **20**, 450–453 (1999).
138. X. J. Xu, Y. Xue, D. Q. Xie and G. S. Yan, *Chem. J. Chinese U.* **20**, 941–947 (1999).
139. Y. H. Lu, H. Xian, D. Q. Xie and G. S. Yan, *Chem. J. Chinese U.* **20**, 1291–1294 (1999).
140. M. L. Yang, Z. M. Sun, D. Q. Xie and G. S. Yan, *Chinese J. Chem. Phys.* **12**, 717–721 (1999).
141. M. L. Yang, Z. M. Sun and G. S. Yan, *Chinese J. Chem. Phys.* **12**, 282–287 (1999).
142. M. L. Yang, Z. M. Sun and G. S. Yan, *J. Atom. Mol. Phys.* **16**, 413–417 (1999).
143. M. L. Yang, Z. M. Sun and G. S. Yan, *Acta Phys-Chim Sin.* **15**, 693–697 (1999).
144. Y. Xue, D. Q. Xie and G. S. Yan, *Acta Phys-Chim Sin.* **15**, 138–142 (1999).
145. M. L. Yang, Z. M. Sun and G. S. Yan, *Acta Chim. Sinica* **57**, 754–759 (1999).
146. X. J. Xu, Y. Xue, D. Q. Xie and G. S. Yan, *Acta Chim. Sinica* **57**, 680–684 (1999).
147. Y. H. Lu, D. Q. Xie, M. H and G. S. Yan, *Chem. Phys. Lett.* **327**, 305–313 (2000).
148. Y. Xue, D. G. Xu, D. Q. Xie and G. S. Yan, *Spectrochim Acta A* **56**, 1929–1938 (2000).
149. X. J. Xu, D. Q. Xie, Y. Xue and G. S. Yan, *Spectrochim Acta A* **56**, 567–574 (2000).
150. M. H. Yang, D. Q. Xie and G. S. Yan, *Sci. China* (*B*) **43**, 196–200 (2000).
151. Y. Xue, D. Q. Xie, and G. S. Yan, *Int. J. Quant. Chem*. **76**, 86–699 (2000).
152. Y. H. Lu, D. Q. Xie, and G. S. Yan, *Int. J. Quant. Chem*. **78**, 269–280 (2000).
153. Y. Xue, D. G. Xu, D. Q. Xie and G. S. Yan, *Chem. J. Chinese U.* **21**, 1293–1298 (2000).
154. D. G. Xu, Y. H. Lu, D. Q. Xie and G. S. Yan, *Chem. J. Chinese U.* **21**, 1884–1887 (2000).
155. H. Y. Xiao, Y. Xue, X. J. Xu, D. Q. Xie and G. S. Yan, *Acta Chim. Sinica* **58**, 414–417 (2000).
156. Y. Xue, Y. Guo, X. J. Xu, D. Q. Xie and G. S. Yan, *Acta Chim. Sinica* **58**, 1254–1258 (2000).
157. Y. H. Lu, Y. Z. Zhou, D. Q. Xie and G. S. Yan, *Acta Chim. Sinica* **58**, 1516–1521 (2000).
158. M. H. Yang, D. Q. Xie and G. S. Yan, *Sci. China* (*B*) **30**, 28–32 (2000).
159. J. K. Xie and G. S. Yan, *Chinese Sci. Bull.* **45**, 2606–2610 (2000).
160. D. Q. Xie, Y. H. Lu, D. G. Xu and G. S. Yan, *Chem. Phys.* **270,** 415–428 (2001).
161. D. Q. Xie, Y. H. Lu and G. S. Yan, *Chem. Phys. Lett.* **339**, 14–22 (2001).
162. J. K. Xie and G. S. Yan, *Chin. Sci. Bull.* **46**, 650–652 (2001).
163. Y. Xue, D. Q. Xie and G. S. Yan, *Chem. J. Chinese U.* **22**, 1189–1192 (2001).
164. Y. Guo, D. Q. Xie, Y. Xue and G. S. Yan, *Chem. J. Chinese U.* **22**, 2061–2064 (2001).
165. H. Zhu, D. Q. Xie and G. S. Yan, *Chem. Phys. Lett*. **351**, 149**–**157 (2002).
166. C. Zhou, D. Q. Xie, R. Q. Chen, G. S. Yan and H. Guo, *Spectrochim Acta A* **58**, 727–746 (2002).
167. H. Zhu, J. Li, D. Q. Xie and G. S. Yan, *Chem. J. Chinese U.* **23**, 2137–2141 (2002).
168. Y. Guo, D. Q. Xie, Y. Xue and G. S. Yan, *Acta Chim. Sinica* **60**, 660–663 (2002).
169. Y. Wu, K. L. Xu, Y. Xue, D. Q. Xie and G. S. Yan, *Acta Chim. Sinica* **60**, 2092–2096 (2002).
170. H. Zhu, D. Q. Xie and G. S. Yan, *J. Chem. Phys*. **24**, 1839–1845 (2003).
171. J. Li, D. Q. Xie and G. S. Yan, *Sci. China* (*B*) **46**, 113–118 (2003).
172. H. Y. Xiao, W. Z. Lai, D. Q. Xie and G. S. Yan, *Sci. China* (*B*) **46**, 425–430 (2003).
173. J. Li, H. Zhu, D. Q. Xie and G. S. Yan, *Chem. J. Chinese U.* **24**, 686–689 (2003).
174. K. L. Xu, D. Q. Xie and G. S. Yan, *Chem. J. Chinese U.* **24**, 2031–2034 (2003).
175. H. Zhang, Y. Xue, K. L. Xu, D. Q. Xie and G. S. Yan, *Acta Chim. Sinica* **61**, 1926–1929 (2003).

176. J. Li, D. Q. Xie, G. S. Yan and D. Q. Xie, *Sci. China* (*B*) **33**, 21–25 (2003).
177. H. Y. Xiao, W. Z. Lai, D. Q. Xie and G. S. Yan, *Sci. China* (*B*) **33**, 239–244 (2003).
178. J. X. Chen, H. Zhu, D. Q. Xie and G. S. Yan, *Acta Chim. Sinica* **62**, 5–9 (2004).
179. K. L. Xu, Y. Wu, D. Q. Xie and G. S. Yan, *Chinese Sci. Bull.* **49**, 535–537 (2004).
180. Y. Z. Zhou, H. Zhu, D. Q. Xie and G. S. Yan, *Chem. J. Chinese U.* **25**, 1081–1084 (2004).
181. K. L. Xu, D. Q. Xie and G. S. Yan, *Acta Chim. Sinica* **62**, 2003–2006 (2004).
182. Y. Xue, H. Zhang, D. Q. Xie and G. S. Yan, *Chem. J. Chinese U.* **26**, 907–911 (2005).
183. Y. Guo, Y. Xue, D. Q. Xie and G. S. Yan, *Chem. J. Chinese U.* **26**, 1686–1689 (2005).
184. H. Zhang, Y. Xue, D. Q. Xie and G. S. Yan, *Acta Chim. Sinica* **63**, 791–796 (2005).
185. L. Jin, Y. Wu, Y. Xue, Y. Guo, D. Q. Xie and G. S. Yan, *Acta Chim. Sinica* **64**, 873–878 (2006).
186. B. He, Y. Xue, Y. Guo and G. S. Yan, *Acta Chim. Sinica* **65**, 481–488 (2007).
187. Y. Zeng, Y. Xue and G. S. Yan, *J. Phys. Chem. B* **112**, 10659–10667 (2008).
188. D. G. Xu and G. S. Yan, *Chem. J. Chinese U.* **29**, 2453–2456 (2008).
189. C. H. Zhang, Y. Xue, Y. Guo and G. S. Yan, *Chem. J. Chinese U.* **29**, 2354–2359 (2008).
190. Y. Y. Sun, C. H. Zhang, Y. Xue and G. S. Yan, *Acta Chim. Sinica* **66**, 751–756 (2008).
191. J. L. Liu, Y. Guo, Y. Xue and G. S. Yan, *Chem. J. Chinese U.* **30**, 100–105 (2009).
192. R. Chen, H. Zhu, D. Q. Xie and G. S. Yan, *Sci. China* (*B*) **52**, 1987–1990 (2009).
193. P. Zou, Q. G. Li, Y. Xue and G. S. Yan, *Acta Chim. Sinica* **67**, 2427–2432 (2009).
194. Q. G. Li, Y. Xue, Y. Guo and G. S. Yan, *Acta Phys–Chim. Sin.* **26**, 1965–1975 (2010).
195. Y. Zeng, Y. Xue and G. S. Yan, *J. Phys. Chem. A* **115**, 4995–5004 (2011).

Theor Chem Acc (2014) 133:1535
DOI 10.1007/s00214-014-1535-0

REGULAR ARTICLE

# Transition between direct gap and indirect gap in two dimensional hydrogenated honeycomb $Si_xGe_{1-x}$ alloys

**Nan Xia · Lan-Feng Yuan · Jinlong Yang**

Received: 24 April 2014 / Accepted: 1 July 2014 / Published online: 12 August 2014
© Springer-Verlag Berlin Heidelberg 2014

**Abstract** Using first-principles calculations, we have explored the structural and electronic properties of fully hydrogenated honeycomb $Si_xGe_{1-x}H$ alloys. Finite band gaps are opened by hydrogenation for $x$ in the whole range from 0 to 1, while their nature and values can be tuned by $x$. When $x$ is <0.7, the band gap is direct (from Γ to Γ). And when $x$ is ≥0.7, the gap turns into indirect (from Γ to M). For all the computed compositions, the two kinds of energy differences between valence band and conduction band, Γ–Γ and Γ–M, are described well by two polynomial functions of $x$. The smaller of the two functions gives a good prediction for the overall band gap at any $x$. The two curves cross at $x = 0.7$, leading to the change of band gap type. At PBE level, the values of band gap for different $x$ spread from 1.09 to 2.29 eV. These findings give a new route to tune the electronic properties of these materials and may have potential applications in nanoscale optoelectronics.

**Keywords** Hydrogenated $Si_xGe_{1-x}$ alloys · Virtual crystal approximation · Band gap engineering · First-principles calculation

Dedicated to Professor Guosen Yan and published as part of the special collection of articles celebrating his 85th birthday.

N. Xia · L.-F. Yuan (✉) · J. Yang (✉)
Hefei National Laboratory for Physical Sciences at Microscale, University of Science and Technology of China, Hefei 230026, China
e-mail: yuanlf@ustc.edu.cn

J. Yang
e-mail: jlyang@ustc.edu.cn

## 1 Introduction

With the extensive applications of graphene in the electronic industry, in the past a few years more and more attentions have been paid to two dimensional (2D) atomically thin sheets, such as boron nitride (h-BN), transition metal dichalcogenides (e.g., $MoS_2$ and $WS_2$), and hybridized $B_xC_yN_z$ [1]. Similar to graphene, these 2D structures possess fantastic properties in various aspects (electronical, magnetical, optical, and mechanical, etc.) and exhibit great application prospects [2–4]. Silicene and germanene have been widely studied experimentally and theoretically [5–7], and it has been mentioned repeatedly that their band structures show linear band crossing at the Fermi level, and thus, the charge carriers behave like a massless Dirac fermion [8], similar to the case of graphene [9].

As two most important materials in the semiconductor industry, Si and Ge are both group 14 elements with similar structural properties; therefore, they can randomly mix to form alloys [10]. It has also been demonstrated that bulk $Si_xGe_{1-x}$ alloys can be fabricated on Si substrates [11]. Not long ago, Padilha et al. [12] suggested that the electronic properties of $Si_xGe_{1-x}$ random alloys in the honeycomb monolayer structure can be tuned by the value of $x$. To open a band gap and regulate the electronic properties of graphene-like materials, a variety of methods have been put forward, such as applying an external electric field [13], introducing hydrogen vacancies [14], uniaxial compression [15], biaxial compressive strain [16], cutting 2D materials into nanoribbons [17], and stacking into bilayer structures [18]. For silicene and germanene, hydrogenation is predicted to be a viable mean to open a finite gap [19, 20]. Therefore, it is highly probable that the 2D hydrogenated $Si_xGe_{1-x}$ alloys also have finite gaps. If this is so, then we get a new parameter to manipulate this gap, i.e., the alloy

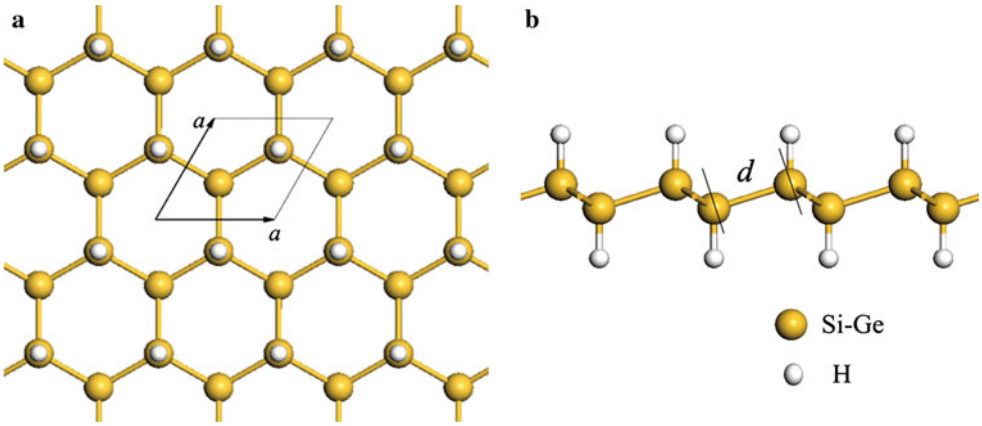


**Fig. 1** Structures of $Si_xGe_{1-x}H$ alloys from the top view (**a**) and from the side view (**b**). The *yellow* and *white spheres* refer to the hybrid Si–Ge atoms and hydrogen atoms, respectively. The rhombus is a unit cell

composition ($x$). In order to explore this route, we hereby investigate the evolution of the band structures of 2D disordered fully hydrogenated $Si_xGe_{1-x}$ alloys (denoted as $Si_xGe_{1-x}H$), via first-principles calculations.

## 2 Methods and computational details

Our ab initio calculations are based on density functional theory (DFT) [21, 22] and are performed by the CASTEP software [23]. The generalized gradient approximation (GGA) with the Perdew–Burke–Ernzerholf (PBE) functional [24] is selected as the exchange correlation potential. For all the calculations, the ultrasoft pseudopotentials are used, with a 600 eV cutoff energy for the plane-wave basis. Both the lattice constants and the atomic positions are fully relaxed. The tolerances for geometry optimizations are $1.0 \times 10^{-5}$ eV/atom for total energy, 0.02 eV/Å for maximum Hellman–Feynman forces, 0.1 GPa for maximum stress, and 0.002 Å for maximum ionic displacement. The periodic boundary condition is applied in the normal direction of the monolayer, with vacuum space of 20 Å to minimize the interlayer interaction. A primitive cell containing two Si (Ge) atoms and two H atoms is used, as shown in Fig. 1. Following the Monkhorst–Pack scheme [25], Brillouin zone integration is carried out at $9 \times 9 \times 1$ k-points for the geometry optimization and $15 \times 15 \times 1$ k-points for the static total energy calculations.

To simulate the electronic structure of these disordered alloys, the virtual crystal approximation (VCA) is used, which is a simple and reasonable approximation for this task. In this approximation, one studies a crystal with the primitive periodicity, but composed of fictitious atoms, which are hybrids of two or more element types [26]. The meaning of "hybrid" is that the potential of a virtual atom is treated as the concentration-weighted average of the constituent potentials, neglecting further compositional disorder effects [27]. VCA is widely used in the literature. For example, Bellaiche et al. [26] successfully employed VCA to study the dielectric and piezoelectric properties of the $Pb(Zr_{0.5}Ti_{0.5})O_3$ perovskite solid solution in its paraelectric and ferroelectric phases. Winkler et al. [28] showed that the VCA approach can be used to study Al/Si disorder in silicates, reproducing the experimental structural parameters.

Employing VCA, a series of $Si_xGe_{1-x}H$ alloys with eleven different compositions have been simulated. The choices for $x$ are from 0 (hydrogenated germanene) to 1 (hydrogenated silicene), with increment of 0.1, in the hope that the properties of an alloy with any $x$ can be roughly estimated based on these eleven data points. There are two common configurations of fully hydrogenated silicene (germanene), i.e., boat like and chair like. It was reported that the chair configurations of silicene and germanene are more stable than the boat ones, by about 10 meV/atom [29]. In our calculations, for three typical alloys ($x = 0.3$, 0.5, and 0.8), the chair configurations are more stable than the boat ones as well, with the energy differences being 12.8, 12.8, and 13.9 meV/atom, respectively. Consequently, we will only consider the chair configurations of $Si_xGe_{1-x}H$ alloys afterward.

## 3 Results and discussions

After geometry optimizations, the calculated lattice parameters $a$ and atom bond lengths $d$ of hydrogenated silicene and germanene are 3.88, 2.35, and 4.06, 2.45 Å respectively, which are consistent with the previous theoretical results 3.884, 2.356 Å [30] and 4.06, 2.46 Å [19]. Upon hydrogenation, the calculated buckling heights $h$ are 0.72 and 0.75 Å, distinctly larger than those of silicene (0.45 Å) and germanene (0.64 Å). Namely, the hydrogenated configurations are more tortuous than the pristine structures. This can be understood in terms of variation in hybridization state along with hydrogenation. In silicene (germanene), the buckled structure gives rise to reduced π–π

**Table 1** Structural and electronic parameters of $Si_xGe_{1-x}H$ alloys in different composition of Si element ($x$)

| $x$ | $a$ (Å) | $\Phi$ (eV) | $E_{\Gamma-\Gamma}$ (eV) (direct) | $E_{\Gamma-M}$ (eV) (indirect) |
|---|---|---|---|---|
| 0 | 4.058 | 4.809 | 1.089 | 1.912 |
| 0.1 | 4.046 | 4.855 | 1.435 | 2.035 |
| 0.2 | 4.035 | 4.870 | 1.710 | 2.135 |
| 0.3 | 4.023 | 4.972 | 1.905 | 2.207 |
| 0.4 | 4.009 | 4.932 | 2.058 | 2.250 |
| 0.5 | 3.998 | 4.950 | 2.157 | 2.271 |
| 0.6 | 3.983 | 4.992 | 2.234 | 2.285 |
| 0.7 | 3.962 | 5.015 | 2.297 | 2.285 |
| 0.8 | 3.941 | 5.028 | 2.327 | 2.262 |
| 0.9 | 3.915 | 5.012 | 2.340 | 2.224 |
| 1 | 3.884 | 5.029 | 2.332 | 2.174 |

The entries $a$, $\Phi$, $E_{\Gamma-\Gamma}$, and $E_{\Gamma-M}$ are the lattice constant, the effective work function, the gaps between conduction band and valence band from Γ to Γ and from Γ to M, respectively

overlap between $p_z$ orbitals of adjacent Si (Ge) atoms, so the hybridization of each Si (Ge) atom is intermediate between $sp^2$ and $sp^3$. After new σ bonds are formed with H atoms, the Si–Ge atoms in $Si_xGe_{1-x}H$ become purely $sp^3$ hybridized. Therefore, the bond angles in $Si_xGe_{1-x}H$ are greater than those in silicene and germanene, resulting in higher degree of buckling.

For all the eleven compositions, the lattice parameters, the effective work functions ($\Phi$), and two kinds of energy differences between valence band and conduction band (Γ–Γ and Γ–M) are listed in Table 1. The lattice parameter $a$ decreases monotonically from 4.058 to 3.884 Å as $x$ increases from 0 to 1, which is naturally owing to the larger atomic radius of Ge than that of Si. The effective work function, defined as the difference in potential energy of one electron between the highest occupied molecular orbital (HOMO) and the vacuum level, ranges from 4.81 to 5.03 eV.

To further illustrate how the composition affects the electronic properties of $Si_xGe_{1-x}H$, the band structures of four typical systems are presented in Fig. 2. In silicene and germanene, the π and π* bands cross at the k-point around the Fermi level, rendering them gapless. On the other hand, all the 2D $Si_xGe_{1-x}H$ alloys have finite band gaps, basically due to the interaction between the $p_z$ orbitals of Si (Ge) and the 1 s orbitals of H atom. The valence band maximum (VBM) is always located at the Γ point. However, the conduction band minimum (CBM) can be either in Γ or in M, depending on the composition. Therefore, hydrogenated silicene is an indirect band gap (2.17 eV) semiconductor, while hydrogenated germanene is a direct band gap (1.09 eV) semiconductor. These results are qualitatively and quantitatively consistent with previous computational

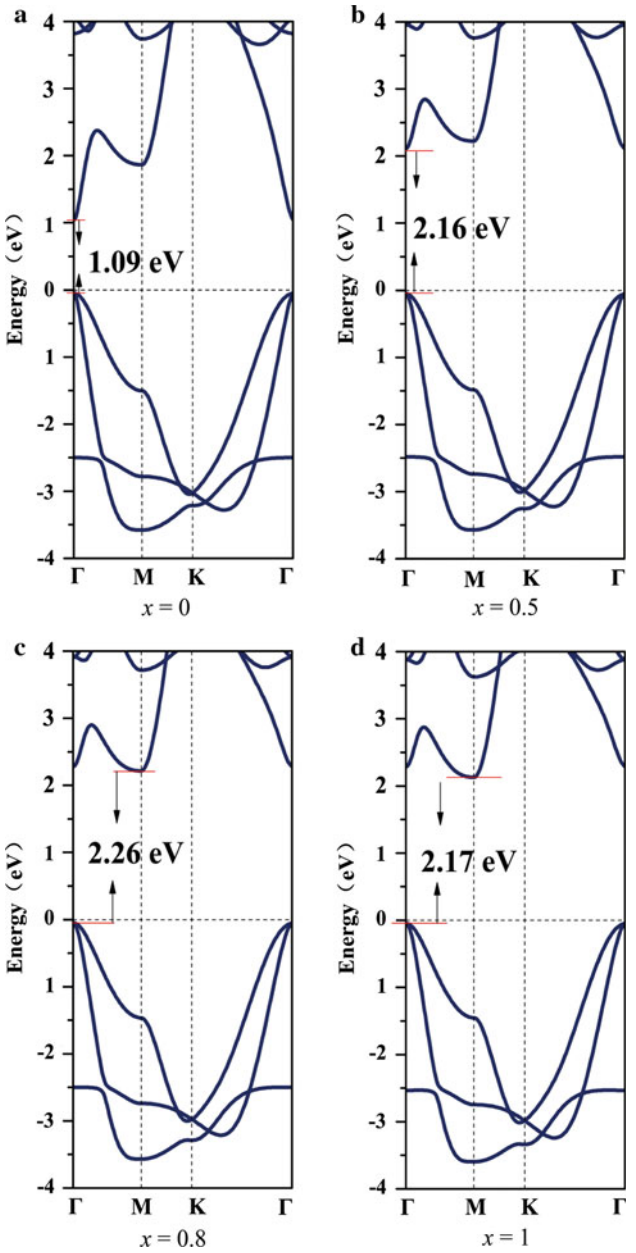


**Fig. 2** Band structures of $Si_xGe_{1-x}H$ alloys with four kinds of composition, i.e. $x = 0$ (**a**), 0.5 (**b**), 0.8 (**c**), 1 (**d**). The band gaps are noted in the picture. The Fermi levels are set to be energy zero

results, for instance, 2.0 eV [29], 2.19 eV [19] and 2.21 eV [14] for hydrogenated silicene, and 0.94 eV [19], 1.4 eV [29] and 1.5 eV [20] for hydrogenated germanene. Among the band gaps of our 11 systems, that of $Si_{0.7}Ge_{0.3}H$ is found to be the biggest, which is an indirect gap of 2.29 eV, while the gap of hydrogenated germanene (1.09 eV) is the smallest. Thus, the band gap of hydrogenated $Si_xGe_{1-x}H$ alloys can be tuned in the range from 1.09 to 2.29 eV by changing the composition. This is reminiscent of the result of Gao et al. [31] that the band gap of hydrogenated

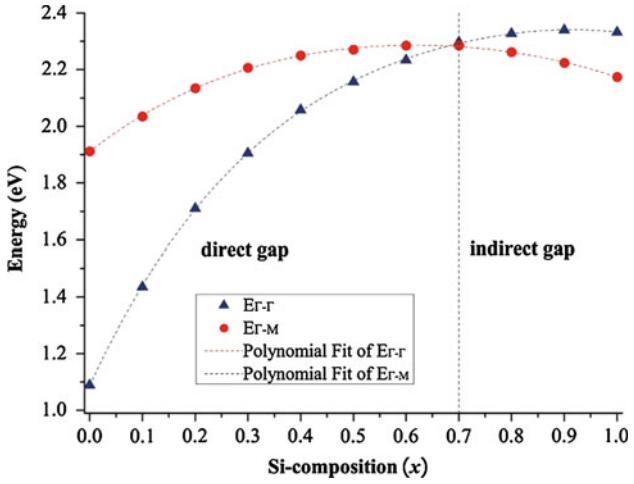


**Fig. 3** Two sets of energy differences between valence and conduction bands of $Si_xGe_{1-x}H$ as functions of Si composition ($x$): Γ–Γ (*triangle dots*) and Γ–M (*round dots*). The corresponding fourth order polynomial fitting curves are displayed as the *dash lines*

graphene can be continuously tuned by H coverage and configuration from 0 to 4.66 eV. That is a tuning in a wider range and with a constant nature of gap (direct), while our result is a tuning in a narrower range and with a variable nature of gap (from direct to indirect).

To gain further understanding on the transition of gap type, we list the Γ–Γ and Γ–M energy differences between valence band and conduction band for each composition in Table 1. We fit the two sets of data by two polynomial functions and find that fourth order polynomials are required to gain satisfactory match, as shown in Fig. 3. The curve for the Γ–Γ gap starts from the lowest value (1.089 eV) at $x = 0$ and increases quickly with $x$. When $x$ approaches 1, this curve becomes flat. It reaches a maximum (2.340 eV) at $x = 0.9$ and drops a little bit (2.332 eV) eventually at $x = 1$. On the other hand, the curve for the Γ–M gap spreads in a much narrower range, from 1.912 to 2.285 eV. The maximum is reached at $x = 0.6$ and 0.7. In the beginning, i.e., for small values of $x$, the Γ–Γ gap is less than the Γ–M gap, so the system is a direct gap semiconductor. The two curves cross roughly at $x = 0.7$. After that, the order between the two gaps is reversed, and the system becomes an indirect gap semiconductor. Therefore, the band gap of any alloy can be represented by the smaller of the two polynomial functions, as listed below (in eV):

$$Eg = \begin{cases} 1.087 + 4.029x - 5.383x^2 + 3.875x^3 - 1.276x^4 (0 \le x < 7) \\ 1.911 + 1.465x - 1.948x^2 + 1.171x^3 - 0.425x^4 (0.7 \le x \le 1) \end{cases}$$

Using this piecewise function, one can describe well the band gap of $Si_xGe_{1-x}H$ for $x$ along the whole range from 0 to 1.

At last, let us discuss the numerical uncertainty of our calculated gaps. There are two levels of errors, one from the treatment to disorder (i.e., VCA) and the other from the selection of functional (i.e., PBE). To check the viability of VCA in our systems, we compare the electronic properties by VCA and by conventional ordered PBE calculations for $Si_{0.5}Ge_{0.5}H$. We employ 6 kinds of supercells, i.e., $n \times n$ for $n = 1$–6, with different atomic arrangements of Si and Ge to simulate the randomized alloy. We test 8 arrangements for the $4 \times 4$ supercell and one arrangement for each of the other supercells. All the VCA and PBE calculations give rise to direct gaps. The band gaps from the supercell calculations are in the range of 1.68–1.72 eV, about 80 % of the VCA value 2.157 eV. Taking into consideration that a more realistic representation of the random alloy would require much larger supercells and many more atomic arrangements, this degree of agreement is acceptable. We acknowledge that VCA is a simple model, and the huge saving in computational cost is a major advantage and the main reason for us to adopt this method.

As for the second factor, GGA is known to tend to underestimate the band gaps of semiconductors and insulators and gives values typically 50–60 % smaller than those from better hybrid DFT methods. The gaps of fully hydrogenated silicene and germanene by HSE06 are reported to be 3.51 eV [32] and 1.56 eV [33], respectively. The optical properties of hydrogenated germanene were investigated by diffuse reflectance absorption (DRA) spectroscopy, and a linear approximation of the absorption edge suggests a band gap of approximately 1.59 eV [33]. There is no experimental data concerning the electronic properties of hydrogenated silicene. Therefore, the scaling factor for band gaps can be estimated as the ratio between the HSE06 to PBE values, which is 1.618 for hydrogenated silicene and 1.431 for hydrogenated germanene. So to compare quantitatively with experiments, it will be advisable to scale our PBE gaps by similar ratios, giving a range of 1.56–3.70 eV.

## 4 Conclusions

In summary, first-principles calculations based on the VCA have been applied to investigate the structural and electronic structures of 2D hydrogenated $Si_xGe_{1-x}$ alloys. At PBE level, the band gap of these systems can be tuned in a range of 1.09–2.29 eV via varying their compositions. For $x < 0.7$, the alloys are direct band gap (Γ–Γ) semiconductors. And after $x$ reaches 0.7, the band gaps transform to indirect (Γ–M). The origin of this transition is the change of the CBM location from Γ to M, or in another word, the crossing of the two curves of the Γ–Γ and Γ–M energy differences versus $x$. We fit the two curves by two polynomials, thus giving a tool to predict the band gap in the whole

range in terms of a piecewise function. Around the transition composition ($x = 0.7$), a small change in composition can lead to qualitative change in electronic and photonic properties for these alloys. Therefore, once combined with advanced Si/Ge nanotechnology, these materials have very valuable potential for band engineering and optical application.

**Acknowledgments** This work is partially supported by the National Key Basic Research Program (Contract No. 2011CB921404), by NSFC (Contract Nos. 21121003, 91021004, 21233007, 21222304), by CAS (Contract Nos. XDB01020300, XDB10030402), and by USTCSCC, SCCAS, Tianjin, and Shanghai Supercomputer Centers.

## References

1. Song X, Hu J, Zeng H (2013) J Mater Chem C 1:2952
2. Santos EJG (2013) J Phys Chem C 117:6420
3. Yan JA, Stein R, Schaefer DM, Wang XQ, Chou MY (2013) Phys Rev B 88:121403
4. Wu IJ, Guo GY (2007) Phys Rev B 76:035343
5. Fleurence A, Friedlein R, Ozaki T, Kawai H, Wang Y, Yamada-Takamura Y (2012) Phys Rev Lett 108:245501
6. Feng B, Ding Z, Meng S, Yao Y, He X, Cheng P, Chen L, Wu K (2012) Nano Lett 12:3507
7. Zheng F, Zhang C (2012) Nanoscale Res Lett 7:1
8. Liu CC, Feng W, Yao Y (2011) Phys Rev Lett 107:076802
9. Novoselov KSA, Geim AK, Morozov SV, Jiang D, Katsnelson M, Grigorieva I, Dubonos S, Firsov A (2005) Nature 438:197
10. Lang DV, People R, Bean JC, Sergent AM (1985) Appl Phys Lett 47:1333
11. Bean JC, Feldman LC, Fiory AT, Nakahara ST, Robinson IK (1984) J Vac Sci Technol A 2:436
12. Padilha JE, Seixas L, Pontes RB, da Silva AJ, Fazzio A (2013) Phys Rev B 88:201106
13. Drummond ND, Zolyomi V, Fal'Ko VI (2012) Phys Rev B 85:075423
14. Pan L, Liu HJ, Wen YW, Tan XJ, Lv HY, Shi J, Tang XF (2012) Appl Surf Sci 258:10135
15. Kaltsas D, Tsatsoulis T, Ziogos OG, Tsetseris L (2013) J Chem Phys 139:124709
16. Houssa M, Pourtois G, Afanas'ev VV, Stesmans A (2010) Appl Phys Lett 96:082111
17. Topsakal M, Ciraci S (2010) Phys Rev B 81:024107
18. Min H, Sahu B, Banerjee SK, MacDonald AH (2007) Phys Rev B 75:155115
19. Wei W, Dai Y, Huang B, Jacob T (2013) Phys Chem Chem Phys 15:8789
20. Voon LCLY, Sandberg E, Aga RS, Farajian AA (2010) Appl Phys Lett 97:163114
21. Hohenberg P, Kohn W (1964) Phys Rev 136:B864
22. Kohn W, Sham LJ (1965) Phys Rev 140:A1133
23. Segall MD, Lindan PJD, Probert MJ, Pickard CJ, Hasnip PJ, Clark SJ, Payne MC (2002) J Phys Condens Matter 14:2717
24. Perdew JP, Burke K, Ernzerhof M (1996) Phys Rev Lett 77:3865
25. Monkhorst HJ, Pack JD (1976) Phys Rev B 13:5188
26. Bellaiche L, Vanderbilt D (2000) Phys Rev B 61:7877
27. Bechiri A, Benmakhlouf F, Bouarissa N (2003) Mater Chem Phys 77:507
28. Winkler B, Pickard C, Milman V (2002) Chem Phys Lett 362:266
29. Houssa M, Scalise E, Sankaran K, Pourtois, G, Afanas'ev VV, Stesmans A (2011) Appl Phys Lett 98:223107
30. Wang XQ, Li HD, Wang JT (2012) Phys Chem Chem Phys 14:3031
31. Gao H, Wang L, Zhao J, Ding F, Lu J (2011) J Phys Chem C 115:3236
32. Zhang P, Li XD, Hu CH, Wu SQ, Zhu ZZ (2012) Phys Lett A376:1230
33. Bianco E, Butler S, Jiang S, Restrepo OD, Windl W, Goldberger JE (2013) ACS Nano 7:4414

Theor Chem Acc (2014) 133:1537
DOI 10.1007/s00214-014-1537-y

REGULAR ARTICLE

# A new ab initio potential energy surface and infrared spectra for the He–$CS_2$ complex

**Ting Yuan · Hua Zhu**

Received: 21 May 2014 / Accepted: 5 July 2014 / Published online: 13 August 2014
© Springer-Verlag Berlin Heidelberg 2014

**Abstract** We report a new three-dimensional potential energy surface for the He–$CS_2$ complex including the $Q_3$ normal mode for the $\upsilon_3$ antisymmetric stretching vibration of the $CS_2$ molecule. The potential energies were calculated at the coupled-cluster singles and doubles with noniterative inclusion of connected triples level with augmented correlation-consistent quadruple-zeta basis set plus midpoint bond functions. Two vibrationally averaged potentials with $CS_2$ at both the ground ($\upsilon = 0$) and the first excited ($\upsilon = 1$) $\upsilon_3$ vibrational states were generated from the integration of the three-dimensional potential over the $Q_3$ coordinate. Both potentials have a T-shaped global minimum and two equivalent linear local minima. The radial discrete variable representation/angular finite basis representation method and the Lanczos algorithm were applied to calculate the rovibrational energy levels. Our calculated results show that the two potentials support eight vibrational bound states. The calculated band origin shift of the complex (0.1759 $cm^{-1}$) agrees very well with the observed one (0.1709 $cm^{-1}$). The predicted infrared spectra and spectroscopic constants based on the two averaged potentials are in excellent agreement with the available experimental values.

**Keywords** Ab initio potential energy surface · Rovibrational energy levels · Infrared spectra · He–$CS_2$

## 1 Introduction

The weak intermolecular interactions and spectroscopy for the van der Waals (vdW) complexes of rare-gas (Rg) atoms with the $CO_2$ or $CS_2$ molecule have attracted considerable attention. Such studies have been aimed at understanding the nature of the intermolecular potential energy surface (PES) and dynamics of these weakly bound molecules. Carbon dioxide complexes have been thoroughly investigated experimentally [1–8] and theoretically [9–23], because $CO_2$ is one of the most important absorbers of infrared radiation in the earth's atmosphere and interstellar chemistry. As an analog of $CO_2$, $CS_2$ is also interesting because sulfur is a key element in chemistry and in the spectroscopy of giant planets [24]. It is interesting to explore the difference of structure and intermolecular dynamics between the $CS_2$ containing complexes and the $CO_2$ containing analogs.

The first spectra of the Ar–$CO_2$ complex were observed by Steed et al. [1] using the microwave spectroscopy. Subsequently, further experimental studies of microwave and infrared spectra for Rg–$CO_2$ (Rg = He, Ne, Ar, Kr) were reported [2, 3, 7, 8]. Along with these experimental studies, a number of theoretical researches have dealt with the construction of the ab initio potential energy surface and the calculation of the rovibrational energy levels. In the previous theoretical calculations [9–17], the $CO_2$ monomer was assumed as a rigid rotor, which is not sufficient for predicting the infrared spectra, since the transition in the

Dedicated to Professor Guosen Yan and published as part of the special collection of articles celebrating his 85th birthday.

**Electronic supplementary material** The online version of this article (doi:10.1007/s00214-014-1537-y) contains supplementary material, which is available to authorized users.

T. Yuan · H. Zhu (✉)
School of Chemistry, Sichuan University,
Chengdu 610064, China
e-mail: zhuhua@scu.edu.cn

T. Yuan · H. Zhu
State Key Laboratory of Biotherapy, Sichuan University,
Chengdu 610064, China

intramolecular vibrational mode is usually involved [25]. In addition, the shifts of the band origin in the infrared spectra cannot be correctly reproduced using the rigid monomer model. One effective way is to take into account the influence of intramolecular vibration mode on the potential energy surface and dynamical calculations [26–32]. To date, we have successfully used this approach to construct the potentials including the dependence on the $Q_3$ normal coordinate of the $CO_2$ molecule and to reproduce the infrared spectra for Rg–$CO_2$ [20–23].

Until now, only a few studies of the complex involving $CS_2$ have appeared [33–38]. Mivehvar et al. [36] first reported the infrared spectra of He–, Ne–, and Ar–$CS_2$ in the region of the $CS_2$ $v_3$ fundamental band around 1,535 $cm^{-1}$. The results showed that the Rg–$CS_2$ complexes have T-shaped structures. The vibrational band origin shifts and spectroscopic constants for Rg–$CS_2$ were also presented in their paper. Subsequently, Farrokhpour and Tozihi [37] constructed the ab initio potential energy surface of the Rg–$CS_2$ complexes (Rg = He, Ne, and Ar) using the coupled-cluster singles and doubles with noniterative inclusion of connected triple [CCSD(T)] theory with aug-cc-pVDZ basis set plus bond functions. Very recently, Zang et al. [38] reported the two-dimensional PESs for the three complexes, which were calculated using aug-cc-pVTZ basis set at CCSD(T) level. Based on the ab initio potential energy surfaces, they further calculated the rovibrational bound states and pure rotational transition frequencies. In the above two theoretical studies, the $CS_2$ molecule was treated as a rigid rotor.

The purpose of this work was to present a reliable three-dimensional potential energy surface involving the antisymmetric $Q_3$ normal mode of $CS_2$ for the He–$CS_2$ complex and to provide more detailed theoretical information on the dynamics including the rovibrational energy levels, bound states, and transition line intensities. The potential-optimized discrete (PODVR) [39, 40] grid points were employed to construct the potential energy surface. The radial discrete variable representation (DVR)/angular finite basis representation (FBR) method and Lanczos algorithm were used to calculate the bound states and rovibrational energy levels. The transition frequencies and line intensities and the band origin shift were also calculated and compared with the available observed results.

## 2 Computational details

### 2.1 Ab initio calculations

The geometry of the He–$CS_2$ complex is defined in Jacobi coordinates: $R$, $\theta$, $Q_3$. $R$ represents the distance from the $CS_2$ center-of-mass to the He atom. $\theta$ is the enclosed angle between the $\boldsymbol{R}$ vector and the molecular axis of $CS_2$. The coordinate $Q_3$ denotes the normal mode for $\upsilon_3$ antisymmetric stretch of $CS_2$. $Q_3$ is defined as $Q_3 = (r_{cs1} - r_{cs2})/\sqrt{2}$, where $r\mathrm{cs}_1$ and $r\mathrm{cs}_2$ are the two C–S bond lengths of $CS_2$, respectively. We used one-dimensional potential for the $Q_3$ coordinate of $CS_2$ to determine the energy levels and wave functions for the $Q_3$ mode. A coordinate scaling method [41] was used to adjust the CCSD(T) potential curve to reproduce the experimental $\upsilon_3$ fundamental frequency value [42], and the scale factor is 0.964322 and 0.978711 for the ground and the $\upsilon_3$ excited states of $CS_2$, respectively. Thus, we generated five PODVR grid points of −0.24995, −0.11881, 0.0, 0.11881, and 0.24995 $a_0$ for the ground state, and −0.24989, −0.11878, 0.0, 0.11878, and 0.24989 $a_0$ for the $\upsilon_3$ excited state.

The intermolecular potential energies of He–$CS_2$ were calculated using the supermolecular approach at the CCSD(T) level [43] for a total of about 1,000 points at each of the ground and the first excited $\upsilon_3$ states of $CS_2$, with $R$ ranging from 4.50 $a_0$ to 22.00 $a_0$ at 26 values, and 13 equidistant angles from $\theta = 0°$ to 180° in a step of 15°. We employed the augmented correlation-consistent quadruple-zeta (aug-cc-pVQZ) basis set [44] for all atoms and the bond functions (3s3p2d1f1g) [45]. The full counterpoise procedure (FCP) [46] was used to correct the basis set superposition error (BSSE).

To test the convergence of the basis set, a few additional calculations using a extrapolation formula [47] were performed to estimate the complete basis set (CBS) limit for two points ($R$, $\theta$) = (3.38 Å, 90.0°) and (4.50 Å, 45.0°) on the potential of He–$CS_2$ with $CS_2$ at the ground state. The ab initio calculated intermolecular energies are −54.06 and −16.44 $cm^{-1}$, respectively, whereas the extrapolation

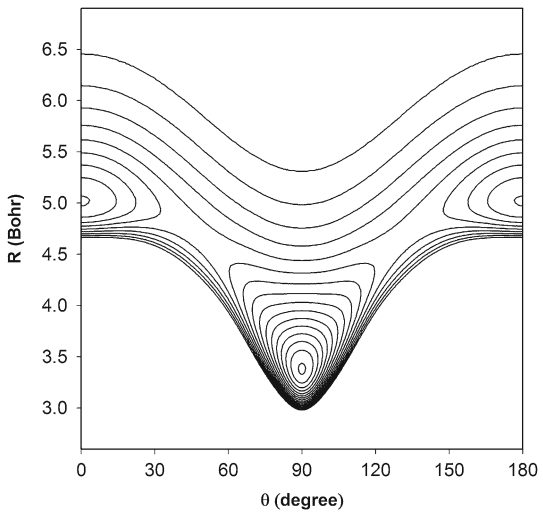


**Fig. 1** Contour plots (in $cm^{-1}$) of the averaged intermolecular potential energy surface for He–$CS_2$ with $CS_2$ at the ground ($\upsilon = 0$) state

**Table 1** Calculated energy levels (in $cm^{-1}$) for the pure vdW vibrational bound states of the He–$CS_2$ complex for the $v = 0$ and 1 states of $CS_2$

| $N$ | Ground state | $\upsilon_4$ State |
|---|---|---|
| 0 | −21.352 | −21.176 |
| 1 | −10.536 | −10.568 |
| 2 | −10.444 | −10.484 |
| 3 | −9.125 | −9.107 |
| 4 | −6.909 | −6.895 |
| 5 | −4.198 | −4.215 |
| 6 | −2.849 | −2.844 |
| 7 | −0.185 | −0.182 |

procedure gave the energies of −54.52 and −16.98 $cm^{-1}$. It is clear that the depth of the potentials presented in this work is only slightly underestimated because of the basis set incompleteness. All the ab initio calculations were carried out using the MOLPRO package [48].

## 2.2 Analytical fitting of the potential energy surface

The vibrationally averaged PESs $V_\upsilon(R, \theta)$ for the He–$CS_2$ complex can be defined as [49].

$$V_v(R,\theta) = \int_{-\infty}^{\infty} \psi_v(Q_3) V(R, Q_3, \theta) \psi_v(Q_3) dQ_3, \quad (1)$$

where $v$ denotes the quantum number for a specific vibrational state of isolated $CS_2$ molecule, and $\psi_v(Q)$ is the corresponding vibrational wave function.

The calculated ab initio potential energies can be fitted to an analytical form, [50–53]

$$V(R,\theta) = V_{\rm sh}(R,\theta) + V_{\rm as}(R,\theta). \quad (2)$$

The short-range part of the interaction is assumed to be

$$V_{\rm sh}(R,\theta) = G(R,\theta) e^{D(\theta) - B(\theta)R} \quad (3)$$

where $G(R, \theta)$, $D(\theta)$, and $B(\theta)$ are expanded as series in Legendre polynomials $P_l(\cos\theta)$,

$$G(R,\theta) = R^{-1} \sum_{i=1}^{2} R^i \sum_{l=0}^{8} g_{i,l} P_l(\cos\theta), \quad (4)$$

$$D(\theta) = \sum_{l=2}^{2} d_l P_l(\cos\theta), \quad (5)$$

$$B(\theta) = \sum_{l=0}^{8} b_l P_l(\cos\theta), \quad (6)$$

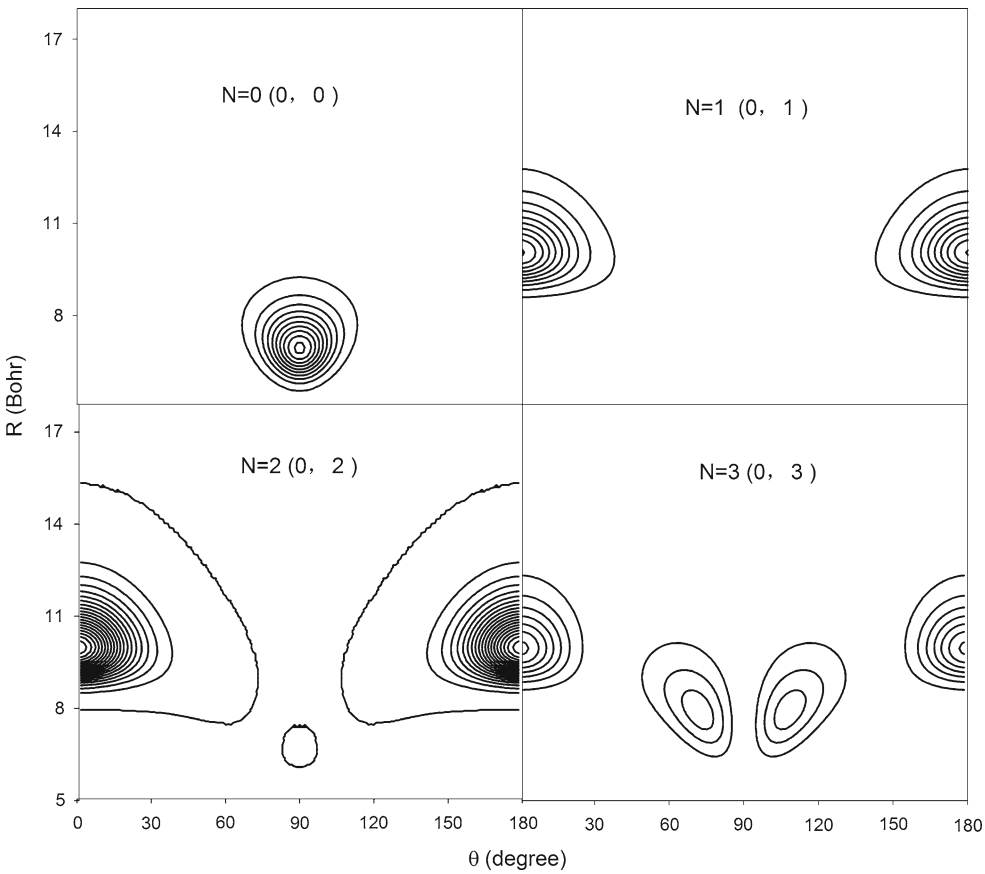


**Fig. 2** Contour plots of the wave functions for the lowest four vibrational states of He–$CS_2$ with $CS_2$ at the ground ($\upsilon = 0$) state

**Table 2** Rovibrational energy levels (in $cm^{-1}$) of He–$CS_2$ for the $v = 0$ and 1 states of $CS_2$

| Level | $J$ | $E$ ($J_{KaKc}$) | | | |
|---|---|---|---|---|---|
| | | Even/even | Even/odd | Odd/even | Odd/odd |
| Ground state | 0 | −21.352 ($0_{00}$) | | | |
| | 1 | | −21.160 ($1_{01}$) | −20.924 ($1_{10}$) | −20.955 ($1_{11}$) |
| | 2 | −20.781 ($2_{02}$)<br>−19.894 ($2_{20}$) | −20.510 ($2_{21}$) | −20.604 ($2_{12}$) | −20.510 ($2_{11}$) |
| | 3 | −19.326 ($3_{22}$) | −20.219 ($3_{03}$)<br>−19.310 ($3_{21}$) | −19.892 ($3_{12}$)<br>−18.230 ($3_{30}$) | −20.079 ($3_{13}$)<br>−18.230 ($3_{31}$) |
| | 4 | −19.485 ($4_{04}$)<br>−18.520 ($4_{22}$)<br>−15.954 ($4_{40}$) | −18.566 ($4_{23}$)<br>−15.954 ($4_{41}$) | −19.382 ($4_{14}$)<br>−17.468 ($4_{32}$) | −19.073 ($4_{13}$)<br>−17.466 ($4_{31}$) |
| | 5 | −17.621 ($5_{24}$)<br>−15.011 ($5_{42}$) | −18.585 ($5_{05}$)<br>−17.518 ($5_{23}$)<br>−15.011 ($5_{41}$) | −18.055 ($5_{14}$)<br>−16.507 ($5_{32}$)<br>−13.085 ($5_{50}$) | −18.516 ($5_{15}$)<br>−16.513 ($5_{33}$)<br>−13.085 ($5_{51}$) |
| $\upsilon_4$ State | 0 | −21.176 ($0_{00}$) | | | |
| | 1 | | −20.985 ($1_{01}$) | −20.750 ($1_{10}$) | −20.780 ($1_{11}$) |
| | 2 | −20.608 ($2_{02}$)<br>−19.723 ($2_{20}$) | −19.726 ($2_{21}$) | −20.431 ($2_{12}$) | −20.339 ($2_{11}$) |
| | 3 | −19.158 ($3_{22}$) | −20.050 ($3_{03}$)<br>−19.143 ($3_{21}$) | −19.725 ($3_{12}$)<br>−18.064 ($3_{30}$) | −19.910 ($3_{13}$)<br>−18.064 ($3_{31}$) |
| | 4 | −19.320 ($4_{04}$)<br>−18.358 ($4_{22}$)<br>−15.795 ($4_{40}$) | −18.404 ($4_{23}$)<br>−15.795 ($4_{41}$) | −19.217 ($4_{14}$)<br>−17.307 ($4_{32}$) | −18.910 ($4_{13}$)<br>−17.306 ($4_{31}$) |
| | 5 | −17.464 ($5_{24}$)<br>−14.859 ($5_{42}$) | −18.425 ($5_{05}$)<br>−17.362 ($5_{23}$)<br>−14.859 ($5_{41}$) | −17.899 ($5_{14}$)<br>−16.353 ($5_{32}$)<br>−12.936 ($5_{50}$) | −18.356 ($5_{15}$)<br>−16.358 ($5_{33}$)<br>−12.936 ($5_{51}$) |

The long-range part $V_{sh}(R, \theta)$ is expressed as,

$$V_{as}(R,\theta) = -\sum_{n=6}^{12}\sum_{l=0}^{8} f_n(B(\theta)R)c_{n,l}R^{-n}P_l(\cos\theta) \tag{7}$$

where $f_n(B(\theta)R$ is employed to damp the long-range force at short intermolecular distance, which is assumed to be in the Tang–Toennies form [54],

$$f_n(x) = 1 - \mathrm{e}^{-x}\sum_{k=0}^{n}\frac{(x)^k}{k!} \tag{8}$$

### 2.3 Calculations of the rovibrational states

The vibrational averaged intermolecular Hamiltonian for the He–$CS_2$ complex in the Jacobi coordinates can be written as [55, 56]

$$\widehat{H} = -\frac{1}{2\mu}\frac{\partial^2}{\partial R^2} + \frac{\hat{j}^2}{2I_v} + \frac{(\hat{\mathbf{J}}-\hat{j})^2}{2\mu R^2} + V_v(R,\theta), \tag{9}$$

where $\mu$ is the reduced mass of the He–$CS_2$ complex, $I_\upsilon = \langle\psi_\upsilon(Q_3)|I_{Q_3}|\psi_\upsilon(Q_3)\rangle$ is the vibrationally averaged rotational moment of inertia of $CS_2$ monomer, $\hat{\mathbf{J}}$, and $\hat{j}$ are the angular momentum operators corresponding to the total and the $CS_2$ monomer rotations. $V_\upsilon(R, \theta)$ is the vibrationally averaged potential in a particular vibrational state $\upsilon$ ($\upsilon = 0,\ 1$) of $CS_2$. The efficient radial DVR/angular FBR method [57, 58] was used to calculate the rovibrational energy levels. In our work, we used 120 sine-DVR [59] points for the $R$ coordinate, 89 basis functions of associated Legendre polynomials, and 90 Gauss–Legendre grids for the angular coordinate. The Lanczos algorithm [60, 61] was employed to efficiently diagonalize the Hamiltonian matrix with 5,000 steps. The parity-adapted rotational basis is defined in the three Euler angles ($\alpha,\ \beta,\ \gamma$) denoting the orientation of BF frame with respect to the SF frame,

$$\begin{aligned} C^{Jp}_{KM}(\alpha,\ \beta,\ \gamma) = [2(1+\delta_{K0})]^{-1/2}[D^{J*}_{MK}(\alpha,\ \beta,\ \gamma) \\ + (-1)^{J+K+p}D^{J*}_{M-K}(\alpha,\ \beta,\ \gamma)], \\ p = 0,\ 1 \end{aligned} \tag{10}$$

where $D^J_{MK}(\alpha,\ \beta,\ \gamma)$is the normalized rotational function. The total parity is given by $(-1)^{J+p}$. We calculated the rovibrational energy levels with the total angular momentum $J \le 8$.

## 3 Features of potential energy surface

The root mean square (rms) errors between the fitted and calculated points at $\upsilon = 0$ and 1 states of $CS_2$ are found to be about 0.04 $cm^{-1}$. The ab initio points and fitted potential

**Table 3** Spectroscopic constants (in $cm^{-1}$, 1 $cm^{-1}$ = 29,979.25 MHz) for the He–$CS_2$ complex at both the ground and $\upsilon_4$ states

| | Ground state | | $\upsilon_4$ State | |
|---|---|---|---|---|
| | Experiment | This work | Experiment | This work |
| $A$ | 0.321565 | 0.316699 | 0.320765 | 0.315786 |
| $B$ | 0.111322 | 0.111404 | 0.110604 | 0.110678 |
| $C$ | 0.080321 | 0.079994 | 0.079845 | 0.079529 |
| $\Delta_K$ | $3.148\times10^{-4}$ | $6.231\times10^{-5}$ | $3.347\times10^{-4}$ | $6.205\times10^{-5}$ |
| $\Delta_{JK}$ | $1.077\times10^{-4}$ | $1.171\times10^{-4}$ | $1.078\times10^{-4}$ | $1.182\times10^{-4}$ |
| $\Delta_J$ | $6.701\times10^{-7}$ | $1.057\times10^{-6}$ | $6.701\times10^{-7}$ | $1.065\times10^{-6}$ |
| $\delta_K$ | $6.347\times10^{-5}$ | $7.302\times10^{-5}$ | $6.446\times10^{-5}$ | $7.407\times10^{-5}$ |

Experimental data are taken from Ref. [36]

parameters for He–$CS_2$ are presented in Tables S1 and S2 in the supplementary material, respectively. The contour plot of $V_\upsilon(R, \theta)$ ($\upsilon = 0$) is shown in Fig. 1. It is clear that the CCSD(T) potential is characterized by a global T-shaped minimum and two linear local minima. The global minimum is situated at $R = 3.38$ Å and $\theta = 90.0°$ with a depth of 54.06 $cm^{-1}$. The two equivalent local minima of $-32.04$ $cm^{-1}$ occur at the linear geometry for $R = 5.02$ Å. A barrier separating the two minima is found at $R = 4.50$ Å and $\theta = 59.50°$ with height of 10.62 $cm^{-1}$, relative to the linear minimum. The barrier of 10.62 $cm^{-1}$ for He–$CS_2$ is higher than that of 2.38 $cm^{-1}$ for He–$CO_2$ [18], which means that the linear minimum of the former is easier to trap the He atom, leading to a less wide delocalized angular distribution.

## 4 Rovibrational bound states

We follow Ref. [6] to label the $\upsilon_3$ antisymmetric stretch of $CS_2$ as the $\upsilon_4$ vibrational mode in the He–$CS_2$ complex. Table 1 presents the energy levels for the total pure vibrational bound states at the $\upsilon = 0$ and 1 states of $CS_2$. One can see that ab initio CCSD(T) potential supports eight vibrational bound states, while He–$CO_2$ only has five bound states [18]. The vibrational ground state of the He–$CS_2$ complex with $CS_2$ at the ground state is bound by 21.35 $cm^{-1}$,corresponding to a zero-point energy of 32.71 $cm^{-1}$. The zero-point energy is over half of the global well depth, similar to other He-containing vdW complexes. Our predicted vibrational band origin for the He–$CS_2$ complex is blue shifted by 0.1759 $cm^{-1}$, very close to the observed value [36] of 0.1709 $cm^{-1}$. Although the band origin shift for He–$CS_2$ is larger (0.1759 vs. 0.1034 $cm^{-1}$) than that for He–$CO_2$ [18], the $CS_2$ and $CO_2$ shifts are small in magnitude and positive in sign, which

**Table 4** Calculated infrared transition frequencies (in $cm^{-1}$) and relative intensities for He–$CS_2$

| $J'_{Ka'Kc'}-J''_{Ka''Kc''}$ | $\upsilon_{cal}$ | $\upsilon_{cal}-\upsilon_{obs}$ | Intensity | $J'_{Ka'Kc'}-J''_{Ka''Kc''}$ | $\upsilon_{cal}$ | $\upsilon_{cal}-\upsilon_{obs}$ | Intensity |
|---|---|---|---|---|---|---|---|
| $5_{05}$–$6_{06}$ | 1,534.4569 | 0.0097 | 0.414 | $3_{12}$–$2_{11}$ | 1,536.1418 | 0.0048 | 0.787 |
| $4_{23}$–$5_{24}$ | 1,534.5733 | 0.0070 | 0.311 | $4_{14}$–$3_{13}$ | 1,536.2178 | 0.0031 | 0.899 |
| $3_{12}$–$4_{13}$ | 1,534.7040 | 0.0051 | 0.555 | $4_{23}$–$3_{22}$ | 1,536.2783 | 0.0036 | 0.503 |
| $3_{21}$–$4_{22}$ | 1,534.7333 | 0.0047 | 0.342 | $5_{05}$–$4_{04}$ | 1,536.4153 | 0.0016 | 0.884 |
| $3_{03}$–$4_{04}$ | 1,534.7904 | 0.0067 | 0.711 | $5_{41}$–$4_{40}$ | 1,536.4512 | 0.0030 | 0.606 |
| $2_{21}$–$3_{22}$ | 1,534.9559 | 0.0056 | 0.280 | $5_{32}$–$4_{31}$ | 1,536.4700 | 0.0034 | 0.221 |
| $2_{12}$–$3_{13}$ | 1,535.0037 | 0.0062 | 0.640 | $5_{23}$–$4_{22}$ | 1,536.5137 | 0.0047 | 0.479 |
| $1_{10}$–$2_{11}$ | 1,535.1170 | 0.0050 | 0.443 | $5_{14}$–$4_{13}$ | 1,536.5294 | 0.0035 | 0.707 |
| $1_{01}$–$2_{02}$ | 1,535.1513 | 0.0054 | 0.671 | $6_{16}$–$5_{15}$ | 1,536.5430 | 0.0012 | 0.660 |
| $4_{14}$–$4_{13}$ | 1,535.2115 | 0.0014 | 0.671 | $6_{25}$–$5_{24}$ | 1,536.6352 | 0.0022 | 0.394 |
| $6_{25}$–$6_{24}$ | 1,535.3146 | −0.0010 | 0.004 | $6_{34}$–$5_{33}$ | 1,536.6517 | 0.0027 | 0.197 |
| $3_{21}$–$3_{22}$ | 1,535.5393 | 0.0054 | 0.382 | $7_{07}$–$6_{06}$ | 1,536.7182 | 0.0001 | 0.778 |
| $1_{10}$–$1_{11}$ | 1,535.5615 | 0.0050 | 0.548 | $7_{43}$–$6_{42}$ | 1,536.8206 | 0.0023 | 0.020 |
| $5_{23}$–$5_{24}$ | 1,535.6147 | 0.0079 | 0.096 | $8_{18}$–$7_{17}$ | 1,536.8558 | −0.0001 | 0.602 |
| $3_{12}$–$3_{13}$ | 1,535.7103 | 0.0068 | 0.139 | $7_{34}$–$6_{33}$ | 1,536.8603 | 0.0044 | 0.143 |
| $1_{01}$–$0_{00}$ | 1,535.7223 | 0.0045 | 0.443 | $7_{16}$–$6_{15}$ | 1,536.8872 | 0.0017 | 0.344 |
| $7_{25}$–$7_{26}$ | 1,535.8068 | 0.0130 | 0.016 | $7_{25}$–$6_{24}$ | 1,536.9253 | 0.0048 | 0.723 |
| $2_{12}$–$1_{11}$ | 1,535.8797 | 0.0043 | 0.548 | $8_{27}$–$7_{26}$ | 1,536.9761 | 0.0010 | 0.179 |
| $5_{14}$–$5_{15}$ | 1,535.9732 | 0.0100 | 0.043 | $8_{45}$–$7_{44}$ | 1,537.0038 | 0.0017 | 0.045 |
| $3_{03}$–$2_{02}$ | 1,536.0864 | 0.0037 | 1.000 | $8_{36}$–$7_{35}$ | 1,537.0188 | 0.0020 | 0.259 |
| $3_{21}$–$2_{20}$ | 1,536.1073 | 0.0046 | 0.367 | Rms error | 0.005 | | |

Experimental data are taken from Ref. [36]

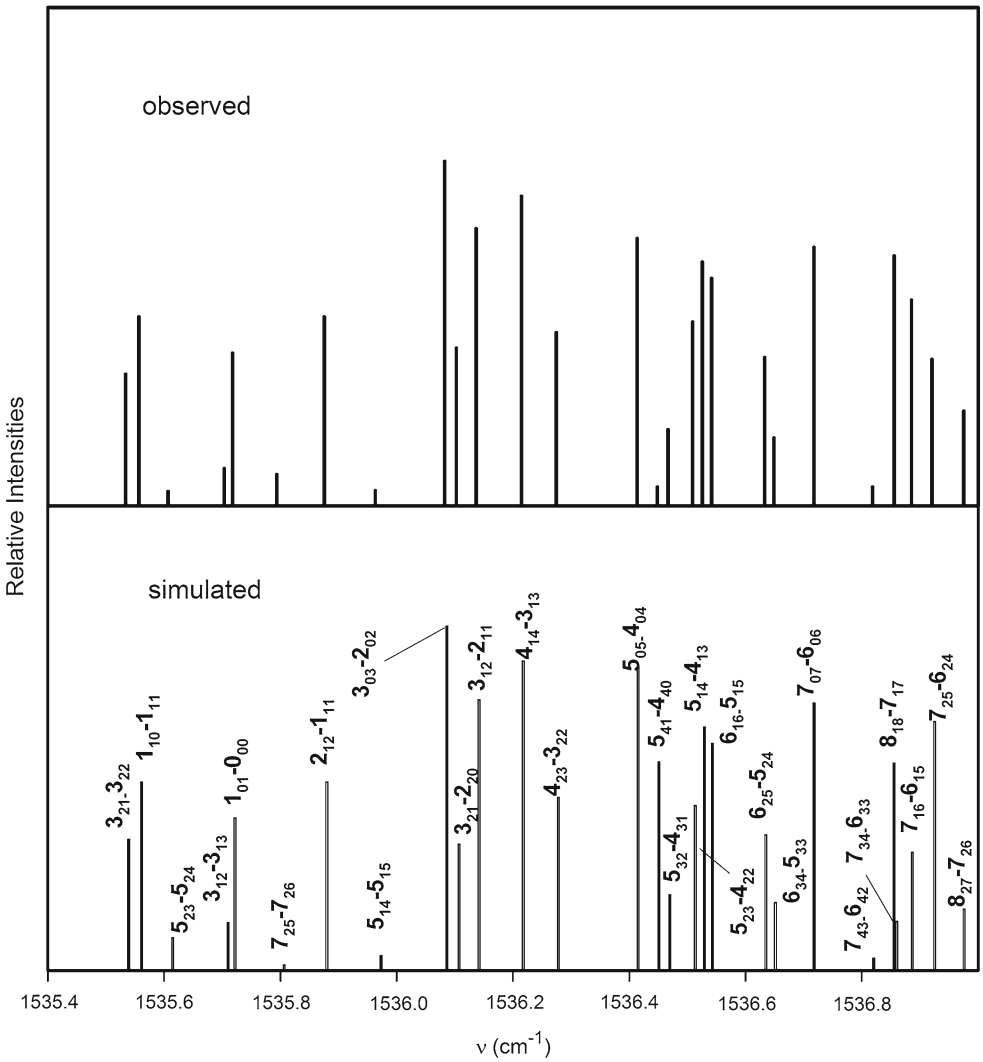


**Fig. 3** Observed and simulated line intensities for the $v_4$ band of He–$CS_2$

shows a slight weakening of the vdW bond upon vibration excitation for the two complexes.

To shed some light on the dynamic of the complex, it is useful to visualize the wave functions. Figure 2 presents the contour plots of the wave functions for the ground and the first three lower excited states of He–$CS_2$ with $CS_2$ at the ground ($\upsilon = 0$) state. The vdW vibrational states are defined by two quantum numbers ($n_s$, $n_b$), respectively, denoting the vdW stretching and bending modes. One can see that the ground state (0, 0) is localized at the T-shaped global minimum. Similar to He–$CO_2$, the wave functions for the lower excited states show predominantly bending character, which means that the potential is too shallow to support stretch vibrations along the $R$ coordinate for the small reduced mass of the complex. However, some significant deviations do exist. For example, the wave function of the first excited state (0, 1) for He–$CS_2$ is distributed less widely than that for He–$CO_2$ along the angular coordinate. The average structures were, respectively, determined from the vibrational ground state wave function of the complex, $\langle R\rangle = \langle\psi_0|R|\psi_0\rangle$ and $\langle\cos^2\theta\rangle = \langle\psi_0|\cos^2\theta|\psi_0\rangle$. The calculated average distance $R$ for the ground state is 3.766 Å, which is about 0.39 Å longer than its equilibrium value, and the angle $\theta$ is 83.53°, the latter is a measure of the average amplitude of the bending from the 90° average configuration, which can be interpreted as an effect of the zero-point vibrational motion of $CS_2$ within the complex. The ground state of the system is quite far from rigid; the radial dispersion and angular dispersion are 0.287 Å and 6.88°, respectively.

The rovibrational energies were assigned by the antisymmetric rotor quantum numbers $J_{KaKc}$. $J$ is the total angular momentum; $K_a$ and $K_c$ denote the projections of $J$ onto the $a$ and $c$ axes in the principal axes of inertia. The rovibrational energy levels consist of four blocks, (even/even), (even/odd), (odd/even), and (odd/odd) for different combination parity of ($j$/$p$). The calculated rovibrational energies for $J \leq 5$ of the vdW ground vibrational state

with $CS_2$ at both the ground ($\upsilon = 0$) and the first excited ($\upsilon = 1)\upsilon_3$ vibrational states are presented in Table 2.

## 5 Infrared spectra

The rovibrational energy levels of the vdW ground and $\upsilon_4$ states for $J \leq 3$ were fitted to a Watson asymmetric top Hamiltonian [62] using the *a*-type reduction in the $I^r$ representation. The fitted molecular spectroscopic constants are given in Table 3 together with the experimental results [36]. It is obvious that the rotational constants A, B, and C agree well with the experimental values. The inertial defect $\Delta_0$ in the ground state of He–$CS_2$ was calculated to be 6.19 amu Å$^2$, whereas for the He–$CO_2$ complex, $\Delta_0$ is 8.5 amu Å$^2$ [18], which indicates that the He–$CS_2$ complex is less floppy than the $CO_2$ analogs.

The calculated infrared transition is defined as the difference between the appropriate rovibrational energies on the upper ($\upsilon = 1$) and lower ($\upsilon = 0$) 2D surface, plus the experimental $CS_2$ band origin energy. The details regarding calculation of the transition intensities can be found in Ref. [63]. The calculated rovibrational transition frequencies and the relative intensities at the effective temperature of $T = 3.0$ K for He–$CS_2$ as well as the comparison with the observed infrared spectra are given in Table 4. The calculated transition frequencies are all in excellent agreement with the experimental values. Most of the calculated frequencies are within 0.005 cm$^{-1}$ of the observed values, and the root mean squares error of the 41 calculated transitions is only 0.005 cm$^{-1}$. Figure 3 plots a portion of the simulated infrared spectra, which is consistent with the observed spectra of Mivehvar et al. [36]. It is clear that both spectra have the $4_{14}$–$3_{13}$, $5_{05}$–$4_{04}$, $3_{12}$–$2_{11}$, and $7_{06}$–$6_{06}$, and the transition from $3_{03}$ to $2_{02}$ is found to be the strongest. Both the transition frequencies and intensities show that the new averaged potentials can reproduce the observed infrared spectra of the He–$CS_2$ complex well.

## 6 Conclusions

We have presented a three-dimensional PES for the He–$CS_2$ complex including the $Q_3$ normal mode of $CS_2$ at the CCSD(T) level with aug-cc-pVQZ basis set plus bond functions. The intermolecular potential was calculated over five PODVR grid points for the $Q_3$ normal mode. Based on the ab initio potential points, two vibrationally averaged PESs of the complex were generated. Each PES has a T-shaped global minimum and two equivalent local minima of linear geometry. The bound rovibrational energy levels of He–$CS_2$ were obtained by employing the radial DVR/angular FBR method and the Lanczos algorithm. The calculated spectroscopic constants and infrared spectra are in good agreement with the available observed values. The experimental band origin shift in the infrared spectra is reproduced very well. The $\upsilon_3$ antisymmetric and $\upsilon_1$ symmetric stretching vibrations of the $CS_2$ molecule will be both considered in the future work, and we will investigate the effect on the potential and spectroscopic properties of He–$CS_2$.

**Acknowledgments** This work was supported by the National Natural Science Foundation of China (Grant No. 21373139).

## References

1. Steed JM, Dixion TA, Klemperer W (1979) J Chem Phys 70:4095
2. Randall RW, Walsh MA, Howard BJ (1988) Faraday Discuss Chem Soc 85:13
3. Fraser GT, Pine AS, Suenram RD (1988) J Chem Phys 88:6157
4. Pine AS, Fraser GT (1988) J Chem Phys 89:100
5. Iida M, Ohsbima Y, Endo Y (1993) J Phys Chem 97:357
6. Weida MJ, Sperhac JM, Nesbitt DJ (1994) J Chem Phys 101:8351
7. Xu YJ, Jäger W (1998) J Mol Spectrosc 192:435
8. Konno T, Fukuda S, Ozaki Y (2006) Chem Phys Lett 421:421
9. Parker GA, Keil M, Kuppermann A (1983) J Chem Phys 78:1145
10. Keil M, Parker GA (1985) J Chem Phys 82:1947
11. Beneventi L, Casavecchia P, Vecchiocattivi F, Volpi GG, Buck U, Lauenstein C, Schinke R (1988) J Chem Phys 89:4671
12. Parker GA, Snow RL, Pack RT (1976) J Chem Phys 64:1668
13. Roche CF, Ernesti A, Huston JM, Dickinson AS (1996) J Chem Phys 104:2156
14. Marshall PJ, Szczesniak MM, Sadlej J, Chalasinski G, ter Horst MA, Jameson CJ (1996) J Chem Phys 104:6569
15. Hutson JM, Ernesti AM, Law M, Roche CF, Wheatley RJ (1996) J Chem Phys 105:9130
16. Yan GS, Yang MH, Xie DQ (1998) J Chem Phys 109:10284
17. Negri F, Ancliotto F, Mistura G, Toigo F (1999) J Chem Phys 111:6439
18. Ran H, Xie DQ (2008) J Chem Phys 128:124323
19. Cui YL, Ran H, Xie DQ (2009) J Chem Phys 130:224311
20. Chen R, Jiao EQ, Zhu H, Xie DQ (2010) J Chem Phys 133:104302
21. Chen R, Zhu H (2012) J Theor Comput Chem 11:1175
22. Chen R, Zhu H, Xie DQ (2011) Chem Phys Lett 511:229
23. Chen M, Zhu H (2012) J Theor Comput Chem 11:537
24. Flaud JM, Camy-Peyret C, Johns JWC (1983) Can J Phys 61:1462
25. Chalasinski G, Szczesniak MM (2000) Chem Rev 100:4227
26. Le Roy RJ, van Kranendonk J (1974) J Chem Phys 61:4750
27. Tennyson J, Sutcliffe BT (1982) J Chem Phys 77:4061
28. Le Roy RJ, Hutson JM (1987) J Chem Phys 86:837
29. Moszynski R, Jeziorski B, Wormer PES, van der Avoird A (1994) Chem Phys Lett 221:161
30. Pedersen TB, Cacheiro JL, Fernandez B, Koch H (2002) J Chem Phys 117:6562
31. Jiang H, Xu MZ, Hutson JM, Bacic Z (2005) J Chem Phys 123:054305
32. Paesani F, Whaley KB (2006) Mol Phys 104:61
33. Jucks KW, Huang ZS, Dayton D, Miller RE, Lafferty WJ (1987) J Chem Phys 86:4341
34. Peebles SA, Sun L, Kuczkowski RL (1999) J Chem Phys 110:6804
35. Newby JJ, Serafin MM, Peebles RA, Peebles SA (2005) Phys Chem Chem Phys 7:487

36. Mivehvar F, Lauzin C, McKellar ARW, Moazzen-Ahmadi N (2012) J Mol Spectrosc 281:24
37. Farrokhpour H, Tozihi M (2013) Mol Phys 111:779
38. Zang LM, Dai W, Zheng LM, Duan CX, Lu YP, Yang MH (2014) J Chem Phys 140:114310
39. Echave J, Clary DC (1992) Chem Phys Lett 190:225
40. Wei H, Carrington T (1992) J Chem Phys 97:3029
41. Bowman JM, Gazdy B (1991) J Chem Phys 94:816
42. Wells JS, Schneider M, Maki AG (1988) J Mol Spectrosc 132:422
43. Raghavachari K, Trucks GW, Pople JA, Head-Gordon M (1989) Chem Phys Lett 157:479
44. Woon DE, Dunning TH (1993) J Chem Phys 98:1358
45. Pedersen TB, Fernandez B, Koch H, Makarewicz J (2001) J Chem Phys 115:8431
46. Boys SF, Bernardi F (1970) Mol Phys 19:553
47. Patel K, Butler PR, Ellis AM, Wheeler MD (2003) J Chem Phys 119:909
48. Werner HJ, Knowles PJ, Amos RD et al. (2000) MOLPRO, version 2000.1, a package of ab initio programs
49. Le Roy RJ, Corey GC, Hutson JM (1982) Faraday Discuss Chem Soc 73:339
50. Misquitta AJ, Bukowski R, Szalewicz K (2000) J Chem Phys 112:5308
51. Murdachaew G, Misquitta AJ, Bukowski R, Szalewicz K (2001) J Chem Phys 114:764
52. Akin-Ojo O, Bukowski R, Szalewicz K (2003) J Chem Phys 119:8379
53. Zhou YZ, Xie DQ (2004) J Chem Phys 121:2630
54. Tang KT, Toennies JP (1984) J Chem Phys 80:3726
55. Tennyson J, Sutcliffe BT (1984) Mol Phys 51:887
56. Miller S, Tennyson J (1988) J Mol Spectrosc 128:132530
57. Lin SY, Guo H (2002) J Chem Phys 117:5183
58. Chen RQ, Ma GB, Guo H (2000) Chem Phys Lett 320:567
59. Colbert DT, Miller WH (1992) J Chem Phys 96:1982
60. Lanczos C (1950) J Res Natl Bur Stand 45:255
61. Guo H, Chen RQ, Xie DQ (2002) J Theor Comput Chem 1:173
62. Watson JKG (1967) J Chem Phys 46:1935
63. Xie DQ, Ran H, Zhou YZ (2007) Int Rev Phys Chem 26:487

Theor Chem Acc (2014) 133:1559
DOI 10.1007/s00214-014-1559-5

REGULAR ARTICLE

# Testing exchange–correlation functionals at fractional electron numbers

**Ali Malek · Degao Peng · Weitao Yang · Robert Balawender · Andrzej Holas**

Received: 22 May 2014 / Accepted: 4 August 2014 / Published online: 7 September 2014
© The Author(s) 2014. This article is published with open access at Springerlink.com

**Abstract** Dependence of the ground-state energy and density on the fractional electron number should be linear, while that of the chemical potential and Fukui function should be constant within the region between integers. In practical calculations with commonly used approximate functionals, results deviate from these ideal conditions. Four indicators are defined here to measure such deviations: from the global and local linearity condition, and from the global and local constancy condition. These indicators are used to test the performance of DFT method with five exchange–correlation functionals, and also the Hartree–Fock method, on a set of high-symmetry atoms: He, Li, Be, Na, Mg. The rCAM-B3LYP functional, having all four indicators small, is found to be the best functional for fractional electron number applications.

**Keywords** Exchange–correlation potentials · Density functional · Fractional particle number

Dedicated to Professor Guosen Yan and published as part of the special collection of articles celebrating his 85th birthday.

**Electronic supplementary material** The online version of this article (doi:10.1007/s00214-014-1559-5) contains supplementary material, which is available to authorized users.

A. Malek (✉) · R. Balawender · A. Holas
Institute of Physical Chemistry of Polish Academy of Sciences, Kasprzaka 44/52, PL-01-224 Warsaw, Poland
e-mail: alimalek2000@gmail.com

D. Peng · W. Yang (✉)
Department of Chemistry, Duke University, Durham, NC 27708, USA
e-mail: weitao.yang@duke.edu

W. Yang
Department of Physics, Duke University, Durham, NC 27708, USA

## 1 Introduction

Density functional theory (DFT) is, at present, the method of choice for the description of the ground-state (GS) properties of quantum systems with relatively low computational complexity. A practical and effective approach for electronic structure calculations is offered by Kohn–Sham (KS) method. The great success of KS-DFT is due to the fact that simple density functional approximations (DFAs) perform remarkably well for a wide range of problems in chemistry and physics, particularly for the prediction of the structure and thermodynamic properties of molecules and solids. DFT owes its power to an efficient formalism founded on the single-determinant state function that should in principle be able to yield the exact energy and density. All the complexity of this theory is hidden in one term—the exchange–correlation functional. This term holds 'the key to the success or failure of DFT' [1]. The main problem is that the explicit form of the exact functional is unknown, and only certain desired properties which should be satisfied by approximate functionals can be formulated [2, 3]. Failures in practical calculations are not the breakdown of the theory itself, but are only due to deficiencies in commonly used approximations [1]. Common approximations for the exchange–correlation functional have been found to give big errors for the linearity condition of fractional charges (electron numbers), leading to delocalization error, and for the constancy condition of fractional spins (the energy of the ensemble constructed from the components of the spin doublet is independent of the spin number), leading to static correlation error [1, 4, 5]. Violation of these conditions underlies the major failures of all known approximate functionals to describe the energy gaps and related properties in strongly correlated systems [6]. The linearity condition of the energy versus

the number of electrons $N$ follows from the zero-temperature limit of the temperature extension of the DFT [7–9] or, alternatively, from the pure states for a collection of replicas at zero temperature [2, 10]. Standard local or semi-local DFAs such as local density approximation (LDA), generalized gradient approximation (GGA) and meta-GGA, result in a very poor description, giving a smooth, convex, almost parabolic, interpolation between the values at integers. Some corrections applied to these functionals straighten the curve for fractional charges but significantly worsen the description at integers. Hartree–Fock (HF) results have the opposite behavior, with a concave interpolation between the integers. However, the hybrid functionals which combine these two ingredients are still quite convex [11, 12]. There have been two strategies to tackle this problem. The first one is the scaling correction method [13–15] or the restoration scheme [16, 17] applied to existing functionals. The second is the construction of new functionals which satisfy the energy linearity condition [11, 18, 19] or the constancy condition of the frontier orbital energy (interpreted as the ionization energy) [20–22]. The "dilemma" of how to define the exchange–correlation potential for fractional $N$ was discussed in early paper [23], while the papers [24, 25] represent the most recent investigations related to the fractional-$N$ problem for density functionals. Recently, an orbital functional based on the particle–particle random phase approximation to many-body theory has been shown to exhibit minimal errors for fractional charges and fractional spins and have many promising features [26, 27].

In this article, we investigate four properties related to fractional number of electrons to test the quality of the exchange–correlation functional. As illustrative example, the results for DFT method with five exchange–correlation functionals (SVWN5, PBE, B3LYP, CAM-B3LYP, rCAM-B3LYP) and the Hartree–Fock method are presented.

## 2 Theoretical background

In the exact DFT [28], the total energy of the system is a functional of the electron density and the external potential $v(\mathbf{r})$,

$$\begin{aligned} E[\rho, v] &= T[\rho] + E_{ee}[\rho] + \int v(\mathbf{r})\rho(\mathbf{r})d\mathbf{r} \\ &= T_s[\rho] + E_{es}[\rho] + E_{xc}[\rho] + \int v(\mathbf{r})\rho(\mathbf{r})d\mathbf{r} \end{aligned} \tag{1}$$

where $T[\rho]$ and $E_{ee}[\rho]$ are the kinetic energy and the electron–electron interaction energy functionals, respectively. Following the Kohn–Sham (KS) scheme, the sum of these two functionals can be represented as the sum of the non-interacting reference KS kinetic energy, $T_s[\rho]$, the electrostatic energy, $E_{es}[\rho]$, and the exchange–correlation energy, $E_{xc}[\rho]$. The GS energy, $E[N, v]$, is the minimum $E[N, v] = \mathrm{Min}_{\rho \to N} E[\rho, v]$ with the constraint $N = \int \rho(\mathbf{r})d\mathbf{r}$. The minimizer is the GS density. The main result of the fractional-number extension of the DFT at zero temperature is that the GS energy is continuous and piecewise linear function of the electron number (charge) [8]. Namely, for the system with fractional charge $N = J \pm \delta$, where $J$ is an integer and $\delta \in [0, 1]$, the GS energy is

$$E_{\pm\delta}[J, v] \equiv E[J \pm \delta, v] = \delta E[J \pm 1, v] + (1 - \delta)E[J, v], \tag{2}$$

and the GS density is a linear mixture of the GS densities of the $J$- and the $(J \pm 1)$-electron number systems,

$$\begin{aligned} \rho_{\pm\delta}(\mathbf{r}; J, v) \equiv \rho(\mathbf{r}; J \pm \delta, v) = \delta\, \rho(\mathbf{r}; J \pm 1, v) \\ + (1 - \delta)\rho(\mathbf{r}; J, v). \end{aligned} \tag{3}$$

The total energy is an implicit functional of the density via the dependence of the molecular orbitals and their occupancies on the density. The term representing the coupling between the electrons and the external potential is an exact, explicit functional of the electron density. The kinetic energy term, expressed as an explicit functional of spinorbitals and occupation numbers, is

$$\breve{T}_s\left[\{n_p\}, \{\chi_p\}\right] = \sum_p n_p \int \chi_p^*(\mathbf{r}) \left(-\frac{1}{2}\nabla_{\mathbf{r}}^2\right) \chi_p(\mathbf{r})d\mathbf{r}. \tag{4}$$

$E_{es}$ represents the classical electrostatic energy

$$E_{es}[\rho] = \frac{1}{2} \int \int \frac{\rho(\mathbf{r})\rho(\mathbf{r}')}{|\mathbf{r} - \mathbf{r}'|} d\mathbf{r}d\mathbf{r}'. \tag{5}$$

Since such $E_{es}[\rho]$ is not linear in $\rho(\mathbf{r})$, it immediately follows that its nonlinearity has to be compensated by the appropriate exchange–correlation term $E_{xc}[\rho]$, or the standard energy expression corrected by some additional terms [29, 30]. Alternatively, both $E_{es}$ and $E_x$ should be expressed in the ensemble terms [31]. In general, if the electrostatic energy for the $(J \pm \delta)$ system is defined as a linear combination of the electrostatic energies for the 'end' points, the form of the electrostatic energy as a functional of density is unknown [32]. Although no explicit form is available for the exact $E_{xc}[\rho]$, much is known about the "proper" way in which approximations for this energy term should be constructed. One of the main challenges for DFT is to keep, as its cornerstone, some element of simplicity [4]. Unfortunately, a simple density functional adopted from the solid-state physics, the LDA, does not perform well in many areas of chemistry. The introduction of the density gradient into the form of the exchange–correlation functional (the GGA or meta-GGA), allows to receive satisfactory results in the

chemical applications. The next major advances came with the inclusion of a fraction of the HF exchange in the $E_{\rm xc}$ functional (hybrid functionals). One of the recent developments in functionals is due to the range separation. The idea is to separate the electron–electron interaction into two parts, the long-range one and the short-range one, and then to treat these parts with different functionals (see Ref. [4] for review).

In practice, the direct extension (to fractional $N$) of DFT is applied, for which the ground-state energy is evaluated as

$$E^{\rm DFA}[N,v] \equiv \underset{\{n_p\},\{\chi_p\}}{\rm Min}\left\{\breve{E}\left[\{n_p\},\{\chi_p\};v\right]\middle|\sum_p n_p = N, n_p\in[0,1], \langle\chi_p \mid \chi_q\rangle = \delta_{pq}\right\} \tag{6}$$

where $\breve{E}\left[\{n_p\},\{\chi_p\}\right]$ is the energy functional defined in terms of commonly used approximations

$$\begin{aligned}\breve{E}\left[\{n_p\},\{\chi_p\},v\right] &= \breve{T}_s\left[\{n_p\},\{\chi_p\}\right] + \int v(\mathbf{r})\breve{\rho}(\mathbf{r};\{n_p\},\{\chi_p\})d\mathbf{r}\\ &+ E_{\rm es}\left[\breve{\rho}\left[\{n_p\},\{\chi_p\}\right]\right] + b_{\rm xc}E_{\rm xc}\left[\breve{\rho}\left[\{n_p\},\{\chi_p\}\right]\right]\\ &- \frac{1}{2}\sum_{pq} n_p n_q\left\{c_{\rm x}\langle\chi_p\chi_q \mid \chi_q\chi_p\rangle + b_{\rm x}^{\rm LR,HF}\langle\chi_p\chi_q \mid \chi_q\chi_p\rangle^{\mu}\right\}\end{aligned} \tag{7}$$

with a set of orthonormal spinorbitals, $\{\chi_p\}$ and their occupation numbers, $\{n_p\}$. Here, the non-integer electron number $N$(fractional charge) is realized indirectly by the constraint on the spinorbital occupancies, $\{n_p\}$. The density of the system (the non-interacting KS density) is

$$\breve{\rho}\left(\mathbf{r};\{n_p\},\{\chi_p\},v\right) = \sum_p n_p\left|\chi_p(\mathbf{r})\right|^2, \tag{8}$$

and can integrate to any nonnegative real number $N = \sum_p n_p$. The GS density $\rho(\mathbf{r};\, N,\, v)$ is obtained from Eq. (8) with $\{\chi_p\}$ and $\{n_p\}$ being the minimizers in Eq. (6). $E_{\rm xc}[\breve{\rho}]$ represents the part of the exchange–correlation energy which depends locally on the density (and on the density derivatives). If $b_{\rm xc} = 0$, there is no correlation part and all exchange is represented by the HF-like exchange. The parameters $c_{\rm x}$ and $b_{\rm x}^{\rm LR,HF}$ determine the portion of the HF exchange in the hybrid and the long-range correction functional, respectively. The parameter $\mu$ defines separation of regions. The spinorbitals $\{\chi_p\}$ and orbital energies $\{\varepsilon_p\}$ are the eigensolutions of the one-electron Hamiltonian with the effective potential $v_{\rm eff}(\mathbf{x})$. The $v_{\rm eff}(\mathbf{x})$ is a local (multiplicative) potential in the original KS method or a non-local potential in a generalized KS method (with hybrid functionals) and in the HF method.

As a consequence of the linearity condition, Eq. (2), the chemical potential (the first derivative of the GS energy with respect to $N$) is constant between the integers

$$\begin{aligned}\mu[J\pm\delta,v] &\equiv \left(\frac{\partial E[N,v]}{\partial N}\right)_v\Bigg|_{N=J\pm\delta}\\ &= \pm(E[J\pm1,v] - E[J,v]),\quad \delta\in(0,1),\end{aligned} \tag{9}$$

and it is related to the frontier (f) eigenvalue [8, 12, 33–35]

$$\mu[J\pm\delta,v] = \varepsilon_f^{\rm DFA}[J\pm\delta,v]. \tag{10}$$

Now, we can formulate the first two indicators for testing the quality of functionals: the relative deviation from the global linearity condition (GLC), Eq. (2), as

$$\Delta_{\pm\delta}^{\rm GLC} = \frac{E_{\pm\delta}^{\rm DFA}}{\delta E_{\pm1}^{\rm DFA} + (1-\delta)E_0^{\rm DFA}} - 1, \tag{11}$$

and the relative deviation from the global constancy condition (GCC), Eqs. (9) and (10), as

$$\Delta_{\pm\delta}^{\rm GCC} \equiv \frac{\varepsilon_f^{\rm DFA}[J\pm\delta]}{\pm\left(E_{\pm1}^{\rm DFA} - E_0^{\rm DFA}\right)} - 1. \tag{12}$$

Here, $E_{\pm\delta}^{\rm DFA} = E^{\rm DFA}[J\pm\delta,v]$.

Besides the linearity condition for the total energy and the constancy condition for the energy of the highest (partially) occupied spinorbital, we can examine the local counterparts of these conditions related to the ground-state density and the Fukui function (FF) [28, 36]. Third indicator tests the fulfillment of the local linearity condition (LLC), Eq. (3). It is the integrated deviation from the LLC, defined as

$$\begin{aligned}\Delta_{\pm\delta}^{\rm LLC} &= (J\pm\delta)^{-1}\int\left|\rho_{\pm\delta}^{\rm DFA}(\mathbf{r}) - \left(\delta\rho_{\pm1}^{\rm DFA}(\mathbf{r}) + (1-\delta)\rho_0^{\rm DFA}(\mathbf{r})\right)\right|d\mathbf{r},\\ \rho_{\pm\delta}^{\rm DFA}(\mathbf{r}) &= \rho(\mathbf{r},J\pm\delta,v).\end{aligned} \tag{13}$$

(The factor $(J\pm\delta)^{-1}$ is omitted in our illustrative example tests as it is irrelevant at comparisons).

The FF (the derivative of the ground-state density, Eq. (3), with respect to the electron number) is independent of the fraction $\delta$ (similarly as the chemical potential)

$$\begin{aligned}f(\mathbf{r};J\pm\delta,v) &\equiv \left(\frac{\partial\rho(\mathbf{r};N,v)}{\partial N}\right)_v\Bigg|_{N=J\pm\delta}\\ &= \pm(\rho(\mathbf{r};J\pm1,v) - \rho(\mathbf{r};J,v))\end{aligned} \tag{14}$$

(this form of FF was noted first in Ref. [37]), and the integrated deviation from this local constancy condition (LCC) is defined as

$$\begin{aligned}\Delta_{\pm\delta}^{\rm LCC} &= C^{\rm LCC}\int\left|f_{\pm\delta}^{\rm DFA}(\mathbf{r}) \mp \left(\rho_{\pm1}^{\rm DFA}(\mathbf{r}) - \rho_0^{\rm DFA}(\mathbf{r})\right)\right|d\mathbf{r},\\ C^{\rm LCC} &= \left(\int\left|\left(\rho_{\pm1}^{\rm DFA}(\mathbf{r}) - \rho_0^{\rm DFA}(\mathbf{r})\right)\right|d\mathbf{r}\right)^{-1}\end{aligned} \tag{15}$$

**Table 1** The average (over the set: Li, Na, Be, Mg) of the test indicator for the global linear condition $\Delta^{\mathrm{GLC}}_{-\delta}$

| | $\delta$ | | | | | | |
|---|---|---|---|---|---|---|---|
| | 0.01 | 0.1 | 0.3 | 0.5 | 0.7 | 0.9 | 0.99 |
| HF | −0.00 [−0.04] | −0.02 [−0.36] | −0.05 [−0.84] | −0.05 [−1.00] | −0.04 [−0.85] | −0.02 [−0.38] | −0.00 [−0.05] |
| SVWN5 | 0.05 [0.27] | 0.48 [2.51] | 1.12 [6.15] | 1.31 [7.66] | 1.07 [6.65] | 0.42 [2.80] | 0.04 [0.25] |
| PBE | 0.05 [0.26] | 0.48 [2.43] | 1.11 [5.92] | 1.31 [7.26] | 1.08 [6.11] | 0.44 [2.29] | 0.04 [0.04] |
| B3LYP | 0.04 [0.21] | 0.40 [1.95] | 0.93 [4.8] | 1.10 [6.01] | 0.91 [5.29] | 0.38 [2.28] | 0.04 [0.21] |
| CAM-B3LYP | 0.02 [0.14] | 0.20 [1.30] | 0.46 [3.2] | 0.55 [4.01] | 0.47 [3.52] | 0.20 [1.50] | 0.02 [0.13] |
| rCAM-B3LYP | 0.00 [0.07] | 0.02 [0.61] | 0.04 [1.50] | 0.05 [1.85] | 0.05 [1.58] | 0.02 [0.61] | 0.00 [0.03] |

In brackets, the average over the set enlarged by He. All values are per thousand. Data for atoms are accessible from Supporting Information

where $f^{\mathrm{DFA}}_{\pm\delta}(\mathbf{r}) \equiv \left(\partial\rho^{\mathrm{DFA}}_{\pm\delta}(\mathbf{r})/\partial\rho^{\mathrm{DFA}}_{\pm\delta}(\mathbf{r})\partial N.\partial N\right)\big|_{N=J\pm\delta}$. (The factor $C^{\mathrm{LCC}}$ is omitted in our illustrative example tests as it is irrelevant at comparisons). Note that $(C^{\mathrm{LCC}})^{-1}$ equals to one when the FF is not negative, but it is larger than one (even two) when FF is negative in some regions as in cases of redox-induced electron transfer [38, 39]. This $\Delta^{\mathrm{LCC}}$ is the last indicator for testing the quality of functionals, proposed in this work. It should be noted that if the integrand in Eqs. (13) and (15) is taken without absolute value operation, the result of integration is exactly zero. According to the proposed definitions of indicators, high quality of a particular DFA is demonstrated when all inequalities

$$\left|\Delta^{GLC}_{\pm\delta}\right| \ll 1, \left|\Delta^{GCC}_{\pm\delta}\right| \ll 1, \Delta^{LGC}_{\pm\delta} \ll 1, \Delta^{LCC}_{\pm\delta} \ll 1, \qquad (16)$$

are satisfied in the whole range $0 < \delta < 1$.

## 3 Illustrative examples and discussion

In this article, the performance of SVWN5 [40] (a LDA-type functional), PBE [41] (a GGA-type functional), B3LYP [42, 43] (a hybrid functional), CAM-B3LYP [44] (a long-range corrected functional), rCAM-B3LYP [11] (a long-range corrected functional with improved description of systems with fractional numbers of electrons), and HF method was tested. To eliminate complication due to the spatial degeneracy, our test set is restricted only to atomic systems with the total angular momentum equal zero, namely to He, Li, Be, Na, Mg atoms. All calculations were performed with cc-pVTZ basis set [45–47] in spin-unrestricted formalism. The FF for the fractional electron system [48], $f^{\mathrm{DFA}}_{\pm\delta}(\mathbf{r})$, was calculated using QM4D program [49] according to methods described in Ref. [48]. Only decreasing electron number process was considered for all systems (lower sign chosen in Eqs. (2), (3), (9)–(15), $\delta = 1$ means a cationic form of an atom). All results are presented per thousand. The results for atoms are accessible from Supporting Information.

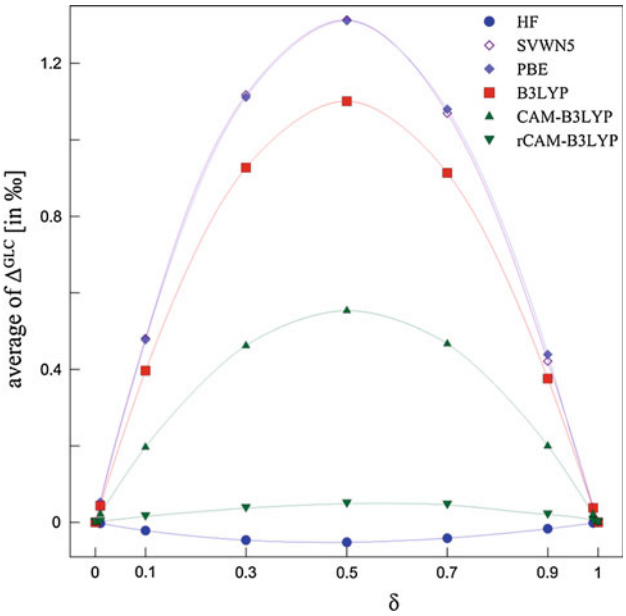


**Fig. 1** The average of $\Delta^{\mathrm{GLC}}_{-\delta}$, Eq. (11), vs. fraction $\delta$

To present our illustrative example results in a condensed form, the average value of an indicator over a set of four atoms, Li, Na, Be, Mg is displayed for each deviation. The results for He are not included, as significantly differing from those of other atoms in many cases: for $\Delta^{\mathrm{GLC}}$ at all methods (see Table 1), for remaining indicators at rCAM-B3LYP. This peculiarity stems from the fact that the two-particle aspects of electron structure in comparison with the single-particle ones are more pronounced for the He atom than for remaining atoms. In all Figures, lines joining calculated points are drawn for eye guidance only.

The results of the global linearity condition testing, Eq. (11), are collected in Table 1 (zero values at $\delta = 0$ and $\delta = 1$ are omitted) and in Fig. 1. As expected, the standard local-potential functionals (SVWN5 and PBE) yield the largest, positive $\Delta^{\mathrm{GLC}}_{-\delta}$. The HF method yields the weakest, negative $\Delta^{\mathrm{GLC}}_{-\delta}$. The B3LYP functional combines these two effects, yielding $\Delta^{\mathrm{GLC}}_{-\delta}$ slightly smaller than those generated by SVWN and PBE functionals,

but still presents a concave curve. A significant improvement is observed for functionals which contain some Coulomb-attenuated exchange (CAM). The rCAM-B3LYP functional yields the smallest GLC deviation. Reasonable explanation of observed tendencies is available, especially of the fact that extreme deviations are observed at $\delta = 0.5$ for all methods. Very weak GLC deviation for the HF method is the effect of the testing set (only atomic systems without spatial degeneracy) used in this article. All the occurring open shell systems at integral $N$ are not spatially degenerate and the HF method for such systems is self-interaction free [31].

At first, it should be noted that the energy expression, Eq. (7), has no explicit $N$ dependence. This dependence is implicit trough the dependence on $\{n_p\}$ and the condition $\sum_p n_p = N$. Namely, the trace of the first-order density matrix (DM), $d_1$, is equal to electron number $N$

$$d_1\left(\mathbf{x};\mathbf{x}';\{n_p\},\{\chi_p\}\right) \equiv \sum_p n_p \chi_p^*(\mathbf{x})\chi_p(\mathbf{x}'), \quad \mathrm{Tr}d_1 = N. \tag{17}$$

In the direct extension of the HF method, the hyper-HF one, the approximate second-order DM, $d_2$, is constructed from the first-order DM as the following determinant

$$\begin{aligned} &d_2(\mathbf{x}_1,\mathbf{x}_2;\mathbf{x}'_1,\mathbf{x}'_2;d_1) \\ &\quad\equiv \frac{1}{2}(d_1(\mathbf{x}_1,\mathbf{x}'_1)d_1(\mathbf{x}_2,\mathbf{x}'_2) - d_1(\mathbf{x}_1,\mathbf{x}'_2)d_1(\mathbf{x}_2,\mathbf{x}'_1)) \\ &\quad= d_2[N,v], \end{aligned} \tag{18}$$

(it is exact for the single Slater determinant). This $d_2$ leads to relations [50] $\mathrm{Tr}d_2[N,v] \geq \frac{1}{2}(N-1)N$, and [31]

$$\Delta E^{\mathrm{HF}}_{\mathrm{ee},\pm\delta} \equiv E^{\mathrm{HF}}_{\mathrm{ee},\pm\delta} - \left(\delta E^{\mathrm{HF}}_{\mathrm{ee},\pm1} + (1-\delta)E^{\mathrm{HF}}_{\mathrm{ee},0}\right) \geq 0. \tag{19}$$

where $E^{\mathrm{HF}}_{\mathrm{ee},\pm\delta} = \mathrm{Tr}d_2[J\pm\delta,v]\hat{V}_{ee}$(the electron–electron energy due to 'generalized Fock' operator).

In the case of atoms considered in this work, the above deviation from the linearity for the electron–electron interaction energy is [31]

$$\Delta E^{\mathrm{HF}}_{\mathrm{ee},\pm\delta} = \delta(1-\delta)J_{ff} \geq 0, \tag{20}$$

(here $J_{\mathrm{ff}}$ is the Coulomb integral for the frontier orbital) with the maximum at $\delta = 0.5$. The shape of this derivation, Eq. (21), was already observed in Fig. 1 of Ref. [51]. When combined with the negative denominator in Eq. (11), it leads to negative $\Delta^{\mathrm{GLC}}_{-\delta}$ for the HF method. Contrary to the hyper-HF method, compensation of the self-interaction errors of $E_{\mathrm{es}}$ and $E_{\mathrm{x}}$ for DFA methods is not complete or absent. Therefore, the deviation from linearity for $E_{\mathrm{es}}$, Eq. (5), is the dominating deviation. It can be easily evaluated as

$$\begin{aligned} \Delta E^{\mathrm{DFA}}_{\mathrm{es},\pm\delta} &\equiv E_{\mathrm{es}}\left[\rho^{\mathrm{DFA}}_{\pm\delta}\right] - \left(\delta E_{\mathrm{es}}\left[\rho^{\mathrm{DFA}}_{\pm1}\right] + (1-\delta)E_{\mathrm{es}}\left[\rho^{\mathrm{DFA}}_{0}\right]\right) \\ &= -\delta(1-\delta)E_{\mathrm{es}}\left[\rho^{\mathrm{DFA}}_{\pm1} - \rho^{\mathrm{DFA}}_{0}\right] \leq 0. \end{aligned} \tag{22}$$

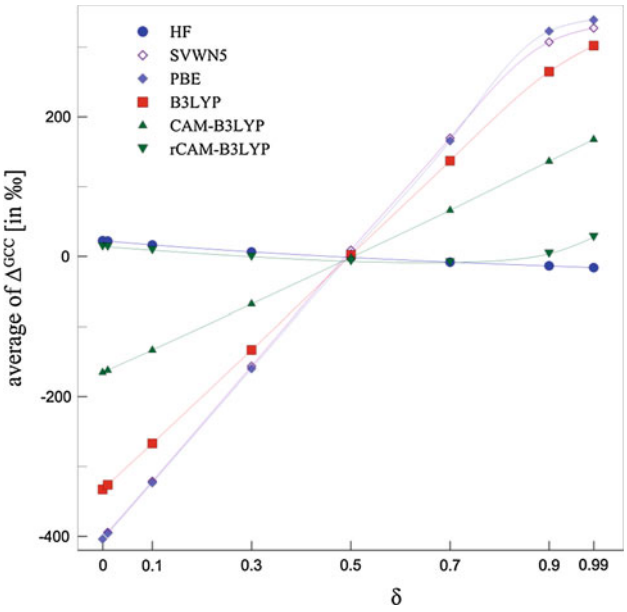


**Fig. 2** The average of $\Delta^{\mathrm{GCC}}_{-\delta}$, Eq. (12), vs. fraction $\delta$

When combined with the negative denominator in Eq. (11), it leads to positive $\Delta^{\mathrm{GLC}}_{-\delta}$ for DFA methods, with the maximum at $\delta = 0.5$.

It should be pointed out that Eqs. (20) and (22) describe the GLC discrepancy of the $E^{\mathrm{HF}}_{\mathrm{ee}}$ and $E^{\mathrm{DFA}}_{\mathrm{es}}$ only approximately due to the following inconsistencies. All three terms $E^{\mathrm{HF}}_{\mathrm{ee},\pm\delta}$, $E^{\mathrm{HF}}_{\mathrm{ee},\pm1}$ and $E^{\mathrm{HF}}_{\mathrm{ee},0}$ are constructed from a common set of orbitals, determined at $N = J \pm \delta$, appropriate for the first term only, while to be consistent, the orbitals determined at $(J \pm 1)$ and $J$ should be applied for remaining two terms. In Eq. (22), a combination of $\rho^{\mathrm{DFA}}_{\pm1}$ and $\rho^{\mathrm{DFA}}_{0}$ is taken for $\rho^{\mathrm{DFA}}_{\pm\delta}$ [like in Eq. (3)], while this density should be constructed from orbitals determined at $N = J \pm \delta$.

The results of the global constancy condition testing, Eq. (12), are presented in Fig. 2. Since the constancy of $\mu[N] = (\partial E[N]/\partial N) = -\partial E_{-\delta}/\partial\delta$ is tested, the discrepancy for the HF method is accounted mainly by $\partial\Delta E^{\mathrm{HF}}_{\mathrm{ee},-\delta}/\partial\delta = -(1-2\delta)J_{\mathrm{ff}}$, see Eq. (20). When combined with the negative denominator in Eq. (12), this produces $\Delta^{\mathrm{GCC}}_{-\delta}$ linearly decreasing, zeroing at $\delta = 0.5$. Similarly, for DFA methods, Eq. (20) should be replaced by Eq. (22), leading to $\Delta^{\mathrm{GCC}}_{-\delta}$ linearly increasing, zeroing at $\delta = 0.5$, and quite large at end points of $\delta$ range, with the smallest absolute values for the rCAM-B3LYP and HF methods. The zeroing at $\delta = 0.5$ is consistent with the transition state approach in which the ionization energy is determined by the highest occupied orbital energy of the intermediate state, $E[J] - E[J-1] \approx \varepsilon_{\mathrm{HOMO}}[J-0.5]$ [52], see also Ref. [53].

As indicated in Eq. (9), the region of $\mu$ constancy is limited to $0 < \delta < 1$. Nevertheless, Fig. 2 includes results at

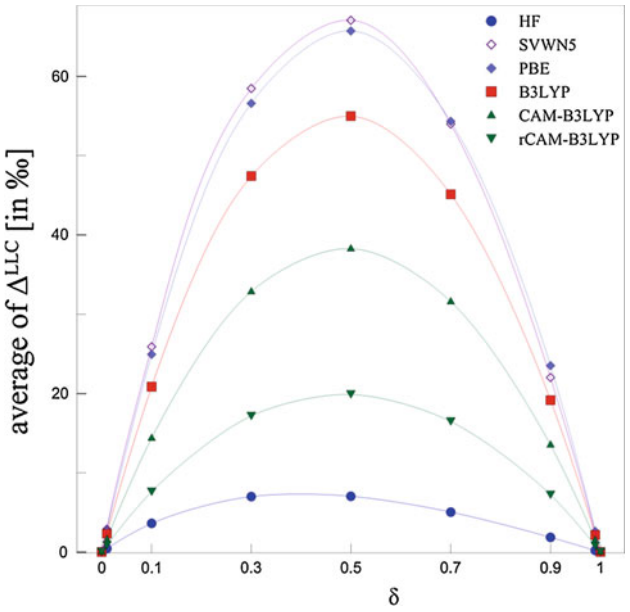


**Fig. 3** The average of $\Delta_{-\delta}^{GCC}$, Eq. (13), vs. fraction $\delta$

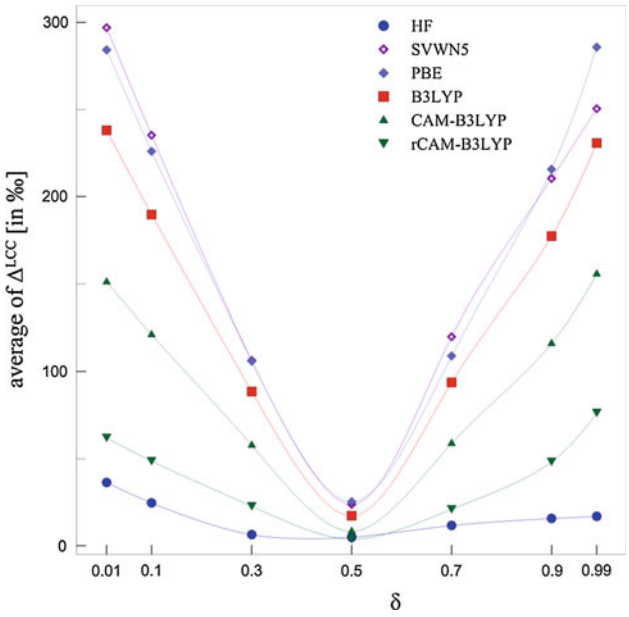


**Fig. 4** The average of $\Delta_{-\delta}^{GCC}$, Eq. (15), vs. fraction $\delta$

$\delta = 0$. With $\varepsilon_f^{DFA}[J-\delta]$ defined to be the frontier (highest occupied) orbital energy, the value of $\Delta_0^{GCC}$ equals $\lim_{\delta\to 0}\Delta_{-\delta}^{GCC}$. It is consistent with $\Delta_{-0.01}^{GCC}$ for all atoms. However, the GCC indicator calculated formally at $\delta = 1$, $\Delta_{-1}^{GCC}$, does not equal $\lim_{\delta\to 1}\Delta_{-\delta}^{GCC}$ and it differs significantly from $\Delta_{-0.99}^{GCC}$ (see Supporting Information). This difference is due to different calculational procedures for determination of $\varepsilon_f^{DFA}[J-\delta]$: at $\delta < 1$, the KS equations are solved self-consistently in the space of $J$ occupied orbitals, while at $\delta = 1$—in the space of $(J-1)$ occupied orbitals. The lowest virtual orbital energy is to be taken as $\varepsilon_f^{DFA}[J-1]$.

The results of the local linearity condition testing, Eq. (13), are shown in Fig. 3. The shapes of plots are similar to those in Fig. 1, but the maximum discrepancies are about 50 times larger. This similarity can be understood with the help of the DFT mapping $\rho \to E[\rho]$ connecting the ground-state density and energy. The maximal discrepancy concerning the density in Fig. 3 correlates with the maximal discrepancy concerning the energy in Fig. 1. Of all DFA methods, the smallest discrepancy is observed for rCAM-B3LYP ($\Delta_{-0.5}^{LLC} = 0.015$). The HF method is even better ($\Delta_{-0.5}^{LLC} = 0.006$).

The results of the local constancy condition testing are shown in Fig. 4. The shapes of plots are similar to those in Fig. 2, provided $\left|\Delta_{-\delta}^{GCC}\right|$ would be plotted there instead of $\Delta_{-\delta}^{GCC}$. The magnitude of discrepancies is practically the same in both figures. This similarity can be viewed as an analog of similarity between the $\Delta_{-\delta}^{GLC}$ and $\Delta_{-\delta}^{LLC}$ plots, but now applied to derivatives with respect to $N$. Again, the performance of the rCAM-B3LYP functional is the best among tested approximate functionals.

## 4 Conclusions

In concluding, our illustrative examples' calculations demonstrate that the performance of the rCAM-B3LYP functional is the best among the tested functionals. Moreover, satisfaction of inequalities (16) is quite reasonable ($\Delta_{-0.5}^{GLC} = 5\times10^{-5}, \Delta_{-0.3}^{GCC} = -4.5\times10^{-4}, \Delta_{-0.5}^{LLC} = 1.5\times10^{-2}, \Delta_{-0.5}^{LCC} = 3.8\times10^{-3}$). The especially small $\Delta^{GLC}$ is due to the fact that the rCAM-B3LYP functional was constructed to minimize just the discrepancy from the GLC. Another general conclusion can be reached: when the chemical potentials and the Fukui function are to be determined, the best results are found at $\delta = 0.5$ for all tested DFAs. It is surprising that the performance of the extended HF method is as good (or even better) as that of DFT with the rCAM-B3lYP functional. Probably, this is due to the particular set of systems (atoms) chosen for tests. In any case, the hyper-HF method should not be used for large systems because important correlation effects are missing.

**Acknowledgments** WY expresses his admiration and happy birthday wish to Professor Guosen Yan. Work of AM, RB and AH has been supported by the International Ph.D. Projects Programme of the Foundation for Polish Science, co-financed from European Regional Development Fund within Innovative Economy Operational Programme "Grants for innovation" and the Interdisciplinary Center for Mathematical and Computational Modeling computational grant.

Work of DP and WY has been supported by the National Science Foundation (CHE 1362927).

**Open Access** This article is distributed under the terms of the Creative Commons Attribution License which permits any use, distribution, and reproduction in any medium, provided the original author(s) and the source are credited.

## References

1. Cohen AJ, Mori-Sanchez P, Yang W (2008) Science 321:792–794
2. Yang W, Zhang Y, Ayers PW (2000) Phys Rev Lett 84:5172–5175
3. Ayers P (2006) Phys Rev A 73:012513
4. Cohen AJ, Mori-Sanchez P, Yang W (2012) Chem Rev 112:289–320
5. Mori-Sanchez P, Cohen AJ, Yang W (2009) Phys Rev Lett 102:066403
6. Mori-Sanchez P, Cohen AJ, Yang W (2008) Phys Rev Lett 100:146401
7. Mermin ND (1965) Phys Rev 137:A1441
8. Perdew JP, Parr RG, Levy M, Balduz JL (1982) Phys Rev Lett 49:1691
9. Balawender R (2012) arXiv:12121367 ePrint archive (http://arxiv.org/abs/1212.1367)
10. Ayers PW (2006) J Math Chem 43:285–303
11. Cohen AJ, Mori-Sanchez P, Yang W (2007) J Chem Phys 126:191109
12. Cohen AJ, Mori-Sánchez P, Yang W (2008) Phys Rev B 77:115123
13. Zheng X, Cohen AJ, Mori-Sanchez P, Hu X, Yang W (2011) Phys Rev Lett 107:026403
14. Stein T, Autschbach J, Govind N, Kronik L, Baer R (2012) J Phys Chem Lett 3:3740–3744
15. Zheng X, Zhou T, Yang W (2013) J Chem Phys 138:174105
16. Stein T, Eisenberg H, Kronik L, Baer R (2010) Phys Rev Lett 105:266802
17. Chai JD, Chen PT (2013) Phys Rev Lett 110:033002
18. Johnson ER, Contreras-Garcia J (2011) J Chem Phys 135:081103
19. Cohen AJ, Mori-Sanchez P, Yang W (2007) J Chem Phys 127:034101
20. Imamura Y, Kobayashi R, Nakai H (2011) Chem Phys Lett 513:130–135
21. Imamura Y, Kobayashi R, Nakai H (2011) J Chem Phys 134:124113
22. Imamura Y, Kobayashi R, Nakai H (2013) Int J Quantum Chem 113:245–251
23. Savin A (1996) In: Seminario JM (ed) Recent Developments and Applications of Modern Density Functional Theory. Elsevier, New York, p 327
24. Levy M, Anderson JSM, Zadeh FH, Ayers PW (2014) J Chem Phys 140:18A538
25. Miranda-Quintana RA, Bochicchio RC (2014) Chem Phys Lett 593:35–39
26. van Aggelen H, Yang Y, Yang W (2013) Phys Rev A 88:030501(R)
27. Yang Y, van Aggelen H, Steinmann SN, Peng D, Yang W (2013) J Chem Phys 139:174110
28. Parr RG, Yang W (1989) Density Functional Theory of Atoms and Molecules. Oxford University Press, New York
29. Kraisler E, Kronik L (2013) Phys Rev Lett 110:126403
30. Perdew JP, Zunger A (1981) Phys Rev B 23:5048
31. Balawender R, Geerlings P (2005) J Chem Phys 123:124102
32. Kleinman L (1997) Phys Rev B 56:12042–12045
33. Almbladh C, von Barth U (1985) Phys Rev B Condens Matter 31:3231–3244
34. Perdew JP (1985) In: Dreizler RM, da Providência J (eds) Density Functional Methods in Physics. NATO ASI Series. Plenum Press, New York
35. Yang W, Cohen AJ, Mori-Sanchez P (2012) J Chem Phys 136:204111
36. Parr RG, Yang W (1984) J Am Chem Soc 106:4049–4050
37. Ayers PW, Levy M (2000) Theor Chem Acc 103:353–360
38. Ayers PW, Morrison RC, Roy RK (2002) J Chem Phys 116:8731–8744
39. Ayers PW (2006) Phys Chem Chem Phys 8:3387–3390
40. Vosko SH, Wilk L, Nusair M (1980) Can J Phys 58:1200–1211
41. Perdew JP, Burke K, Ernzerhof M (1996) Phys Rev Lett 77:3865–3868
42. Lee C, Yang W, Parr RG (1988) Phys Rev B 37:785–789
43. Becke AD (1988) Phys Rev A 38:3098–3100
44. Yanai T, Tew DP, Handy NC (2004) Chem Phys Lett 393:51–57
45. Dunning TH (1989) J Chem Phys 90:1007
46. Woon DE, Dunning TH (1995) J Chem Phys 103:4572
47. Kendall RA, Dunning TH, Harrison RJ (1992) J Chem Phys 96:6796
48. Yang W, Cohen AJ, De Proft F, Geerlings P (2012) J Chem Phys 136:144110
49. Parveen S, Chandra AK, Zeegers-Huyskens T (2009) J Phys Chem A 113:6182–6191
50. Lieb E (1981) Phys Rev Lett 46:457–459
51. Perdew JP, Ruzsinszky A, Csonka GI, Vydrov OA, Scuseria GE, Staroverov VN, Tao JM (2007) Phys Rev A 76:040501
52. Slater JC (1972) Adv Quantum Chem 6:1–92
53. Gaiduk AP, Mizzi D, Staroverov VN (2012) Phys Rev A 86:052518

Theor Chem Acc (2014) 133:1556
DOI 10.1007/s00214-014-1556-8

REGULAR ARTICLE

# Stereoselective inclusion mechanism of ketoprofen into β-cyclodextrin: insights from molecular dynamics simulations and free energy calculations

**Mingsong Shi · Chunchun Zhang · Yani Xie · Dingguo Xu**

Received: 22 May 2014 / Accepted: 29 July 2014 / Published online: 26 August 2014
© Springer-Verlag Berlin Heidelberg 2014

**Abstract** The host–guest inclusion mechanism formed between β-cyclodextrin and those poorly water-soluble drug molecules has important applications in supramolecular chemistry, biology and pharmacy. In this work, the chiral recognition ability of β-cyclodextrin to one of non-steroidal anti-inflammatory drugs, ketoprofen, has been systematically investigated using molecular dynamics and free energy simulation methods. The *R*- and *S*-enantiomers of ketoprofen were explicitly bound within the cyclodextrin cavity in our simulations, respectively. In consistent with experimental observations, tiny structural difference between two isomers could be observed. Calculated absolute binding free energies using adapted biasing force (ABF) method and MM/GBSA approach for both isomers are comparable to experimental values. Significant binding fluctuations along the MD trajectory have been observed. The free energy profiles calculated using two different approaches reveal that the ketoprofen prefers binding in the cavity with the carboxylate group facing the wider edge of β-cyclodextrin. Similar free energy profiles for two enantiomers obtained using ABF calculations indicate that it is very hard to separate and identify the chiral conjugates within the framework of the natural β-cyclodextrin.

**Keywords** Molecular dynamics · ABF · β-Cyclodextrin · Ketoprofen · Chiral recognition

Dedicated to Professor Guosen Yan and published as part of the special collection of articles celebrating his 85th birthday.

**Electronic supplementary material** The online version of this article (doi:10.1007/s00214-014-1556-8) contains supplementary material, which is available to authorized users.

M. Shi · D. Xu (✉)
MOE Key Laboratory of Green Chemistry and Technology, College of Chemistry, Sichuan University, Chengdu 610064, Sichuan, People's Republic of China
e-mail: dgxu@scu.edu.cn

C. Zhang (✉) · Y. Xie
Analytical and Testing Center, Sichuan University, Chengdu 610064, Sichuan, People's Republic of China
e-mail: cczh@scu.edu.cn

## 1 Introduction

The interaction or recognition mechanism of host–guest systems constitutes the core part of supramolecular chemistry, for which the main driving force of the formation of the systems is considered to be the hydrophobic interactions. Correct understanding or quantification of the intermolecular interaction would be particularly important for the "rational planning of new supramolecular systems, including intelligent materials, as well as for developing new biologically active agents" [1]. Among host–guest systems, the inclusion complexes formed between natural cyclodextrins (CDs) with small organic molecules, *esp.* those hydrophobic molecules, represents a typical example in this field and thus attracts a lot of attentions [2–9].

CDs are cyclic oligomers of glucose units. The most common natural CDs are composed of 6 (α), 7 (β) or 8 (γ) pyranose units connected by α-1,4 glycosidic linkage. Due to $^4C_1$ chair conformation of the pyranose units, the overall topology of these CDs can be described as a toroid/hollow truncated cone shape. The significant different hydrophilicity of their exterior environment and interior cavity makes the CDs very unique in the supramolecular chemistry. They can easily bind lipophilic molecules to form a host–guest inclusion complex and thus change the chemical, physical or even biological properties of these ligands. Such ability

makes them widely applied in pharmaceutical development, drug delivery or food industry. People have pursued their usage in the synthesis of some certain mechanically interlocked molecular architecture, such as rotaxanes [10] and catenanes [11]. The photochemistry of molecules hosted by CDs is also of particular interests, e.g., arenes [12]. In this work, we will focus on the detailed chiral recognition mechanism of β-CD complexed with a widely used anti-inflammatory drug, *ketoprofen*. The schematic representations of β-CD and ketoprofen are given in Scheme 1.

Ketoprofen (IUPACE name of (*R*/*S*)2-(3-benzoylphenyl) propionic acid) has long been considered to be the nonsteroidal anti-inflammatory drug (NSAID) with analgesic and antipyretic effects [13]. It has also served as one of pain relief drugs. Ketoprofen is usually marketed as 50:50 racemic mixtures of (*R*-) and (*S*-)enantiomers, but with poor solubility. It was demonstrated that only *S*-enantiomer has anti-inflammatory activity, while same functions can be found for other profen drugs such as ibuprofen and flurbiprofen. However, the chiral inversion of the *R*- to *S*-enantiomers of profen drugs has been observed in vivo, e.g., in pigs [14]. Based on this, the physiological functions of (*R*-)ketoprofen should not be totally neglected and might deserve some more researches. More importantly, some experimental studies have proved that (*R*-)flurbiprofen can be involved in the antitumor activity in mouse. Clearly, we cannot simply neglect either enantiomer. Due to the importance of the enantiomer drugs in the drug delivery, it might be interesting to pursue the synthesis, separation or chemical properties for different enantiomers. The recognition mechanism and binding structures of β-CD with ketoprofen have been reported in some detail from both experimental and theoretical sides [15–19]. However, little was known about the difference of the binding features, such as binding free energies or structures, for both enantiomers of ketoprofen. Recently, to tackle the photochemistry characteristics of (*R*-) and (*S*-)ketoprofen and their chiral recognition in β-CD, it was investigated by Marconi et al. [17] using various experimental techniques such as circular dichroism, isothermal titration calorimetry and NMR. For the association constants for both enantiomers, the experiments gave almost identical values considering experimental uncertainty. Based on circular dichroism and 2D ROESY spectra, tiny structural difference can be probed for both enantiomers. Therefore, it should be pointed out that it is very difficult to use experimental tools to get stereoselective recognition ability of β-CD versus (*R*-) and (*S*-)ketoprofen. Given the practically enantio-differentiated anti-inflammatory and analgesic activities of ketoprofen, it is then necessary to understand the detailed recognition mechanism for both chiral isomers from theoretical view.

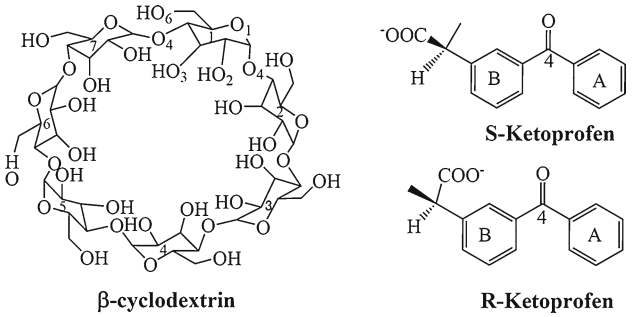


**Scheme 1** Schematic representations and definition of atoms of β-cyclodextrin and (*S*-) and (*R*-)ketoprofen molecules

Besides the stereoselective recognition mechanism of β-CD with ketoprofen, there is another interesting issue not quite well understood. For the profen drugs, there are two sides which bear different polarizability as shown in Scheme 1, with polar carboxylate group at one side and nonpolar aromatic group at the other side. So far there is no definite study to say which rim of the β-CD the carboxylate group is bound with. Indeed, some controversies were reported for other profen drugs, such as ibuprofen. The X-ray structure of the inclusion complex formed between β-CD and *S*-ibuprofen reported by Braga et al. [20] clearly indicates that the carboxylate group of the ligand faces the smaller rim of the β-CD. On the contrary, another crystallographic structure of *S*-ibuprofen complexed by a heptakis-substituted β-CD shows that the carboxylate group is facing the bigger rim [21]. In addition, theoretical simulations reported by Cai et al. [22] on steroid drugs recognized by β-CD indicate that the different binding orientations could lead to closed binding free energy profiles along the binding coordinates as well as the association constants. Such observations could further suggest that the formation of inclusion complex has some complicated processes. Therefore, to obtain a complete understanding of the β-CD bound with ketoprofen molecule or other small ligands, it is highly desired to perform extensive simulations on all of possible binding orientations for different enantiomers.

In this work, to obtain a complete understanding of the binding characteristics of ketoprofen/β-CD inclusion complex, we then build four possible binding structures for two ketoprofen enantiomers as shown in Scheme 2. The absolute binding free energies will then be calculated based on molecular mechanics-generalized born surface area (MM-GBSA) method. To understand the detailed formation processes of each inclusion complex, the potential of mean force (PMF) profiles along the inclusion coordinates will be computed using adapted biasing forcing (ABF) method.

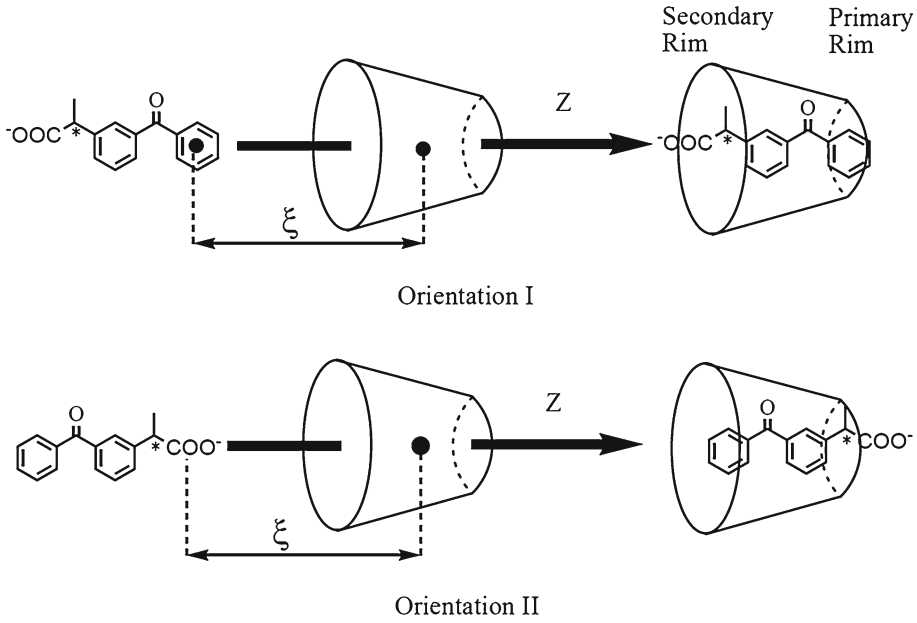


**Scheme 2** Schematic representations of two different inclusion directions of ketoprofen threading through the cavity of β-CD. The origin is set at the center of mass of seven glycosidic oxygen atoms of β-CD. The narrower edge is usually called as primary rim, while the wider edge as secondary rim

## 2 Computational details

### 2.1 Models of β-CD/ketoprofen inclusion complex

There is no published X-ray structure for β-CD/ketoprofen inclusion complex. To investigate the dynamics properties of this inclusion complex, it would be necessary to construct the model of inclusion complex firstly. It should be pointed out that since there are two isomers for ketoprofen molecule, we then docked *R*- and *S*-ketoprofen into β-CD cavity using AutoDock 4.2 program, respectively [23]. In addition, since there are also two possible binding orientations for each enantiomer as shown in Schemes 1 and 2, the structures for each orientation of different enantiomers with the lowest binding energy were chosen for the following extensive molecular dynamics simulation. For convenience, the glucose units of cyclodextrin are labeled from G1 to G7. We simply give the name for each binding orientation as **R-I**, **R-II** for (*R*-) ketoprofen, while **S-I** and **S-II** for (*S*-)ketoprofen, respectively. In binding orientation **I**, the carboxyl group is facing the secondary rim, while the carboxyl group stays at the primary rim in binding orientation **II**. Throughout the simulation, the stoichemistry of β-CD and ketoprofen is maintained to be 1:1 ratio, which has been suggested by many experimental works.

The obtained systems were firstly solvated in a pre-equilibrated TIP3P [24] water box. The typical size of the water box is calculated to be about 44 Å × 44 Å × 40 Å, consisting of 179 solute atoms and about 1800 solvent molecules. To prepare suitable force field for the ketoprofen molecule, we employed the standard Amber general amber force field (GAFF) generation procedure. First of all, the geometry optimizations of ketoprofen at HF/6-31G* level of theory were carried out using gaussian09 suite of program [25]. The partial atomic charges were then calculated using the restrained electrostatic potential (RESP) protocol after structure optimization and electrostatic potential calculations using B3LYP/6-31G* method. The force field parameters for the ligands generated using the Antechamber program were then described by GAFF module. The force field of β-cyclodextrin is expressed using Glycam06 carbohydrate parameters [26] in this work, which has been proved to accurately and efficiently represent carbohydrates. The periodic boundary conditions and an 8 Å cutoff for non-bond interactions were applied. The particle mesh ewald (PME) algorithm [27] was used to calculate the long-range electrostatic interactions. The positions of water molecules were relaxed by 500 steps of steepest descent (SD) and 1000 steps of conjugate gradient (CG) minimization approach with all of solute molecules fixed at their original positions. Further 10,000 steps of CG full minimization were carried out for total system. The obtained systems were gradually heated to 300 K in 20 ps in the NVT ensemble, followed by 20 ns equilibration simulation under 1 atm pressure. Subsequently, further 20 ns MD simulations in the isothermal–isobaric NPT ensemble were performed for data analysis. Newton's equations of atomic motion were integrated by the Verlet algorithm with a 2-fs time step. SHAKE algorithm [28] was applied to constraint bond stretching of the covalent bonds involving hydrogen atoms. All of MD simulations were performed using PMEMD module of CUDA version implemented in AMBER 12 software package.

### 2.2 Binding free energy calculations

To quantitatively assess the binding affinity of β-CD in complex with ketoprofen molecule, it is necessary to calculate the binding free energy for the inclusion complex.

Several methods have been proposed for calculating absolute binding free energy, e.g., linear response approximation (LRA) [29], linear interaction energy (LIE) [30–32], molecular mechanics Poisson Boltzmann (or generalized Born) surface area (MM-PB/GBSA) [33, 34], solvated interaction energy (SIE) [35], or free energy pathway method [36]. In this work, the binding free energy is calculated using MM-GBSA [33] method.

For the calculation of binding free energy in MM-GBSA framework, it has been discussed extensively [37–41]. Only a short description is summarized here:

$$\Delta G_{\text{binding}} = \Delta G_{\text{complex}} - \Delta G_{\beta\text{ - CD}} - \Delta G_{\text{ketoprofen}} \quad (1)$$

$$G = E_{\text{gas}} + G_{\text{sol}} - \text{TS} \quad (2)$$

$$E_{\text{gas}} = E_{\text{int}} + E_{\text{vdW}} + E_{\text{ele}} \quad (3)$$

$$G_{\text{sol}} = G_{\text{GB}} + G_{\text{np}} \quad (4)$$

$\Delta G_{\text{complex}}$, $\Delta G_{\beta\text{ - CD}}$ and $\Delta G_{\text{ketoprofen}}$ are free energies of the complex, the β-CD and ketoprofen, respectively. Each term can be obtained according to Eq. (2). Practically, they are calculated as the statistical averages over frames extracted from MD trajectories. The solvation free energy ($G_{\text{sol}}$) can be divided into polar ($G_{\text{GB}}$) and nonpolar ($G_{\text{np}}$) contributions. The polar solvation contribution is calculated by solving the Generalized Born (GB) equation [42]. Dielectric constants ($\varepsilon$) for solute and solvent were selected to be 1 and 80, respectively. The nonpolar contribution due to cavity formation and van der Waals interactions between the solute and the solvent can be estimated by the equation of $\gamma \cdot \text{SA} + b$, where $\gamma = 0.0072$ kcal/Å$^2$, $b = 0.0$ kcal/mol. The SA is defined as the solvent accessible surface area, which was estimated using the program MSMS [43]. For each complex system, binding energies were averaged over 1,000 frames of the 20-ns MD trajectory. It has long been recognized that the inclusion of entropic effect in the calculation of total binding free energy can largely reduce the difference between theoretical and experimental values [44]. Entropy contributions are from changes in the degrees of freedom including translation, rotation and vibration. The translational, rotational and vibrational entropy terms are functions of the mass and moments of inertia of the molecule and thus can be calculated using the standard equations of statistical mechanics [45]. In this work, vibrational entropy contributions were estimated using the normal mode analysis approach [46]. Due to the system size is just moderate, the $-T\Delta S$ was averaged over 200 snapshots of the MD trajectory.

### 2.3 Formation of inclusion complex

As suggested in Scheme 2, two possible binding models with different position of the propionic acid end have been proposed for the molecules in profen family recognized by β-CD. Although the absolute binding free energy calculated using MM-GBSA method can provide some insights into the interaction affinity between β-CD and ligands, the detailed process to form the inclusion complex cannot be entirely revealed. Furthermore, the chiral recognition processes might be another interesting issue for the β-CD/ketoprofen inclusion complex. To address the formation of inclusion complexes, we further carried out extensive simulations of the inclusion processes using the adaptive biasing force (ABF) method [47]. MD simulations were performed using NAMD program [48], for which the initial system is constructed using the following strategy to avoid artificial impacts. As shown in Scheme 2, we randomly put the ketoprofen isomers outside the secondary (bigger) rim of the cavity of β-CD. We then simulate the translocation process through the cavity starting from the secondary rim, and finally moving out via the primary rim. The origin is defined as the center of mass of seven oxygen atoms (O4) of glycosidic linkage of the β-CD. In the present ABF calculations, we have two possible binding processes for each isomer: One is aromatic ring *A* enters the cavity first, and the second is the carboxylate group moves into the cavity first. Then, the order parameter or the inclusion coordinate should be defined correspondingly. For the first case, the orientation I, the order parameter ($\xi$), which ranges from $-16$ to 14 Å, was chosen as the projection of the distance between the origin and the center of mass of the aromatic ring *A* of ketoprofen on the *z*-axis. For the second case, the orientation II, the order parameter ($\xi$), which ranges from $-16$ to 14 Å, was chosen as the projection of the distance between the origin and the center of the mass of the carboxylate group of ketoprofen on the *z*-axis. The inclusion pathway was then divided into six consecutive windows to increase the computational efficiency. Each window was further divided into consecutive bins with bin width of 0.1 Å. For each window, up to 5 ns of MD trajectory was generated, resulted in a total of 30 ns simulation time. Instantaneous values of the forces, the first-order derivative of free energy with respect to the defined order parameter, were accrued in each bin to calculate the mean force value. Total of 1,500 force samples were accumulated in each bin prior to application of the adaptive bias. For the setup protocol of MD simulations, which is essentially the same as we did in previous section using Amber program, except the integration step is set as 1 fs time step in ABF calculations.

## 3 Results and discussion

### 3.1 Structures of the inclusion complexes

In this work, one of our major objectives is to understand the mechanism of chiral recognition of β-CD with

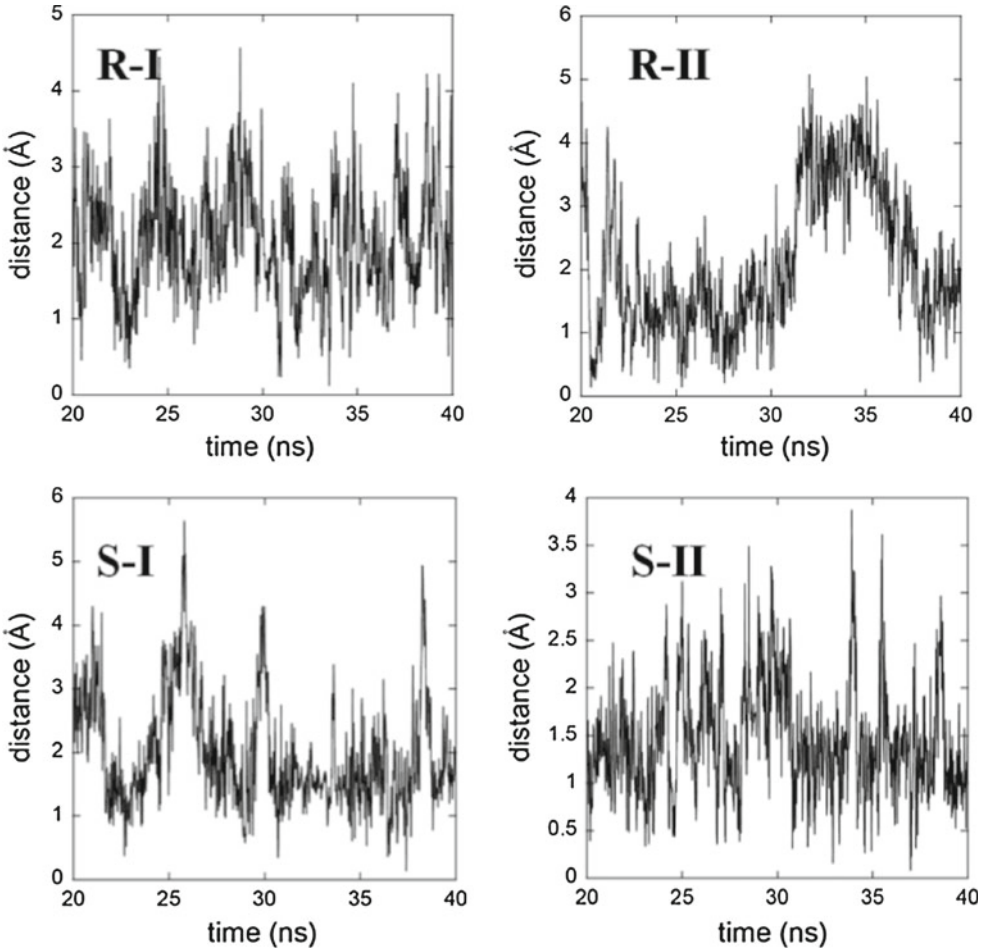


**Fig. 1** Distance between C4 atom and the center of mass of glycosidic oxygen atoms of β-cyclodextrin along the simulation time for four binding models

ketoprofen enantiomers. The phenomenon called chiral discrimination in the host–guest interaction has been observed in experimental way [49]. Here, we performed extensive MD simulations to examine the dynamic effects of β-CD interacting with the enantiomers of the ketoprofen.

Throughout the molecular dynamics simulations, all four inclusion complexes formed between ketoprofen and β-CD were maintained very well judged by the distance between the C4 atom of ketoprofen and the center of mass of glycosidic oxygen atoms as shown in Fig. 1. It looks like that for the *R*-ketoprofen, the binding orientation **I (R-I)** is much more stable than the other binding orientation (**R-II**) according to different binding fluctuation, while the difference between **S-I** and **S-II** models is smaller. Therefore, it could be deduced that a little smaller difference of binding affinity in *S*-conformation than that in *R*-conformation is expected. To get a direct view of the structural change along the simulation time, we further plotted corresponding snapshots from 20 ns to 40 ns for each binding conformer in Figs. 2 and 3. In most of simulation time, the ligand molecule is inserted into the cavity in tilted direction, which would ensure that the sugar ring has more interactions with aromatic rings of guest molecule. Such phenomenon has been found in the simulation of β-CD/steroid drug systems investigated by Cai et al. [22]. At least one aromatic ring (*A* or *B*) of ketoprofen was found to be included in the cavity during the simulation, but some apparent fluctuations of the binding position could be observed. Such pattern could partially indicate the hydrophobic interaction plays important role in the guest molecule recognition by β-cyclodextrin. For clarity, the time course profiles of the distance between the center of mass of aromatic ring *A* ($d^A_{\mathrm{cm}}$) or *B* ($d^B_{\mathrm{cm}}$) and the center of mass of the glycosidic oxygen atoms of the host molecule are depicted in Fig. 4. It should be noted that this distance could only be used to elucidate the fluctuations for the binding status of the aromatic rings, but not for the estimation of binding stability, since this distance is different from the definition of order parameter ($\xi$) used in free energy pathway calculations as we gave above. Clearly, different binding performance for chiral isomers can be observed. For the orientation **I**, along the simulation trajectory, we can see that the carboxylate group always points outward and cannot be included into the cavity of β-CD. Such binding pattern requires that at least one of aromatic rings of ketoprofen is recognized by the hydrophobic interior environment of β-CD. According

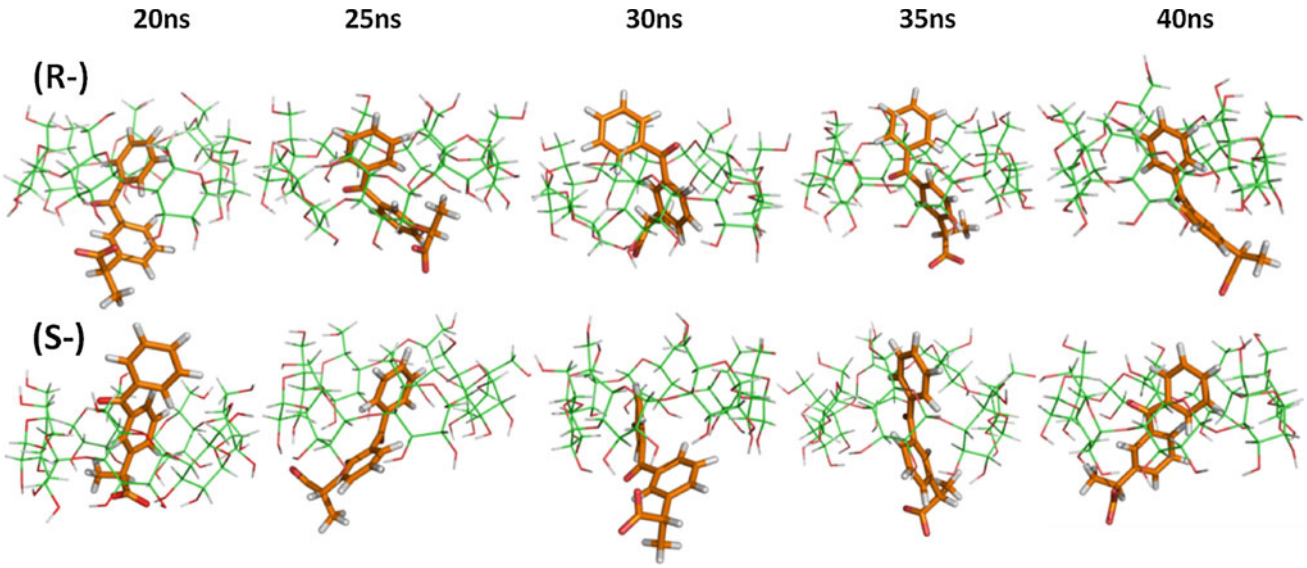


**Fig. 2** *Snapshots* of the inclusion complexes formed by the β-CD and (*R*-) and (*S*-)ketoprofen along the dynamics simulation time in orientation **I**, respectively. For clarity, the water molecules have been removed. The ketoprofen is plotted using stick style, while line style for β-CD

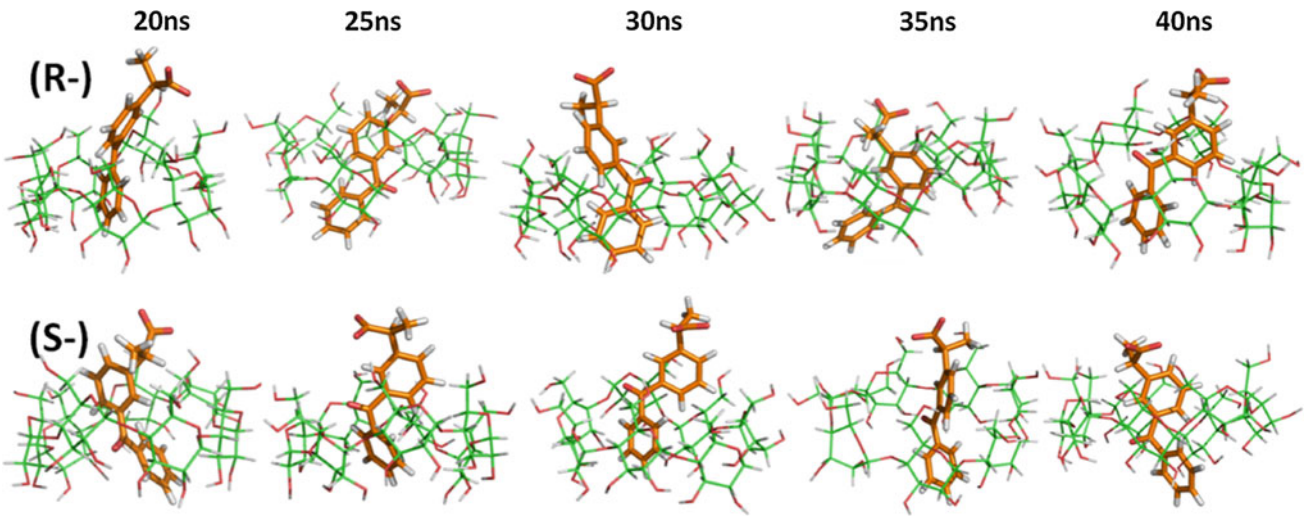


**Fig. 3** Snapshots of the inclusion complexes formed by the β-CD and (*R*-) and (*S*-)ketoprofen along the dynamics simulation time in orientation **II**, respectively. For clarity, the water molecules have been removed. The ketoprofen is plotted using stick style, while line style for β-CD

to the snapshots given in Fig. 2 and the relative position analysis between the benzene rings and β-CD in Fig. 4, the substantial fluctuation of the binding of the benzene rings is quite clear. That means both aromatic rings have chance to be included into the cavity. It thus suggests that β-CD cannot identify any specific aromatic ring of included ligand. If we recall the NMR spectroscopy of the inclusion complex of β-CD/ketoprofen [17], experimental work indicated that both rings (*A* and *B*) can be deeply embedded in the cavity with very close chemical shifts. Our results are then in reasonably agreement with this observation. For the binding orientation **II**, a little different binding pattern could be observed. Especially, we can see that ring *A* of *R*-II and ring *B* of *S*-II seem to be dominantly recognized by β-CD cavity. Such binding feature might be inconsistent with the experimental observations. This feature should be further examined by binding free energy calculations.

It is also interesting to examine the possibility of hydrogen bond formed between host and guest molecules, since there are a lot of hydroxyl groups in β-cyclodextrin and one carboxylate group in ketoprofen. We summarized the hydrogen bond occupancy analysis results in Table 1 over the MD trajectories for all four inclusion complexes. Quite low hydrogen bond occupancies were found between host

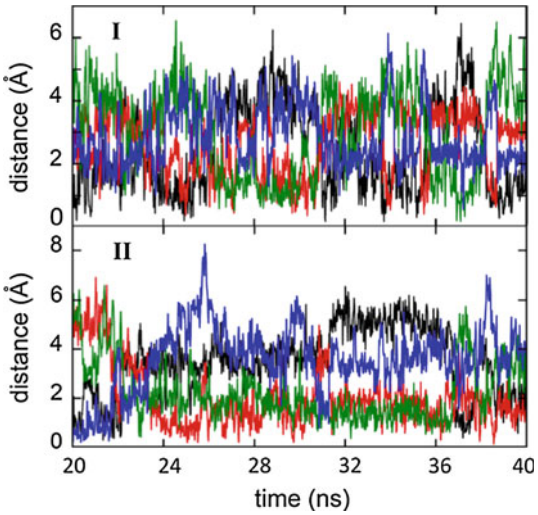


**Fig. 4** Distances between the aromatic rings of ketoprofen and the center of mass of seven glycosidic oxygen atoms of β-CD in binding orientation **I** (*panel I*) and in binding orientation **II** (*panel II*). For the binding of *R*-ketoprofen, $d^A_{cm}$ is colored in *black*, and $d^B_{cm}$ is colored in *green*. For the binding of *S*-ketoprofen, $d^A_{cm}$ is colored in *red*, and $d^B_{cm}$ is colored in *blue*

**Table 1** Hydrogen bonds network analysis for interactions between β-CD and (*R*-) and (*S*-)ketoprofen (KET)

| H-bond | Occupancy (%) | | | |
|---|---|---|---|---|
| | *R*-I | *S*-I | *R*-II | *S*-II |
| KET:O1···G7:O3 | 18.0 | – | – | – |
| KET:O3···G1:O2 | 13.8 | 16.1 | – | – |
| KET:O3···G1:O3 | 13.6 | 19.2 | – | – |
| KET:O1···G1:O2 | 13.4 | 18.6 | – | – |
| KET:O3···G7:O3 | 12.6 | – | – | – |
| KET:O1···G1:O3 | 10.8 | 16.9 | – | – |
| KET:O1···G5:O6 | – | – | 21.6 | – |
| KET:O1···G4:O6 | – | – | 12.4 | – |
| KET:O3···G5:O6 | – | – | 11.1 | – |
| KET:O1···G6:O6 | – | – | – | 14.2 |
| KET:O3···G6:O6 | – | – | – | 13.3 |
| KET:O1···G7:O6 | – | – | – | 11.8 |

Occupancy is in unit of percentage of the investigated time period (20 ns) during which specific hydrogen bonds are formed. The hydrogen bond is defined as the distance of acceptor and donor atoms shorter than 3.0 Å, and the internal angle of acceptor···H-donor is larger than 120°

and guest molecules. The biggest occupancy rate is just about 20 %. This supports from another angle that the hydrophobic interaction is possible the dominant factor in the stabilization of the inclusion complex. The electrostatic interactions should be considered to be a minor factor in the host–guest recognition. Indeed, the polar carboxylate group of ketoprofen is exposed to solvent molecules in almost most of simulation time no matter which rim it faces. However, the existence of the carboxyl group might be an issue to affect the formation of inclusion complex and the drug releasing, which we will discuss below using free energy calculations.

### 3.2 Binding free energy

Although binding models obtained from MD simulations can provide some insights into the guest molecule recognition, it is still difficult to identify which model is the favored one. Some quantitative measurements, such as absolute binding free energy calculation, can help us to get useful ideas. Due to chiral discrimination, different binding free energy for *R*- and *S*-enantiomers should be expected. Such results have been observed for the binding of ketoprofen, although researchers attributed the slight energetic difference into experimental uncertainty and thus cannot tell which the favored binding conformer is [17]. In this work, calculated absolute binding free energies are summarized in Table 2 for two binding orientations of both isomers, and the measured association free energies from different experimental sources [17, 18, 50–52] are included for comparison. The uncertainties for all of terms are included in the parentheses, which were calculated as the root mean square error for all of frames extracted in the MM/GBSA running. Overall, the calculated entropies for four binding models are negative, at the same time the enthalpies are also negative. This can suggest that the formation of inclusion complexes is an enthalpy driven process. For both *R*- and *S*-ketoprofen in binding orientation **I**, the calculated average binding free energy is around 3.8 kcal/mol, which is in excellent agreement with experimental values of ~4.0 kcal/mol listed in Table 2. On the other hand, for the orientation **II**, a little larger difference between experimental and theoretical values could be observed. This could suggest that for the inclusion complexes formed by β-CD and ketoprofen, the binding orientation **I**, the propionic acid group of ketoprofen facing the wider rim of β-CD, is more likely the favored conformer, no matter *R*- or *S*-isomer.

On the other hand, since marked ketoprofen is often in a molar ratio of 50:50 racemic nature, little efforts have been applied to examine the binding difference between two chiral models. Recently, to understand the chiral photoreaction properties, Marconi et al. [17] examined the stereoselective binding affinity of β-CD bound with ketoprofen enantiomers. It is not surprised that only very tiny difference for the binding free energies can be observed, −3.95 kcal/mol (**S**) versus 3.76 kcal/mol (**R**). The experimental work by Marconi et al. [17] suggests that β-CD can bind *S*-ketoprofen slightly stronger than its *R*-chiral conjugate, although they put this to be within experimental uncertainty. Our

**Table 2** Calculated absolute binding free energies for β-CD/(*R*-) and (*S*-)ketoprofen inclusion complex using MM/GBSA approach (comparison with experimental values)

We, in this work, calculated separately binding free energies of two binding orientations (**I** and **II**) for *R*- and *S*-ketoprofen isomers embedded into the β-CD cavity. Only Ref. [17] reports the binding free energies for two *R*- and *S*-ketoprofen enantiomers, other experimental work reports the binding free energies for the binding of ketoprofen with *R* and *S* isomers of 50:50 ratio

| Energy (kcal/mol) | *R*-ketoprofen | | *S*-ketoprofen | |
|---|---|---|---|---|
| | **I** | **II** | **I** | **II** |
| $\langle \Delta E_{ele} \rangle$ | −22.70 (3.21) | −25.34 (2.69) | −21.56 (3.47) | −25.09 (2.59) |
| $\langle \Delta E_{vdw} \rangle$ | −26.82 (16.71) | −19.56 (10.31) | −29.23 (16.70) | −20.18 (9.77) |
| $\langle \Delta G_{sol,nonpolar} \rangle$ | −2.98 (0.31) | −3.06 (0.27) | −2.93 (0.32) | −3.08 (0.26) |
| $\langle \Delta E_{gas} \rangle$ | −49.53 (16.71) | −44.90 (10.00) | −50.79 (15.81) | −45.26 (10.36) |
| $\langle \Delta G_{sol,GB} \rangle$ | 28.75 (12.57) | 26.28 (8.59) | 29.72 (12.28) | 25.56 (7.81) |
| $\langle \Delta E_{gas} + G_{sol} \rangle$ | −20.78 (4.78) | −18.62 (2.35) | −21.08 (4.37) | −19.70 (3.36) |
| $\langle -T\Delta S \rangle$ | 17.11 (2.20) | 16.26 (1.68) | 17.21 (1.94) | 16.57 (1.89) |
| $\langle \Delta G_{binding} \rangle$ | −3.67 | −2.36 | −3.87 | −3.13 |
| $\Delta G^{exp}_{binding}$ | −3.76 [17] | | −3.95 [17] | |
| | −3.96 [50] | | | |
| | −3.90 [51] | | | |
| | −3.97 [18] | | | |
| | −4.13 [52] | | | |

results are quite close this value, *esp.*, the binding orientation **I** with the calculated absolute binding free energies are −3.87 kcal/mol for **S-I**, while −3.67 kcal/mol for **R-I**. For the binding orientation **I**, the difference of binding free energy between two enantiomers is calculated to be 0.2 kcal/mol, which agrees well with experimental difference of 0.19 kcal/mol [17] as shown in Table 2. Our results are also in consistent with a recent computational work, which suggests that the β-cyclodextrin binds (*S*-)ketoprofen a little tightly than (*R*-)ketoprofen [53].

Another interesting issue is that for both chiral isomers, the stronger binding affinity can be observed for orientation **I** than orientation **II**, *esp.* the *R*-isomer, which is consistent with our MD simulation result as described in above section. However, the negative binding free energies for the orientation **II** still suggest that such an inclusion conformation should not be totally neglected. Indeed, our simulation on the orientation **II** has confirmed that this conformer for both enantiomers is pretty stable as shown in Fig. 1. In addition, X-ray structure has proved the existence of the orientation **II** for the ibuprofen/β-CD inclusion complex [20]. It should be noted that the deviation of the calculated binding free energies of orientation **II** is a bit larger than those of orientation **I**. Based on the calculated absolute binding free energies, we then suggest that the preferred binding mode of ketoprofen by the natural β-cyclodextrin might take the orientation **I** for both isomers no matter it is in *R*- or *S*-isomer. Of course, such conclusion awaits more accurate experimental work to confirm. To this end, there is no contradiction between our results and a recent NMR study on the inclusion of *R*- and *S*-ketoprofen, in which Marconi et al. [17] concluded that the carboxyl group of ketoprofen exposed to the solvent from secondary edge of the host.

Usually, there are two major factors that could affect the substrate binding, i.e., the electrostatic ($\Delta E_{ele} + \Delta G_{sol,\,GB}$) and nonpolar ($\Delta E_{vdW} + \Delta G_{sol,\,np}$) terms. It has long been accepted that the recognition of lipophilic molecules by β-CD is mainly due to hydrophobic interactions. The structural feature of aromatic included in the cavity revealed by MD simulation can support this proposal. Further, from Table 2, it can be seen that all four conformers agree this very well. For example, the electrostatic terms are calculated to be about 6.1, 1.0, 8.2 and 0.5 kcal/mol for **R-I**, **R-II**, **S-I** and **S-II** inclusion complexes, respectively. The electrostatic interaction is canceled out by the polar part of solvation. Positive values for electrostatic contribution indicate that polar interactions between host and guest molecules clearly disfavor the molecular recognition in the β-CD based inclusion complexes. In contrast, van der Waals interactions have dominantly favorable contributions to the binding affinity, as does the nonpolar part of solvation. The calculated total nonpolar terms are −29.8, −22.1, −31.2 and −23.2 kcal/mol for **R-I**, **R-II**, **S-I** and **S-II** inclusion complexes, respectively. Quite interestingly, much larger nonpolar terms for the orientation **I** than the orientation **II** can be obtained in our simulations. This is also in consistent with our deduction of stronger binding affinity for orientation **I** than orientation **II**, since the hydrophobic interaction is the dominant factor in the formation of host–guest system we studied in this work.

### 3.3 ABF calculations

The binding free energies obtained using MM/GBSA method can explain the recognition driving force to some extent. However, it cannot tell us how the drug molecule is included into the cavity of host molecule. At the same

time, it cannot identify the drug releasing direction and possible rate. To solve the problem, it is then necessary to examine the detailed energetic performance for the binding processes along the inclusion coordinates as depicted in Scheme 2. Calculated free energy profiles along the inclusion pathway for two binding orientations of *R*- and *S*-ketoprofen using ABF method are given in Figs. 5 and 6, respectively.

The free energy profile derived from ABF calculation could be integrated along the order parameters ($\xi$) to obtain a quantitative estimation of the association constant, $K_a$ [54]. When ketoprofen penetrates through the β-CD cavity, the sampled volume was restricted to a cylinder defined by the area ($A_{CD}$) available for in-plane movement of the guest molecule in the cavity ($A_{CD} = \pi r^2$) and the linear trajectory perpendicular to this area [55].

$$K_a = N_A A_{CD} \int \exp\left(-\frac{\Delta A(\xi)}{RT}\right) d\xi, \quad (5)$$

where $K_a$ is the system association constant with an unit of $M^{-1}$, $N_A = 6.02 \times 10^{23}$ is the Avogadro constant and the temperature $T$ is chosen at 300 K. For the choice of radius of the cylinder, it could be calculated to be the average radius along the ligand penetrating the cavity along the *z*-axis direction. In this work, we simply take the value of $r = 2$Å as suggested by Auletta et al. [55]. The integration ranged over the whole sampled pathway. The association free energy can be obtained again according to the relationship of $\Delta G = -\mathrm{RT} \ln K_a$. Calculated association constants and binding free energies of $\Delta G$ are listed in Table 3. The calculated association free energies are in excellent agreement with those values obtained using MM/GBSA method. Similarly, the association of *S*-isomer is systematically stronger than *R*-enantiomer, but with pretty small difference. For the binding orientation **I**, the results can be comparable to experimental values very well, with typical error less than 1.0 kcal/mol. These results could further indicate ABF method is one of suitable methods to address the energetic profiles for the formation of inclusion complexes. On the other hand, the results for the binding orientation **II** is not as good as those in orientation I. Considering the computational accuracy, our simulation results within both MM/GBSA and ABF frameworks seem to support that the inclusion complex formed in binding orientation **I** would be more likely the binding model observed in experimental way.

Since our simulations suggest that the model in orientation **I** would be the favored one, we will then focus on the free energy profiles depicted in Fig. 5. The overall topology of the free energy profiles for **R-I** and **S-I** is quite similar, which means that only a little difference can be observed in the chiral recognition. This is reasonable since there is only tiny difference for the chiral inclusion process revealed by

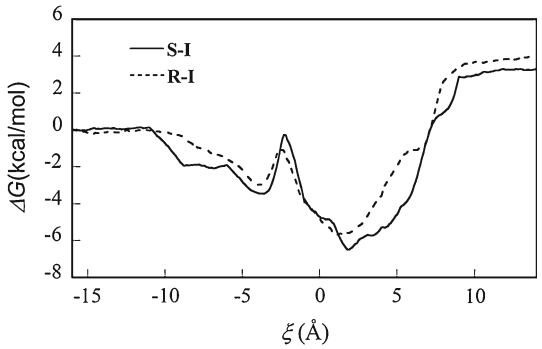


**Fig. 5** Free energy profiles via ABF calculations for the inclusion of ketoprofen into β-CD along the *z*-axis in binding orientation **I**, *S*-ketoprofen (*solid line*), *R*-ketoprofen (*dash line*)

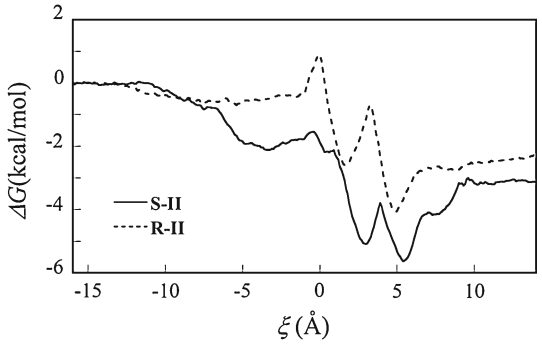


**Fig. 6** Free energy profiles via ABF calculations for the inclusion of ketoprofen into β-CD cavity in binding orientation **II**, *S*-ketoprofen (*solid line*), *R*-ketoprofen (*dash line*)

**Table 3** Calculated association constants and association free energies for all four binding models, and the experimental values from Ref. [17] are also included for comparison

| Models | $K_a$ ($M^{-1}$) | $\Delta G$ (kcal/mol) |
|---|---|---|
| **S-I** | 632.5 | −3.85 |
| **R-I** | 221.1 | −3.22 |
| **S-II** | 176.5 | −3.08 |
| **R-II** | 13.3 | −1.53 |
| Exp. [17] | | −3.95 (*S*) |
| | | −3.76 (*R*) |

*S* denotes the included compound is in *S*-enantiomer, while *R* represents the ligand is in its *R*-chiral conjugate

NMR experiments [17]. On the other hand, there are two distinguished energy minima along the order parameter, ca. $\xi = -3.6$ and 1.9 Å for **S-I**, while $\xi = -3.9$ and 1.1 Å for **R-I**, respectively. We then plotted corresponding snapshots in Fig. 7 for the inclusion of *S*-ketoprofen, and Fig. 8 for the inclusion of *R*-ketoprofen, which are all extracted from ABF trajectories. For the second minimum of **S-I**

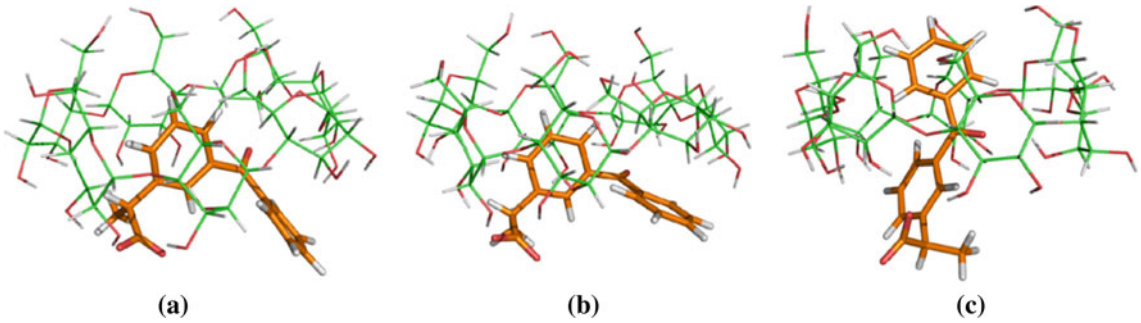


**Fig. 7** Snapshots of the inclusion complexes of *S*-ketoprofen with β-CD at the inflection points along the free energy curve in orientation I. **a** Near the first minimum, ca. $\xi = -3.6$ Å, **b** near the maximum, ca. $\xi = -2.6$ Å, **c** near the second minimum, ca. $\xi = 1.9$ Å

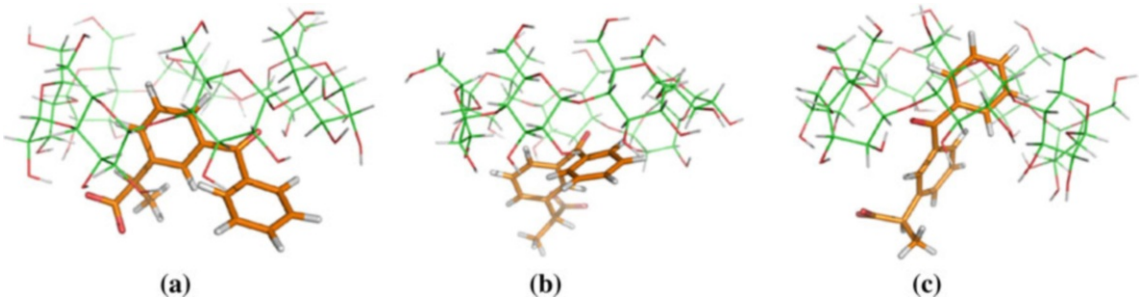


**Fig. 8** *Snapshots* of the inclusion complexes of *R*-ketoprofen with β-CD at the inflection points along the free energy curve in orientation I. **a** Near the first minimum, ca. $\xi = -3.9$ Å, **b** near the maximum, ca. $\xi = -2.3$ Å, **c** near the second minimum, ca. $\xi = 1.1$ Å

($\xi = 1.9$ Å) and **R-I** ($\xi = 1.1$ Å) models, two aromatic rings are fully inserted into the β-CD cavity to maximum the hydrophobic interactions, while the carboxyl group is facing the wider rim just as we have observed in MD simulations. Surprisingly, instead of the ring *A* included in the cavity, we can see that for the first minima at $\xi = -3.6$ Å (**S-I**) and $-3.9$ Å (**R-I**), the ring *B* is included by β-CD cavity. One barrier at $\xi = -2.3$ Å (**S-I**) and $-2.6$ Å (**R-I**) with a moderate barrier height can be observed to connect these two free energy minima, and the structures for two isomers are presented in Figs. 7 and 8, respectively. It looks like that this barrier stays at the stage of the ring *A* beginning entering the cavity, but not fully bounded. Such geometry transformation characteristics could explain why we can see significant fluctuations in the ligand binding dynamics presented above. However, if we carefully examine the structures, we may partially attribute this barrier to the carboxyl group of ketoprofen, which could form hydrogen bond network with hydroxyl groups around the secondary rim. To understand this issue, we then calculated the hydrogen bond occupancy between the carboxylate group and sugar hydroxyl groups within the ABF simulation window of [$-6.0$ and $-1.0$ Å]. The hydrogen bond occupancy for this oxygen atom is calculated to be about 35 %. Clearly, albeit the ring *A* is not included by the cavity, the existence of hydrogen bond between the carboxyl group and β-CD could still anchor the ketoprofen a little while. That will make the ring *B* has the chance to be bound in the cavity. Therefore, although the polar interaction has been proved to be a minor factor to stabilize the host–guest system, it still should be considered as one of the key factors to affect the formation of the inclusion complex.

Although we pull the ketoprofen from the wide edge to narrow rim in the ABF calculations, we can still take a look at the free energy in a recursive way. Quite interestingly, no barrier can be located for the ligand migration from the narrow rim into the cavity, for which the carboxyl group enters the cavity firstly. However, the barrier occurs along the *z*-axis positive direction, which means to enter the cavity from the wider edge, and it has to overcome a barrier height of 3.0 and 2.7 kcal/mol for *S*- and *R*-ketoprofen according to our calculations, respectively. In other words, we might safely conclude that to form the ketoprofen/β-CD inclusion complex, the polar carboxyl group will enter the cavity first, but finally two aromatic rings will be bound in the cavity as shown in Fig. 7. It should be emphasized here that the hydrophobic interactions constitute the major factor in the final formation of inclusion complex. Accounting for the ketoprofen releasing direction, it depends on the binding position of the carboxyl group, i.e., where the

carboxyl group occurs, and the releasing the drug could move out more easily through this direction. About 10 kcal/mol energy has to be overcome for bounded ligand to migrate from the cavity through the narrow edge. We might dedicate this carboxyl group as one of manipulate factors for the drug releasing issue. This is quite smart of nature. According to our simulations, it is thus possible to design some new drugs with a desired releasing rate.

## 4 Conclusion

Correct understanding the inclusion mechanism of β-CD complexed with small drug molecules would be of particular importance in the drug delivery. We, in this work, systematically investigated the free energy profiles of the inclusion complexes formed between natural β-CD and ketoprofen enantiomers. Our results support that the *R*- and *S*-ketoprofen prefer binding β-CD with their carboxylate groups facing the wider edge of the cavity (binding orientation **I**). Additionally, both MM/GBSA and ABF approaches suggest that β-CD has stronger affinity with *S*- than *R*-ketoprofen, which is also consistent with NMR measurement. Calculated binding free energies for the model of **S-I** and **R-I** using MM/GBSA and ABF are very close to the experimental values, which further confirm that both methods are suitable to deal with the recognition problem related with host–guest supramolecular system. It has also been proved that natural β-CD might not be a good chiral separation matter due to similar binding performance of ketoprofen enantiomers into the cavity. Therefore, various substituted CDs might be good candidates to fulfill this object. Nonetheless, our simulations reveal that the ketoprofen might move out more easily from the cavity via the position of carboxyl group occurring. This carboxyl group can be denoted as one of manipulate factors in the drug releasing. It is our hope that this could be helpful for the further drug design with desired drug releasing rate.

**Acknowledgments** This work was funded by National Science Foundation of China (Nos. 21073125 and 31170675) and the Program for New Century Excellent Talents in University (no. NCET-10-0606) to D. X., and by SRF for ROCS, SEM (No. 20111568-8-5) to C. Z. Parts of the results described in this paper are obtained on the Deepcomp7000 of Supercomputing Center, Computer Network Information Center of Chinese Academy of Sciences.

## References

1. Schneider H (2009) Angew Chem Int Ed 48:3924–3977
2. Fromming KH, Szejtli J (1994) Cyclodextrins in pharmacy. Kluwer, Dordrecht
3. Irie T, Uekama K (1999) Adv Drug Deliv Rev 36:101–123
4. Davis ME, Brewster ME (2004) Nature Rev Drug Discov 3:1023–1035
5. Del Valle EMM (2004) Process Biochem 39:1033–1046
6. Brewster ME, Loftsson T (2007) Adv Drug Deliv Rev 59:645–666
7. Loftsson T, Duchene D (2007) Int J Pharm 329:1–11
8. Nagaruju M, Sastry GN (2009) J Phys Chem A 113:9533–9542
9. Pandey S, Kumar B, Vijayendra Swamy SM, Gupta A (2010) Int J Pharm Technol 2:281–319
10. Stanier CA, O'Connell MJ, Anderson HL, Clegg W (2001) Chem Commun 5:493–494
11. Kuhnert N, Tang B (2006) Tetrahedron Lett 47:2985–2988
12. Avakyan VG, Nazarov VB, Alfimov MV, Bagatur'yants AA (1999) Russ Chem Bull 48:1833–1844
13. Kantor TG (1986) Pharmacotherapy 6:93–103
14. Neirinckx E, Croubels S, Remon JP, Devreese M, De Backer P, Vervaet C (2011) Vet J 190:290–292
15. Lu W, Zhang Q, Zheng L, Wang H, Li R, Zhang L, Shen W, Tu X (2004) Biol Pharm Bull 27:1515–1520
16. Maestrelli F, Gonzalez-Rodriguez ML, Rabasco AM, Mura P (2005) Int J Pharm 298:55–67
17. Marconi G, Mezzina E, Manet I, Manoli F, Zmabelli B, Monti S (2011) Photochem Photobiol Sci 10:48–59
18. Mura P, Bettinetti GP, Manderioli A, Faucci MT, Bramanti G, Sorrenti M (1998) Int J Pharm 166:189–203
19. Tayade PT, Vavia PR (2006) Ind J Pharm Sci 68:164–170
20. Braga SS, Goncalves IS, Herdtweck E, Teixeira-Dias JJC (2003) New J Chem 27:597–601
21. Brown G, Caira M, Nassimbeni L, Van Outtshoorn B (1996) J Incl Phenom Mol Recognit Chem 26:281–294
22. Cai W, Sun T, Liu P, Chipot C, Shao X (2009) J Phys Chem B 113:7836–7843
23. Morris GM, Huey R, Lindstrom W, Sanner MF, Belew RK, Goodsell DS, Olson AJ (2009) J Comput Chem 16:2785–2791
24. Jorgensen WL, Chandrasekhar J, Madura JD, Impey RW, Klein ML (1983) J Chem Phys 79:926–935
25. Frisch MJ, Trucks GW, Schlegel HB, Scuseria GE, Robb MA, Cheeseman JR, Scalmani G, Barone V, Mennucci B, Petersson GA, Nakatsuji H, Caricato M, Li X, Hratchian HP, Izmaylov AF, Bloino J, Zheng G, Sonnenberg JL, Hada M, Ehara M, Toyota K, Fukuda R, Hasegawa J, Ishida M, Nakajima T, Honda Y, Kitao O, Nakai H, Vreven T, Montgomery JA Jr, Peralta JE, Ogliaro F, Bearpark M, Heyd JJ, Brothers E, Kudin KN, Staroverov VN, Kobayashi R, Normand J, Raghavachari K, Rendell A, Burant JC, Iyengar SS, Tomasi J, Cossi M, Rega N, Millam JM, Klene M, Knox JE, Cross JB, Bakken V, Adamo C, Jaramillo J, Gomperts R, Stratmann RE, Yazyev O, Austin AJ, Cammi R, Pomelli C, Ochterski W, Martin RL, Morokuma K, Zakrzewski VG, Voth A, Salvador P, Dannenberg JJ, Dapprich S, Daniels AD, Farkas O, Foresman JB, Ortiz JV, Cioslowski J, Fox DJ (2009) Gaussian 09, Revision A.01. Gaussian, Inc., Wallingford CT
26. Kirschner KN, Yongye AB, Tschampel SM, González-outeiriño J, Daniels CR, Foley BLW, Wood RJ (2008) J Comput Chem 29:622–655
27. Darden TA, York D, Pedersen L (1993) J Chem Phys 98:10089
28. Ryckaert J-P, Ciccotti G, Berendsen HJC (1977) J Comput Phys 23:327–341
29. Lee FS, Chu ZT, Bolger MB, Warshel A (1992) Prot Eng 5:215–228
30. Åqvist J, Medina C, Samuelsson JE (1994) Prot Eng 7:385–391
31. Bren U, Martínek V, Florián J (2006) J Phys Chem B 110:10557–10566
32. Perdih A, Bren U, Solmajer T (2009) J Mol Model 15:983–996
33. Srinivasan J, Cheatham TE, Cieplak P, Kollman PA, Case DA (1998) J Am Chem Soc 120:9401–9409

34. Lee MS, Salsbury FR, Olson MA (2004) J Comput Chem 25:1967–1978
35. Naïm M, Bhat S, Rankin KN, Dennis S, Chowdhury SF, Siddiqi I, Drabik P, Sulea T, Bayly CI, Jakalian A, Purisima EO (2007) J Chem Inf Model 47:122–133
36. Gilson MK, Zhou H (2007) Annu Rev Biophys Biomol Struct 36:21–42
37. Kollman PA, Massova I, Reyes C, Kuhn B, Huo S, Chong L, Lee M, Lee T, Duan Y, Donini O, Wang W, Cieplak P, Srinivasan J, Case DA, Cheatham III TE (2000) Acc Chem Res 33:889-897
38. Hou T, Wang J, Li Y, Wang W (2011) J Comput Chem 32:866–877
39. Rizzo RC, Toba S, Kuntz ID (2004) J Med Chem 47:3065–3074
40. Strockbine B,Rizzo RC (2007) Proteins: Struct Funct Bioinform 67:630-642
41. Yang C, Sun H, Chen J, Coleska ZN, Wang S (2009) J Am Chem Soc 131:13709–13721
42. Onufriev A, Bashford D, Case DA (2000) J Phys Chem B 104:3712–3720
43. Sanner MF, Olson AJ, Spehner JC (1996) Biopolymers 38:305–320
44. Zoete V, Meuwly M, Karplus M (2005) Proteins 61:79–93
45. McQuarrie DA (2000) Statistical mechanics. University Science Books, Sausalito
46. Case DA (1994) Curr Opin Strut Biol 4:285–290
47. Darve E, Rodriigues-Gomez D, Pohorille A (2008) J Chem Phys 128:144120
48. Phillips JC, Braun R, Wang W, Gumbart J, Tajkhorshid E, Villa E, Chipot C, Skeel L, Schulten K (2005) J Comput Chem 26:1781–1802
49. Mason SF (1989) Chirality 1:183–191
50. Faucci MT, Melani F, Mura P (2002) Chem Phys Lett 358:383–390
51. Katritzky AR, Fara DC, Yang H, Karelson M, Suzuki T, Solovev VP, Varnek A (2004) J Chem Inf Comput Sci 44:529–541
52. Waters LJ, Bedford S, Parkes GMB, Mitchell JC (2010) Thermochim Acta 511:102–106
53. Felton LA, Popescu C, Wiley C, Esposito EX, Lefevre P, Hopfinger AJ (2014) AAPS Pharm Sci Technol 15:872–881
54. Shoup D, Szabo A (1982) Biophys J 40:33–39
55. Auletta T, de Jong MR, Mulder A, van Veggel FCJM, Huskens J, Reinhoudt DN, Zou S, Zapotoczny S, Schonherr H, Vancso GJ, Kuipers L (2004) J Am Chem Soc 126:1577–1584

Theor Chem Acc (2014) 133:1529
DOI 10.1007/s00214-014-1529-y

REGULAR ARTICLE

# State-to-state quantum dynamics of the $N(^4S) + C_2(\tilde{X}^1\Sigma^+) \rightarrow CN(\tilde{X}^2\Sigma^+) + C(^3P)$ reaction

**Xixi Hu · Changjian Xie · Daiqian Xie**

Received: 23 May 2014 / Accepted: 23 June 2014 / Published online: 8 July 2014
© Springer-Verlag Berlin Heidelberg 2014

**Abstract** Quantum dynamics of the $N(^4S) + C_2(\tilde{X}\,^1\Sigma^+) \rightarrow CN(\tilde{X}^2\Sigma^+) + C(^3P)$ reaction was investigated on a global potential energy surface for the $\tilde{a}^4A''$ state of $C_2N$ using a Chebyshev real wave packet method. This reaction is barrierless and has two deep wells corresponding to the CCN and CNC species, respectively. The numerous oscillations in reaction probabilities and highly excited rovibrational states of the product CN reflect the large exothermicity of the reaction and the feature of the potential. As expected for a complex-forming reaction, the rotational state distributions of the CN product were highly excited. The calculated vibrational state distributions of the CN product are in reasonably good agreement with the experimental results. The differential cross sections were found to be dominated by scattering in both forward and backward directions with a forward bias, suggesting that the reaction is not completely statistic and the lifetime of the reaction intermediate is not particularly long.

**Keywords** Quantum dynamics · Wave packet propagation · Reaction probability · Cross section

Dedicated to Professor Guosen Yan and published as part of the special collection of articles celebrating his 85th birthday.

X. Hu · C. Xie · D. Xie (✉)
Institute of Theoretical and Computational Chemistry, Key Laboratory of Mesoscopic Chemistry, School of Chemistry and Chemical Engineering, Nanjing University, Nanjing 210093, Jiangsu, China
e-mail: dqxie@nju.edu.cn

D. Xie
Synergetic Innovation Center of Quantum Information and Quantum Physics, University of Science and Technology of China, Hefei 230026, Anhui, China

## 1 Introduction

The CN radical is ubiquitous in the interstellar medium and has been observed in the dense clouds and around circumstellar envelopes [1–5], which is produced by the reactions such as [6, 7]

$$N + CH \rightarrow CN + H, \quad (1)$$

$$N + C_2 \rightarrow CN + C. \quad (2)$$

Both reactions also play important roles in the formation of CN (and $N_2$ indirectly) in interstellar clouds [8, 9]. For reaction (1), its rate constants were measured recently over the range of 56 K $\leq T \leq$ 296 K, which were excellently reproduced by our quantum mechanical calculations [10]. Based on the new rate constants, the CN abundance generated from the Nautilus gas-grain model is significantly less than the previous estimation, suggesting that this reaction is only a relatively minor source of the CN radical in dense clouds [10]. In addition, we further investigated quantum dynamics of reaction (1), which gave an intimate insight into the underlying reaction mechanism at a state-to-state level [11].

For reaction (2), both $N(^4S) + C_2(\tilde{X}^1\Sigma^+)$ and $N(^4S) + C_2(\tilde{a}^3\Pi_u)$ reactions lead to the products of $C(^3P)$ and $CN(\tilde{X}^2\Sigma^+)$. The rate constant of the $N(^4S) + C_2(\tilde{a}\,^3\Pi_u)$ reaction at room temperature was found to be $2.8 \times 10^{-11}$ cm$^3$ mol$^{-1}$ s$^{-1}$ from an experimental study by Becker et al. [12]. Very recently, Loison et al. [13] measured rate constants for the $N(^4S) + C_2(\tilde{X}^1\Sigma^+)$ reaction, which turned out to be much larger than the estimated value for the $N(^4S) + C_2(\tilde{a}^3\Pi_u)$ reaction. Astrochemical simulations showed that the title reaction should be dominant in the formation of CN in dense interstellar medium [13]. In addition, the vibrational distributions of the CN product produced by the exoergic indirect reaction (2) have

been measured by Daugey et al. [14, 15] with laser-induced fluorescence, which were found to be non-statistical. High-resolution photoelectron spectra of $C_2N^-$ obtained by using slow electron velocity-map imaging provided the first measurement of the low-lying $\tilde{a}^4\Sigma^-$ state of $C_2N$ [16].

Theoretically, geometric and vibrational characterizations of the low-lying electronic states of the $C_2N$ molecule have been calculated by several groups at various ab initio levels [17–23]. Near-equilibrium potential energy surface (PES) for the $\tilde{a}^4\Sigma^-$ state of the $C_2N$ radical has been constructed using correlated CCSD(T) method to study the ro-vibrational spectra by Hill et al. [22]. Very recently, we constructed a global PES for the $\tilde{a}^4A''$ state of $C_2N$ and calculated the rate constants of the title reaction, which showed good agreement with the recent experimental results [13]. To the best of our knowledge, there has been no theoretical study on the reaction dynamics of the title reaction, due to the lack of a global PES before.

In this work, we for the first time present an exact quantum mechanical study of the state-to-state integral and differential cross sections for the title reaction at the collision energies ranging from 0 to 0.16 eV, based on our new PES. This paper is organized as follows. In Sect. 2, we describe the ab initio calculations used to construct the PES and the details of the quantum mechanical calculations. The main characteristics of the PES, reaction probabilities, and cross sections are presented and discussed in Sect. 3. Finally, Sect. 4 gives a short summary.

## 2 Computational details

### 2.1 Potential energy surface

The title reaction can proceed adiabatically on the $\tilde{a}^4A''$ state, which is $\tilde{a}^4\Sigma^-$ in the linear geometries. The ab initio calculations were performed using internally contracted multi-reference configuration interaction method with Davidson correction (MRCI + Q) [24–26] employing the augmented correlation consistent polarized valence triple zeta (aug-cc-pVTZ) basis set, as implemented in the MOLPRO 2010 package [27]. All CI wave functions were based on the nature orbitals obtained from the state-averaged completed active space self-consistent field (SA-CASSCF) calculations for equally weighted $\tilde{a}^4A''$, $\tilde{b}^4A''$, and $\tilde{c}^4A'$ states. A full-valence active space involving 13 electrons in 12 orbitals was used in the CASSCF procedure, and three 1 s orbitals for both nitrogen and carbon atoms were kept doubly occupied but fully optimized. In the subsequent MRCI calculations, three 1*s* orbitals and one 2*s* orbital of the nitrogen atom were frozen. A total number of contracted configurations are typically 9795174.

**Table 1** Low-lying vibrational energy levels ($cm^{-1}$) of $C_2N$

| $(n_1, n_2, n_3)$ | $E$ | $(n_1, n_2, n_3)$ | $E$ |
|---|---|---|---|
| (0, 0, 0) | 0.0 | (2, 1, 0) | 2,851.4 |
| (0, 1 ,0) | 522.5 | (0, 6, 0) | 2,897.4 |
| (0, 2, 0) | 1,014.7 | (1, 0, 1) | 2,984.5 |
| (1, 0, 0) | 1,165.3 | (1, 4, 0) | 3,150.3 |
| | $(1{,}170 \pm 8)$[a] | (0, 3, 1) | 3,263.9 |
| (0, 3, 0) | 1,503.9 | (2, 2, 0) | 3,344.3 |
| (1, 1, 0) | 1,692.4 | (0, 7, 0) | 3,350.1 |
| (0, 0, 1) | 1,812.9 | (3, 0, 0) | 3,463.1 |
| (0, 4, 0) | 1,974.9 | (1, 1, 1) | 3,501.7 |
| (1, 2, 0) | 2,185.7 | (0, 0, 2) | 3,571.0 |
| (2, 0, 0) | 2,319.4 | (1, 5, 0) | 3,620.2 |
| (0, 1, 1) | 2,327.1 | (0, 4, 1) | 3,716.2 |
| (0, 5, 0) | 2,443.2 | (0, 8, 0) | 3,791.6 |
| (1, 3, 0) | 2,677.9 | (2, 3, 0) | 3,839.1 |
| (0, 2, 1) | 2,794.1 | (1, 2, 1) | 3,969.1 |

[a] Experimental value taken from Garand et al. [16]

The internal coordinates ($R_{NC}$, $R_{CC}$, $\theta_{N-C-C}$) were used to give a better description of the global PES. The PES was fitted with spline interpolation based on about 13,000 ab initio points ranging from $1.7 \le R_{NC}/a_0 \le 15.0$, $1.75 \le R_{CC}/a_0 \le 14.0$, and $0 \le \theta_{N-C-C}/\text{deg} \le 180$. The permutation symmetry of the two carbon atoms was kept by selecting the shorter NC bond as the NC coordinate in interpolation.

### 2.2 Vibrational energy levels

The vibrational energy levels of the $C_2N$ intermediate were calculated by solving the time-independent Schrödinger vibrational equation in the Jacobi coordinates ($R$, $r$, $\gamma$) using the Lanczos algorithm [28]. All energy levels were generated by carrying out about 2000 Lanczos recursion steps. For the two Jacobi radial coordinates $R$ and $r$, 120 potential-optimized discrete variable representation (PODVR) points [29] were used. And 110 Gauss–Legendre grid points [30] were used for the angular variable $\gamma$. The calculated energy levels, given in Table 1, are converged to be 0.01 $cm^{-1}$ or better.

### 2.3 Quantum dynamics

The reactive scattering dynamics were investigated using the Chebyshev real wave packet (CRWP) method. Since the details of the method can be found in earlier papers [31–34], only a brief description is given here. The Hamiltonian in the reactant Jacobi coordinates ($R$, $r$, $\gamma$) can be written as ($\hbar = 1$),

$$\hat{H} = -\frac{1}{2\mu_R}\frac{\partial^2}{\partial R^2} - \frac{1}{2\mu_r}\frac{\partial^2}{\partial r^2} + \frac{(\hat{J}-\hat{j})^2}{2\mu_R R^2} + \frac{\hat{j}^2}{2\mu_r r^2} + V(R, r, \gamma), \quad (3)$$

**Table 2** Numerical parameters (in atomic units) used in the wave packet calculations

| | |
|---|---|
| Grid/basis ranges and sizes | $R \in [0.01, 19.0],\ N_R^1 = 511,\ N_R^2 = 269$ |
| | $r \in [1.7, 15.7],\ N_r^1 = 323,\ N_r^2 = 59$ |
| | $\gamma \in [0, 180^\circ], j = 0 \sim j_{\max} = 300, N_j = 301$ |
| Projection | $R'_\infty = 12.0$ |
| Initial wave packet | $R_0 = 11.0, \delta = 0.1, E_0 = 0.05$ eV |
| Damping function | $D = \begin{cases} \exp[-0.01(\frac{R-14.0}{5.0})^2], & 14.0 \le R \le 19.0 \\ \exp[-0.09(\frac{r-14.9}{0.8})^2 - 0.007], & 14.9 < r \le 15.7 \\ \exp[-0.007(\frac{r-13.9}{1.0})^2], & 13.9 \le r \le 14.9 \\ 1, & \text{otherwise} \end{cases}$ |
| Spectral range | Potential energy cutoff: 7.5 eV |
| | Rotational kinetic energy cutoff: 5.5 eV |
| Propagation step | 60,000 |

where $\mu_r$ and $\mu_R$ are the reduced masses of the diatomic $C_2$ and $C_2N$, respectively. $J$ and $j$ denote the total and $C_2$ rotational angular momentum. The reactant Jacobi coordinates ($R$, $r$, $\gamma$) represent the distance between the N atom and the $C_2$ center, the $C_2$ bond length, and the angle between $R$ and $r$, respectively.

The Hamiltonian and wave packet were discretized in a mixed basis/grid representation [35]. To make the calculations efficient, an $L$-shaped grid was used for the radial coordinate [34]. For each total angular momentum $J$ and parity $p$, the wave function in the body-fixed (BF) frame can be expanded as,

$$\left|\Psi^{Jp}\right\rangle = \sum_{\alpha_r \alpha_R jK} C^{Jp}_{\alpha_r \alpha_R jK} |\alpha_r\rangle |\alpha_R\rangle |jK, Jp\rangle, \tag{4}$$

where $\alpha_r$ and $\alpha_R$ denote the grid indices for the two radial coordinates, and $K$ is the projection of $J$ onto the BF $z$-axis. The parity-adapted angular basis can be written as

$$\begin{aligned} |jK; Jp\rangle &= (2 + 2\delta_{K,0})^{-1/2} \\ &\times \Big( |JK\rangle |jK\rangle + p(-1)^J |J - K\rangle |j - K\rangle \Big), \end{aligned} \tag{5}$$

where $|jK\rangle \equiv Y_j^K(\gamma, 0)$ are normalized associated Legendre functions and $|JK\rangle \equiv \sqrt{(2J+1)/8\pi^2} D^J_{KM}$ are the parity-adapted normalized rotation matrix elements with the Wigner rotation functions $D^J_{KM}$ [36].

The initial wave packet $|\Psi_i\rangle$ in the space-fixed frame is defined as [35],

$$|\Psi_i\rangle = N e^{-(R-R_0)^2/2\delta^2} \cos k_0 R \left|\varphi_{v_i j_i}\right\rangle |j_i l_i, Jp\rangle, \tag{6}$$

where $N$ is a normalization factor, $R_0$ and $\delta$ represent, respectively, the initial position and width of the Gaussian function, $k_0 = \sqrt{2\mu_R E_0}$ is the mean momentum and $\left|\varphi_{v_i j_i}\right\rangle$ ($v_i = 0, j_i = 0$) is the eigenfunction of the initial rovibrational state of $C_2$. The initial wave function was transformed into the BF frame before propagation.

The propagation of the wave packet $|\Psi_k\rangle$ was performed using the modified Chebyshev recursion relation [37–39],

$$|\Psi_k\rangle = 2D\hat{H}_s |\Psi_{k-1}\rangle - D^2 |\Psi_{k-2}\rangle,\ k \ge 2, \tag{7}$$

where $D$ is a damping function. The propagation begins with $|\Psi_0\rangle = |\Psi_i\rangle$ and $|\Psi_1\rangle = D\hat{H}_s |\Psi_0\rangle$. The scaled Hamiltonian $\hat{H}_s$ is defined as

$$\hat{H}_s = (\hat{H} - H^+)/H^-, \tag{8}$$

in which $H^+$ and $H^-$ are the spectral medium and half width of the Hamiltonian, respectively, which can be calculated from the upper and lower spectral limits of the Hamiltonian ($H_{\max}$ and $H_{\min}$) with the relation $H^\pm = (H_{\max} \pm H_{\min})/2$.

The coordinate transformation method [34] was used to carry out final state projection in the product channel, which yields the $S$-matrix elements ($S^J_{v_f j_f K_f \leftarrow v_i j_i K_i}(E)$). The state-to-state integral cross section (ICS) can be then evaluated as

$$\begin{aligned} \sigma_{v_f j_f \leftarrow v_i j_i}(E) &= \frac{\pi}{(2j_i + 1) k^2_{v_i j_i}} \\ &\times \sum_{K_i} \sum_{K_f} \sum_J (2J+1) \left| S^J_{v_f j_f K_f \leftarrow v_i j_i K_i}(E) \right|^2, \end{aligned} \tag{9}$$

and the state-to-state differential cross section (DCS) is calculated as

$$\begin{aligned} &\frac{\mathrm{d}\sigma_{v_f j_f \leftarrow v_i j_i}(\vartheta, E)}{\mathrm{d}\Omega} \\ &= \frac{\pi}{(2j_i + 1)} \sum_{K_i} \sum_{K_f} \left| \frac{1}{2ik_{v_i j_i}} \sum_J (2J+1) d^J_{K_f K_i}(\vartheta) S^J_{v_f j_f K_f \leftarrow v_i j_i K_i}(E) \right|^2, \end{aligned} \tag{10}$$

in which $k_{v_i j_i}$ is the initial translational wave vector, $\vartheta$ is the scattering angle between the scattered CN + C product and the incoming N + $C_2$ reactant, and $d^J_{K_f K_i}(\vartheta)$ are the reduced Wigner rotational matrix elements [36].

The optimal numerical parameters listed in Table 2 were determined based on extensive convergence tests

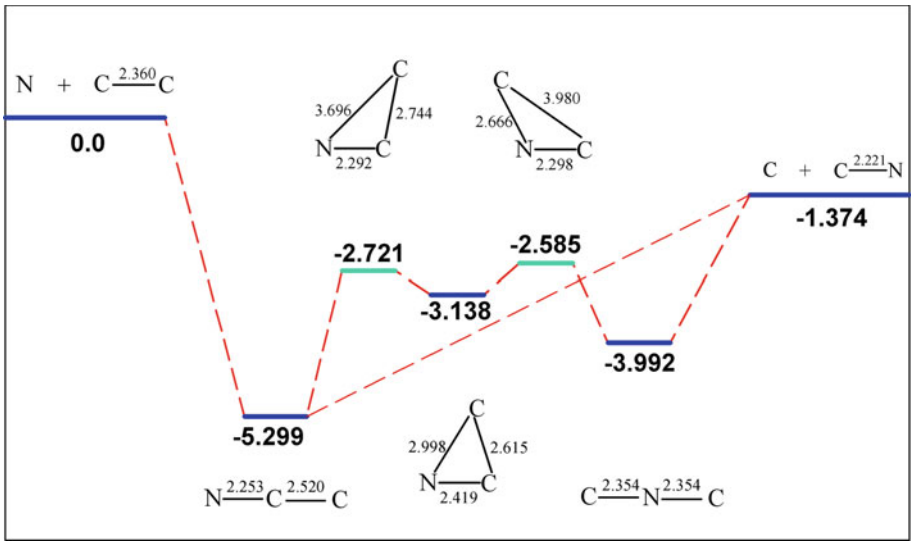


**Fig. 1** Energy diagram of the $N(^4S) + C_2(X^1\Sigma^+)$ reaction. The energies (in eV) are relative to the reactant. The geometries are presented with bond lengths (in bohr)

with respect to $J = 0$ reaction probability. A total of 60,000 Chebyshev propagation steps and large basis dimension were necessary for converging reaction probabilities due to deep wells in the reaction path. Partial waves for $J \leq 94$ were included to converge the ICS to 0.16 eV. For $J \leq 70$, a maximum $K$ value of 30 was found to converge the probabilities well, whereas $K_{max} = 45$ was used for $70 < J \leq 94$.

## 3 Results and discussion

### 3.1 Potential energy surface

The energies and geometries of the stationary points on the PES along the reaction pathways are shown in Fig. 1. The calculated exothermicity of the reaction is 1.322 eV including the zero point energies, which reasonably agrees with the experimental value of (1.48 ± 0.07) eV, estimated from the difference between the dissociation energies of $C_2(\tilde{X}^1\Sigma^+)$ and $CN(\tilde{X}^2\Sigma^+)$, which are (6.29 ± 0.02) [40] and (7.77 ± 0.05) eV [41], respectively. For the geometry of the global minimum, our result of ($2.253a_0$, $2.520a_0$, 180.0°) is in good agreement with the CCSD(T)/VQZ-F12 result of ($2.25a_0$, $2.51a_0$, 180.0°) by Hill et al. [22]. The reaction path shows no barrier and has two deep wells, corresponding to the linear $C_2N$ and CNC species, which are connected by two transition states and one intermediate. It is worth noting that there are conical intersections between the $\tilde{a}^4A''$ and $\tilde{b}^4A''$ states near the global minimum, which are not considered in the present work.

The vibrational energy levels, listed in Table 1, are labeled by three vibrational quantum numbers $n_1$, $n_2$, and $n_3$, representing the symmetric stretching, bending, and anti-symmetric stretching vibrations, respectively. The calculated fundamental frequencies of (1,165.3, 522.5, 1,812.9) $cm^{-1}$ are in good agreement with the anharmonic frequencies (1,178.5, 443.2, 1,821.8) $cm^{-1}$ of Hill et al. [22]. They are also consistent well with the harmonic fundamental frequencies reported by several groups, which are (1,111, 433, 1,915) $cm^{-1}$ at the CASSCF/cc-pVDZ level, (1,138, 434, 1,826) $cm^{-1}$ at the CCSD(T)/TZ2P level [19], and (1,101, 473, 1,910) $cm^{-1}$ at the CASSCF/6s4p2d2f level of theory [20]. Moreover, the fundamental frequency of 1,165.3 $cm^{-1}$ for the symmetric stretching vibrational mode is in excellent agreement with the experimental value of (1,170 ± 8) $cm^{-1}$ by Garand et al. [16].

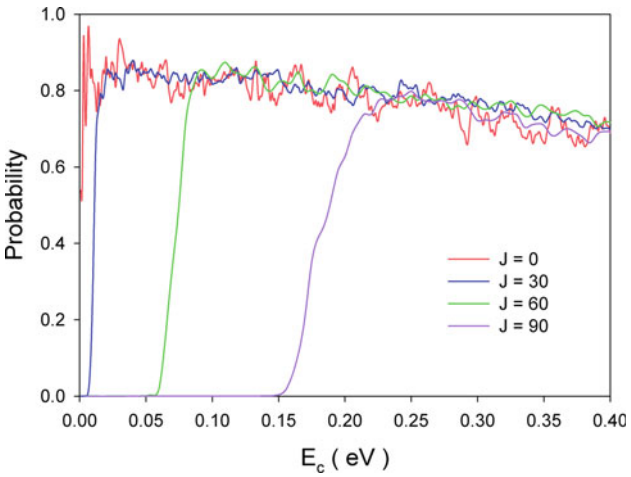


**Fig. 2** Calculated reaction probabilities for $J = 0$, 30, 60, and 90 as a function of collision energy

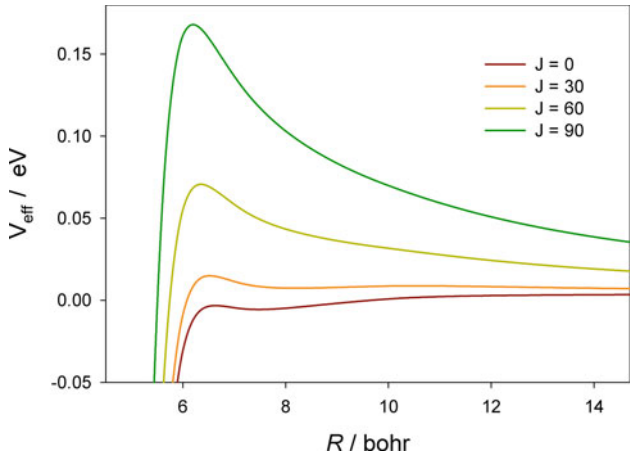


**Fig. 3** The effective potential energies including centrifugal potential as a function of Jacobi coordinate $R$ with optimized $r$ and $\gamma$ in the $N + C_2$ entrance channel at $J = 0$, 30, 60, and 90

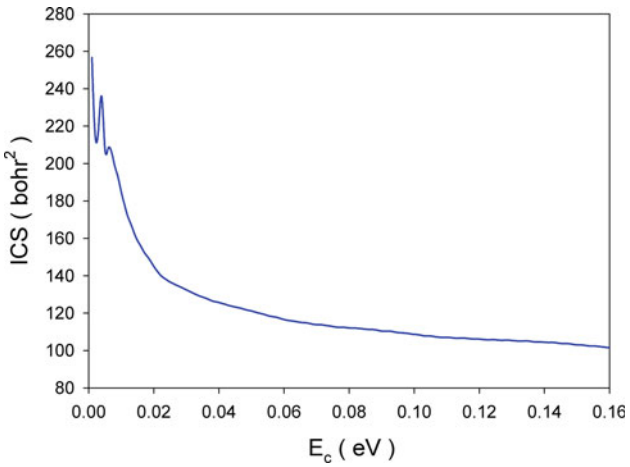


**Fig. 4** Calculated total ICS for title reaction as a function of collision energy

## 3.2 Reaction probabilities

The reaction probabilities for $J = 0$, 30, 60, and 90 are shown in Fig. 2 as a function of the collision energy $E_c$. It is worth noting that the probabilities are basically around a value of 0.8, which shows the high reactivity of this reaction. There is no energy threshold for $J = 0$ reaction probability, consistent with the fact that the PES has no intrinsic barrier in the reactant channel. The threshold appears when $J > 0$ and gradually gets larger, since the effective potential turns to be a higher barrier as $J$ increases due to the centrifugal potential $J(J + 1)/2\mu_R R^2$, as shown in Fig. 3. Moreover, the reaction probabilities consist of numerous sharp oscillations, which correspond to resonances supported by the two deep potential wells.

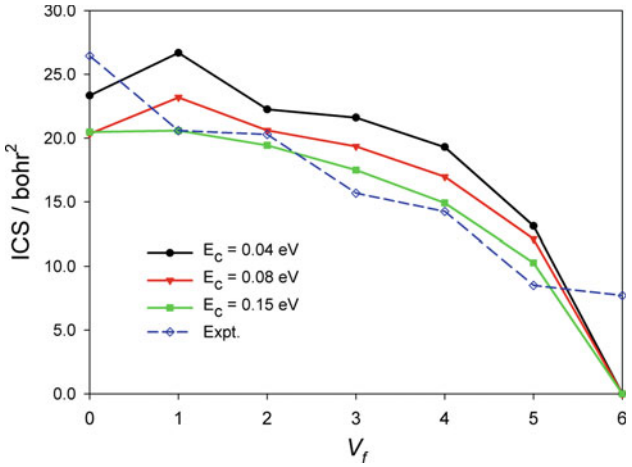


**Fig. 5** Calculated product vibrational state distributions at $E_c = 0.04$, 0.08, and 0.15 eV. The experimental values over the room temperature are taken from Ref. [14]

## 3.3 Cross sections

The total ICS calculated by summing over partial waves ($J \leq 94$) is shown in Fig. 4. In consistent to the reaction probabilities, the total ICS shows no threshold. In general, the ICS decreases monotonically with the increase of the collision energy, due to the barrierless reaction path and complex-forming mechanism.

Figure 5 presents the vibrational state distributions of the CN product at collision energies of 0.04, 0.08, and 0.15 eV, obtained by summing all rotational state populations in each vibrational channel. It can be seen that the CN vibration is excited up to 6 quanta. At a collision energy of 0.04 or 0.08 eV, a slight population inversion appears, which implies the non-statistical nature of the reaction. At higher energies, the vibrational state populations decrease with the vibrational quantum number $v_f$, consistent with the complex-forming mechanism. For comparison, the vibrational distribution measured at a distance of 4 mm from the reactant mixing zone by Daugey et al. [14] is also plotted in Fig. 5. It can be seen that their overall trends are similar. Since the reaction was investigated experimentally above room temperature, the reactant $C_2$, which is a mixture of $C_2(\tilde{X}^1\Sigma^+)$ and $C_2$ $(\tilde{a}^3\Pi_u)$, contains both ground and excited ro-vibrational states, whereas we considered only the reaction between $N(^4S)$ and $C_2(\tilde{X}^1\Sigma^+)$ in the specific initial state ($v_i = 0, j_i = 0$). This should be the major reason for the experiment–theory discrepancy.

So far, there has been no measured rotational state distribution of the CN product or theoretical prediction for the title reaction. The CN rotational state resolved ICSs at collision energy of 0.04, 0.08, and 0.15 eV are plotted in Fig. 6. The CN rotational state is highly excited up to

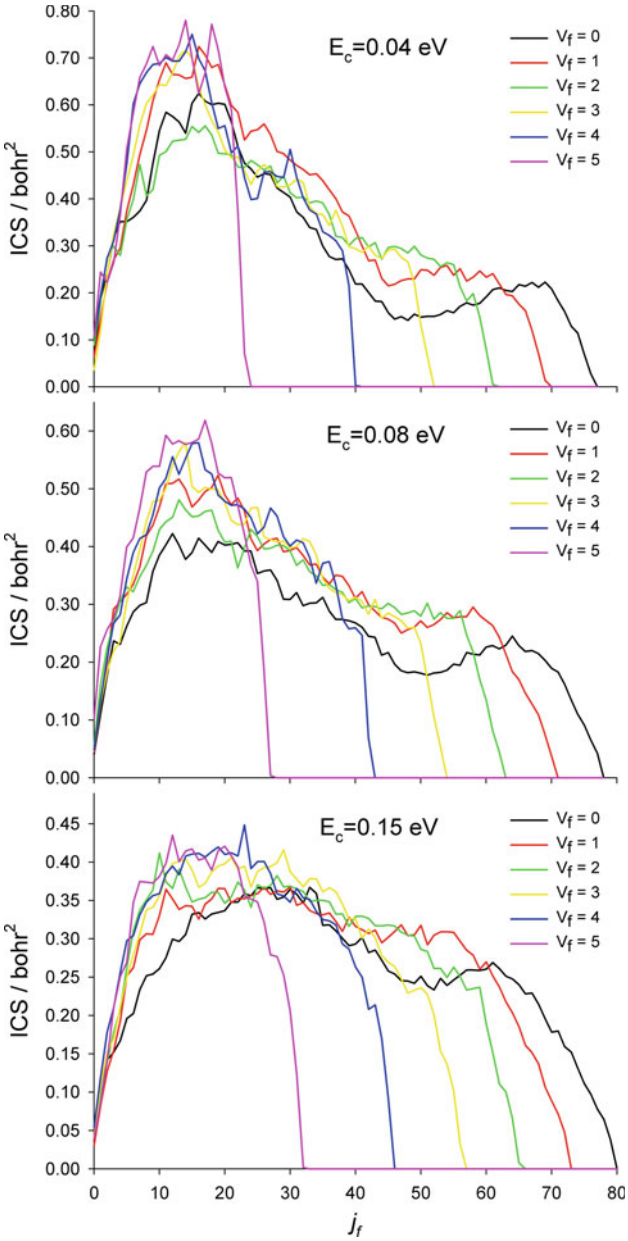


**Fig. 6** Calculated product rotational state distributions at $E_c = 0.04$, 0.08, and 0.15 eV

more than 76 quanta in the ground vibrational state, since the reaction is largely exothermic. The number of rotational excited states decreases with the increase of the vibrational quantum number. The oscillatory structures in all populations are obviously caused by resonances.

The DCSs at collision energies of 0.04, 0.08, and 0.15 eV are presented in Fig. 7. It can be seen that the DCSs are dominated by scattering in both forward and backward directions, also consistent with the complex-forming mechanism. However, the DCSs are not entirely symmetric. The forward bias is similar to the N + CH and

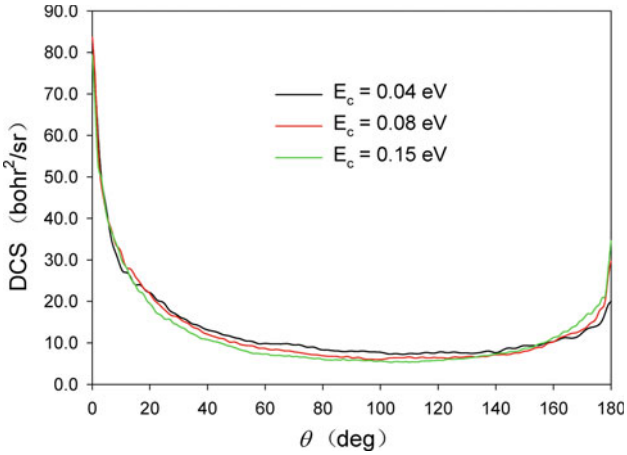


**Fig. 7** Calculated total DCSs for the title reaction as a function of scattering angle at $E_c = 0.04$, 0.08, and 0.15 eV

O + NH reactions [11, 42], suggesting that the reaction is non-statistic and the lifetime of reaction intermediate is not particularly long.

## 4 Conclusions

In this work, we reported the state-to-state quantum dynamics of the $N(^4S) + C_2(\tilde{X}^1\Sigma^+)$ reaction, based on a new global PES of the $\tilde{a}^4A''$ state for $C_2N$. The PES was fitted from more than 13,000 ab initio points calculated at the MRCI + Q level using the aug-cc-pVTZ basis set. The reaction path is barrierless and has two deep wells corresponding to the linear CCN and CNC species. The resonances supported by these deep wells manifest in reaction probabilities as numerous oscillations. The vibrational and rotational states of the CN product are highly excited. The agreement with the available experimental vibrational state distributions of the product CN is reasonably good. The DCSs were found to be dominated by scattering in both forward and backward directions with a forward bias, providing evidence for the non-statistic behavior of this complex-forming reaction.

**Acknowledgments** This work was supported by the National Natural Science Foundation of China (21133006, 21273104, and 91221301) and the Ministry of Science and Technology (2013CB834601).

## References

1. Suzuki H, Yamamoto S, Ohishi M, Kaifu N, Ishikawa S, Hirahara Y, Takano S (1992) Astrophys J 392(2):551
2. Ohishi M, Kaifu N (1998) Faraday Discuss 109:205
3. Ungerechts H, Bergin EA, Goldsmith PF, Irvine WM, Schloerb FP, Snell RL (1997) Astrophys J 482(1):245
4. Bachiller R, Fuente A, Bujarrabal V, Colomer F, Loup C, Omont A, de Jong T (1997) Astron Astrophys 319(1):235

5. Bakker EJ, van Dishoeck EF, Waters L, Schoenmaker T (1997) Astron Astrophys 323(2):469
6. Federman SR, Strom CJ, Lambert DL, Cardelli JA, Smith VV, Joseph CL (1994) Astrophys J 424(2):772
7. Klisch E, Klaus T, Belov SP, Winnewisser G, Herbst E (1995) Astron Astrophys 304(1):L5
8. Hily-Blant P, Walmsley M, des Forets GP, Flower D (2010) Astron Astrophys 513:A41
9. Daranlot J, Hincelin U, Bergeat A, Costes M, Loison J-C, Wakelam V, Hickson KM (2012) Proc Natl Acad Sci USA 109(26):10233
10. Daranlot J, Hu X, Xie C, Loison J-C, Caubet P, Costes M, Wakelam V, Xie D, Guo H, Hickson KM (2013) Phys Chem Chem Phys 15(33):13888
11. Hu X, Xie C, Xie D, Guo H (2013) J Chem Phys 139(12):124313
12. Becker KH, Donner B, Dinis CMF, Geiger H, Schmidt F, Wiesen P (2000) Z Phys Chem 214:503
13. Loison J-C, Hu X, Han S, Hickson KM, Guo H, Xie D (2014) Phys Chem Chem Phys 16(27):14212
14. Daugey N, Bergeat A, Schuck A, Caubet P, Dorthe G (1997) Chem Phys 222(1):87
15. Daugey N, Bergeat A, Loison JC, Schuck A, Caubet P, Dorthe G (2000) Chem Phys Lett 324(1–3):1
16. Garand E, Yacovitch TI, Neumark DM (2009) J Chem Phys 130(6):064304
17. Thomson C (1973) J Chem Phys 58(3):841
18. Gabriel W, Reinsch EA, Rosmus P (1994) Chem Phys Lett 231(1):13
19. Martin JML, Taylor PR, Francois JP, Gijbels R (1994) Chem Phys Lett 226(5–6):475
20. Pd R, Chandra P (2001) J Chem Phys 114(4):1589
21. Ehara M, Gour JR, Piecuch P (2009) Mol Phys 107(8–12):871
22. Hill JG, Mitrushchenkov A, Yousaf KE, Peterson KA (2011) J Chem Phys 135(14):144309
23. Hansen JA, Piecuch P, Lutz JJ, Gour JR (2011) Phys Scr 84(2):028110
24. Langhoff SR, Davidson ER (1974) Int J Quantum Chem 8(1):61
25. Knowles PJ, Werner HJ (1988) Chem Phys Lett 145(6):514
26. Werner HJ, Knowles PJ (1988) J Chem Phys 89(9):5803
27. Werner H-J, Knowles PJ, Knizia G, Manby FR, Schütz M, Celani P, Korona T, Lindh R, Mitrushenkov A, Rauhut G, Shamasundar KR, Adler TB, Amos RD, Bernhardsson A, Berning A, Cooper DL, Deegan MJO, Dobbyn AJ, Eckert F, Goll E, Hampel C, Hesselmann A, Hetzer G, Hrenar T, Jansen G, Koppl C, Liu Y, Lloyd AW, Mata RA, May AJ, McNicholas SJ, Meyer W, Mura ME, Nicklass A, O'Neill DP, Palmieri P, Pflüger K, Pitzer R, Reiher M, Shiozaki T, Stoll H, Stone AJ, Tarroni R, Thorsteinsson T, Wang M, Wolf A (2010) MOLPRO 2010.1
28. Lanczos C (1950) J Res Natl Bur Stand 45(4):255
29. Echave J, Clary DC (1992) Chem Phys Lett 190(3-4):225
30. Lill JV, Parker GA, Light JC (1982) Chem Phys Lett 89(6):483
31. Sun Z, Lin X, Lee S-Y, Zhang DH (2009) J Phys Chem A 113(16):4145
32. Sun Z, Lee S-Y, Guo H, Zhang DH (2009) J Chem Phys 130(17):174102
33. Ma J, Lin SY, Guo H, Sun Z, Zhang DH, Xie D (2010) J Chem Phys 133(5):054302
34. Sun Z, Guo H, Zhang DH (2010) J Chem Phys 132(8):084112
35. Lin S, Guo H (2006) Phys Rev A 74(2):022703
36. Zare RN (1988) Angular Momentum. Wiley, New York
37. Mandelshtam VA, Taylor HS (1995) J Chem Phys 103(8):2903
38. Gray SK, Balint-Kurti GG (1998) J Chem Phys 108(3):950
39. Chen RQ, Guo H (1996) J Chem Phys 105(9):3569
40. Urdahl RS, Bao YH, Jackson WM (1991) Chem Phys Lett 178(4):425
41. Costes M, Naulin C, Dorthe G (1990) Astron Astrophys 232(1):270
42. Li A, Xie C, Xie D, Guo H (2013) J Chem Phys 138(2):024308

Theor Chem Acc (2014) 133:1549
DOI 10.1007/s00214-014-1549-7

REGULAR ARTICLE

# Mechanism and regioselectivity of the cycloaddition between nitrone and dirhodium vinylcarbene catalyzed by $Rh_2(O_2CH)_4$: a computational study

**Xin Yang · Pan Xu · Ying Xue**

Received: 24 May 2014 / Accepted: 16 July 2014 / Published online: 9 August 2014
© Springer-Verlag Berlin Heidelberg 2014

**Abstract** The B3LYP density functional studies on the cycloaddition between nitrone and dirhodium vinylcarbene with subsequent cascade carbenoid aromatic cycloaddition/N–O cleavage and rearrangement revealed the energetics and the geometries of important intermediates and transition states in the catalytic cycle. The reaction initially occurs through a stepwise [3+2]-cycloaddition in which the dirhodium carbene activates the adjacent vinyl group for [3+2]-cycloaddition by the nitrone. Driven by the reactivity of the carbene carbon, intramolecular cyclopropanation takes place to release the catalyst, followed by the electrocyclic opening of the cyclopropane ring to form a seven-membered ring intermediate. N–O cleavage and [1,7]-oxygen migration to final product proceed in a single step with a high activation energy. With *meta*-substituent (Cl) in the *N*-aryl group, the charge density of chlorine's *ortho*-site decreases due to the negative inductive effect of chlorine. Therefore, as compared to the electrophilic addition on the $C^8$ atom, the electrophilic addition on the $C^9$ site owns a significantly incensement on the energy barrier of cyclopropane (**TSIII** and **TSIX**). In addition, according to the calculations, the basicity of the product **4** is stronger than that of the product **5**. So an acidic compound 1,1,1,3,3,3-hexafluoro-2-propanol added in the experimental study (Wang et al. in Angew Chem Int Ed 51:5907–5910, 2012) more easily reacts with **4** than **5** and thus promotes the formation of product **4**.

**Keywords** Dirhodium vinylcarbene · DFT calculation · Transition state · Reaction mechanism · Regioselectivity

## 1 Introduction

Diazo compounds have been extensively studied during the last few decades, and their value in organic synthesis is well known [1–5]. Transition-metal carbenoids derived from reactions of diazo compounds with a variety of metal complex are versatile intermediates in organic synthesis [6]. For several years, the rhodium-catalyzed reactions of donor/acceptor-substituted carbenoids have been explored, and the results showed that those carbenoids display much greater chemoselectivity when compared to the more conventional acceptor-substituted carbenoids [7–10]. A clear example of this effect is seen in a Hammett study of intermolecular cyclopropanation of *para*-substituted styrenes (Scheme 1) [11]. Electronic character of styrenes [$\rho$ value of $-0.9$ ($\sigma^+$ scale)] can strongly affect the relative rates of reaction of methyl phenyldiazoacetate with various styrenes, while ethyl diazoacetate shows virtually no selectivity [11]. The greater chemoselectivity of the donor/acceptor carbenoids has opened up a number of reactions that were previously not viable with conventional carbenoids. In particular, vinylcarbene intermediates derived from vinyldiazoacetates exhibit a high level of selectivity in cyclopropanation [12–14] and carbon–hydrogen insertion reaction [15–17] and can participate in a diverse array of more elaborate transformation [15, 18, 19], such as the

Dedicated to Professor Guosen Yan and published as part of the special collection of articles celebrating his 85th birthday.

**Electronic supplementary material** The online version of this article (doi:10.1007/s00214-014-1549-7) contains supplementary material, which is available to authorized users.

X. Yang · P. Xu · Y. Xue (✉)
Key Laboratory of Green Chemistry and Technology in Ministry of Education, College of Chemistry, Sichuan University, Chengdu 610064, People's Republic of China
e-mail: yxue@scu.edu.cn

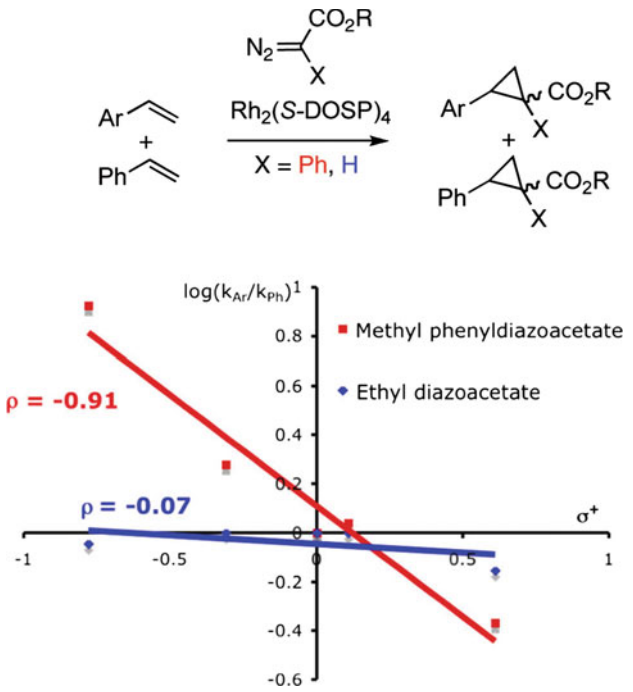


**Scheme 1** Competition reaction with styrene. Using metal carbenoids. Reproduced with permission from Ref. [11] Copyright 2000, ScienceDirect

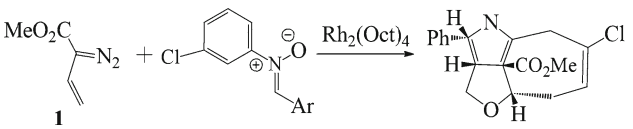


**Scheme 2** Dirhodium vinylcarbene-induced nitrone cycloaddition with subsequent cascade carbenoid aromatic cycloaddition/N–O cleavage and rearrangement (CACR)

combined C–H insertion/cope rearrangement [18], and the ylide formation/[2,3]-sigmatropic rearrangement/oxy-cope rearrangement/ene reaction cascade sequence [19]. Furthermore, their propensity for formal [3+2] [20–22] and [4+3] [23–26] cycloaddition reactions has been demonstrated.

Recently, Doyle et al. reported an efficient and highly regioselective cycloaddition reaction between the vinylcarbene from methyl 2-diazo-3-butenoate **1** and diverse nitrones catalyzed by rhodium octanoate [$Rh_2(Oct)_4$] (Scheme 2) [27]. The dirhodium vinylcarbene induced nitrone cycloaddition with subsequent cascade carbenoid aromatic cycloaddition/N–O cleavage, and rearrangement (CACR) gave products which have both oxygen and nitrogen-fused rings and a quaternary carbon in the middle. The compound structure obtained by X-ray diffraction of a single crystal reveals that extensive rearrangement has occurred, and the carboxylate group from the vinyldiazoacetate is bound to the quaternary carbon that connects the tricycle. Even though the reactions were carried out at room temperature, the products of the process were formed with remarkable specificity, and this type of reaction can be used as a general and selective method for preparation of multi-functionalized tricyclic heterocycles through an abnormal cascade process. A further surprising feature of the reactions is that, with *meta*- and *ortho*-substituents on the *N*-aryl group, cyclopropanation could have occurred on either side of the *N*-aryl bond, which would have led to the formation of two regioisomers; however, only a single regioisomer was formed in high yields. Therefore, this multi-step cascade process occurred with very high regiocontrol. This class of reaction has already become a standard method for laboratory and is being considered as a promising protocol for commercial process [28–30].

In light of the experimental results and for further development of the CACR chemistry, it was felt that the deeper understanding of the reaction mechanism, in particular the origins of the observed selectivity on the molecular scale, was indispensable. We report herein the pathways of the rhodium-catalyzed reactions of methyl 2-diazo-3-butenoate and nitrone by using the density functional calculations, which provide the first qualitative account of the experimental data, as well as the structures of important intermediates and transition states involved in the catalytic cycle. The calculations explain how the CACR happens and disclose the reason why the reaction can have such high regioselectivity. It is worthwhile to mention that this is the first report on reaction mechanism for the CACR reaction in detail. The theoretical analysis of the properties of intermediates and transition states revealed unique roles of the rhodium carbene. The studies and mechanistic insights obtained herein can ultimately provide value in accelerating the design and optimization of catalytic processes of transition-metal-catalyzed carbene procedures.

## 2 Computational methods

### 2.1 Models

In the present work, we have studied a catalytic model reaction between vinylcarbenoid complex **2** and nitrone **3** to form two different products **4** and **5** using dirhodium tetrakis (formate), $Rh_2(O_2CH)_4$, as a model of a common catalyst [31–34] (Scheme 3). Product **4** is in accord with the actual synthetic compound. The reaction to generating product **5** has not been reported in the literature and was investigated herein for comparison in regioselectivity. These model reactions serve to investigate the fundamental properties of the dirhodium carbene complex, as well as the mechanism and regioselectivity of CACR reactions. The vinylcarbenoid model **2** has been described in previous

**Scheme 3** Model reactions for the computational studies

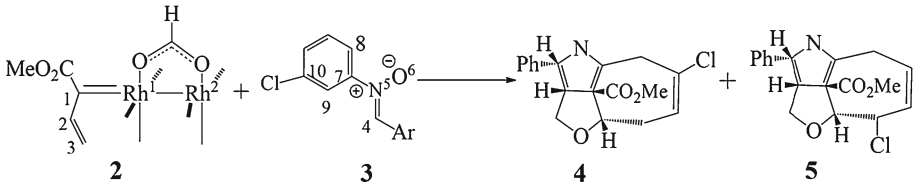


**2** **3** **4** **5**

computational studies on cyclopropanation chemistry [31, 34]. This study is focused on an analysis of how the rhodium carbenoid reacts with the nitrone. For detailed discussions on the formation of the reactive vinylcarbenoid complex, see Refs. [31, 34].

### 2.2 Computational details

All of the calculations were performed with the Gaussian 09 software package [35]. Density functional theory (DFT) was employed using the three-parameter hybrid functional B3LYP [36, 37] to locate stationary points on the potential energy surface (PES). Structures were optimized with a basis set consisting of the 1997 stuttgart relativistic small-core effective core-potential and basis set [Stuttgart RSC 1997 ECP] [38–40] for Rh, augmented with a 4f-function ($\zeta_f$(Rh) = 1.350) [31] and the split valence basis set 6-31G(d,p) for all other atoms (C, H, N, Cl and O). The method and the basis sets used here are known to give reliable results for rhodium (carbene) reactions [5]. This composite basis set is abbreviated 6-31G(d,p)[Rh-RSC+4f]. The main discussion is based on single-point energies calculated at the B3LYP/6-311+G(2d,2p)[Rh-RSC+4f]//B3LYP/6-31G(d,p)[Rh-RSC+4f] level of theory, with zero-point energy corrections calculated at the B3LYP/6-31G(d,p)[Rh-RSC+4f] level and Gibbs free energies calculated at the B3LYP/6-31G(d,p)[Rh-RSC+4f] level of theory. Heavy-atom basis set definitions and corresponding pseudopotential parameters were obtained from the EMSL basis set exchange library [41, 42]. Each stationary point was adequately characterized by normal coordinate analysis (only one imaginary for a transition state and no imaginary frequencies for an equilibrium structure). The intrinsic reaction coordinate (IRC) analysis [43] was carried out throughout the reaction pathways to confirm that all stationary points are smoothly connected to each other.

To evaluate the effect of the solvent polarity on the energetics of CACR reactions, a single-point energy calculation was performed with self-consistent reaction field (SCRF) method [based on the SMD model [44], $\varepsilon = 10.125$ for dichloroethane (DCE)]. Natural population analysis and natural bond orbital (NBO) analyses were carried out at the same level as the one used for geometry optimization [45, 46]. All charge distribution analyses discussed throughout this article are made on the basis of the nature population analysis.

## 3 Results and discussion

### 3.1 Reaction to produce the real product 4

First, we investigated the reactions of **3** with vinylcarbenoid complex **2** to generate product **4** as a basic model reaction. Scheme 4 shows the reaction course that the catalytic cycle involves five steps. The free energy profile of this CACR reaction in the gas phase is given in Fig. 1. First, **3** and **2** interact through a stepwise [3+2] cycloaddition to form the complex **III**. The formation of C–O bond proceeds via **TSI** with an activation free energy of 2.8 kcal/mol, which is followed by the formation of C–C bond with the activation free energy barrier of 4.5 kcal/mol. Subsequent intramolecular cyclopropanation by the rhodium carbene on the nitrogen-bound aryl group is proposed to form intermediate **V** via two transition states **TSIII** and **TSIV** with the free energy barriers of 10.2 and 7.6 kcal/mol, respectively, and the catalyst is regenerated. The next step toward the final product first involves an electrocyclic opening of the cyclopropane ring (aromatic cycloaddition) to form intermediate **VI** via **TSV** with a free energy barrier 4.5 kcal/mol. Unexpected and unique N–O bond cleavage and [1,7]-oxygen migration then take place through **TSVI** with the largest free energy barrier of 22.2 kcal/mol followed by a downhill path to the final product with large exothermicity (64.7 kcal/mol). In **TSVI**, the cleavage of N–O bond and migration of oxygen to conjugated olefinic carbon atom take place simultaneously in a single step. No intermediates were located near **TSVI** along the intrinsic reaction coordinate.

To probe the solvent effect on the reaction energetics, SCRF calculations (SMD model) were performed based on the gas-phase geometry. Dichloroethane (DCE, $\varepsilon = 10.125$) was investigated as the solvent because it is used for the CACR reaction in practice. The relative free energies of the stationary points on the potential energy surface in DCE are also given in Fig. 1 (in blue). The free energy profile did not change very much from the one in the gas-phase calculations. The N–O cleavage and [1,7]-oxygen migration processes have the largest free energy barrier (19.6 kcal/mol in DCE). Therefore, this step can be regarded as the rate-determining step (RDS). Moreover, the free energy barrier for **TSVI** has a small decrease, and the energy barrier for cyclopropanation has a slight increase. As compared to the free energy profile in gas phase, the [1,7]-oxygen migration

**Scheme 4** Pathway of the $Rh_2(O_2CH)_4$-catalyzed CACR reaction of **2** and **3** to produce **4**

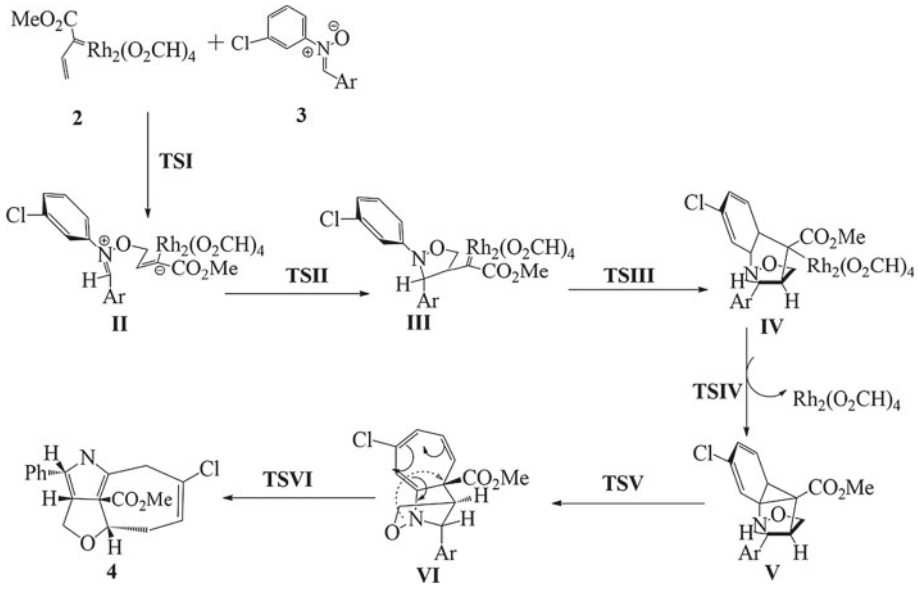


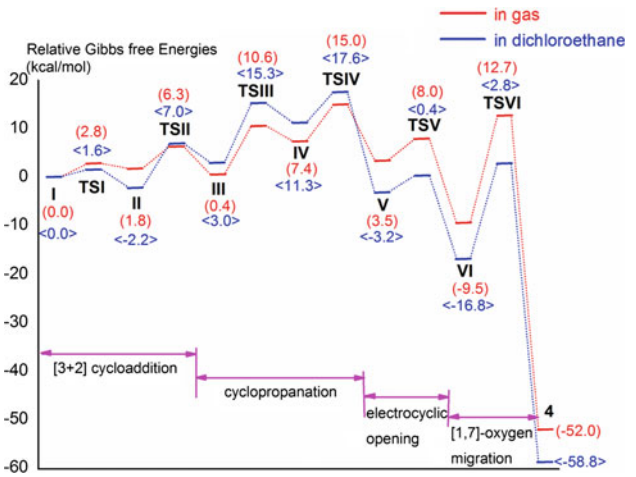


**Fig. 1** Free energy profile of the $Rh_2(O_2CH)_4$-catalyzed CACR reaction of **2** and **3** to produce **4** at the B3LYP/6-311+G(2d,2p)[Rh-RSC+4f]//B3LYP/6-31G(d,p)[Rh-RSC+4f] level. The result of the free energies in gas phase is given in *red*, and the result of the free energies in DCE is shown in *blue*

step has the highest energy barrier, which suggests that how to overcome the energetic bottleneck for the [1,7]-oxygen migration becomes very crucial for accelerating the reaction rate.

The 3D structures of representative stationary points are shown in Fig. 2. The $Rh^1$–$Rh^2$ bond of **I** has no significant change toward the formation of the complex **III** (2.479 → 2.474 Å). The $Rh^1$–$C^1$ bond of **I** (2.036 Å) has a significant increase in first to form the intermediate **II** (2.103 Å) and then shortens through the C–C bond formation stage **TSII** (2.063 Å) to form the complex **III** (1.981 Å, 5.8 % decrease), which indicates that **II** barely has the character of carbene complex. To probe the function of the nuclear structure of the dirhodium catalyst, we analyzed the nature of the Rh–Rh–C π and σ-bond systems in **II** (carbene complex). Important orbital of **II** is shown in Fig. 3. LUMO of the complex **II** was found to be exactly what is expected and composed mainly of the carbene 2p orbital, which accepts rather small back-donation form the $Rh^1$ $4d_{xz}$ orbital to form an extended π*-system that possesses a strongly electrophilic carbene carbon.

Analysis of the charge distribution during the reaction course was found to be informative and showed strong parallelism between this realistic model to form **4** (Fig. 4a), and the model to form **5** discussed later (Fig. 4b). The nitrone moiety releases negative charge ($C^4$: +0.03 → +0.16, $O^6$: −0.51 → −0.42) upon formation of **II**, and the negative charge moves largely into the vinylcarbene carbon $C^1$ (+0.04 → −0.12) and the $N^5$ atom (+0.09 → +0.01). In the $C^2$–$C^4$ bond formation stage (**TSII**), the nitrogen moiety becomes less positive ($N^5$: +0.01 → −0.15, $C^4$: +0.16 → −0.06), and the carbene carbon becomes cationic (−0.12 → +0.16).In the complex **IV**, the benzene ring attached to $N^5$ atom significantly becomes more positive ($C^7$: +0.15 → +0.31), because the negative charge moves largely from the p-type orbital of the $C^7$ into the $C^1$ atom. The Charge of the $Rh^1$ and $Rh^2$ atoms changes just a little during the $C^1$–$C^8$ bond formation ($Rh^1$: +0.44 → +0.47; $Rh^2$: +0.51 → +0.55).However, in the $C^1$–$C^7$ bond formation, $Rh^1$ and $Rh^2$ lose a lot of negative charge ($Rh^1$: +0.47 → +0.68; $Rh^2$: +0.55 → +0.68) and $C^7$ becomes less positive (+0.31 → +0.13), which is in accord with the removing of the donation from carbene to Rh. In the electrocyclic reaction TS (**TSV**), the $C^1$–$C^7$ and $C^1$–$C^8$ bond significantly shorten (1.580–1.503 and 1.537–1.490 Å, respectively.), and $C^7$ and $C^8$ atom lose negative charge ($C^7$: +0.13 → +0.20, $C^8$: −0.26 → −0.19). The negative

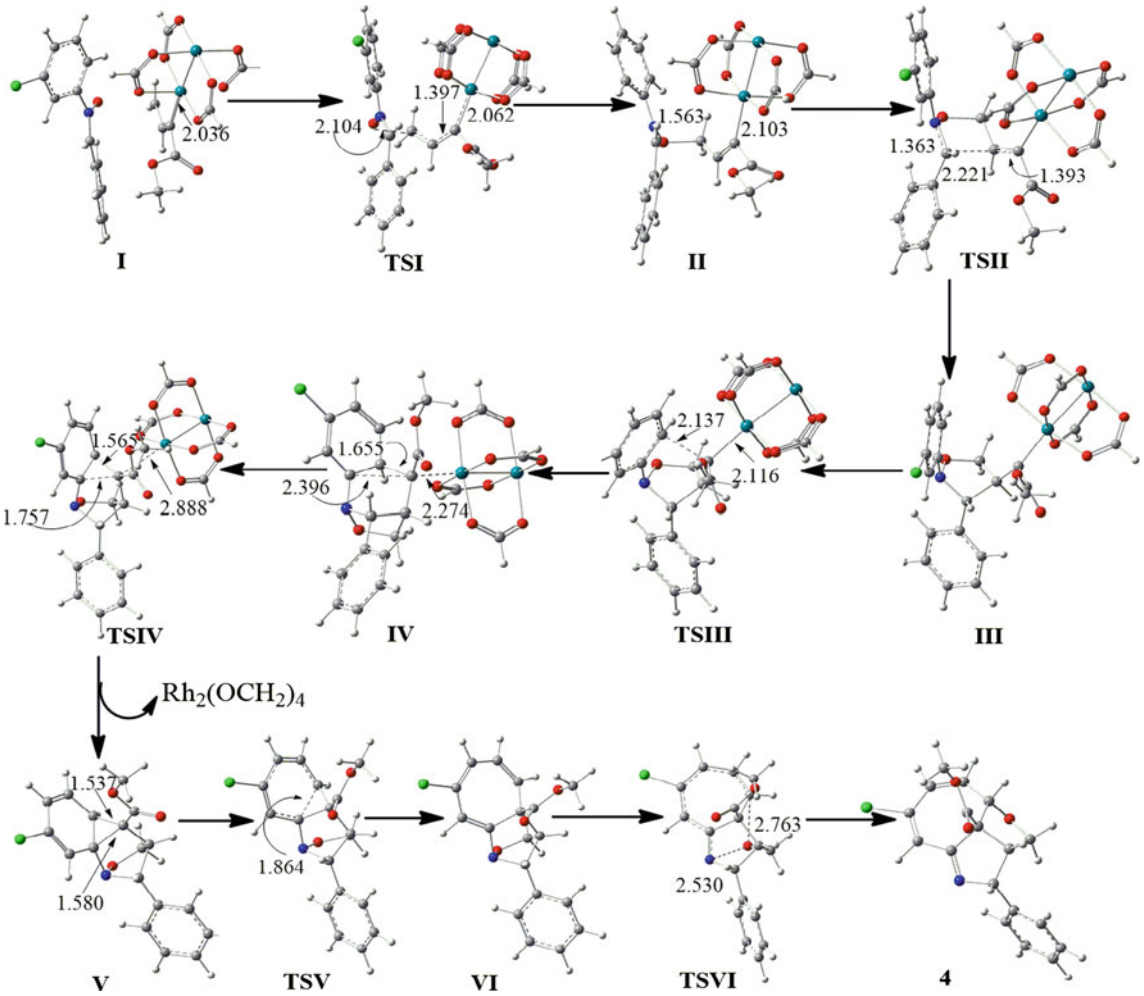


**Fig. 2** B3LYP/6-31G(d,p)[Rh-RSC+4f] structures of stationary points in CACR reaction of **2** and **3**–**4**. The *numbers* refer to bond length (Å)

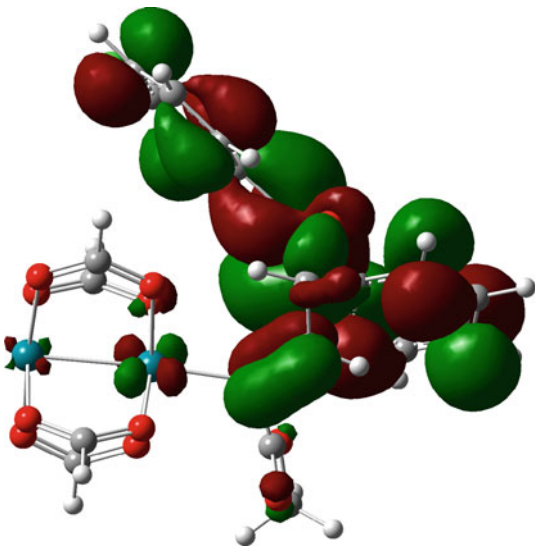

**Fig. 3** Electronic structure and shape of the frontier electronic level (LUMO) of complex **II**

charge moves largely into the $C^1$ atom (−0.16 → −0.22). In [1,7]-oxygen migration step, the $C^7$–$N^5$ bond shortens (1.449 Å → 1.282 Å), and the benzene ring attached to $N^5$ loses negative charge ($C^7$: +0.20 → +0.25, $C^8$: −0.19 → +0.06). The nitrone moiety becomes negatively charged ($N^5$ decrease by +0.21) because of forming of the $C^7$–$N^5$ $\pi$-bonding electrons. Some negative charge is also transferred to the $O^6$ atom (−0.13).

### 3.2 Reaction to produce isomer **5**

Furthermore, to prove the reasonableness of the mechanism proposed for the above catalytic system and gain insight into the influencing factors for highly regioselectivity for the present reaction, the other reaction of nitrone **3** with dirhodium vinylcarbene **2** to produce **5** was investigated. The free energy profile along the reaction progress is shown in Fig. 5. To make a concise expression, the detailed reaction mechanism to form **5** is shown in Fig. 6.

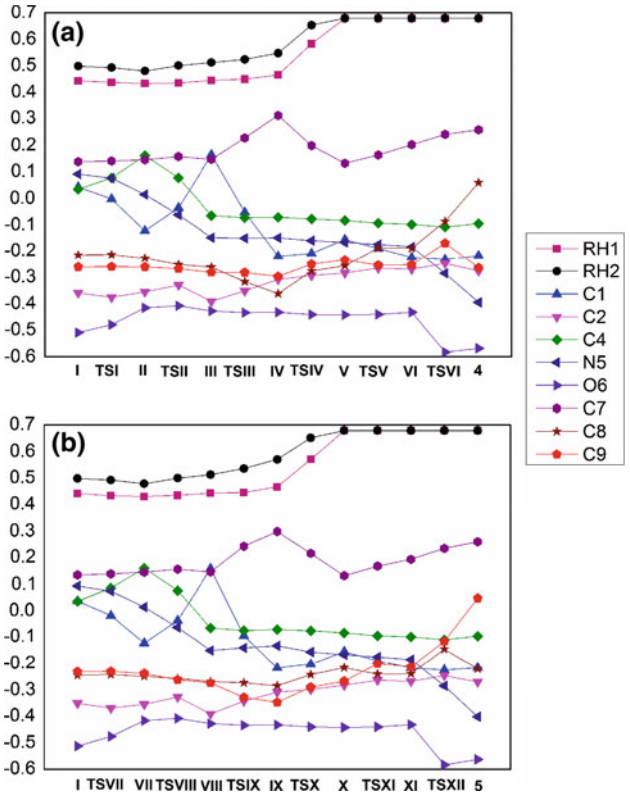


**Fig. 4** Charge distribution along the reaction coordinate for **a** the reaction to **4** and **b** the reaction to **5**

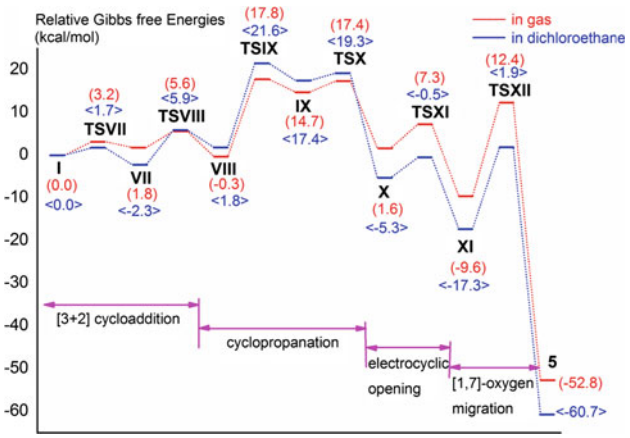


**Fig. 5** Free energy profile of the $Rh_2(O_2CH)_4$-catalyzed CACR reaction of **2** and **3** to produce **5** at the B3LYP/6-311+G(2d,2p)[Rh-RSC+4f]//B3LYP/6-31G(d,p)[Rh-RSC+4f] level. The result of the free energies in gas phase is given in *red*, and the result of the free energies in DCE is shown in *blue*

The reaction pathway and the energetics obtained for this reaction are essentially the same as those of the reaction to form **4** (Fig. 1). The CACR reaction also starts with the [3+2]-cycloaddition. This step goes through stepwise mechanism via **TSVII** and **TSVIII** with low free energy barriers of 3.2 and 3.8 kcal/mol, respectively, in the gas phase. The charge distribution shows the same tendency as found for the reaction to form **4**. In the next cyclopropanation step, carbene atom $C^1$ reacts with $C^9$ instead of $C^8$ to form the intermediate **IX**. Unlike the result in the reaction to obtain **4**, the $C^1$–$C^9$ bond formation step process via transition state **TSIX** with a significantly higher activation free energy (18.1 kcal/mol in gas phase). In the next electrocyclic opening of the cyclopropane ring, the free energy barrier for overcoming **TSXI** is much lower ($\Delta G^{\neq} = 5.7$ kca/mol). Downhill from **TSXI**, seven-membered ring intermediate **XI** is formed. Since the activation of the N–O bond is poor, the electrophile attack of O to $C^9$ via a concerted transition state **TSXII** requires a higher Gibbs free energy of activation of 22.0 kcal/mol in gas phase, which is nearly identical with that of the reaction to form **4** (22.2 kcal/mol). When taking the solvent effect into consideration, the energy profile has a little different from that in gas phase. The step of [1,7]-oxygen migration also bears a large free energy barrier (19.2 kcal/mol), which indicates that the oxygen migration is also difficulty in all cases. However, in the reaction to form **5**, the $C^1$–$C^9$ bond formation bears the largest energy barrier (19.8 kcal/mol) and the cyclopropanation step has become the rate-determining step (RDS).

Two reactions mentioned above affording **4** and **5** are two parallel. Based on our calculational results, although the free energy barrier of RDS to **5** is larger than that to **4**, the difference between those two reactions is small. So the reaction dynamics is not the main factor responsive to the fact that the amount of product **4** dominates over **5** in DCE. We noted that an acidic additive 1,1,1,3,3,3-hexafluoro-2-propanol (HFIP) was used to capture the basic product in the experiment research [27]. So the proportion of alkaline dissociation equilibrium constant $K_b$ values of products **4** and **5** was also calculated in our study according to the Eqs. (1) and (2).

$$\mathrm{B} + \mathrm{H}^+ \overset{\Delta G_B^{\theta}}{\rightleftharpoons} \mathrm{BH}^+ \tag{1}$$

$$\frac{K_{b,4}}{K_{b,5}} = \exp\left(-\frac{\Delta G_4^{\theta} - \Delta G_5^{\theta}}{RT}\right) = \exp\left(\frac{G_4^{\theta} - G_{\mathrm{H4}^+}^{\theta} - G_5^{\theta} + G_{\mathrm{H5}^+}^{\theta}}{RT}\right) \tag{2}$$

where $\Delta G_4^{\theta}$ and $\Delta G_5^{\theta}$ are the free energy changes of reactions corresponding to producing **4** and **5** in the standard state, respectively. $R$ is mole gas constant, and $T$ equals to 298.15 K. Table 1 lists the Gibbs free energies of product **4** and **5**, as well as their corresponding protonated substances $\mathbf{H4}^+$ and $\mathbf{H5}^+$. It is easy to find that the basicity of the product **4** is stronger than that of the product **5**. As a

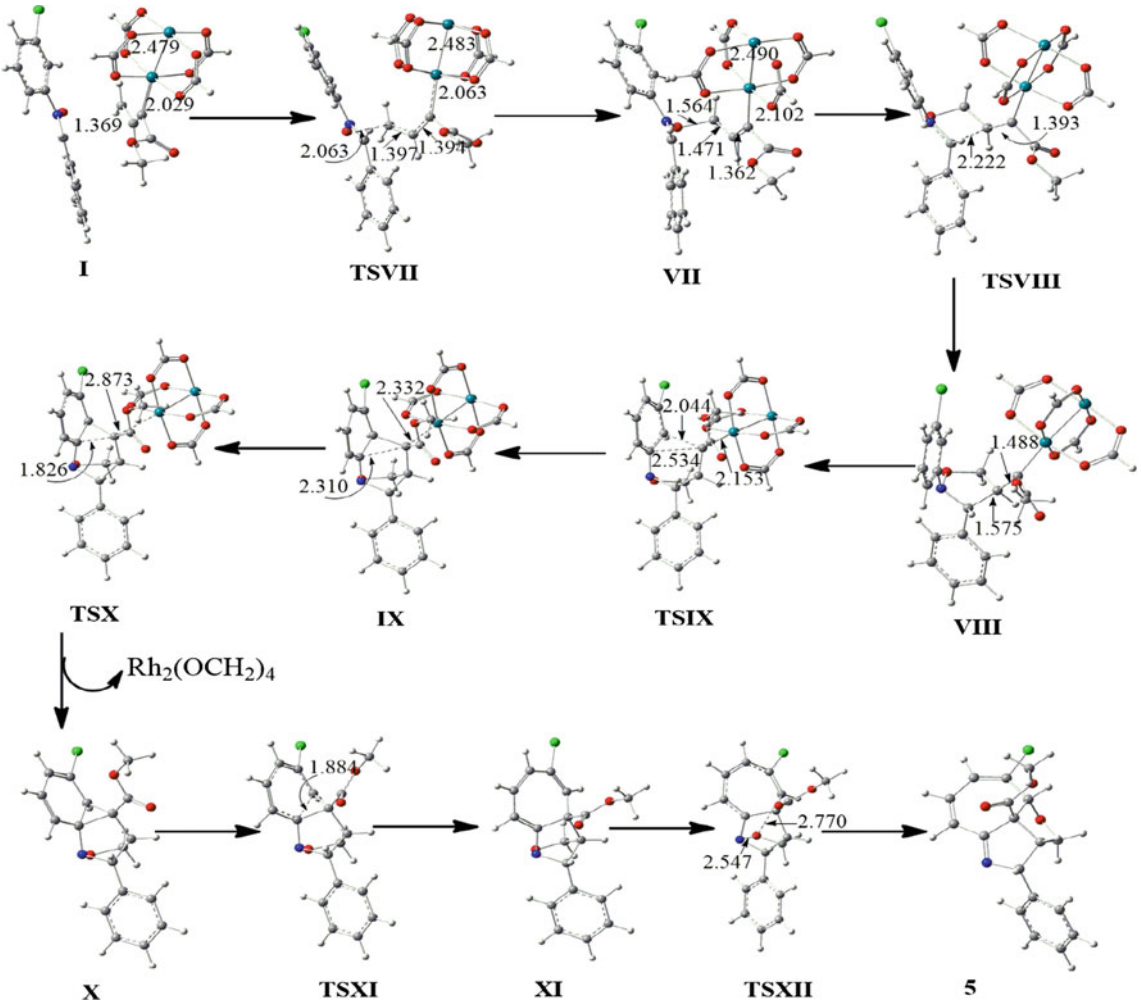


**Fig. 6** B3LYP/6-31G(d,p)[Rh-RSC+4f] structures of stationary points in CACR reaction of **2** and **3**–**5**. The *numbers* refer to bond length (Å)

**Table 1** Gibbs free energy (in kcal/mol) of product **4** and **5**, and their corresponding protonated substances **H4**$^+$ and **H5**$^+$ in DCE

| Substance **B** | **4** | **H4**$^+$ | **5** | **H5**$^+$ |
|---|---|---|---|---|
| $G_B^{\theta}$/kcal mol$^{-1}$ | −1,435.3 | −1,437.0 | −1,437.2 | −1,438.1 |

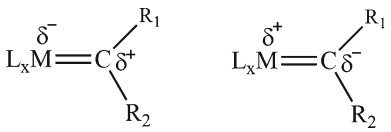


**Fig. 7** Fischer and Schrock-type carbenoids

result, HFIP more easily reacts with **4** than **5**, and thus, the reaction equilibrium will move to the formation of product **4**, which is consistent with the experimental results that the reaction between **1** and **3** has high regioselectivity.

It is well known that rhodium carbenoids are Fischer-type carbenoids (see Fig. 7). From the charge distribution along the reactions, it is clear that the carbene $C^1$ atom occurs electrophilic addition, along with a significant reduction of its charge. When there is an electron-withdrawing group such as chlorine at $C^{10}$ of nitrone,the charge density of chlorine's *ortho*-site decreases due to the negative inductive effect of chlorine. On the other hand, the electron density on $C^8$ is slightly affected by the negative inductive effect of chlorine. Therefore, the electrophilic addition is more likely to occur at $C^8$ site, rather than $C^9$ site.

## 4 Conclusion

On the basis of our theoretical computations, we have developed a mechanistic proposal for the CACR reaction. The present studies have revealed, for the first time, the

energetics, the electronic nature, and the 3-D structures of the intermediates and the transition states in the catalytic cycle of the dirhodium vinylcarbene-induced nitrone cycloaddition with subsequent cascade carbenoid aromatic cycloaddition/N–O cleavage and rearrangement. The reaction of vinyldiazoacetate-induced nitrone starts from the stepwise [3+2] cycloaddition. Subsequent intramolecular cyclopropanation and electrocyclic opening of the cyclopropane ring by the rhodium carbene on the nitrogen-bound aryl group take place to form a heptatomic ring intermediate. A [1,7]-oxygen migration to final product occurs via a concerted transition state. The reactions to form **4** and **5** have similar mechanisms, and the step of cyclopropanation is the regioselectivity determining step. With *meta*-substituent (Cl) on the *N*-aryl group, the charge density of chlorine's *ortho*-site decreases due to the negative inductive effect of chlorine. Therefore, as compared to the electrophilic addition on the $C^8$ atom, the electrophilic addition on the $C^9$ site owns a significantly incensement on the energy barrier of cyclopropane (**TSIII** and **TSIX**). Since the basicity of the product **4** is stronger than that of the product **5**, the acidic additive HFIP promotes the formation of product **4**.

## 5 Supporting information

The optimized Cartesian coordinates and geometrical structures of all stationary points along the potential energy profiles. This material is available free of charge via the Internet at http://springerlink.lib.tsinghua.edu.cn/content/.

**Acknowledgments** This project has been supported by the National Natural Science Foundation of China (Grant No. 21173151) and by National Basic Research Program of China of Ministry of Science and Technology of China (973 Program, Grant No. 2011CB201202).

## References

1. Selander N, Fokin VV (2012) J Am Chem Soc 134:2477–2480
2. Nadeau E, Ventura DL, Brekan JA, Davies HML (2010) J Org Chem 75:1927–1939
3. Cui X, Xu X, Lu H, Zhu S, Wojtas L, Zhang XP (2011) J Am Chem Soc 133:3304–3307
4. Takeda K, Oohara T, Shimada N, Nambu H, Hashimoto S (2011) Chem Eur J 17:13992–13998
5. Hansen JH, Gregg TM, Ovalles SR, Lian Y, Autschbach J, Davies HML (2011) J Am Chem Soc 133:5076–5085
6. Doyle MP, McKervey MA, Ye T (1998) Modern catalytic methods for organic synthesis with diazo compounds. Wiley, London
7. Davies HML, Antoulinakis EG (2004) Intermolecular metal-catalyzed carbenoid cyclopropanations. In: Organic reactions, vol 57. Wiley, USA
8. Davies HM, Beckwith RE (2003) Chem Rev 103:2861–2904
9. Davies HM, Loe O, Budynina E, Averina E, Ivanova O, Yashin N, Kuznetsova T, Zefirov N, VanZanten A, Mullaugh K (2004) Synthesis 2004:2595–2608
10. Davies HM, Manning JR (2008) Nature 451:417–424
11. Davies HM, Panaro SA (2000) Tetrahedron 56:4871–4880
12. Qin C, Boyarskikh V, Hansen JH, Hardcastle KI, Musaev DG, Davies HML (2011) J Am Chem Soc 133:19198–19204
13. Davies HM, Morton D (2011) Chem Soc Rev 40:1857–1869
14. Lu H, Dzik WI, Xu X, Wojtas L, de Bruin B, Zhang XP (2011) J Am Chem Soc 133:8518–8521
15. Lian Y, Davies HML (2011) J Am Chem Soc 133:11940–11943
16. Davies HM, Denton JR (2009) Chem Soc Rev 38:3061–3071
17. Doyle MP, Duffy R, Ratnikov M, Zhou L (2009) Chem Rev 110:704–724
18. Davies HML, Stafford DG, Doan BD, Houser JH (1998) J Am Chem Soc 120:3326–3331
19. Parr BT, Li Z, Davies HM (2011) Chem Sci 2:2378–2382
20. Barluenga J, Lonzi G, Riesgo L, López LA, Tomás M (2010) J Am Chem Soc 132:13200–13202
21. Lian Y, Davies HML (2009) J Am Chem Soc 132:440–441
22. Davies HML, Xiang B, Kong N, Stafford DG (2001) J Am Chem Soc 123:7461–7462
23. Reddy RP, Davies HML (2007) J Am Chem Soc 129:10312–10313
24. Schwartz BD, Denton JR, Lian Y, Davies HML, Williams CM (2009) J Am Chem Soc 131:8329–8332
25. Lian Y, Miller LC, Born S, Sarpong R, Davies HML (2010) J Am Chem Soc 132:12422–12425
26. Miller LC, Ndungu JM, Sarpong R (2009) Angew Chem Int Ed 48:2398–2402
27. Wang X, Abrahams QM, Zavalij PY, Doyle MP (2012) Angew Chem Int Ed 51:5907–5910
28. Tabolin AA, Ioffe SL (2014) Chem Rev 114. doi:10.1021/cr400196x
29. Xu X, Doyle MP (2014) Acc Chem Res 47:1396–1405
30. Xu X, Leszczynski JS, Mason SM, Zavalij PY, Doyle MP (2014) Chem Commun 50:2462–2464
31. Hansen J, Autschbach J, Davies HML (2009) J Org Chem 74:6555–6563
32. Nakamura E, Yoshikai N, Yamanaka M (2002) J Am Chem Soc 124:7181–7192
33. Yoshikai N, Nakamura E (2003) Adv Synth Catal 345:1159–1171
34. Nowlan DT, Gregg TM, Davies HML, Singleton DA (2003) J Am Chem Soc 125:15902–15911
35. Frisch MJGWT, Schlegel HB, Scuseria GE, Robb MA, Cheeseman JR, Scalmani G, Barone V, Mennucci B, Petersson GA, Nakatsuji H, Caricato M, Li X, Hratchian HP, Izmaylov AF, Bloino J, Zheng G, Sonnenberg JL, Hada M, Ehara M, Toyota K, Fukuda R, Hasegawa J, Ishida M, Nakajima T, Honda Y, Kitao O, Nakai H, Vreven T, Montgomery JA Jr, Peralta JE, Ogliaro F, Bearpark M, Heyd JJ, Brothers E, Kudin KN, Staroverov VN, Kobayashi R, Normand J, Raghavachari K, Rendell A, Burant JC, Iyengar SS, Tomasi J, Cossi M, Rega N, Millam JM, Klene M, Knox JE, Cross JB, Bakken V, Adamo C, Jaramillo J, Gomperts R, Stratmann RE, Yazyev O, Austin AJ, Cammi R, Pomelli C, Ochterski JW, Martin RL, Morokuma K, Zakrzewski VG, Voth GA, Salvador P, Dannenberg JJ, Dapprich S, Daniels AD, Farkas O, Foresman JB, Ortiz JV, Cioslowski J, Fox DJ (2009) Gaussian 09, revision A.1. Gaussian Inc, Wallingford, CT
36. Becke AD (1993) J Chem Phys 98:5648–5652
37. Lee C, Yang W, Parr RG (1988) Phys Rev B 37:785–789
38. Kaupp M, Schleyer PVR, Stoll H, Preuss H (1991) J Chem Phys 94:1360–1366
39. Bergner A, Dolg M, Küchle W, Stoll H, Preuß H (1993) Mol Phys 80:1431–1441
40. Dolg M, Stoll H, Preuss H, Pitzer RM (1993) J Phys Chem 97:5852–5859
41. Feller D (1996) J Comput Chem 17:1571–1586

42. Schuchardt KL, Didier BT, Elsethagen T, Sun L, Gurumoorthi V, Chase J, Li J, Windus TL (2007) J Chem Inf Model 47:1045–1052
43. Foresman JB, Keith TA, Wiberg KB, Snoonian J, Frisch MJ (1996) J Phys Chem 100:16098–16104
44. Marenich AV, Cramer CJ, Truhlar DG (2009) J Phys Chem B 113:6378–6396
45. Reed AE, Curtiss LA, Weinhold F (1988) Chem Rev 88:899–926
46. Yang X, Fan L, Xue Y (2014) RSC Adv 4:30108–30117

Theor Chem Acc (2014) 133:1566
DOI 10.1007/s00214-014-1566-6

REGULAR ARTICLE

# Theoretical study on the working mechanism of a reversible light-driven rotary molecular motor

**Lili Wang · Xin Che · Huiliang Li · Jun Gao · Chengbu Liu**

Received: 24 May 2014 / Accepted: 13 August 2014 / Published online: 27 August 2014
© Springer-Verlag Berlin Heidelberg 2014

**Abstract** Recent progress in the experimental design and synthesis of artificial light-driven molecular motors has made it possible to reverse the light-powered rotation of a molecular motor during the rotary process with multilevel control of rotary motion. With the interconversion between the photochemically generated less-stable isomers in one unidirectional rotary cycle with the stable isomers in the other cycle, the clockwise and anticlockwise rotations can be regulated with configuration inversion at the stereogenic centre. In this work, we report theoretical calculations by using density functional theory and time-dependent density functional theory, revealing the working mechanism of the clockwise and anticlockwise rotations. Specifically, by locating the relevant stationary points along the excited-state and ground-state reaction paths, the clockwise and anticlockwise rotary cycles are explored in great detail, which is of complementary importance in understanding the overall rotary process of the reversible rotation.

**Keywords** Light-driven molecular motor · Rotation reversal · Working mechanism · TD-DFT

## 1 Introduction

Molecular motor, in general, is a kind a nano-machine which can perform continuously mechanical functions by converting external energy to repetitive 360° motion. There are various molecular motors in nature, existing in the biological systems such as ATPase, dimeric kinesin, myosin, and dynein, which accomplish the extremely delicate and intricate microscopic works that compose the brilliant biological world. According to the different driven forces, it can be sorted as chemical [1], electrical, thermal, and light-driven molecular motors. On the other hand, due to the rapid development of the 'bottom-up' approach for experimental chemists, studies focusing on the design and synthesis of molecular-level machines that mimic the basic functions in nature have increased dramatically in the past decade. Although it is still far to construct artificial molecular motor that can perform integrated functions for realistic works, people have been able to design and to synthesis some relatively simple molecular motors which possess linear or rotary movement working under ambient conditions.

An eligible biological or artificial molecular motor that can be operated effectively at molecular level should work against the random thermal Brownian motion, which means the unidirectionality and controllability of the motor are essential criteria. The artificially designed molecular motors in laboratory that are powered by different energy sources and possess various mechanical motions have been

Dedicated to Professor Guosen Yan and published as part of the special collection of articles celebrating his 85th birthday.

**Electronic supplementary material** The online version of this article (doi:10.1007/s00214-014-1566-6) contains supplementary material, which is available to authorized users.

L. Wang
Advanced Research Center for Optics, Shandong University, Jinan 250100, People's Republic of China

L. Wang · X. Che · H. Li · J. Gao (✉) · C. Liu
School of Chemistry and Chemical Engineering, Shandong University, Jinan 250100, People's Republic of China
e-mail: gaojun@sdu.edu.cn

L. Wang
State Key Laboratories of Transducer Technology, Shanghai Institute of Microsystem and Information Technology, Chinese Academy of Sciences, Shanghai 200050, People's Republic of China

inspired extensively by the pioneering synthetic unidirectional rotary molecular motors presented by Feringa [2, 3] and Kelly [4, 5] and their co-workers over the last 15 years.

One of the most interesting characteristics of the rotary motors existing in biological systems is the reversal of the direction of rotation [6]. Recently, a new molecular motor (henceforth denoted motor **1**) driven by light, whose rotation direction can be controlled to be capable of performing reversible mechanical works by certain chemical catalysis epimerization, has been reported by Feringa et al. [7]. The design of motor **1** is based on one of the typical second-generation molecular motor (shown in Scheme 1) by replacing the methyl substituent at the stereogenic centre 2′ position with electron-withdrawing—$CONMe_2$ group at the 3′ position [7, 8]. In this way, the bidirectional 360° rotary cycle of motor **1** can be achieved, and the concerted working mechanism was experimentally observed, as shown in Fig. 1. According to the relative rotating between the upper rotor and lower stator, the two rotating cycles are named *clockwise* rotation and *anticlockwise* rotation, respectively.

Computational studies complement these experimental efforts and provide more insights into the rationale of the working mechanism, which could be helpful for the design and operation of these high rotational frequency motors in functional devices [9–12]. Moreover, quantum chemical studies could be regarded as the first step before exploring the rotary cycle of such motors by making them work as practical molecular machines. Some theoretical studies focusing on the working mechanisms of different light-driven molecular motors have been reported widely. Grimm et al. [13] have investigated the photochemical steps of a Feringa alkene-based molecular motor by using Car–Parrinello molecular dynamics simulations and thermal steps by semiempirical AM1 method, which has revealed the important role of methyl groups in determining the unidirectionality of the rotation. Excited-state dynamics studies of fluorene-based molecular motor also include TD-DFT simulation [14] and semiclassical trajectory surface hopping (TSH) simulations combined with orthogonalization-corrected OM2 Hamiltonian and multireference configuration interaction treatment (OM2/MRCI) by Filatov et al. [15]. Recently, the detailed photoisomerization processes of a redesigned stilbene-based light-driven molecular motor were specified by Liu and Morokuma [16] with CASPT2//CASSCF calculations. On the contrary, Perez-Hernandez and González [17] mainly focused on the possible reaction paths and corresponding transition states in the ground state.

As for the working mechanism of motor **1**, despite the experimental observation has shown the bidirectional rotations, a detailed understanding of the excited-state photoisomerization and ground-state thermal helix inversion following the rotary motion is still of essential importance considering improved design of reversible light-driven rotary molecular motors in the future.

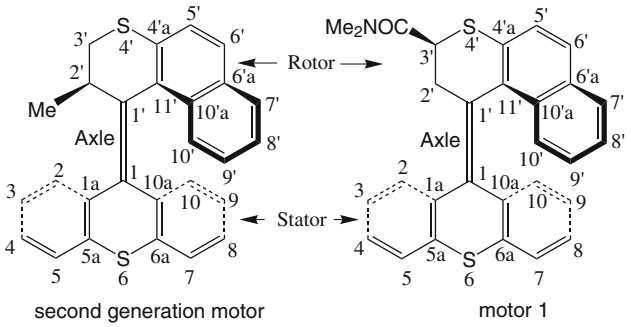


**Scheme 1** Second-generation (*left panel*) and redesigned reversible rotary motor **1** (*right panel*). With dihedral angles defined as follows, $\theta$ = C11′–C1′–C1–C10a, $\alpha$ = C1–C1′–C11′–C10′a, $\alpha'$ = C1′–C1–C10a–C10, $\beta$ = C1–C1′–C2′–C3′, and $\beta'$ = C1′–C1–C1a–C2

We report quantum chemical calculations in this work by using density functional theory (DFT) [18–24] and time-dependent density functional theory (TD-DFT) [25–29], which illustrate the overall rotary process including both the excited-state photoisomerization and the ground-state thermal helix inversion steps at the same level of theory. It is found that the long-range corrected (LC) density functional CAM-B3LYP [30] is able to demonstrate the unidirectionality of the photoisomerizations in the *clockwise* and *anticlockwise* rotary processes. By computing the potential energy curves (PECs) of the ground state and three lowest excited states, the different profiles of these states in the power-stroke photochemical reactions have been revealed.

## 2 Computational methods

The complete understanding of the rotary cycle of motor **1** involves the description of both photoisomerization reaction and thermal helix inversion steps. Therefore, the selection of a rational computational method that is equally good at describing excited-state and ground-state potential energy surfaces at the same level of theory is of fundamental importance. Although the widely used globally hybrid density functional B3LYP [18, 21, 31] is recognized as one of the most accurate for ground-state structures, energies, and frequencies [18, 21], there are still some limitations for handling partial $\pi$-bond breaking or interactions dominated by medium-range correlation energy such as overestimate of rotation barriers [32], failure to give correct excitation energies [33–35], and shortcomings in some other cases [36]. Hence, CAM-B3LYP was employed in the work motivated by its merit in describing the excited-state potential energy surfaces as well as relatively accurate ground-state energy barriers as demonstrated by Rostov et al. [34, 35].

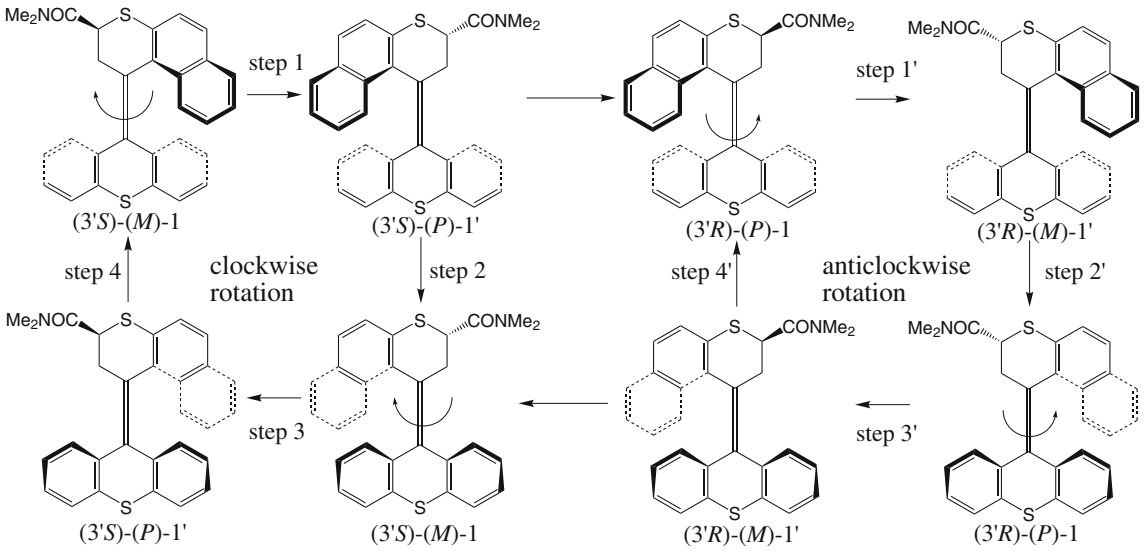


**Fig. 1** Schematic *clockwise* and *anticlockwise* rotary cycles of motor **1**

**Table 1** CAM-B3LYP and B3LYP ground-state geometric parameters and relative energetic differences of two most stable structures (3′*S*)-(*M*)-1 and (3′*R*)-(*P*)-1 with different basis sets

| Isomer | Method | Basis set | $\theta$ | $\alpha$ | $\alpha'$ | $\beta$ | $\beta'$ | C1′–C1 | $\Delta G$ |
|---|---|---|---|---|---|---|---|---|---|
| (3′*S*)-(*M*)-1 | CAM-B3LYP | 6−31G+(d,p) | 0.2 (177.3) | −63.4 | −50.5 | −107.1 | 52.4 | 1.348 | 0.0 |
| | | 6−311G++(d,p) | 0.5 (177.3) | −63.6 | −51.0 | −107.2 | 52.9 | 1.343 | 0.0 |
| | B3LYP | 6−31G+(d,p) | −0.9 (176.5) | −63.1 | −49.9 | −107.0 | 51.7 | 1.359 | 0.2 |
| | | 6−311G++(d,p) | −0.6 (176.7) | −63.4 | −50.4 | −107.1 | 52.2 | 1.354 | 0.2 |
| (3′*R*)-(*P*)-1) | CAM-B3LYP | 6−31G+(d,p) | −177.2 (−0.2) | 63.5 | 50.4 | 107.0 | −52.5 | 1.348 | 0.0 |
| | | 6−311G++(d,p) | −177.3 (−0.5) | 63.6 | 51.0 | 107.2 | −52.9 | 1.343 | 0.0 |
| | B3LYP | 6−31G+(d,p) | −176.3 (1.1) | 63.0 | 50.0 | 106.6 | −51.9 | 1.359 | 0.0 |
| | | 6−311G++(d,p) | −176.4 (0.7) | 63.4 | 50.6 | 106.7 | −52.5 | 1.354 | 0.0 |

The definition of dihedral angles is listed in Scheme 1. Dihedral angles in degrees, bond lengths in angstrom, and relative energies in kJ mol$^{-1}$. $\Delta G$ is the relative energy differences between (3′*S*)-(*M*)-1 and (3′*R*)-(*P*)-1 computed at the same level of theory

In order to explore the rotary cycle of motor 1 with clarity and simplicity, each 360° rotation process of *clockwise* and *anticlockwise* is divided into two identical rotary halves due to the symmetric chemical structure of the lower stator, i.e., every 180° half includes a photochemical and a thermal step (step 1 and step 2 for *clockwise* rotation and step 1′ and step 2′ for *anticlockwise* rotation as shown in Fig. 1). The two most stable stationary points ((3′*S*)-(*M*)-1 and (3′*R*)-(*P*)-1) on the ground state were located by geometry optimizations and frequency calculations using long-range corrected hybrid density functional CAM-B3LYP in combination with the 6−31+G(d,p) basis set. As a complementary comparison, geometry optimizations and frequency calculations with B3LYP functional and 6−31+G(d,p) basis set were also performed to ensure the reliability of CAM-B3LYP for ground-state properties (see Table 1 in following section).

Starting from (3′*S*)-(*M*)-1 and (3′*R*)-(*P*)-1) as the most stable structures on the ground state in each rotary cycle, constrained geometry optimizations along the dihedral angle C11′–C1′–C1–C10a ($\theta$ in Table 1) with an interval of 10° were carried out with the same DFT methodology to identify the ground-state PECs. Then, based on the ground-state minima and PECs, the excited-state PECs in each rotary cycle ((3′*S*)-(*P*)-1′ and (3′*R*)-(*M*)-1′) including the three lowest electronic excited states ($S_1$, $S_2$, and $S_3$) were evaluated by TD-DFT single-point calculations at CAM-B3LYP/6−311++G(d,p) level of theory, where triple-ζ quality and more diffuse functions are included (basis set effect on the ground-state geometries also discussed in Table 1). It should be noticed that during the Franck–Condon (FC) relaxation, i.e. analytic TD-DFT gradients [28, 37] calculations from (3′*S*)-(*M*)-1 and (3′*R*)-(*P*)-1 structures, 6−31+G(d,p) basis set and

Tamm–Dancoff approximation (TDA) [38] were employed in order to give balanced results between accuracy and efficiency. Afterwards, TD-DFT single-point excitation energies of the TDA optimized geometries were calculated at 311++G(d,p) level.

The less-stable structures (3′*S*)-(*P*)-1 and (3′*R*)-(*M*)-1 can be recognized as products of photoisomerizations, whereafter the transition state search was carried out by constrained geometry optimization along the relevant dihedral angle $\alpha$ shown in Scheme 1. The saddle-point structure for each curve was taken out and was optimized to a transition structure at B3LYP/6−31G+(d,p) level of theory using the standard transition state search algorithms implemented in Gaussian 09 [39]. After a transition structure is optimized, the geometries and energies were refined using B3LYP/6−311G++(d,p) and CAM-B3LYP/6−311G++(d,p) together with the frequency calculations in order to confirm all the transition structures have only one imaginary frequency and to obtain thermal corrected free energies. Also, intrinsic reaction coordinate calculations were done to make sure the reactants and products do connected by a given transition structure.

All calculations in this work were performed with Gaussian 09 package of programs [39].

## 3 Results and discussions

### 3.1 The (3′*S*)-(*P*)-1 and (3′*R*)-(*M*)-1 isomers

Taken as the preliminary photochemical reactants in each rotary cycle, the ground-state geometric parameters and relative energy difference of (3′*S*)-(*M*)-1 and (3′*R*)-(*P*)-1 were computed by CAM-B3LYP and B3LYP with different basis sets, respectively, as shown in Table 1.

It can be known from Fig. 1 the stable mirror opposite enantiomer (3′*R*)-(*P*)-1 which can be obtained by base-catalysed epimerization of the less-stable (3′*S*)-(*P*)-1′ should be of the same stereogenic structure and energetic stability with (3′*S*)-(*M*)-1. It is confirmed by the comparison in Table 1, in which the maximum disparities are 0.1°, 0.0 Å, and 0.0 kJ mol$^{-1}$ for CAM-B3LYP/6−31G+(d,p), 0.0°, 0.0 Å, and 0.0 kJ mol$^{-1}$ for CAM-B3LYP/6−311G++(d,p), 0.4°, 0.0 Å, and 0.2 kJ mol$^{-1}$ for B3LYP/6−31G+(d,p), and 0.4°, 0.0 Å, and 0.2 kJ mol$^{-1}$ for B3LYP/6−311G++(d,p) in dihedral angles, C1′–C1 bonds, and relative energies. Moreover, the increase in the size of the basis set from 6−31G+(d,p) to 6−311G++(d,p) has similar and minor effect on the chemical structures, with maximum disparities of 0.5° and 0.005 Å for CAM-B3LYP, and 0.6° and 0.005 Å for B3LYP.

From this point of view, both functionals combined with each of two basis sets give reasonably good description of the ground-state geometry and energy. Importantly, CAM-B3LYP predicts (3′*S*)-(*M*)-1 and (3′*R*)-(*P*)-1 to be exactly identical, which proves that this functional is capable of yielding accurate ground-state results needed for the calculations in this work.

### 3.2 FC relaxation and potential energy curves

As the first power stroke in the rotary cycle, the irradiation of light promotes the two initial structures in each cycle, (3′*S*)-(*M*)-1 and (3′*R*)-(*P*)-1, to the higher energy excited electronic states, followed by an ultrafast relaxation to the $S_1$ minimum region, which can be evidenced by the electronic structure analyses for the three lowest electronic excited states. (For detailed discussion, please refer to the Supporting Information.) The energy difference between vertical and adiabatic excitation energy is the driving force of the photoisomerization process, and the isomer is considered to go down to the ground state near the twisted perpendicular conical intersection. Therefore, the directionality of the photoinitiated rotation around C1′–C1 is controlled by the FC relaxation and can be reflected by the shape of PECs on the excited state. Some key parameters of excitation energy and geometry variation during this process are collected and shown in Table 2.

**Table 2** $S_1$ vertical (VEE) and adiabatic (AEE) excitation energies (eV) of (3′*S*)-(*M*)-1 and (3′*R*)-(*P*)-1 calculated at CAM-B3LYP with 6−31G+(d,p) and 6−311G++(d,p) level of theory

| Isomer | Basis set | $\lambda^{b}_{max}$ | VEE | AEE | Geometry change | |
|---|---|---|---|---|---|---|
| | | | | | $\Delta\theta$ | ΔC1′–C1 |
| (3′*S*)-(*M*)-1 | 6−31G+(d,p) | 3.97 | 4.14 | 2.99 | 0.2 → −57.5 | 1.348 → 1.447 |
| | 6−311G++(d,p)[a] | | 4.14 | 3.01 | – | – |
| (3′*R*)-(*P*)-1 | 6−31G+(d,p) | 3.97 | 4.14 | 2.99 | −177.2 → −126.4 | 1.348 → 1.447 |
| | 6−311G++(d,p)[a] | | 4.14 | 3.01 | – | – |

[a] The excitation energies are computed from the geometries optimized with 6−31G+(d,p) basis set

[b] Experimental absorption maximum taken from Ref. [7]

It can be seen from Table 2 how well CAM-B3LYP can describe the excitation energies of the excited electronic states. The vertical excitation energies (∼0.15 eV higher than the experimental values) are in reasonable agreement with the experimental absorption maxima which should correspond to the vertical approximation, as the calculated adiabatic excitation energies are ∼0.90 eV lower than the experimental values. The basis set effect was evaluated by single-point calculations increasing basis set from 6−31G+(d,p) to 6−311G++(d,p) and only shows marginal difference (∼0.02 eV in adiabatic excitation energies). With regard to the geometry changes during the FC relaxation of the two isomers, there are both similarity and difference. While a pronounced elongation of ∼0.1 Å in C1′–C1 bond is observed for both isomers, the driving forces on the relative rotation between rotor and stator of (3′*S*)-(*M*)-1 and (3′*R*)-(*P*)-1 are of opposite directions which can be observed clearly in Fig. 2.

In Fig. 2, the $S_0$ minimum energy path (MEP) and the single-point excitation energies of the first three excited states for (3′*S*)-(*M*)-1 and (3′*R*)-(*P*)-1 are shown. It should be pointed out that the aim of the research is to elucidate the reversible rotation processes and to understand the working mechanism of the motor; therefore, the expensive excited-state potential energy surface calculation was not performed. Furthermore, although CAM-B3LYP functional performs well for the excitation energy calculation, it is a single-reference method and is well known not as good as multireference methods in describing conical intersections. Instead, the nature of the excited-states MEPs was estimated by computing the single-point excitation energies of the first three excited states from the optimized geometries on $S_0$ MEP, and still some interesting features are revealed.

As shown in Fig. 2, the key feature is the inversion symmetry of the PECs of the two isomers. As for the (3′*S*)-(*M*)-1 isomer, the FC relaxation on the excited state follows the $S_1$ PEC after the molecule is excited, which results from the barrierless feature of the first excited state and high energy barriers on the second and third excited states. The descent of energy from the FC point on the $S_1$ PEC drives the excited state isomerization towards the twisted intermediate conformation (3′*S*)-(*M*)-1*. The dihedral angle $\theta$ changes from ∼0° to −60° roughly, suggesting an efficient *clockwise* initial rotation. While for the (3′*R*)-(*P*)-1 isomer, the PECs feature similar characteristics with that of the (3′*S*)-(*M*)-1 isomer, except the dihedral angle $\theta$ changes from ∼−180° to ∼−120° towards (3′*R*)-(*P*)-1* and is in an *anticlockwise* fashion.

As indicated in the discussion above, both $S_1$ and $S_0$ PECs in Fig. 2 cannot be capable of locating the conical intersections between the excited state and ground state. Nevertheless, an excitation energy of approximately zero is shown at −130° for (3′*S*)-(*M*)-1 and at −50° for (3′*R*)-(*P*)-1, which indicates that the conical intersection is in the range of (−60°, −130°) for (3′*S*)-(*M*)-1 and (−120°, −50°) for (3′*R*)-(*P*)-1, respectively. Such assumption can be further confirmed by carrying out ground-state geometry optimizations from twisted (3′*S*)-(*M*)-1* and (3′*R*)-(*P*)-1* conformations to locate the less-stable photochemical products. Interestingly, it was observed that in the intermediate (3′*S*)-(*M*)-1* and (3′*R*)-(*P*)-1* conformations, the orientation of phenyl rings on the stator has changed from pointing-in the plane to pointing-out direction. Furthermore, when optimized to the ground-state minima from the excited-state intermediates (3′*S*)-(*M*)-1* and (3′*R*)-(*P*)-1*, the orientation of phenyl rings on the stator was preserved and less-stable structures (named as (3′*S*)-(*P*)-1 and (3′*R*)-(*M*)-1) different with that in the original working mechanism (shown in Fig. 1) were obtained. The photochemical products (3′*S*)-(*P*)-1 and (3′*R*)-(*M*)-1 suggest that motor 1 should work in a slightly different manner that does lead to the experimentally observed thermal barriers.

### 3.3 Working cycles and transition states

Taken as the rate-determining steps in the overall rotary cycle, the thermal helix inversions of step 2 and step 2′ start from the photoisomerized (3′*S*)-(*P*)-1 in the clockwise

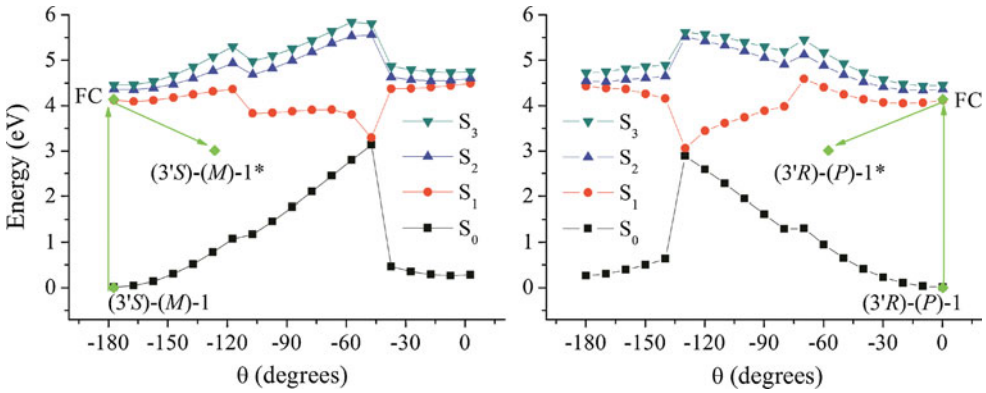


**Fig. 2** FC relaxation directions and excitation energies with $S_0$ MEPs for (3′*S*)-(*M*)-1 (*left panel*) and (3′*R*)-(*P*)-1 (*right panel*). The photoisomerization directions indicated by *green arrows*

rotation and from (3′*R*)-(*M*)-1 in the anticlockwise rotation, during the first half of each rotary cycle. The location of transition states is of utmost importance in determining the rotary frequency and in understanding the working mechanism of the motor. To this aim, two-dimensional relaxed potential energy scans are carried out by changing torsional angle $\alpha$ and $\alpha'$ in order to get suitable starting geometries for the geometry optimizations of transition states. After the corresponding transition states are optimized, all of the requisite frequency and intrinsic reaction coordinate calculations are performed to get the free energies and to verify the reactants and products mediated by the transition states. (The atomic coordinates of optimized ground and excited-state stationary points are provided in Supporting Information.) By means of locating all the possible stationary points, the proposed feasible working cycles for the clockwise and anticlockwise rotations are shown in Fig. 3. The exclusive *syn-fold* structures (3′*S*)-(*P*)-1 and (3′*R*)-(*M*)-1 of the photochemical products have been theoretically predicted, which means that there is an *anti-fold* → *syn-fold* geometrical transformation during the rotary process. All the five isomers of motor 1 in step 1 and step 2 of clockwise rotation and another five isomers in step 1′ and step 2′ are depicted in Fig. 4, where also given are the relative stabilities of different isomers with respect to the *global* stable isomer in each rotary cycle.

As shown clearly in Fig. 4, the clockwise and anticlockwise rotary cycles show highly symmetric characteristic, which has an opposite rotary direction but nearly equivalent relative free energies for all the corresponding isomers

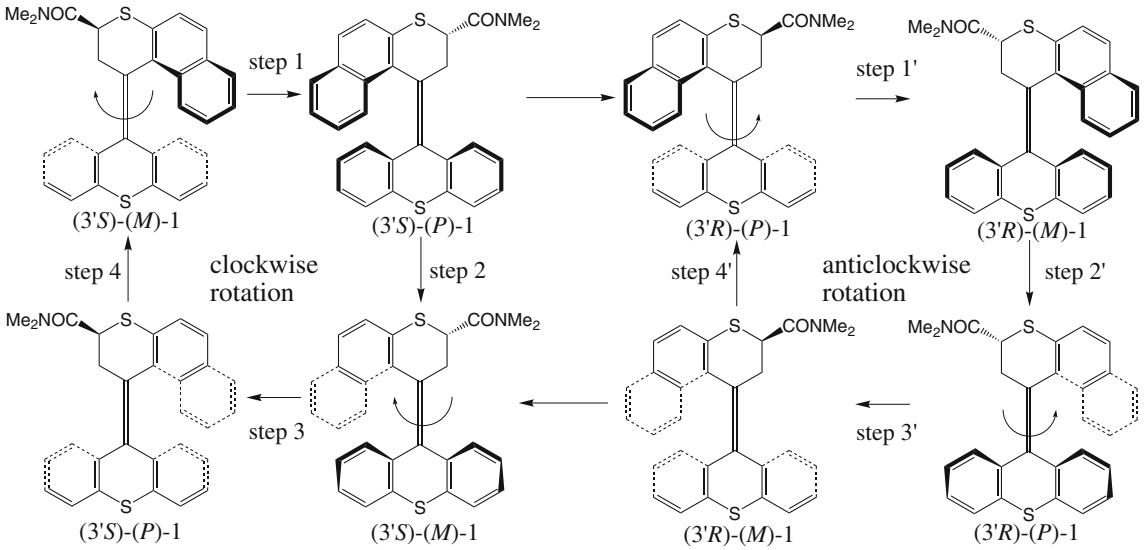


**Fig. 3** Proposed feasible working cycles for the *clockwise* and *anticlockwise* rotations

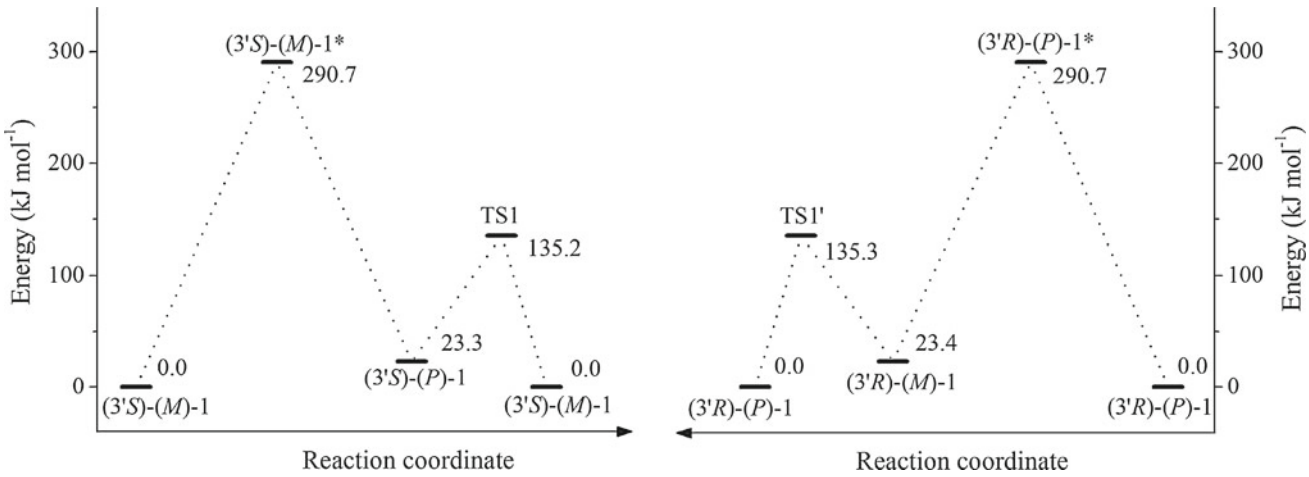


**Fig. 4** Relative free energies (in kJ mol$^{-1}$) at CAM-B3LYP/6−31G+(d,p) level of theory with respect to the most stable isomers of motor 1 in the *clockwise* and *anticlockwise* rotations

in each cycle. The step 1 of the clockwise rotation and step 1′ of the anticlockwise rotation are the power stroke photochemical steps, which go through the excited-state intermediates (3′*S*)-(*M*)-1* and (3′*R*)-(*P*)-1*, respectively. The subsequent concerted thermal helix inversion steps are accomplished via the transition states TS1 and TS1′. The Gibbs free energies for the thermal isomerizations were found experimentally to be 107.9 kJ $mol^{-1}$ for the energetically downhill isomerization and 120.1 kJ $mol^{-1}$ for the uphill isomerization [7]. Accordingly, the obtained activation barriers for the downhill isomerization (from (3′*S*)-(*P*)-1 to TS1 for step 2 and from (3′*R*)-(*M*)-1 to TS1′ for step 2′) and the uphill isomerization (from (3′*S*)-(*M*)-1 to TS1 for step 2 and from (3′*R*)-(*P*)-1 to TS1′ for step 2′) are about 111.9 and 135.2 kJ $mol^{-1}$, which is in good agreement with the experimental ones. Also compared with the experimental results is the temperature effect on the rate constant of the thermal downhill isomerization process which gives the same trend as provided by the experiment (See Supporting Information for more detail).

As for the different photoisomerization products compared with that observed from the experiment, our calculations do predict the *syn-fold* conformers in both clockwise and anticlockwise rotary cycles. Although there is lack of evidence for the existence of *syn-fold* isomers of motor 1, both experimental and theoretical studies have identified the *syn-fold* conformers as possible chemical constitutions for certain second-generation light-driven molecular motors with analogous structure [17, 40].

## 4 Conclusions

In summary, using long-range corrected density functional CAM-B3LYP, we have explored the working mechanism of a recently synthesized reversible light-driven molecular motor in detail by locating all the stationary points along the reaction paths. The different profiles of the ground-state and three lowest excited-states PECs were evaluated, by which the unidirectional *clockwise* and *anticlockwise* rotary motions of the photoisomerizations can be well understood. Although the appreciable structures of the conical intersections of $S_0/S_1$ are not accurately located, we are able to obtain the less-stable photochemical products by optimizing the highly twisted molecular structures within a large range to the ground state. Interestingly, the photoisomerization products show *syn-fold* conformations which are slightly different with that in the experiments, for which there are possible evidences both from experimental and theoretical studies of light-driven molecular motors with similar structures. Finally, by comparing the excitation energies and calculated free-energy barriers with the experimental values, it has been found that the CAM-B3LYP function cannot only give good description of excited states, but also show good performance for the thermal helix reactions.

**Acknowledgments** This work is supported by the National Natural Science Foundation of China (Nos. 91127014 and 21373124), State Key Laboratory of Sensor Technology Fund (No. SKT1202), and China Postdoctoral Science Foundation (No. 2012M521319). It is also supported by the National Supercomputer Center in Jinan and Shandong University High Performance Computing Center.

## References

1. Kelly TR, Cai XL, Damkaci F, Panicker SB, Tu B, Bushell SM, Cornella I, Piggott MJ, Salives R, Cavero M, Zhao YJ, Jasmin S (2007) Progress toward a rationally designed, chemically powered rotary molecular motor. J Am Chem Soc 129(2):376–386
2. Harada N, Koumura N, Feringa B (1997) Chemistry of unique chiral olefins. 3. Synthesis and absolute stereochemistry of trans- and cis-1,1′,2,2′,3,3′,4,4′-octahydro-3,3′-dimethyl-4,4′-biphenanthrylidenes. J Am Chem Soc 119(31):7256–7264
3. Koumura N, Zijlstra RWJ, van Delden RA, Harada N, Feringa B (1999) Light-driven monodirectional molecular rotor. Nature 401(6749):152–155
4. Kelly TR, De Silva H, Silva RA (1999) Unidirectional rotary motion in a molecular system. Nature 401(6749):150–152
5. Kelly TR (2001) Progress toward a rationally designed molecular motor. Acc Chem Res 34(6):514–522
6. Henningsen U, Schliwa M (1997) Reversal in the direction of movement of a molecular motor. Nature 389(6646):93–96
7. Ruangsupapichat N, Pollard MM, Harutyunyan SR, Feringa BL (2011) Reversing the direction in a light-driven rotary molecular motor. Nat Chem 3(1):53–60
8. Koumura N, Geertsema EM, van Gelder MB, Meetsma A, Feringa BL (2002) Second generation light-driven molecular motors. Unidirectional rotation controlled by a single stereogenic center with near-perfect photoequilibria and acceleration of the speed of rotation by structural modification. J Am Chem Soc 124(18):5037–5051
9. Amatatsu Y (2011) Theoretical design of a light-driven molecular rotary motor with low energy helical inversion: 9-(5-methyl-2-phenyl-2-cyclopenten-1-ylidene)-9H-fluorene. J Phys Chem A 115(46):13611–13618
10. Amatatsu Y (2012) Theoretical design of a fluorene-based light-driven molecular rotary motor with constant rotation. J Phys Chem A 116(41):10182–10193
11. Fang C, Oruganti B, Durbeej B (2014) Computational study of the working mechanism and rate acceleration of overcrowded alkene-based light-driven rotary molecular motors. RSC Adv 4(20):10240–10251
12. García-Iriepa C, Marazzi M, Zapata F, Valentini A, Sampedro D, Frutos LM (2013) Chiral hydrogen bond environment providing unidirectional rotation in photoactive molecular motors. J Phys Chem Lett 4(9):1389–1396
13. Grimm S, Brauchle C, Frank I (2005) Light-driven unidirectional rotation in a molecule: ROKS simulation. ChemPhysChem 6(9):1943–1947
14. Kazaryan A, Kistemaker JCM, Schäfer LV, Browne WR, Feringa BL, Filatov M (2010) Understanding the dynamics behind the photoisomerization of a light-driven fluorene molecular rotary motor. J Phys Chem A 114(15):5058–5067
15. Kazaryan A, Lan ZG, Schafer LV, Thiel W, Filatov M (2011) Surface hopping excited-state dynamics study of the

photoisomerization of a light-driven fluorene molecular rotary motor. J Chem Theory Comput 7(7):2189–2199
16. Liu F, Morokuma K (2012) Computational study on the working mechanism of a stilbene light-driven molecular rotary motor: sloped minimal energy path and unidirectional nonadiabatic photoisomerization. J Am Chem Soc 134(10):4864–4876
17. Perez-Hernandez G, Gonzalez L (2010) Mechanistic insight into light-driven molecular rotors: a conformational search in chiral overcrowded alkenes by a pseudo-random approach. Phys Chem Chem Phys 12(38):12279–12289
18. Lee CT, Yang WT, Parr RG (1988) Development of the Colle–Salvetti correlation-energy formula into a functional of the electron density. Phys Rev B 37(2):785–789
19. Becke AD (1992) Density-functional thermochemistry. II. The effect of the Perdew–Wang generalized-gradient correlation correction. J Chem Phys 97(12):9173–9177
20. Becke AD (1992) Density-functional thermochemistry. I. The effect of the exchange-only gradient correction. J Chem Phys 96(3):2155–2160
21. Becke AD (1993) Density-functional thermochemistry. III. The role of exact exchange. J Chem Phys 98(7):5648–5652
22. Becke AD (1996) Density-functional thermochemistry. IV. A new dynamical correlation functional and implications for exact-exchange mixing. J Chem Phys 104(3):1040–1046
23. Becke AD (1997) Density-functional thermochemistry. V. Systematic optimization of exchange-correlation functionals. J Chem Phys 107(20):8554–8560
24. Arabi AA, Becke AD (2012) Assessment of the PW86+ PBE+ XDM density functional on van der Waals complexes at non-equilibrium geometries. J Chem Phys 137(1):7
25. Runge E, Gross EKU (1984) Density-functional theory for time-dependent systems. Phys Rev Lett 52(12):997–1000
26. Bauernschmitt R, Ahlrichs R (1996) Treatment of electronic excitations within the adiabatic approximation of time dependent density functional theory. Chem Phys Lett 256(4–5):454–464
27. Casida ME, Jamorski C, Casida KC, Salahub DR (1998) Molecular excitation energies to high-lying bound states from time-dependent density-functional response theory: characterization and correction of the time-dependent local density approximation ionization threshold. J Chem Phys 108(11):4439–4449
28. Furche F, Ahlrichs R (2002) Adiabatic time-dependent density functional methods for excited state properties. J Chem Phys 117(16):7433–7447
29. Marques MAL, Gross EKU (2004) Time-dependent density functional theory. Annu Rev Phys Chem 55:427–455
30. Yanai T, Tew DP, Handy NC (2004) A new hybrid exchange-correlation functional using the Coulomb-attenuating method (CAM-B3LYP). Chem Phys Lett 393(1–3):51–57
31. Stephens PJ, Devlin FJ, Chabalowski CF, Frisch MJ (1994) Ab initio calculation of vibrational absorption and circular dichroism spectra using density functional force fields. J Phys Chem 98(45):11623–11627
32. Cheol HC, Miklos K, Alfred K (1997) Limitations of current density functional theories for the description of partial pi-bond breaking. Chem Phys Lett 276(3–4):266–268
33. Chai JD, Head-Gordon M (2008) Systematic optimization of long-range corrected hybrid density functionals. J Chem Phys 128(8):084106
34. Rostov IV, Amos RD, Kobayashi R, Scalmani G, Frisch MJ (2010) Studies of the ground and excited-state surfaces of the retinal chromophore using CAM-B3LYP. J Phys Chem B 114(16):5547–5555
35. Rostov IV, Kobayashi R, Amos RD (2012) Comparing long-range corrected functionals in the cis–trans isomerisation of the retinal chromophore. Mol Phys 110(19–20):2329–2336
36. Zhao Y, Truhlar DG (2008) Density functionals with broad applicability in chemistry. Acc Chem Res 41(2):157–167
37. Scalmani G, Frisch MJ, Mennucci B, Tomasi J, Cammi R, Barone V (2006) Geometries and properties of excited states in the gas phase and in solution: theory and application of a time-dependent density functional theory polarizable continuum model. J Chem Phys 124(9):094107
38. Hirata S, Head-Gordon M (1999) Time-dependent density functional theory within the Tamm–Dancoff approximation. Chem Phys Lett 314(3–4):291–299
39. Frisch MJ, Trucks GW, Schlegel HB, Scuseria GE, Robb MA, Cheeseman JR, Scalmani G, Barone V, Mennucci B, Petersson GA, Nakatsuji H, Caricato M, Li X, Hratchian HP, Izmaylov AF, Bloino J, Zheng G, Sonnenberg JL, Hada M, Ehara M, Toyota K, Fukuda R, Hasegawa J, Ishida M, Nakajima T, Honda Y, Kitao O, Nakai H, Vreven T, Montgomery JA, Peralta JE, Ogliaro F, Bearpark M, Heyd JJ, Brothers E, Kudin KN, Staroverov VN, Kobayashi R, Normand J, Raghavachari K, Rendell A, Burant JC, Iyengar SS, Tomasi J, Cossi M, Rega N, Millam JM, Klene M, Knox JE, Cross JB, Bakken V, Adamo C, Jaramillo J, Gomperts R, Stratmann RE, Yazyev O, Austin AJ, Cammi R, Pomelli C, Ochterski JW, Martin RL, Morokuma K, Zakrzewski VG, Voth GA, Salvador P, Dannenberg JJ, Dapprich S, Daniels AD, Farkas, Foresman JB, Ortiz JV, Cioslowski J, Fox DJ (2009) Gaussian 09, Revision C.01, Wallingford, CT
40. Klok M, Walko M, Geertsema EM, Ruangsupapichat N, Kistemaker JCM, Meetsma A, Feringa BL (2008) New mechanistic insight in the thermal Helix inversion of second-generation molecular motors. Chem Eur J 14(35):11183–11193

Theor Chem Acc (2014) 133:1532
DOI 10.1007/s00214-014-1532-3

REGULAR ARTICLE

# The combined CASPT2 and CASSCF studies on photolysis of 3-thienyldiazomethane and subsequent reactions

**Pei-Jie Guan · Wei-Hai Fang**

Received: 26 May 2014 / Accepted: 28 June 2014 / Published online: 9 August 2014
© Springer-Verlag Berlin Heidelberg 2014

**Abstract** The triplet 3-thienylcarbene and α-thial-methylenecyclopropene were observed as the main products upon photolysis ($\lambda > 540$ nm) of 3-thienyldiazomethane (3-TD) under the matrix-isolated conditions. The underlying mechanism was explored by the combined CASPT2 and CASSCF calculation in the present work. The $S_1$, $T_2$, and $T_1$ surfaces were found to be quasi-degenerate over a wide structural region. Meanwhile, there is a relatively strong spin–orbit interaction between the $S_1$ and $T_2$ states, due to the sulfur-atom effect. As a result, the triplet 3-thienylcarbene can be formed with a noticeable efficiency. The $S_1$ minimum and $S_1/S_0$ intersection structures for 3-TD were predicted to be undistinguishable by the present CASPT2//CASSCF calculations. Therefore, the $S_1 \rightarrow S_0$ internal conversion that occurs in the vicinity of the $S_1/S_0$ intersection ($S_1$ minimum) is in competition with the $S_1 \rightarrow T_1$ intersystem crossing through the three-surface ($S_1$, $T_2$, and $T_1$) intersection region. Once the excited 3-TD molecule returns to the $S_0$ state, the singlet 3-thienylcarbene can be generated with a considerable efficiency, which is followed by the carbene rearrangement, leading to the final product of α-thial-methylenecyclopropene (α-TMC). The concerted $N_2$ loss and rearrangement in the excited state was proposed for the α-TMC formation in previous experimental study, which is not supported by the present CASPT2//CASSCF calculation. The reason for this might come from the matrix effect, which is open for further study.

**Keywords** 3-Thienyldiazomethane · Photodissociation · Ab initio calculation

## 1 Introduction

Diazomethane and its derivatives have been widely used as reagents in synthetic organic chemistry. For example, they were employed as methylating agents in cyclopropanation reactions with olefins [1–4] and for one-carbon chain elongation by insertion into the primary C–H bond [5]. Diazomethane derivatives can function as photochemical precursors of singlet carbenes, which are the reactive intermediates and play important role in many branches of chemistry [6–10]. Mechanistic study on how to form the singlet carbene from these precursors has a long and venerable history [6, 11] and is still active area in the fields of chemical kinetics and physical organic chemistry [12–16]. The photolysis of diazomethane has been extensively studied from experimental and theoretical viewpoints [13, 17–21]. Upon irradiation of diazomethane ($CH_2N_2$) in the gas phase, methylene ($CH_2$) was observed as the initial product in different singlet states that are dependent on excitation wavelengths (a weak $n \rightarrow \pi^*$ transition at 300–500 nm and a strong $\pi \rightarrow \pi^*$ transition at 200–260 nm) [17–20]. It has been argued whether the dissociation of $CH_2N_2$ to $CH_2 + N_2$ occurs in the excited electronic state [13, 21].

Ultrafast time-resolved spectroscopic techniques have been used to probe the excited-state dynamics of aryl diazocompounds and the formation of reactive carbene intermediates [22–29]. The excited-state lifetimes of

Dedicated to Professor Guosen Yan and published as part of the special collection of articles celebrating his 85th birthday.

P.-J. Guan · W.-H. Fang (✉)
Key Laboratory of Theoretical and Computational Photochemistry, Ministry of Education, College of Chemistry, Beijing Normal University, Beijing 100875, China
e-mail: Fangwh@bnu.edu.cn

*p*-biphenylyldiazomethane ($BpCN_2H$) and *p*-biphenylyldiazoethane ($BpCN_2CH_3$) were inferred to be within 300 fs by femtosecond time-resolved UV–vis transient absorption studies [23–27]. The experimentally observed absorption bands at ~360 nm were assigned to the singlet carbenes ($^1BpCH$ and $^1BpCCH_3$) with their lifetimes changed from a few hundreds of picoseconds in acetonitrile to ~10 ps in a carbene scavenging solvent of methanol. Meanwhile, the quantum yield for formation of $^1BpCCH_3$ was determined to be much lower than that for formation of $^1BpCH$. It was proposed that the excited state of $BpCN_2CH_3$ underwent 1,2-H shift in concert with $N_2$ extrusion [24, 25]. Subsequently, the direct experimental evidence for the rearrangement in the excited states was obtained by ultrafast time-resolved IR spectroscopic study of alkyl diazoester ($CH_3CN_2CO_2CH_3$) in chloroform [29].

It is well known that singlet carbenes are primarily released by photodissociation of aryl diazocompounds [23–29]. The nascent singlet carbene can undergo either intramolecular or intermolecular reactions to form final products. As organic reactive intermediates, heteroaryl carbenes have been extensively investigated in the past several decades, due to their importance in astronomical environments [30]. A major channel for formation of heteroaryl carbene involves pyrolysis and photolysis of heteroaryl diazocompounds, such as thienyldiazomethanes. Because of the interaction between the heteroaryl ring and electron-rich diazo groups, thienyldiazomethanes were expected to exhibit some unique characters. Early in 1978, Shechter and co-workers studied pyrolysis of 2-thienyldiazomethane and its methyl-substituted analogs [31]. Heteroaryl carbenes were inferred to be reactive intermediates, and the main products were observed to be unsaturated thiocarbonyls and 1,2-di(2-thienyl)ethylenes. The primary product has been proposed to be 3-thienylcarbene upon photolysis of 3-thienyldiazomethane in argon at 10 K with $\lambda > 450$ nm [32]. In order to determine whether the triplet 3-thienylcarbene is formed initially, a spectroscopic study has been performed on photochemistry of furyl- and thienyldiazomethanes by IR, UV/vis, and EPR spectroscopy [16]. The conformational isomers of 3-thienylcarbene exhibit a weak electronic absorption of triplet characteristic in the visible spectrum ($\lambda_{max} = 467$ nm) and an unusually large difference in zero-field splitting parameters in the EPR spectrum, which afford strong evidence for formation of the triplet 3-thienylcarbene. However, the underlying mechanism is still unclear up to now.

Photolysis of diazomethane and its aryl-substituted derivatives has been a subject of numerous ab initio calculations and dynamics simulations in order to explore the mechanism for formation of singlet carbene [13, 15, 20, 21, 33]. However, how the triplet 3-thienylcarbene is produced from the photolysis of 3-thienyldiazomethane was not explored from theoretical viewpoint up to now. In the present work, we performed the combined CASPT2//CASSCF study on structures and reactivity of 3-thienyldiazomethane in the ground and low-lying excited states, which enable us to understand mechanism of 3-thienylcarbenes generated by the photolysis of 3-thienyldiazomethane at $\lambda > 540$ nm. Meanwhile, 3-thienylcarbene rearrangements in singlet and triplet states were determined on the basis of the CASSCF optimized stationary and intersection structures as well as the CASPT2 calculated relative energies. We believe that the present study provides new insights into mechanism for formation of 3-thienylcarbene, which is very helpful for understanding mechanistic photochemistry of heteroaryl diazocompounds.

## 2 Computational details

Stationary structures in the ground and low-lying excited states were fully optimized at the level of the complete active space self-consistent field (CASSCF), which was confirmed to be appropriate for the potential energy surface (PES) topology analysis of diazocompounds [13, 20]. All the optimized stationary structures were characterized as minima or saddle points on PESs by frequency analysis. The minimum-energy structures on intersection seams of different electronic states were determined with the state-averaged CASSCF wave functions to ensure a balanced description of multi-states at the intersection area. On the basis of the CASSCF optimized structures for the stationary and intersection points, the energies were recomputed with the CASPT2 method (the complete active space perturbation theory to second order). The combined CASPT2//CASSCF calculation was extensively used to study excited-state behavior of different systems [34–37] and proven to be well suited for the accurate description of the lowest-lying electronic states. The active space of the present CASSCF calculation for 3-thienyldiazomethane is comprised of twelve electrons distributed in eleven orbitals, assigned as CAS(12,11) hereafter, which is composed of all $\pi$ and $\pi^*$ orbitals. Since the C–N fission occurs in the process of $N_2$ extrusion, the C–N $\sigma$ and $\sigma^*$ orbitals are included in the active space. As for 3-thienylcarbene and its rearrangement reactions, we chose eight electrons in eight orbitals as the active space, which originate from four $\pi$ and $\pi^*$ orbitals in the thiophene ring, the C–S $\sigma$ and $\sigma^*$ orbitals, and the two singly occupied orbitals of the carbene C atom. The 6-31G* basis set was used for all CASSCF and CASPT2 calculations, which were carried out with Gaussian 09 and Molcas 7.4 software packages [38, 39].

## 3 Results and discussion

### 3.1 The lowest-lying electronic states

Photochemistry of 3-thienyldiazomethane (3-TD) was investigated with excitation wavelength of 543 nm or longer [16]. In order to identify the initial state populated by irradiation at ~540 nm, geometric structures of 3-TD in the lowest-lying electronic states were optimized at the CAS(12,11)/6-31G* level and the obtained results were shown in Fig. 1, along with the selected bond parameters.

As expected, the C=N=N moiety has a linear configuration in the ground-state ($S_0$) equilibrium structure of 3-TD (3-TD_$S_0$_min). However, the C–N=N angle becomes ~126° in the minimum-energy structures of the lowest excited singlet ($S_1$) and triplet ($T_1$) states, which are referred to as 3-TD_$S_1$_min and 3-TD_$T_1$_min, respectively. Meanwhile, the C–N bond is mainly of a single-bond character in 3-TD_$S_1$_min and 3-TD_$T_1$_min. On the basis of the CAS(12,11)/6-31G* calculation for 3-thienyldiazomethane in the low-lying electronic states, eleven active orbitals are schematically shown in Fig. 2 and are labeled by AO$i$ ($i$ = 1–11). Two singly occupied orbitals of the $S_1$ or $T_1$ state are found to be AO6 (the out-of-plane C–N bonding π orbital) and AO8 (the in-plane N=N anti-bonding π* orbital). It is evident that the $S_1$ or $T_1$ state originates from π → π* transition localized in the C–N–N structural region. The second excited singlet ($S_2$) and triplet ($T_2$) states are of the ππ* nature and are mainly localized in the thiophene ring with a considerable delocalization into the C–N–N region, since two unpaired electrons for the $S_2$ and $T_2$ states are mainly distributed in AO5, AO9, and AO10 in Fig. 2.

On the basis of the CAS(12,11)/6-31G* optimized 3-TD_$S_0$_min structure, the vertical excitation energies to the $S_1$ and $S_2$ states were calculated to be 58.4 and 108.8 kcal/mol

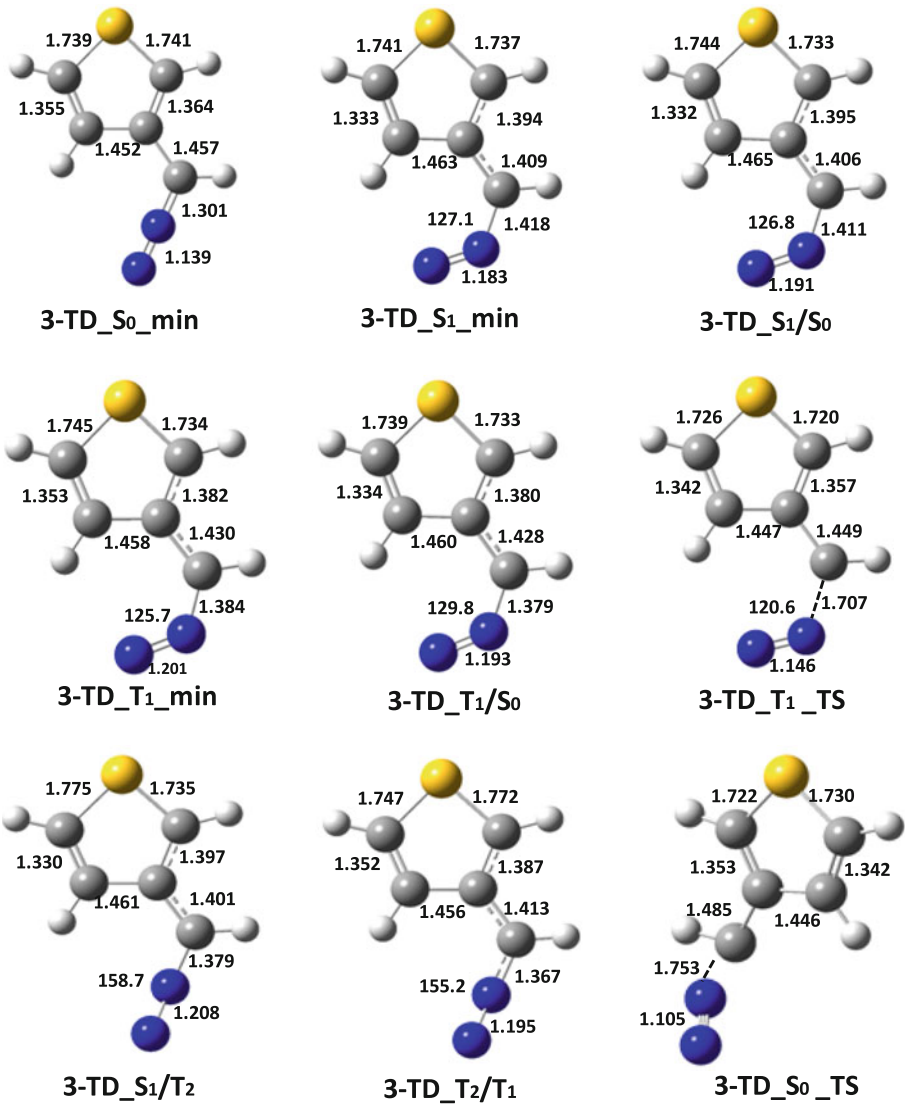


**Fig. 1** CASSCF optimized stationary and intersection structures, along with the selected bond lengths in angstrom

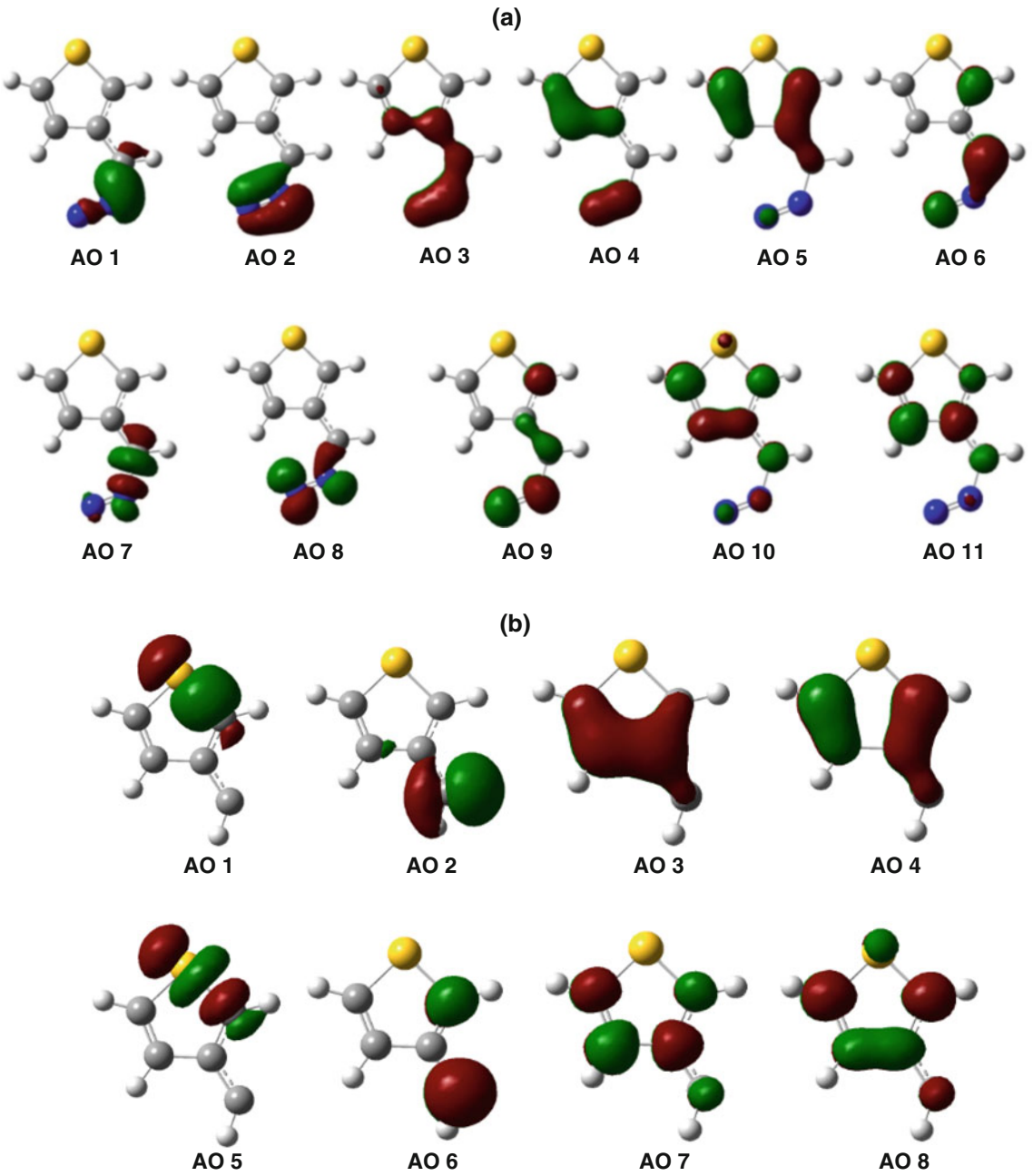


**Fig. 2** Active orbitals of the CASSCF calculations for 3-thienyldiazomethane (**a**) and 3-thienylcarbene (**b**)

at the CASPT2//CAS(12,11)/6-31G* level of theory. In comparison with the absorption peak of 494 nm (57.9 kcal/mol) for 3-thienyldiazomethane in acetonitrile solution [16], we come into conclusion that the $S_1$ state is initially populated upon photolysis of 3-TD at 490 nm and longer wavelengths.

### 3.2 Formation of the singlet 3-thienylcarbene

It has been established that 3-thienylcarbene (3-TC) is energetically lower in the lowest triplet state than in the lowest singlet state [16], which are, respectively, referred to as 3-TC_$T_1$ and 3-TC_$S_1$ hereafter. Once the 3-TD molecule is excited to the $S_1$ state, the C–N bond cleavage might occur along the $S_1$ pathway. Direct extrusion of molecular nitrogen from 3-TD on the $S_1$ state was traced by the CAS(12,11)/6-31G* stepwise optimizations, followed by the CASPT2 single-point energy correction. The barrier height for the C–N bond cleavage on the $S_1$ state was estimated to be 69.5 and 39.7 kcal/mol with respect to the $S_0$ and $S_1$ minima, respectively. It is evident that the direct

$S_1$ C–N fission is inaccessible in energy upon photolysis of 3-TD in the wavelength range of 490–540 nm. Therefore, there is little possibility that the singlet 3-thienylcarbene (3-TC_$S_1$) is directly formed along the $S_1$ pathway.

From the $S_1$ state, there are mainly two non-radiative pathways for the 3-TD molecule to deactivate: internal conversion (IC) to the $S_0$ state and intersystem crossing (ISC) to a triplet state. Here, we pay attention to the $S_1 \rightarrow S_0$ IC process and the subsequent formation of the singlet 3-thienylcarbene along the $S_0$ pathway. The minimum-energy conical intersection between $S_1$ and $S_0$ was determined by the two state-averaged CAS(8,7)/6-31G* calculations, referred to as 3-TD_$S_1$/$S_0$. It was found that the 3-TD_$S_1$_min and 3-TD_$S_1$/$S_0$ structures are not distinguishable from each other. As a result, the IC process from $S_1$ to $S_0$ takes place very effectively, leading to the 3-TD molecule in a hot $S_0$ state. A transition state, 3-TD_$S_0$_TS, was determined on the $S_0$ pathway from 3-TD_$S_0$_min to the singlet 3-thienylcarbene and $N_2$. The barrier height was predicted to be 32.1 kcal/mol at the CASPT2//CAS(12,11)/6-31G* level of theory. The present CASPT2//CASSCF calculation reveals that the singlet 3-thienylcarbene (3-TC_$S_1$) can be formed with a considerable efficiency upon irradiation of 3-thienyldiazomethane at ~540 nm.

### 3.3 Formation of the triplet 3-thienylcarbene

In addition to the $S_1 \rightarrow S_0$ IC process, the $S_1 \rightarrow T_1$ intersystem crossing is another important pathway for the $S_1$ deactivation, which is probably responsible for the triplet 3-thienylcarbene observed experimentally [16]. The minimum-energy crossing point between singlet and triplet states was optimized at the state-averaged CAS(12,11)/6-31G* level. The optimized structure was confirmed to be the crossing point between the $S_1$ and $T_2$ states by the CASSCF wave functions and electron populations, referred to as 3-TD_$S_1$/$T_2$ hereafter. As shown in Fig. 1, the 3-TD_$S_1$/$T_2$ structure is still in the $S_1$ Franck–Condon (FC) region and has its relative energy of 52.5 kcal/mol at the CASPT2//CAS(12,11)/6-31G* level. As pointed out before, the two unpaired π electrons in the $T_2$ state are mainly distributed in the thiophene ring and the C=N bond is mainly of a double-bond character. In addition, the C=N bond fission from the $T_2$ state is adiabatically correlated with an excited triplet state of 3-thienylcarbene, which is not favorable in energy. Thus, there is little possibility for the C=N bond to break along the $T_2$ pathway to the triplet 3-thienylcarbene observed experimentally.

To explore the possibility of the $T_2 \rightarrow T_1$ internal conversion, a conical intersection between the $T_1$ and $T_2$ states was determined by the state-averaged CAS(12,11)/6-31G* optimization, referred to as 3-TD_$T_2$/$T_1$ hereafter. As shown in Fig. 1, 3-TD_$T_2$/$T_1$ is similar to 3-TD_$S_1$/$T_2$ in structure. It is found that a small difference in 3-TD_$T_2$/$T_1$ and 3-TD_$S_1$/$T_2$ structures originates mainly from the redistribution of the conjugated π electrons, which will not result in a large change in energy. The energy difference between 3-TD_$T_2$/$T_1$ and 3-TD_$S_1$/$T_2$ was predicted to be 2.6 kcal/mol by the CASPT2/CAS(12,11)/6-31G* calculations. Test single-point energy calculations at the CASPT2/CAS(12,11)/6-31G* level for a series of the structures show that the $S_1$, $T_2$, and $T_1$ states are nearly degenerate in the structural region from 3-TD_$S_1$/$T_2$ to 3-TD_$T_2$/$T_1$. As discussed before, the $T_2$ state is of the $^3\pi\pi^*$ character localized in the thiophene ring. Because of a heavy-atom effect of sulfur, there is a relatively strong spin–orbit interaction between the $S_1$ and $T_2$ states, which enhances considerably the rate of the $S_1 \rightarrow T_2$ process. The spin–orbit coupling (SOC) between $S_1$ and $T_2$ was calculated to be 35.1 $cm^{-1}$ in the vicinity of the 3-TD_$S_1$/$T_2$ structure by using a one-electron operator, and effective nuclear charges for spin–orbit interaction implemented in Gaussian 03 software package. In addition, the time scale for the $T_2 \rightarrow T_1$ internal conversion process in the vicinity of the 3-TD_$T_2$/$T_1$ conical intersection is expected to be on the order of a vibrational period [40]. Thus, the $S_1 \rightarrow T_1$ intersystem crossing occurs efficiently in the structural region from 3-TD_$S_1$/$T_2$ to 3-TD_$T_2$/$T_1$, due to a function of the $T_2$ state as a bridge [41, 42].

The C–N bond cleavage of 3-thienyldiazomethane was determined to be the most probable pathway on the $T_1$ state, leading to formation of the triplet 3-TC and $N_2$. A transition state of 3-TD_$T_1$_TS was obtained on the $T_1$ pathway, which was confirmed to be the saddle point on the $T_1$ pathway from 3-TD_$T_1$_min to $N_2$ and 3-TC_$T_1$_min (the equilibrium geometry of 3-thienylcarbene in the $T_1$ state). The barrier height was calculated to be 13.1 and 34.8 kcal/mol with respect to the $T_1$ and $S_0$ vibrational zero levels, respectively. Formation of the triplet 3-thienylcarbene along the $T_1$ pathway is favorable in energy upon irradiation of 3-thienyldiazomethane at ~540 nm.

### 3.4 Formation of α-thial-methylenecyclopropene

Upon irradiation of 3-thienyldiazomethane (3-TD) at $\lambda > 534$ nm [16], α-thial-methylenecyclopropene (α-TMC) was observed as one of the main products in Ar or $N_2$ at 10 K. There are two possible mechanisms responsible for the α-TMC formation, the concerted $N_2$ loss and rearrangement in the excited state of the diazo precursor [16, 24, 29] and the stepwise process of molecular nitrogen extrusion followed by carbene isomerization in the ground state [27, 32, 43]. The concerted process from 3-TD to α-TMC involves formation of the C–C bond and fissions of the C–N and C–S bonds simultaneously. Because the initial relaxation from the $S_1$ Franck–Condon (FC) structure

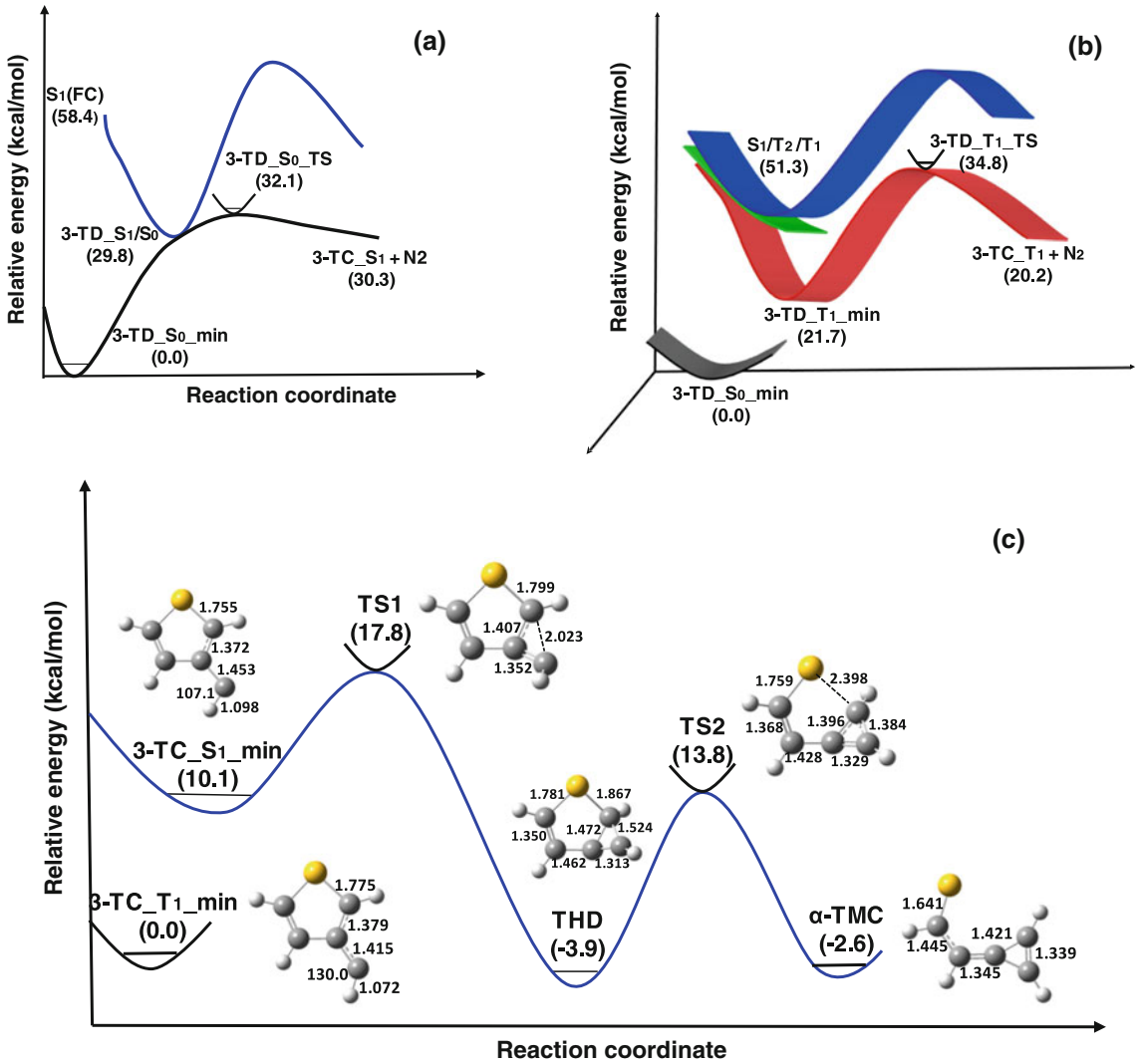


**Fig. 3** Schematical potential energy profiles for formation of the singlet 3-thienylcarbene (**a**), for formation of the triplet 3-thienylcarbene (**b**), and for rearrangement of the singlet 3-thienylcarbene (**c**). The stationary structures on the reaction pathways and their relative energies (kcal/mol) are given, together with some key bond lengths (Å) in the related structures

to 3-TD_$S_1$_Min is downhill process, the concerted process takes place in the $S_1$ state with little possibility. In order to explore the possibility that the concerted process occurs in the $S_0$ state, the $S_0$ potential energy surface was scanned as a function of the C–N and C–S distances with the other bond parameters optimized fully. The scanned $S_0$ potential energy surface shows clearly that the reaction from 3-TD to α-TMC proceeds in a stepwise way. The first step involves the C–N bond fission of 3-TD_$S_0$ yielding singlet 3-thienylcarbene (3-TC_$S_1$), which is followed by the C–S bond fission and isomerization to α-TMC.

As pointed out before, the direct $S_1$ C–N fission is inaccessible in energy upon photolysis of 3-TD at $\lambda > 540$ nm. Since the ultrafast $S_1 \rightarrow S_0$ internal conversion occurs at the vicinity of the 3-TD_$S_1$/$S_0$ conical intersection, the singlet 3-thienylcarbene (3-TC_$S_1$) was formed from 3-TD_$S_0$ with a barrier of 32.1 kcal/mol, which is considered as the first step (3-TD_$S_0$ → 3-TC_$S_1$ + $N_2$) for formation of α-TMC from the 3-TD photolysis. An intermediate was determined on the pathway from 3-TC_$S_1$ to α-TMC, which is assigned as 1H-2-thiabicyclo[3.1.0]hexa-3,5-diene (THD) observed experimentally [16]. As shown in Fig. 3, the barrier height was calculated to be 7.7 kcal/mol at the CASPT2//CAS(8,8)/6-31G* level for the second step of 3-TC_$S_1$ → THD, while the third step of THD → α-TMC has a barrier of 17.7 kcal/mol at the same level of theory.

On the basis of the CASSCF calculated frequencies for the stationary structures on the pathway from 3-TD_$S_0$ to α-TMC + $N_2$ and the CASPT2 calculated barrier heights, the RRKM rate theory [43] was used to estimate rate constants for each step of the sequential reaction with the CASPT2//CAS(12,11)/6-31G* calculated vertical

excitation energies of 58.4 kcal/mol as the available energies. The calculated rate constants indicate that the 3-TC_$S_1$ formation is the rate-determining step and the rate constant of the THD formation is about 100 times larger than that on the third step from THD to α-TMC. As a result, the THD intermediate might be observed experimentally, when the sequential reaction is in its stationary state. However, there is little possibility to have the singlet 3-thienylcarbene observed under the experimental condition. A minor amount of a species was assigned as THD, which is based on a comparison of experimental and the computed IR spectra [16].

## 4 Summary

In the present work, we performed the combined CASPT2//CASSCF study on photodissociation of 3-thienyldiazomethane (3-TD) and the subsequent reactions. Upon irradiation of 3-TD at ~540 nm, the $S_1(^1\pi\pi^*)$ state is initially populated, which originates from one-electron excitation from the out-of-plane C–N π orbital to the in-plane N=N π* orbital. From the $S_1$ state, there are three possible non-radiative pathways for the 3-TD molecule to deactivate: the direct $S_1$ reactions, internal conversion (IC) to the $S_0$ state, and intersystem crossing (ISC) to a triplet state. The CASPT2//CASSCF calculated results provide a strong evidence that the C–N bond fission and the concerted $N_2$ loss take place in the $S_1$ state with little possibility. On the basis of CASSCF optimized structures for the $S_1/T_2$ and $T_2/T_1$ intersections as well as the CASPT2//CASSCF calculated relative energies, it is found that the $S_1$, $T_2$, and $T_1$ surfaces are near degenerate over a wide structural region. Because of the heavy-atom effect of sulfur, there is a relatively strong spin–orbit interaction between the $S_1$ and $T_2$ states, which enhances considerably the rate of the $S_1 \rightarrow T_2$ process. In addition, the time scale for the $T_2 \rightarrow T_1$ internal conversion process is expected to be on the order of a vibrational period in the vicinity of $T_2/T_1$ conical intersection. Thus, the $S_1 \rightarrow T_1$ intersystem crossing occurs efficiently with a function of the $T_2$ state as a bridge, once the 3-TD molecule is populated in the $S_1$ state. A barrier of 13.1 kcal/mol was determined by the CASPT2//CASSCF calculation on the $T_1$ pathway from the triplet 3-thienyldiazomethane (3-TD_$T_1$) to the triplet 3-thienylcarbene (3-TC_$T_1$). All of these enable us to understand mechanism of 3-thienylcarbenes generated by the photolysis of 3-thienyldiazomethane at $\lambda > 540$ nm [16].

The 3-TD_$S_1$_min and 3-TD_$S_1/S_0$ structures were found to be undistinguishable by the present CASPT2//CASSCF calculations. Therefore, the $S_1 \rightarrow S_0$ IC process takes place very effectively after irradiation of the 3-TD molecule to the $S_1$ state, which is at least in competition with the $S_1 \rightarrow T_1$ ISC process. Once the 3-TD molecule returns to the hot $S_0$ state, the singlet 3-thienylcarbene (3-TC_$S_1$) can be formed with a barrier of 32.1 kcal/mol on the pathway. Since the singlet 3-thienylcarbene is very reactive, the α-thial-methylenecyclopropene (α-TMC) can be formed easily, which has been observed as one of the main products upon photolysis of 3-TD in Ar or $N_2$ at 10 K. An intermediate was determined on the pathway from 3-TC_$S_1$ to α-TMC, which is assigned as 1H-2-thiabicyclo[3.1.0]hexa-3,5-diene (THD). The calculated rate constant for formation of THD from 3-TC_$S_1$ is about 100 times larger than that for the reaction of THD → α-TMC, which might be responsible for a minor amount of a species observed experimentally [16]. Finally, it should be pointed out that the concerted $N_2$ loss and rearrangement in the excited state was proposed for the α-TMC formation upon photolysis of 3-TD in Ar or $N_2$ at 10 K [16], which is not supported by the present CASPT2//CASSCF calculations. The reason for this might come from the matrix effect of Ar or $N_2$ at 10 K, and the related studies are still in progress and will be reported in due time.

**Acknowledgments** This work was supported by grants from the NSFC (Grant No. 21033002) and from the Major State Basic Research Development Programs (Grant No. 2011CB808503).

## References

1. Coelho PS, Brustad EM, Kannan A, Arnold FH (2013) Science 339:307
2. Morandi B, Carreira EM (2012) Science 335:1471
3. Kaschel J, Schneider TF, Werz DB (2012) Angew Chem Int Ed 51:7085
4. Phillips DL, Fang W-H, Zheng X (2001) J Am Chem Soc 123:4197
5. Lo VK-Y, Guo Z, Choi MK-W, Yu W-Y, Huang J-S, Che C-M (2012) J Am Chem Soc 134:7588
6. Kirmse W (1971) Carbene chemistry. Academic Press, New York
7. Durr H, Abdel-Wahab A-M (1995) A CRC handbook of organic photochemistry and photobiology. CRC Press, Boca Raton
8. Pan W, Balci M, Shevlin PB (1997) J Am Chem Soc 119:5035
9. McKee ML, Shevlin PB, Zottola M (2001) J Am Chem Soc 123:9418
10. Moss RA, Platz MS Jr, Jones M (2004) Reactive intermediate chemistry. Wiley, New York
11. Rudolf P, Buback J, Aulbach J, Nuernberger P, Brixner T (2010) J Am Chem Soc 132:15213
12. Arenas JF, Lopez-Tocon I, Otero JC, Soto J (2002) J Am Chem Soc 124:1729
13. Lee H, Miyamoto Y, Tateyama Y (2009) J Org Chem 74:562
14. Burdzinski G, Platz MS (2010) J Phys Org Chem 23:308
15. Zhang Y, Vyas S, Hadad CM, Platz MS (2010) J Phys Chem A 114:5902
16. Pharr CR, Kopff LA, Bennett B, Reid SA, McMahon RJ (2012) J Am Chem Soc 134:6443
17. Herzberg G (1966) Molecular spectra and molecular structure. III. Electronic spectra and electronic structure of polyatomic molecules. Van Nostrand, Princeton
18. Wolf RJ, Hase WL (1978) J Phys Chem 82:1850
19. Seburg RA, McMahon RJ (1992) J Am Chem Soc 114:7183

20. Yamamoto N, Bernardi F, Bottoni A, Olivucci M, Robb MA, Wilsey S (1994) J Am Chem Soc 116:2064
21. Arenas JF, Lopez-Toco I, Otero NJC, Soto J (2002) J Am Chem Soc 124:1728
22. Peon J, Polshakov D, Kohler B (2002) J Am Chem Soc 124:6428
23. Wang J, Burdzinski G, Gustafson TL, Platz MS (2006) J Org Chem 71:6221
24. Wang J, Burdzinski G, Gustafson TL, Platz MS (2007) J Am Chem Soc 129:2597
25. Wang J, Kubicki J, Hilinski EF, Mecklenburg SL, Gustafson TL, Platz MS (2007) J Am Chem Soc 129:13683
26. Wang J, Kubicki J, Gustafson TL, Platz MS (2008) J Am Chem Soc 130:2304
27. Wang J, Burdzinski G, Kubicki J, Platz MS (2008) J Am Chem Soc 130:11195
28. Zhang Y, Burdzinski G, Kubicki J, Vyas S, Hadad CM, Sliwa M, Poizat O, Buntinx G, Platz MS (2009) J Am Chem Soc 131:13784
29. Burdzinski G, Zhang Y, Selvaraj P, Sliwa M, Platz MS (2010) J Am Chem Soc 132:2126
30. Kaiser RI (2002) Chem Rev 102:1309 and references therein
31. Hoffman RV, Orphanides GG, Shechter H (1978) J Am Chem Soc 100:7927
32. Albers R, Sander W (1997) J Org Chem 62:761
33. Kerkines ISK, Cyarsky P, Mavridis A (2005) J Phys Chem 109:10148
34. Han J, Chen XB, Shen L, Chen Y, Fang W-H, Wang HB (2011) Chem Eur J 17:13971
35. Han J, Shen L, Chen XB, Fang W-H (2013) J Mater Chem C 1:4227
36. Liu FY, Morokuma K (2013) J Am Chem Soc 135:10693
37. Xiao HY, Maeda S, Morokuma K (2013) J Phys Chem A 117:7001
38. Gaussian 09, Revision A.1, Frisch MJ, Trucks GW, Schlegel HB, Scuseria GE, Robb MA, Cheeseman JR, Scalmani G, Barone V, Mennucci B, Petersson GA, Nakatsuji H, Caricato M, Li X, Hratchian HP, Izmaylov AF, Bloino J, Zheng G, Sonnenberg JL, Hada M, Ehara M, Toyota K, Fukuda R, Hasegawa J, Ishida M, Nakajima T, Honda Y, Kitao O, Nakai H, Vreven T, Montgomery JA Jr, Peralta JE, Ogliaro F, Bearpark M, Heyd JJ, Brothers E, Kudin KN, Staroverov VN, Kobayashi R, Normand J, Raghavachari K, Rendell A, Burant JC, Iyengar SS, Tomasi J, Cossi M, Rega N, Millam NJ, Klene M, Knox JE, Cross JB, Bakken V, Adamo C, Jaramillo J, Gomperts R, Stratmann RE, Yazyev O, Austin AJ, Cammi R, Pomelli C, Ochterski JW, Martin RL, Morokuma K, Zakrzewski VG, Voth GA, Salvador P, Dannenberg JJ, Dapprich S, Daniels AD, Farkas Ö, Foresman JB, Ortiz JV, Cioslowski J, Fox DJ (2009) Gaussian, Inc., Wallingford CT
39. Molcas 7.4: Aquilante F, De Vico L, Ferre N, Ghigo G, Malmqvist P-A, Neogrady P, Pedersen TB, Pitonak M, Reiher M, Roos BO, Serrano-Andres L, Urban M, Veryazov V, Lindh R (2010) J Comput Chem 31:224. Code development: Veryazov V, Widmark P-O, Serrano-Andres L, Lindh R, Roos BO (2004) Int J Quantum Chem 100:626
40. Bernardi F, Olivucci M, Robb MA (1996) Chem Soc Rev 25:321
41. Fang W-H, Phillips DL (2002) Chem Phys Chem 3:889
42. Cui G, Fang W-H (2013) J Chem Phys 138:044315
43. Burdzinski G, Wang J, Gustafson TL, Platz MS (2008) J Am Chem Soc 130:3746

Theor Chem Acc (2014) 133:1579
DOI 10.1007/s00214-014-1579-1

REGULAR ARTICLE

# Analysis of a failure of the CC2 coupled-cluster method for bond lengths of SnO and PbO

**Zhifan Wang · Fan Wang**

Received: 27 May 2014 / Accepted: 4 September 2014 / Published online: 18 September 2014
© Springer-Verlag Berlin Heidelberg 2014

**Abstract** CC2 model is found to overestimate bond lengths of SnO and PbO by about 0.25 Å, while both second-order Møller–Plesset perturbation theory and coupled-cluster singles and doubles give reasonable results. Previously, analysis shows that the $[[U, T_1], T_1]$ term in the doubles equation of CC2 is the origin of failure for CC2 and some truncated CC models have been suggested to achieve reasonable result for ozone, where CC2 is unable to obtain a stable structure. However, these remedies are unable to afford reasonable bond lengths of SnO and PbO. Based on a term-wise analysis, our results indicate that the $[U, T_1]$ term results in failure of CC2. CC2 model by removing this term will provide results that agree well with those of MP2. Furthermore, the $[[U, T_2], T_1]$ term absent in the CC2 while present in doubles equation of CCSD can balance this $[U, T_1]$ term and CC2 model augmented with this term is able to afford reasonable results for PbO, SnO and ozone.

**Keywords** Coupled-cluster theory · CC2 · Unexpected failure

Dedicated to Professor Guosen Yan and published as part of the special collection of articles celebrating his 85th birthday.

Z. Wang
College of Chemistry, Sichuan University, Chengdu 610064, People's Republic of China

F. Wang (✉)
Institute of Atomic and Molecular Physics, Sichuan University, Chengdu 610064, People's Republic of China
e-mail: wangf44@gmail.com

## 1 Introduction

Coupled-cluster (CC) theory [1–3] is one of the most commonly used non-variational methods in quantum chemistry which shows good performance on correlation energies and properties for single-reference systems. Accuracy of results improves rapidly within the hierarchy of truncated coupled-cluster methods: CCS, CCSD [4] and CCSDT [5]. However, computational costs also increase rapidly and scalings of CCS, CCSD and CCSDT are $N^4$, $N^6$ and $N^8$, respectively, where N represents system size. On the other hand, some intermediate models like CC2 [6], CCSD(T) [7] and CC3 [8], which scale as $N^5$, non-iteratively $N^7$ and iteratively $N^7$, respectively, have been developed to achieve results with similar accuracy to those of the more expensive CC methods.

The CC2 model was developed by Christiansen et al. [6] as an approximation to the CCSD method and is mainly used for excited states [9–14]. Some benchmark calculations indicate that excitation energies with CC2 are even in better agreement with those high-level approaches such as CC3 and CCSDR(3) [15] than those of CCSD especially for valence-type excitations of single-reference molecules [16–19]. Due to its success and relatively low computational cost, various variants of CC2 by employing resolution of identity (RI) [20, 21], density fitting [10, 11], spin-component scaling [22, 23], localized orbitals [20, 21, 24], reduction of virtual spaces [25], etc. have been proposed to reduce computational effort even further. In addition, CC2 with a scaling of $N^4$ based on tensor hypercontraction [26, 27], scaled opposite-spin [28], pair natural orbital [29, 30] or Laplace transformation [24, 31] has also been developed. These developments enable applications of CC2 to ground- and excited-state energies of large molecules. Besides energies, analytical gradients [32–34] and Hessian [35] as well

as properties for ground and excited states based on CC2 have also been implemented.

CC2 can be understood as a generalization of second-order Møller–Plesset perturbation theory with an iterative treatment on single excitations. Equation for single excitation amplitudes in CC2 is the same as that in CCSD, and it is expected to provide results with similar accuracy to MP2. Recently, we calculated bond lengths and harmonic frequencies of some closed-shell diatomic heavy-element compounds with CC approaches and MP2 [36]. CC2 is found to perform poorly for PbO and SnO, and their bond lengths are calculated to be about 0.25 Å longer than those with CCSD and MP2 as well as experimental data. Bond lengths for monoxides of this group by various methods as well as experimental data [37] are listed in Table 1, and it can be seen from this table that bond lengths for CO and SiO with CC2 are somewhat larger than those of MP2, while performance of CC2 deteriorates for heavy-element compounds. It has been noticed that CC2 is sensitive to strong electron correlation effects [22]. In fact, strong correlation does not necessarily mean large deviation between CC2 and MP2 according to our results [36]. Bond lengths of AuH and $Au_2$ with CC2 agree reasonably with those of MP2, although electron correlation reduces bond lengths of these two molecules by about 0.1 Å at MP2 level [36]. One may argue that CC2 is mainly developed to calculate excitation energies. Pilot calculations indeed show that transition energies to the lowest several excited states of PbO at experimental bond length with CC2 agree reasonably with those based on equation-of-motion CCSD (EOM-CCSD) [38] and differences are <0.1 eV. However, equilibrium bond length for the lowest spin-singlet excited state with CC2 is still about 0.15 Å longer than that with EOM-CCSD and EOM-CCSDT. This shows poor performance of CC2 on the ground state structure will inevitably affect its performance on structures of excited states. It should be noted that bond lengths with CCSD(T) for SnO and PbO in Table 1 are overestimated by about 0.08 Å, which is due to the employed basis set as well as the frozen inner-shell electrons.

Recently, Pabst et al. [39] reported that CC2 leads to a severe failure in calculation of the equilibrium structure and vibrational frequencies of ozone where MP2 and CCSD provide reasonable results. They carried out a term-wise analysis on CC2 equations and found that the $[[H, T_1], T_1]$ term in the doubles equation was the origin of this failure. Unfortunately, our calculations indicate that modified CC2 approaches suggested by them that could achieve reasonable structure for ozone fail for SnO and PbO. In this work, a term-wise analysis of CC2 on potential energy surface of PbO is performed following closely the work by Pabst et al. An alternative remedy is suggested to achieve reasonable results for bond lengths of PbO and SnO.

**Table 1** Bond lengths (in Å) for monoxides of group IV

| | MP2 | CC2 | CCSD | CCSD(T) | Exp.[a] |
|---|---|---|---|---|---|
| CO | 1.138 | 1.149 | 1.129 | 1.136 | 1.128 |
| SiO | 1.534 | 1.563 | 1.515 | 1.527 | 1.510 |
| GeO | 1.658 | 1.726 | 1.634 | 1.649 | 1.625 |
| SnO | 1.908 | 2.148 | 1.875 | 1.900 | 1.833 |
| PbO | 2.027 | 2.247 | 1.952 | 2.015 | 1.922 |

[a] Ref. [37]

## 2 Theory

CC2 is an approximation to CCSD and we will start from CCSD equations. Total energy in CCSD can be written as the following:

$$E_{\mathrm{CCSD}} = \langle \Phi_0 | H \exp(T_1 + T_2) | \Phi_0 \rangle, \tag{1}$$

where $H$ is the Hamiltonian, $\Phi_0$ is the HF wavefunction of the corresponding $H$, $T_1$ and $T_2$ are single and double excitation operator, respectively, and are defined as the following

$$T_1 = \sum_{i,a} t_i^a a_a^+ a_i, \quad T_2 = \frac{1}{4} \sum_{a,b,i,j} t_{ij}^{ab} a_a^+ a_i a_b^+ a_j, \tag{2}$$

where $i, j, \ldots$ $(a, b, \ldots)$ are indices for occupied (virtual) spin orbitals in $\Phi_0$. The cluster amplitudes $t_i^a$ and $t_{ij}^{ab}$ in $T_1$ and $T_2$ are determined based on the following equations in CCSD:

$$\left\langle \Phi_i^a \right| \exp(-T_1 - T_2) H \exp(T_1 + T_2) \left| \Phi_0 \right\rangle = 0, \tag{3}$$

$$\left\langle \Phi_{ij}^{ab} \right| \exp(-T_1 - T_2) H \exp(T_1 + T_2) \left| \Phi_0 \right\rangle = 0, \tag{4}$$

where $\Phi_i^a$ and $\Phi_{ij}^{ab}$ are singly and doubly excited determinant with respect to $\Phi_0$, respectively. The Hamiltonian $H$ can be divided into the one-electron Fock operator $F$ and the two-electron perturbation $U$: $H = F + U$, where $F$ is treated as zeroth order and $U$ as first order. The $F$ operator will be diagonal when canonical molecular orbitals (MO) are used. With this division and canonical MO, the above equations can be written as

$$E_{\mathrm{CCSD}} = \langle \Phi_0 | H + [H, T_2] + 1/2[[H, T_1], T_1] | \Phi_0 \rangle, \tag{5}$$

$$\begin{aligned} &\left\langle \Phi_i^a \right| H + [F, T_1] + [U, T_1] + [H, T_2] + 1/2[[H, T_1], T_1] \\ &\quad + [[H, T_2], T_1] + 1/6[[[H, T_1]T_1]T_1] | \Phi_0 \rangle = 0, \end{aligned} \tag{6}$$

$$\begin{aligned} &\left\langle \Phi_{ij}^{ab} \right| U + [F, T_2] + [U, T_1] + 1/2[[H, T_1], T_1] \\ &\quad + 1/6[[[H, T_1], T_1], T_1] + 1/24[[[[H, T_1], T_1], T_1], T_1] \\ &\quad + [U, T_2] + [[H, T_2], T_1] + 1/2[[[H, T_2], T_1], T_1] \\ &\quad + 1/2[[H, T_2], T_2] | \Phi_0 \rangle = 0. \end{aligned} \tag{7}$$

Based on the Brillouin theorem, it can readily be shown that $T_1$ is of second order and $T_2$ is of first order in $U$. However, orbital relaxation is described mainly by $T_1$ and it will be of zeroth order if non-HF wavefunction is employed. In CC2 approach, $T_1$ is set as zeroth order in $U$ and $T_2$ is approximated to be correct through first order. Total energy in CC2 is thus correct to second order in $U$. Total energy and singles equation in CC2 are the same as those in CCSD in Eqs. (5) and (6), while the following doubles equation is employed in CC2:

$$\begin{aligned}&\left\langle \Phi_{ij}^{ab}\middle| U + [F,T_2] + [U,T_1] + 1/2[[H,T_1],T_1] \right.\\ &\quad + 1/6[[[H,T_1]T_1]T_1] \\ &\quad \left. + 1/24[[[[H,T_1],T_1]T_1]T_1]|\Phi_0\right\rangle = 0.\end{aligned} \tag{8}$$

By comparing Eqs. (7) and (8), it can be seen that the last four terms in the doubles equation of CCSD are neglected. In the present work, CC2 was implemented by calculating each term in Eqs. (5, 6) and (8) separately through an interface to the CFOUR program package [40] so that a term-wise analysis on CC2 equation can be carried out. Furthermore, the last four terms in Eq. (7) were also implemented in a term-wise way.

## 3 Results and discussion

All calculations in this paper were performed by the CFOUR program package. The energy-consistent pseudopotential developed by the Stuttgart/Cologne groups, i.e., ECP28MDF and ECP60MDF [41] are employed for Sn and Pb and the corresponding cc-pVTZ-PP basis set [42] is adopted. For C, Si, Ge and O, the cc-pVTZ basis set is used [43]. $4s^2 4p^6 4d^{10}$ electrons of Sn,$5s^2 5p^6 5d^{10}$ electrons of Pb and $1s^2$ electrons of O are kept frozen in correlation calculations. Equilibrium bond length of SnO and PbO was obtained by fitting total energies at five points with a space of 0.02 Å around the equilibrium bond length with a polynomial function up to fourth order.

Total energies of PbO, norms of the $T_1$- and $T_2$-amplitude vectors ($\|T_1\|$ and $\|T_2\|$) at different bond lengths with MP2, CC2, CCSD and CCSDT are demonstrated in Fig. 1. It can be seen from this figure that total energies with CC2 are much too low compared with those of MP2, CCSD and CCSDT. In addition, underestimation of CC2 energies with respect to the other approaches is more pronounced at larger bond length which results in a too long bond length with CC2. Significant underestimation of total energies with CC2 is accompanied by large $\|T_1\|$ and $\|T_2\|$ of CC2. $\|T_1\|$ and $\|T_2\|$ with CCSD and CCSDT increase slightly with bond length while those with CC2 grow much more rapidly.

Performance of CC2 on PbO is similar to that on ozone as in Ref. [39], where $\|T_1\|$ and $\|T_2\|$ are overestimated and

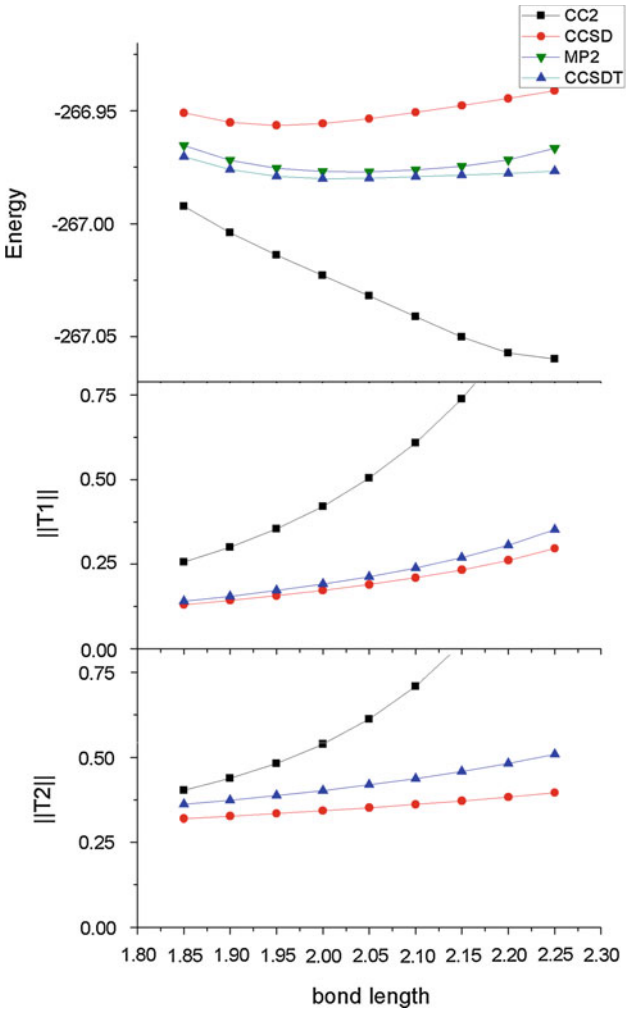


**Fig. 1** Potential energy curve of PbO with MP2, CC2, CCSD, CCSDT as well as $\|T_1\|$ and $\|T_2\|$ for CC2, CCSD and CCSDT at different bond lengths

the total energy is underestimated significantly by CC2. After a term-wise analysis, the $[[U, T_1], T_1]$ term in doubles equation is identified as the main origin of failure of CC2 on ozone. The following truncated CC2 models have been suggested to achieve reasonable results for structure of ozone: (1) CC2-no$T_1$q: deleting the $[[U, T_1], T_1]$ term in Eqs. (5–7), i.e., the third term on r.h.s. of Eq. (5) and the fourth term on l.h.s. of Eqs. (6) and (7): (2) CC2-$T_1$l($\mu_2$): Total energy and singles equation are the same as those in CC2, while only the linear terms in $T_1$ and $T_2$, i.e., the first three terms on l.h.s. of Eq. (7) are retained in doubles equation.

These truncated CC2 models are applied to potential energy curve of PbO and the results together with $\|T_1\|$ and $\|T_2\|$ of these models are illustrated in Fig. 2. It can be seen from this figure that none of these two models is able to provide a reasonable equilibrium bond length of PbO. Energies

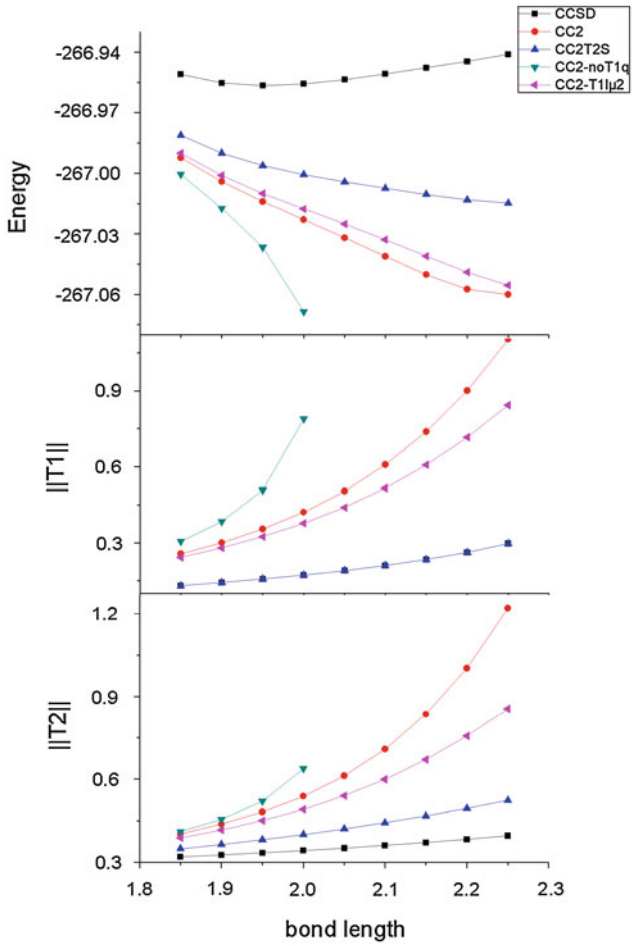


**Fig. 2** Potential energy curve of PbO as well as $\|T_1\|$ and $\|T_2\|$ for CC2, CC2-$T_1$lu2, CC2-no$T_1$q, CC2T2S and CCSD with respect to bond lengths

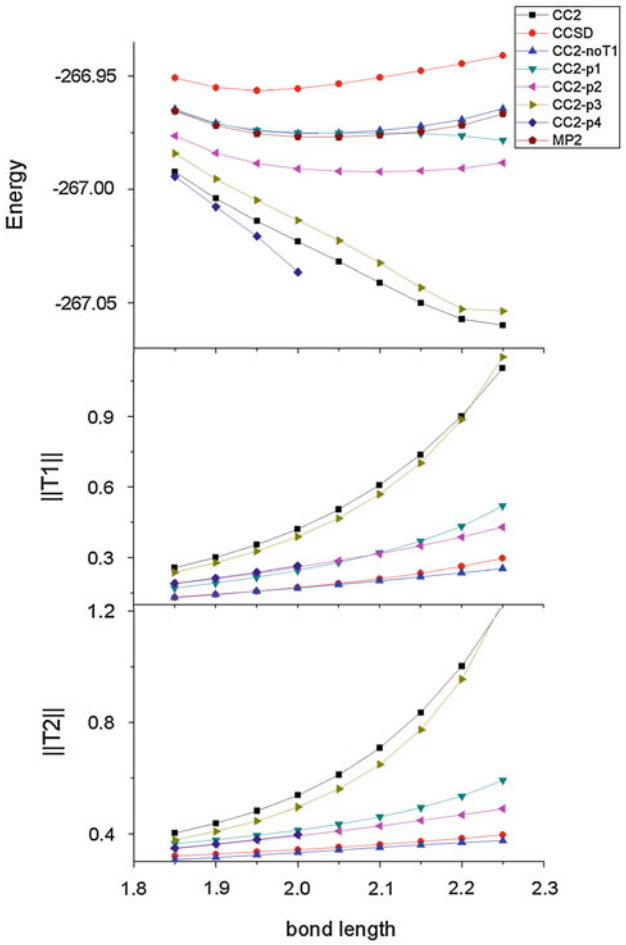


**Fig. 3** Potential energy curve of PbO as well as $\|T_1\|$ and $\|T_2\|$ for MP2, CC2, CCSD, CC2-no$T_1$, CC2-p1, CC2-p2, CC2-p3, CC2-p4

of CC2-$T_1$l($\mu_2$) are slightly higher than those with CC2, while CC2-no$T_1$q gives rise to energies that are even lower. Performance of these models on $\|T_1\|$ and $\|T_2\|$ is consistent with their performance on energies, where large $\|T_1\|$ and $\|T_2\|$ correspond to lower energies. Furthermore, it is difficult to achieve converged results at large bond length with CC2-no$T_1$q. One may suspect that this is because electron correlation effect is more pronounced in PbO than that in ozone. However, as we have shown in our previous work [36] that large correlation effect does not necessarily mean failure of CC2. Electron correlation reduces bond length of $Au_2$ by about 0.17 Å at MP2 level, while bond length with CC2 is only about 0.005 Å shorter than that with MP2. According to our calculations, the largest absolute $T_1$ amplitude for ozone at CCSD level is 0.073 and it is indeed smaller than that for PbO, i.e., 0.103. On the other hand, the largest $T_2$ amplitude for ozone at CCSD level is 0.213, while it is only 0.077 for PbO. This indicates that the origin of failure of CC2 for ozone may be different from that for PbO.

One can see from these results that the failure of CC2 on PbO is closely related to the abnormally large $\|T_1\|$ and $\|T_2\|$. $T_1$ is treated as zeroth order in CC2, and the maximum absolute $T_1$ amplitude is indeed larger than the maximum absolute $T_2$ amplitude. However, contribution to correlation energy from $T_1$ is smaller than that of $T_2$ by two orders of magnitude. This indicates that failure of CC2 should mainly come from the too large$\|T_2\|$, instead of $\|T_1\|$. However, it is still unclear whether this overestimation of $\|T_2\|$ stems from large $\|T_1\|$ or from some unbalanced terms in the doubles equation of CC2. To clarify this point, the converged $T_1$ amplitudes from CCSD calculation are plugged into the doubles equation of CC2, and this method is termed as CC2$T_2$S. Results of CC2$T_2$S are also plotted in Fig. 2. It can be seen from this figure that $\|T_2\|$ with CC2$T_2$S is indeed much smaller. Unfortunately, bond length with CC2$T_2$S is still too long, which means $\|T_2\|$ from CC2 equation even with reasonable $T_1$ amplitudes is still overestimated, especially at long bond length range. This implies some unbalanced term in the doubles equation should be the origin of failure of CC2.

**Table 2** Bond lengths (in Å) of SnO and PbO

| Method | MP2 | CC2 | CC2-noT$_1$ | CC2-p2 | CCSD | CCSDT |
|---|---|---|---|---|---|---|
| SnO | 1.908 | 2.148 | 1.903 | 1.922 | 1.875 | 1.898 |
| PbO | 2.027 | 2.247 | 2.014 | 2.091 | 1.952 | 2.004 |

The fourth term in the doubles equation in CC2, i.e., Eq. (8), was identified as the origin of failure of CC2 previously. However, removing this term could not afford improved bond length for PbO. The last two terms should only have minor contribution to $T_2$ amplitudes since they are cubic and quartic terms in $T_1$, respectively. The first two terms on l.h.s. of Eq. (8) give rise to MP2 results. Besides these two terms, the most important contribution to $T_2$ amplitudes should thus be the $[U, T_1]$ term. To investigate importance of this term, we proposed the truncated CC2-noT$_1$ model where this $[U, T_1]$ term is removed from the doubles equation of CC2. Results of this model are plotted in Fig. 3 together with those of MP2 and CCSD, and one can see from this figure that CC2-noT$_1$ is able to achieve reasonable bond length for PbO. Furthermore, energies with CC2-noT$_1$ are in close agreement with those of MP2 and $\|T_1\|$ and $\|T_2\|$ of CC2-noT$_1$ are even smaller than those with CCSD. The $[U, T_1]$ term is the most important coupling term between $T_1$ and $T_2$ operators in doubles equation, and omitting this term in CC2 will thus give rise to results that closely resemble those of MP2. Bond lengths of PbO and SnO with CC2-noT$_1$are listed in Table 2 together with results of MP2, CCSD and CCSDT. It can be seen from this table that bond length with CC2-noT$_1$ is about 0.01 Å shorter than that with MP2. CC2 has been developed mainly for excitation energies, and the $[U, T_1]$ term is critical to couple single and double excitations. Excitation energies based on CC2-noT1 formulation will give rise to excitation energies of similar accuracy to that of CIS and CC2-noT1 should thus not be used for excitation energies.

Our result indicates that failure of CC2 is due to the unbalanced $[U, T_1]$ term in doubles equation. Considering that CCSD is able to provide reasonable bond length of PbO, the $[U, T_1]$ term must be balanced by one or any combination of the addition four terms in doubles equation of CCSD: $[U, T_2]$, $[[U, T_2], T_1]$, $[[U, T_2], T_2]$ and $[[[U, T_2], T_1], T_1]$. To further investigate this point, we proposed four models: CC2-pn with $n = 1,2,3,4$, and CC2-pn means the CC2 model with the additional n-th term from these four additional members included in the doubles equation. Results of these four models are demonstrated in Fig. 3. One can see from this figure that energies with CC2-p1 are rather close to those of CC2-noT$_1$ for bond lengths below 2.10 Å, but performance of this model deteriorate at longer bond lengths. On the other hand, energies of CC2-p3 are only slightly higher than those of CC2 and converged results cannot be obtained with the CC2-p4 model when bond length exceeds 2.0 Å. It is interesting to note that although energies with CC2-p4 are even lower than those of CC2, $\|T_1\|$ and $\|T_2\|$ with this model are smaller than those with CC2. According to this figure, the CC2-p2 model improves upon CC2 model to a large extent and reasonable bond length of PbO can be achieved with this model. These results show that the $[U, T_1]$ term in doubles equation which result in large error on bond length of PbO in CC2 can somehow be balanced by the $[[U, T_2], T_1]$ term in CCSD. Bond lengths of PbO and SnO with CC2-p2 are

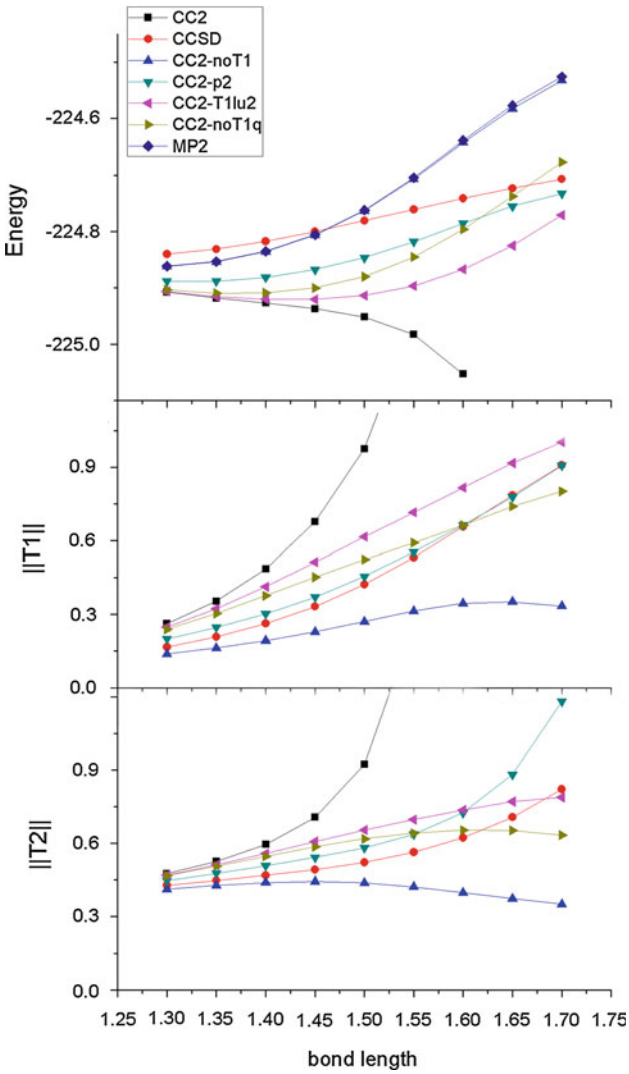


**Fig. 4** Potential energy curve as well as $\|T_1\|$ and $\|T_2\|$ of ozone with MP2, CC2, CCSD, CC2-noT$_1$q, CC2-T$_1$l($\mu_2$), CC2-noT$_1$ and CC2-p2

**Table 3** Bond lengths (in Å) of $Bi_2$, TlH, $Sb_2$ and InH

| | MP2 | CC2 | CC2-noT1 | CC2-p2 | CCSD | CCSD(T) |
|---|---|---|---|---|---|---|
| InH | 1.860 | 1.861 | 1.860 | 1.864 | 1.871 | 1.873 |
| TlH | 1.926 | 1.927 | 1.927 | 1.926 | 1.944 | 1.946 |
| $Sb_2$ | 2.559 | 2.585 | 2.558 | 2.532 | 2.506 | 2.532 |
| $Bi_2$ | 2.733 | 2.765 | 2.732 | 2.696 | 2.661 | 2.691 |

also listed in Table 2. Compared with results of MP2, CC2-p2 overestimates this bond length by about 0.06 Å for PbO and 0.01 Å for SnO.

To further demonstrate the reliability of the CC2-no$T_1$ and CC2-p2 models, potential energy curve of ozone is calculated with these two models and results are plotted in Fig. 4 together with those given by CC2-no$T_1$q, CC2-$T_1$l($\mu_2$), CC2, MP2 and CCSD. It can be seen from this figure that CC2-no$T_1$q and CC2-$T_1$l($\mu_2$) models yield reasonable result for ozone, which is consistent with results in Ref. [39]. On the other hand, results of the two models suggested in this work also agree qualitatively with those of MP2 and CCSD. Unsurprisingly, energies with CC2-no$T_1$ are in good agreement with those of MP2.

Bond lengths of InH, TlH, $Sb_2$ and $Bi_2$ have also been calculated with CC2-noT1, CC2-p2, MP2, CC2, CCSD and CCSD(T), and results are listed in Table 3. Basis set and ECPs employed in these calculations are the same as those for SnO and PbO. Electron correlation effect for InH and TlH is insignificant where bond lengths with CC2 for these two molecules are in good agreement with those with MP2. On the other hand, electron correlation effect somewhat more pronounced for $Sb_2$ and $Bi_2$ and CC2 bond lengths are about 0.03 Å larger than that of MP2. Bond lengths with CC2-no$T_1$ closely resemble those with MP2 as expected and differences are about 0.001 Å. On the other hand, results with CC2-p2 for InH and TlH are in good agreement with those of CC2, while they are shorter than those with CC2 and are in better agreement with CCSD and CCSD(T) results.

## 4 Conclusion

CC2 model fails to achieve equilibrium structure for ozone, and bond lengths with CC2 are overestimated by about 0.25 Å for PbO and SnO. In a previous analysis, the $[[U, T_1], T_1]$ term in the doubles equation is identified as the origin of the failure of CC2 and some truncated CC2 models have been proposed to provide reasonable results for ozone. Unfortunately, these models are unable to give rise to reasonable bond length for PbO. Based on a term-wise analysis of CC2, we show that the $[U, T_1]$ term in the doubles equation result in this failure of CC2. This term is the most important term that couples $T_1$ amplitudes with $T_2$ amplitudes and truncated CC2 model by removing this term from the doubles equation provide results that are in close agreement with those of MP2. Furthermore, we also found that the $[[U, T_2], T_1]$ term that is absent in CC2 equation can balance this $[U, T_1]$ term. CC2 model augmented with this term in the doubles equation is able to afford reasonable bond lengths of PbO and SnO as well as equilibrium structure for ozone.

It should be noted that the computational scaling of the $[[U, T_2], T_1]$ term is $N^6$, and performance of CC2-no$T_1$ closely resembles that of MP2. The purpose of this work is to provide an understanding on failure of CC2, instead of proposing some improved models. On the other hand, CC2 is developed mainly to calculate excitation energies, while MP2 should be preferred to calculate ground state energy. Indeed, excitation energies for PbO at equilibrium bond length of PbO with CC2 are in good agreement with those of EOM-CCSD. However, its poor performance on ground-state structure leads to its significant overestimation of excited state bond length. Reasonable energy for excited state may be obtained by summation of excitation energy with CC2 and ground state energy from MP2. The suggested approach is similar to CIS(D) [44] and ADC(2) [45], where the MP2 ground state energies are employed. However, it is well known that CC2 usually provides better excitation energies than CIS(D) and ADC(2) and the suggested approach may still outperform CIS(D), ADC(2) and even CC2 itself in determining excited state structures.

**Acknowledgments** We thank the National Nature Science Foundation of China (Grant No. 21273155) for financial support.

## References

1. Taylor PR (1994) Lecture notes in quantum chemistry II. In: Roos BO (ed) European summer school in quantum chemistry. Springer, Berlin, p 125
2. Gauss J (1998) Encyclopedia of computational chemistry. In: Schleyer PVR, Allinger NL, Clark T, Gasteiger J, Kollmann PA, Schaefer HF, Schreiner PR (eds). Wiley, New York, p 615
3. Bartlett RJ, Musiał M (2007) Rev Mod Phys 79:291
4. Purvis GD III, Bartlett RJ (1982) J Chem Phys 76:1910
5. Noga J, Bartlett RJ (1988) J Chem Phys 89:3401
6. Christiansen O, Koch H, Jørgensen P (1995) Chem Phys Lett 243:409
7. Raghavachari K, Trucks GW, Pople JA, Head-Gordon M (1989) Chem Phys Lett 157:479

8. Koch H, Christiansen O, Jørgensen P, Sanchez de Merás AM, Helgaker T (1997) J Chem Phys 106:1808
9. Hättig C (2003) J Chem Phys 118:7751
10. Kats D, Korona T, Schutz M (2006) J Chem Phys 125:104106
11. Kats D, Korona T, Schutz M (2007) J Chem Phys 127:064107
12. Borges I, Aquino AJA, Barbatti M, Lischka H (2009) Int J Quant Chem 109:2348
13. Etinski M, Fleig T, Marian CM (2009) J Phys Chem A 113:11809
14. Rocha-Rinza T, Christiansen O (2009) Chem Phys Lett 482:44
15. Christiansen O, Koch H, Jørgensen P (1996) J Chem Phys 105:1451
16. Schreiber M, Silva-Junior MR, Sauer SPA, Thiel W (2008) J Chem Phys 128:134110
17. Falden HH, Falster-Hansen KR, Bak KL, Rettrup S, Sauer SP (2009) J Phys Chem A 113:11995
18. Sauer SP, Schreiber M, Silva-Junior MR, Thiel W (2009) J Chem Theor Comput 5:555
19. Silva-Junior MR, Sauer SPA, Schreiber M, Thiel W (2010) Mol Phys 108:453
20. Hättig C, Weigend F (2000) J Chem Phys 113:5154
21. Köhn A, Hättig C (2003) J Chem Phys 119:5021
22. Hellweg A, Grün SA, Hättig C (2008) Phys Chem Chem Phys 10:4119
23. Hellweg A (2011) J Chem Phys 134:064103
24. Freundorfer K, Kats D, Korona T, Schütz M (2010) J Chem Phys 133:244110
25. Send R, Kaila VR, Sundholm D (2011) J Chem Phys 134:214114
26. Hohenstein EG, Kokkila SI, Parrish RM, Martínez TJ (2013) J Phys Chem B 117:12972
27. Hohenstein EG, Kokkila SI, Parrish RM, Martinez TJ (2013) J Chem Phys 138:124111
28. Winter NO, Hattig C (2011) J Chem Phys 134:184101
29. Helmich B, Hättig C (2011) J Chem Phys 135:214106
30. Helmich B, Hattig C (2013) J Chem Phys 139:084114
31. Ledermuller K, Kats D, Schutz M (2013) J Chem Phys 139:084111
32. Köhn A, Hättig C (2003) J Chem Phys 119:5021
33. Winter NOC, Hättig C (2012) Chem Phys 401:217
34. Ledermüller K, Schütz M (2014) J Chem Phys 140:164113
35. Friese DH, Hättig C, Koßmann J (2013) J Chem Theor Comput 9:1469
36. Wang Z, Wang F (2013) Phys Chem Chem Phys 15:17922
37. Huber KP, Herzberg G (1979) Molecular spectra and molecular structure, constants of diatomic molecules. Van Nostrand Rienhold, New York
38. Geertsen J, Rittby M, Bartlett RJ (1989) Chem Phys Lett 164:57
39. Pabst M, Köhn A, Gauss J, Stanton JF (2010) Chem Phys Lett 495:135
40. CFOUR, a quantum chemical program package written by Stanton JF, Gauss J, Harding ME, Szalay PG with contributions from Auer AA, Bartlett RJ, Benedikt U, Berger C, Bernholdt DE, Bomble YJ, Cheng L, Christiansen O, Heckert M, Heun O, Huber C, Jagau T-C, Jonsson D, Jusélius J, Klein K, Lauderdale WJ, Matthews DA, Metzroth T, Mück LA, O'Neill DP, Price DR, Prochnow E, Puzzarini C, Ruud K, Schiffmann F, Schwalbach W, Stopkowicz S, Tajti A, Vázquez J, Wang F, Watts JD and the integral packages MOLECULE (Almlöf J, Taylor PR), PROPS (Taylor PR), ABACUS (Helgaker T, Aa Jensen HJ, Jørgensen P, Olsen J), and ECP routines by Mitin AV, van Wüllen C. For the current version. http://www.cfour.de
41. Metz B, Stoll H, Dolg M (2000) J Chem Phys 113:2563
42. Peterson KA (2003) J Chem Phys 119:11099
43. Dunning TH (1989) J Chem Phys 90:1007
44. Head-Gordon M, Rico RJ, Oumi M, Lee TJ (1994) Chem Phys Lett 219:21
45. Trofimov A, Schirmer J (1995) J Phys B 28:2299

Theor Chem Acc (2014) 133:1542
DOI 10.1007/s00214-014-1542-1

REGULAR ARTICLE

# Electrostatic potentials of camptothecin and its analogues

**Jianyong Lei · Yun Chen · Xuejun Feng · Jian Jin · Jiande Gu**

Received: 28 May 2014 / Accepted: 11 July 2014 / Published online: 12 August 2014
© Springer-Verlag Berlin Heidelberg 2014

**Abstract** In order to understand the influences of the modification of E-ring on the main frame of camptothecin (CPT), studies of the E-ring modification resulted changes in the stability and the electrostatic potential around the main frame of CPT were performed by the density functional theory. The results of present study indicate that the stability of the close-ring lactone form of CPT and homocamptothecin (hCPT) is similar to their open-ring hydroxylate forms, especially when in aqueous solutions. As an E-ring-modified CPT analogue, hCPT has essentially the same electrostatic potential (ESP) as CPT around the main frame (from A- to D-ring). However, the electrostatic potentials of the open-ring compounds are more negative around the main frame than that of CPT. The changes in the ESP of the CPT derivatives are found to be correlated with the corresponding dipole moments. Since electrostatic potential could influence the π–π stacking pattern between CPT (and its analogues) and the DNA bases, present study suggests that this π–π interaction of the open-ring forms of CPT and hCPT might be different from that of the close-ring lactone form. The information revealed in this study sheds light on the developments of new CPT-type antitumor drugs.

**Keywords** Electrostatic potentials · Camptothecin · π–π Interaction

Dedicated to Professor Guosen Yan and published as part of the special collection of articles celebrating his 85th birthday.

J. Lei · Y. Chen · J. Jin (✉)
School of Medicine and Pharmaceutics, Jiangnan University, Jiangsu, Wuxi 214122, People's Republic of China
e-mail: jinjian31@hotmail.com

X. Feng (✉)
School of Petrochemical Engineering, Changzhou University, Changzhou 213164, People's Republic of China
e-mail: xuejun-f@163.com

J. Gu (✉)
Drug Design and Discovery Center, State Key Laboratory of Drug Research, Shanghai Institute of Materia Medica, Shanghai Institutes for Biological Sciences, CAS, Shanghai 201203, People's Republic of China
e-mail: Jiande@icnanotox.org

## 1 Introduction

Camptothecin (CPT, see Fig. 1) and its analogues are antitumor drugs, which strongly inhibit nucleic acid synthesis and initiate DNA strand breaks [1–4]. Structure-activity studies indicate that their activity is due to an action on topoisomerase I [5, 6].

CPT and its analogues are found to intercalate between DNA bases of both strands at the enzyme-induced nick in the eukaryotic DNA topoisomerase I. The binding pattern consists of stacking interactions with the bases of DNA, H-bonding with residual Asp, and water-bridged H-bonding interactions with the active site phosphotyrosine and Asn [7]. Based on the crystal structure of the topoisomerase I and DNA complex, Kerrigan and Pilch predicted that the closed lactone form (E-ring) of CPT might also bind to residuals Arg and Asp of the topoisomerase and guanine and ribose moieties of DNA through H-bonding [8]. Molecular modeling studies suggested that both stacking and H-bonding interactions played important roles in stabilizing the CPT-topoisomerase I–DNA complex [9].

The lactone moiety (a six-membered α-hydroxylactone) within CPT can be hydrolyzed at physiological condition, forming the open-ring carboxylate structure [2]. Compared with the closed lactone form, the open carboxylate form of

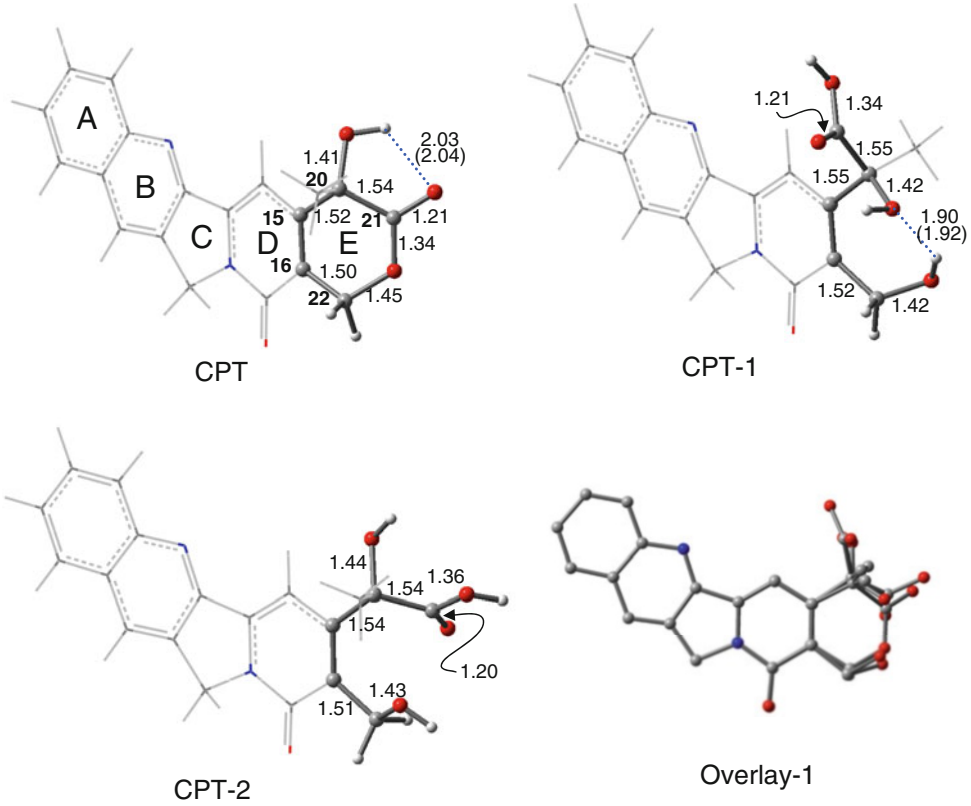


**Fig. 1** The optimized structures of the lactone form of CPT and its hydrolyzed open-ring hydroxylate forms. Calculated at the B3LYP/6-311G(d,p) level of theory. Numbering scheme is in *black*. The values in *parenthesis* were evaluated at the M06-2X/6-311G(d,p) level of theory. *Color* representations: *red* for oxygen, *gray* for carbon, *blue* for nitrogen, and *white* for hydrogen. Atomic distances are in Å. Overlay-1 is the overlay structures of CPT, CPT-1, and CPT-2. Hydrogen atoms have been omitted in Overlay-1 for clarity

CPT (and its analogues) provides more H-bonding sites. Therefore, the open carboxylate form is expected to bind more tightly to the topoisomerase I. Furthermore, opening of the E-ring may influence the electrostatic potential around main frame of CPT.

As an E-ring-modified CPT, homocamptothecin (hCPT, see Fig. 2) bears a seven-membered β-hydroxylactone ring. This E-ring-expanded compound exhibits enhanced lactone stability due to the reduced electrophilicity of a β-hydroxylactone [10–12]. However, there are still 20 % of hCPT adopt the open-ring form [12]. Moreover, the expanded E-ring in hCPT provides more H-bonding sites than that of CPT.

Theoretical study at different levels of theory suggested that the alteration of the electrostatic potential might affect the π–π stacking with the DNA bases [13]. Since the orientation of the π–π stacking between the main frame of CPT and the DNA bases could be a main factor contributing to the stability of the CPT-topoisomerase I–DNA complex [14], the knowledge of the influences of the modification of E-ring on the main frame of CPT is crucial for improving the selectivity of CPT-related compounds. Here, we report the density functional theory study of the influences of the E-ring modifications on the electrostatic potential of the main frame of CPT. The information revealed in this study sheds light on the developments of new CPT-type antitumor drugs.

## 2 Methods

The B3LYP [15, 16] and M06-2X [17] functionals with basis sets of triple-ζ quality plus polarization functions (denoted 6-311G(d,p)) [18, 19] were used to determine the local minimal geometries, energetics, and vibrational frequencies of CPT and hCPT (and their corresponding open-ring forms as well). For better description of long-range interactions, diffuse functions were also included (6-311 + G(d,p)) in the determination of the electrostatic potentials. These compounds were also been optimized using the polarizable continuum model (PCM) [20] with a dielectric constant of water ($\varepsilon = 78.39$) in order to evaluate the energies of the systems in a polarizable medium. It should be noted that this PCM model used in the present study only accounts for the influences of the polarizable surroundings; the important effects of the micro-hydration could not be included in this approach. Therefore, the PCM model only to some extent approximates the real situation of aqueous solution. The GAUSSIAN 09 program [21] was used for all computations.

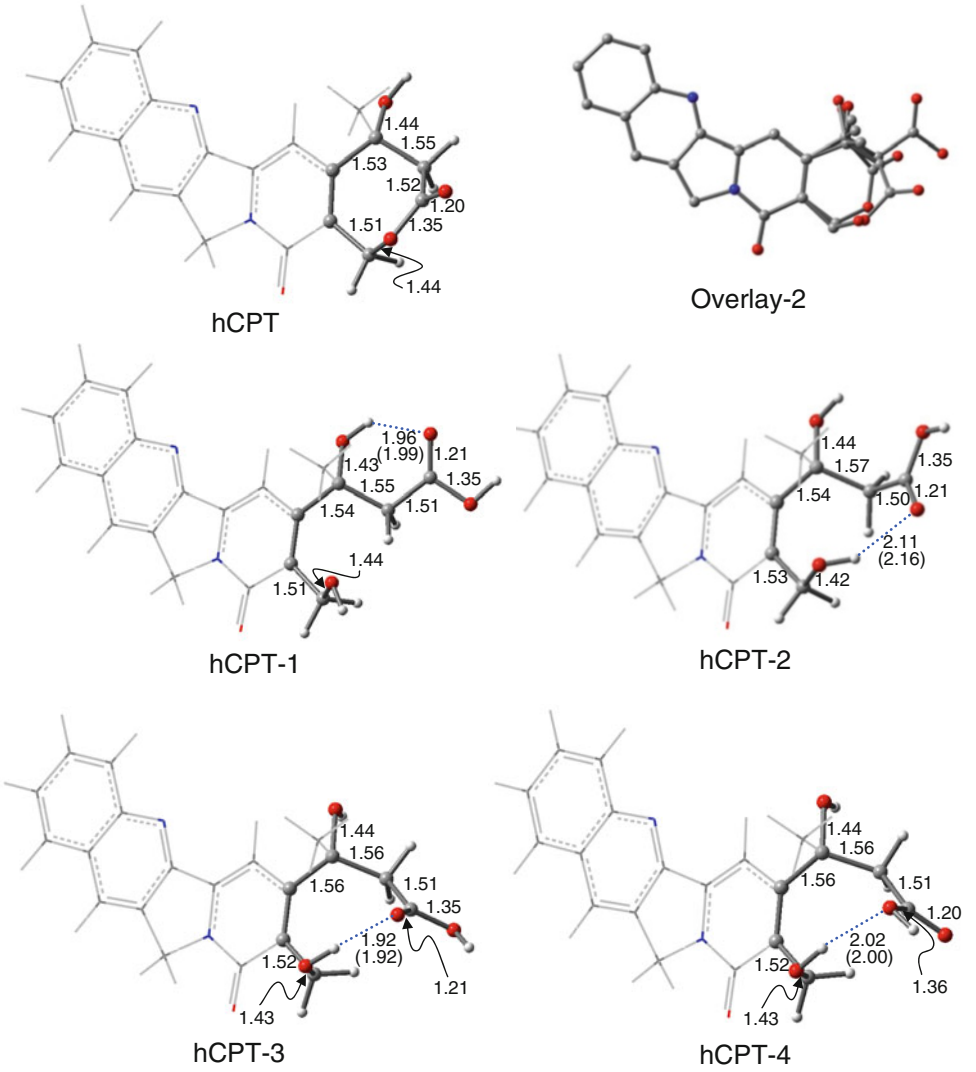


**Fig. 2** The optimized structures of the lactone form of hCPT and its hydrolyzed open-ring hydroxylate forms. Calculated at the B3LYP/6-311G(d,p) level of theory. The values in parenthesis were evaluated at the M06-2X/6-311G(d,p) level of theory. Color representations: red for oxygen, gray for carbon, blue for nitrogen, and white for hydrogen. Atomic distances are in Å. Overlay-2 is the overlay structures of CPT, hCPT, and hCPT-1. Hydrogen atoms have been omitted in Overlay-2 for clarity

## 3 Results and discussions

### 3.1 Geometry and energy properties

Both B3LYP and M06-2X functionals predict the similar geometries for all the species. The main difference in the geometric parameters is that the intra-molecular H-bond length predicted by the M06-2X functional is 0.05 Å longer than that predicted by the B3LYP approach at most. Moreover, the geometries of the CPT and hCPT derivatives optimized with the PCM model are also close to the corresponding compounds optimized in the gas phase. Therefore, the discussion below is mainly based on the results obtained at the B3LYP/6-311G(d,p) level of theory in the gas phase. The optimized geometries of CPT and the corresponding open-ring compounds (CPT-1 and CPT-2, see Fig. 1) reveal that the geometric variations due to the E-ring opening mainly limited on the E-ring. In general, the C–C bond distances of the E-ring moiety in the open-ring forms increase slightly as compared to those in the lactone form. Specifically, C15–C20 distance increases 0.03 Å in CPT-1 (1.55 Å) and 0.02 Å in CPT-2 (1.54 Å), and C16–C22 distance elongates 0.02 Å in CPT-1 (1.52 Å) and 0.01 Å in CPT-2 (1.51 Å), respectively, as compared to those in CPT. Moreover, C20–O bond length also increases in the open carboxylate forms (1.42 Å in CPT-1 and 1.44 Å in CPT-2 vs. 1.41 Å in CPT). The main difference between CPT-1 and CPT-2 is that there is an intra-molecular H-bond in the

opened E-ring moiety of CPT-1. To form this intra-molecular H-bond, the OH group at the C20 position in CPT-1 has to rotate around C15–C20 bond to the opposite position after the hydration of CPT. Compared with CPT-1, the relative positions of C20, C21, and C22 of the opened E-ring moiety in CPT-2 are close to those of CPT. The geometric feature of CPT-2 indicates that CPT-2 is the direct product of the hydration of CPT. On the other hand, the overlay of the structures of CPT, CPT-1, and CPT-2 indicates that the geometries of the A-, B-, C-, and D-rings of CPT do not change significantly in response to the hydrolysis of the lactone form.

Similarly, the optimized geometries of hCPT and its hydrolysis products (hCPT-1, hCPT-2, hCPT-3, and hCPT-4, Fig. 2) demonstrate that the introduction of $CH_2$ group at the α-position of the lactone moiety does not lead to geometric variations in the main frame (A-, B-, C-, and D-rings) of CPT (see Overlay-2 in Fig. 2). However, the C–C bond distances of the E-ring moiety increase in the open-ring carboxylate forms as compared to those in the lactone form of hCPT. It is important to note that the intra-molecular H-bond in the α-hydroxylactone moiety of CPT does not exist in hCPT. Nevertheless, in the hydrolysis products of hCPT, intra-molecular H-bond can be identified at various sites of the E-ring moiety. In hCPT-1, the intra-molecular H-bond through the proton of the β-hydroxyl group and the carbonyl oxygen of carboxylate group forms a six-membered ring structure as can be seen in Fig. 2. For other conformers of the open-ring carboxylate forms of hCPT, the intra-molecular H-bond is found to be involved in the ω-hydroxyl group and in the carboxylate group. The formation of intra-molecular H-bond is expected to be one of the important factors that stabilize the systems.

The relative energies (relative to the close-ring lactone form) summarized in Table 1 reveal that the stability of the open-ring form of CPT is similar to that of the lactone form. The energy of CPT-1 is about 2.5 kcal/mol lower than that of CPT, while the energy of CPT-2 is about 2.5 kcal/mol higher than that of CPT at the B3LYP/6-311G(d,p) level of theory. Therefore, the balance between the open-ring carboxylate form and the close-ring lactone form could be easily shifted in different environments. The higher stability of CPT-1 as compared to CPT-2 should be attributed to the existence of the intra-molecular H-bond in the former.

On the other hand, two of the open-ring forms of hCPT (hCPT-1 and hCPT-2) are considerably more stable than the lactone form of hCPT. The energy of hCPT-1 and hCPT-2 is about 10.1 kcal/mol and 5.7 kcal/mol lower than that of hCPT, respectively. These two structures should dominate the open carboxylate form of hCPT. Although the structures of hCPT-3 and hCPT-4 are similar, the total energy of hCPT-3 is about 3 kcal/mol lower than that of hCPT-4. The stronger intra-molecular H-bondingin hCPT-3 (with O···H distance of 1.92 Å in hCPT-3 vs. 2.02 Å in hCPT-4) should be the main contribution of this energy difference.

Including the polarizable medium slightly raises the stability of the close-ring form of camptothecin. Using the PCM model, the energy variations between the open-ring (CPT-1) and close-ring form of CPT are <0.1 kcal/mol. On the other hand, CPT-2 in the aqueous solutions is approximately 4 kcal/mol less stable than CPT (predicted by the B3LYP functional). Due to the existence of the polarizable surroundings, the energy variations between the open-ring and close-ring form of hCPT are <5.0 kcal/mol. All of the open-ring forms of hCPT derivatives are more stable than the close-ring form with the exception of hCPT-4, which is about 3 kcal/mol less stable than hCPT.

Compared with the B3LYP functional, the M06-2X functional predicts that the open-ring structures are more stable. The relative energies of the open-ring forms of CPT and hCPT evaluated by the M06-2X approach are about

**Table 1** Energy properties (in kcal/mol) and dipole moments (μ, in Debye) of the optimized structures of CPT and hCPT

| | ΔE | $\Delta E^0$ | ΔG | ΔE(PCM)[a] | μ |
|---|---|---|---|---|---|
| CPT + $H_2O$ | 0.0 | 0.0 | 0.0 | 0.0 | 6.5 (6.5) |
| CPT-1 | −2.49 (−6.73) | 1.17 (−3.09) | 10.27 (6.04) | −0.06 (−4.13) | 6.9 (6.8) |
| CPT-2 | 2.47 (−2.86) | 5.40 (0.18) | 14.70 (9.53) | 4.09 (−1.47) | 2.1 (2.0) |
| hCPT + $H_2O$ | 0.0 | 0.0 | 0.0 | 0.0 | 7.1 (7.0) |
| hCPT-1 | −10.14 (−12.29) | −6.94 (−9.15) | 1.83 (−0.26) | −4.84 (−7.09) | 1.4 (1.5) |
| hCPT-2 | −5.69 (−9.14) | −2.50 (−5.92) | 6.48 (3.40) | −0.87 (−4.03) | 4.4 (4.1) |
| hCPT-3 | −3.091 (−5.82) | 0.12 (−2.53) | 9.14 (6.64) | −0.02 (−2.72) | 4.8 (5.0) |
| hCPT-4 | 0.162 (−2.46) | 3.45 (0.93) | 12.59 (9.94) | 3.03 (0.38) | 5.0 (5.0) |

Calculated at the B3LYP/6-311G(d,p) level of theory. The values in parenthesis were evaluated at the M06-2X/6-311G(d,p) level of theory. ΔE is the energy relative to the total energy of the close-ring lactone form and one water molecule; $\Delta E^0$ is the zero-point-energy corrected ΔE; ΔG is the free energy difference at 298 K

[a] Using the polarizable continuum model with a dielectric constant of water (ε = 78.39)

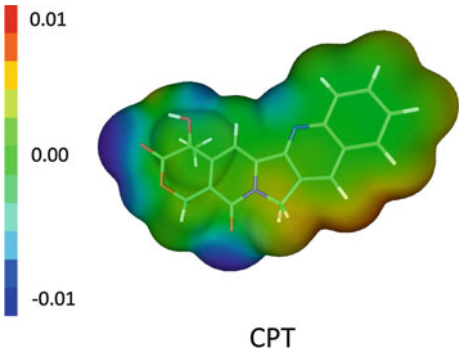


**Fig. 3** The electrostatic potential (ESP) map of CPT. The ESP is mapped on the iso-surface of electron density with iso-value of 0.0005. The ESP color ranges from −0.01 (*blue*) to 0.01 (*red*). Unit is in au

2–5 kcal/mol lower than those by the B3LYP method. In the PCM-modeled aqueous solutions, the open-ring derivatives are more stable than the corresponding close-ring compounds in the M06-2X studies (except for hCPT-4, which is 0.4 kcal/mol higher than hCPT in energy). Since all the energy differences between the close-ring lactone form of CPT and hCPT are close to the corresponding open-ring hydroxylate forms, one may expect that both forms exist in aqueous solutions.

### 3.2 Electrostatic potential and dipole moment

Electrostatic potential (ESP) around the molecular surface is one of the crucial properties of activity of a drug. Changes in electrostatic potential might result in changes in the interaction patterns between a drug and the corresponding reaction site. Moreover, changes in electrostatic potential could influence the transportation process of a drug. The electrostatic potential of CPT mapped on its electron density iso-surface (with iso-value of 0.0005 au) is depicted in Fig. 3. On this iso-surface, negative ESP (colored in blue) regions spread around the oxygen and the nitrogen atoms. Meanwhile, a slightly positive ESP (in orange) area locates on the vicinity of the edge of the carbon side of the B- and C-ring. Electrostatic potential is essentially zero (in green) on the iso-surface of the A-ring moiety of CPT.

As expected, the alteration of the E-ring of CPT could result in dramatic changes in the electrostatic potential around its neighborhood. The electrostatic potential

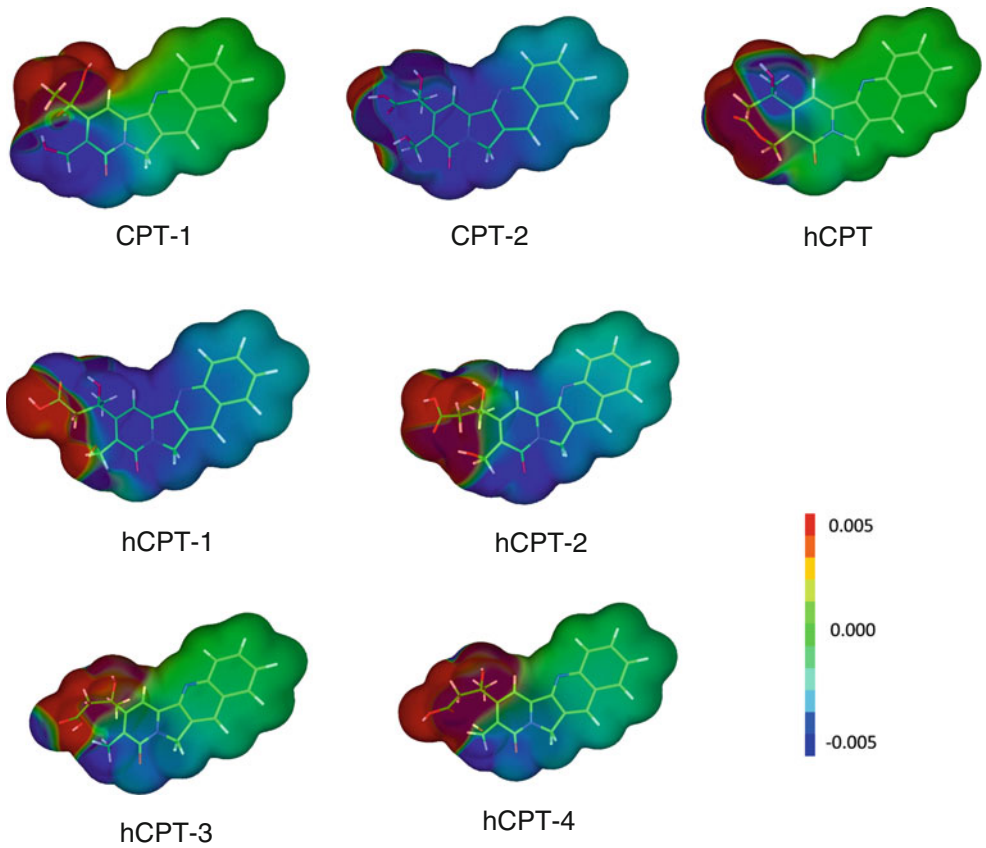


**Fig. 4** The electrostatic potential difference (ESPD) maps of the E-ring-modified compounds of CPT. The ESPD is mapped on the iso-surface of electron density with iso-value of 0.0005. The ESPD color ranges from −0.005 (*blue*) to 0.005 (*red*). Unit is in au

difference (ESPD) between CPT-1 and CPT mapped on the electron density iso-surface in Fig. 4 demonstrates that the change in the electrostatic potential only limited on the iso-surface around the E- and D-ring. The electrostatic potential of the main frame from A- to C-ring is effectively unaffected in CPT-1. However, the other form of the open-ring hydroxylate compound, CPT-2, has substantial changes in its electrostatic potential due to the structural variations of the E-ring of CPT. The ESPD map of CPT-2 reveals that the electrostatic potential is notably more negative around the main frame of CPT-2 as compared to that of CPT.

The influence of the E-ring modification on the electrostatic potential is primarily limited on the E-ring moiety of hCPT, as revealed in its ESPD map. Therefore, the binding pattern of stacking interactions with the bases of DNA should be the same for CPT, CPT-1, and hCPT. On the other hand, the ESPs of the hydrolyzed products of hCPT decrease over the main frame, ranging from A- to D-ring, as compared to that of CPT. ESPD maps depicted in Fig. 4 show that the decrease of ESP around the B-, C-, and D-ring moiety of the main frame of hCPT-1 is the most obvious among the four open-ring structures of hCPT. Meanwhile, the ESPD map of hCPT-2 demonstrates moderate decrease in the ESP around the main frame. The reduction of ESP over the A- and B-ring of hCPT-3 and hCPT-4 is less significant as illustrated by the corresponding ESPD maps.

It is interesting to note that the changes in the ESP of the CPT derivatives can be correlated with the corresponding dipole moments. Similar dipole moments are found for CPT, CPT-1, and hCPT (6.5, 6.9, and 7.1 Debye, respectively), which matches the near-zero ESPD around the main frame for the corresponding compounds. Meanwhile, small dipole moments of hCPT-1 (1.4 Debye) and CPT-2 (2.1 Debye) correlate the significant ESP reduce on their iso-surfaces around B-, C-, and D-rings. Moderate dipole moments of hCPT-2 (4.4 Debye), hCPT-3 (4.8 Debye), and hCPT-4 (5.0 Debye) associated with the observable ESP lessen on the C- and D-rings as shown in the ESPD maps.

## 4 Concluding remarks

The results of present study indicate that the stability of the close-ring lactone form of CPT and hCPT is similar to their open-ring hydroxylate forms, especially when in aqueous solutions. E-ring modification of hCPT essentially does not alter the ESP around the main frame (from A- to D-ring) as compared to that of CPT. However, the electrostatic potential of the open-ring compounds around is more negative around the main frame than that of CPT. The changes in the ESP of the different structures of the CPT derivatives are found to be correlated with the corresponding dipole moments. Significant decreases of the ESP around the A-, B-, C-, and D-ring of CPT-2 and hCPT-1 are found to be associated with the dramatic reduce of their dipole moments, while minor changes in the ESP over the A-, B-, C-, and D-ring region of CPT, CPT-1, and hCPT can be correlated with their similar dipole moments.

Since electrostatic potential could influence the π–π stacking pattern between CPT (and its analogues) and the DNA bases, present study suggests that this π–π interaction of the open-ring forms of CPT and hCPT might be different from that of the close-ring lactone form.

**Acknowledgments** This research was supported by National Natural Science Foundation of China (30772586) and Jiangsu Natural Science Foundation of China (BK2009071).

## References

1. Thomas CJ, Rahier NJ, Hecht SM (2004) Bioorg Med Chem 12:1585–1604
2. Hartmann JT, Lipp HP (2006) Drug Saf 29:209–230
3. Hsiang Y, Hertzberg R, Hecht S, Liu LF (1985) J Biol Chem 260:14873–14878
4. Hsiang Y, Lihou MG, Liu LF (1989) Cancer Res 49:5077–5082
5. Jaxel C, Kohn KW, Wai MC, Wall Mo E, Pommier Y (1989) Cancer Res 49:1465–1469
6. Fan Y, Shi LM, Kohn KW, Pommier Y, Weistein JN (2001) J Med Chem 44:3254–3263
7. Staker BL, Hjerrild K, Feese MD, Behnke CA, Burgin AB, Stewart L (2002) Proc Natl Acad Sci USA 99:15387–15392
8. Kerrigan JE, Pilch DS (2001) Biochemistry 40:9792–9798
9. Fan Y, Weinstein JN, Kohn KW, Shi LM, Pommier Y (1998) J Med Chem 41:2216–2226
10. Lesueur-Ginot L, Demarquay D, Kiss R, Kasprzyk PG, Dassonneville L, Bailly C, Camara J, Lavergne O, Bigg DCH (1999) Cancer Res 59:2939–2943
11. Chauvier D, Chourpa I, Maizieres M, Riou J-F, Dauchez M, Alix AJP, Manfait M (2003) J Mol Struct 651–653:55–65
12. Demarquay D, Huchet M, Coulomb H, Lesueur-Ginot L, Lavergne O, Camara J, Kasprzyk PG, Prevost G, Bigg DCH (2004) Cancer Res 64:4942–4949
13. Xiao X, Cushman M (2005) J Org Chem 70:9584–9587
14. Xiao X, Cushman M (2005) J Am Chem Soc 127:9960–9961
15. Beck AD (1993) J Chem Phys 98:5648–5652
16. Lee C, Yang W, Parr RG (1988) Phys Rev B 37:785–789
17. Zhao Y, Truhlar DG (2008) Acc Chem Res 41:157–167
18. McLean AD, Chandler GS (1980) J Chem Phys 72:5639
19. Krishnan R, Binkley JS, Seeger R, Pople JA (1980) J Chem Phys 72:650
20. Cossi M, Barone V, Cammi R, Tomasi J (1996) Chem Phys Lett 255:327–335
21. Frisch MJ et al (2010) Gaussian 09, (version b.01). (Gaussian, Inc., Wallingford CT)

Theor Chem Acc (2014) 133:1555
DOI 10.1007/s00214-014-1555-9

REGULAR ARTICLE

# A comparison study of the H + $CH_4$ and H + $SiH_4$ reactions with eight-dimensional quantum dynamics: normal mode versus local mode in the reactant molecule vibration

**Yan Wang · Jun Li · Hua Guo · Minghui Yang**

Received: 29 May 2014 / Accepted: 29 July 2014 / Published online: 24 August 2014
© Springer-Verlag Berlin Heidelberg 2014

**Abstract** While molecular vibration of $CH_4$ is well described by the normal-mode paradigm, the local mode picture is more suitable for understanding the $SiH_4$ stretching vibrational motion. To compare the roles of the two types of molecular vibration in reaction dynamics, the H + $CH_4$ → $H_2$ + $CH_3$ and H + $SiH_4$ → $H_2$ + $SiH_3$ reactions have been investigated using an eight-dimensional (8D) quantum dynamics method in which the nonreacting $XH_3$ (X = C, Si) group keeps its $C_{3v}$ symmetry in the reaction. The reaction probabilities, integral cross sections and thermal rate constants in the temperature range of 200–2,000 K were calculated for both reactions. Strong mode specificity was found in both reactions, and the differences were rationalized by the vibrational characteristics of the $CH_4$ and $SiH_4$ reactants.

**Keywords** Quantum dynamics · H + $CH_4$ · H + $SiH_4$ · Normal mode · Local mode

Dedicated to Professor Guosen Yan and published as part of the special collection of articles celebrating his 85th birthday.

Y. Wang · M. Yang (✉)
Key Laboratory of Magnetic Resonance in Biological Systems, Wuhan Center for Magnetic Resonance, State Key Laboratory of Magnetic Resonance and Atomic and Molecular Physics, Wuhan Institute of Physics and Mathematics, Chinese Academy of Sciences, Wuhan 430071, People's Republic of China
e-mail: yangmh@wipm.ac.cn

Y. Wang
School of Chemical and Environmental Engineering, Hubei University for Nationalities, Enshi 445000, People's Republic of China

J. Li · H. Guo
Department of Chemistry and Chemical Biology, University of New Mexico, Albuquerque, NM 87131, USA

## 1 Introduction

Based on observations in atom–diatom reactions, Polanyi summarized the role played by various forms of energy in promoting reactivity. For a reaction with an "early" (reactant-like) barrier, translational energy is more effective than vibrational energy. However, for a reaction with a "late" (product-like) barrier, vibrational energy has higher efficacy in promoting reaction [1]. Much effort has been made to test Polanyi's rules in reactions involving polyatomic molecules, both experimentally [2–6] and theoretically [7–10]. The results indicated that Polanyi's rules are mostly upheld, but the capacity of various reactant vibrational modes for promoting reactivity may be different. These studies have stimulated new models to understand mode specificity in chemical reactions [11–15].

The vibration of a polyatomic molecule is traditionally described with the normal-mode paradigm, in which each normal-mode vibration involves a particular form of synchronized atomic motion [16, 17]. For example, the vibration of $CH_4$ is classified into four normal modes: the symmetric stretching mode ($\nu_1$), the asymmetric bending mode ($\nu_2$), the asymmetric stretching mode ($\nu_3$) and the symmetric bending mode ($\nu_4$, also known as umbrella mode). These synchronized motions involve all atoms in the molecule, and the energy deposited in each vibrational mode can be used to promote reactivity in a reaction. Previous studies have indicated that all excitations of the $CH_4$ vibration could enhance the H + $CH_4$ reaction with different levels of efficacy [18–20].

In some molecules, the normal-mode picture is inadequate and a local mode description of molecular vibration may be more suitable. A good example is the $SiH_4$ molecule, in which the four Si–H bonds vibrate nearly independently due to weak kinetic coupling among these stretching

modes [21–24]. The ro-vibrational spectrum of $SiH_4$ has been extensively investigated as a model to understand the local mode vibration by Zhu et al. [25, 26]. The $SiH_4$ molecule is a spherical top in its vibrational ground state. Upon the Si–H vibrational excitation, however, its rotational spectrum displayed symmetric top characters. The differences observed in the $SiH_4$ ro-vibrational spectra could be used to assign the stretching excited states, which are better described in the local mode regime. Theoretically, Halonen and Child [23] have developed a theory to calculate the different kinetic and potential couplings and analyzed the conditions under which the local mode vibration could be observed.

As a prototype of polyatomic reactions, the dynamics of the $H + CH_4$ reaction has attracted significant interests over the past decades, both experimentally [2, 27, 28] and theoretically [19, 20, 29–38]. As a full-dimensional quantum dynamics calculation is still difficult to perform, a number of reduced-dimensional models have been proposed. For example, Takayanagi [38] reported a three-dimensional study by approximating $H + CH_4$ with a collinear four-atomic system. Yu and Nyman [37] included the umbrella mode in their four-dimensional treatment within the rotating bond approximation (RBA). Wang and Bowman [36] performed a six-dimensional calculation by approximating $CH_4$ with a triatomic molecule. A semi-rigid vibrating rotor target (SVRT) model proposed by Zhang has been applied to this reaction in which the reacting polyatomic molecule $CH_4$ is treated as a semi-rigid vibrating rotor [35]. Last but not least, Palma and Clary [39] have suggested a quantum mechanics model for the $X + YCZ_3$ reactions, in which the nonreacting $CZ_3$ group is restricted to $C_{3v}$ symmetry. Based on this model, Yang and Zhang [20] reported a seven-dimensional initial state-selected time-dependent wave packet study, and Zhang et al. [32] have carried out an eight-dimensional transition-state wave packet study of $H + CH_4$ reaction. Very recently, Manthe et al. [31] studied initial state-selected reaction probabilities for this reaction with a full-dimension MCTDH (multi-configuration time-dependent Hartree) method, and Zhang et al. reported a six-dimensional state-to-state quantum dynamics study of this reaction [29].

Experimentally, the dynamics of the $F + SiH_4$ [40, 41] and $Cl + SiH_4$ [42, 43] reactions have been studied recently by Yang et al. However, no experimental study of the $H + SiH_4$ reaction has been reported. Theoretically, Espinosa-Garcia et al. [44] have developed an analytic potential energy surface (PES) for the $H + SiH_4$ reaction. Based on this PES, rate constants and kinetic isotope effects were studied using variational transition-state theory by the same authors [44] and later using a semi-classical quantum instanton method by Zhao et al. [45]. Recently, Bian et al. constructed a global twelve-dimensional ab initio PES for the $H + SiH_4$ reaction [46] and studied the dynamics with quasi-classical trajectory calculations [47, 48] and the kinetics with variational transition-state theory [49].

In this work, a reduced-dimensional quantum dynamics study of the $H + SiH_4$ reaction is performed to explore the role of local mode in the reaction dynamics, using the PES of Espinosa-Garcia et al. [44] (denoted as SiH5-EGSC-1998). For comparison, the quantum dynamics calculations for the $H + CH_4$ reaction have also been carried out on a PES also developed by Espinosa-Garcia [50] (denoted as CH5-EG-2002). This PES is completely symmetric with respect to the permutation of the four $CH_4$ hydrogen atoms and has been carefully calibrated [50]. This permutation symmetry is absent in the PES developed by Jordan and Gilbert [51] (denoted as JG-PES), and the calculated potential energy is dependent on the order of four hydrogen atoms, although the JG-PES has been used in most previous quantum dynamics studies. The SiH5-EGSC-1998 and CH5-EG-2002 PESs have recently been employed to calculate the thermal rate constants using variational transition-state theory [44, 50] and semi-classical methods [45, 52], thus providing theoretical data to compare with. For these reasons, these PESs are selected in this work, although several more accurate PESs exist [53–55]. For the quantum dynamical calculations, a recently developed eight-dimensional (8D) quantum mechanical (QM) Hamiltonian is employed [19]. This 8D QM model is similar to the pioneering work of Palma and Clary [39] for the $X + YCZ_3 \rightarrow XY + CZ_3$ reaction and has recently been applied to the $H/O(^3P) + CH_4$ reactions [9, 19] and the $CH_4$ dissociative chemisorption on Ni(111) [8], and the results were in good agreement with experimental observations.

The paper is organized as follows. In Sect. 2, the 8D QM method is briefly described. The reaction probabilities, integral cross sections and thermal rate constants for both reactions are presented in Sect. 3. This is followed by a discussion of these results in Sect. 4. Finally, conclusions are given in Sect. 5.

## 2 Methodology

### 2.1 The coordinate system

The eight-dimensional model for the $X + YCZ_3 \rightarrow XY + CZ_3$ reaction is described in a Jacobi coordinate system as shown in Fig. 1: $\boldsymbol{R}$ is the vector from the center of mass of $YCZ_3$ to X; $\boldsymbol{r}$ is the vector from the center of mass of $CZ_3$ to Y. The $CZ_3$ group could be defined with polar coordinates ($\rho$, $\chi$) [32, 55] or Cartesian coordinates ($x$, $s$) [39, 56]. Here, $\rho$ is the bond length of CZ, and $\chi$ is the angle between a CZ bond and vector $\boldsymbol{S}$, which is the symmetry axis of $CZ_3$; $x$ denotes the distance between atom Z

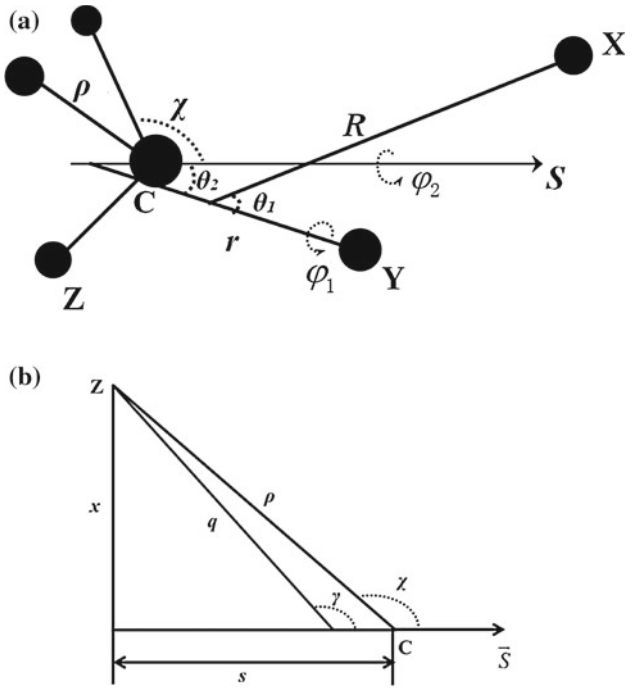


**Fig. 1** **a** Jacobi coordinate system of the X + $YCZ_3$ model; **b** Cartesian coordinates and polar coordinates of $CZ_3$ group

and the symmetry axis $\boldsymbol{S}$ and $s$ the distance between atom C and the center of three Z atoms. $\theta_1$ is the bending angle between the vectors $\boldsymbol{R}$ and $\boldsymbol{r}$ and $\varphi_1$ is the azimuthal angle of the rotation of $YCZ_3$ around the vector $\boldsymbol{r}$; $\theta_2$ is the bending angle between vectors $\boldsymbol{r}$ and $\boldsymbol{S}$ and $\varphi_2$ is the azimuthal angle of the rotation of $CZ_3$ around the vector $\boldsymbol{S}$.

Four frames were introduced to describe the angular coordinates and rotation of the system: the space-fixed frame, the body-fixed frame ($XYCZ_3$-fixed frame), the $YCZ_3$-fixed frame and the $CZ_3$-fixed frame. The $z$-axis of the body-fixed frame lies along the vector $\boldsymbol{R}$, and the vector $\boldsymbol{r}$ is always in the $xz$-plane of the frame. The $z$-axis of the $YCZ_3$-fixed frame lies along the vector $\boldsymbol{r}$, and the vector $\boldsymbol{S}$ is always in the $xz$-plane of the frame. The $z$-axis of the $CZ_3$-fixed frame lies along its symmetry axis, the vector $\boldsymbol{S}$, and the first Z atom is always in the $xz$-plane of the frame. The four frames form three pairs of related space and body-fixed frames.

## 2.2 The model Hamiltonian

By restricting the nonreacting $CZ_3$ group in $C_{3v}$ symmetry, the eight-dimensional model Hamiltonian for $XYCZ_3$ system is given by

$$\hat{H} = -\frac{1}{2\mu_R}\frac{\partial^2}{\partial R^2} - \frac{1}{2\mu_r}\frac{\partial^2}{\partial r^2} + \frac{(\hat{J}_{tot}-\hat{J})^2}{2\mu_R R^2} + \frac{\hat{l}^2}{2\mu_r r^2} + \hat{K}^{vib}_{CZ_3} + \hat{K}^{rot}_{CZ_3} + V(R,r,x,s,\theta_1,\varphi_1,\theta_2,\varphi_2), \quad (1)$$

where $\mu_R$ is the reduced mass of the X + $YCZ_3$ system and $\mu_r$ is the reduced mass of Y + $CZ_3$. The first two terms are the kinetic energy operators for $R$ and $r$, respectively; $\hat{J}_{tot}$ is the total angular momentum operator of the system. $\hat{J}$ is the rotational angular momentum operator of $YCZ_3$, and $\hat{l}$ is the orbital angular momentum operator of atom Y with respect to $CZ_3$. $\hat{K}^{vib}_{CZ_3}$ and $\hat{K}^{rot}_{CZ_3}$ are the vibrational and rotational kinetic energy operators of $CZ_3$, respectively. Due to the symmetry requirement and definition of the $CZ_3$-fixed frame, no vibration–rotation coupling exists in this eight-dimensional Hamiltonian. The last term $V(R,r,x,s,\theta_1,\varphi_1,\theta_2,\varphi_2)$ in Hamiltonian is the potential energy.

The vibrational and rotational kinetic operators of the $CZ_3$ group could be expressed with a new scaled-polar coordinate system ($q$, $\gamma$), with $q = \sqrt{x^2+y^2}$ and $\gamma = \arctan(-x/y)$, here $y = \sqrt{\frac{m_C}{m_C+3m_Z}}s$. The explicit form of the operators is

$$\hat{K}^{vib}_{CZ_3} = \frac{1}{2\mu_x}\left(\frac{\partial^2}{\partial q^2} + \frac{1}{q^2}\frac{\partial^2}{\partial \gamma^2} + \frac{1}{4q^2}\right), \quad (2)$$

with $\mu_x = 3m_Z$ and the integral element as $\partial q \partial \gamma$, and

$$\hat{K}^{rot}_{CZ_3} = \frac{1}{2I_A}\hat{j}^2 + \left(\frac{1}{2I_C} + \frac{1}{2I_A}\right)\hat{j}^2_z, \quad (3)$$

with $\hat{j}$ as the rotational angular momentum of $CZ_3$ and $\hat{j}_z$ its z-component. The rotational inertia $I_A$ and $I_C$ are defined as [39],

$$I_A = \frac{3}{2}m_Z\left[x^2 + \frac{2m_C}{m_C+3m_Z}s^2\right], \quad (4)$$

$$I_C = 3m_Z x^2. \quad (5)$$

## 2.3 Wavefunction and reaction flux

For the case of $J_{tot} = 0$, the wave packet is expanded as a linear combination of the product of the basis sets for $R$, $r$, $q$, $\gamma$ and the parity-adapted rotational basis functions.

$$\Psi^{\varepsilon} = \sum_{n_Z,n_r,n_q,n_\gamma}\sum_{Jljk} c^{\varepsilon}_{n_Z n_r n_q n_\gamma Jljk}(t) G_{n_R}(R) F_{n_r}(r) Q_{n_q}(q) H_{n_\gamma}(\gamma) \Phi^{\varepsilon}_{Jljk}(\hat{r},\hat{S}), \quad (6)$$

$k$ is the projection of $j$ onto the $C_{3v}$ symmetry axis $\boldsymbol{S}$, and $\varepsilon$ is the parity under space inversion. The parity-adapted rotational basis function is expressed as

$$\Phi^{\varepsilon}_{Jljk}(\hat{r},\hat{S}) = \sqrt{\frac{1}{2(1+\delta_{k0})}} \times \left[\Phi_{Jljk}(\hat{r},\hat{S}) + \varepsilon(-1)^{J+l+j+k}\Phi_{Jlj-k}(\hat{r},\hat{S})\right], \quad (7)$$

with

$$\Phi_{Jjlk}(\hat{r},\hat{S}) = \sum_m \bar{D}^J_{0m}(\hat{r})\sqrt{\frac{2l+1}{2J+1}}\langle jml0|Jm\rangle \bar{D}^j_{mk}(\hat{S}), \quad (8)$$

where $\bar{D}^J_{MK}$ is the normalized Wigner rotational matrix and $\langle jmj'm'|JM\rangle$ the Clebsch-Gordan coefficient [57].

The time-dependent wave packet method was used to solve the Schrödinger equation with an initial wave packet consisting of a Gaussian wave packet and a particular ro-vibrational state of $XH_4$ (X = C, Si)

$$\Psi^{\varepsilon}(t=0) = Ne^{-[(R-R_0)/\alpha]^2}e^{i\kappa_0 R}\psi_{XH_4}, \quad (9)$$

where $N$, $R_0$, $\alpha$, $\kappa_0$ are, respectively, the normalization factor, position, half-width and central energy of the Gaussian wave packet. $\psi_{XH_4}$ is the ro-vibrational wavefunction of $XH_4$, which has been predetermined in the reactant asymptote. In this work, the rotationless reactants were used.

### 2.4 Analysis of the reaction path Hamiltonian

The reaction path Hamiltonian [58] for both reactions was determined using POLYRATE 9.7 [59], starting from the saddle point geometry and going downhill to both directions in mass-weighted Cartesian coordinates using the Page and McIver's method [60] with a step size of $1.9 \times 10^{-4}$ u$^{1/2}\cdot a_0$. Along the minimum energy path (MEP), the reaction coordinate ($s$) is defined as the signed distance from the saddle point ($s = 0$), with $s > 0$ referring to the product side and $s < 0$ to the reactant side. The reaction path was followed between $s = -1.5$ and $s = 1.5$ u$^{1/2}\cdot a_0$, and the Hessian matrix was calculated every 10 points. These parameters have been tested for convergence. All calculations were carried out in mass-scaled coordinates with a reduced mass equal to 1 u. Along the MEP, a generalized normal-mode analysis was performed by projecting these modes along the reaction path as well as overall rotations and translations. With such information, the vibrationally adiabatic potentials were determined as:

$$V_a(n,s) = V_{MEP}(s) + \varepsilon_{int}(n,s), \quad (10)$$

where $V_{MEP}(s)$ is the potential energy of the MEP with its zero at the reactants, and $\varepsilon_{int}(n,s)$ is the vibrational energy at $s$ from the generalized normal-mode vibrations orthogonal to the reaction coordinate. $V_a(n = 0, s)$ corresponds to the ground vibrational state adiabatic potential, $V_a^G(s)$.

## 3 Results

### 3.1 Basis set

In this work, an $L$-shaped wavefunction expansion for $R$ and $r$ was used to reduce the size of the basis set [61].

**Table 1** Parameter used in dynamics calculations

| | $H + CH_4$ | $H + SiH_4$ |
|---|---|---|
| $N_R$ | 85/26 | 160/80 |
| ($R_{min}$, $R_{max}$) | (2.5, 15.0)[a] | (3.0, 11.0)[a] |
| $N_r$ | 5/25 | 6/28 |
| ($r_{min}$, $r_{max}$) | (1.0, 5.0)[a] | (1.5, 5.5)[a] |
| $N_q$ | 4 | 4 |
| $N_\gamma$ | 5 | 5 |
| $J_{max}$ | 45 | 72 |
| $l_{max}$ | 27 | 48 |
| $j_{max}$ | 18 | 24 |
| $k_{max}$ | 6 | 6 |
| $N_{rot}$ | 18,654 | 62,048 |
| $N_{tot}$ | $3.5 \times 10^8$ | $3.4 \times 10^9$ |

[a] Unit in $a_0$

For the $H + SiH_4$ reaction, a total of 160 sine basis functions ranging from 3.0 to 11.0 $a_0$ were used for the $R$ basis set expansion with 80 nodes in the interaction region, and 6 and 28 basis functions of $r$ were used in the asymptotic and interaction regions, respectively. For the vibration of the $CZ_3$ group, 4 and 5 basis functions were used for coordinates $q$ and $\gamma$, respectively. The size of the rotational basis functions is controlled by the parameters, $J_{max} = 72$, $l_{max} = 48$, $j_{max} = 24$ and $k_{max} = 6$. After considering parity and $C_{3v}$ symmetry, the size of rotational basis functions is 62,048 and the size of the total basis functions is ~3.4 billion. These parameters are listed on Table 1. For comparison, the corresponding values for the $H + CH_4$ reaction are also listed on this table. Due to the small mass of C, the size of basis set for the $H + CH_4$ reaction is smaller than that for the $H + SiH_4$ reaction.

### 3.2 Total reaction probabilities

For the $H + CH_4$ reaction, total reaction probabilities were calculated with nonrotating $CH_4$ initially in 5 vibrational states which labeled as ($v_1$, $v_2$, $v_3$, $v_4$): (1) the ground vibrational state (0, 0, 0, 0) with a zero point energy of 4,872.29 cm$^{-1}$, (2) the excited states of the umbrella mode (0, 0, 0, 1) and (0, 0, 0, 2) with excitation energies of 1,288.18 cm$^{-1}$ (0.160 eV) and 2,543.35 cm$^{-1}$ (0.315 eV), (3) the symmetric stretching excited state (1, 0, 0, 0) with an excitation energy of 2,822.18 cm$^{-1}$ (0.350 eV) and (4) the asymmetric stretching vibrational state (0, 0, 1, 0) with an excitation energy of 2,949.29 cm$^{-1}$ (0.366 eV). These excitation energies are listed in Table 2 and compared with the experimental values [62]. Note that the relatively large errors are due to inaccuracies in the PES. It is also clear that the frequency for the (0, 1, 0, 0) state has a large discrepancy with the corresponding experimental value, due

**Table 2** Vibration frequencies of $CH_4$ and $SiH_4$ ($cm^{-1}$)

| | $CH_4$ | | $SiH_4$ | |
|---|---|---|---|---|
| | Cal | Exp[a] | Cal | Exp[b] |
| (0, 0, 0, 0) | 4,872.29 | | 3,364.02 | |
| (0, 0, 0, 1) | 1,288.18 | 1,367 | 851.22 | 914 |
| (0, 1, 0, 0) | 2,517.06 | 1,583 | 1,677.36 | 975 |
| (0, 0, 0, 2) | 2,543.35 | | 1,686.89 | |
| (1, 0, 0, 0) | 2,822.16 | 3,026 | 1,992.27 | 2,187 |
| (0, 0, 1, 0) | 2,949.29 | 3,157 | 2,075.69 | 2,191 |

[a] Reference [62]

[b] Reference [63]

presumably to the fact that the bending motion is not compatible with the $C_{3v}$ symmetry of the $CZ_3$ moiety [9]. As a result, the dynamics calculations for this state were not attempted.

Figure 2 shows the total reaction probabilities ($J = 0$) as a function of the translational energy and total energy relative to H + $CH_4$(0, 0, 0, 0), respectively. From the figure, all vibrational excitations of $CH_4$ appear to enhance the reactivity and the excitation energies were partially utilized to reduce the reaction threshold. At low collision energies, the reactivity is apparently enhanced by the symmetric stretching (1, 0, 0, 0) and asymmetric stretching (0, 0, 1, 0) excited states. However, the reaction probabilities as a function of total energy show that the translational energy is the most effective in promoting the reaction. These observations are consistent with our previous results on the earlier JG-PES [19].

The calculated energies of the six low-lying vibrational states of $SiH_4$ are also listed in Table 2 and compared with the experimental values [63]. Again, the (0, 1, 0, 0) state is poorly described by the 8D model and is not included in the dynamics calculations. The total reaction probabilities for the H + $SiH_4$ reaction were calculated with nonrotating $SiH_4$ initially in these five vibrational states and are shown in Fig. 3. The efficacies of the two umbrella excitations are very similar for both the H + $SiH_4$ and H + $CH_4$ reactions:

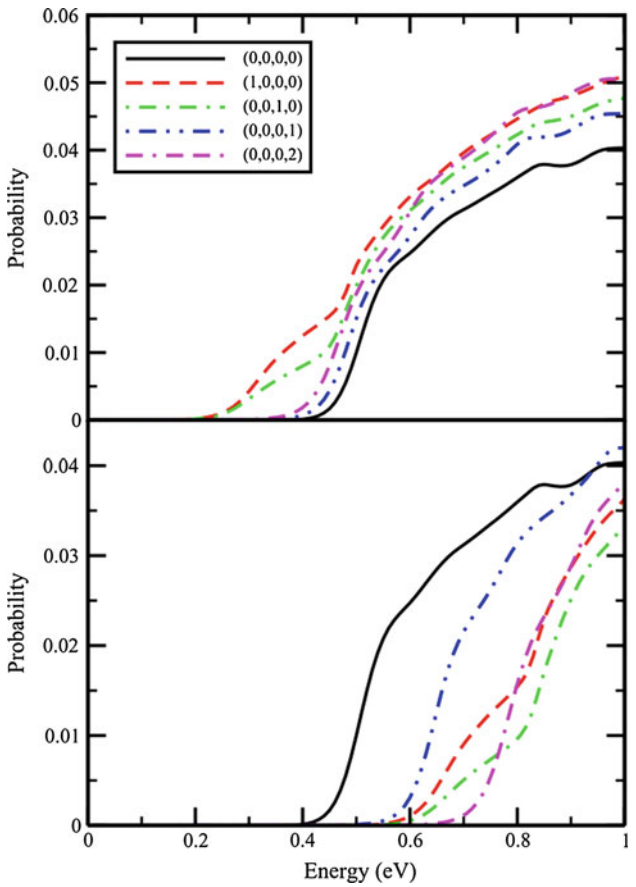


**Fig. 2** Total reaction probabilities for the H + $CH_4$ reaction from different initial vibrational states of $CH_4$ as a function of translational energy (*upper panel*) and as a function of total energy measured with respect to H + $CH_4$ (0, 0, 0, 0) (*lower panel*)

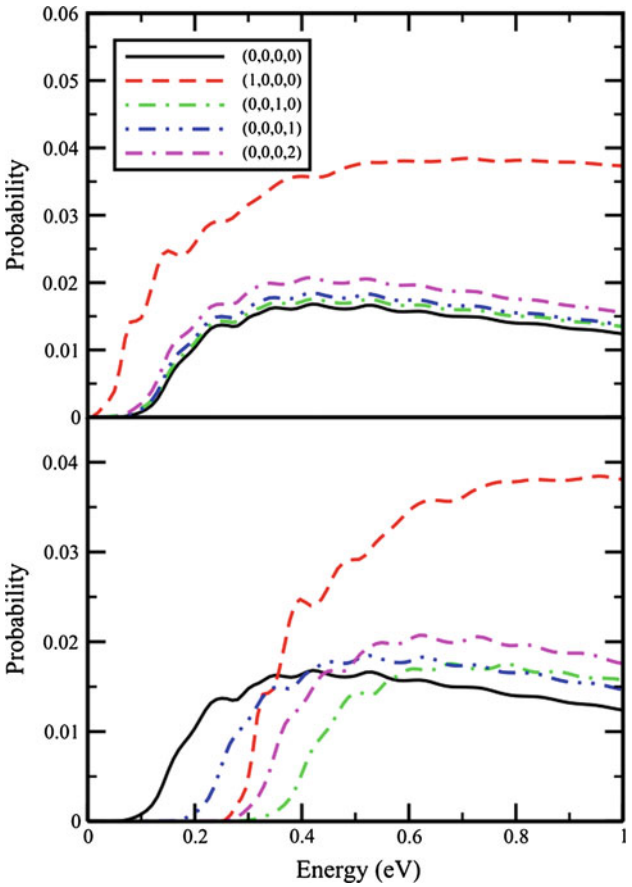


**Fig. 3** Total reaction probabilities for the H + $SiH_4$ reaction from different initial vibrational states of $SiH_4$ as a function of translational energy (*upper panel*) and as a function of total energy measured with respect to H + $SiH_4$ (0, 0, 0, 0) (*lower panel*)

(0, 0, 0, 2) > (0, 0, 0, 1). For the two stretching excitations of $SiH_4$, although the frequencies of $\nu_1$ (2,187 $cm^{-1}$) and $\nu_3$ (2,191 $cm^{-1}$) modes are close in energies, they show very different efficacies in reducing the reaction threshold. From Fig. 3, the (1, 0, 0, 0) excitation pronouncedly enhances the reactivity while the (0, 0, 1, 0) excitation has a minor effect on the reactivity. In the H + $CH_4$ reaction, two stretching excitations were found to have roughly the same efficacy in promoting the reaction. Similar behaviors have also been found in the previous studies of the O + $CH_4$ reaction with a four-dimensional model by Palma and Clary [64] and an eight-dimensional model by Liu and coworkers [9].

### 3.3 Integral cross sections and thermal rate constants

The integral cross section (ICS) for a specific initial state is obtained by summing the total reaction probabilities over all the partial waves,

$$\sigma_i(E) = \frac{1}{2J+1}\frac{\pi}{2\mu E}\sum_{J_{\text{tot}}}(2J_{\text{tot}}+1)P_i^{J_{\text{tot}}}(E). \quad (11)$$

In this work, the $J_{\text{tot}} > 0$ partial waves were calculated with the centrifugal-sudden (CS) approximation [65, 66]. For H + $CH_4$, the maximum value of $J_{\text{tot}}$ needed to converge the ICS is $J_{\text{tot}} = 40$. And for H + $SiH_4$, the corresponding value is $J_{\text{tot}} = 50$. The ICSs have been multiplied by a factor of 4 to account for all possible reaction channels. The results for ICS are plotted on Figs. 4 and 5.

The ICS curves are very similar to the reaction probability curves for both reactions. As shown in Fig. 4, all vibrational excitations of $CH_4$ promote the H + $CH_4$ reaction, consistent with the previous calculations [19]. It should be noted that the calculated values of the ICS are close to those obtained on the JG-PES [19] but almost 10 times larger than that obtained using recently developed ab initio PESs [55]. The lower panel of Fig. 4 shows that the ground-state reaction yields the largest ICS throughout the energy range. For the H + $SiH_4$ reaction, the H + $SiH_4$(1, 0, 0, 0) reaction has the largest contribution to the reaction when the total energy is above 0.33 eV and the ground-state reaction dominates the reactivity when the total energy is below 0.33 eV. The efficacy of the $SiH_4$(1, 0, 0, 0) excitation for the promotion of reactivity is rather pronounced. From the upper panels of Fig. 5, the ICS for the H + $SiH_4$(1, 0, 0, 0) reaction is overall 2 times larger than that for the H + $SiH_4$(0, 0, 0, 2) reaction. Overall, the ICS values for the (0, 0, 0, 1), (0, 0, 1, 0) and (0, 0, 0, 2) excitations of $SiH_4$ are very close to each other over the entire collision energy range studied here.

The rate coefficients are calculated from the Boltzmann average of the cross sections for the five vibrational states considered in this work,

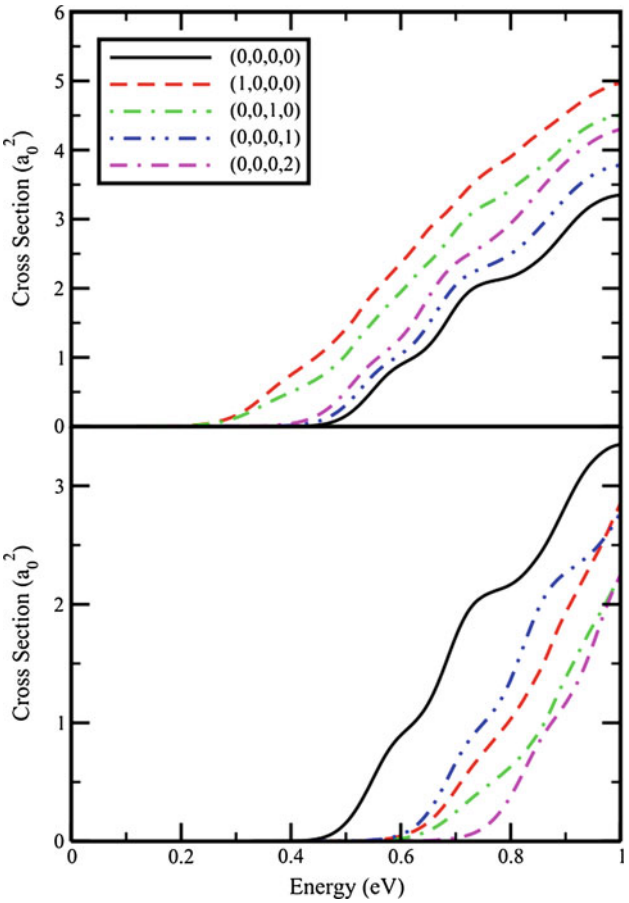


**Fig. 4** Integral cross sections for the H + $CH_4$ reaction from different initial vibrational states of $CH_4$ as a function of translational energy (*upper panel*) and as a function of total energy measured with respect to H + $CH_4$ (0, 0, 0, 0) (*lower panel*)

$$k_i(T) = \left(\frac{8kT}{\pi\mu}\right)^{1/2}(k_{\text{B}}T)^{-2}\int_0^{\infty} E_{\text{t}}\exp(-E_{\text{t}}/kT)\sigma_{\text{i}}(E_{\text{t}})\text{d}E_{\text{t}}, \quad (12)$$

where $k_{\text{B}}$ is the Boltzmann constant and $\mu$ is the reduced mass of the scattering coordinate. These rate coefficients are presented in Figs. 6 and 7. For comparison purposes, the calculated values with two other theoretical, the canonical variational theory (CVT) [44, 50] and quantum instanton (QI) methods [45, 52], as well as experimental values [67–71] are also showed in the figures. These theoretical calculations have been performed on the same PESs. For the H + $CH_4$ reaction, the 8D QM calculated values satisfactorily described the rate constants in the temperature range of 200–2,000 K and are in good agreement with the results calculated using other theoretical methods. For the H + $SiH_4$ reaction, on the other hand, the 8D QM rate coefficients are overall smaller than the experimental and QI values, which are quite close, by a factor of 1.5, and are slightly larger at low temperature but about 2 times smaller

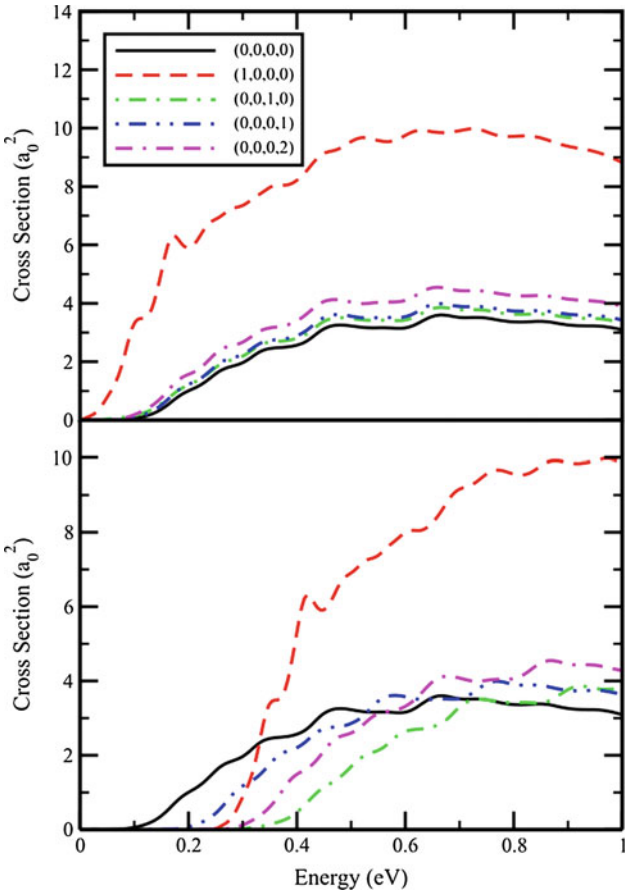


**Fig. 5** Integral cross sections for the H + $SiH_4$ reaction from different initial vibrational states of $SiH_4$ as a function of translational energy (*upper panel*) and as a function of total energy measured with respect to H + $SiH_4$ (0, 0, 0, 0) (*lower panel*)

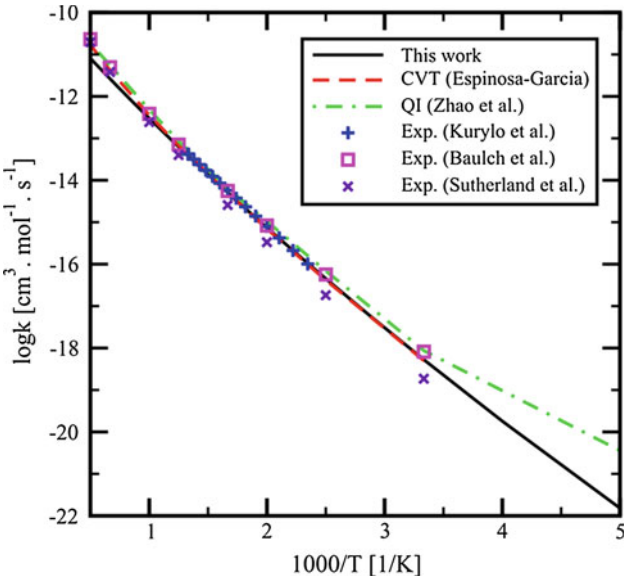


**Fig. 6** Arrhenius plot of thermal rate coefficients for the H + $CH_4$ reaction, in comparison with other theoretical [50, 52] and experimental rate constants [67–69]

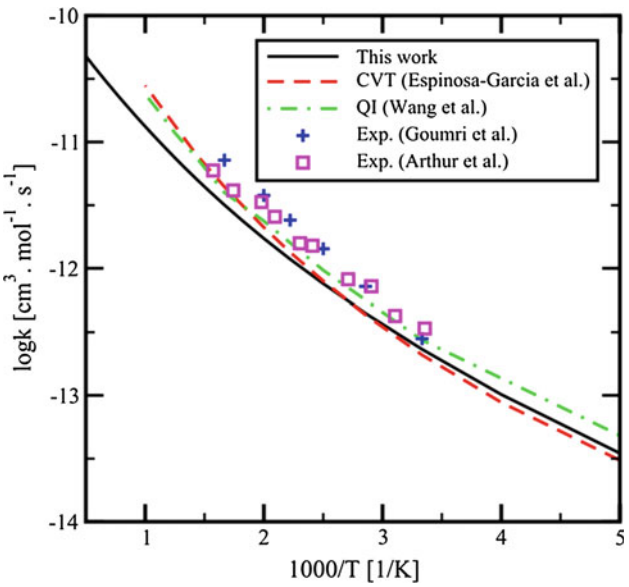


**Fig. 7** Arrhenius plot of thermal rate coefficients for the H + $SiH_4$ reaction, in comparison with other theoretical [44, 45] and experimental rate constants [70, 71]

at high temperatures than the CVT values. The discrepancy between 8D QM and CVT rate constant at high temperatures indicates that higher vibrational excited state may have considerable contributions to the reactivity.

## 4 Discussion

The differences in mode specificity between the two reactions can be explained by the vibrational character of the $XH_4$ reactant molecules. The (1, 0, 0, 0) and (0, 0, 1, 0) stretching modes of $CH_4$ are best described by the normal-mode picture, while those of $SiH_4$ have different characters from the $CH_4$ molecule, as the vibrational excitation is localized in each Si–H bond. These differences are clearly shown in Fig. 8, where the corresponding wavefunctions are displayed in the ($r$, $q$) coordinates. For $CH_4$, the wavefunction is normal as the node is along either the ($r + q$) or ($r - q$) normal coordinate. In the classical picture, this corresponds to synchronized vibrational motions involving all atoms. On the other hand, the wavefunctions for $SiH_4$ are largely local, as the node is along either the $r$ or $q$ coordinate. Classically, this represents vibrational motion in either the C–Y or C–$Z_3$ bond. It is important at this point to stress that the 8D model used here does not have full permutation symmetry. As a result, the C–Y and C–Z bonds are not treated as equals. In particular, the wavefunction of

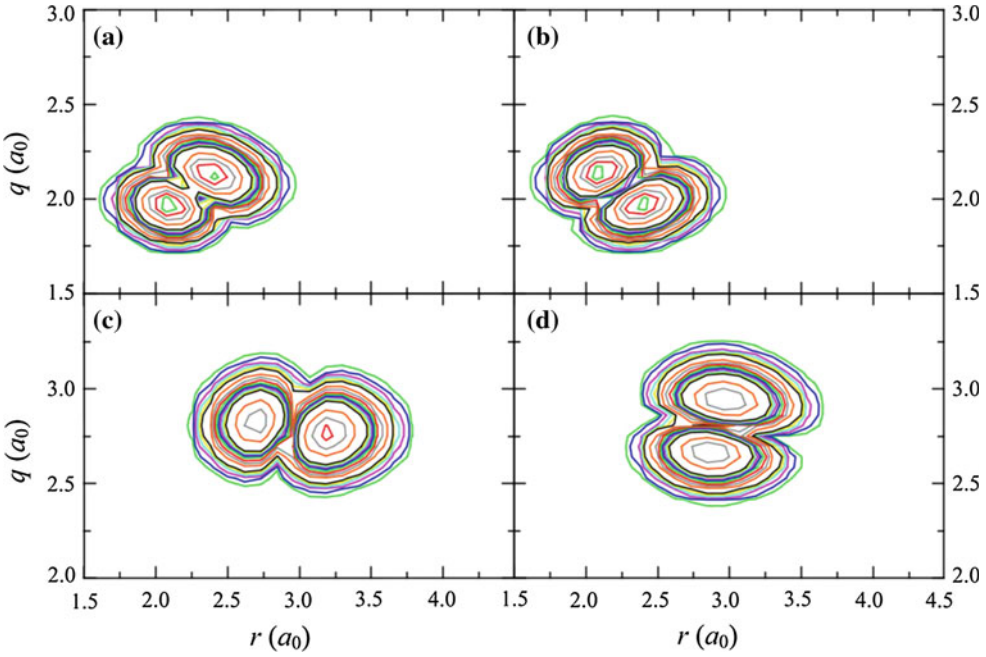


**Fig. 8** The contour plots of $|\psi_{XH_4}(r,q)|^2$ with integration over other coordinates. **a**, **b** (1, 0, 0, 0) and (0, 0, 1, 0) states of $CH_4$ and **c**, **d** (1, 0, 0, 0) and (0, 0, 1, 0) states of $SiH_4$, respectively

$SiH_4$ in full dimension should be a linear combination of all four local modes with equal weights [23]. Consequently, the description of the reactant vibrational and reaction dynamics within the 8D model is approximate in nature. Nevertheless, this reduced-dimensional model captures the essence of the normal versus local vibrations, as evidenced by the reasonably good agreement with experimental vibrational frequencies in Table 2.

The results in Sect. 3 clearly demonstrated that the energy deposited into vibration can be used to overcome the reaction barrier. From Fig. 2, for example, 0.212 eV out of 0.350 eV for the (1, 0, 0, 0) excitation energy and 0.212 eV out of 0.366 eV for the (0, 0, 1, 0) excitation energy are used to reduce the reaction threshold for the H + $CH_4$ reaction, respectively. The corresponding percentages are 60 % and 58 %, clearly larger than the average value of 25 %. The dominance of the local mode features in the $SiH_4$ helps to promote its reaction with H even more effectively. The effect of the symmetric stretching mode is much more prominent in the $SiH_4$ + H reaction than that in the $CH_4$ + H reaction. This is clearly seen in Fig. 5, where the $SiH_4$(1, 0, 0, 0) excited reactivity is much larger than both the ground and other excited vibrational states.

A word of caution concerning the limitations of the reduced-dimensionality model used in this work is in order. As mentioned above, the lack of permutation symmetry in this model prevents the proper treatment of the four equivalent X–H bonds in $XH_4$. As a result, the local mode wavefunctions for both the (1, 0, 0, 0) and (0, 0, 1, 0) states of $SiH_4$ are not properly symmetrized. In particular, the full-dimensional (1, 0, 0, 0) state should also include excitation of the three C–Z bonds by symmetry. On the other hand, the reduced-dimensional wavefunction has only a node in the $r$ coordinate along the C–Y bond. Furthermore, the attribution of the vibrational excitation to all three C–Z bonds for the (0, 0, 1, 0) state in our reduced-dimensional model is probably not a realistic representation of the local mode vibration in this molecule. Hence, the strong mode specificity observed in our reduced-dimensional model calculations is expected to be much less pronounced in full-dimensional dynamics.

To further illustrate the influence of the local mode vibration of $SiH_4$ during the H + $SiH_4$ reaction, we have computed the vibrationally adiabatic reaction paths for the corresponding vibrational excitation in $SiH_4$ in full dimension, which are presented in Fig. 9. For comparison, the corresponding results for the $CH_4$ + H reaction are also included in the same figure. Despite the fact that the reaction paths are qualitatively similar for these two reactions, the extent of localization is different. As shown in the figure, the symmetric stretching mode of both the isolated $CH_4$ and $SiH_4$ molecules involves all four bonds. However, as the H collisional partner approaches, the (1, 0, 0, 0) vibration localized to the proximal C–H or Si–H bond involved in the reaction, but with different extents. At $s = -0.95$, the $SiH_4$ vibration is already exclusively in the proximal Si–H bond, while the $CH_4$ vibration has still some residual normal-mode character. This is readily understood as the former has very weak coupling among the four Si–H stretching vibrations, while the coupling is moderate in $CH_4$ [22].

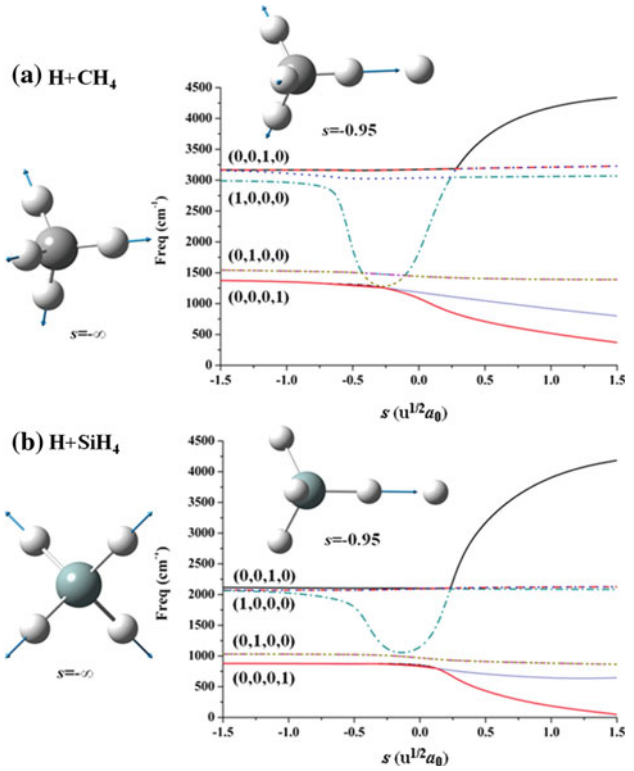


**Fig. 9** Vibrationally adiabatic reaction paths for both the H + $CH_4$ (*upper panel*) and H + $SiH_4$ (*lower panel*) reactions on the PESs of Espinosa-Garcia et al. [44, 50]. The vibrational modes of the $CH_4$ or $SiH_4$ reactant in the reactant asymptote are labeled. The normal-mode vibrational vectors are also given for the isolated reactant ($s = -\infty$) and the reactive system at $s = -0.95$

At this point, it is interesting to consider isotopically substituted methane as a prototype for local excitation. Due to the larger differences in the vibrational frequencies in $CHD_3$, the C–H and C–D stretches do not couple anymore. The $\nu_1$ mode of $CHD_3$ is the C–H local mode, and the $\nu_3$ mode is localized in the C–D stretches. A recent study [72] of the H + $HCD_3 \rightarrow H_2 + CD_3$ reaction has showed that the C–H excitation led to a much large enhancement than the bending or umbrella mode. Similar results have also been obtained in the studies of the Cl + $CHD_3 \rightarrow$ HCl + $CD_3$ reaction [7, 73]. These results together with the current study of the H + $SiH_4$ reaction demonstrate that the high efficiency promotes the reaction by local mode excitation.

Very recently, we have proposed the sudden vector projection (SVP) model [14, 15], which complements the adiabatic picture described in Fig. 9. Assuming the collision process is much faster than the intramolecular vibrational energy redistribution (IVR), the mode specificity in a bimolecular reaction is attributed to the projection of the reactant normal-mode vectors on to the reaction coordinate vector at the transition state. Although the H + $CH_4$ reaction has been analyzed in another publication [74] based on ab initio data, we repeat here the calculation on the CH5-EG-2002 PES. The SVP values are 0.51, 0.00, 0.28 and 0.038 for the symmetric stretching, bending, asymmetric stretching and umbrella modes of $CH_4$. These values are similar to those reported elsewhere [74], where the validity of the SVP predictions has been discussed. The same SVP calculations have been done on the (SiH5-EGSC-1998) PES as well for the H + $SiH_4$ reaction, and the corresponding SVP values are 0.47, 0.001, 0.27 and 0.001. In both systems, the SVP model predicts a larger enhancement effect for the symmetric stretching mode than that for the asymmetric mode, and small efficacies of the bending modes for enhancing the reactions. Both predictions are consistent with the 8D results presented above, although the SVP model seems to underestimate the bending modes.

## 5 Conclusions

In this work, an eight-dimensional quantum dynamics study has been carried out for both the H + $CH_4$ and H + $SiH_4$ reactions on two analytic PESs developed by Espinosa-Garcia and coworkers [44, 50]. The quantum dynamics are based on a reduced-dimensional model originally proposed by Palma and Clary [39] and reformulated by introducing a coordinate transform [19]. The 8D model includes representatives of all $XH_4$ vibrational modes, thus presenting a realistic reduced-dimensional model for the $X + YCZ_3 \rightarrow XY + CZ_3$ type reactions.

The total reaction probabilities and integral cross sections were obtained for reactants initially in the ground and four excited vibrational states. Strong mode specificity was found in both reactions. The mode specificity was analyzed and found to be consistent with the SVP predictions. In addition, the ability to enhance the reactivity is also correlated with the normal or local mode characters of the reactant molecules. For both reactions, the thermal rate coefficients were also calculated by averaging the contributions from all five initial vibrational states. The quantum dynamical rate coefficients are in reasonably good agreement with the experiment measurements and other theoretical calculated values.

This work demonstrates that the effects of reactant local modes on reaction dynamics could be studied using the 8D quantum dynamics method. On the other hand, it should be noted that the results are not expected to be quantitative due to the limitations of the reduced-dimensional model. An ultimate understanding of the mode specificity in these reactions can only be achieved with full dimensionality.

**Acknowledgments** This work was supported by National Science Foundation of China (Projects No. 21221064 and 21373266 to MY) and US Department of Energy (DE-FG02-05ER15694 to HG).

## References


1. Polanyi JC (1972) Acc Chem Res 5:161
2. Zhang WQ, Zhou Y, Wu GR, Lu YP, Pan HL, Fu BN, Shuai QA, Liu L, Liu S, Zhang LL, Jiang B, Dai DX, Lee SY, Xie Z, Braams BJ, Bowman JM, Collins MA, Zhang DH, Yang XM (2010) Proc Natl Acad Sci USA 107:12782
3. Zhang WQ, Kawamata H, Liu KP (2009) Science 325:303
4. Wang FY, Liu KP (2010) Chem Sci 1:126
5. Wang FY, Lin JS, Liu KP (2011) Science 331:900
6. Lin JJ, Zhou JG, Shiu WC, Liu KP (2003) Science 300:966
7. Zhang ZJ, Zhou Y, Zhang DH, Czako G, Bowman JM (2012) J Phys Chem Lett 3:3416
8. Jiang B, Liu R, Li J, Xie DQ, Yang MH, Guo H (2013) Chem Sci 4:3249
9. Liu R, Yang MH, Czako G, Bowman JM, Li J, Guo H (2012) J Phys Chem Lett 3:3776
10. Czako G, Bowman JM (2011) Science 334:343
11. Duncan WT, Truong TN (1995) J Chem Phys 103:9642
12. Yoon S, Holiday RJ, Sibert EL III, Crim FF (2003) J Chem Phys 119:9568
13. Yan S, Wu Y-T, Liu K (2008) Proc Natl Acad Sci USA 105:12667
14. Jiang B, Guo H (2013) J Chem Phys 138:234104
15. Jiang B, Guo H (2013) J Am Chem Soc 135:15251
16. Wilson EB, Decius JC, Cross PC (1955) Molecular vibrations. Dover, New York
17. Ma GB, Guo H (1999) J Chem Phys 111:4032
18. Palma J, Echave J, Clary DC (2002) J Phys Chem A 106:8256
19. Liu R, Xiong HW, Yang MH (2012) J Chem Phys 137:174113
20. Yang MH, Zhang DH, Lee SY (2002) J Chem Phys 117:9539
21. Halonen L, Carrington T (1988) J Chem Phys 88:4171
22. Halonen L (1998) Adv Chem Phys 104:41
23. Halonen L, Child MS (1983) J Chem Phys 79:4355
24. Halonen L, Noid DW, Child MS (1983) J Chem Phys 78:2803
25. Zhu QS, Zhang BS, Ma YR, Qian HB (1989) Chem Phys Lett 164:596
26. Zhu QS, Zhang BS, Ma YR, Qian HB (1990) Spectrochim Acta A 46:1217
27. Camden JP, Bechtel HA, Brown DJA, Zare RN (2005) J Chem Phys 123:134301
28. Camden JP, Hu WF, Bechtel HA, Brown DJA, Martin MR, Zare RN, Lendvay G, Troya D, Schatz GC (2006) J Phys Chem A 110:677
29. Liu S, Chen J, Zhang ZJ, Zhang DH (2013) J Chem Phys 138:011101
30. Welsch R, Manthe U (2012) J Chem Phys 137:244106
31. Schiffel G, Manthe U (2010) J Chem Phys 133:174124
32. Zhang LL, Lu YP, Lee SY, Zhang DH (2007) J Chem Phys 127(23):4313
33. Yang MH, Lee SY, Zhang DH (2007) J Chem Phys 126:064303
34. Kerkeni B, Clary DC (2004) J Chem Phys 120:2308
35. Zhang X, Yang GH, Han KL, Wang ML, Zhang JZH (2003) J Chem Phys 118:9266
36. Wang DY, Bowman JM (2001) J Chem Phys 115:2055
37. Yu HG, Nyman G (1999) J Chem Phys 111:3508
38. Takayanagi T (1996) J Chem Phys 104:2237
39. Palma J, Clary DC (2000) J Chem Phys 112:1859
40. Shen GL, Yang XM, Shu JN, Yang CH, Lee YT (2006) J Chem Phys 125:133103
41. Zhang WQ, Wu GR (2009) Pan, H. L. Q. Shuai, B. Jiang, D. X. Dai and X. M. Yang. J Phys Chem A 113:4652
42. Wu GR, Zhang WQ, Pan HL, Shuai QA, Yang JY, Jiang B, Dai DX, Yang XM (2010) Phys Chem Chem Phys 12:9469
43. Xiao CF, Shen GL, Wang XY, Yang XM (2011) Chin J Chem Phys 24:4
44. Espinosa-Garcia J, Sanson J, Corchado JC (1998) J Chem Phys 109:466
45. Wang WJ, Feng SL, Zhao Y (2007) J Chem Phys 126:114307
46. Wang MH, Sun XM, Bian WS, Cai ZT (2006) J Chem Phys 124:234311
47. Wang MH, Sun XM, Bian WS (2008) J Chem Phys 129:084309
48. Cao JW, Zhang ZJ, Zhang CF, Liu K, Wang MH, Bian WS (2009) Proc Natl Acad Sci USA 106:13180
49. Cao JW, Zhang ZJ, Zhang CF, Bian WS, Guo Y (2011) J Chem Phys 134:024315
50. Espinosa-Garcia J (2002) J Chem Phys 116:10664
51. Jordan MJT, Gilbert RG (1995) J Chem Phys 102:5669
52. Zhao Y, Yamamoto T, Miller WH (2004) J Chem Phys 120:3100
53. Espinosa-Garcia J (2008) Phys Chem Chem Phys 10:1277
54. Xie Z, Braams BJ, Bowman JM (2005) J Chem Phys 122:224307
55. Zhou Y, Fu BN, Wang CR, Collins MA, Zhang DH (2011) J Chem Phys 134:064323
56. Palma J, Clary DC (2000) Phys Chem Chem Phys 2:4105
57. Zare RN (1988) Angular momentum. Wiley, New York
58. Miller WH, Handy NC, Adams JE (1980) J Chem Phys 72:99
59. Corchado JC, Chuang Y–Y, Fast PL, Hu W-P, Liu Y-P, Lynch GC, Nguyen KA, Jackels CF, Fernandez Ramos A, Ellingson BA, Lynch BJ, Zheng J, Melissas VS, Villà J, Rossi I, Coitiño EL, Pu J, Albu TV, Steckler R, Garrett BC, Isaacson AD, Truhlar DG (2007) Polyrate, version 9.7, University of Minnesota, Minneapolis
60. Page M, McIver JW (1988) J Chem Phys 88:922
61. Zhang DH, Collins MA, Lee SY (2000) Science 290:961
62. Gray DL, Robiette AG (1979) Mol Phys 37:1901
63. Lide DR (1998) CRC handbook of chemistry and physics, 79th edn. CRC, New York
64. Palma J, Clary DC (2001) J Chem Phys 115:2188
65. Pack RT (1974) J Chem Phys 60:633
66. McGuire P, Kouri DJ (1974) J Chem Phys 60:2488
67. Kurylo MJ, Timmons RB (1969) J Chem Phys 50:5076
68. Baulch DL, Cobos CJ, Cox RA, Esser C, Frank P, Just T, Kerr JA, Pilling MJ, Troe J, Walker RW, Warnatz J (1992) J Phys Chem Ref Data 21:411
69. Sutherland JW, Su MC, Michael JV (2001) Int J Chem Kinet 33:669
70. Goumri A, Yuan WJ, Ding LY, Shi YC, Marshall P (1993) Chem Phys 177:233
71. Arthur NL, Miles LA (1997) J Chem Soc, Faraday Trans 93:4259
72. Zhou Y, Wang CR, Zhang DH (2011) J Chem Phys 135:024313
73. Wang FY, Lin JS, Cheng Y, Liu KP (2013) J Phys Chem Lett 4:323
74. Jiang B, Guo H (in press) J Chin Chem Soc. doi:10.1002/jccs.201400158

Theor Chem Acc (2014) 133:1574
DOI 10.1007/s00214-014-1574-6

REGULAR ARTICLE

# How the molecular face and the interaction vary as H atom approach $H_2$ molecule

**Dong-Xia Zhao · Zhong-Zhi Yang**

Received: 30 May 2014 / Accepted: 26 August 2014 / Published online: 23 September 2014
© Springer-Verlag Berlin Heidelberg 2014

**Abstract** First, we briefly introduce the potential acting on one electron in a molecule (PAEM). Second, based on PAEM, the molecular intrinsic characteristic contours (MICC) is defined uniquely and intrinsically, and then, the electron density distribution is mapped on the MICC which is called molecular face (MF), an identification card, which is an intrinsic characteristic "face" or "fingerprint" for a molecule. Third, the polarization phenomena have been quantitatively demonstrated, i.e., the changing features of the spatial characteristic and the frontier electron density on the MF surface have been shown for reaction $H_2 + H \rightarrow H + H_2$, denoted as $H1 - H2 + H3 \rightarrow H1 + H2 - H3$, along the linear reaction path, which is compared with those quantities of the reaction $H + H \rightarrow H_2$ process. Furthermore, the conversion between the van der Waals interaction and chemical bonding during the process of $H1 - H2 + H3 \rightarrow H1 + H2 - H3$ reaction is shown by the PAEM-MO diagram, which provides insight into the characteristic of the interaction between two atoms: At the starting step of the reaction, the interaction between H1 and H2 atoms is chemically bonded, while the interaction between H2 and H3 is van der Waals interaction, and the contour of H2 atom in $H_2$ molecule does not overlap with that of the H3 atom, which means that the electron interflow between H1 and H2 atoms is free and the electron interflow between H2 and H3 atoms is blocked by a PAEM barrier or must tunnel the barrier. At the transition state, both the pair of H1 and H2 and the pair of H2 and H3 are chemically bonded.

**Keywords** Molecular face · The potential acting on one electron within a Molecule (PAEM) · $H_2 + H \rightarrow H + H_2$ reaction · PAEM-MO diagram · Conversion between van der Waals interaction and chemical bonding

## 1 Introduction

One is used to say and to visualize an object with shape, size and color. Scientists often do the same things for molecules. Molecular shape and size are basic and fundamental concepts [1–12]. It is just through their boundary surfaces that molecules recognize, communicate and interact with each other. Therefore, molecular contour is essential in describing molecular properties, particularly in solutions [6–9]. Most molecular properties, even the chemical processes of life and physiology, are strongly dependent on molecular shape and size.

In this paper, we will demonstrate how the molecular face (MF) and the interaction character (van der Waals or chemical bonding) vary during the process of an H atom approaching a $H_2$ molecule as an example.

Usually, a molecular shape is visualized by a set of overlapping hard spheres with the corresponding van der Waals (vdW) radii. There are mainly three kinds of surfaces based on this idea: the vdW surface (vdWS), the solvent-accessible surface (SAS) [13] and the molecular (or solvent excluded) surface (MS or SES) [14, 15]. The vdWS is formed by centering the spheres with properly chosen vdW radii at the positions of atomic nuclei. The SAS and MS are often used for dealing with solvation of solutes and

Dedicated to Professor Guosen Yan and published as part of the special collection of articles celebrating his 85th birthday.

D.-X. Zhao · Z.-Z. Yang (✉)
School of Chemistry and Chemical Engineering, Liaoning Normal University, Dalian, China
e-mail: zzyang@lnnu.edu.cn

D.-X. Zhao
e-mail: zhaodx@lnnu.edu.cn

macromolecules. The SAS was first proposed by Lee and Richards as the locus of the center of an imaginary hard probe sphere when it rolls over the vdWS of the macromolecule. Later, Richards defined MS as the part of the surface of the solvent probe sphere that faces the macromolecule. As the simplest model, the vdWS and the volume it enclosed (van der Waals volume) are trivial to be programmed and able to be calculated analytically [6, 16, 17]. A large number of articles on algorithms for computing SAS and MS and the corresponding volumes can be found. The researches until 1996, including Connolly's dot surface [18], the parametric representations introduced by Duncan and Olson [19] and GEPOL proposed by Silla et al. [20], have been reviewed by Connolly in detail [21]. Many new approaches have also been reported recently [22–35]. An analytic method for reproducing Lee-Richards molecular volume [10] was proposed to yield an efficient solvent representation in simulations of biopolymers by Lee et al., Pomelli and Tomasi et al. [22, 23] presented the DefPOL program, which is more efficient to describe solvent effects on molecular system of large size. Wiser and coworkers presented the NLR optimization to accelerate the computation of hard-sphere molecular surfaces [24]. However, a problem for all of these approaches is the choice of an appropriate set of vdW radii or an assumed probe radius. The vdW radius is not a unique and fixed parameter characteristic of an atom. In general, vdW radii of same atom accepted by different authors vary by about 10 % [26]. This ambiguity can lead to a difference of about 12 % in calculating the vdW volume [29].

As a quantum chemical approach, electron density has been employed to give a sort of molecular boundary surface in many studies [1, 30–33]. Boyd [30] discussed the relative sizes of atoms from H to Xe based on the electron density distribution by using a cutoff value $10^{-4}$ of electron density. Bader and coworkers proposed the surface of constant electron density (usually typical values of 0.001 or 0.002 a.u.) to describe the shape and size of diatomic molecules [31–33]. They also demonstrated that the 0.002 a.u. isosurface of electron density is closely related in size to Corley–Pauling–Koltun (CPK) surfaces for hydrocarbons. Mezey proposed a method for topological analysis of contour surfaces represented by electron isodensity-fused spheres, which is called the molecular isodensity contour (MIDCO), and the MIDCO surfaces of biopolymers are constructed by a set of molecular density fragments [1]. Recently, isosurface function of promolecule electron density has also been presented by Mitchell and Spackman [34]. The molecular surface areas and volumes based on electron density are, of course, sensitive to selection of the cutoff value of electron density, and the choice of the cutoff value could not be determined intrinsically. Moreover, a single cutoff value is found not to be suitable for all molecular species [35]. For example, Stefanovich used an isodensity cutoff value of 0.001 a.u. to calculate the solvation energies of neutral and ionic species. However, the solvation energies of anions were found to be underestimated, while solvation energies of cations overestimated, and the assignment of a cutoff value to be employed for a zwitterionic system becomes ambiguous, i.e., the cutoff value applicable for neutral species would not appear to be suitable for both positive and negative ones. Thus, the previous methods and models, including the hard-sphere models and the electron density approach, have not yet provided an intrinsic and unique representation to molecular shape and size.

Recently, by using the classical turning point of electron movement in a molecule, the molecular intrinsic characteristic contour (MICC) [36–39] has been proposed by Yang and his workers. Furthermore, we define the MF that is the MICC mapped with the electron density [40]. MF is such a unique and intrinsic 3D picture that provides both molecular spatial appearance and molecular frontier electron density, an intuitive and instructive identification card for a molecule. Studies on some small molecules show that the MF is a reasonable representation [41–44]. In the previous researches, we have defined and calculated a set of atomic and ionic characteristic boundary radii in the spirit of this model [45–47]. The atomic characteristic radii [45, 48, 49] show a close correlation with the commonly used vdW atomic radii, and the surface derived by this sort of radius is taken as the accurate classical turning point surface to resemble by Ayers [50] and is called the atomic turning radius by Dekock et al. [51] in their investigation and classification of the atomic radii. The ionic characteristic radii [47, 52] also correlate quite well with Pauling ionic radii, as well as Shannon and Prewitt ionic radii. Moreover, the MF model was used to study the shape changing and polarization of some reactions, H + H, H + F, and HCl + $CH_3CH$=CH, and so on [37, 39, 53–58]. Very recently, we proposed and constructed the PAEM-MO diagram which is used to give a rule of distinguishing chemical bonding from van der Waals interaction [59]. Herein, both MF model and PAEM-MO diagram will be used to investigate the process of $H_2 + H \rightarrow H + H_2$ reaction to show the conversion between the chemical bonding and vdW interaction.

The following sections describe the MF model, computational algorithm, results and a brief summary.

## 2 Formalism of the molecular face (MF)

### 2.1 The potential acting on one electron in a molecule and its 3D representation

The potential acting on one electron in a molecule (PAEM) [36, 37, 59, 60] was formulated in previous

studies. It should be emphasized that the electron considered in this kind of the potential belongs to this molecule rather than an external test electron. As we know, however, the positive unit charge in defining the molecular electrostatic potential (MEP) [61–63] is an external test charge that does not belong to the molecule and only electrostatically interacts with all electrons and nuclei of the molecule. In addition, there are various potentials in atomic and molecular descriptions and studies [64–83], which are of some significance that will not be introduced here.

If one electron in a molecule locates at position $\mathbf{r}_1$, it feels a potential coming from the remaining particles of the molecule, the $N$-1 remaining electrons and all nuclei. This potential acting on this electron in a molecule (PAEM), the $V(\mathbf{r}_1)$ at a position $\mathbf{r}_1$ can be expressed

$$V(\mathbf{r}_1) = -\sum_A \frac{Z_A}{r_{1A}} + \frac{1}{\rho(\mathbf{r}_1)} \int \frac{\rho_2(\mathbf{r}_1, \mathbf{r}_2)}{|\mathbf{r}_1 - \mathbf{r}_2|} \mathrm{d}\mathbf{r}_2 \tag{1}$$

in which the first term is the attractive potential provided by all nuclei, and the second term is the potential which is the interaction energy of this electron of interest with all the remaining electrons of the molecular system. In Eq. (1), $Z_\mathrm{A}$ is the charge on nucleus A, $r_{1\mathrm{A}}$ stands for the distance of nucleus A to the electron considered, summation involving index A is over atomic nuclei, $\mathbf{r}_1$ and $\mathbf{r}_2$ denote the electronic coordinates, $\rho(\mathbf{r}_1)$ is the one-electron density function of finding an electron at position $\mathbf{r}_1$, and $\rho_2(\mathbf{r}_1, \mathbf{r}_2)$ is the two-electron density function of finding an electron at position $\mathbf{r}_1$ and at the same time another electron at position $\mathbf{r}_2$.

In the ab initio configuration interaction (CI) method, the one-electron density function can be deduced as,

$$\begin{aligned}\rho(\mathbf{r}_1) = &\sum_I \sum_J \sum_{i_1 \in I} \sum_{j_1 \in J} c_\mathrm{I} c_\mathrm{J}^* (-1)^{s-t} \delta_{\{I-i_1\}\{J-j_1\}} \\ &\times \left[ f_{i_1}^{\alpha}(\mathbf{r}_1) f_{j_1}^{*\alpha}(\mathbf{r}_1) + f_{i_1}^{\beta}(\mathbf{r}_1) f_{j_1}^{*\beta}(\mathbf{r}_1) \right]\end{aligned} \tag{2}$$

Here $c_\mathrm{I}$ is the configuration interaction coefficient summation, $f_{i_1}^{\alpha}(\mathbf{r}_1)$ is the $i_1$-th molecular orbital (MO) with $\alpha$ spin corresponding to the $s$-th row in the determinant $I$, and $f_{j_1}^{*\alpha}(\mathbf{r}_1)$ is the complex conjugate of the $j_1$-th molecular orbital (MO) with $\alpha$ spin corresponding to the $t$-th row in the determinant $J$. Summation involving index $I$ and $J$ is over the configurations. Summation involving index $i_1$ and $j_1$ is over the molecular orbitals. The Kronecker delta, $\delta_{\{I-i_1\}\{J-j_1\}}$, is defined to be unity when $\{I - i_1\}$ equals $\{J - j_1\}$ and zero otherwise.

The spatial two-electron density function can practically be expressed by the following formula,

$$\begin{aligned}&\rho_2(\mathbf{r}_1, \mathbf{r}_2) \\ &= \sum_{I,J} c_I c_J^* \sum_{\substack{i_1 \in I \\ j_1 \in J \\ i_1 < i_2 \\ j_1 < j_2}} (-1)^{s+t-u-v} \delta_{\{I-i_1-i_2\}\{J-j_1-j_2\}} \cdot \\ &\{ f_{i_1}^{\alpha}(\mathbf{r}_1) f_{j_1}^{\alpha}(\mathbf{r}_1) f_{i_2}^{\alpha}(\mathbf{r}_2) f_{j_2}^{\alpha}(\mathbf{r}_2) + f_{i_1}^{\alpha}(\mathbf{r}_1) f_{j_1}^{\alpha}(\mathbf{r}_1) f_{i_2}^{\beta}(\mathbf{r}_2) f_{j_2}^{\beta}(\mathbf{r}_2) \\ &- f_{i_1}^{\alpha}(\mathbf{r}_1) f_{j_2}^{\alpha}(\mathbf{r}_1) f_{i_2}^{\alpha}(\mathbf{r}_2) f_{j_1}^{\alpha}(\mathbf{r}_2) - f_{i_1}^{\alpha}(\mathbf{r}_1) f_{j_2}^{\alpha}(\mathbf{r}_1) f_{i_2}^{\beta}(\mathbf{r}_2) f_{j_1}^{\beta}(\mathbf{r}_2) \\ &- f_{i_2}^{\alpha}(\mathbf{r}_1) f_{j_1}^{\alpha}(\mathbf{r}_1) f_{i_1}^{\alpha}(\mathbf{r}_2) f_{j_2}^{\alpha}(\mathbf{r}_2) - f_{i_2}^{\alpha}(\mathbf{r}_1) f_{j_1}^{\alpha}(\mathbf{r}_1) f_{i_1}^{\beta}(\mathbf{r}_2) f_{j_2}^{\beta}(\mathbf{r}_2) \\ &+ f_{i_2}^{\alpha}(\mathbf{r}_1) f_{j_2}^{\alpha}(\mathbf{r}_1) f_{i_1}^{\alpha}(\mathbf{r}_2) f_{j_1}^{\alpha}(\mathbf{r}_2) + f_{i_2}^{\alpha}(\mathbf{r}_1) f_{j_2}^{\alpha}(\mathbf{r}_1) f_{i_1}^{\beta}(\mathbf{r}_2) f_{j_1}^{\beta}(\mathbf{r}_2) \\ &+ f_{i_1}^{\beta}(\mathbf{r}_1) f_{j_1}^{\beta}(\mathbf{r}_1) f_{i_2}^{\alpha}(\mathbf{r}_2) f_{j_2}^{\alpha}(\mathbf{r}_2) + f_{i_1}^{\beta}(\mathbf{r}_1) f_{j_1}^{\beta}(\mathbf{r}_1) f_{i_2}^{\beta}(\mathbf{r}_2) f_{j_2}^{\beta}(\mathbf{r}_2) \\ &- f_{i_1}^{\beta}(\mathbf{r}_1) f_{j_2}^{\beta}(\mathbf{r}_1) f_{i_2}^{\alpha}(\mathbf{r}_2) f_{j_1}^{\alpha}(\mathbf{r}_2) - f_{i_1}^{\beta}(\mathbf{r}_1) f_{j_2}^{\beta}(\mathbf{r}_1) f_{i_2}^{\beta}(\mathbf{r}_2) f_{j_1}^{\beta}(\mathbf{r}_2) \\ &- f_{i_2}^{\beta}(\mathbf{r}_1) f_{j_1}^{\beta}(\mathbf{r}_1) f_{i_1}^{\alpha}(\mathbf{r}_2) f_{j_2}^{\alpha}(\mathbf{r}_2) - f_{i_2}^{\beta}(\mathbf{r}_1) f_{j_1}^{\beta}(\mathbf{r}_1) f_{i_1}^{\beta}(\mathbf{r}_2) f_{j_2}^{\beta}(\mathbf{r}_2) \\ &+ f_{i_2}^{\beta}(\mathbf{r}_1) f_{j_2}^{\beta}(\mathbf{r}_1) f_{i_1}^{\alpha}(\mathbf{r}_2) f_{j_1}^{\alpha}(\mathbf{r}_2) + f_{i_2}^{\beta}(\mathbf{r}_1) f_{j_2}^{\beta}(\mathbf{r}_1) f_{i_1}^{\beta}(\mathbf{r}_2) f_{j_1}^{\beta}(\mathbf{r}_2) \}\end{aligned} \tag{3}$$

where $\delta_{\{I-i_1-i_2\}\{J-j_1-j_2\}}$ is equal to 1, if the cofactor $\{I - i_1 - i_2\}$ of the determinant $I$ is equal to the cofactor $\{J - j_1 - j_2\}$ of the determinant $J$, and otherwise is zero.

Based on the expressions of the electron density $\rho(\mathbf{r}_1)$ Eq. (2), and the two-electron density function $\rho_2(\mathbf{r}_1, \mathbf{r}_2)$, Eq. (3), we can obtain the concrete expression of PAEM defined in Eq. (1) and can then calculate it by using an ab initio CI method and an our in-house program.

### 2.2 Definition of molecular intrinsic characteristic contour (MICC)

The idea for this definition can be considered as follows [36, 37, 40]. When an electron moves in a molecule, its kinetic energy varies with its relative position to the other particles of the molecule. If its energy is equal to its felt potential, i.e., the average kinetic energy of this electron at this point equals zero, then this position $\mathbf{r}$ is a classical turning point of this electron movement. Supposing that the one-electron energy at $\mathbf{r}$ is equal to minus of the first ionization potential of the molecule, then we have the formula, $V(\mathbf{r}) = -I$, i.e., the classical turning point equation of this electron movement, where $V(\mathbf{r})$ is the PAEM defined by Eq. (1) and $I$ is the first ionization potential of the molecule. We assume that such a point $\mathbf{r}$ is termed as an intrinsic characteristic contour point of this molecule. The set of all the intrinsic characteristic points defines the molecular intrinsic characteristic contour (MICC), which can be expressed as:

$$\boldsymbol{G}(-I) = \{\mathbf{r} : V(\mathbf{r}) = -I\} \tag{4}$$

in which $\boldsymbol{G}$ denotes the MICC, i.e., the MICC is composed of all the classical turning points of electron movement in

the molecule and is an iso-PAEM contour where PAEM (or one-electron energy) equals the negative value of the ionization potential of the molecule. In other words, if one electron located on the MICC obtains an equivalent energy of the molecular first ionization potential, it becomes a free electron.

### 2.3 Program and calculation

By using the ab initio MELD program [84] developed by Davidson et al. and a separated program developed by our own, the PAEM was calculated. The SDCI calculation in MELD program with the near Hartree–Fock quality Gaussian type orbital basis sets [85] was used to calculate the molecular integrals in the expression of the PAEM. At the same level of ab initio method, the vertical ionization potentials of a molecular system in its ground state were also calculated if there is no experimental value can be utilized. According to the classical turning point of electron movement, the molecular intrinsic characteristic contour (MICC) points were calculated one by one for a molecule, then collected, and thereby a MICC was drawn. All of the numerical computations were carried out on a SGI O-300 server. Based on this model, we have, respectively, studied the MICCs of a number of molecular systems in their ground states.

The calculation of the PAEM and MICC in our model for a molecule can be summarized in the following three steps:

(a) Calculate the molecular integrals in Eqs. (2) and (3). Here, we utilize the MELD program [84] developed by Davidson et al. to perform the ab initio calculations. All calculations were carried out on an O300 server (16 × 500 MHz MIPS R14000 CPU) and a SGI Octane2 workstation (2 × 400 MHz MIPS R12000 CPU). Then, by using a program of our own, calculate the PAEM and physical quantities expressed by Eqs. (2) and (3), including the electron density.
(b) Calculate the MICC points. According to the classical turning point equation, Eq. (4), the MICC points are obtained by a large number of calculations. The vertical ionization potential $I$ that we have used is the experimental vertical ionization potential or the calculated value by the accurate ab initio CI method.
(c) Sketch the MICC. Collecting all the MICC points, a 3D picture of MICC can be drawn. Besides this, significantly, the electron density distribution on the MICC is also mapped out. Matlab [86] was used to depict and to obtain visualization plots of the MF.

## 3 Results and discussion

### 3.1 3D Representations of the PAEM and MF: HI molecule as an example

Using the formulism and computational method mentioned above, we have studied the potentials acting on an electron for some molecules. Here, take HI molecule as an example to demonstrate the procedure of obtaining the PAEM and MF as follows.

We put I atom at the origin of the coordinate system and H atom at the $X$-axis. The equilibrium bond length of the HI molecule is 3.041 a.u. (experimental value) [87]. Since HI has an axial symmetry around its molecular axis that contains the two nuclei, it is sufficient to only represent the PAEM $V(\mathbf{r}_1)$ where $\mathbf{r}_1$ is on a plane that passes through the molecular axis.

First of all, the calculations of the $V(x_1)$ were carried out along the molecular axis, the $x$-axis. When $\mathbf{r}_1$ runs on the molecular plane, the $xy$ plane, i.e., taking a lot of net points on the $xy$ plane, the calculated $V(\mathbf{r}_1)$ is displayed in the $z$-axis, then a 3D representation of the PAEM $V(\mathbf{r}_1)$ is brought out and drawn in Fig. 1. The near-nucleus region is the area that is located around a nucleus of a molecule. For the PAEM of HI molecule, there are two deep potential wells which originate from the nuclear attraction, a

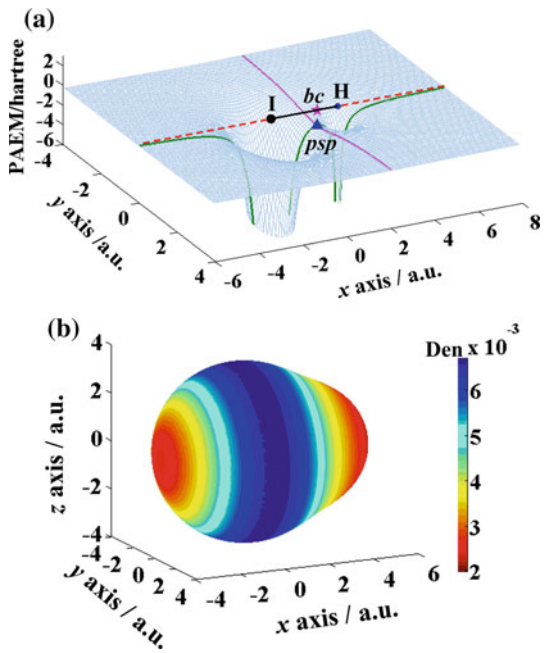


**Fig. 1** **a** The 3D graph of the PAEM for HI molecule on $xy$ plane (Molecular Plane). All quantities are in atomic units in this paper. **b** The molecular intrinsic characteristic contour with electronic density (MICCED or MF) of HI molecule

wider potential well corresponding to the I atom of the larger nuclear charge and a narrower potential well relating to the H atom of the smaller nuclear charge. The PAEM surface between the two wells has a saddle shape with a saddle point at $x_1 = 2.10$, $y_1 = 0.0$, $V(2.10,0.0) = -1.5726$ hartree which is called PAEM saddle point (psp). The corresponding electronic position of the PAEM saddle point between the H and I atoms is named the bond center (bc), marked by star. The corresponding PAEM of this point is called the height of PAEM barrier. The vast remaining part is the out-bond region of the PAEM, the rest area subtracting the near-nuclei and bond regions from the total PAEM. In this region, the potential gradually ascends with enlarging the distance between the electron and nucleus and then approaches to zero at the infinite, which is a correct asymptotic behavior.

Then, Eq. (4), called equation of the classical turning point, is performed to obtain the MICC points of HI molecule. At the same time, the electron density at every MICC point is calculated. Thus, we collect the MICC point and their corresponding electron density. As result, a colorful picture of molecular intrinsic characteristic contour with electron density (MICCED or MF) is obtained, as shown in Fig. 1b, where the color scale indicates the electron density distributed on the MICC, i.e., the red color area denotes lower electron density and the blue area has larger one. It can be found that the MF contains not only the spatial shape and size but also the electron distribution on the MICC. Therefore, it provides insight into a significant feature of both molecular spatial appearance and frontier electron density mapped on the MICC, an intuitive picture of molecular fingerprint or face, which is denoted as MF.

### 3.2 The changing pictures of the molecular face (MF) for the reaction $H_2 + H \rightarrow H + H_2$ at different internuclear distances along the energy-favorite linear reaction path

Now, the typical three-atomic exchange reaction $H_2 + H \rightarrow H + H_2$ is taken as an example to show both its spatial and electronic MF varying pictures, along the energy-favorite collinear reaction path [88–90], the route of the intrinsic reaction coordinate [91]. The calculations were performed by a program at the ab initio CI level based on the MELD program package developed by Davidson et al. [84] and a separate program with 18s15p3d basis set for each H atom.

The coordinate system is chosen as follows: along the collinear approaching line (the chemical bond direction in $H_2$ molecule), the atoms from left to right are the two H atoms of the hydrogen molecule and the approaching H atom, denoted as H1, H2 and H3 atoms. The structural formula, H1($R_1$)H2($R_2$)H3, where $R_1$ is the distance between H1 and H2 atoms, $R_2$ is the distance between H2 and H3 atoms, is used to denote the corresponding state at each point of the IRC route.

The vivid changing pictures of MFs during the process of the H atom approaching hydrogen molecule drawn along their IRC route are shown in Fig. 2b–h, in which the dark blue region has large electron density while the dark red region has small electron density, and the value of MFED or MF is denoted by the color scale (marked by Den) on the right side of the picture. Figure 2 shows a series of MF pictures at different distances of the process of H atom approaching $H_2$ molecule, a reaction of $H_3$ system. As the H atom, going along the linear reaction path, is 4.33 a.u. close to the adjacent H atom of the $H_2$ molecule that has a nuclear separation 1.4011 a.u., i.e., the geometry H1(1.4011)H2(4.33)H3, both the $H_2$ part and the H part have stretched their hands and increased their electron density around the active areas, even with a weak green signal from the $H_2$ right hand, as depicted in Fig. 2c. About the transition state structure, as shown in Fig. 2h, the $H_3$ linear reaction is symmetric. After this step, the right H3 atom and the middle H2 atom are combining while the left H1 atom leaving, whose MF pictures are just the images of Fig. 2a–g about the middle vertical plane.

In order to quantitatively describe and compare the changing features of different MFs along the IRC route, several characteristic parameters of the molecular intrinsic characteristic contour (MICC) and its corresponding electron density (MFED) are defined and exhibited in Fig. 2b. For example, in the molecular cross section including atoms H1, H2 and H3, the horizontal straight line passing through all nuclei has four intersection points with the molecular contour of $H_3$ system, so $R_l$(H1), $R_r$(H2) and $R_l$(H3) and $R_r$(H3) are in turn defined as the distances from the left side of H1 atom, the right side of H2 atom, the left side of H3 atom, the right side of H3 atom to the intersection points, and the corresponding electron density on these points are denoted by $Den_l$(H1), $Den_r$(H2) and $Den_l$(H3) and $Den_r$(H3), respectively. The vertical straight line passing through nucleus H1 has two intersection points with the MF, and then, the distance from nucleus H1 to one of the intersection points is denoted $R_v$(H1), the corresponding electron density is represented by $Den_v$(H1). The calculated numerical values of some characteristic quantities of MICC and MFED at different geometries for the $H_3$ system are listed in Table 1.

The polarization phenomena, including both the deformation of spatial shape and the charge of the frontier electron density, are clearly demonstrated by the characteristic quantities, as given in Table 1, for the $H_3$ reaction, particularly the $R_r$(H2) and $R_l$(H3) that denote the reaction sites of $H_2$ molecule part and H atom part, respectively. The streching of both parts for the reaction process is obviously seen from the following change of $R_r$(H2) values (from

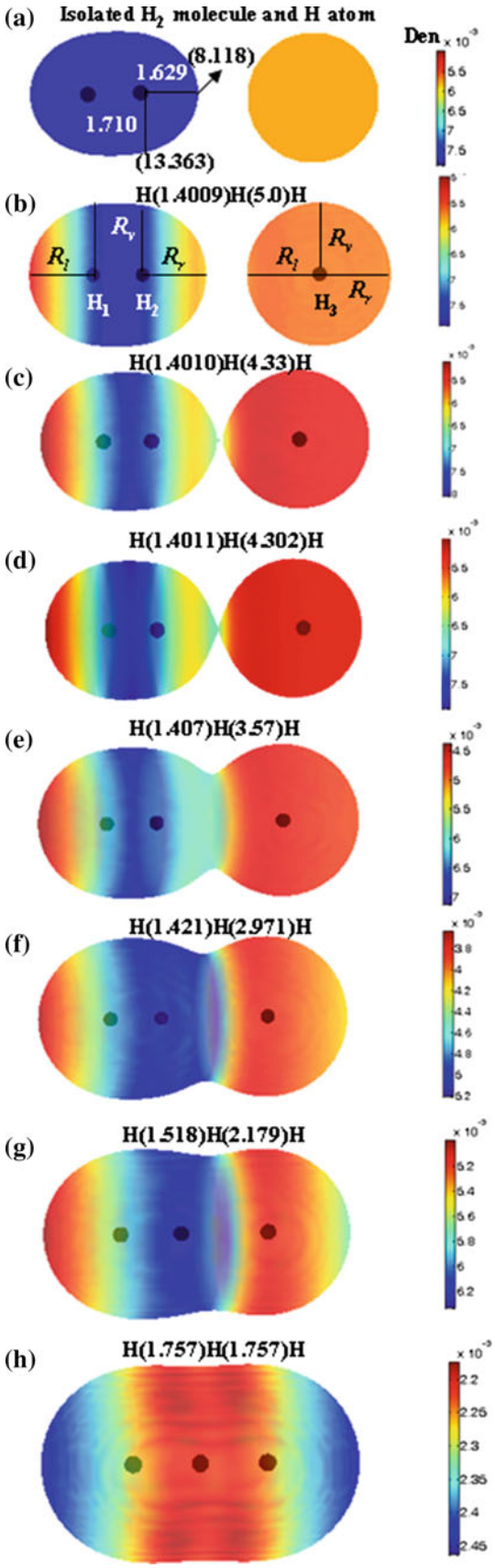


**Fig. 2** 3D MF of the energy-favorite linear $H_2 + H \rightarrow H + H_2$ reaction system at the nuclear arrangement along IRC reaction route during the process of H atom gradually approaching to $H_2$ molecule. **a** The isolated $H_2$ molecule and H atom; **b–h** corresponding to the nuclear separation of H(1.4009)H(5.0)H, H(1.4010)H(4.33)H, H(1.4011)H(4.27)H, H(1.4070)H(3.57)H, H(1.421)H(3.57)H, H(1.421)H(2.971)H, H(1.518)H(2.179)H and H(1.757)H(1.757)H of the linear $H_3$ reaction system, respectively

1.8012 to 1.9793 a.u.) and $R_l$(H3) values (from 2.0532 to 2.2899 a.u.). Correspondingly, the values of the frontier electron densities have the following changes: $Den_r$(H2) from $5.921 \times 10^{-3}$ to $6.541 \times 10^{-3}$ a.u. and $Den_l$(H3) from $5.664 \times 10^{-3}$ to $6.533 \times 10^{-3}$ a.u. listed in Table 1. The following four paragraphs are given for more detailed descriptions.

If the H atom and $H_2$ molecule are separate, the MF of the H atom is round with a boundary radius of 2.00 a.u. and the electron density of $5.832 \times 10^{-3}$ a.u., and the MF of the $H_2$ part is like an egg with nearly uniform electron distribution on the MF frontier surface, which is shown in Fig. 2a.

As the H atom along the linear reaction path is 5.00 far from the adjacent H atom of the $H_2$ moiety that is at nuclear separation 1.4009, or simply denoted by H(1.4009)H(5.0)H, the 3D MF is shown in Fig. 2b, where the color indicates the electron density on the MF surface (the red or blue area has lower or higher electron density). Obviously, there are $H_2$ molecular and H atomic regions, and between them there is a medium that is a classically forbidden region for the electronic motion. The H atom looks still round with nearly uniform electron density on MF, while the MF region of the $H_2$ part is clearly polarized in the electron distribution although its equilibrium nuclear separation is still 1.4009, around the middle of the $H_2$ region, the electron density (blue) is larger than that around the two end sides, and the left one being red and the right one being yellow (yellow has higher electron density than red but blue has the highest). It seems that the $H_2$ part defends its covalent bond concentrating its electrons around the middle of the $H_2$ bond but giving a bit warning with its yellow right hand to the attacking H atom.

The Fig. 2d of the geometry H(1.4011)H(4.302)H shows a critical step along the $H_3$ reaction path, where only one touching point appears between the two MF regions. Here, the two regions are more significantly deformed and polarized, particularly around the touching tip. It seems that both the $H_2$ molecule and H atom regions stretch their body to welcome each other with the green hands, implying that they both intensify their electron density on the adjacent active areas, which just belong to the bonding domain described by the Hellmann–Feynman theorem [92]. This means both regions have strengthened their interaction.

**Table 1** The molecular intrinsic characteristic quantities (MICC and MFED) of the $H_3$ systems, distances in a.u., electron densities in $\times 10^{-3}$ a.u

| $R_1$ | $R_2$ | $R_v$(H1) | $R_l$(H1) | $R_v$(H2) | $R_r$(H2) | $R_v$(H3) | $R_l$(H3) | $R_r$(H3) |
|---|---|---|---|---|---|---|---|---|
| 1.4009 | 5.000 | 1.9728 | 1.8222 | 1.9606 | 1.8012 | 2.0178 | 2.0532 | 2.0134 |
| 1.4010 | 4.500 | 1.9890 | 1.8263 | 1.9762 | 1.8304 | 2.0335 | 2.1221 | 2.0283 |
| 1.4011 | 4.330 | 1.9902 | 1.8293 | 1.9790 | 1.9010 | 2.0405 | 2.2125 | 2.0356 |
| 1.4011 | 4.302 | 1.9962 | 1.8328 | 1.9861 | 1.9972 | 2.0431 | 2.2994 | 2.0375 |
| 1.4011 | 4.290 | 1.9924 | 1.8339 | 1.9835 | | 2.0438 | | 2.0380 |
| 1.4011 | 4.270 | 1.9892 | 1.8310 | 1.9788 | | 2.0407 | | 2.0340 |
| 1.4070 | 3.571 | 2.0412 | 1.8849 | 2.0363 | | 2.1144 | | 2.1006 |
| 1.4210 | 2.971 | 2.1794 | 1.9828 | 2.1478 | | 2.2209 | | 2.1901 |
| 1.5180 | 2.179 | 2.4459 | 2.2495 | 2.4120 | | 2.4461 | | 2.3621 |
| 1.7570 | 1.757 | 2.5484 | 2.4068 | 2.5117 | | 2.5484 | | 2.4068 |
| $R_1$ | $R_2$ | $Den_v$(H1) | $Den_l$(H1) | $Den_v$(H2) | $Den_r$(H2) | $Den_v$(H3) | $Den_l$(H3) | $Den_r$(H3) |
| 1.4010 | 5.000 | 7.596 | 5.109 | 7.760 | 5.921 | 5.616 | 5.664 | 5.646 |
| 1.4010 | 4.500 | 7.337 | 5.064 | 7.518 | 6.568 | 5.444 | 6.003 | 5.490 |
| 1.4011 | 4.330 | 7.313 | 5.060 | 7.448 | 6.697 | 5.366 | 6.382 | 5.436 |
| 1.4011 | 4.302 | 7.220 | 5.024 | 7.339 | 6.541 | 5.339 | 6.533 | 5.417 |
| 1.4011 | 4.290 | 7.275 | 5.014 | 7.376 | | 5.331 | | 5.409 |
| 1.4011 | 4.270 | 7.333 | 5.053 | 7.452 | | 5.365 | | 5.435 |
| 1.4070 | 3.571 | 6.561 | 4.500 | 6.560 | | 4.632 | | 4.831 |
| 1.4210 | 2.971 | 4.843 | 3.696 | 5.060 | | 3.762 | | 4.158 |
| 1.5180 | 2.179 | 2.701 | 2.239 | 2.783 | | 2.486 | | 3.124 |
| 1.7570 | 1.757 | 2.164 | 2.310 | 2.226 | | 2.164 | | 2.310 |

Obviously, the other areas on the MF of the $H_3$ system vary accordingly.

The picture for the transition state structure, H(1.757)H(1.757)H, that has the highest energy for the linear $H_3$ reaction has been shown in Fig. 2h. Remarkably, the middle of the original $H_2$ part becomes dark red, which means that the electron density strongly decreases making its bond much weaker. This is consistent with that this transition structure has the highest energy along the reaction path. It is also seen that the electrons increase around the two end sides of the system. About this transition state structure, the $H_3$ linear reaction is symmetric. After this stage, the right and the middle H atoms combine while the left H atom leaves, whose MF pictures are just the images of Fig. 2a–c about the middle vertical plane.

In addition, we have also investigated the MF changing pictures for $H + H \rightarrow H_2$ reaction, which provides a comparison with the $H_3$ system. For an easy comparison with $H_3$ system, the two H atoms in $H_2$ system are marked by H2 and H3 atoms. When two isolated H2 and H3 atoms approach each other, the MFs have investigated. The calculated numerical values of some characteristic quantities of MICC and MFED for the chosen $H_2$ geometries are listed in Table 2. Figure 3 only depicts the MFs where the distances between two H atoms are in turn 7.0, 5.0, 4.314, 1.757 and 1.4009 a.u. (equilibrium geometry) with the same color bar, the scale of electron density. When the distance between two H atoms is 4.314 a.u., the two atoms touch each other and begin to form a body (contacting point).

It can be seen from Tables 1 and 2 that the contacting distance between the H2 and H3 atoms in $H_2$ system is 4.314 a.u., but that is 4.302 a.u. for $H_2 + H$ system. Before they arrive at their respective contacting point, for two H atomic system, the MICCs in three directions gradually shrink as a result of a decrease in the distance between two H atoms in $H_2$ system, while the MICCs in three directions gradually swell as a result of a decrease in the distance between the $H_2$ and H parts in $H_3$ system.

### 3.3 Conversion between van der Waals interaction and chemical bonding based on PAEM-MO diagram

We have constructed the PAEM-MO diagram, i.e., the local PAEM curve between two atoms inserted with the molecule orbitals with their main atomic components, from which a rule is provided for distinguishing chemical bonding from van der Waals interaction between two atoms [59]. Here, for $H_2 + H \rightarrow H + H_2$ reactions, we just take three points on the reaction route, namely H(1.4009)H(5.0)H, H(1.4011)H(4.302)H and H(1.757)H(1.757)H, to demonstrate the conversion between van der Waals interaction and chemical bonding.

As the H atom along the linear reaction path is 5.00 a.u. far from the adjacent H atom of the $H_2$ molecule whose

**Table 2** The molecular intrinsic characteristic quantities (MICC and MFED) of the $H_2$ systems, distances in a.u., electron densities in $\times 10^{-3}$ a.u

| $R_2$ | $R_r$(H2) | $Den_r$(H2) | $R_l$(H3) | $Den_l$(H3) | $R_v$(H3) | $Den_v$(H3) |
|---|---|---|---|---|---|---|
| 5.0 | 2.0760 | 4.957 | 1.9904 | 7.387 | 2.0739 | 5.073 |
| 4.5 | 2.0901 | 4.565 | 2.0176 | 9.975 | 2.0840 | 4.962 |
| 4.4 | 2.0919 | 4.499 | 2.0498 | 10.733 | 2.0834 | 4.958 |
| 4.35 | 2.0937 | 4.479 | 2.0744 | 11.151 | 2.0829 | 4.961 |
| 4.33 | 2.0942 | 4.470 | 2.1214 | 11.326 | 2.0826 | 4.963 |
| 4.32 | 2.0945 | 4.464 | 2.1455 | 11.415 | 2.0824 | 4.964 |
| 4.315 | 2.0945 | 4.462 | 2.1573 | 11.461 | 2.0823 | 4.965 |
| 4.314 | 2.0946 | 4.461 | | | 2.0823 | 4.965 |
| 4.313 | 2.0946 | 4.461 | | | 2.0823 | 4.965 |
| 4.31 | 2.0946 | 4.459 | | | 2.0822 | 4.966 |
| 4.3 | 2.0946 | 4.449 | | | 2.0817 | 4.965 |
| 4.2 | 2.0947 | 4.385 | | | 2.0791 | 4.983 |
| 4.1 | 2.0973 | 4.301 | | | 2.0773 | 5.113 |
| 4.0 | 2.0953 | 4.268 | | | 2.0736 | 5.137 |
| 3.5 | 2.0605 | 4.363 | | | 2.0352 | 5.532 |
| 3.0 | 1.9881 | 4.746 | | | 1.9661 | 6.468 |
| 2.5 | 1.8945 | 5.182 | | | 1.8675 | 8.251 |
| 2.0 | 1.7452 | 6.728 | | | 1.7631 | 10.886 |
| 1.4009 | 1.5089 | 10.575 | | | 1.6409 | 15.561 |

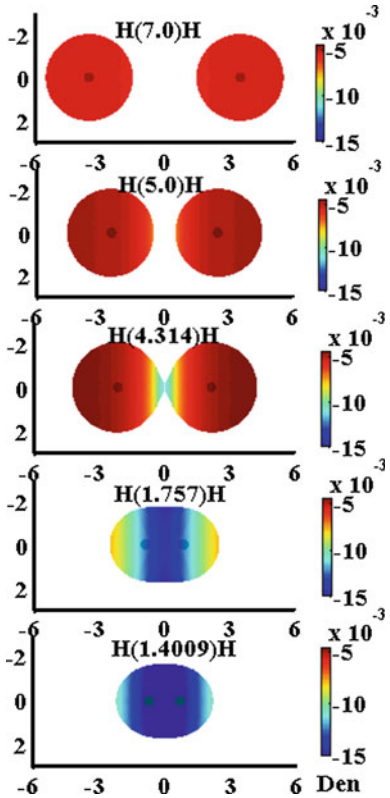


**Fig. 3** 3D MF of the $H_2$ molecule at the nuclear arrangement. The nuclear separation of H(7.0)H, H(5.0)H, H(4.3314)H, H(1.757)H, H(1.4009)H (equilibrium) of the $H + H \rightarrow H_2$ reaction, respectively

nuclear separation is 1.4009 a.u., named H(1.4009)H(5.0) H, the PAEM-MO diagram is described in Fig. 5a, along the line of the three H atoms. The PAEM barrier top between two H atoms in the $H_2$ molecule is −1.9127 hartree, while the PAEM barrier top between isolated H atom and the adjacent H atom of the $H_2$ molecule is −0.4097 hartree. The 3 electrons of the $H_3$ system distribute 2 molecular orbitals, 1σ and 2σ, whose energies are −0.5971 and −0.4995 hartree, respectively. The electrons of 1σ MO are dominantly located on the H–H chemical bond of the $H_2$ molecule with bonding character, and one electron in 2σ MO is dominantly located on the $H_3$ atom. The 1σ and 2σ in energy are higher than the barrier top of −1.9127 hartree between H1 and H2 atoms, while they are lower than the barrier top −0.4097 hartree, which implies that is a chemical bonding between the H1 and H2 atoms, while the interaction between H2 and H3 atoms belongs to a van der Waals interaction.

As shown in Fig. 2d, when the distance between $H_2$ molecule and H atom is 4.302 a.u., denoted by H(1.4011) H(4.27)H, there is one touching point between the $H_2$ molecule and H atom along the $H_3$ reaction path, based on their MF. For this critical point, the PAEM-MO diagram is correspondingly depicted in Fig. 4b where the PAEM barrier top between two H atoms in the $H_2$ molecule is −1.9174 hartree, while the PAEM barrier top between the coming H atom and the adjacent H atom of the $H_2$ molecule

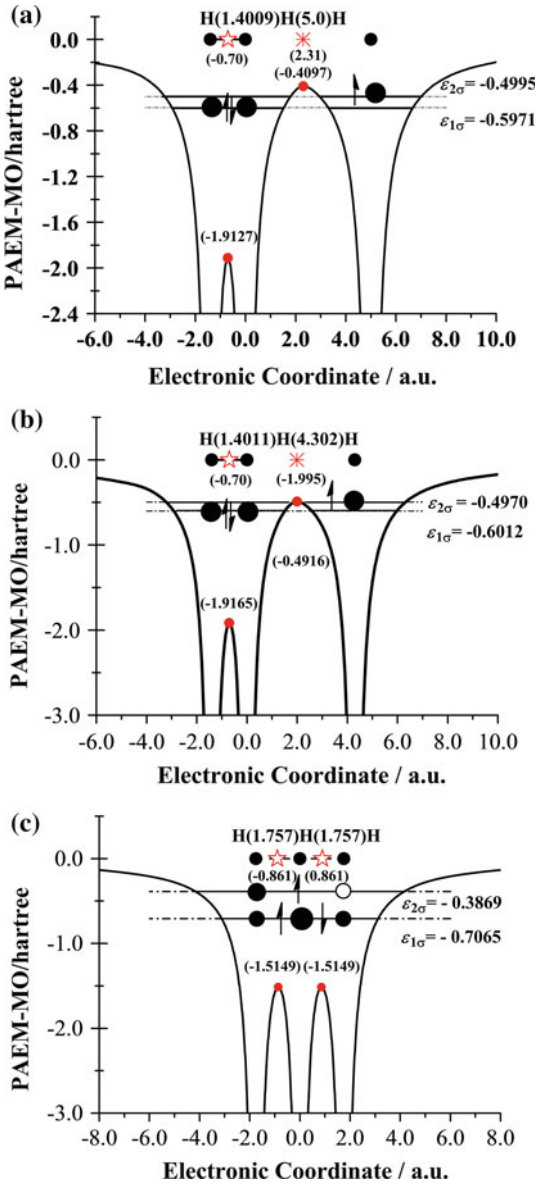


**Fig. 4** The PAEM-MO diagrams along the nuclear line of the energy-favorite linear $H_2 + H \rightarrow H + H_2$ reaction system at the nuclear arrangement. **a** From the left to the right the H–H distances are, respectively, 1.4009 and 5.0 a.u., denoted as H(1.4009)H(5.0)H. **b** At the nuclear separation of H(1.4011)H(4.302)H. **c** The structure of transition state H(1.757)H(1.757)H

is −0.4958 hartree. The three electrons of the $H_3$ system distribute two molecular orbitals, 1σ and 2σ, whose energies are −0.6015 and −0.4968 hartree, respectively. The electrons of 1σ MO are dominantly located on the $H_1$–$H_2$ region, and one electron in 2σ MO is dominantly located on the H3 atom. The 1σ and 2σ in energy are higher than the barrier top of −1.9174 hartree, while 1σ MO in energy is

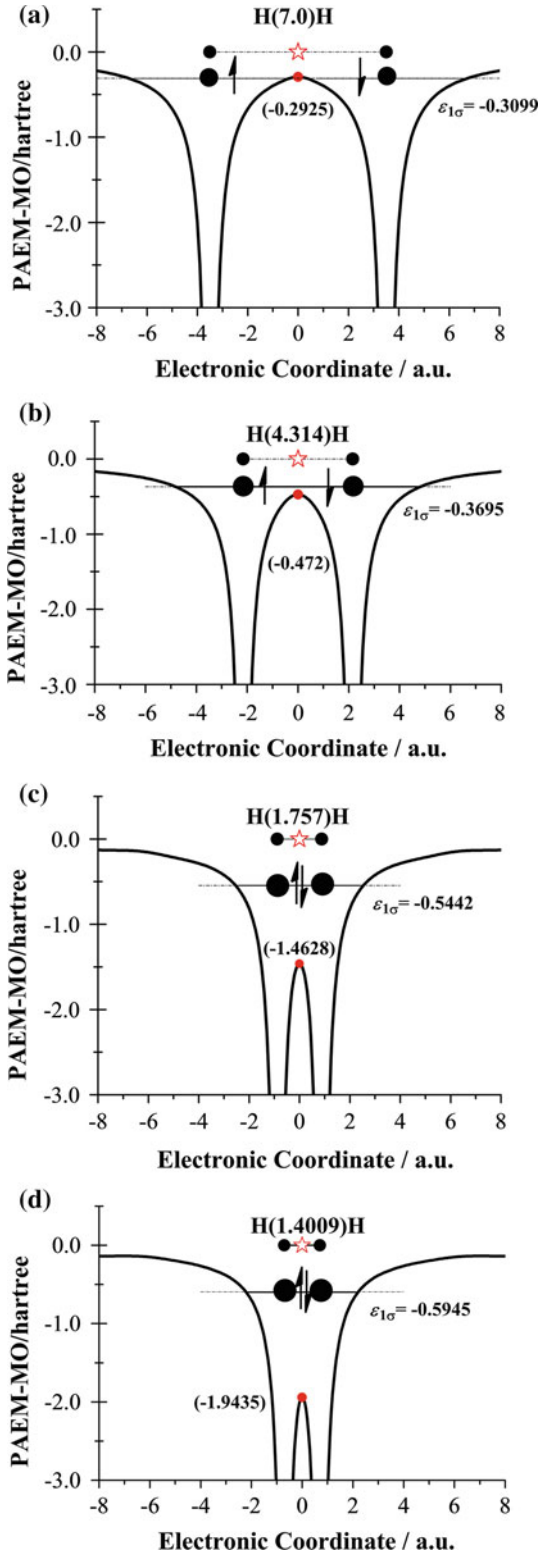


**Fig. 5** The PAEM-MO diagrams of $H_2$ system at the nuclear arrangement. **a** H(7.0)H, **b** H(4.314)H, **c** H(1.757)H, H(1.4009)H

lower than the barrier top of −0.4958 hartree and 2σ MO in energy (−0.4968 hartree) is almost at the same level of the barrier top (−0.4958 hartree). It is shown that the interaction between H1 and H2 atoms still belongs to the chemical bonding, but the interaction between $H_2$ molecule and isolated H3 atom start chemical bonding from van der Waals, in terms of PAEM-MO diagram.

As $H_2$ molecule gradually approaches to H atom, the distance between H1 and H2 atoms gradually enlarges and separation between H2 and H3 atoms shortens. Along the IRC of the linear $H_3$ reaction, the geometry H(1.757) H(1.757)H in energy is highest, being the transition state. The three H atoms have formed one body, as described by the MF in Fig. 2h. Figure 4c shows its corresponding PAEM-MO diagram where the PAEM barrier tops between two adjacent H atoms are −1.5149 hartree. The three electrons of the $H_3$ system occupied 1σ and 2σ MOs whose energies are −0.7065 and −0.3869 hartree, respectively. 1σ and 2σ MOs in energy in this case are higher than the PAEM barrier top (−1.5149 hartree). It is shown that the interaction between H2 and H3 has become chemical bonding. It is demonstrated from the Fig. 4a, b and c that there is conversion between van der Waals interaction and chemical bonding in the linear $H_3$ reaction ($H_2 + H \rightarrow H + H_2$).

In addition, Fig. 5a–d displays the PAEM-MO diagrams of the H(7.0)H, H(4.314)H, H(1.757)H and H(1.4009) H for $H + H \rightarrow H_2$ reaction, respectively. Corresponding, four out of their PAEM-MO diagrams are shown in Fig. 5a–d, where the PAEM barrier tops are, respectively, −0.2925, −0.4720, −1.4628 and 1.9435 hartree, and the 1σ MO energies are in turn −0.3099, −0.3695, −0.5442 and −0.5945 hartree. As a consequence of comparing their respective PAEM barrier and the MO energy, H(7.0)H is van der Waals interaction, while H(4.314)H, H(1.757)H and H(1.4009)H are chemical bonding.

## 4 Summary

The method for defining molecular intrinsic characteristic contour (MICC) and then the MF that is the MICC mapped by the electron density (MFED) is formulated. This is based on the intrinsic motion of an electron within a molecule and rigorously calculated by an accurate ab initio method. MF is a molecular turning surface for electron motion and provides a unique and intrinsic description of both the molecular boundary surface and the frontier electron density.

To sum up, some features can be abstracted for the MF change and PAEM-MO diagram for a molecular reaction system: (a) In the respect of spatial polarization, the adjacent active areas of MF regions of two reactants may stretch to welcome each other; the nearer they approach, the larger stretching they make, and then they touch and bond together while the rest part of the reaction system may have the concerted changing. (b) In the respect of polarization of the electron cloud, during the approaching process of reactants, the electron density on the MF contour usually concentrates onto the reaction active areas to strengthen the interaction of two reactants while accordingly lessening the electron density of other areas, especially from the bond-breaking region. This may provide a pattern of recognition strategies between molecules. (c) At the critical point, two reactant MF regions have only one touching point with the largest stretching in shape and the most polarization in the electron density, particularly on the active reaction areas. It might practically be assumed that only one touching point reached by two reacting MF regions represents the starting point of forming or breaking the chemical bonding between reactants. (d) In addition, it was shown that the chemical bonding or van der Waals interaction between two adjacent atoms can be distinguished by the barrier height of the potential acting on an electron (PAEM) compared with the valence bounding MO energy levels, i.e., by the PAEM-MO diagram. (e) In most cases, the MF and PAEM-MO diagram give consistent distinction of chemical bonding from van der Waals interaction, but MF gazes at the shape, while the frontier electron density and PAEM-MO diagram focuses on the electronic structure, namely the potential, bonding and the electron interflow.

Really, we need to do more studies on the PAEM, MF and PAEM-MO diagram for more molecular systems later on.

**Acknowledgments** The authors are very grateful to Prof. E. R. Davidson for providing us the MELD package and other kind helps. The authors give great thanks to the editor and reviewers for their suggestions and comments that help us a lot for improving our manuscript. Thanks are also given to the support of the National Natural Science Foundation of China (Nos. 21133005 and 21073080), as well as program for Liaoning Excellent Talents in University LNET (LJQ2013111), and Natural Science Foundation of Liaoning (2014020150).

## References

1. Mezey PG (1993) Shape in chemistry: an introduction to molecular shape and topology. VCH, New York
2. Mezey PG (1998) The proof of the metric properties of a fuzzy chirality measure of molecular electron density clouds. J Mol Struct THEOCHEM 455(2–3):183–190
3. Kourtzi Z, Kanwisher N (2001) Representation of perceived object shape by the human lateral occipital complex. Science 293(5534):1506–1509
4. Puntes VF, Krishnan KM, Alivisatos AP (2001) Colloidal nanocrystal shape and size control: the case of cobalt. Science 291:2115–2117
5. Hansen PL (2002) Atom-resolved imaging of dynamic shape changes in supported copper nanocrystals. Science 295(5562):2053–2055

6. Meyer AY (1986) The size of molecules. Chem Soc Rev 15(4):449–474
7. Leach AR (1996) Molecular modelling: principles and applications. Addison Wesley Longman Limited, London
8. Lim C, Chan SL, Tole P (eds) (1994) In structure and reactivity in aqueous solution. ACS, Washington
9. Jackson RM, Sternberg MJE (1993) Protein surface area defined. Nature 366:638
10. Lee MS, Feig M, Salsbury FR Jr, Brooks CL III (2003) New analytic approximation to the standard molecular volume definition and its application to generalized born calculations. J Comput Chem 24(11):1348–1356
11. Chothia C, Janin J (1975) Principles of protein–protein recognition. Nature 256(5520):705–708
12. Exner TE, Keil M, Brickmann J (2002) Pattern recognition strategies for molecular surfaces. I. Pattern generation using fuzzy set theory. J Comput Chem 23(2):1176–1187
13. Lee B, Richards FM (1971) The interpretation of protein structures: estimation of static accessibility. J Mol Biol 55(3):379–383
14. Richards FM (1977) Areas, volumes, packing and protein structure. Annu Rev Biophys Bioeng 6:151–176
15. Greer J, Bush BL (1978) Macromolecular shape and surface maps by solvent exclusion. Proc Natl Acad Sci USA 75(1):303–307
16. Gibson KD, Scheraga HA (1987) Exact calculation of the volume and surface area of fused hard-sphere molecules with unequal atomic radii. Mol Phys 62(5):1247–1265
17. Petitjean M (1994) On the analytical calculation of van der Waals surfaces and volumes: some numerical aspects. J Comput Chem 15(5):507–523
18. Connolly ML (1983) Solvent-accessible surfaces of proteins and nucleic acids. Science 221(4621):709–713
19. Duncan BS, Olson AJ (1993) Approximation and characterization of molecular surfaces. Biopolymers 33(2):219–229
20. Pascual-Ahuir JL, Silla E, Tuñón I (1994) An improved description of molecular surfaces. III. A new algorithm for the computation of a solvent-excluding surface. J Comput Chem 15(10):1127–1138
21. Connolly ML (1996) Molecular surfaces: a review, Part 5: solvent-accessible surfaces. Netw Sci
22. Cossi M, Mennucci B, Cammi R (1996) Analytical first derivatives of molecular surfaces with respect to nuclear coordinates. J Comput Chem 17(1):57–73
23. Pomelli CS, Tomasi J, Cammi R (2001) A Symmetry adapted tessellation of the GEPOL surface: applications to molecular properties in solution. J Comput Chem 22(12):1262–1272
24. Weiser J, Shenkin PS, Still WC (1999) Optimization of Gaussian surface calculations and extension to solvent-accessible surface areas. J Comput Chem 20(7):688–703
25. Cai WS, Zhang MS, Maigret B (1998) New approach for representation of molecular surface. J Comput Chem 19(16):1805–1815
26. Paci E, Velikson B (1997) On the volume of macromolecules. Biopolymers 41(7):785–797
27. Laug P, Borouchaki H (2003) Generation of finite element meshes on molecular surfaces. Int J Quantum Chem 93(2):131–138
28. Tsodikov OV, Record MTJ, Sergeev YV (2002) Novel computer program for fast exact calculation of accessible and molecular surface areas and average surface curvature. J Comput Chem 23(6):600–609
29. Richards FM (1974) The interpretation of protein structures: total volume, group volume distributions and packing density. J Mol Biol 82(1):1–14
30. Boyd R (1977) The relative sizes of atoms. J Phys B Atom Mol Phys 10(12):2283–2291
31. Bader RFW, Marshall TC, James RC, Cheng C (1987) Properties of atoms in molecules: atomic volumes. J Am Chem Soc 109(26):7968–7979
32. Bader RFW, Henneker WH, Cade PE (1967) Molecular charge distributions and chemical binding. II. First-row diatomic hydrides, AH. J Chem Phys 47(9):3381–3402
33. Bader RFW, Keaveny I, Cade PE (2004) Molecular charge distributions and chemical binding. J Chem Phys 46(9):3341–3363
34. Mitchell AS, Spackman MA (2000) Molecular surfaces from the promolecule: a comparison with Hartree-Fock ab initio electron density surfaces. J Comput Chem 21(11):933–942
35. Stefanovich EV, Truong TN (1995) Optimized atomic radii for quantum dielectric continuum solvation models. Chem Phys Lett 244(1):65–74
36. Yang ZZ, Zhao DX (1998) A characteristic molecular contour evaluated by a theoretical method. Chem Phys Lett 292(4–6):387–394
37. Yang ZZ, Zhao DX, Wu Y (2004) Polarization and bonding of the intrinsic characteristic contours of hydrogen and fluorine atoms of forming a hydrogen fluoride molecule based on an ab initio study. J Chem Phys 121(8):3452–3462
38. Zhao DX, Gong LD, Yang ZZ (2002) Exploration of the potential acting on an electron within diatomic molecules. Chin Sci Bull 47(8):635–640
39. Zhao DX, Yang ZZ (2002) The changing features of the molecular intrinsic characteristic contours of $H_2$ molecule in the ground and first excited states calculated by an ab initio method. J Mol Struct (Theochem) 579(1):73–84
40. Zhao DX, Yang ZZ (2008) Molecular face: a novel molecular model showing both molecular spatial contour and frontier electron density. J Theor Comput Chem 7(3):303–315
41. Gong LD, Zhao DX, Yang ZZ (2003) The molecular intrinsic characteristic contours (MICCs) of some small organic molecules. J Mol Struct (Theochem) 636(1):57–70. doi:10.1016/S0166-1280(03)00419-6
42. Gong LD, Zhao DX, Yang ZZ (2003) Molecular intrinsic characteristic contours of small organic molecules containing oxygen atom. Chin Sci Bull 48(18):1943–1946
43. Gong LD, Zhao DX, Yang ZZ (2005) Theory on the molecular characteristic contour (II): molecular intrinsic characteristic contours of several typical organic molecules. Sci China Ser B Chem 48(2):89–100
44. Yang ZZ, Gong LD, Zhao DX, Zhang MB (2005) Method and algorithm of obtaining the molecular intrinsic characteristic contours (MICCs) of organic molecules. J Comput Chem 26(1):35–47
45. Yang ZZ, Davidson ER (1997) Evaluation of a characteristic atomic radius by an ab Initio method. Int J Quantum Chem 62(1):47–53
46. Zhang MB, Zhao DX, Yang ZZ (2005) The characteristic boundary radii of atoms. J Theor Comput Chem 4(1):281–288
47. Yang ZZ, Li GH, Zhao DX, He HB, Sun RA (1998) Theoretical study on characteristic ionic radii. Chin Sci Bull 43(17):1452–1455
48. Yang ZZ, Niu SY (1991) A sort of radius to describe the size of an atom. Chin Sci Bull 36(11):964–965
49. Niu SY, Yang ZZ (1994) A new scale of atomic radius: atomic boundary radius (in Chinese). Acta Chim Sin 52(6):551–555
50. Ayers PW (2001) Strategies for computing chemical reactivity indices. Theor Chem Acc 106(4):271–279
51. DeKock RL, Strikwerda JR, Yu EX (2012) Atomic size, ionization energy, polarizability, asymptotic behavior, and the Slater-Zener model. Chem Phys Lett 547:120–126
52. Yang ZZ, Tang SQ, Niu SY (1996) Boundary radii of cations (in Chinese). Acta Chim Sin 54(9):846–852
53. Yang ZZ, Ding YL, Zhao DX (2009) Theoretical analysis of gas-phase front-side attack identity $S_N2$(C) and $S_N2$(Si) reactions with retention of configuration. J Phys Chem A 113(28):5432–5445
54. Ding YL, Gong LD, Zhao DX, Zhang MB, Yang ZZ (2009) Studies on nucleophilic substitution reactions at carbon ($S_N2$(C)) and

silicon ($S_N2$(Si)) in terms of ab initio, potential acting on an electron in a molecule and molecular face theory. J Theor Comput Chem 8(Supp. 1):983–1001
55. Yang ZZ, Ding YL, Zhao DX (2008) Insight into Markovnikov reactions of alkenes in terms of ab initio and molecular face theory. ChemPhysChem 9(16):2379–2389. doi:10.1002/cphc.200800364
56. Zhang M-B, Gong LD (2012) Evolution of the molecular face during the reaction process of $F^-$+CH3Cl → CH3F + $Cl^-$. Acta Phys Chim Sin 28(5):1020–1026. doi:10.3866/PKU.WHXB201203082
57. Ding Y-L, Li E-B, Gong L-D (2012) Dynamic changing features of the molecular face for interaction of a rare gas atom with a hydrogen molecule. Int J Quantum Chem 112(12):2515–2524. doi:10.1002/qua.23249
58. Zhang MB, Yang ZZ (2005) Computational study on the reaction $CH_2CH_2$ + F → $CH_2CHF$ + H. J Phys Chem A 109(21):4816–4823
59. Zhao DX, Yang ZZ (2014) Investigation of the distinction between van der Waals interaction and chemical bonding based on the PAEM-MO diagram. J Comput Chem 35(13):965–977. doi:10.1002/jcc.23570
60. Zhao DX, Gong LD, Yang ZZ (2005) The relations of bond length and force constant with the potential acting on an electron in a molecule. J Phys Chem A 109(44):10121–10128
61. Politzer P, Truhlar DG (1981) Chemical applications of atomic and molecular electrostatic potentials. Plenum, New York
62. Politzer P, Murray JS (1996) Molecular electrostatic potentials: concepts and applications. In: Murray JS, Sen K (eds) Theoretical and Computational Chemistry, vol 3. Elsevier, Amsterdam, p 664
63. Politzer P, Murray JS, Lane P (2003) Electrostatic potentials and covalent radii. J Comput Chem 24(4):505–511
64. Levine RD, Bernstein RB (1987) Molecular reaction dynamics and chemical reactivity. Oxford University Press, New York
65. Eyring H, Walter J, Kimball G (1944) Quantum chemistry. Wiley, New York
66. Levine IN (2000) Quantum chemistry, 5th edn. Prentice-Hall Inc., New Jersey
67. Hartree DR (1928) The wave mechanics of an atom with a non-Coulomb central field. Part I. Theory and methods. Proc Camb Phil Soc 24:89–110. doi:10.1017/S0305004100011919
68. Slater JC (1951) A simplification of the Hartree-Fock method. Phys Rev 81:385–390. doi:10.1103/PhysRev.81.385
69. Kohn W, Sham LJ (1965) Self-consistent equations including exchange and correlation effects. Phys Rev A 140(4):1133–1138
70. Dirac PAM (1930) Note on exchange phenomena in the Thomas atom. Proc Camb Phil Soc 26:376–385. doi:10.1017/S0305004100016108
71. Bader RFW (1990) Atoms in molecules-a quantum theory. Oxford University Press, New York
72. Gáspár R (2000) Concerning an approximation of the Hartree-Fock potential by a universal potential function. J Mol Struct THEOCHEM 501–502:1–15
73. Colle R, Salvetti O (1993) A non-local representation of the effective potential due to a molecular fragment. Theor Chim Acta 86(6):451–465
74. Zhang Y, Tai-Sung GL, Yang W (1999) A pseudobond approach to combining quantum mechanical and molecular mechanical methods. J Chem Phys 110(1):46–54
75. Poteau R, Alary F, Makarim HAE, Heully JL, Barthelat JC, Daudey JP (2001) Effective group potentials. 2. Extraction and transferability for chemical groups involved in covalent or donor–acceptor bonds. J Phys Chem A 105(1):206–214
76. Ayers PW, Parr RG (2001) Variational principles for describing chemical reactions. Reactivity indices based on the external potential. J Am Chem Soc 123(9):2007–2017
77. Chan WT, Hamilton IP (1998) Valence shell structures in the distributions of the Laplacian of the electron density and the one-electron potential for diatomic molecules. J Chem Phys 108(6):2473–2485
78. von Armin M, Peyerimhoff SD (1993) Effective potentials for spectator groups in molecular systems. Transition energies and transition moments. Chem Phys Lett 210(4–6):488–494
79. Hunter G (1996) Atoms in molecules from the exact one-electron wave function. Can J Chem 74(6):1008–1013
80. Mishra PC, Kumar A (1999) Modified hybridization displacement charge scheme for π-electron systems: study of molecular electrostatic potential maps. Int J Quantum Chem 71(2):191–200
81. Donald E, Williams AA (1999) Site charge models for molecular electrostatic potentials of cycloalkanes and tetrahedrane. J Comput Chem 20(6):579–585
82. Sundholm D, Olsen J (1993) The exactness of the extended Koopmans' theorem: a numerical study. J Chem Phys 98(5):3999–4002
83. Ohta K, Yoshioka Y, Morokuma K, Kitaura K (1983) The effective fragment potential method an approximate ab initio MO method for large melecules. Chem Phys Lett 101(1):12–17
84. Davidson ER (1990) MELD Program, MELD program description in MOTECC. ESCOM, New York
85. Partridge H (1987) Near Hartree-Fock quality GTO basis sets for the second-row atoms. J Chem Phys 87:6643–6647
86. Mathworks (2005) Matlab. 7.0 (Release 14) edn. The Mathworks, Natick
87. Lide DR (ed) (2003) CRC handbook of chemistry and physics, vol 84th ed. CRC Press, Boca Raton
88. Liu B (1973) Ab initio potential energy surface for linear $H_3$. J Chem Phys 58(5):1925–1937. doi:10.1063/1.1679454
89. Siegbahn P, Liu B (1978) An accurate three-dimensional potential energy surface for H3. J Chem Phys 68(5):2457–2465
90. Wright JS, Kruus E (1986) MRD-CI potential surfaces using balanced basis sets. IV. The H2 molecule and the H3 surface. J Chem Phys 85(12):7251–7260
91. Fukui K, Kato S, Fujimoto H (1975) Constituent analysis of the potential gradient along a reaction coordinate. Method and an application to methane + tritium reaction. J Am Chem Soc 97(1):1–7
92. Feynman RP (1939) Forces in molecules. Phys Rev 56:340–343

Theor Chem Acc (2014) 133:1558
DOI 10.1007/s00214-014-1558-6

REGULAR ARTICLE

# State-to-state quantum versus classical dynamics study of the OH + CO → H + $CO_2$ reaction in full dimensions ($J = 0$): checking the validity of the quasi-classical trajectory method

**Shu Liu · Jun Chen · Bina Fu · Dong H. Zhang**

Received: 31 May 2014 / Accepted: 3 August 2014 / Published online: 24 August 2014
© Springer-Verlag Berlin Heidelberg 2014

**Abstract** We report full-dimensional state-to-state quantum mechanical (QM) and quasi-classical trajectory (QCT) calculations on the title reaction for the ground rovibrational initial state with total angular momentum fixed at zero on the accurate potential energy (PES) constructed recently by using permutation-invariant polynomial–neural network method (Li et al. in J Chem Phys 140:044327, 2014), to check the validity of the QCT method for the reaction. It is found that the QM state-to-state results strongly depend on the resonance structures in reaction, but the collision energy-averaged results show a smooth change with the increase of collision energy. Overall, the agreement between collision energy-averaged QM and QCT state-to-state results is satisfactory, in particular at high collision energy region, indicating that the QCT method is rather accurate on describing dynamics of the reaction on the PES. On the other hand, because earlier studies revealed the QCT results on the PES do not agree very well with the experimental measurements available, more theoretical and experimental studies should be carried out to achieve a full understanding on the dynamics of this benchmark complex-forming reaction.

**Keywords** Complex-forming reaction · State-to-state · Quantum dynamics · Quasi-classical trajectory

Dedicated to Professor Guosen Yan and published as part of the special collection of articles celebrating his 85th birthday.

S. Liu · J. Chen · B. Fu · D. H. Zhang (✉)
State Key Laboratory of Molecular Reaction Dynamics and Center for Theoretical Computational Chemistry, Dalian Institute of Chemical Physics, Chinese Academy of Sciences, Dalian 116023, P.R. China
e-mail: zhangdh@dicp.ac.cn

## 1 Introduction

Because of its crucial role in the conversion of CO to $CO_2$, the OH + CO → H + $CO_2$ reaction is important to both atmospheric [1] and combustion chemistry [2]. This exothermic reaction proceeds via two pathways with the formation of HOCO intermediate complex in *trans* and *cis* deep wells, representing a prototype for complex-forming four-atom reactions, just as $H_2$ + OH → H + $H_2O$ is for direct four-atom reactions. Over the years, a large number of experimental studies have been devoted to this reaction, both for kinetic and dynamical properties. The measured thermal rate constants are nearly independent of temperature between 80 and 500 K, but increase sharply with temperature above 500 K [3–5]. This strong non-Arrhenius behavior has been attributed to the intricate minimum energy paths (MEP), which have near-isoenergetic barriers in the entrance (OH + CO) and exit (H + $CO_2$) channels. The molecular beam experiment carried out by Alagia et al. showed peaks both in the forward and backward directions, indicating the existence of reasonable long-lived intermediate species [6, 7].

Theoretically, the OH + CO reaction presents a great challenge to both potential energy surface (PES) construction and quantum dynamics. Much of the earlier work on the development of the global PES has been pioneered by Schatz and coworkers [8–10], by using a relatively small number of ab initio points. Following that, a few better PESs have been constructed and widely used, such as the YMS, LTSH, and VvHK PES [11–13], but they were still not sufficiently accurate for dynamical studies. The situation has been greatly improved, thanks to new PESs based on large numbers of high-level ab initio points. In 2012, Li et al. developed a global PES [14] and its modified version [15] using the permutation-invariant polynomial (PIP)

method [16]. Subsequently, Chen et al. reported another PES using the neural network (NN) method [17], with data points spreading in a more complete configuration space [18]. It was shown that the NN PES fits the ab initio points much better than the PIP PES. Very recently, Li et al. reported a new full-dimensional global PES based on the same ab initio data set generated by Chen et al. [18], but fit using the newly proposed permutation-invariant polynomial–neural network (PIP–NN) method [19, 20], which can be considered as the most accurate PES so far for the title reaction [21].

Because of the presence of three heavy atoms and a relatively long-lived intermediate complex, the rigorous quantum scattering calculations of this reaction is difficult. Extensive quantum mechanical (QM) studies were only carried out for the total reaction probabilities and rate constants on different PESs [21–26]. In 2011, we performed the first full-dimensional state-to-state quantum dynamics calculation for total angular momentum $J = 0$ on LTSH PES for the title reaction, for the ground and two vibrationally excited initial states [27, 28]. It was found that the initial CO vibrational excitation essentially has the same effect on the product energy partition as the reagent translational excitation, while the initial OH excitation leads to slightly more internal energy of $CO_2$. However, because the total reaction probabilities for $J = 0$ obtained on the LTSH PES were found to be substantially larger than those on the more accurate NN [18] and PIP–NN [21] PESs, state-to-state dynamics calculations on the NN or PIP–NN PES are highly desired to theoretically study product state distribution of this important reaction.

Although the quantum wave packet methods have been developed to compute differential cross sections (DCS) for direct four-atom reactions, such as the $HD + OH \rightarrow H_2O + D$ [29, 30], which achieved excellent agreement with high-resolution crossed-molecular beam experiments, it is still not feasible at present to compute final state resolved cross sections for complex-forming four-atom reactions due to the long wave packet propagation time and huge basis sets required. Quasi-classical trajectory (QCT) calculations of the title complex-forming reaction were carried out extensively on different PESs [12, 15, 21, 31–34]. Detailed dynamics features, i.e., DCS, product translational energy, vibrational and rotational state distributions, as well as the excitation functions and rate constants were calculated and compared with available experimental results. The recent QM and QCT study on the new PIP–NN PES indicated better agreement with both experimental kinetic and dynamical data than on previous PESs, but the differences still remain between QCT and experimental DCS [21]. Therefore, it is important to test the validity of the QCT method to describe chemical reaction dynamics for the title reaction.

In this article, we perform the full-dimensional (6D) state-to-state QM and QCT studies from the ground rovibrational initial state for the $OH + CO \rightarrow H + CO_2$ reaction on the new PIP–NN PES. Both QM and QCT calculations were carried out at the total angular momentum (impact parameter) fixed at zero. The rest of this paper is organized as follows. In Sec. II, we present the theory of the full-dimensional state-to-state quantum dynamics treatment to diatom–diatom reactions and some computational details. Sec. III contains our results, including QM and QCT total reaction probabilities, product distributions and energy partitioning information for this reaction. In Section IV we summarize our conclusions.

## 2 Theory

The QM calculations were carried out using the multi-step reactant-product decoupling (MRPD) scheme based time-dependent wave packet (TDWP) method [30, 35–37]. The basic strategy of the RPD scheme is to partition the full time-dependent (TD) wavefunction into a sum of reactant component ($\Psi_r$) and all product components ($\Psi_p$, $p = 1, 2, 3, \ldots$) that satisfy the following decoupled equations,

$$\begin{aligned} i\hbar\frac{\partial}{\partial t}|\Psi_r(t)\rangle &= H|\Psi_r(t)\rangle - i\sum_p V_p|\Psi_r(t)\rangle \\ i\hbar\frac{\partial}{\partial t}|\Psi_p(t)\rangle &= H|\Psi_p(t)\rangle + iV_p|\Psi_r(t)\rangle, \end{aligned} \tag{1}$$

where $-iV_p$ is the negative imaginary potential (absorption potential) employed to prevent the wavefunction $\Psi_r(t)$ from entering the $p$th product arrangement. The solution for $\Psi_r(t)$ can be propagated in the reactant Jacobi coordinates just as for total reaction probability calculations,

$$\Psi_r(t + \Delta) = e^{-V_p\Delta/\hbar}e^{-(i/\hbar)H\Delta}\Psi_r(t). \tag{2}$$

Every product wave function, $\Psi_p$, can be propagated in its own coordinates as in a normal wave packet propagation except for a source term, $\xi_p$, prepared by Eq. 2,

$$\begin{aligned} \Psi_p(t + \Delta) = e^{-(i/\hbar)H\Delta}\Psi_p(t) + \xi_p(t) &= e^{-(i/\hbar)H\Delta}\Psi_p(t) \\ &+ \left(1 - e^{-V_p\Delta/\hbar}\right)\Psi_r(t + \Delta). \end{aligned} \tag{3}$$

In the original RPD approach, the source term $\xi_p(t) = (1 - e^{-V_p\Delta/\hbar})\Psi_r(t)$ is saved and transformed from reactant to product Jacobi coordinates at every propagation time step. To reduce the computational cost, we use MRPD by saving and transforming the source term at every $M$ time steps in the actual calculation,

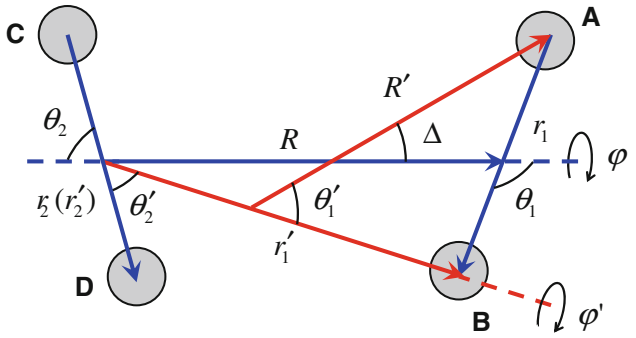


**Fig. 1** The reagent Jacobi coordinates $(R, r_1, r_2, \theta_1, \theta_2, \varphi)$ for the AB + CD diatom–diatom arrangement, and product Jacobi coordinates $(R', r_1', r_2', \theta_1', \theta_2', \varphi')$ for the A + BCD atom–triatom arrangement. $\Delta$ is the angle between $\hat{R}$ and $\hat{R}'$

$$\begin{aligned}
&\Psi_r(t+\Delta) = e^{-V_p M\Delta/\hbar} e^{-(i/\hbar)H\Delta}\Psi_r(t),\\
&\text{when } mod((t+\Delta)-t_0, M\Delta) = 0,\\
&\Psi_p(t+\Delta) = e^{-(i/\hbar)H\Delta}\Psi_p(t) + \left(1 - e^{-V_p M\Delta/\hbar}\right)\Psi_r(t+\Delta),
\end{aligned} \tag{4}$$

where $t_0$ is the starting point for performing wave function transformation. At other time steps, we carried out the standard split-operator propagation for $\Psi_r(t)$ and $\Psi_p(t)$ without the absorption potential, $V_p$, related terms. In this way, we can cut the computational time for wave function transformation from reactant coordinates to product coordinates by a factor of $M$. Finally, one can extract the final state information, such as state-to-state $S$ matrix elements or reaction probabilities, from the Fourier transformation of $\Psi_p(t)$.

The coordinate systems and wavefunctions representations for both diatom–diatom and atom–triatom scattering studies are outlined here. For details, please refer Refs. [38, 39]. Figure 1 shows the reagent Jacobi coordinates $(R, r_1, r_2, \theta_1, \theta_2, \varphi)$ for the OH + CO diatom–diatom arrangement, and product Jacobi coordinates $(R', r_1', r_2', \theta_1', \theta_2', \varphi')$ for the H + $CO_2$ atom–triatom arrangement. As can be seen $r_2$ and $r_2'$ share the same vector.

The system Hamiltonian in the OH + CO arrangement for a given total angular momentum $J$ can be written as

$$\begin{aligned}
H = &-\frac{\hbar^2}{2\mu}\frac{\partial^2}{\partial R^2} + \frac{(\mathbf{J}-\mathbf{j}_{12})^2}{2\mu R^2} + \frac{\mathbf{j}_1^2}{2\mu_1 r_1^2} + \frac{\mathbf{j}_2^2}{2\mu_2 r_2^2}\\
&+ V(R, r_1, r_2, \theta_1, \theta_2, \varphi) + h_1(r_1) + h_2(r_2),
\end{aligned} \tag{5}$$

where $\mu$ is the reduced mass between the center of mass of OH and CO, $\mathbf{J}$ is the total angular momentum operator, $\mathbf{j}_1$ and $\mathbf{j}_2$ are the rotational angular momentum operators of OH and CO, which are coupled to form $\mathbf{j}_{12}$. The diatomic reference Hamiltonian $h_i(r_i)$ $(i = 1, 2)$ is defined as

$$h_i(r_i) = -\frac{\hbar^2}{2\mu_i}\frac{\partial^2}{\partial r_i^2} + V_i(r_i). \tag{6}$$

The time-dependent wave function can be expanded in terms of the translational basis of R, the vibrational basis $\phi_{v_i}(r_i)$, and the BF rovibrational eigenfunction as

$$\begin{aligned}
\Psi^{JM\epsilon}_{v_0 j_0 K_0}(\mathbf{R}, \mathbf{r_1}, \mathbf{r_2}, t) = &\sum_{n,v,j,K} F^{JM\epsilon}_{nvjK, v_0 j_0 K_0}(t) u_n^{v_1}(R)\phi_{v_1}(r_1)\phi_{v_2}\\
&\times (r_2)\mathscr{Y}^{JM\epsilon}_{jK}(\hat{R}, \hat{r}_1, \hat{r}_2).
\end{aligned} \tag{7}$$

The BF total angular momentum eigenfunctions can be written as,

$$\begin{aligned}
\mathscr{Y}^{JM\epsilon}_{jK} = &(1+\delta_{K0})^{-1/2}\sqrt{\frac{2J+1}{8\pi}}\Big[D^{J*}_{K,M} Y^{j_{12}K}_{j_1 j_2}\\
&+ \epsilon(-1)^{j_1+j_2+j_{12}+J} D^{J*}_{-K,M} Y^{j_{12}-K}_{j_1 j_2}\Big]
\end{aligned} \tag{8}$$

$$\equiv \mathscr{D}^{J*}_{K,M} Y^{j_{12}K}_{j_1 j_2} + \epsilon(-1)^{\tilde{j}} \mathscr{D}^{J*}_{-K,M} Y^{j_{12}-K}_{j_1 j_2} \tag{9}$$

where $D^J_{K,M}(\Theta\Phi\Psi)$ is the Wigner rotation matrix [40] with three Euler angles $(\Theta\Phi\Psi)$, $\epsilon$ is the parity of the system defined as $\epsilon = (-1)^{j_1+j_2+L}$ with $L$ being the orbital angular momentum, and $Y^{j_{12}K}_{j_1 j_2}$ is the angular momentum eigenfunction of $\mathbf{j}_{12}$,

$$Y^{j_{12}K}_{j_1 j_2} = \sum_{m_1} \langle j_1 m_1 j_2 K - m_1 | j_{12} K\rangle y_{j_1 m_1}(\theta_1, 0) y_{j_2 K-m_1}(\theta_2, \phi) \tag{10}$$

where $y_{jm}$ are spherical harmonics.

For the H + $CO_2$ arrangement, similarly to the discussion about OH + CO arrangement, we have the same forms of equations, except the quantities with unprimed indices replaced by primed ones. The system Hamiltonian for the H + $CO_2$ arrangement, corresponding to Eq. (5),

$$\begin{aligned}
H = &-\frac{\hbar^2}{2\mu'}\frac{\partial^2}{\partial R'^2} + \frac{(\mathbf{J}-\mathbf{j}'_{12})^2}{2\mu' R'^2} + \frac{\mathbf{j}'^2_1}{2\mu'_1 r'^2_1} + \frac{\mathbf{j}'^2_2}{2\mu'_2 r'^2_2}\\
&+ V(R', r_1', r_2', \theta_1', \theta_2', \varphi') + h_1(r_1') + h_2(r_2'),
\end{aligned} \tag{11}$$

where $\mu'$ is the reduced mass between the center-of-mass of H and $CO_2$, $\mathbf{j}'_{12}$ is the total angular momentum operator of $CO_2$, $\mathbf{j}'_2$ is the rotational angular momentum operator of CO, and $\mathbf{j}'_1 = \mathbf{j}'_{12} - \mathbf{j}'_2$ is the orbital angular momentum of $CO_2$. The reference vibrational Hamiltonian $h_i(r_i')$ $(i = 1, 2)$ is defined as

$$h_i(r'_i) = -\frac{\hbar^2}{2\mu'_i}\frac{\partial^2}{\partial r'^2_i} + V_i(r_i'). \tag{12}$$

Corresponding to the Eq. 7, we have

$$\Psi_i^{JM\epsilon}(\mathbf{R}', \mathbf{r}'_1, \mathbf{r}'_2, t) = \sum_{n',v',j',K'} F^{JM\epsilon}_{n'v'j'K',i}(t) u^{v'_1}_{n'}(R')\phi_{v'_1}(r'_1)\phi_{v'_2} \times (r'_2)\mathscr{Y}^{JM\epsilon}_{j'K'}(\hat{R}', \hat{r'}_1, \hat{r'}_2), \quad (13)$$

It should be pointed out here that the functional form for the product arrangement basis (primed) are different with the one for the reagent arrangement basis (unprimed).

The BF total angular momentum basis $\mathscr{Y}^{JM\epsilon}_{j'K'}(\hat{R}', \hat{r'}_1, \hat{r'}_2)$ in Eq. 13 are defined as,

$$\mathscr{Y}^{JM\epsilon}_{j'K'} = (1+\delta_{K'0})^{-1/2}\sqrt{\frac{2J+1}{8\pi}}\left[D^{J*}_{K'M}Y^{j'_{12}K'}_{j'_1j'_2} + \epsilon(-1)^{j'_1+j'_2+j'_{12}}D^{J*}_{-K'M}Y^{j'_{12}-K'}_{j'_1j'_2}\right] \quad (14)$$

$$\equiv \mathscr{D}^{J*}_{K'M}Y^{j'_{12}K'}_{j'_1j'_2} + \epsilon(-1)^{\tilde{j}'}\mathscr{D}^{J*}_{-K'M}Y^{j'_{12}-K'}_{j'_1j'_2} \quad (15)$$

$\epsilon$ is the total parity of the system defined as $\epsilon_0(-1)^J$ with $\epsilon_0$ being the parity of the system. $Y^{j'_{12}K'}_{j'_1j'_2}$ is the angular momentum eigenfunction of $\mathbf{j}'_{12}$ defined as,

$$Y^{j'_{12}K'}_{j'_1j'_2} = \sum_m D^{j'_{12}*}_{K'm}(\chi, \theta'_1, \varphi')\sqrt{\frac{2j'_1+1}{4\pi}}\langle j'_2\, m\, j'_1\, 0|j'_{12}m\rangle y_{j'_2\,m}(\theta'_2, 0) \quad (16)$$

and $y_{jm}$ are spherical harmonics. Note that in Eq. 15, the restriction $\epsilon(-1)^{j'_1+j'_2+j'_{12}} = 1$ for $K' = 0$ partitions the whole rotational basis set into even and odd parities. Thus a $K' = 0$ initial state can only appear in one of these two parity blocks. For $K' > 0$, however, there is no such restriction, the basis set is the same for even and odd parities. Hence a $K' > 0$ initial state can appear in both parities.

We used the same parameters in Ref. [28], except for a larger asymptotic region with 60 sine basis functions for the R' from 1.0 to 13.0 $a_0$ in continuous propagation atom–triatom coordinates. A total number of 45,000 time steps with a time increment of 10 a.u. were used to accomplish the wave packet propagation from reagent channel to product channel. To minimize the computational cost, the coordinate transformation, which transfers the no-return part of reacted wave packets from the diatom–diatom coordinates to atom–triatom coordinates, was carried out at every 12 time steps. Even so, it is very time consuming to carry out the wave packet propagation in the reactant and product arrangements and to make the coordinate transformation.

The QCT calculations used essentially the same method as in the previous work [21]. Briefly, reactive scattering at the collision energy below 0.4 eV was simulated using the VENUS code [41]. The initial OH and CO reactants in their respective ground rovibrational states are separated by 6.0 Å and the trajectories are terminated when products (or reactants for non-reactive trajectories) reached a separation of 6.0 Å. The propagation time step was selected to be 3 a.u., and exceptionally long trajectories were halted if the propagation time reached a pre-specified value (36 ps). The scattering parameters (vibrational phases, and spatial orientation of the initial reactants) were selected with a Monte Carlo approach. The gradient of the PES was obtained numerically by the central-difference algorithm.

## 3 Results

Figure 2 shows the QM total reaction probabilities for $J = 0$ ground initial state on the PIP–NN PES from the summation of the state-to-state reaction probabilities obtained by using the RPD approach, in comparison with those from the initial state selected wave packet (ISSWP) approach only using reactant Jacobi coordinates. As can be seen, the agreement between the total reaction probabilities from RPD and ISSWP calculations is very good, indicating the RPD partition of the wave function as well as the continuous propagation in atom–triatom coordinates is of high accuracy. The QCT reaction probabilities for some collision energies on the same PES are represented by red dots, which show the same trend as the QM curve, although many narrow but overlapping resonances exist on QM probabilities apparently due to the long-lived HOCO complex. Obviously, the reaction probabilities are quite small, indicating this bimolecular reaction is very inefficient, despite its low energy barriers along the MEP. The present QM probabilities are substantially different from those obtained on the LTSH PES, not only for the magnitude of the reaction probabilities but also for the position of narrow resonance peaks. Based on the accuracy of the ab initio method used in generating energy points for the PIP–NN PES and the extremely small fitting errors [21], the current QM probabilities on the PIP–NN PES should be much more reliable as compared to the results on the LTSH PES.

Figure 3 shows the $CO_2$ product vibrational state distributions at $E_c = 0.1$ and 0.4 eV obtained by the QM calculation on the PIP–NN PES. For $CO_2$, because the symmetric stretching vibrational frequency $\nu_1$ is very close to the double of the bending frequency $\nu_2$, there are strong Fermi resonances between levels (100) and (020), and their corresponding overtones. In addition, with the increase of $CO_2$ rotational angular momentum, the number of vibrational states proliferates rapidly. Therefore, it is extremely hard to make a complete assignment of all the vibrational states, and we only managed to assign some of the vibrational states with low excitation energies. As seen from Fig. 3a at $E_c = 0.1$ eV, the $CO_2$ products are dominantly excited in bending and symmetric modes, but essentially have no excitation in the antisymmetric stretching mode. It is interesting that quite large population is seen from the

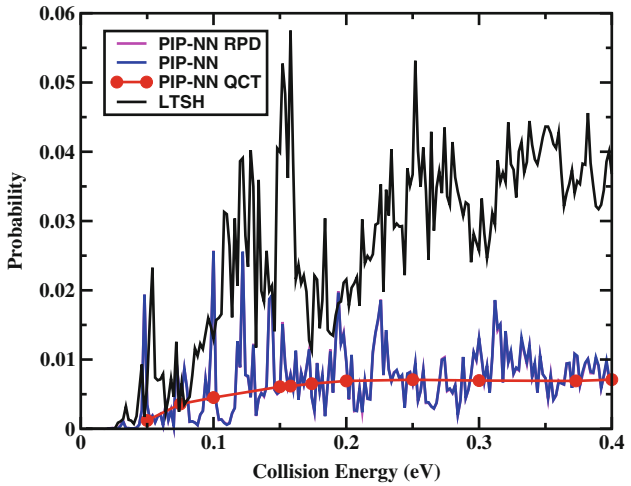


**Fig. 2** Total reaction probabilities for $J = 0$ ground initial state on the PIP–NN PES, including QM results obtained from state-to-state RPD and ISSWP calculations, and QCT results for some collision energy, in comparison with QM probabilities on the LTSH PES

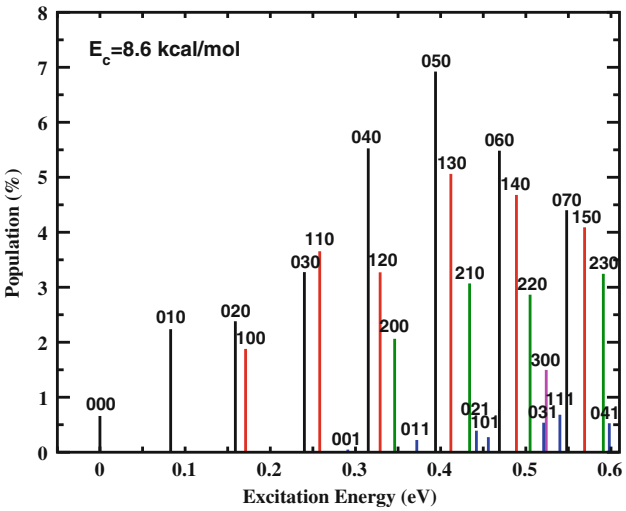


**Fig. 4** Product vibrational state distributions below 0.6 eV for total angular momentum $J = 0$ at $E_c = 8.6$ kcal/mol obtained by adding the sublevels of each bending mode together

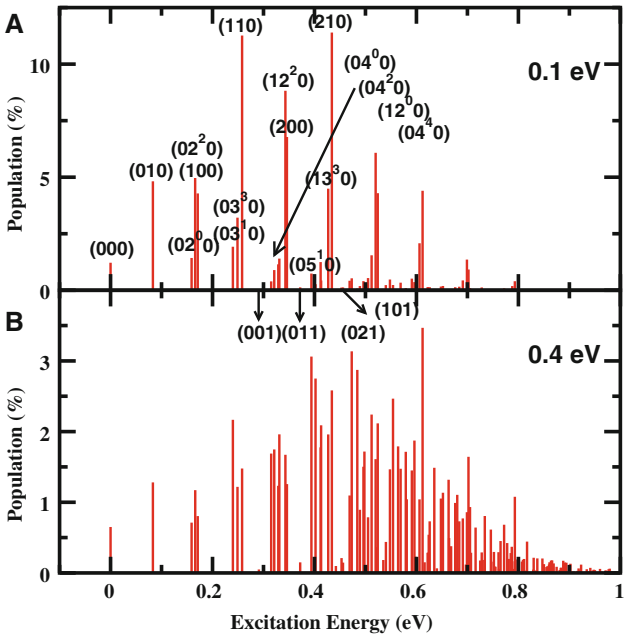


**Fig. 3** Product vibrational state distributions of $CO_2$ for total angular momentum $J = 0$ at $E_c = 0.1$ (**a**) and 0.4 eV (**b**) obtained by the QM calculation

simultaneous excitations of combined bending and symmetric modes, such as (110), ($12^20$) and (210). With the increase of collision energy, higher vibrationally excited states of $CO_2$ become populated as shown in Fig. 3b. The largest population for a single vibrational state decreases substantially, from 11 % at $E_c = 0.1$ eV to merely 3.5 % at $E_c = 0.4$ eV. Contrary to highly bending and symmetric stretching excitation, the population of the antisymmetric stretching states, even with one quantum number, is still small at $E_c = 0.4$ eV. Because the CO bond is substantially excited vibrationally in the complex wells as found in Ref. [25], it clearly reflects the fact that the reaction system has to put much of the available energy on the reaction coordinate to overcome the exit channel barrier. In the mean time, the substantial excitation of bending vibration are consistent with the geometry of the exit channel *cis*-H-OCO transition state, where O–C–O has an angle of 157°. The excitation in the symmetric stretching modes can likely be attributed to the Fermi-link with bending mode. The vibrational distributions on the LTSH PES in Ref. [27] are less excited than the present results. At $E_c = 0.1$ eV, the LTSH distribution peaks at (000) state with 36 % population, and is limited to a small number of states with energy below 0.25 eV. The peak moves slightly to ($02^20$) state at $E_c = 0.4$ eV. We also found more populations with antisymmetric stretching excited on the LTSH PES. As we have discussed in Ref. [18], in contrast to the tight exit *cis*-H-OCO transition state on the PIP–NN PES, the exit channel of LTSH PES is much wider, resulting in larger probabilities for the complex decaying into product channel and larger total reaction probabilities. And the bending angle of O-C-O changes slower to the linear product on the LTSH PES, leading to the cooler vibrational excitation patterns.

The QCT product vibrational state distribution at $E_c = 8.6$ kcal/mol for this reaction has been determined using a normal-mode analysis method on PIP (CCSD-2/d) PES in an earlier work, as shown in Fig. 3 of Ref. [33]. To compare with that, we added the sublevels of each bending mode together in QM distribution. Because of the difficulty

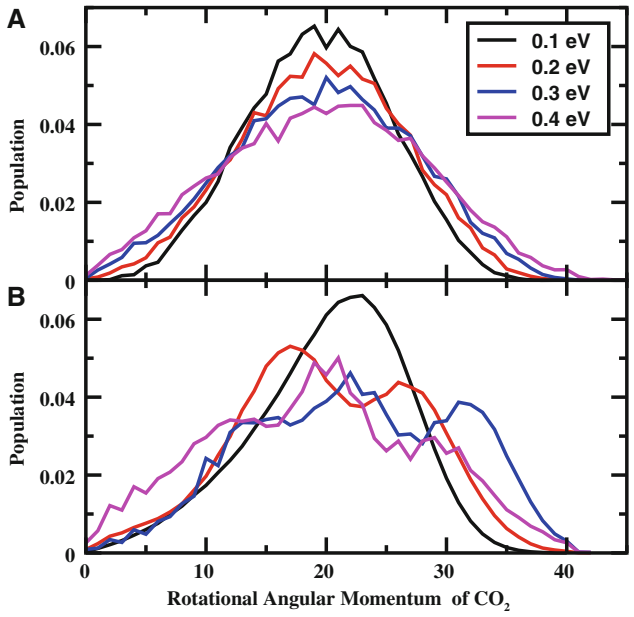


**Fig. 5** Normalized product $CO_2$ rotational state distributions for total angular momentum $J = 0$ at some collision energy, obtained by QCT (**a**) and QM (**b**) calculations

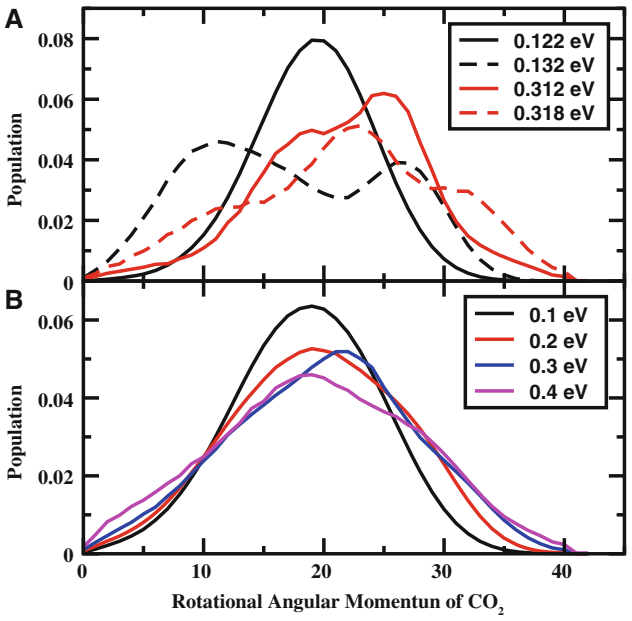


**Fig. 6** Normalized QM product $CO_2$ rotational state distributions for total angular momentum $J = 0$, at peak and dip positions of total probability (**a**), and after Gaussian function-weighted averaging (**b**)

on assigning vibrational states in high energy region, Fig. 4 only includes the treated QM distribution below 0.6 eV. Although the QCT and QM calculations were carried out on different PESs and different impact parameters, the trends of the two distributions are quite similar: the populations in each group (distinguished by symmetric stretching mode) firstly increase and then decrease with the increase of bending quantum number in general, despite the slight differences in the population of a single state and the position of peaks. However, the ratio of symmetric stretching excitations in the QM distribution is larger than that in the QCT one.

Figure 5 shows the normalized $CO_2$ rotational state distributions at some collision energies, with all vibrational states included. As seen, the reaction leads to substantial rotational excitations. Overall, the two sets of distributions calculated by QCT and QM methods are similar except some details. With the increase of collision energy, the QCT distribution becomes slightly broader, with the peak nearly fixed at the rotational angular moment of roughly 20. In contrast, the variation of QM distributions with the collision energies is more complicated. The behavior of QM rotational state distribution at $E_c = 0.1$ eV is similar to that of QCT results, except slightly higher peak for the QM distribution. However, as the collision energy increases, the QM distribution turns to show oscillatory structures which can be attributed to resonances during the reaction.

To further investigate this, we depict in Fig. 6a the QM rotational state distributions, respectively, at two pairs of collision energies (0.122/0.132 and 0.312/0.318 eV), where the total reaction probability exhibits a pronounced peak and a dip nearby as shown in Fig. 2. The behavior of these distributions is quite different, indicating the QM rotational state distributions depend strongly on the reaction resonances. To eliminate the influence of resonances, we averaged the QM populations using a Gaussian function weighting for each collision energy. As a result, the resonance-smoothing QM distributions shown in Fig. 6b are in very good agreement with QCT results. In addition, the rotational state distributions shown in Fig. 5b are quite different from those on the LTSH PES in Ref. [27], where the $CO_2$ products were shown to be more rotationally excited as the collision energy increases. The present PES is substantially more accurate and thus the current dynamics results are more reliable. The small variation of rotational state distributions with collision energy in this study reflects the fact that the HOCO intermediate complex lives sufficiently long in the wells in the collision energy region we studied.

Figure 7a, b compare the normalized product translational energy distributions on the PIP–NN PES calculated by QM and QCT methods at the collision energies of 0.1 and 0.4 eV, respectively. The zero point energy (ZPE) problem is an important issue in QCT calculations. As for this reaction, some $CO_2$ products can emerge with the vibrational energies below its ZPE level. Hence, we have shown the QCT results without (blue curve) and with ZPE constraint (magenta curve). The ZPE constraint results are

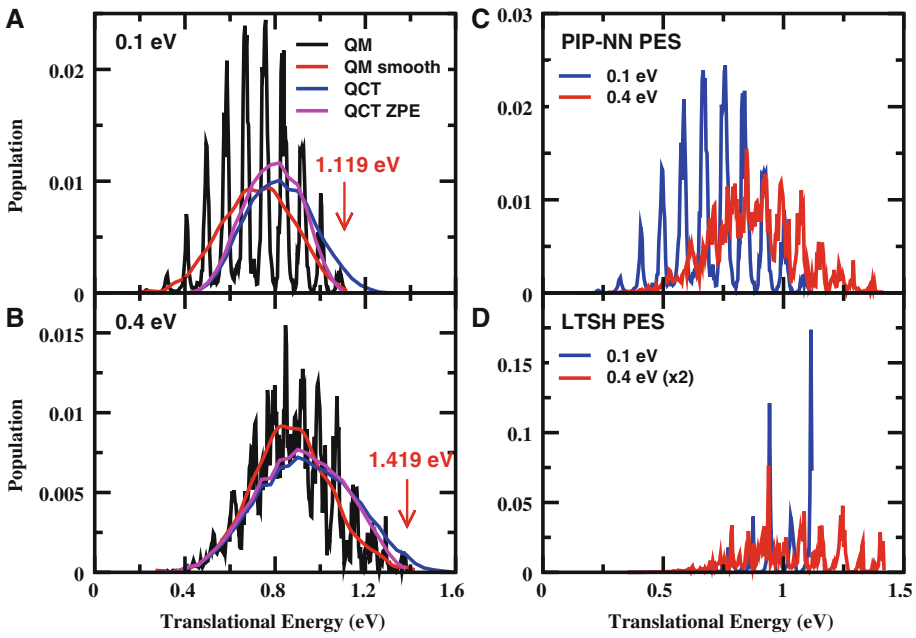


**Fig. 7** Normalized product translational energy distributions on the PIP–NN PES at $E_c = 0.1$ (**a**) and 0.4 eV (**b**) obtained by both QM and QCT calculations, in comparison with QM results on the LTSH PES (**c**, **d**). The maximum translational energy determined by the ZPE level of $CO_2$ is indicated by the *arrow*

analyzed for those trajectories in which $CO_2$ has at least the corresponding ZPE. It can be seen that the ZPE constraint QCT distributions are similar to the original QCT distributions, except at high translational energy region. At $E_c = 0.1$ eV, the QM distribution is lower in translational energy by about 0.1 eV than the QCT distributions, indicating the QM calculation yields a higher internal energy distribution. This discrepancy possibly results from the tunneling and ZPE effects that QCT calculation does not consider in the reaction. While $E_c = 0.4$ eV, the agreement between the QM and QCT distributions are quite good, except that the QCT distributions slightly overestimate populations at high translational energy region.

To investigate the influence of the reactant translational energy on the product translational energy, we show the QM product translational energy distributions on the PIP–NN PES at $E_c = 0.1$ and 0.4 eV in Fig. 7(c), together with the previous QM results on the LTSH PES in Fig. 7(d). On the whole, the two batches of results on the two different PESs are rather different. At $E_c = 0.1$ eV, the product translational energy obtained on the PIP–NN PES peaks roughly at 0.72 eV, whereas the peak of translational energy distribution on the LTSH PES nearly reaches the maximum of available translational energy, in accord with the previous calculation that only the $CO_2$ vibrational states with low excitation energies are mainly populated [27]. With the increase of collision energy, the product translational energy distribution on the PIP–NN PES shifts substantially to higher energy, although more rovibrational states are populated as discussed above, indicating the reactant collision energy transforms substantially into the translational motion of products. Similar trend is seen from the

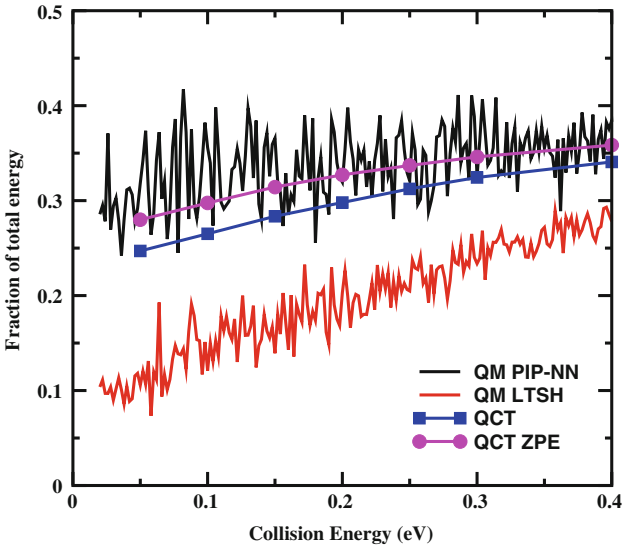


**Fig. 8** The fraction of the total available energy in product channel going into internal rovibrational motion of $CO_2$ as a function of collision energy, together with the QCT results on the same PES and QM result on the LTSH PES

product translational energy distributions on the LTSH PES in Fig. 7(d).

Figure 8 shows the fraction of the total available energy in product channel (with respect to the ground state $CO_2$) going into internal rovibrational motion of the product as a function of collision energy from the QM and QCT calculations. It can be seen that although the QM curve fluctuates rapidly just like the total reaction probability shown in Fig. 2, the average value increases steadily with the collision

energy from 28 % at $E_c = 0.1$ eV to 37 % at $E_c = 0.4$ eV. The QCT fractions for some collision energies on the same PES and their ZPE constrained results are represented by blue and magenta dots, with the latter agreeing well with the QM results except in low energy region. As we know the partial wave average will wash out most oscillatory structures exhibited in the total reaction probability as well as in the fraction of the total available energy going into $CO_2$ rovibrational excitation, and thus the QM energy partition will be much smoother if seen from the integral cross section, which results in better agreement with the QM and QCT result. The QM results calculated on the LTSH PES, indicated by red curve, underestimated this fraction in the entire energy region considered here, implying that the total available energy goes into the translational motion of the product more efficiently. At $E_c = 8.6$ kcal/mol, the QM fraction of the available energy released into product translation, $< f_T >$, is 0.618 on the PIP–NN PES. It is lower than both the molecular beam experimental value of 0.70 [7], and the QM value of 0.738 on the LTSH PES, suggesting more excitation in the internal degrees of freedom of $CO_2$ on the PIP–NN PES. Furthermore, if we assume the $CO_2$ rotational constant does not change substantially for various vibrational states, we can get the approximate fraction of energy going into product rotation, only 1.72 % on the PIP–NN PES at $E_c = 8.6$ kcal/mol due to the tiny rotational constant of $CO_2$, much smaller than the QCT value of 9.36 % from VENUS code. However, the VENUS code also provided an uncertainty in rotational energy close to the rotational energy itself, indicating that QCT result given by VENUS code excessively overestimated product rotational energy by including part of vibrational energy in bending modes in particular when $CO_2$ vibrates close to linear geometry. The QCT fraction can be reduced to 3.92 % by using the minimum rotation energy of each trajectory instead of the average value, but is still larger than the quantum result. It is worthwhile to point out that our QM and QCT calculations are for $J = 0$, while rotational energy in product may increase with the increase of $J$.

## 4 Conclusions

We performed full-dimensional (6D) state-to-state QM and QCT calculations for the ground rovibrational initial state for the $OH + CO \rightarrow H + CO_2$ reaction on the new PIP–NN PES, with the total angular momentum (impact parameter) fixed at zero. It is found that the QM rovibrational distributions of $CO_2$ strongly depend on the resonance structures of the reaction, but the collision energy-averaged distributions show a smooth change with the increase of collision energy. It turns out that the vibrational excitations in $CO_2$ bending and symmetric stretching modes are quite substantial and increase with the increase of collision energy. Very little excitation in $CO_2$ antisymmetric stretching states is observed. The rotational distributions of $CO_2$ do not change substantially with the collision energy, peaking at angular momentum of about 20. Overall, the agreement between collision energy-averaged QM and QCT state-to-state results is satisfactory, in particular at high collision energy region, indicating that the QCT method is rather accurate on describing dynamics of this complex-forming reaction on the PIP–NN PES.

On the other hand, since the QCT results on this PIP–NN PES do not agree very well with the experimental measurements available [21], the present PIP–NN PES may not be sufficiently accurate for the dynamics studies of the reaction at the state-to-state level. More efforts therefore should be devoted to the construction of more accurate PESs for this benchmark complex-forming reaction. In the meanwhile, because the PIP–NN PES was fitted very well to such a large number of ab initio energy points calculated at a high-level theory [18], it is highly desirable to carry out more experimental investigations on the reaction to eliminate possible uncertainties from experiment.

**Acknowledgments** This work was supported by the National Natural Science Foundation of China (Grant No. 90921014), Ministry of Science and Technology of China (2013CB834601), and the Chinese Academy of Sciences.

## References

1. Finlayson-Pitts BJ, Pitts JN (2000) Chemistry of the upper and lower atmosphere. Academic press, San Diego
2. Miller JA, Kee RJ, Westbrook CK (1990) Annu Rev Phys Chem 41:345–387
3. Ravishankara AR, Thompson RL (1983) Chem Phys Lett 99:377–381
4. Frost MJ, Sharkey P, Smith IWM (1991) Faraday Discuss Chem Soc 91:305–317
5. Golden DM, Smith GP, McEwen AB, Yu CL, Eiteneer B, Frenklach M, Vaghjiani GL, Ravishankara AR, Tully FP (1998) J Phys Chem A 102:8598–8606
6. Alagia M, Balucani N, Casavecchia P, Stranges D, Volpi GG (1993) J Chem Phys 98:8341
7. Casavecchia P, Balucani N, Volpi GG (1995) Chemical dynamics and kinetics of small free radicals, part I. In: Wagner AF, Liu K (eds) World Scientific, Singapore
8. Schatz GC, Fitzcharles MS, Harding LB (1987) Faraday Discuss Chem Soc 84:359–369
9. Kudla K, Schatz GC, Wagner AF (1991) J Chem Phys 95:1635
10. Bradley KS, Schatz GC (1997) J Chem Phys 106:8464
11. Yu HG, Muckerman JT, Sears TJ (2001) Chem Phys Lett 349:547–554
12. Lakin MJ, Troya D, Schatz GC, Harding LB (2003) J Chem Phys 119:5848
13. Valero R, van Hemert MC, Kroes GJ (2004) Chem Phys Lett 393:236–244
14. Li J, Wang Y, Jiang B, Ma J, Dawes R, Xie D, Bowman JM, Guo H (2012) J Chem Phys 136:041103

15. Li J, Xie C, Ma J, Wang Y, Dawes R, Xie D, Bowman JM, Guo H (2012) J Phys Chem A 116:5057–5067
16. Bowman JM, Czakó G, Fu B (2011) Phys Chem Chem Phys 13:8094
17. Behler J (2011) Phys Chem Chem Phys 13:17930
18. Chen J, Xu X, Zhang DH (2013) J Chem Phys 138:221104
19. Jiang B, Guo H (2013) J Chem Phys 139:054112
20. Li J, Jiang B, Guo H (2013) J Chem Phys 139:204103
21. Li J, Chen J, Zhang DH, Guo H (2014) J Chem Phys 140:044327
22. Zhang DH, Zhang JZH (1995) J Chem Phys 103:6512
23. Valero R, McCormack DA, Kroes GJ (2004) J Chem Phys 120:4263
24. Medvedev DM, Gray SK, Goldfield EM, Lakin MJ, Troya D, Schatz GC (2004) J Chem Phys 120:1231
25. Liu S, Xu X, Zhang DH (2012) Theor Chem Acc 131:1068
26. Ma J, Li J, Guo H (2012) J Phys Chem Lett 3:2482–2486
27. Liu S, Xu X, Zhang DH (2011) J Chem Phys 135:141108
28. Wang C, Liu S, Zhang DH (2012) Chem Phys Lett 537:16–20
29. Xiao C, Xu X, Liu S, Wang T, Dong W, Yang T, Sun Z, Dai D, Zhang DH, Yang X (2011) Science 333:440
30. Liu S, Xu X, Zhang DH (2012) J Chem Phys 136:144302
31. García E, Saracibar A, Zuazo L, Laganà A (2007) Chem Phys 332:162–175
32. García E, Corchado JC, Espinosa-García J (2012) J Comput Theor Chem 990:47–52
33. Corchado JC, Espinosa-García J, Li J, Guo H (2013) J Phys Chem A 117:11648–11654
34. Xie C, Li J, Xie D, Guo H (2012) J Chem Phys 137:024308
35. Althorpe SC, Kouri DJ, Hoffman DK (1997) J Chem Phys 106:7629–7636
36. Cvitaš MT, Althorpe SC (2009) J Phys Chem A 113:4557–4569
37. Cvitaš MT, Althorpe SC (2011) J Chem Phys 134:024309
38. Zhang DH, Zhang JZH (1994) J Chem Phys 101:1146
39. Zhang DH, Light JC (1996) J Chem Phys 104:4544–4553
40. Rose ME (1957) Elementary theory of angular momentum. Wiley, New York
41. Hase WL, Duchovic RJ, Hu X, Komornicki A, Lim KF, Lu DH, Peslherbe GH, Swamy KN, Linde SRV, Varandas A, Wang H, Wolf RJ (1996) Quantum Chem Prog Exch Bull 16:671

Theor Chem Acc (2014) 133:1565
DOI 10.1007/s00214-014-1565-7

REGULAR ARTICLE

# NO adsorption and transformation on the BaO surfaces from density functional theory calculations

**Nai-Xia Lu · Jing-Cong Tao · Xin Xu**

Received: 31 May 2014 / Accepted: 8 August 2014 / Published online: 5 September 2014
© Springer-Verlag Berlin Heidelberg 2014

**Abstract** Density functional theory combined with embedded cluster model calculations have been used to investigate the NO adsorption and transformation reactions on the BaO(100) surfaces. NO is found to adsorb on the anion sites to form a $NO_2^{2-}$ species, which can then couple with another NO to form a $N_2O_3^{2-}$ species. These surface species provide an alternative explanation for the infrared bands that were used to be assigned to the nitrite/nitrate and hyponitrite species. The calculations suggest a large intrinsic barrier for the transformation from $N_2O_3^{2-}$ to $N_2O_2^{2-}$. The latter species acts as a chemisorbed $N_2O$, which is envisioned as a key intermediate for further NO reduction. The present study provides a detailed description at the molecular level for the NO/BaO(100) system, which shed some light on the $NO_x$ storage–reduction systems, as well as NO direct decomposition.

**Keywords** $NO_x$ storage and reduction · BaO · $NO_x$ trap · Lean-burn · DFT · Vibrational properties

Dedicated to Professor Guosen Yan and published as part of the special collection of articles celebrating his 85th birthday.

**Electronic supplementary material** The online version of this article (doi:10.1007/s00214-014-1565-7) contains supplementary material, which is available to authorized users.

N.-X. Lu · J.-C. Tao (✉)
Laiwu Vocational and Technical College, Laiwu 271100, China
e-mail: jingcongtao@gmail.com

X. Xu (✉)
Shanghai Key Laboratory of Molecular Catalysis and Innovative Materials, MOE Laboratory for Computational Physical Science, Department of Chemistry, Fudan University, Shanghai 200433, China
e-mail: xxchem@fudan.edu.cn

## 1 Introduction

The need for fuel economy and consequently a reduction in $CO_2$ emissions for environmental protection has brought about the lean-burn engine technology with high air/fuel ratio for motor vehicles. In such a circumstance, however, the conventional three-way catalysts (TWC) in removing engine exhausts, notably CO, hydrocarbons (HC) and nitrogen oxides ($NO_x$), are no longer effective in removal of $NO_x$. One promising solution to this problem is to use the so-called $NO_x$ storage–reduction (NSR) catalyst [1–5]. The concept of NSR is that $NO_x$ is first stored under the lean condition over the catalyst, which is regenerated during the short periods of rich conditions, where $NO_x$ is released and subsequently reduced with HC, $H_2$ and CO to form $N_2$, $H_2O$ and $CO_2$ [6–8]. A typical NSR catalyst consists of noble metals (generally Pt) for the purposes of NO oxidation/reduction, and materials with Lewis basicity (notably a metal oxide like BaO) for the purposes of $NO_x$ storage, which are dispersed on a high surface area support like $\gamma$–$Al_2O_3$ [1, 6–8]. To further improve the performance of the catalysts in regard of $NO_x$ storage ability, temperature stability, regeneration times, and sulfur resistance, a good knowledge about the storage and transformation mechanisms is vital.

Despite the fact that huge efforts have been dedicated to kinetic measurements and spectroscopic characterizations [e.g., 1–31], certain key aspects concerning the mechanistic features of the NSR processes remain elusive, such that no clear understanding of this catalytic system has emerged [1, 5]. The difficulty arises not only from the variations of the operation conditions, but also from the complexity of both the reactant gas mixture (i.e., NO, $NO_2$, $O_2$, $H_2O$, $CO_2$, etc.) and the catalyst material (e.g., Pt/Ba/$\gamma$–$Al_2O_3$) with the abundance of the different adsorption and reaction sites. To

build a comprehensive understanding of the mechanism and to set up a predictive kinetic model concerning how different reactant gases adsorb, react and even compete against each other for active sites, and how different components of catalyst materials interplay to enhance or depress the reaction activity, model catalysts and model reactant gases have to be employed to individually probe the adsorption and chemistry on different sites [10–14, 17–28]. Along this line, the present work focuses only on NO, which is the main form of $NO_x$ in exhaust gas, adsorbed on and reacted with BaO, which is the primary storage material, with embedded cluster model calculations using density functional theory. The results shall be best compared with the experiments concerning NO adsorption and reactions on BaO surfaces by surface chemistry approaches [12, 13, 15, 23, 26].

In a NSR catalytic system, it is generally believed that NO is first oxidized to $NO_2$ on noble metal sites,

$$NO + \frac{1}{2}O_2 \overset{Pt}{\rightleftharpoons} NO_2 \tag{1}$$

which is then stored on BaO as nitrites ($NO_2^-$) and nitrates ($NO_3^-$) [6–11]. However, such a conversion was shown to be kinetically limited at lower temperature and thermodynamically limited at higher temperature [1, 11]. For example, Muncrief et al. [11] reported a <30 % steady-state NO to $NO_2$ conversion at temperatures below 250 °C and above 450 °C, with a maximum conversion of 60 % around 350 °C on a $Pt/Ba/Al_2O_3$ catalyst for a gas feed of 500 ppm NO and 5 % $O_2$ flowing at 200 $cm^3$/min. Hence, understanding the NO adsorption and transformations is an important issue in unraveling the $NO_x$ storage mechanism.

In experiments, the ad-species of NO exposure on barium-containing catalysts is complicated and controversial. The NO storage on monolith experiments showed that negligible conversion of NO to $NO_2$ occurred with the Pt-free catalyst, and catalysts with >1 % Pt loading had significantly improved the trapping efficiencies [21]. These experiments suggested the importance of a Pt–Ba couple and associated spillover processes that enhanced the storage [10, 18, 21]. Temperature-programmed desorption (TPD) experiments were carried by Mahzoul et al. [19], which also confirmed the role of platinum. Nevertheless, they showed that NO storage was already significant even if no oxygen was present in the gas phase and even in the absence of platinum [19]. Hence, their experiments suggested that BaO alone is reactive toward pure NO. The X-ray photoelectron spectroscopy (XPS) has been used to characterize the ad-species of NO on a 15–20 Å BaO film deposited on the aluminum substrate [12], where the influence of the substrate was actually minimized. The nitrogen and oxygen core level spectra acquired following NO exposure strongly suggested that new ad-species had formed, which were primarily ascribed as a nitrite-like species ($NO_2^-$), accompanied by the formation of a small amount of nitrate-like ad-species ($NO_3^-$) [12]. These results were, however, not supported by a later XPS and TPD investigation on BaO layers deposited on Cu(111) surfaces [23], which concluded that BaO itself did not readily trap NO. A systematic study of the $Pt/Ba/Al_2O_3$ system was performed by Prinetto et al. [13]. The evolutions of the surface species were monitored with FT-IR where $Pt/Ba/Al_2O_3$, $Pt/Al_2O_3$, $BaO/Al_2O_3$, and $Al_2O_3$ were exposed independently to NO or $NO_2$ in $O_2$. A couple of sharp bands at 1,375 and 1,310 $cm^{-1}$, a complex absorption at 1,050–950 $cm^{-1}$ with maximum at 1,025 $cm^{-1}$ and bands of minor intensity at 1,600, 1,470, and 1,220–1,180 $cm^{-1}$ were observed upon NO adsorption on either $Ba/Al_2O_3$ or $Pt/Ba/Al_2O_3$ [13]. Regardless of the presence of platinum or not, there was little difference on the IR spectra for these two systems [13]. Based on these results, the formation of nitrites ($NO_2^-$), nitrates ($NO_3^-$), and hyponitrite ($N_2O_2^{2-}$) species was assumed, and a mechanism was postulated [13]

$$2\,NO + O^{2-}_{(s)} \longrightarrow NO^- + NO^-_{2(s)} \tag{2}$$

$$4\,NO + 2\,O^{2-}_{(s)} \longrightarrow 3\ NO^-_{(s)} + NO^-_{3(s)} \tag{3}$$

$$2\,NO^-_{(s)} \longrightarrow N_2O^{2-}_{2(s)} \tag{4}$$

However, it should be noted that these seemingly simple steps are actually sum of several elementary reaction steps, which already includes some uncertainties. For example, the suggested formation of the hyponitrite species involves coupling of two negative species ($NO^-$), which is suspicious due to the large electrostatic repulsion.

In NSR, conversion to $N_2$ is also thought to occur over noble metal sites, which generally involves NO dissociation to form atomic N and O on platinum, where $N_2O$ was found to be an important product at lower temperature when the NO coverage is higher [1, 11, 18, 21, 29]. Although the primary focus of this study is the NSR system, direct decomposition of NO is also of interest. In fact, decomposition of NO over metal oxides in no presence of noble metals has been actively studied [31–35]. For example, Lunsford and co-workers have studied the BaO supported MgO systems using in situ Raman spectroscopy. This system was claimed to be particularly active for NO decomposition at Ba loadings of 11 mol% or greater, where a nitro species was assumed to be an intermediate in the catalytic cycle [31]. Recently, NO direct decomposition on the $BaO/Y_2O_3$ catalyst was reported by Ishihara et al. [35]. $N_2O$, nitrite and nitrate species were supposed to form based on IR spectra. Thus, the disproportional reactions of NO were suggested to occur [35]:

$$3\,NO \longrightarrow N_2 + NO_3 \quad (5)$$

$$3\,NO \longrightarrow N_2O + NO_2 \quad (6)$$

Clearly, Eqs. 5 and 6 do not refer to elementary steps and the mechanistic details remain to be clarified.

Identification of reaction pathways and intermediates by means of experiments represents a great challenge, while theoretical calculations can help to gain a more clear-cut answer for a given model system. So far, only a few theoretical calculations, based on either periodic-slab models [36, 37] or cluster models [38–40] have been carried out to investigate the interaction of NO with the BaO surfaces. It was generally agreed that NO adsorbs on the oxygen anion sites to form a $NO_2^{2-}$ species [38, 39]. However, the subsequent reactions of the surface species and the possible reaction paths that lead to the formation of the possible hyponitrite ($N_2O_2^{2-}$) species and the release of $N_2O$ have not yet been explored.

Thermodynamics for NO decomposition on MgO has been studied using cluster model calculations, where no transition states have been characterized [41]. A $N_2O_3^{2-}$ species was proposed to be an important intermediate in the NO decomposition process [41]. Unlike the neutral $N_2O_2$ dimer, it was noticed that anionic dimeric species such as $N_2O_2^{-}$ and $N_2O_2^{2-}$ present a much shorter N–N bond, typical of the N–N double bond [42, 43]. Therefore, charge transfer from the adsorption site to the ad-species was essential to activate the adsorbed precursors for the production of molecular $N_2O$ [42]. On MgO, the lattice sites were found to interact with NO very weakly [41], while chemisorbed species was formed only at low-coordination anions (steps, edges, or corners) or oxygen vacancies [42, 43]. As it is well known that the surface basicity of the cubic alkaline earth oxides (MgO, CaO, SrO, and BaO) increases going down the series as a result of the reduction of the Madelung potential with the crystal lattice expansion [44], the more basic anions on the BaO surfaces are expected to facilitate the NO adsorption and subsequent reactions.

The present theoretical study deals with NO adsorption and transformation on BaO surfaces. It aims, on the one side, at providing a detailed understanding of NO and BaO interactions at the molecular level, and on the other side, at complementing the available experimental work to gain, in particular, a better assignment of the species observed in the IR spectra.

## 2 Computational details

Density functional theory (DFT) calculations were carried out using the gradient-corrected Becke three-parameter hybrid exchange functional [45–49] in combination with the correlation functional of Lee, Yang, and Parr [50] (B3LYP). Recently, the inter-conversion between $NO_2$ and $N_2O_4$ has been studied using the B3LYP functional and several ab initio methods (MP2, CCSD(T), etc.). The results indicated that the B3LYP functional led to good energetics for these conversions [51].

An embedded cluster model approach was adopted to describe the BaO(100) surface as well as the low-coordination surface sties. A $Ba_{16}O_{16}$ cluster was chosen to represent the BaO(100) terrace sites ($O_{5c}$), while $Ba_{12}O_{12}$ and $Ba_{10}O_{10}$ were used as models for the four-coordinated edge sites ($O_{4c}$), and the three-coordinated corner sites ($O_{3c}$), respectively (see Fig. 1). These cluster models were constructed in fulfillment of some general requirements, namely the neutrality principle, the stoichiometry principle, and the coordination principle [52–56]. All these clusters were embedded in a large array of $\pm 2$ point charges (PCs), which were aimed to reproduce the Madelung potential at the adsorption sites. A Ba–O lattice distance of 2.76 Å was assumed [57]. To avoid the artificial polarization of the $O^{2-}$ anions at the cluster border induced by the PCs, the positive PCs at the interface were replaced by the total ion effective core potentials (TIPs) [58–60] to ensure a proper description of the Pauli repulsion. No basis functions were associated with the TIPs. The Ba atoms in the clusters were also treated with the effective core potentials (ECPs) originally developed by Hay and Wadt [61]. These were the small core ECPs with the contraction scheme generally known as LANL2DZ. The O and N atoms were described with a 6–31+G* basis set [62, 63].

Geometry optimizations were performed by means of analytical gradients with no symmetry constraints. The adsorbed NO molecules and atoms in clusters which were not in direct contact with the TIPs were included in the geometry optimization. Vibration frequencies were computed by determining the second derivatives of the total energy with respect to the internal coordinates. No scaling factors were applied when comparing the calculated frequencies with the experimental ones.

The adsorption enthalpy changes at room temperature were calculated using the formula:

$$\Delta H_{ad} = H_{tot}^{clus+ad} - H_{tot}^{clus} - H_{tot}^{ad} \quad (7)$$

where $H_{tot}^{clus+ad}$, $H_{tot}^{clus}$, and $H_{tot}^{ad}$ refer to the total enthalpy of the full system (BaO cluster + adsorbate), the enthalpy of the bare BaO cluster, and the enthalpy of the gas-phase molecules, respectively. According to this definition, $\Delta H_{ad} < 0$ stands for an exothermic adsorption.

Cluster models have generally been recognized as a useful tool to facilitate analysis and to be able to treat the neutral (e.g., NO and NO dimer) and charged adsorbates (e.g., nitrite and nitrate) on metal oxide surfaces even-handedly [64]. Previously, the same methodology has been used to study the $O_2$ dissociation mechanisms over the BaO(100)

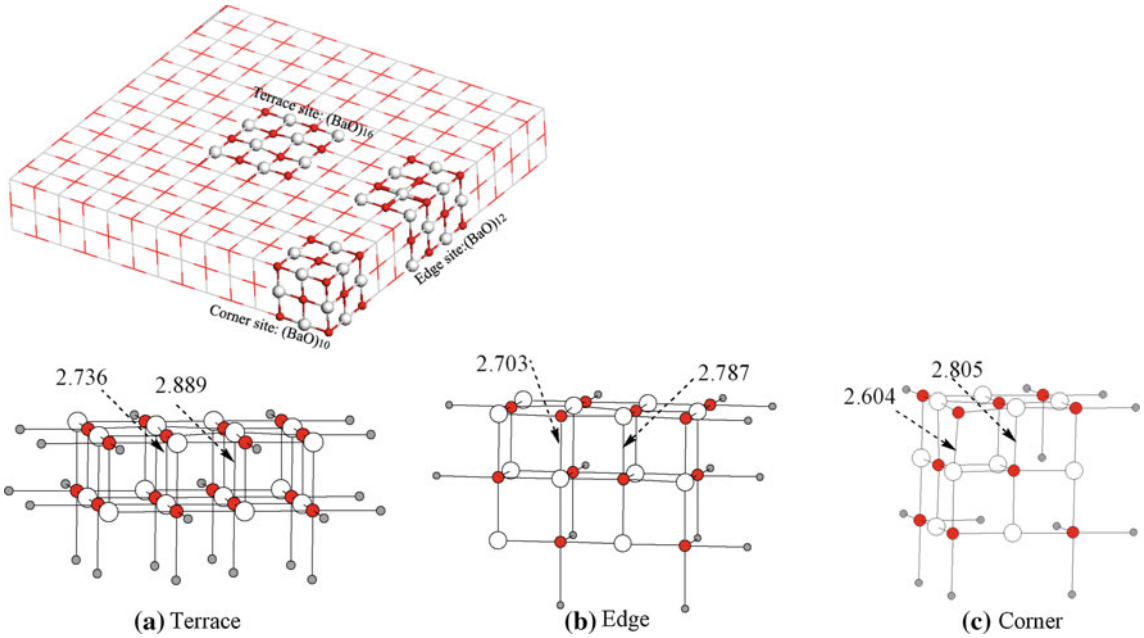


**Fig. 1** Cluster models used in the present work: **a** $(BaO)_{16}$ for terrace sites, **b** $(BaO)_{12}$ for edge sites, and **c** $(BaO)_{10}$ for corner sites. *Red spheres* stand for $O^{2-}$, while *large white spheres* for $Ba^{2+}$. *Small gray spheres* refer to the point charges (PCs) that are in close contact with $O^{2-}$ in the clusters as described by the total ion effective core potentials (TIPs). The rest of PCs are not shown

surface [65]. Other related studies, in particular, regarding the cluster size and embedding method [64–67], have well documented the validity of the present methodology [64–77].

All calculations were performed with the Gaussian 03 suite of program [62].

## 3 Results and discussion

### 3.1 One NO adsorption

On the terrace sites of the BaO(100) surfaces, our calculations predict that NO binds, with the N-down orientation, quite strongly to the $O_{5c}$ anion sites [see Fig. 2(**1**)]. The adsorption energy is calculated to be $\Delta H_{ad} = -28.4$ kcal/mol (see Table 1). Mulliken analysis shows that the unpaired spin density is almost entirely localized on the adsorbed NO (0.95, as shown in Table S1 in the supporting information, SI). Upon adsorption, the NO moiety is negatively charged (−0.89), such that partial charge is transferred from the surface anion ($O_s$) to the antibonding $\pi^*$ orbital of the adsorbed NO, resulting in an elongation of the N–O bond length from 1.158 Å in the gas phase to 1.291 Å on the surfaces. As a relatively short $O_s$–N bond (1.516 Å) is formed, the adsorption of NO on the $O_s$ site can be formally regarded as the formation of a $NO_2^{2-}$ species:

$$NO + O^{2-}_{(s)} \longrightarrow NO^{2-}_{2\,(s)} \quad (8)$$

This was first postulated by Lunsford based on the results of the electron paramagnetic resonance (EPR) technique on MgO [78] and was later supported by the observation on CaO [79]. Certainly, $NO_2^{2-}$ is unstable as an isolated species. It is stabilized on the surfaces by the Madelung potential.

As expected, the reactivity on the low-coordination sites for such an adsorption is much higher than that on the terrace sites due to the increased basicity of $O_s$ [44]. For instance, The NO adsorption energies on the $O_{4c}$ edge sites, or the $O_{3c}$ corner sites, are calculated to be −38.8 and −46.1 kcal/mol, respectively (Table 1). The stronger interactions are also reflected in the shorter $O_s$–N distances of 1.461 Å, and 1.423 Å on the $O_{4c}$ and $O_{3c}$ sites, respectively (Table S1). Spin densities (0.92) are nearly localized on the NO moieties which carrier more negative charges (−0.98), as compared to that on the terrace site, in accord with the increased adsorption energies.

Previously, a detailed comparison between the slab model and the embedded cluster model has been carried out in the study of the $O_2$ dissociation mechanisms over the BaO(100) surface [65]. A general agreement on the reaction trend was observed with these two methods. The calculations for NO adsorption are also generally in agreement with previous slab model [36, 37] and cluster model [38, 39] calculations. For example, with cluster models [38], Pacchioni et al. calculated the adsorption energies for NO on the $O_{5c}$ terrace and $O_{4c}$ step sites to be −18.4, and −38.0 kcal/mol, respectively. It is interesting to note that

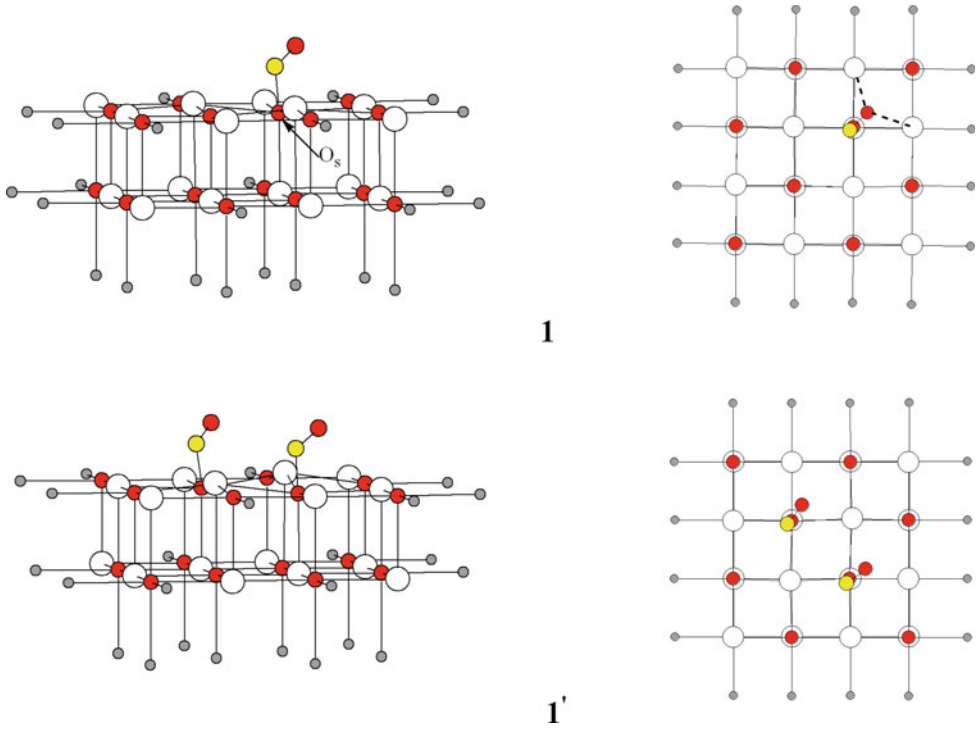


**Fig. 2** Optimized structures. **1** for one NO molecule adsorbed on an $O_{5c}$ anion site at the terrace of BaO (*left*, *side view*; *right*, *top view*); **1′** for two NO molecules adsorbed on two neighboring $O_{5c}$ anion sites at the terrace of BaO (*left*, *side view*; *right*, *top view*). *Color codes*: *yellow spheres* for N, *red spheres* for O, *large white spheres* for Ba and *small gray spheres* for TIPs. Geometric details are given in Table S1 in supporting information (SI)

**Table 1** The adsorption energies $\Delta H_{ad}$ (kcal/mol)[a] for one and two NO (the triplet state) adsorbed on the surface anion sites ($O_s$) of BaO[b]

| Adsorption geometry | Terrace | Edge | Corner |
|---|---|---|---|
| One NO adsorption (**1**) | −28.4 | −38.8 | −46.1 |
| Two NO adsorption (**1′**) | −58.1 | −66.9 | −70.2 |

a The adsorption energies are calculated according to $\Delta H_{ad} = H_{tot}^{clus+n*NO} - H_{tot}^{clus} - n*H_{tot}^{NO}$, where $n = 1, 2$

b The corresponding adsorption configurations are illustrated in Fig. 2

although a similar stability on the $O_{4c}$ sites was obtained, their adsorption energies on the $O_{5c}$ terrace sites were predicted to be less stable by ~10 kcal/mol than ours. The discrepancy is probably due to the difference in cluster size and the allowed surface relaxation. For adsorption on the terrace sites, besides the adsorbed NO molecule, the four-center ions of the $(BaO)_{16}$ cluster have been included in the present geometry optimization, while in the previous work [38], only the central O atom of the $(BaO)_9$ cluster was free to relax. The contribution to the adsorption energy associated with the surface relaxation can be significant. In our case, if only the central oxide anion was involved in the geometry optimization, the adsorption energy was found to decrease by ~4 kcal/mol. On the other hand, the effect of surface relaxation is usually well considered in the slab model calculations. For instance, the binding energies for NO adsorption on the BaO(100) surface were reported to be about −34 kcal/mol at a coverage of 0.25 [36, 37].

The frequency analysis shows that the N–O stretch band appears at 1,317 $cm^{-1}$ on the BaO terrace sites (Table 3), which may be compared to, for example, the observed frequency (1,300 $cm^{-1}$) for NO exposure on the $BaO/Y_2O_3$ catalyst [35]. With the decreasing of the coordination number of the adsorption sites, the N–O stretch band experiences a red shift to 1,241 $cm^{-1}$ on the $O_{4c}$ edge sites, and to 1,096 $cm^{-1}$ on the $O_{3c}$ corner sites, respectively. Therefore, we are inclined to associate the $NO_2^{2-}$ species with the broad band at 1,206 $cm^{-1}$ that was observed by Sedlmair et al. [15] in their IR experiments, although they tentatively assigned this band to the bridged bidentate nitrites.

### 3.2 Two NO adsorption

A key theoretical concept in understanding the interaction between $NO_x$ and the basic metal oxides is a pairwise, cooperative adsorption mechanism [36]:

$$M^{2+} - NO_x + NO_x - O^{2-} \longrightarrow M^{2+} - (NO_x)^{\delta-}/(NO_x)^{\delta+} - O^{2-} \quad (9)$$

where $NO_x$ molecules, adsorbed on metal cation sites, and oxygen anion sites, respectively, accept and donate electrons. Such a unique ability of $NO_x$ is a consequence of their high electron affinity and low ionization energy. The electron transfer between two $NO_x$ adsorbates in close proximity through the substrate results in a substantial increase of the adsorption energies for the pair in comparison with two individual adsorbates in isolation. This effect

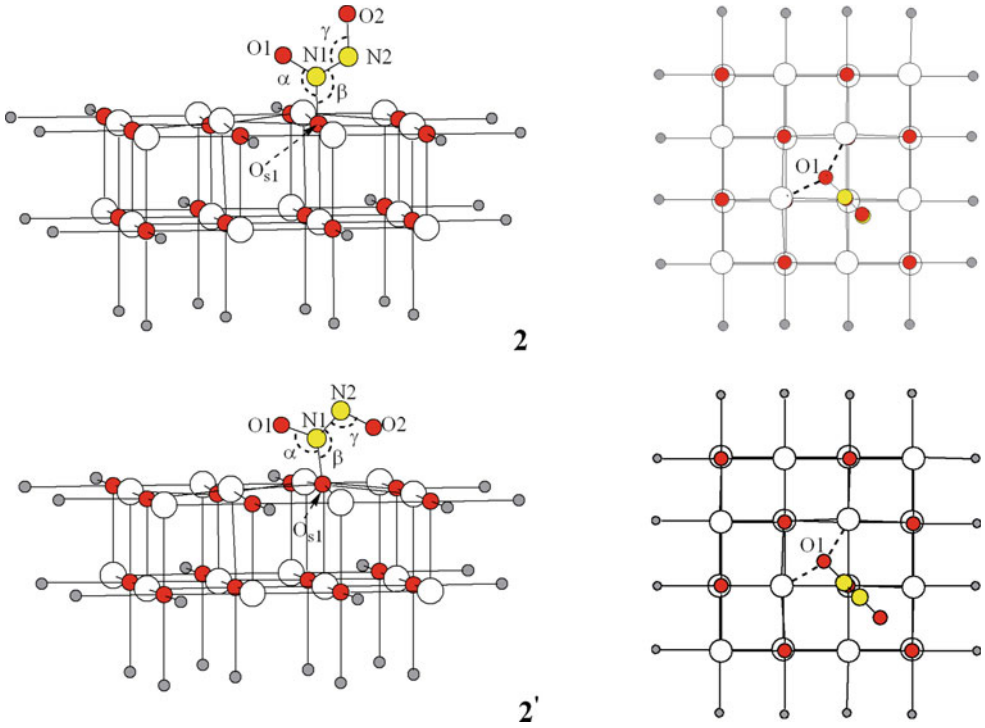


**Fig. 3** Optimized structures for NO dimer adsorbed on an $O_{5c}$ anion site at the terrace of BaO, forming *cis*-$N_2O_3^{2-}$ (**2**) and *trans*-$N_2O_3^{2-}$(**2′**) (*left*, *side view*; *right*, *top view*). *Color codes*: *yellow spheres* for N, *red spheres* for O, *large white spheres* for Ba and *small gray spheres* for TIPs. Geometric details are given in Table S1 in supporting information (SI)

has been observed for the (NO, $NO_2$), ($NO_2$, $NO_2$), ($NO_2$, $NO_3$) pairs, but not for the (NO, NO) pair [36].

Adsorption of two NO molecules on the BaO surfaces is studied in the present work, where both NO molecules are found to adsorb on the O anion sites. The adsorption configuration on two adjacent $O_{5c}$ sites is shown in Fig. 2 (**1′**), while geometries for some other configurations may be found in Table S1 in SI. As shown in Table 1, the adsorption energy per molecule on a terrace site is −29.05 kcal/mol, no matter the electronic state is set to either a triplet or an open-shell singlet. This energy actually compares well with the adsorption energy of the singly adsorbed molecule, indicating that there is little enhanced pairwise cooperative effect. The same is true if two NO molecules are adsorbed on a pair of $O_{5c}$ and $O_{4c}$ sites. Interestingly, if adsorption occurs on a pair of ($O_{5c}$, $O_{3c}$) sites, a repulsion of 3.8 kcal/mol is encountered (see Table 1).

The coverage dependence of NO adsorption on the BaO(100) surface was reported with the slab model calculations [37]. The results showed that the binding strength of NO on the anion sites almost linearly decreased with the increasing coverage from 34.6 kcal/mol at $\theta = 0.125$–23.1 kcal/mol at $\theta = 0.5$. Therefore, as indicated by the present cluster model calculations and the previous slab model calculations [37], some other adsorption configurations containing NO dimer may be more favorable at higher NO coverage.

As described above, the isolated NO binds strongly on the $O_s$ sites to form a $NO_2^{2-}$ species even on the terrace sites of BaO. As both the $NO_2^{2-}$ species and the free NO molecule carry one unpaired electron on the N atom, respectively, a singlet $N_2O_3^{2-}$ species would be formed by coupling the two radical-like groups (see Fig. 3):

$$NO^{2-}_{2\,(s)} + NO \longrightarrow N_2O^{2-}_{3\,(s)} \tag{10}$$

The $N_2O_3^{2-}$ complex can also be regarded as the adsorption of a NO dimer ($N_2O_2$) on the surface O anion site. These have been studied before on MgO [41], as well as BaO [39]. The configurations of the $N_2O_3^{2-}$ surface complexes can be assigned to *cis*-$N_2O_3^{2-}$ and *trans*-$N_2O_3^{2-}$ with respect to *cis*-$N_2O_2$ and *trans*-$N_2O_2$, respectively. The corresponding geometrical parameters are listed in Table S2 in SI. The N–N bond length is dramatically reduced from 1.96 Å for *cis*-$N_2O_2$ in the gas phase [42] to 1.29–1.32 Å, depending on the orientation, while the N–O bond length is drastically elongated from 1.16 Å in the gas phase [42] to 1.30–1.34 Å. Mulliken charge analysis shows that the adsorbed NO dimer on the terrace anion sites almost obtains one electron (−0.84 for the *cis* form and −0.75 for the *trans* form), which is increased to −1.0 and −1.3 for the low-coordination anion sites on the edges and corners, respectively (see Table S2 in SI). Such an electron transfer from the surface anion sites to the NO dimer reinforces the bond strength of N–N, while weakens the N–O bond simultaneously, which then triggers the direct dissociation channel from $N_2O_3^{2-}$ into $N_2O$ as described in the next section.

**Table 2** The adsorption energies $\Delta H_{ad}$ (kcal/mol)[a] for a NO dimer adsorbed on the surface anion sites ($O_s$) of BaO[b]

| Adsorption geometry | Terrace | Edge | Corner |
|---|---|---|---|
| *cis*-$N_2O_3^{2-}$ (**2**) | −41.4 | −58.3 | −89.7 |
| *trans*-$N_2O_3^{2-}$ (**2′**) | −41.0 | −68.5 | −89.9 |

[a] The adsorption energies are calculated according to $\Delta H_{ad} = H_{tot}^{clus+(NO)_2} - H_{tot}^{clus} - 2 * H_{tot}^{NO}$

[b] The corresponding adsorption configurations are illustrated in Fig. 3

The adsorption energies of the NO dimer on the terrace as well as edge and corner anion sites are summarized in Table 2. On the terrace sites, the stability of the *cis*- and *trans*-$N_2O_3^{2-}$ is similar with an exothermicity of ~41 kcal/mol with respect to two free NO molecules. On the low-coordination anion sites, the $N_2O_3^{2-}$ species are calculated to be more stable. On the edge sites, formations of the *cis*- and *trans*-$N_2O_3^{2-}$ species are exothermic by 58.3 and 68.5 kcal/mol, respectively, while on the corner sites, both *cis*- and *trans*-$N_2O_3^{2-}$ show a large stability with the adsorption energy of about −90 kcal/mol.

The formation of the stable $N_2O_3^{2-}$ species represents the N–N bond formation which should be identified by the IR spectra. Previously, the bands around 1,310 and 1,375 $cm^{-1}$ as observed by Prinetto et al. [13] and the peak around 1,380 $cm^{-1}$ as observed by Sedlmair et al. [15] were associated with the N–N stretching in the $N_2O_2^{2-}$ species. This is fairly reasonable if one compares them with the N–N stretching in the $Na_2N_2O_2$ salts, which appear around 1,314 and 1,419 $cm^{-1}$ [80]. However, as listed in Table 3, our calculated N–N stretching frequencies are also around 1,354 $cm^{-1}$ for *cis*-$N_2O_3^{2-}$ and 1,413 $cm^{-1}$ for *trans*-$N_2O_3^{2-}$, even though the corresponding peak appears at much low region of 1,120 $cm^{-1}$ in the $Na_2N_2O_3$ salts [80]. Hence, a band of the same nature may appear at different position on surfaces and in compounds. The present calculations offer a new insight into the assignment of the N–N stretching bands, which may indicate the formation of the $N_2O_3^{2-}$ species on the surfaces.

### 3.3 $N_2O_3^{2-}$ dissociation

The proposed mechanisms for NO decomposition via $N_2O_3^{2-}$ species are presented in Scheme 1. It is initialized by the formation of species **1** ($NO_2^{2-}$) via the adsorption of an NO molecule on the oxygen anion sites, then followed by the coupling of the second gas-phase NO to **1** to produce **2** (*cis*-$N_2O_3^{2-}$) or **2′** (*trans*-$N_2O_3^{2-}$), depending on the orientation. The dissociation of species **2** (**2′**) occurs through the cleavage of one of the N–O bonds, leading to the formation of species **3**(**3′**), which corresponds to a $N_2O_2^{2-}$ species plus a peroxide species of $O_2^{2-}$ on the surface. A rearrangement of $N_2O_2^{2-}$ generates the lattice oxygen anion with an electrostatically adsorbed $N_2O$ as in **4**(**4′**). The final step is envisioned as the desorption of $N_2O$, leaving the peroxide on the surfaces.

The transition states and intermediates in the dissociation processes on the terrace sites are presented in Figs. 4 and 5, respectively. The corresponding enthalpy changes, defined in Scheme 1, are summarized in Table 4, which are depicted in Fig. 6. The detailed geometric parameters are given in Tables S3 and S4 in SI.

**Table 3** Calculated vibrational frequencies ($cm^{-1}$) for the adsorption species on the BaO terrace sites

The experimental IR spectra for free molecules[a] , ions in compounds[a] and the NO/BaO/$Al_2O_3$ system[b] are also listed for comparison

[a] Data from Ref. [63] for free molecules and ions in compounds

[b] From IR spectra for NO/BaO/$Al_2O_3$ at room temperature [13]

[c] Assigned to the surface $N_2O_2^{2-}$ species [13]

[d] Assigned to the surface $NO_2^-$ species [13]

[e] Assigned to the surface $NO_3^-$ species [13]

| | $\nu_1$ (N–N stretch) | $\nu_2$ (N–O stretch) |
|---|---|---|
| *Calc.* | | |
| NO adsorption (1) | – | 1,317 |
| Two NO adsorption (1′) | – | 1,313 (symmetry), 1,309 (asymmetry) |
| *cis*-$N_2O_3^{2-}$ (2) | 1,354 | 1,410 |
| *trans*-$N_2O_3^{2-}$ (2′) | 1,413 | 1,282 |
| *trans*-$N_2O_2^{2-}$ (3) | 1,279 | 1,417 |
| *cis*-$N_2O_2^{2-}$ (3′) | 1,380 | 1,241 |
| adsorbed $N_2O$ (4) | 1,884 | 1,118 |
| adsorbed $N_2O$ (4′) | 2,378 | 1,315 |
| *Expt.* | | |
| NO[a] | – | 1,876 |
| $N_2O$[a] | 2,224 | 1,285 |
| $NO_2^-$ [a] | – | 1,260 (asymmetry), 1,330 (sym.) |
| $NO_3^-$ [a] | – | 1,380 (asymmetry), 1,050 (sym.) |
| $N_2O_3^{2-}$[a] | 1,120, 1,100 | 1,400, 1,380 (asymmetry $NO_2$), 1,280 (sym. $NO_2$), 980, 970 |
| *cis*-$N_2O_2^{2-}$[a] | 1,314 | 1,057 (sym.), 857 (asymmetry) |
| *trans*-$N_2O_2^{2-}$[a] | 1,419 | 1,120 (sym.), 1,030 (asymmetry) |
| NO/BaO/$Al_2O_3$[b] | 1375[c], 1310[c] | 1,050–950[c], 1,220–1,180[d], 1,600[d], 1470[e] |

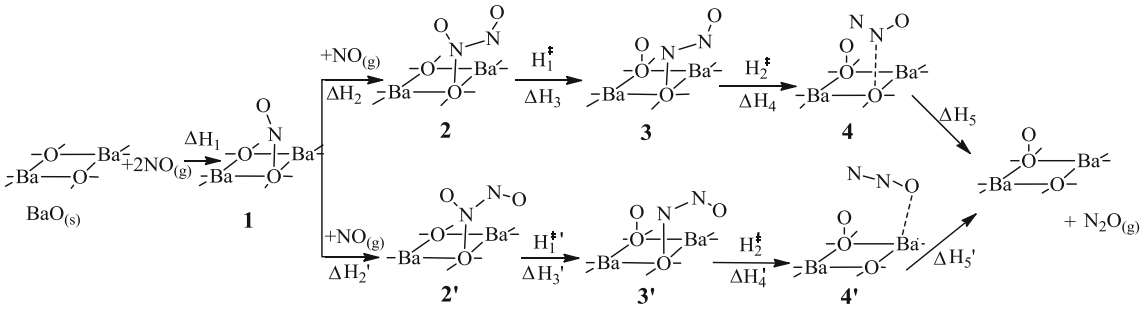


**Scheme 1** The possible reaction pathways of NO decomposition on BaO (100) surfaces

We first look at the dissociation of *cis*-$N_2O_3^{2-}$ (**2**) on the terrace sites of the BaO surfaces. A transition state (**TS1** in Fig. 4) is located, which clearly indicates the cleavage of a N–O bond and the formation of an $O_s$–O bond. The as-formed **3** is lower lying by 12.5 kcal/mol on the terrace with respect to **2**. Notably in **3**, a surface peroxide species ($O_2^{2-}$) can be envisioned. This is characterized by an $O_s$−O bond length of 1.523 Å as shown in Table S4 in SI, which approaches to the bond length of a standard peroxo species (1.49 ± 0.02 Å, [81]). Meanwhile, a relatively short $O_s$–N bond with the distance of 1.46 Å is maintained, which is accompanied by a N–N bond of 1.30 Å (See Table S4). The latter compares well with the N–N distance in the standard $N_2O_2^{2-}$ species (1.27 Å [80]). We thus assign this entity as a surface $N_2O_2^{2-}$ species. It has to be noted that the transformation from the $N_2O_3^{2-}$ (**2**) species to the $N_2O_2^{2-}$ species in **3** on the terrace sites needs to surmount an intrinsic reaction barrier of 52.8 kcal/mol. Hence, it is necessary to increase the reaction temperature to facilitate the $N_2O_2^{2-}$ formation.

Thereafter, **3** experiences a geometry relaxation and leads to the formation of **4** by overcoming a reaction barrier of 25.0 kcal/mol on the terrace sites via **TS2**. The geometrical features of **TS2** (see Fig. 4 and Table S3 in SI) clearly indicate the $N_2O$ formation with the N–N bond length of 1.18 Å and the N–O length of 1.28 Å, which is accompanied by a strongly elongated $O_s$–N bond (2.11 Å). In **4** on the terrace, the as-formed $N_2O$ is found to be adsorbed on the surface anion site via the middle N atom (see Fig. 5). There is still a sizable charge transfer from $O_s$ to $N_2O$ (0.57 as listed in Table S4 in SI), leading to a NNO which is bent by 138°, instead of adopting a linear NNO structure as in free $N_2O$. We find that there is an energy cost of 10.2 kcal/mol from **3** to **4**.

Now, we look at the dissociation of *trans*-$N_2O_3^{2-}$ (**2′**) on the terrace site of the BaO surfaces. As shown in Fig. 6, the dissociation route is basically the same as that of the *cis*-$N_2O_3^{2-}$ species. The whole energetics is more favorable, as compared to the dissociation of *cis*-$N_2O_3^{2-}$ (**2**), due to a more favorable electrostatic interaction between the trans-configurations of the ad-species and the surfaces. Indeed, **TS1′** is 5.7 kcal/mol lower lying than **TS1**, while **TS2′** is 17.3 kcal/mol more stable than **TS2**. The geometry features of $N_2O$ in **4′** are shown in Fig. 5 and Table S4 in SI. The adsorbed $N_2O$ is nearly linear (177°), which is nearly charge neutral. Hence, one may consider the $N_2O_2^{2-}$ species in **3**(**3′**) as a chemisorbed $N_2O$ on the surface, the $N_2O$ moiety in **4**, in particular **4′,** shall be considered as a physisorbed species.

The energy profiles show that the dissociation of $N_2O_3^{2-}$ on the terrace sites is characterized by a large barrier encountered at **TS1**(**TS1′**) for the formation of $N_2O_2^{2-}$, followed by a small barrier at **TS2**(**TS2′**) which eventually leads to the $N_2O$ formation. Hence, if the first barrier can be overcome, e.g., with the help of other components in the catalyst at high temperature, it is possible that NO undergoes direct dissociation over BaO as it was observed in the BaO/MgO [31] or BaO/$Y_2O_3$ [35] system. On the other hand, we conclude that NO initially adsorbs on BaO as $NO_2^{2-}$ and $N_2O_3^{2-}$ at low temperature in no presence of $O_2$ and Pt.

We have also examined the dissociation of $N_2O_3^{2-}$ on the low-coordination sites of the BaO surfaces. The corresponding enthalpy changes are also summarized in Table 4 and depicted in Fig. 6. The detailed geometric parameters may be found in SI. Even though the intrinsic barriers to transform $N_2O_3^{2-}$ (**2** or **2′**) to $N_2O_2^{2-}$ (**3** or **3′**) remain to be high (54.8–62.1 kcal/mol), the strong basicity of the low-coordination sites is found to significantly enhance the stabilities of the $N_2O_3^{2-}$ species, which actually brings the transition states (**TS1** or **TS1′**) lower (by −3.5 to −30.0 kcal/mol) than the entrance level (**BaO + 2 NO**), rendering these dissociation processes having no apparent barriers. Therefore, the $N_2O_3^{2-}$ dissociation on the low-coordination surface sites is predicted to be easier than that on the terrace sites. In addition, the increased basicity from terrace to edge to corner sites has significantly increased the amount of the change transfer from 0.57 to 0.90 to 1.34 from the surfaces to the $N_2O$ moiety (see Table S4 in SI), which stabilizes the bent $N_2O$ in **4**. In fact, both **TS2** and **TS2′** are found to connect with **4** on the low-coordination sites.

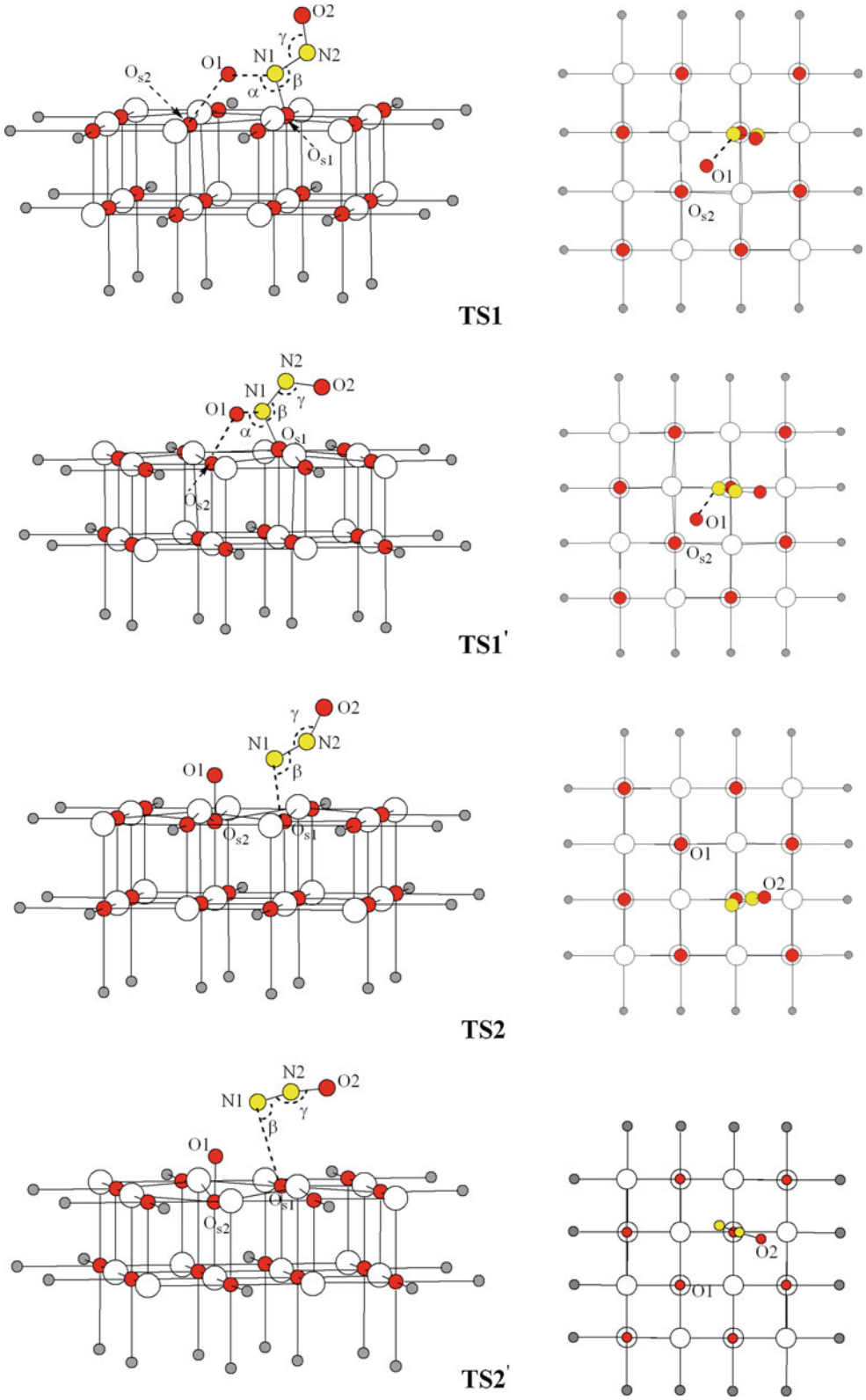


**Fig. 4** Optimized transition state (TS) structures on the terrace sites of BaO (*left*, *side view*; *right*, *top view*): TS1 and TS1′ correspond to the dissociation of *cis*-$N_2O_3^{2-}$ and *trans*-$N_2O_3^{2-}$, respectively, to form *cis*-$N_2O_2^{2-}$ and *trans*-$N_2O_2^{2-}$; TS2 and TS2′ correspond to the dissociation of *cis*-$N_2O_2^{2-}$ and *trans*-$N_2O_2^{2-}$, respectively, to form physisorbed $N_2O$. *Color codes*: *yellow spheres* for N, *red spheres* for O, *large white spheres* for Ba and *small gray spheres* for TIPs. Geometric details may be found in supporting information (SI)

The calculated N–N–O asymmetric stretching mode in **4** appears at 1,884 $cm^{-1}$ on the terrace sites, 1,756 $cm^{-1}$ on the edge sites, and 1,570 $cm^{-1}$ on the corner sites, which are comparable to the experimental band observed around 1,780 $cm^{-1}$ for NO adsorbed on $BaO/Y_2O_3$ [35]. On the other hand, the calculated N–N–O asymmetric vibration

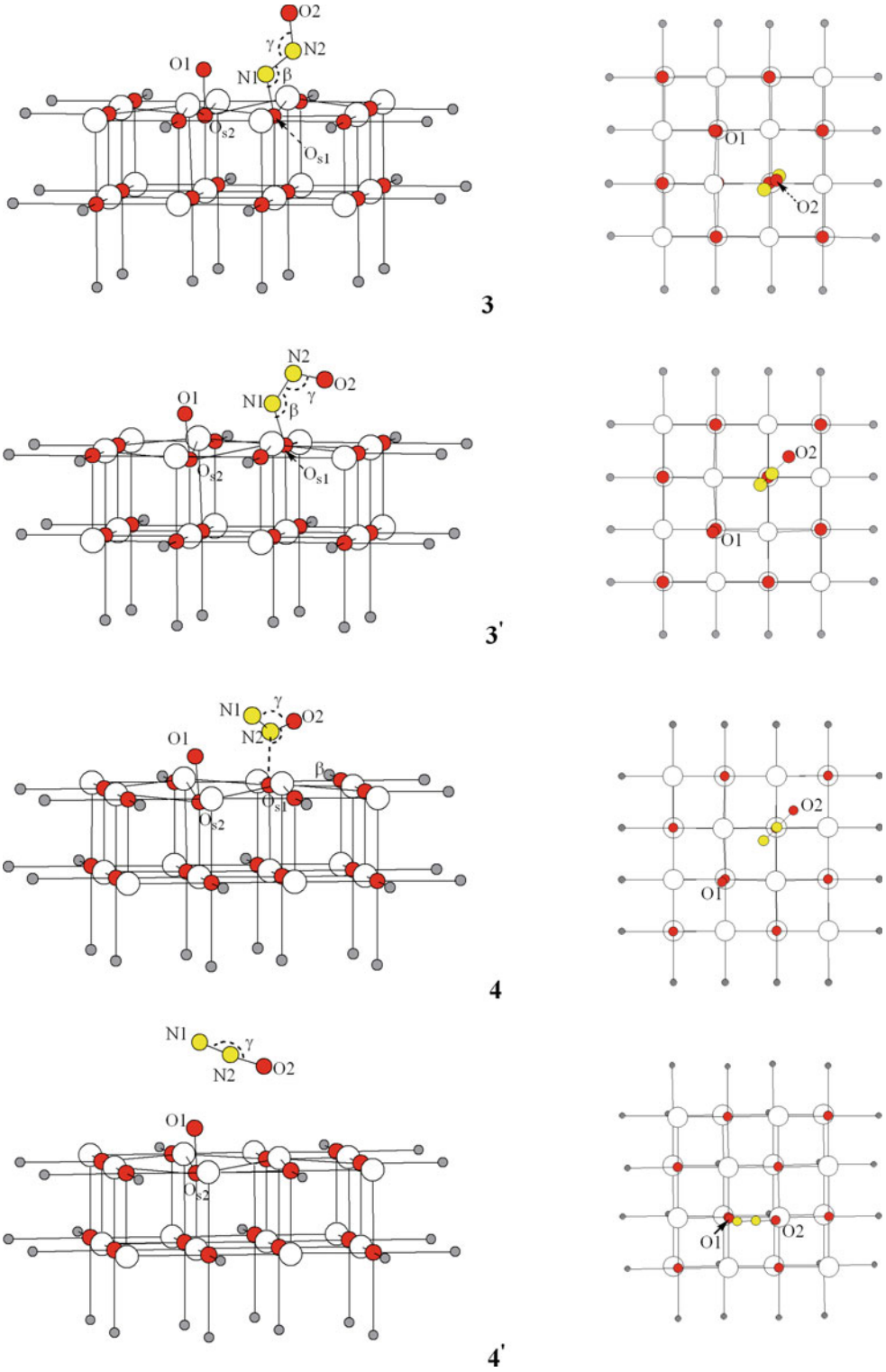


**Fig. 5** Optimized structures on the terrace sites of BaO (*left*, *side view*; *right*, *top view*): **3** and **3′** correspond to *trans*-$N_2O_2^{2-}$ and *cis*-$N_2O_2^{2-}$, respectively, plus a surface $O_2^{2-}$ species. **4** and **4′** correspond to a physically adsorbed $N_2O$ plus a surface $O_2^{2-}$ species. *Color codes*: *yellow spheres* for N, *red spheres* for O, *large white spheres* for Ba and *small gray spheres* for TIPs. Geometric details may be found in supporting information (SI)

**Table 4** Reaction enthalpy changes and intrinsic activation barriers (kcal/mol) for reaction paths defined in Scheme 1

| | $\Delta H_1$ | $\Delta H_2$ | $H_1^{\ddagger}$ | $\Delta H_3$ | $H_2^{\ddagger}$ | $\Delta H_4$ | $\Delta H_5$ | $\Delta H_2'$ | $H_1^{\ddagger\prime}$ | $\Delta H_3'$ | $H_2^{\ddagger\prime}$ | $\Delta H_4'$ | $\Delta H_5'$ |
|---|---|---|---|---|---|---|---|---|---|---|---|---|---|
| Terrace | −28.4 | −13.0 | 52.8 | −12.5 | 25.0 | 10.2 | −0.6 | −12.6 | 47.7 | −14.8 | 7.7 | 6.1 | 5.5 |
| Edge | −38.8 | −19.5 | 54.8 | −2.7 | 28.1 | 2.0 | 16.6 | −29.7 | 58.3 | −5.7 | 22.9 | – | 5.6 |
| Corner | −46.1 | −43.6 | 62.1 | 9.1 | 45.1 | 5.7 | 33.8 | −43.8 | 59.9 | 1.7 | 36.7 | – | 5.2 |

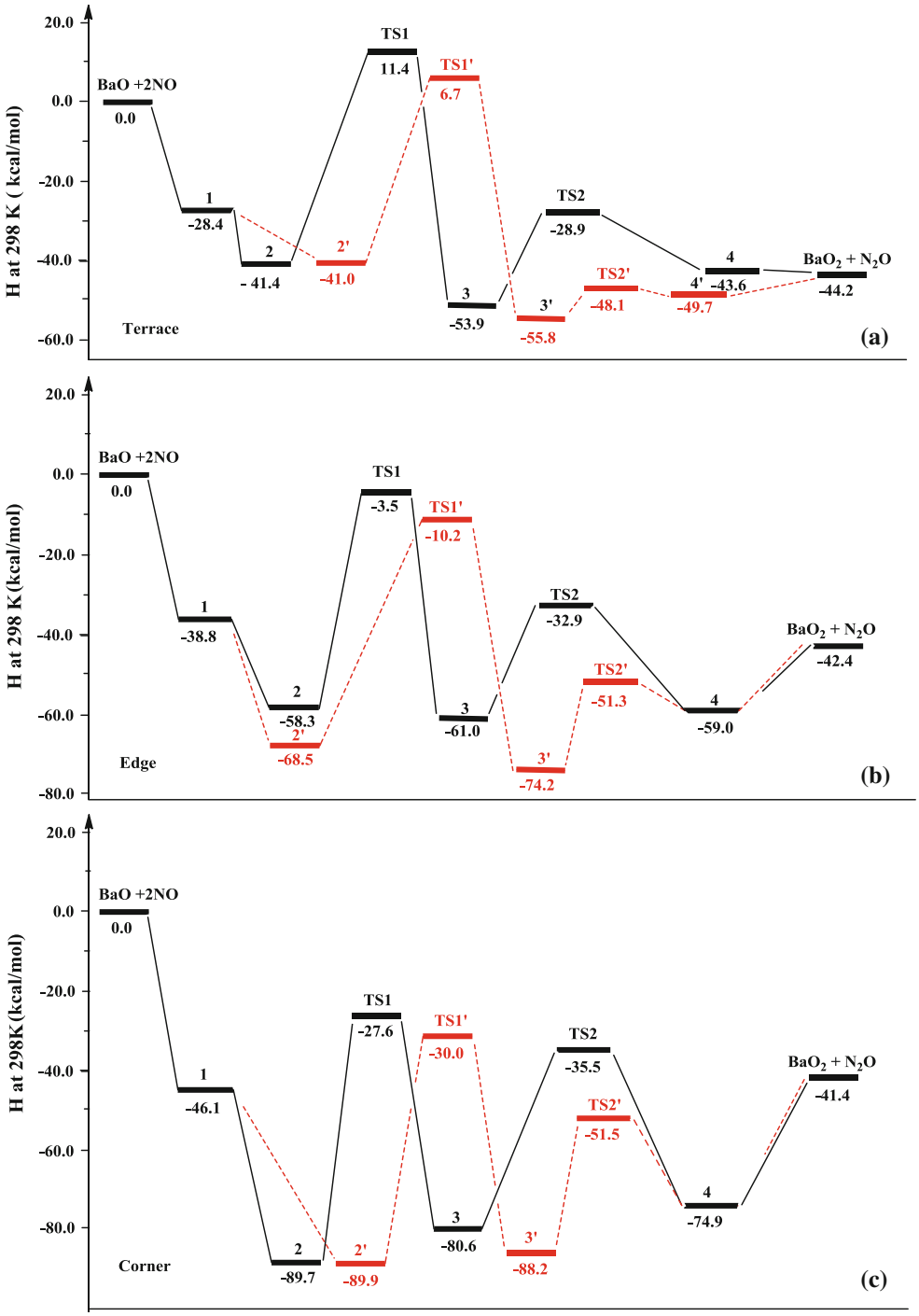


**Fig. 6** Energy profiles for NO adsorption and transformations on the **a** terrace **b** edge and **c** corner sites of BaO surfaces. The reaction schemes are defined in Scheme 1. The profiles bifurcate at the formation of *cis*- and *trans*-$N_2O_3^{2-}$ (**2** and **2′**, respectively) species

frequency in **4′** is around 2,377 $cm^{-1}$ on the terrace. This is in good agreement with the experimentally observed band at 2,350 $cm^{-1}$ for the NO/BaO/$Y_2O_3$ system [35] and is also close to that in the free $N_2O$ [81]. All in all, our calculations support that the peaks around 1,780 and 2,350 $cm^{-1}$ are from $N_2O$, in accordance with the assignments reported by Ishihara et al. [35] for the NO/BaO/$Y_2O_3$ systems.

It is particularly interesting to compare the calculated N–N stretching spectra in $N_2O_2^{2-}$ with those observed in experiments for the NSR systems [13, 15]. In fact, the calculated bands are around 1,279 and 1,380 $cm^{-1}$, which compare fairly well with the bands centered at 1,310 and 1,375 $cm^{-1}$ as observed by Prinetto et al. [13] and 1,380 $cm^{-1}$ as observed by Sedlmair et al. [15], which were assigned to the $N_2O_2^{2-}$ species. Hence, our calculations support that the surface $N_2O_2^{2-}$ will also contribute to the strong peaks observed around 1,310–1,380 $cm^{-1}$ if the barriers from **TS1** (**TS1′**) can be effectively overcome.

## 4 Concluding remarks

It is commonly reported that conversion of NO to $NO_2$ over noble metals is required for $NO_x$ storage, while NO reduction also occurs over noble metals [6–10]. Due to the complexity of the NSR system, however, the understanding of the single role of BaO is still incomplete. Some reports suggested that BaO is inactive toward NO [10, 23], while some others showed that NO trapping is already significant on BaO alone [11, 12]. The present work presents a theoretic study on NO adsorption and reaction on BaO, trying to clarify this issue.

The XPS experiments by Schmitz and Baird have highlighted the importance of BaO [12]. Considering that $NO_x$ in exhaust gas is primarily NO and that the surface area of the oxides far exceeds that of the dispersed noble metals, they proposed a unique mechanism that the initial trapping is dominated by the molecular adsorption of NO on BaO to form a nitrite-like ($NO_2^-$) ad-species [12]. Our calculations support this view of molecular adsorption of NO on BaO, although we are inclined to favor the picture that NO adsorbs on the surface anion sites to form $NO_2^{2-}$, which is in agreement with the results from the EPR study of NO on the low-coordination sites on MgO and CaO surfaces [78, 79].

A key theoretical concept in understanding the interaction between $NO_x$ and the basic metal oxides is a pairwise, cooperative adsorption mechanism [36], which is shown not to be effective for the (NO, NO) pair on BaO. At high NO pressure, dimerization is favored, in particular, on the low-coordination anion sites to form $N_2O_3^{2-}$. Although the surface $N_2O_2^{2-}$ species is a commonly assumed key intermediate in the NSR system, our calculations suggest that it has to surmount an intrinsic barrier of 50 kcal/mol for its formation. Notably, the high basicity of the low-coordination anion sites on BaO will bring the corresponding transition states below the entrance level, which shall facilitate the $N_2O_2^{2-}$ formation.

Our calculations show that if this barrier can be overcome, the transformation from the surface $N_2O_2^{2-}$ species to $N_2O$ is facile. Indeed, the formation of $N_2O$ has been observed in some NSR and related systems [10, 25, 29, 33, 35]. It is well known that $N_2O$ can be further reduced to $N_2$ on the metal oxide surfaces [82], which has been characterized with embedded cluster models for BaO(100) [83]. Hence, it is envisioned that BaO not only plays a role in NO storage, but also affects in a way the NO reduction.

The net reaction studied in the present work may be summarized as

$$2\,NO + O^{2-}_{(s)} \longrightarrow N_2O + O^{2-}_{2\,(s)} \qquad (11)$$

It would be anticipated that the surface peroxide species may, in turn, serve as an active oxidant for further NO storage to form $NO_2^-$ and $NO_3^-$ [13, 15, 21, 31, 40], which deserves a detailed investigation.

Some calculated vibrational frequencies of the intermediates are summarized in Table 3, which shall be helpful to assign the bands observed in the experiments. In Table 3, we have also listed the experimental results for the corresponding free molecules (NO and $N_2O$) and ions ($NO_2^-$, $NO_3^-$, $N_2O_3^{2-}$ and $N_2O_2^{2-}$) in compounds [80]. These are the reference numbers with which the IR spectra for surface species in the NSR systems are compared [84]. One has to note that coordination on surfaces will change the peak positions dramatically and the bands from various $N_xO_y^{\delta}$ species overlap. All of these have made the assignment of the corresponding vibrational spectra complicated and controversial. Indeed, the surface $NO_2^{2-}$ and $N_2O_3^{2-}$ species provide an alternative explanation of the experimentally observed IR spectra which were previously assigned to the nitrite/nitrate and hyponitrite species [13, 15].

Further investigation is necessary to see how different reactant gases adsorb, react and even compete against each other for a specific active site, and how the interplay between different components in a real NSR catalyst will change the energy profiles or even change the reaction mechanisms.

**Acknowledgments** This work was supported by the Ministry of Science and Technology (2013CB834606, 2011CB808505), National Natural Science Foundation of China (21133004), and the Natural Science Foundation of Shandong Province (ZR2010BM041), China.

## References

1. Epling WS, Campbell LE, Yezerets A, Currier NW, Parks JE II (2004) Overview of the fundamental reactions and degradation mechanisms of NOx storage/reduction catalysts. Catal Rev Sci Eng 46:163–245
2. Liu ZM, Woo SI (2006) Recent advances in catalytic DeNOx science and technology. Catal Rev Sci Eng 48:43–89
3. Roy S, Baiker A (2009) NOx storage–reduction catalysis: from mechanism and materials properties to storage–reduction performance. Chem Rev 109:4054–4091
4. Granger P, Parvulescu VI (2011) Catalytic NOx abatement systems for mobile sources: from three-way to lean burn after-treatment technologies. Chem Rev 111:3155–3207
5. Szanyi J, Yi CW, Mudiyanselage K, Kwak JH (2013) Understanding automotive exhaust catalysts using a surface science approach: model NOx storage materials. Top Catal 56:1420–1440
6. Takahashi N, Shinjoh H, Iijima T, Suzuki T, Yamazaki K, Yokota K, Suzuki H, Miyoshi N, Matsumoto S, Tanizawa T, Tanaka T, Tateishi S, Kasahara K (1996) The new concept 3-way catalyst for automotive lean-burn engine: NOx storage and reduction catalyst. Catal Today 27:63–69
7. Matsumoto S (1996) DeNOx catalyst for automotive lean-burn engine. Catal Today 29:43–45
8. Bögner W, Krämer M, Krutzsch B, Pischinger S, Voigtländer D, Wenninger G, Wirbeleit F, Brogan MS, Brisley J, Webster DE (1995) Removal of nitrogen oxides from the exhaust of a lean-tune gasoline engine. Appl Catal B Environ 7:153–171

9. Lietti L, Forzatti P, Nova I, Tronconi E (2001) NOx storage reduction over Pt-Ba/$\gamma$–$Al_2O_3$ catalyst. J Catal 204:175–191
10. Fridell E, Skoglundh M, Westerberg B, Johansson S, Smedler G (1999) NOx storage in barium-containing catalysts. J Catal 183:196–209
11. Muncrief RL, Khanna P, Kabin KS, Harold MP (2004) Mechanistic and kinetic studies of NOx storage and reduction on Pt/BaO/$Al_2O_3$. Catal Today 98:393–402
12. Schmitz PJ, Baird RJ (2002) NO and $NO_2$ adsorption on barium oxide: model study of the trapping stage of NOx conversion via lean NOx traps. J Phys Chem B 106:4172–4180
13. Prinetto F, Ghiotti G, Nova I, Lietti L, Tronconi E, Forzatti P (2001) FT-IR and TPD investigation of the NOx storage properties of BaO/$Al_2O_3$ and Pt-BaO/$Al_2O_3$ catalysts. J Phys Chem B 105:12732–12745
14. Fridell E, Persson H, Olsson L, Westerberg B, Amberntsson A, Skoglundh M (2001) Model studies of NOx storage and sulphur deactivation of NOx storage catalyst. Top Catal 16(17): 133–137
15. Sedlmair C, Seshan K, Jentys A, Lercher JA (2003) Elementary steps of NOx adsorption and surface reaction on a commercial storage–reduction catalyst. J Catal 214:308–316
16. Fridell E, Persson H, Westerberg B, Olsson L, Skoglundh M (2000) The mechanism for NOx storage. Catal Lett 66:71–74
17. Westerberg B, Fridell E (2001) A transient FTIR study of species formed during NOx storage in the Pt/BaO/$Al_2O_3$ system. J Mol Catal A Chem 165:249–263
18. Olsson L, Persson H, Fridell E, Skoglundh M, Andersson B (2001) A kinetic study of NO oxidation and NOx storage on Pt/$Al_2O_3$ and Pt/BaO/$Al_2O_3$. J Phys Chem B 105:6895–6906
19. Mahzoul H, Brilhac JF, Gilot P (1999) Experimental and mechanistic study of NOx adsorption over NOx trap catalysts. Appl Catal B Environ 20:47–55
20. Su Y, Amiridis MD (2004) In situ FTIR studies of the mechanism of NOx storage and reduction on Pt/Ba/$Al_2O_3$ catalysts. Catal Today 96:31–41
21. Kabin KS, Khanna P, Muncrief RL, Medhekar W, Harold MP (2006) Monolith and TAP reactor studies of NOx storage on Pt/BaO/$Al_2O_3$: elucidating the mechanistic pathways and roles of Pt. Catal Today 114:72–85
22. Desikusumastuti A, Happel M, Dumbuya K, Staudt T, Laurin M, Gottfried JM, Steinrück H-P, Libuda J (2008) Modeling NOx storage materials: on the formation of surface nitrites and nitrates and their identification by vibrational spectroscopy. J Phys Chem C 112:6477–6486
23. Tsami A, Grillo F, Bowker M, Nix RM (2006) Model NSR catalysts: fabrication and reactivity of barium oxide layers on Cu(111). Surf Sci 600:3403–3418
24. Szanyi J, Kwak JH, Hanson J, Wang C, Szailer T, Peden CHF (2005) Changing Morphology of BaO/$Al_2O_3$ during $NO_2$ Uptake and Release. J Phys Chem B 109:7339–7344
25. Hess C, Lunsford JH (2002) Mechanism for $NO_2$ storage in barium oxide supported on magnesium oxides studies by in situ Raman spectroscopy. J Phys Chem B 106:6358–6360
26. Chi Y, Chuang SSC (2003) Infrared and TPD studies of nitrates adsorbed on $Tb_4O_7$, $La_2O_3$, BaO, and MgO/$\gamma$–$Al_2O_3$. J Phys Chem B 107:1982–1987
27. Cheng L, Ge Q (2008) Effect of BaO morphology on NOx abatement: $NO_2$ interaction with Unsupported and $\gamma$–$Al_2O_3$-supported BaO. J Phys Chem C 112:16924–16931
28. Cheng L, Ge Q (2007) Effect of $\gamma$–$Al_2O_3$ substrate on $NO_2$ interaction with supported BaO clusters. Surf Sci 601:L65–L68
29. Burch R, Fornasiero P, Watling TC (1998) Kinetics and mechanism of the reduction of NO by n-Octane over Pt/$Al_2O_3$ under lean-burn conditions. J Catal 176:204–214
30. Broqvist P, Gronbeck H, Fridell E (2004) Characterization of NOx species adsorbed on BaO: experiment and theory. J Phys Chem B 108:3523–3530
31. Xie S, Mestl G, Rosynek MP, Lunsford JH (1997) Decomposition of nitric oxide over barium oxide supported on magnesium oxide. 1. Catalytic results and in situ Raman spectroscopic evidence for a barium–nitro intermediate. J Am Chem Soc 119:10186–10191
32. Klingenberg B, Vannice MA (1999) NO adsorption and decomposition on $La_2O_3$ studied by DRIFTS. Appl Catal B Environ 21:19–33
33. Wang Y, Jacobi K, Ertl G (2003) Interaction of NO with the Stoichiometric $RuO_2$(110) Surface. J Phys Chem B 107:13918–13924
34. Rodriguez JA, Azad S, Wang L-Q, García J, Etxeberria A, Gonzalez L (2003) Electronic and chemical properties of mixed-metal oxides: adsorption and reaction of NO on SrTiO(100). J Chem Phys 118:6562–6571
35. Ishihara T, Goto K (2011) Direct decomposition of NO over BaO/$Y_2O_3$ catalyst. Catal Today 164:484–488
36. Schneider WF (2004) Qualitative differences in the adsorption chemistry of acidic ($CO_2$, SOx) and amphiphilic (NOx) species on the alkaline earth oxides. J Phys Chem B 108:273–282
37. Tutuianu M, Inderwildi OR, Bessler WG, Warnatz J (2006) Competitive adsorption of NO, $NO_2$, $CO_2$, and $H_2O$ on BaO(100): a quantum chemical study. J Phys Chem B 110:17484–17492
38. Marta Branda M, Valentin CD, Pacchioni G (2004) NO and $NO_2$ adsorption on terrace, step, and corner sites of the BaO Surface from DFT Calculations. J Phys Chem B 108:4752–4758
39. Ferullo RM, Fuente SA, Branda MM, Castellani NJ (2007) Theoretical study of $N_2O_2$ interaction with BaO(1 0 0) surface. J Mol Struct THEOCHEM 818:57–64
40. Zubieta C, Castellani NJ, Ferullo RM (1009) High reactivity of nitric oxide with peroxo groups on BaO particles DFT calculations. Comput Theor Chem 2013:1–7
41. Lu X, Xu X, Wang N, Zhang Q (1999) Adsorption and decomposition of NO on magnesium oxide: a quantum chemical study. J Phys Chem B 103:5657–5664
42. Valentin CD, Pacchioni G, Abbet S, Heiz U (2002) Conversion of NO to $N_2O$ on MgO Thin Films. J Phys Chem B 106:7666–7673
43. Valentin CD, Pacchioni G, Bernasconi M (2006) Ab Initio molecular dynamics simulation of NO reactivity on the CaO(001) Surface. J Phys Chem B 110:8357–8362
44. Pacchioni G, Ricart JM, Illas F (1994) Ab initio cluster model calculations on the chemisorption of $CO_2$ and $SO_2$ probe molecules on MgO and CaO (100) Surfaces. A theoretical measure of oxide basicity. J Am Chem Soc 116:10152–10158
45. Beck AD (1988) Density-functional exchange-energy approximation with correct asymptotic behavior. Phys Rev A 38:3098–3100
46. Becke AD (1993) Density functional thermochemistry. III. The role of exact exchange. J Chem Phys 98:5648–5652
47. Slater JC (1974) Quantum theory of molecules and solids, vol 4. McGraw-Hill, New York
48. Vosko SH, Wilk L, Nusair M (1980) Accurate spin-dependent electron liquid correlation energies for local spin density calculations: a critical analysis. Can J Phys 58:1200–1211
49. Stephens PJ, Devlin FJ, Chabalowski CF, Frisch MJ (1994) Ab initio calculation of vibrational absorption and circular dichroism spectra using density functional force fields. J Phys Chem 98:11623–11627
50. Lee C, Yang W, Parr RG (1988) Development of the Colle–Salvetti correlation-energy formula into a functional of the electron density. Phys Rev B 37:785–789
51. Liu W-G, Goddard WA III (2012) First-principles study of the role of interconversion between $NO_2$, $N_2O_4$, cis-ONO–NO, and *trans*-ONO–NO in chemical processes. J Am Chem Soc 134:12970–12978

52. Xu X, Lu X, Wang NQ, Zhang QE (1995) Charge-Consistency Modelling of CO/NiO(100) Chemisorption System. Chem Phys Lett 235:541–547
53. Xu X, Lu X, Wang NQ, Zhang QE (2004) Cluster modeling of chemisorption and reactions on metal oxide surfaces. Acta Phys Chim Sin 20:1045–1054
54. Xu X, Nakatsuji H, Lu X, Ehara M, Cai Y, Wang NQ, Zhang QE (1999) On the cluster modeling of metal oxides: case study of MgO and CO/MgO adsorption system. Theor Chem Acc 102:170–179
55. Lu X, Xu X, Wang NQ, Zhang QE, Ehara M, Nakatsuji H (1998) Cluster modeling of metal oxides: how to cut out a cluster? Chem Phys Lett 291:445–452
56. Xu X, Nakatsuji H, Ehara M, Lu X, Wang NQ, Zhang QE (1998) Cluster modeling of metal oxides: the influence of the surrounding point charges on the embedded cluster. Chem Phys Lett 292:282–288
57. Wyckoff RWG (1963) Crystal structures, 2nd edn. Interscience, New York
58. Winter NW, Pitzer RM, Temple DK (1987) Theoretical study of a Cu+ ion impurity in a NaF host. J Chem Phys 86:3549–3556
59. Nygren MA, Petterson LG, Barandiaran Z, Seijo L (1994) Bonding between CO and the MgO(001) surface: a modified picture. J Chem Phys 100:2010–2018
60. Wadt WR, Hay PJ (1985) Ab initio effective core potentials for molecular calculations. Potentials for main group elements Na to Bi. J Chem Phys 82:284–288
61. Wadt WR, Hay PJ (1985) Ab initio effective core potentials for molecular calculations. Potentials for K to Au including the outermost core orbitals. J Chem Phys 82:299–310
62. Frisch MJ et al (2003) Gaussian03. Gaussian Inc., Pittsburgh
63. Hehre WJ, Ditchfield R, Pople JA (1972) Self-consistent molecular-orbital methods. XII. Further extensions of Gaussian-type basis sets for use in molecular-orbital studies of organic molecules. J Chem Phys 56:2257–2261
64. Miletic M, Gland JL, Hass KC, Schneider WF (2003) First-principles characterization of NOx adsorption on MgO. J Phys Chem B 107:157–163
65. Lu N-X, Fu G, Xu X, Wan HL (2008) Mechanisms for $O_2$ dissociation over the BaO (100) surface. J Chem Phys 128:034702 1–9
66. Grönbeck H, Broqvist P, Panas I (2006) Fundamental aspects of NOx adsorption on BaO. Surf Sci 600:403–408
67. Valentin CD, Figini A, Pacchioni G (2004) Adsorption of NO and NO2 on terrace and step sites and on oxygen vacancies of the CaO(001) Surface. Surf Sci 556:145–158
68. Lu X, Xu X, Wang NQ, Zhang QE (1999) $N_2O$ decomposition on MgO and Li/MgO catalysts: a quantum chemical study. J Phys Chem B 103:3373–3379
69. Lu X, Xu X, Wang NQ, Zhang QE, Ehara M, Nakatsuji H (1999) Heterolytic adsorption of $H_2$ on ZnO(100) surface: an ab initio SPC cluster model study. J Phys Chem B103:2689–2695
70. Lu X, Xu X, Wang NQ, Zhang QE (2000) Chemisorption-induced oligomerization of CO over strongly basic sites of MgO solid: a hybrid B3LYP study. J Phys Chem B104:10024–10031
71. Fu G, Xu X, Lu X, Wan HL (2005) Mechanisms of initial propane activation on molybdenum oxides: a density functional theory study. J Phys Chem B 109:6416–6421
72. Fu G, Xu X, Lu X, Wan HL (2005) Mechanisms of methane activation and transformation on molybdenum oxide based catalysts. J Am Chem Soc 127:3989–3996
73. Fu G, Xu X, Wan HL (2006) Mechanism of methane oxidation by transition metal oxides: a cluster model study. Catal Today 117:133–137
74. Fu G, Yi XD, Huang CJ, Xu X, Weng WZ, Xia WS, Wan HL (2007) Developing selective oxidation catalysts of light alkanes: from fundamental understanding to rational design. Surf Rev Lett 14:645–656
75. Lu NX, Xu X (2011) Theoretical study of $NO_x/CO_2/H_2O$ adsorption on BaO(001) surface. Acta Chim Sin 69:1264–1268
76. Yuan R-M, Fu G, Xu X, Wan HL (2011) Brønsted-NH4 + mechanism versus nitrite mechanism: new insight into the selective catalytic reduction of NO by NH3. Phys Chem Chem Phys 13:453–460
77. Yuan R-M, Fu G, Xu X, Wan HL (2011) Mechanisms of selective catalytic oxidation (SCO) of ammonia over vanadium oxides. J Phys Chem C 115:21218–21229
78. Lunsford JH (1967) EPR study of NO adsorbed on magnesium oxide. J Chem Phys 46:4347–4351
79. Paganini MC, Chiesa M, Martino P, Giamello E (2002) EPR study of the surface basicity of calcium oxide. 1. The CaO–NO chemistry. J Phys Chem B 106:12531–12536
80. Laane J, Olsen JR (1980) Characterization of nitrogen oxides by vibrational spectroscopy. Prog Inorg Chem 27:465–513
81. Palmer MS, Neurock M (2002) Periodic density functional theory study of the dissociative adsorption of molecular oxygen over $La_2O_3$. J Phys Chem B 106:6543–6547
82. Kapteijn F, Rodriguez-Mirasol J, Moulijn JA (1996) Heterogeneous catalytic decomposition of nitrous oxide. Appl Catal B Environ 9:25–64
83. Karlsen EJ, Pettersson LGM (2002) N2O decomposition over BaO: including effects of coverage. J Phys Chem B 106:5719–5721
84. Hadjiivanov KI (2000) Identification of Neutral and charged NxOy surface species by IR spectroscopy. Catal Rev Sci Eng 42:71–144

Theor Chem Acc (2014) 133:1568
DOI 10.1007/s00214-014-1568-4

REGULAR ARTICLE

# Microwave and infrared spectra of CO–$(pH_2)_2$, CO–$(oD_2)_2$, and mixed CO–$pH_2$–He trimers

**Xiao-Long Zhang · Hui Li · Robert J. Le Roy · Pierre-Nicholas Roy**

Received: 31 May 2014 / Accepted: 19 August 2014 / Published online: 6 September 2014
© Springer-Verlag Berlin Heidelberg 2014

**Abstract** The microwave and infrared spectra of CO–$(pH_2)_2$, CO–$(oD_2)_2$, and CO–$pH_2$–He trimers are predicted by performing exact bound state calculations on the global potential energy surfaces defined as the sum of accurately known two-body $pH_2$–CO or $oD_2$–CO (in Li et al. J Chem Phys 139:164315, 2013), $pH_2$–$pH_2$ or $oD_2$–$oD_2$ (in Patkowski et al. J Chem Phys 129:094304, 2008), and $pH_2$–He pair potentials. A total of four transitions have been reported to date, three in the infrared region, and one in the microwave region, which are in good agreement with our theoretical predictions. Based on selection rules, new transitions for $J \leq 3$ have been predicted, and the corresponding transition intensities at different temperatures are also calculated. These predictions will serve as a guide for new experiments. The weak and tentatively assigned transitions are verified by our calculations. Three-body effects and the quality of the potential are discussed. A reduced-dimension treatment of the $pH_2$ or $oD_2$ rotation has been employed by applying the hindered-rotor averaging technique of Li et al. (J Chem Phys 133:104305, 2010). A technique for displaying the three-dimensional $pH_2$ or $oD_2$ density in the body-fixed frame is used and shows that in the ground state, the two $pH_2$ or two $oD_2$ molecules are localized, while the He's are delocalized.

**Keywords** Microwave spectra · Infrared spectra · CO–$(pH_2)_2$ trimers · CO–$(oD_2)_2$ trimers · CO–$pH_2$–He trimers · Reduced-dimension treatment · Exact bound state calculations · Three-body effects

Dedicated to Professor Guosen Yan and published as part of the special collection of articles celebrating his 85th birthday.

**Electronic supplementary material** The online version of this article (doi:10.1007/s00214-014-1568-4) contains supplementary material, which is available to authorized users.

X.-L. Zhang · H. Li (✉)
Institute of Theoretical Chemistry, State Key Laboratory of Theoretical and Computational Chemistry, Jilin University, 2519 Jiefang Road, Changchun 130023, People's Republic of China
e-mail: Prof_huili@jlu.edu.cn

H. Li · R. J. Le Roy · P.-N. Roy
Department of Chemistry, University of Waterloo, Waterloo, ON N2L 3G1, Canada
e-mail: leroy@uwaterloo.ca

P.-N. Roy
e-mail: pnroy@uwaterloo.ca

## 1 Introduction

At a very low temperature (<2 K), high-resolution infrared or microwave spectra of a single chromophore molecule doped in helium droplets or clusters have provided a unique opportunity to study quantum solvation and microscopic superfluidity [1–20]. Para-hydrogen ($pH_2$) or ortho-deuterium ($oD_2$), like $^4$He atoms, are bosons. Similarly, a chromophore molecule embedded in $pH_2$ or $oD_2$ clusters can also be considered as a possible route to investigate quantum solvation and the superfluidity of $pH_2$ or $oD_2$ [21–30]. Recently, combining experimental measurements and theoretical simulations, superfluid response for $pH_2$ to dopant rotation has been first elucidated in CO2–$(pH_2)_N$ clusters [26]. However, due to localization effects, the superfluid fraction of larger doped hydrogen clusters becomes suppressed. Carbon monoxide (CO) is a gentler probe molecule with much weaker and less anisotropic interaction with $pH_2$ and a relatively large rotational constant. These features lead to a delocalized distribution of $pH_2$ molecules with respect to CO. Persistent molecular

superfluid response to dopant rotation in $CO–(pH_2)_N$ clusters has been observed, and this conclusion is supported by both microwave spectroscopy and the theoretical analysis [31].

An understanding of the experimental spectra at the microscopic scale requires complementary computer simulation studies based on accurate intermolecular potential energy functions. Very recently, two reliable ab initio analytical potential energy surfaces (PESs) for $H_2$–CO dimer have been reported, referred to hereafter $V_{12}$ [32, 33] and $V_{MLRQ}$ [34], respectively. Both PESs explicitly account for the intra-molecular C–O stretch coordinate and allow to describe the infrared spectrum in the region of the fundamental stretching vibration of C–O around 2,143.2712 $cm^{-1}$. The predicted infrared spectra calculated from these two PESs have already been shown to agree extremely well with the experimental spectra of the $pH_2$– and $oH_2$–CO dimers [32–34]. Studies of $CO–(pH_2)_2$ trimer are important for testing the accuracy of pair-wise additive approach by sum of two-body potentials to simulate systems with tens of $pH_2$ molecules, looking for three-body effects, and for testing the validity of quantum Monte Carlo methods for molecular clusters, since comparisons with exact quantum results are possible.

Although a large number of infrared and microwave transitions were recorded and assigned for CO–He and $CO–pH_2$ dimers [33, 35–37], only a few transitions for $CO–(pH_2)_2$, $CO–(oD_2)_2$, and $CO–pH_2$–He trimers were reported, and some weak or tentatively assigned transitions remain to be verified or reassigned [22, 31]. Therefore, reliable theoretical predictions based on exact quantum calculations will provide valuable guidance in confirming or reassigning the measured infrared spectra. Previous work on exact quantum calculations of infrared and microwave spectra for trimer complexes containing one CO, $CO_2$, $N_2O$, and OCS molecule attached to two He atoms have been reported, by Wang and Carrington [38–41] and by Li et al. [42], which yield excellent agreement with experiment observations. Exact rovibrational spectra calculations for the trimer containing a single chromophore molecule doped with two $pH_2$ molecules, such as $CO_2–(pH_2)_2$, were first reported by Li et al. [27] by applying the hindered-rotor averaging technique to treat $pH_2$ as a point-like particle and consequently reduce the dimension of the potential enemy surface. To date, however, exact quantum calculations for the trimer containing a chromophore molecule doped with two $oD_2$ or with mixed $pH_2$ and He have not been reported. Further more, exact quantum calculations for $CO–(pH_2)_N$ clusters have only been limited to $CO–pH_2$ dimer. In the present paper, we extend such exact quantum calculations to the cases of two $pH_2$, or two $oD_2$, or mixed $pH_2$ and He, attached to one CO dopant molecule. The results are used to help assign or confirm the experimental spectra of $CO–(pH_2)_2$, $CO–(oD_2)_2$, and $CO–pH_2$–He.

## 2 Computational methods

### 2.1 Geometry and reduced-dimension treatment

There are six atoms in $CO–(pH_2)_2$ system, and it takes a 12-dimensional (12D) PES to describe the interaction within the system. If we treat linear CO and the two $H_2$ as rigid molecules, taking only the intermolecular coordinates into consideration, there are still nine intermolecular degrees of freedom. The geometry of this complex in which CO is rigidly linear, and can be described naturally using the Jacobi coordinates ($q_1$, $q_2$, $\vartheta_1$, $\vartheta_2$, $\vartheta_3$, $\vartheta_4$, $\varphi$, $\varphi_1$, $\varphi_2$) is shown on the left panel of Fig. 1, where $q_1$ and $q_2$ are the distances from the center of mass of CO to the centers of mass of the two $H_2$ molecules, $\vartheta_1$ and $\vartheta_2$ are the angles between $\mathbf{q_1}$ or $\mathbf{q_2}$ and a vector pointing from atom O to atom C, $\vartheta_3$ and $\vartheta_4$ are the angles between $\mathbf{q_1}$ and a vector pointing from atom $H_2$ to atom $H_1$, and from $\mathbf{q_2}$ to a vector pointing from atom $H_4$ to atom $H_3$, $\varphi$ is the dihedral angle between two planes defined by vector $\mathbf{q_1}$ and $\mathbf{q_2}$ with the

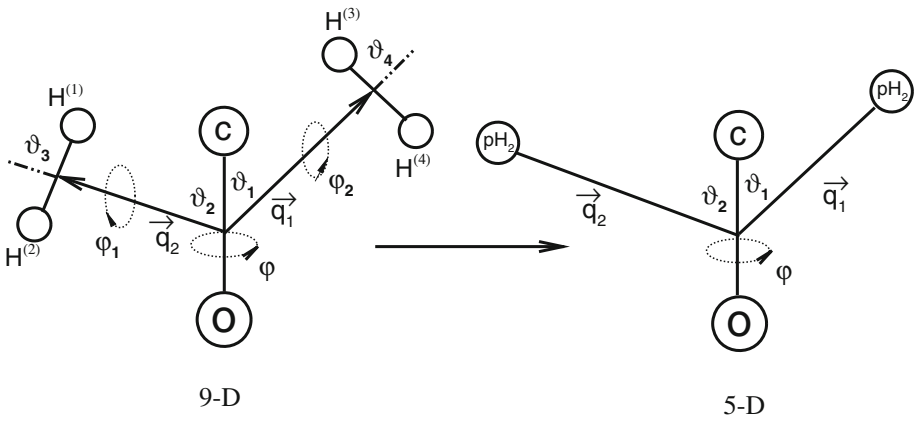


**Fig. 1** Jacobi coordinates for the $CO–(H_2)_2$ complex: left side, the geometry describe with nine dimensions of intermolecular coordinates; right side, the geometry described with five dimensions of intermolecular coordinates and with the two para-hydrogen treated as spherical particles

axis of the CO molecule, $\varphi_1$ and $\varphi_2$ are the azimuthal angles for rotation of $H_1$–$H_2$ and $H_3$–$H_4$ about vectors $\mathbf{q_1}$ or $\mathbf{q_2}$, respectively.

It is still difficult to solve the nine-dimensional intermolecular Schrodinger equation. However, because the nuclear spins are anti-parallel for para-hydrogen, the rotational angular momentum, $J$, must be even. We know that the ground-state rotational wave function of an isolated ground-state ($J = 0$) $H_2$ molecule is precisely spherically symmetric, and the energy spacing to its first-excited ($J = 2$) level is relatively large (354.3735 $cm^{-1}$). It is therefore desirable to treat $pH_2$ as a spherical particle. Following this approximation, the nine-dimensional intermolecular coordinates for a CO–$(pH_2)_2$ complex can be reduced to five coordinates ($q_1$, $q_2$, $\vartheta_1$, $\vartheta_2$, $\varphi$) shown on the right panel of Fig. 1, greatly reducing the computational effort. However, it should be noted that $pH_2$ is not truly spherical when interacting with other species. A simple spherical average over the orientations of the $H_2$ moiety does not provide an accurate description [43].

The rotational constant for $pH_2$(59.322 $cm^{-1}$) is more than 31 times larger than that of CO in its ground (1.9225288 $cm^{-1}$) or excited state (1.9050256 $cm^{-1}$) [44]. It therefore seems reasonable to perform a Born–Oppenheimer-type separation of the fast rotational motion of $pH_2$ from the relative slower CO rotation. Recently, Li, Roy, and Le Roy introduced a much better reduced-dimension description which they call an "adiabatic-hindered-rotor (AHR)" method. This approximation yields an effective $pH_2$-{linear molecule} interactions that are an order of magnitude more accurate than those obtained using a simple spherical-average approximation. We expect that with such an AHR approximation, the CO–$(pH_2)_2$ trimer can be accurately described with the left over five degrees of freedom shown in the right panel of Fig. 1. Based on our previous tests for CO–$oD_2$ dimer, as shown in Table 2 of Ref. [43], we found the AHR treatment of $oD_2$ is still feasible and reliable, and the differences between {2D–4D} are smaller than 0.092 $cm^{-1}$ for vibrational levels, which are about six times better than those obtained by spherical treatment. Therefore, similar treatment has been applied for the other two trimers of CO–$(oD_2)_2$ and CO–$pH_2$–He.

The rovibrational energy levels of CO–$(pH_2)_2$, CO–$(oD_2)_2$, and CO–$pH_2$–He were calculated using the radial discrete variable representation (DVR) and parity-adapted angular finite basis representation (FBR) methods described in Section II. The potential we used for each trimer is a sum of three pair potentials. The CO–$pH_2$, CO–$oD_2$, and $oD_2$–$oD_2$ potentials were generated by an "adiabatic-hindered-rotor" average treatment of the $H_2$ or $D_2$ rotation using dimer potentials taken from Refs. [32, 34, 45], while $pH_2$–$pH_2$ potentials were generated by a "spherical" average treatment of the $H_2$ rotation using dimer potential taken from Ref. [45]. For CO–$pH_2$–He and CO–$(He)_2$ complexes, the CO–$pH_2$, CO–He, and He–He potentials of Refs. [34, 46, 47] were used. The rotational constants $B_{CO}$ required for these calculations were fixed at the experimental values of 1.9225288 and 1.9050256 $cm^{-1}$ for CO in their ground ($\upsilon_3 = 0$) and excited ($\upsilon_3 = 1$) states [44], respectively. In our calculations, the masses were set at 1.00782503207 u for H, 2.0141017778 u for D, 4.00260324 u for $^4$He, 15.994914635 u for $^{16}$O, and 12. u for $^{12}$C. An 40-point sine DVR grid range from 3.0 to 30.0 bohr was used for the radial $r_1$ or $r_2$ stretching coordinate. For the angular basis, we use $l_{max} = m_{max} = 25$; 30 Gauss–Legendre quadrature points were used for the integration over $\theta_1$ or $\theta_2$, while 64 equally spaced points in the range [0, 2π] were used for the integration over $\phi$. It is useful to apply a potential ceiling value to reduce the spectral range and accelerate the convergence of the Lanczos calculation [48]. In our calculations, we use a ceiling of 1,000 $cm^{-1}$ and have confirmed that low-lying energy levels change by less than 0.001 $cm^{-1}$ when the ceiling is raised to 10,000 $cm^{-1}$.

## 2.2 Hamiltonian and basis functions

Following our previous work for $CO_2$–$(pH_2)_2$ trimer [27], in Radau coordinate, we use the Hamiltonian and basis functions based mainly on the work of Wang et al. [39] and on fundamental ideas presented by Mladenovic [49]. In recent years, this approach have been successfully used to treat $N_2O$–$(He)_2$, CO–$(He)_2$, $CO_2$–$(He)_2$, OCS–$(He)_2$, and $CO_2$–$(pH_2)_2$ complexes. The method is briefly reviewed here, and the reader is referred to Refs. [39] and [27] for further details. With the AHR approximation, the rovibrational Hamiltonian of the CO–$(pH_2)_2$ complex in the CO molecule-fixed frame has the form (in a.u.) [39, 49–51],

$$\hat{H} = \hat{T}_{str} + \hat{T}_{diag} + \hat{T}_{off} + \hat{T}_{Cor} + \bar{V}(r_1, r_2, \theta_1, \theta_2, \phi) \tag{1}$$

in which

$$\hat{T}_{str} = -\frac{1}{2m_{H_2}}\frac{\partial^2}{\partial r_1^2} - \frac{1}{2m_{H_2}}\frac{\partial^2}{\partial r_2^2} \tag{2}$$

$$\begin{aligned}\hat{T}_{diag} = &-\left(\frac{1}{2m_{H_2}r_1^2} + B_{CO}\right)\left[\frac{\partial^2}{\partial\theta_1^2} + \cot\theta_1\frac{\partial}{\partial\theta_1} - \frac{1}{\sin^2\theta_1}(\hat{J}_z - \hat{l}_{2z})^2\right] \\ &+ \left(\frac{1}{2m_{H_2}r_2^2} + B_{CO}\right)\hat{l}_2^2 + B_{CO}[\hat{J}^2 - 2(\hat{J}_z - \hat{l}_{2z})^2 - 2\hat{J}_z\hat{l}_{2z}]\end{aligned} \tag{3}$$

$$\hat{T}_{off} = B_{CO}[\hat{l}_{2+}\hat{a}_1^- + \hat{l}_{2-}\hat{a}_1^+] \tag{4}$$

$$\hat{T}_{Cor} = -B_{CO}[\hat{J}_-\hat{a}_1^+ + \hat{J}_+\hat{a}_1^- + \hat{J}_-\hat{l}_{2+} + \hat{J}_+\hat{l}_{2-}] \tag{5}$$

where

$$\hat{J}_{\pm} = \hat{J}_x \pm i\hat{J}_y, \quad \hat{l}_{2\pm} = \hat{l}_{2x} \pm i\hat{l}_{2y} \tag{6}$$

$$\hat{a}_1^{\pm} = \pm\frac{\partial}{\partial\theta_1} - \cot\theta_1(\hat{J}_z - \hat{l}_{2z}) \tag{7}$$

The details of the coordinate system are shown in Fig. 2. $r_1$ and $r_2$ are the lengths of Radau (or orthogonalized satellite) vectors $\mathbf{r_1}$ and $\mathbf{r_2}$, which are linear combinations of the Jacobi vectors $\mathbf{q_1}$ and $\mathbf{q_2}$ running from the center of mass of CO to the centers of the $pH_2$ molecules [49]. The polyspherical angles ($\theta_1$, $\theta_2$, $\phi$) are determined by the three vectors ($\mathbf{r_0}$, $\mathbf{r_1}$, $\mathbf{r_2}$). $\theta_1$ is the angle between the dopant axis $\mathbf{r_0}$ and $\mathbf{r_1}$, $\theta_2$ and $\phi$ are the polar angles that specify the orientation of $\mathbf{r_2}$ with respect to the CO molecule-fixed frame. $m_{H2}$ is the mass of the $pH_2$ molecule and $B_{CO}$ is the rotation constant of CO. The operators $\mathbf{J_x}$, $\mathbf{J_y}$, and $\mathbf{J_z}$ are the components of the total angular momentum operator $\mathbf{J}$ in the body-fixed frame, the $z$ axis of the body-fixed frame lies along the Jacobi radial vector $\mathbf{r_0}$, and the $x$ axis is in the plane that contains $\mathbf{r_0}$ and one $pH_2$ molecule. Here, $\overline{V}(r_1, r_2, \theta_1, \theta_2, \phi)$ is the total potential energy function which is represented as a sum of two two-dimensional AHR $pH_2$–CO potentials [34, 43] plus the one-dimensional AHR $pH_2$–$pH_2$ intermolecular potential [45]. The above Hamiltonian contains full vibration–rotation coupling.

A sine DVR grid [52] is used for the $r_1$ and $r_2$ degrees of freedom, while parity-adapted rovibrational basis functions are used for the angular part. A complete product basis function is

$$u^{J,M,P}_{l_1,l_2,m_2,K} = \frac{1}{\sqrt{2(1+\delta_{m_2,0}\delta_{K,0})}}[|l_1, l_2, m_2, K; J, M\rangle + (-1)^{J+P}|l_1, l_2, -m_2, -K; J, M\rangle] \tag{8}$$

where $K > 0$, and $P = 0$ and 1 correspond to even and odd parities, respectively. If $K = 0$, then it is necessary to apply the constraint $m_2 \geq 0$ to get rid of the redundant basis. The combination $m_2 = K = 0$ and $(-1)^{J+P} = -1$ is not allowed. The parity-adapted basis makes it possible to calculate even and odd parity levels separately. Within each parity block, we use the symmetry-adapted Lanczos algorithm (SAL) [53, 54] to compute states that are symmetric (A) and antisymmetric (B) with respect to exchange of the two $pH_2$ or $oD_2$ in trimers of CO–$(pH_2)_2$ or CO–$(oD_2)_2$, while no exchange symmetry applied for CO–$pH_2$–He Trimer.

## 3 Results and discussion

### 3.1 Features of the five-dimensional potential energy surface

Figure 3 shows how the well depth of our vibrationally averaged five-dimensional $V_{MLRQ}$ ground-state PES for

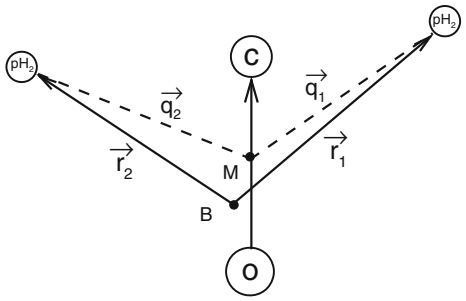


**Fig. 2** M is the center of mass of CO, and B is the canonical point for the Radau vectors. $\mathbf{q_1}$ and $\mathbf{q_2}$ are Jacobi vectors. $\mathbf{r_1}$ and $\mathbf{r_2}$ are Radau vectors. $\phi$ is a dihedral angle between $\mathbf{r_1}$ and $\mathbf{r_2}$ around $\mathbf{r_0}$. $\theta_1(\theta_2)$ are angles between $\mathbf{r_0}$ and $\mathbf{r_1}(\mathbf{r_2})$

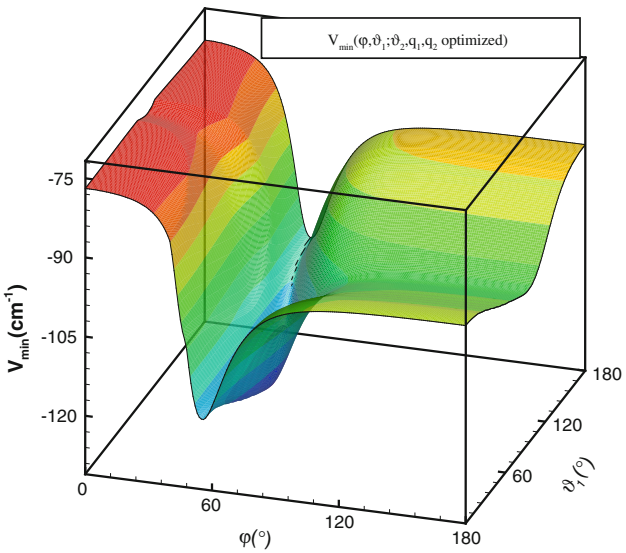


**Fig. 3** Minimum energy on our vibrationally averaged five-dimensional PES for CO($\upsilon = 0$)–$(pH_2)_2$ trimer as a function of angles $\varphi$ and $\vartheta_1$, for optimized values of $\vartheta_2$, $q_1$, and $q_2$

CO($\upsilon = 0$)–$(pH_2)_2$ system depends on $\varphi$ and $\vartheta_1$, when $\vartheta_2$, $q_1$, $q_2$ are optimized to minimize the energy for each ($\varphi$, $\vartheta_1$). As seen there, the global minima with well depth of $-126.06$ cm$^{-1}$ occur at the geometries ($\vartheta_1 = 95.6°$, $\vartheta_2 = 95.6°$) with $q_1 = q_2 = 3.57$ Å and $\varphi = 58.0°$ (or by symmetry of $\varphi = 302.0°$). Between these two identical global minima, there exists a saddle point with energy $-101.90$ cm$^{-1}$ located at $\vartheta_1 = \vartheta_2 = 95.3°$ with $q_1 = q_2 = 3.57$ Å and $\varphi = 180.0°$, which corresponds to a coplanar geometry with the two $pH_2$ molecules on opposites of the CO molecule. In addition, Fig. 3 also shows local minimum with energy of $-77.59$ cm$^{-1}$ occurs at the coplanar geometry ($\vartheta_1 = 94.7°$, $\vartheta_2 = 180.0°$) with $q_1 = 3.56$ Å, $q_2 = 7.01$ Å, and $\varphi = 0.0°$. Parameters characterizing the various stationary configurations and energies for the CO–$(pH_2)_2$ trimer are summarized in Table 1, where

**Table 1** Properties of stationary points of the CO($\upsilon = 0$)–$(pH_2)_2$ potential energy surface, and comparisons with those results for CO($\upsilon = 0$)–$(oD_2)_2$ and CO($\upsilon = 0$)–$(He)_2$ surfaces

| | Global minimum | Saddle point | Local minimum |
|---|---|---|---|
| CO–$(pH_{2)2}(V_{MLRQ})$ | {3.57, 3.57, 95.6, 95.6, 58.0, −126.06} | {3.57, 3.57, 95.3, 95.3, 180.0, −101.90} | {3.56, 7.01, 94.7, 180.0, 0.0, −77.59} |
| CO–$(pH_2)_2(V_{12})$ | {3.57, 3.57, 94.7, 94.7, 58.0, −126.22} | {3.57, 3.57, 94.7, 94.7, 180.0, −102.07} | {3.56, 7.01, 94.0, 180.0, 0.0, −77.74} |
| CO–$(oD_2)_2(V_{MLRQ})$ | {3.57, 3.57, 95.2, 95.2, 58.0, −126.91} | {3.56, 3.56, 94.6, 94.6, 180.0, −102.76} | {3.56, 7.01, 96.0, 180.0, 0.0, −78.07} |
| CO–$(He)_2(V_{MLRQ})$ | {3.39, 3.39, 120.8, 120.8, 51.9, −53.47} | {3.39, 3.39, 120.8, 120.8, 180.0, −45.90} | {3.37, 6.31, 118.3, 0.0, 0.0, −32.22} |

All entries are given as $\{q_1[\text{Å}], q_2[\text{Å}], \vartheta_1^\circ, \vartheta_2^\circ, \varphi^\circ, \Delta V[\text{cm}^{-1}]\}$

they are consistent with corresponding values obtained on $V_{12}$ PES, and compared with properties of the analogous CO–$(oD_2)_2$ and CO–$(He)_2$ species. As shown in Table 1, all the stationary points (the global minimum, saddle point, and local minimum) for CO–$(pH_2)_2$ are more than twice as deep as those of CO–$(He)_2$. This will be mostly due to the polarizability of $pH_2$ (5.414 au) [55] is four times larger than that for He (1.383 au) [56]. Comparing CO–$(pH_2)_2$ and CO–$(oD_2)_2$ yields the differences at the global minimum, saddle point, and local minimum are 0.85, 0.86, and 0.48 $cm^{-1}$, respectively. Those differences originate from the fact that $B_{D2}/B_{H2} \approx 0.5$, which means the solution of the two-dimensional angular rotational equation for $oD_2$ systems will have substantially larger contributions from basis functions corresponding to $L > 0$ [43], where $L$ is the angular momentum quantum number of $H_2$ rotation. Figure 4 shows the minimum energy paths between equivalent global minima as a function of $\varphi$, for optimized values of $\vartheta_1$, $\vartheta_2$, $q_1$ and $q_2$.

As clearly shown in Fig. 4(b), the comparison between CO–$(pH_2)_2$ and CO–$(He)_2$ shows that the anisotropy with respect to the dihedral torsional motion of the two $pH_2$ molecules in CO–$(pH_2)_2$ (48.47 $cm^{-1}$) is more than twice as strong as that for the analogous motion in the CO–$(He)_2$ (21.25 $cm^{-1}$) complex. It also shows that the barrier between two adjacent minima of CO–$(pH_2)_2$ (24.16 $cm^{-1}$) is more than three times higher than that for CO–$(He)_2$ (7.57 $cm^{-1}$). As would be expected, these barrier heights are approximately equal to the well depths for $pH_2$–$pH_2$ (24.71 $cm^{-1}$) [45] and He–He (7.65 $cm^{-1}$) [47] dimers, respectively. These differences in PESs will still be reflected in the different spectra of the Trimers.

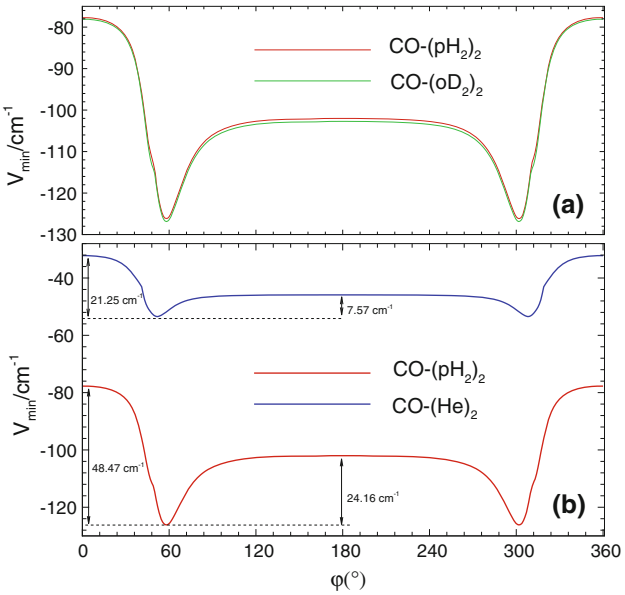


**Fig. 4** Minimum energy path on our vibrationally averaged five-dimensional PES for CO($\upsilon = 0$)–$(pH_2)_2$ trimer as functions of angle $\varphi$ for optimized values of $\vartheta_1$, $\vartheta_2$, and $q_1$, $q_2$

## 3.2 Rovibrational energy levels and band origin shifts

The calculated intermolecular rovibrational energy levels for the ground ($\upsilon = 0$) states of CO–$(pH_2)_2$, CO–$(oD_2)_2$, and CO–$pH_2$–He trimers with $J = 0$, 1, 2, and 3 are listed in Table 2, which are relative to the corresponding zero point energies of −42.907, −59.326, and −26.671 $cm^{-1}$, respectively. Those for excited ($\upsilon = 1$) (not shown here) are very similar and listed in Table S1 of the supplementary material. The rovibrational energy levels are labeled by quantum numbers ($J$, $P$, $n_{J,P}$). The only good quantum numbers are the overall angular momentum $J$ and parity $P$ = e or f. The label $n_{J,P}$ numbers consecutive states for each (J,P). As shown in Table 2, symmetry (A) and antisymmetry (B) are used to label the symmetries with respect to permutation of the two $pH_2$ or $oD_2$ molecules, (A, e) and (B, e) for even parity and (A, f) and (B, f) for odd parity. Because of the zero nuclear spin of the $^4$He, $pH_2$, $oD_2$, therefore for CO–$(pH_2)_2$, CO–$(He)_2$ and CO–$(oD_2)_2$ trimers, only (A, e) and (A, f) states are physically allowed. However, for CO–$pH_2$–He trimer, without exchange symmetry between $pH_2$ and He, only even and odd parity blocks are used to sort the rovibrational energy levels.

In order to assign the torsional motion states for CO–$(pH_2)_2$ trimer, it is very useful to yield a one-dimensional representation of the partial wave functions along the

**Table 2** Calculated $J = 0$, 1, 2, 3 rovibrational energy levels (in $cm^{-1}$) for CO($\upsilon = 0$)–($pH_2$)$_2$, CO($\upsilon = 0$)–($oD_2$)$_2$, and CO($\upsilon = 0$)–$pH_2$–He complexes, which are relative to the corresponding zero point energies of −42.907, −59.326, and −26.671 $cm^{-1}$, respectively

| CO($\upsilon = 0$)–($pH_2$)$_2$ | | | | CO($\upsilon = 0$)–($oD_2$)$_2$ | | | | CO($\upsilon = 0$)–$pH_2$–He | |
|---|---|---|---|---|---|---|---|---|---|
| (A,e) | (B,e) | (A,f) | (B,f) | (A,e) | (B,e) | (A,f) | (B,f) | e | f |
| $J = 0$ | | | | | | | | | |
| 0.000 (0) | 5.477 | 14.782 | 3.407 (1) | 0.000 (0) | 4.852 | 12.839 | 2.728 (1) | 0.000 (0) | 4.065 (1) |
| 5.340 (2) | 12.753 | 22.294 | 10.947 (3) | 7.299 (2) | 13.559 | 22.401 | 11.516 (3) | 2.580 (2) | 8.378 (3) |
| 6.951 | 14.491 | 24.140 | 14.932 | 7.915 | 15.141 | 23.522 | 14.116 | 4.991 | 11.280 |
| 11.901 (4) | 18.603 | 27.663 | 19.647 (5) | 11.140 (4) | 18.436 | 27.299 | 16.553 (5) | 6.651 | 11.407 |
| $J = 1$ | | | | | | | | | |
| 3.597 | 1.352 | 0.736 | 1.136 | 3.001 | 0.773 | 0.399 | 0.692 | 1.197 | 0.517 |
| 7.662 | 3.943 | 3.438 | 5.973 | 6.038 | 3.103 | 3.005 | 5.219 | 4.058 | 0.985 |
| 11.532 | 7.972 | 7.398 | 6.078 | 11.856 | 8.093 | 5.977 | 7.956 | 4.362 | 3.091 |
| 14.271 | 8.708 | 7.745 | 8.125 | 13.123 | 9.437 | 7.752 | 8.283 | 5.354 | 3.897 |
| $J = 2$ | | | | | | | | | |
| 2.083 | 2.426 | 4.126 | 2.945 | 1.181 | 1.410 | 2.508 | 1.650 | 1.494 | 2.319 |
| 4.074 | 4.758 | 4.865 | 4.857 | 2.521 | 3.910 | 3.740 | 3.830 | 1.778 | 3.235 |
| 4.558 | 7.337 | 8.609 | 5.168 | 3.754 | 5.958 | 6.839 | 3.941 | 3.080 | 4.848 |
| 7.307 | 8.967 | 9.926 | 10.283 | 6.659 | 8.591 | 9.742 | 8.589 | 4.197 | 5.198 |
| $J = 3$ | | | | | | | | | |
| 6.326 | 5.199 | 4.022 | 4.234 | 3.707 | 2.947 | 2.317 | 2.476 | 3.969 | 2.792 |
| 6.776 | 6.713 | 6.193 | 6.436 | 4.832 | 4.896 | 3.770 | 4.986 | 4.501 | 3.097 |
| 7.754 | 6.974 | 6.443 | 7.612 | 5.785 | 5.104 | 4.858 | 5.264 | 6.028 | 4.150 |
| 10.860 | 8.148 | 7.705 | 9.314 | 8.049 | 5.270 | 5.790 | 7.075 | 6.309 | 5.538 |

The torsional motion assignments are indicated in parentheses as $\upsilon_t$

dihedral angle $\phi$. In terms of the basis functions and Radau coordinate system, the wavefunction for the $n$'th energy level for a given set of $\{J, M, P\}$ quantum numbers is,

$$\Psi_n^{J,M,P}(r_1, r_2, \theta_1, \theta_2, \phi; \alpha, \beta, \gamma) = \sum_{\alpha_1,\alpha_2,l_1,l_2,m_2,K} \langle \theta_1, \theta_2, \phi; \alpha, \beta, \gamma \mid l_1, l_2, m_2; J, K, M, P \rangle \langle r_1 \mid \alpha_1 \rangle \langle r_2 \mid \alpha_2 \rangle \times \left\langle \alpha_1, \alpha_2, l_1, l_2, m_2; J, K, M, P \,\middle|\, \Psi_n^{J,M,P} \right\rangle, \quad (9)$$

in which $\langle r_j \mid \alpha_j \rangle$ is a localized DVR basis function for particle $j$, and the coefficient $\left\langle \alpha_1, \alpha_2, l_1, l_2, m_2; J, K, M, P \,\middle|\, \Psi_n^{J,M,P} \right\rangle$ is an eigenvector obtained via Lanczos diagonalization. The one-dimensional wave function along the dihedral angle $\phi$, $\Psi_n^{J,M,P}$ is defined as

$$\psi^{J,M,P,n}(\phi) = \int dr_1 dr_2 \sin\theta_1 d\theta_1 \sin\theta_2 d\theta_2 \Psi_n^{J,M,P} \times (r_1, r_2, \theta_1, \theta_2, \phi; \alpha, \beta, \gamma) \quad (10)$$

The above integral can be evaluated on the same grid as the potential integral. The torsional motion states for CO–($pH_2$)$_2$ trimer are assigned and indicated in parentheses as ($\upsilon_t$) in Table 2, using the partial wave functions, which are yielded by integrating over all degrees of freedom except the dihedral angle $\phi$. We make the assignment based on the nodal structure of the partial wave function shown in Fig. 5.

Table 3 presents the calculated zero point energies (ZPEs) and band origin shifts for CO containing dimer or trimer complexes formed from CO($\upsilon$) with one or two $pH_2$, $oD_2$, He, or mixed one $pH_2$ and one He. ZPEs are relative to the energies at the dissociation limits for corresponding dimers or trimers. All the band origin shifts are calculated by $\Delta\upsilon_0 = E_{\upsilon=1}^{\mathrm{ZPE}} - E_{\upsilon=0}^{\mathrm{ZPE}}$. As shown in Table 3, the band origin shift for CO–($pH_2$)$_2$ trimer predicted by our five-dimensional reduced-dimension $V_{MLRQ}$ PES is −0.369 $cm^{-1}$, which is almost twice the value of −0.179 $cm^{-1}$ for CO–$pH_2$ dimer and slightly lower than the estimated experimental value of −0.355 $cm^{-1}$ [31], which was indirectly determined by combining the microwave and the a-type infrared transitions, assuming that the rotational frequencies are the same in the ground and first-excited vibrational states. For CO–($oD_2$)$_2$ or CO–(He)$_2$ trimer, the predicted band origin shift of −0.420 or −0.049 $cm^{-1}$, is approximately equal to twice of −0.206 or −0.024 $cm^{-1}$ for CO–$oD_2$ or CO–He dimer.

For CO–$pH_2$–He trimer, two CO–He potentials of CBS + Corr [57] and V333 [46] were used for comparison. The CBS + Corr surface by Peterson and McBane was a three-dimensional ab initio PES that explicitly incorporates dependence on the C–O stretching, obtained with state-of-the-art ab initio and extrapolation methods. The V333 surface [46] by Chuaqui et al. [57] was a two-dimensional PES with CO fixed at its equilibrium geometry, obtained by fitting

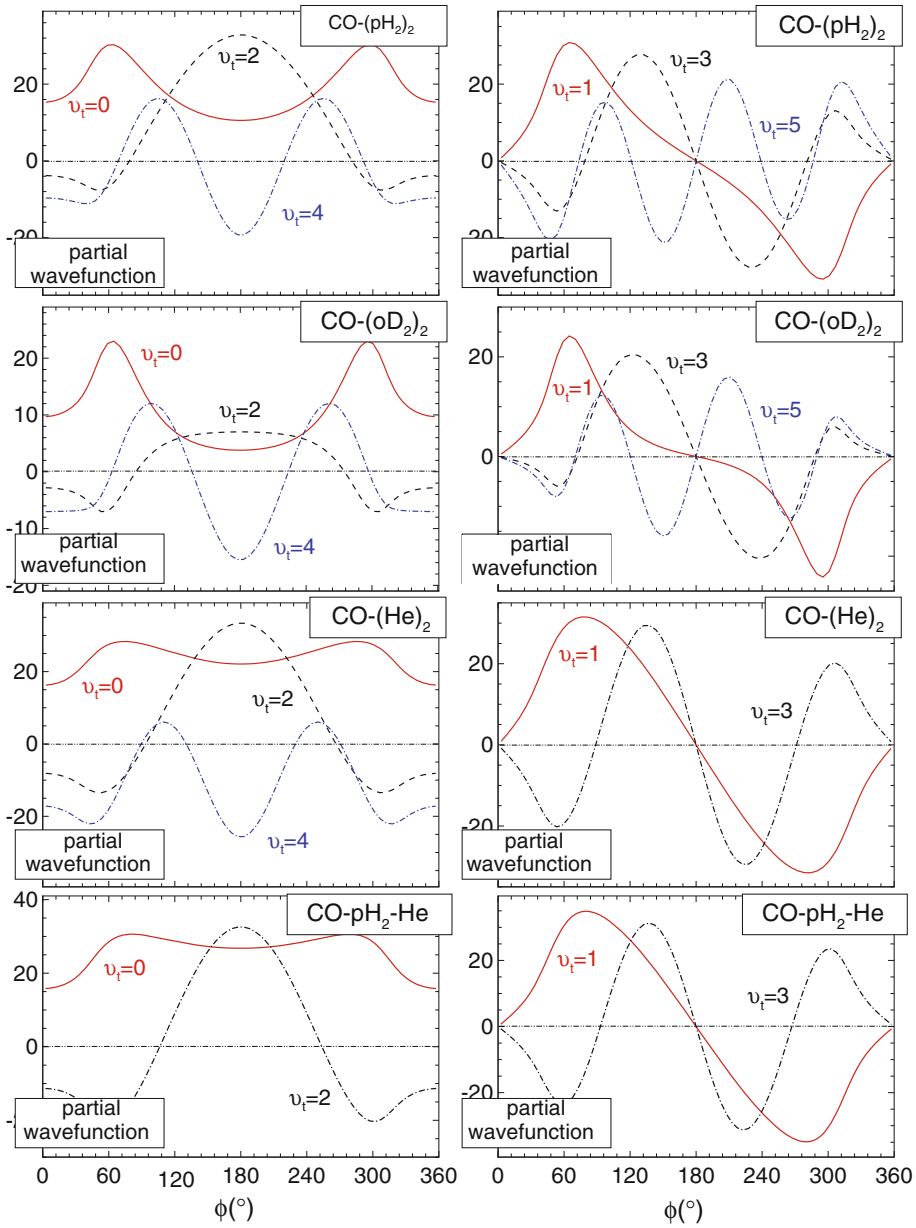


**Fig. 5** Partial wave functions for the torsional motion $\upsilon_t$ of CO–$(pH_2)_2$ complex as a function of the azimuthal angle $\phi$, compared with those of CO–$(oD_2)_2$, CO–$(He)_2$, CO–$pH_2$–He complexes

a potential to observed transitions near the fundamental band of CO. As we expected, the calculated band origin shift for CO–$pH_2$–He trimer is $-0.205$ cm$^{-1}$ on CBS + Corr potential for CO–He, which is approximately equal to the sum of the band origin shifts of $-0.179$ and $-0.024$ cm$^{-1}$ for CO–$pH_2$ and CO–He dimers, respectively. This indicates that the density for $pH_2$ or He in CO–$pH_2$–He trimer has very similar distribution as that in their dimers. Due to V333 potential for CO–He without taking into account the CO vibration, the predicted band origin shift on this surface for CO–$pH_2$–He trimer is $-0.019$ cm$^{-1}$ different from that on CBS + Corr potential, which is very close to the calculated shift value of $-0.024$ cm$^{-1}$ for CO–He dimer.

### 3.3 Predicted microwave and infrared transitions

For CO–$(pH_2)_2$, the predicted microwave (MW) and infrared (IR) transition frequencies (cm$^{-1}$) from our AHR 5D $V_{MLRQ}$ potential are listed in Tables 4 and 5, respectively, and compared with those calculated on $V_{12}$ potential and experimental results. The lower and upper states involved in the transitions are numbered with the set of parameters ($J$, $P$, $n_{J,P}$). For infrared transitions, to compare our computed energy transitions directly with experimental results, we calculate IR rovibrational transitions from

$$\upsilon = \upsilon_0(\mathrm{CO}) + E^{\mathrm{upper}}_{v=1} - E^{\mathrm{lower}}_{v=0} \tag{11}$$

**Table 3** The zero point energies (ZPEs) and band origin shifts for the complexes formed from stretch CO($\upsilon$) with one or two $pH_2$, $oD_2$, or mixed one $pH_2$ and one He

| Complexes | $E_{v=0}^{ZPE}$ | $E_{v=1}^{ZPE}$ | $\Delta\upsilon_0$(calc.) | $\Delta\upsilon_0$(obs.) |
|---|---|---|---|---|
| CO($\upsilon$)–$pH_2$ | −19.371 | −19.550 | −0.179 | −0.179[a] |
| CO($\upsilon$)–$(pH_2)_2$ | −42.907 | −43.276 | −0.369 | −0.355[b] |
| CO($\upsilon$)–$oD_2$ | −25.630 | −25.836 | −0.206 | −0.202[c] |
| CO($\upsilon$)–$(oD_2)_2$ | −59.326 | −59.746 | −0.420 | |
| CO($\upsilon$)–He[f] | −6.431 | −6.455 | −0.024 | −0.025[d] |
| CO($\upsilon$)–$(He)_2$[f] | −13.130 | −13.179 | −0.049 | −0.049[e] |
| CO($\upsilon$)–$pH_2$–He[g] | −26.671 | −26.857 | −0.186 | |
| CO($\upsilon$)–$pH_2$–He[f] | −26.459 | −26.664 | −0.205 | |

ZPEs are relative to the energies at the dissociation limits for corresponding dimers or trimers. $\Delta\upsilon_0 = E_{\upsilon=1}^{ZPE} - E_{\upsilon=0}^{ZPE}$ is the resulting band origin shifts. All energies are in $cm^{-1}$

[a] Reference [35]. [b] Reference [31]. [c] Reference [58]

[d] Reference [36]. [e] Reference [38]

[f] This calculation is with the CBS + Corr potential [57]

[g] This calculation is with the V333 potential [46]

where, $\upsilon_0$(CO) = 2,143.2712 $cm^{-1}$ is the experimental fundamental vibrational transition frequency of a free CO molecule.

As shown in column 2 of Tables 4 or 5, the transition energies yielded by our $V_{MLRQ}$ PES are seen to agree very well with the experimental values shown in column 3 of Tables 4 or 5. The differences seen in column 5 are very small both for microwave and infrared transitions, yielding a root-mean-square (rms) discrepancy of only 0.010 $cm^{-1}$ for all 4 observed transitions (1 for MW and 3 for IR), and also consistent with those obtained on the $V_{12}$ potential as shown in column 5 with the same rms discrepancy for those 4 experimental transitions. To predict more possible microwave and infrared transitions for CO–$(pH_2)_2$ trimer, the line strength and relative intensity at temperatures 0.6 K (effective experimental rotational temperature) are also computed from the wave functions. Note that the line strength does not depend on the temperature. Subject to the selection rules $\Delta J = 0, \pm 1$, $\Delta P$ = e ↔ f, and with line strength larger than $10^{-3}(\mu_{CO}^2)$, 64 possible allowed transitions for MW and 129 for IR with $J \leq 3$ and $n \leq 4$ are predicted. To select most possible microwave and infrared transitions for CO–$(pH_2)_2$ trimer, all the relative intensities at temperature 0.6 K are calculated, and expressed relative to (1, f, 2)−(0, e, 1) transition, whose intensity is set to 1. With the restriction of the relative intensity larger than $10^{-3}$, only 15 strongest transitions for MW and 18 for IR are kept and listed in Tables 4 and 5, respectively. The predicted 129 line strengths and 18 relative intensities for CO–$(pH_2)_2$ trimer at temperature of 0.6 K are clearly illustrated in the uppermost segment of Fig. 6.

For CO–$(oD_2)_2$ and CO–$pH_2$–He, the predicted infrared transition frequencies expressed relative to the band origin 2,143.2712 $cm^{-1}$ of a free CO from our AHR 5D $V_{MLRQ}$ potential are given in Tables 6 and 7, respectively. The lower and upper states involved in the transitions are also numbered with the set of parameters ($J$, $P$, $n_{J,P}$). Only the transitions between A+ and A− states are physically allowed for CO–$(oD_2)_2$, but this restriction does not apply to CO–$pH_2$–He. Subject to overall selection rules $\Delta J = 0$, $\pm 1$, $\Delta P$ = e ↔ f, with line strength larger than $10^{-3}$ $(\mu_{CO}^2)$, $J \leq 3$ and $n \leq 4$, 149 line strengths and 32 most possible allowed IR transitions at temperature of 0.6 K for

**Table 4** Predicted microwave frequencies ($cm^{-1}$), line strengths, and relative intensities at temperature of 0.6 K for CO–$(pH_2)_2$ complex from vibrationally averaged five-dimensional $V_{12}$ or $V_{MLRQ}$ PES, comparison with experimental results

The lower and upper states involved in the transitions are numbered with the set of parameters ($J$, $P$, $n_{J,P}$). The line strength values are multiplied by 100

| Transitions | | | Diff. (Calc. − Obs.) | | Line | Intensity |
|---|---|---|---|---|---|---|
| Upper–lower | $V_{MLRQ}$ | Obs. | $V_{12}$ | $V_{MLRQ}$ | strength | (0.6 K) |
| (1, f, 1)–(0, e, 1) | 0.736 | 0.741 | 0.002 | −0.005 | 0.061 | 0.047 |
| (2, f, 2)–(2, e, 1) | 2.783 | | | | 1.853 | 0.010 |
| (1, e, 1)–(1, f, 1) | 2.862 | | | | 0.957 | 0.126 |
| (1, f, 2)–(0, e, 1) | 3.438 | | | | 1.294 | 1.000 |
| (2, e, 3)–(1, f, 1) | 3.822 | | | | 0.679 | 0.090 |
| (3, f, 2)–(2, e, 1) | 4.110 | | | | 0.521 | 0.003 |
| (1, f, 3)–(2, e, 1) | 5.315 | | | | 0.225 | 0.001 |
| (3, f, 4)–(2, e, 1) | 5.622 | | | | 0.162 | 0.001 |
| (0, e, 3)–(1, f, 1) | 6.951 | | | | 0.205 | 0.158 |
| (2, f, 3)–(2, e, 1) | 6.526 | | | | 0.312 | 0.002 |
| (1, e, 2)–(1, f, 1) | 6.926 | | | | 0.079 | 0.011 |
| (1, f, 3)–(0, e, 1) | 7.236 | | | | 0.105 | 0.082 |
| (1, f, 4)–(0, e, 1) | 7.398 | | | | 0.326 | 0.252 |
| (2, f, 4)–(2, e, 1) | 7.844 | | | | 0.489 | 0.003 |
| (1, e, 3)–(1, f, 1) | 10.796 | | | | 0.141 | 0.019 |

**Table 5** Predicted infrared transition frequencies ($cm^{-1}$), line strengths, and relative intensities at temperature of 0.6 K for CO–$(pH_2)_2$ complex from vibrationally averaged five-dimensional $V_{12}$ or $V_{MLRQ}$ PES, comparison with experimental results

| Transitions | | | Diff. (calc. − obs.) | | Line | Intensity |
|---|---|---|---|---|---|---|
| Upper–lower | $V_{MLRQ}$ | Obs. | $V_{12}$ | $V_{MLRQ}$ | Strength | (0.6 K) |
| (0, e,1)–(1, f, 1) | 2,142.167 | | | | 0.062 | 0.008 |
| (1, f, 1)–(0, e, 1) | 2,143.638 | 2,143.657 | 0.007 | 0.019 | 0.001 | 0.051 |
| (2, e, 1)–(1, f, 1) | 2,144.250 | | | | 0.051 | 0.007 |
| (2, f, 1)–(2, e, 1) | 2,144.945 | | | | 0.100 | 0.001 |
| (2, f, 2)–(2, e, 1) | 2,145.671 | | | | 1.848 | 0.010 |
| (1, e, 1)–(1, f, 1) | 2,145.747 | | | | 0.959 | 0.127 |
| (1, f, 2)–(0, e, 1) | 2,146.324 | 2,146.330 | 0.015 | 0.006 | 1.293 | 1.000 |
| (2, e, 3)–(1, f, 1) | 2,146.713 | 2,146.712 | 0.011 | −0.001 | 0.673 | 0.089 |
| (3, f, 2)–(2, e, 1) | 2,147.586 | | | | 0.514 | 0.003 |
| (1, f, 3)–(2, e, 1) | 2,148.201 | | | | 0.224 | 0.001 |
| (3, f, 4)–(2, e, 1) | 2,148:893 | | | | 0:161 | 0.001 |
| (0, e, 3)–(1, f, 1) | 2,149.108 | | | | 0.204 | 0.027 |
| (2, f, 3)–(2, e, 1) | 2,149.414 | | | | 0.311 | 0.002 |
| (1, e, 2)–(1, f, 1) | 2,149.809 | | | | 0.079 | 0.010 |
| (1, f, 3)–(0, e, 1) | 2,150.283 | | | | 0.103 | 0.079 |
| (1, f, 4)–(0, e, 1) | 2,150.637 | | | | 0.330 | 0.256 |
| (2, f, 4)–(2, e, 1) | 2,150.733 | | | | 0.498 | 0.003 |
| (1, e, 3)–(1, f, 1) | 2,153.693 | | | | 0.141 | 0.019 |

The lower and upper states involved in the transitions are numbered with the set of parameters ($J$, $P$, $n_{J,P}$). The line strength values are multiplied by 10

CO–$(oD_2)_2$, and 118 line strengths and 37 most possible IR transitions for CO–$pH_2$–He are predicted, and shown in the middle and lowermost segments of Fig. 6, respectively. Although MW or IR transitions for CO–$(oD_2)_2$ have not been reported yet, one transition marked "m" in Fig. 7 of Ref. [22] was tentatively assigned as b-type $R(0)$ of the mixed ternary cluster CO–$pH_2$–He. Based on the calculated line position and intensity, this line may correspond to the (1, f, 4)–(0, e, 1) transition. We are confident for this assignment, not only because the calculated transition at 2,146.958 $cm^{-1}$ are in good agreement with the experimental position at 2,146.93 $cm^{-1}$, but also the relative intensity for (1, f, 4)–(0, e, 1) at temperature 0.6 K is the strongest among all predicted transitions for CO–$pH_2$–He complex.

### 3.4 The wave functions and "solvent" density distributions

Examining the wave function of some of the vibrational states with $\upsilon = 0$ and $J = 0$ helps us to understand the nature about the motions of the $pH_2$, $oD_2$, and He in their complexes. We are most interested in the $\phi$ dependence of the wave function because this coordinate plays an important role in assigning and understanding many vibrational states. Figure 5 shows the reduced wave functions with (A,e) symmetry and (B,f) symmetry for $\upsilon_t = 0$, 1, 2, 3, 4, and 5 levels of CO–$(pH_2)_2$, obtained by integrating the wave function over the coordinates of $r_1$, $r_2$, $\theta_1$ and $\theta_2$ at each value of $\phi$, and compared with those of CO–$(oD_2)_2$, CO–$(He)_2$, and CO–$pH_2$–He trimers. As shown in Fig. 5, the wave functions for the $\upsilon_t = 1$, 3, and 5 levels shown on the right side have strikingly regular nodal structures along the $\phi$ coordinate with exact zero at $\phi = 0$ or $\phi = 180°$, which implies that there is little coupling between $\phi$ with the other coordinates. While the wave functions for $\upsilon_t = 0$, 2, and 4 levels shown on the left side have no strict characteristics as torsional states, which is probably due to the fact that there is strong coupling between $\phi$ with the other coordinates that distort their character. For CO–$(He)_2$ and CO–$pH_2$–He trimers, there exist strong coupling between many (A,e) or (A,f) states, and it is hard to assign those states as torsional motions; thus, we only presented the lowest possible torsion states with $\upsilon_t < 4$. In Fig. 5, it can be clearly seen that the wave functions for the $\upsilon_t = 0$, 2, and 4 levels are quite different between the CO–$(pH_2)_2$ and CO–$(He)_2$ complexes, but very similar for CO–$(pH_2)_2$ and CO–$(oD_2)_2$, and for CO–$(He)_2$ and CO–$pH_2$–He complexes. In particular, for the $\upsilon_t = 0$ and 1 levels, the highly localized distribution for $pH_2$ or $oD_2$ in CO–$(pH_2)_2$ or CO–$(oD_2)_2$ complexes contrasts sharply with that for He in CO–$(He)_2$ or CO–$pH_2$–He complexes. In addition to the expected excluded volumes near $\phi = 0$ and $\phi = 360$, for the ground state of CO–$(pH_2)_2$ or CO–$(oD_2)_2$, there are local maxima at $\phi = 58$ and $\phi = 302°$ corresponding to the $pH_2$ or $oD_2$ particles lying at global minimum positions, while the He distribution in CO–$(He)_2$ or CO–$pH_2$–He is delocalized, even with a lot of distribution at $\phi = 180°$.

Figure 7 shows the three-dimensional density for the two $pH_2$ molecules (upper), two He atoms (middle), or mixed

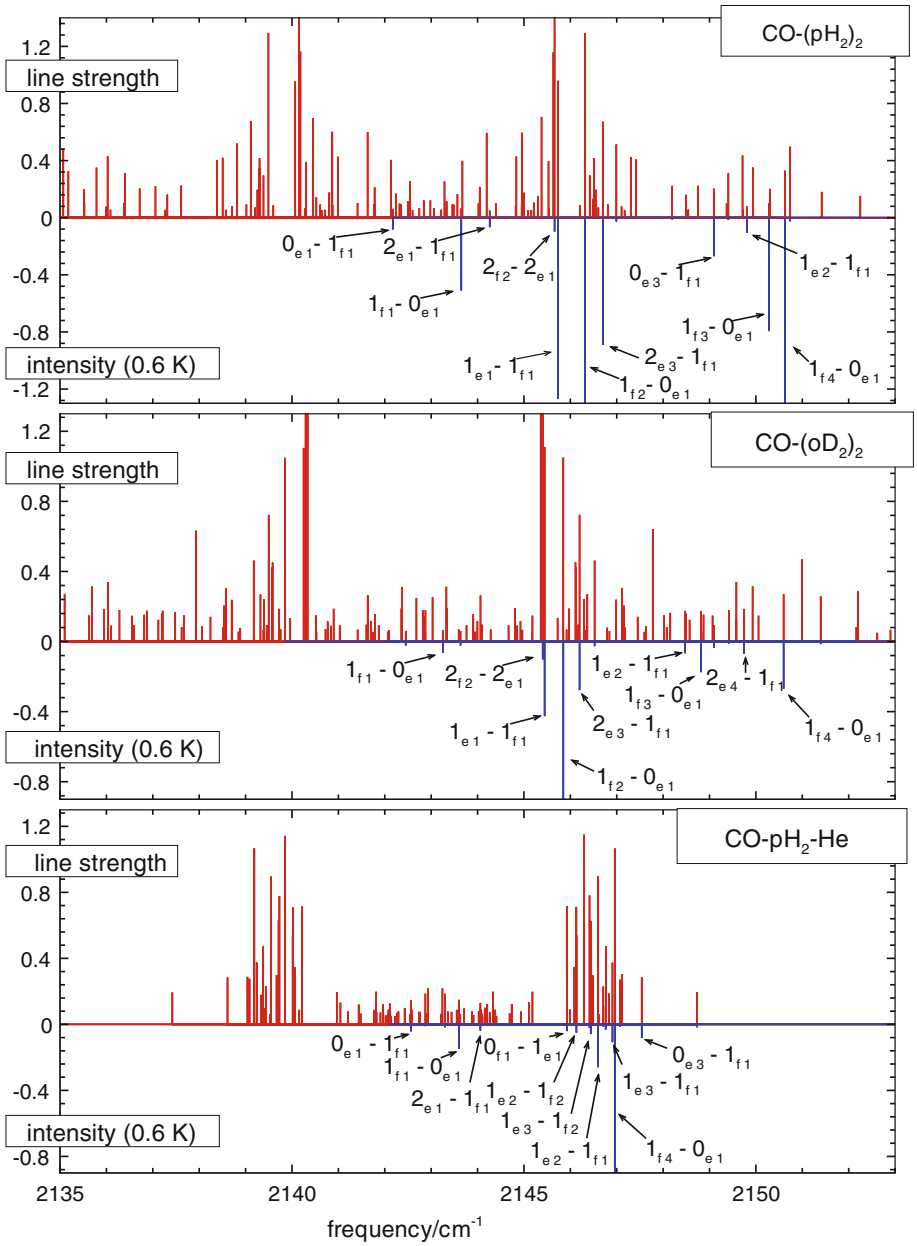


**Fig. 6** Calculated infrared spectra of CO–$(pH_2)_2$ (*upper panel*), CO–$(oD_2)_2$ (*middle panel*), and CO–$pH_2$–He (*lower panel*) for line strength (*upward pointing lines*) and relative intensity at 0.6 K (*downward pointing lines*), respectively. The intensities are expressed relative to (1, f, 2)–(0, e, 1) transition of CO–$(pH_2)_2$ or CO–$(oD_2)_2$, and (1, f, 4)–(0, e, 1) transition of CO–$pH_2$–He complexes, respectively, whose intensity is equal 1. All the line strength values are multiplied by 10. The relative intensity of CO–$(pH_2)_2$ are also multiplied by 100

one $pH_2$ and one He (bottom) in the body-fixed frame, as calculated for the ground state of CO–$(pH_2)_2$, CO–$(He)_2$, or CO–$pH_2$–He using the procedure described in Ref. [27]. It is very useful to develop some intuitive feeling regarding the nature of these species. Iso-surfaces are used to represent the three-dimensional densities, and the z axis is defined to lie on the CO molecular axis. One significant feature of these representations is the fact that the two $pH_2$ molecules or two He molecules appear to have very different density distributions. It is clear that the density distribution of the first $pH_2$ or He particle in CO–$(pH_2)_2$ or CO–$(He)_2$ trimer is represented as a at disk and somewhat delocalized in the yz plane, while that of the second $pH_2$ in CO–$(pH_2)_2$ trimer is highly localized, with two density maxima at regions associated with the $pH_2$–$pH_2$ potential minimum. In contrast, the density distribution of the second helium atom in CO–$(He)_2$ trimer (middle panel) is highly delocalized relative to the first, being distributed on an incomplete ring wrapped around the CO molecule. For CO–$pH_2$–He trimer, the density for $pH_2$ as particle-1 is located in the *yz* plane as reference, while the density for He as particle-2 is relative to $pH_2$. As shown in the lowest panel of Fig. 7, the more localized He distribution in CO–$pH_2$–He than in CO–$(He)_2$ is related to the stronger interaction (deeper well) between the $pH_2$–He interaction than the He–He one. For all three cases, the density for particle-2 is excluded from the region near particle-1 by the short-range repulsive wall of the $pH_2$–$pH_2$, He–He, or $pH_2$–He potential.

**Table 6** Predicted infrared transition frequencies ($cm^{-1}$), line strengths, and relative intensities at temperature of 0.6 K for CO–$(oD_2)_2$ complex from vibrationally averaged five-dimensional $V_{MLRQ}$ PES

| Transitions | | Line | Intensity |
|---|---|---|---|
| Upper–lower | Calc. | Strength | (0.6 K) |
| (1, f, 2)–(0, e, 1) | 2,145.849 | 1.050 | 1.000 |
| (1, e, 1)–(1, f, 1) | 2,145.445 | 1.111 | 0.406 |
| (2, e, 3)–(1, f, 1) | 2,146.199 | 0.723 | 0.264 |
| (1, f, 4)–(0, e, 1) | 2,150.597 | 0.270 | 0.257 |
| (1, f, 3)–(0, e, 1) | 2,148.813 | 0.175 | 0.167 |
| (2, f, 2)–(2, e, 1) | 2,145.404 | 1.726 | 0.097 |
| (1, e, 3)–(1, f, 1) | 2,154.309 | 0.241 | 0.088 |
| (0,e, 2)–(1, f, 1) | 2,149.747 | 0.186 | 0.068 |
| (1, e, 2)–(1, f, 1) | 2,148.475 | 0.175 | 0.064 |
| (1, f, 1)–(0, e, 1) | 2,143.251 | 0.064 | 0.061 |
| (2, e, 4)–(1, f, 1) | 2,149.096 | 0.093 | 0.034 |
| (3, f, 3)–(2, e, 1) | 2,146.523 | 0.462 | 0.026 |
| (0, e, 1)–(1, f, 1) | 2,142.452 | 0.061 | 0.022 |
| (2, e, 1)–(1, f, 1) | 2,143.633 | 0.060 | 0.022 |
| (2, f, 4)–(2, e, 1) | 2,151.396 | 0.258 | 0.014 |
| (1, f, 4)–(2, e, 1) | 2,149.416 | 0.179 | 0.010 |
| (2, f, 3)–(2, e, 1) | 2,148.495 | 0.160 | 0.009 |
| (3, f, 4)–(2, e, 1) | 2,147.451 | 0.141 | 0.008 |
| (3, e, 2)–(3, f, 1) | 2,145.361 | 1.616 | 0.006 |
| (1, f, 2)–(2, e, 1) | 2,144.668 | 0.093 | 0.005 |
| (1, f, 3)–(2, e, 1) | 2,147.632 | 0.086 | 0.005 |
| (1, f, 1)–(2, e, 1) | 2,142.070 | 0.057 | 0.003 |
| (3, f, 4)–(2, e, 2) | 2,146.111 | 0.452 | 0.001 |
| (3, e, 3)–(2, f, 1) | 2,146.119 | 0.423 | 0.001 |
| (1, f, 1)–(1, e, 1) | 2,140.250 | 1.105 | 0.001 |
| (0, e, 1)–(1, f, 2) | 2,139.846 | 1.049 | 0.001 |
| (1, f, 2)–(2, e, 2) | 2,143.328 | 0.313 | 0.001 |
| (1, e, 3)–(2, f, 1) | 2,152.200 | 0.287 | 0.001 |
| (1, e, 2)–(2, f, 1) | 2,146.366 | 0.271 | 0.001 |
| (2, f, 2)–(2, e, 2) | 2,144.063 | 0.263 | 0.001 |
| (2, e, 4)–(2, f, 1) | 2,146.988 | 0.239 | 0.001 |
| (1, f, 3)–(2, e, 2) | 2,146.292 | 0.243 | 0.001 |

The lower and upper states involved in the transitions are numbered with the set of parameters ($J$, $P$, $n_{J,P}$). The line strength values are multiplied by 10

**Table 7** Predicted infrared transition frequencies ($cm^{-1}$), line strengths, and relative intensities at temperature of 0.6 K for CO–$pH_2$–He complex from vibrationally averaged five-dimensional $V_{MLRQ}$ PES

| Transitions | | Line | Intensity |
|---|---|---|---|
| Upper–lower | Calc. | Strength | (0.6 K) |
| (1, f, 4)–(0, e, 1) | 2,146.958[a] | 1.066 | 1.000 |
| (1, e, 2)–(1, f, 1) | 2,146.599 | 0.898 | 0.244 |
| (1, f, 1)–(0, e, 1) | 2,143.601 | 0.149 | 0.140 |
| (1, e, 3)–(1, f, 1) | 2,146.908 | 0.374 | 0.102 |
| (0, e, 3)–(1, f, 1) | 2,147.539 | 0.285 | 0.077 |
| (1, e, 3)–(1, f, 2) | 2,146.440 | 0.627 | 0.055 |
| (1, e, 2)–(1, f, 2) | 2,146.131 | 0.540 | 0.048 |
| (0, e, 1)–(1, f, 1) | 2,142.569 | 0.148 | 0.040 |
| (0, f, 1)–(1, e, 1) | 2,145.929 | 0.715 | 0.038 |
| (2, e, 1)–(1, f, 1) | 2,144.061 | 0.130 | 0.035 |
| (2, e, 4)–(1, f, 1) | 2,146.761 | 0.112 | 0.030 |
| (2, f, 3)–(2, e, 1) | 2,146.413 | 0.781 | 0.020 |
| (0, e, 4)–(1, f, 2) | 2,148.729 | 0.194 | 0.017 |
| (1, e, 1)–(1, f, 2) | 2,143.299 | 0.186 | 0.016 |
| (2, f, 4)–(1, e, 1) | 2,147.067 | 0.271 | 0.014 |
| (2, f, 4)–(2, e, 1) | 2,146.770 | 0.474 | 0.012 |
| (2, f, 3)–(1, e, 1) | 2,146.710 | 0.229 | 0.012 |
| (1, f, 2)–(1, e, 1) | 2,142.876 | 0.186 | 0.010 |
| (2, f, 3)–(2, e, 2) | 2,146.129 | 0.712 | 0.009 |
| (3, f, 4)–(2, e, 1) | 2,147.113 | 0.303 | 0.008 |
| (2, e, 2)–(1, f, 2) | 2,143.881 | 0.079 | 0.007 |
| (2, f, 1)–(1, e, 1) | 2,144.209 | 0.122 | 0.006 |
| (2, e, 1)–(1, f, 2) | 2,143.593 | 0.060 | 0.005 |
| (2, f, 4)–(2, e, 2) | 2,146.486 | 0.297 | 0.004 |
| (1, f, 1)–(2, e, 1) | 2,142.108 | 0.127 | 0.003 |
| (0, f, 3)–(1, e, 1) | 2,153.142 | 0.062 | 0.003 |
| (3, f, 4)–(2, e, 2) | 2,146.829 | 0.187 | 0.002 |
| (3, f, 1)–(2, e, 1) | 2,144.382 | 0.072 | 0.002 |
| (3, f, 2)–(2, e, 1) | 2,144.691 | 0.066 | 0.002 |
| (1, f, 2)–(2, e, 1) | 2,142.579 | 0.060 | 0.002 |
| (2, f, 1)–(2, e, 1) | 2,143.912 | 0.057 | 0.001 |
| (3, e, 3)–(3, f, 1) | 2,146.297 | 1.150 | 0.001 |
| (1, f, 2)–(2, e, 2) | 2,142.295 | 0.078 | 0.001 |
| (3, e, 3)–(2, f, 1) | 2,146.770 | 0.268 | 0.001 |
| (3, f, 1)–(2, e, 2) | 2,144.098 | 0.065 | 0.001 |
| (2, f, 1)–(2, e, 2) | 2,143.628 | 0.063 | 0.001 |
| (3, f, 2)–(2, e, 2) | 2,144.407 | 0.051 | 0.001 |

The lower and upper states involved in the transitions are numbered with the set of parameters ($J$, $P$, $n_{J,P}$). The line strength values are multiplied by 10

[a] The observed value is 2,146.93 $cm^{-1}$

Figure 8 shows the "Solvent" $pH_2$(upper panels), He (middle panels), and $pH_2$–He (lower panels) densities in the first three torsional levels of CO–$(pH_2)_2$, CO–$(He)_2$, and CO–$pH_2$–He, respectively. For the $\upsilon_t = 0$ ground states, the density distribution patterns of particle-2 across three complexes are quite different, while for $\upsilon_t = 1$, 2, and 3 excited states, the density distribution patterns are similar among the three species, because at these levels energy patterns are determined by the nodal structures instead of inter-particle interactions and can be explained by a simple one-dimensional particle-in-a-box model along the $\phi$ coordinate [27, 39].

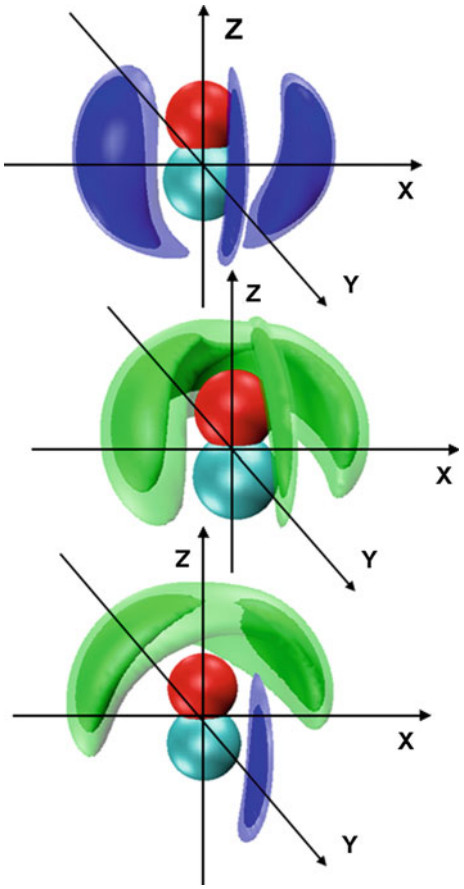


**Fig. 7** Three-dimensional representations of the $pH_2$ density for the ground state CO–$(pH_2)_2$ trimer (*upper panel*) in the body-fixed frame, compared with the helium atom density for a ground-state CO–$(He)_2$ trimer (*middle panel*) and the $pH_2$–He density of a ground-state CO–$pH_2$–He trimer (*lower panel*). The position of the first $pH_2$ or He defines the location of the *yz* plane, while the density of the second pH2 or He particle is shown in the *xy* plane. These results were obtained with the values of the Gaussian standard deviations defining the densities set at $\sigma_x = \sigma_z = 0.25$ Å and $\sigma_y = 0.1$ Å for particle-1 and at $\sigma_x = \sigma_y = \sigma_z = 0.25$ Å for particle-2

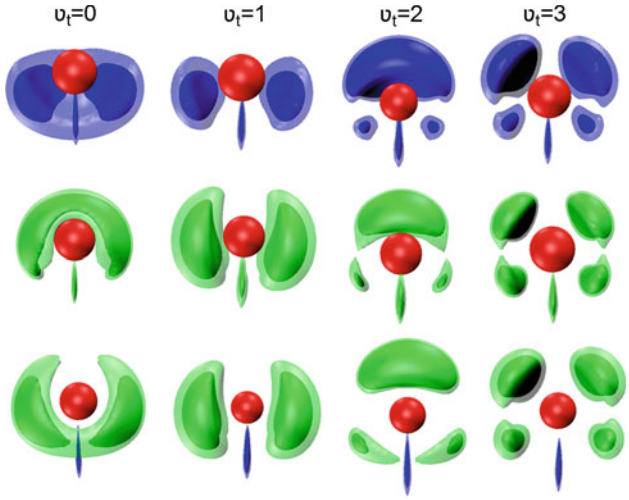


**Fig. 8** Three-dimensional representations of the "solvent" ($pH_2$, He and $pH_2$–He) density for CO–$(pH_2)_2$ (*upper panels*), CO–$(He)_2$ (*middle panels*), and CO–$pH_2$–He (*lower panels*) trimers in their four lowest torsion vibrational levels

## 4 Conclusions

Predicted rovibrational energy levels, microwave, and infrared spectra for CO–$(pH_2)_2$, CO–$(oD_2)_2$, and CO–$pH_2$–He complexes have been obtained from the vibrationally averaged five-dimensional PESs as a sum of accurate CO–$pH_2$, CO–$oD_2$, or CO–He and $pH_2$–$pH_2$, $oD_2$–$oD_2$, or $pH_2$–He pair potentials. For CO–$(pH_2)_2$ complex, it is remarkable that the predictions are in good agreement with the experimental measurements of the microwave and infrared transitions, showing that the spectrum can be reliably predicted by this additive approach. Small remaining differences between experiment and theory may in part be due to our neglect of three-body contributions to the interaction energy. For CO–$(oD_2)_2$ trimer, the infrared spectrum has been predicted for the first time. For CO–$pH_2$–He, one observed IR transition tentatively assigned as b-type $R(0)$ was confirmed based on the calculated line position and intensity. Although many of the transitions for those three complexes have not been observed, our predictions will be a good guidance for future experimental research. The calculated band origin shift from vibrationally averaged five-dimensional PESs associated with the fundamental transition of CO is $-0.369$ cm$^{-1}$ for CO–$(pH_2)_2$, which is also in good agreement with the experimental value of $-0.355$ cm$^{-1}$. The band origin shifts for CO–$(oD_2)_2$ and CO–$pH_2$–He are also predicted for the first time. In any case, the result indicates that a reduced-dimension treatment of $pH_2$ or $oD_2$ rotation based on a "adiabatic-hindered-rotor" average over its relative orientations can yield accurate spectra predictions. Three-dimensional representation of the $pH_2$, $oD_2$, or He density in the body-fixed frame is very useful to develop some intuitive feeling regarding the nature of these species, and it clearly shows the density distribution of the second $pH_2$, $oD_2$, or He relative to the first one. The $pH_2$ and $oD_2$ distributions in the vibrational ground state of CO–$(pH_2)_2$ and CO–$(oD_2)_2$ are highly localized, with two maxima, while the He distribution in CO–$(He)_2$ or CO–$pH_2$–He is delocalized, with one maximum lying in an incomplete ring wrapped around the CO molecule axis at the O end.

**Acknowledgments** The authors thank Professor Piotr Jankowski (Nicolaus Copernicus University) for providing us with his $V_{12}$ potential for the $H_2$–CO complex. This research has been supported by the National Natural Science Foundation of China (Grant Nos. 21003058 and 21273094), the Program for New Century Excellent Talents in University, and the Natural Sciences and Engineering Research

Council of Canada (NSERC). We acknowledge the High Performance Computing Center (HPCC) of Jilin University for supercomputer time.

## References


1. Grebenev S, Toennies JP, Vilesov AF (1998) Science 279:2083
2. Nauta K, Miller RE (2001) J Chem Phys 115:10254
3. Tang J, Xu Y, McKellar ARW, Jäger W (2002) Science 297:2030
4. Lehnig R, Jäger W (2006) Chem Phys Lett 424:146
5. Tang J, McKellar ARW (2003) J Chem Phys 119:754
6. Surin LA, Potapov AV, Dumesh BS, Schlemmer S, Xu Y, Raston PL, Jäger W (2008) Phys Rev Lett 101:233401
7. Tang J, McKellar ARW (2004) J Chem Phys 121:181
8. Tang J, McKellar ARW, Mezzacapo F, Moroni S (2004) Phys Rev Lett 92:145503
9. McKellar ARW (2008) J Chem Phys 128:044308
10. Xu Y, Jäger W (2003) J Chem Phys 119:5457
11. McKellar ARW, Xu Y, Jäger W (2006) Phys Rev Lett 97:183401
12. Tang J, McKellar ARW (2003) J Chem Phys 119:5467
13. McKellar ARW, Xu Y, Jäger W (2007) J Phys Chem A 111:7329
14. Li H, Ma YT (2012) J Chem Phys 137:234310
15. Wang L, Xie DQ, Le Roy RJ, Roy P-N (2012) J Chem Phys 137:104311
16. McKellar ARW (2007) J Chem Phys 127:044315
17. Knaap CJ, Xu Y, Jäger W (2011) Mol Spectrosc 268:130
18. Xu Y, Blinov N, Jäger W, Roy P-N (2006) J Chem Phys 124:081101
19. Toennies JP (2013) Mol Phys 111:1879
20. Zeng T, Roy P-N (2014) Rep Prog Phys 77:046601
21. Grebenev S, Sartakov B, Toennies JP, Vilesov AF (2000) Science 289:1532
22. Moroni S, Botti M, De Palo S, McKellar ARW (2005) J Chem Phys 122:094314
23. Tang J, McKellar ARW (2004) J Chem Phys 121:3087
24. Tang J, McKellar ARW (2005) J Chem Phys 123:114314
25. Michaud J, Xu Y, Jäger W (2008) J Chem Phys 129:144311
26. Li H, Le Roy RJ, Roy P-N, McKellar ARW (2010) Phys Rev Lett 105:133401
27. Li H, McKellar ARW, Le Roy RJ, Roy P-N (2011) J Phys Chem A 115:7327
28. Li H, Roy P-N, Le Roy RJ (2010) J Chem Phys 132:214309
29. Zeng T, Guillon G, Cantin JT, Roy P-N (2013) J Phys Chem Lett 4:239
30. Wang L, Xie DQ, Le Roy RJ, Roy P-N (2013) J Chem Phys 139:034312
31. Raston PL, Jager W, Li H, Le Roy RJ, Roy P-N (2012) Phys Rev Lett 108:253402
32. Jankowski P, McKellar ARW, Szalewicz K (2012) Science 336:1147
33. Jankowski P, Surin LA, Potapov A, Schlemmer S, McKellar ARW, Szalewicz K (2013) J Chem Phys 138:084307
34. Li H, Zhang XL, Le Roy RJ, Roy P-N (2013) J Chem Phys 139:164315
35. McKellar ARW (1998) J Chem Phys 108:1811
36. McKellar ARW, Xu Y, Jäger W, Bissonnette C (1999) J Chem Phys 110,10766
37. Surin LA, Roth DA, Pak I, Dumesh BS, Lewen F, Winnewisser G (2000) J Chem Phys 112:4064
38. Wang XG, Carrington T Jr, McKellar ARW (2009) J Phys Chem A 113:13331
39. Wang XG, Carrington T Jr, Tang J, McKellar ARW (2005) J Chem Phys 123:34301
40. Wang XG, Carrington T Jr (2010) Can J Phys 88:779
41. Tang J, McKellar ARW, Wang XG, Carrington T Jr (2009) Can J Phys 87:417
42. Li H, Liu YD, Jäger W, Le Roy RJ, Roy P-N (2010) Can J Phys 88:1146
43. Li H, Roy P-N, Le Roy RJ (2010) J Chem Phys 133:104305
44. Telle H, Telle U (1981) J Mol Spectrosc 85:248
45. Patkowski K, Cencek W, Jankowski P, Szalewicz K, Mehl JB, Garberoglio G, Harvey AH (2008) J Chem Phys 129:094304
46. Chuaqui CE, Le Roy RJ, McKellar ARW (1994) J Chem Phys 101:39
47. Jeziorska M, Cencek W, Patkowski K, Jeziorski B, Szalewicz K (2007) J Chem Phys 127:124303
48. Bramley MJ, Tromp JW, Carrington T Jr, Corey GC (1994) J Chem Phys 100:6175
49. Mladeovic M (2000) J Chem Phys 112:1070
50. Gatti F, Lung C, Menou M, Justum Y, Nauts A, Chapuisat X (1998) J Chem Phys 108:8804
51. Yu HG (2002) Chem Phys Lett 365:189
52. Light JC, Hamilton IP, Lill JV (1985) J Chem Phys 82:1400
53. Chen R, Guo H (2001) J Chem Phys 114:1467
54. Wang XG, Carrington T Jr (2001) J Chem Phys 114:1473
55. Bishop DM, Cheung LM (1980) J Chem Phys 72:5125
56. Parker GA, Snow RL, Pack RT (1976) J Chem Phys 64:1668
57. Peterson KA, McBane GC (2005) J Chem Phys 123:084314
58. McKellar ARW (1991) Chem Phys Lett 186:58

Theor Chem Acc (2014) 133:1557
DOI 10.1007/s00214-014-1557-7

REGULAR ARTICLE

# Numerical solution of solvent reorganization energy and its application in electron transfer reaction

**Ting-Jun Bi · Mei-Jun Ming · Hai-Sheng Ren · Jian-Yi Ma · Xiang-Yuan Li**

Received: 31 May 2014 / Accepted: 31 July 2014 / Published online: 27 August 2014
© Springer-Verlag Berlin Heidelberg 2014

**Abstract** According to our recent studies on the nonequilibrium solvation, the solvent reorganization energy $\lambda_s$ is found to be the cost of maintaining the residual polarization, which equilibrates with the constraining extra electric field. In this work, a matrix form of $\lambda_s$ has been formulated based our new analytical expression of the solvent reorganization energy. By means of the integral equation formulation-polarizable continuum model (IEF-PCM), a new numerical algorithm for $\lambda_s$ has been implemented as a subroutine coupled with the Q-Chem package. Then, we have performed a comparison of numerical results with analytical solution obtained by two-sphere model for $\lambda_s$ in self-exchange electron transfer (ET) reaction of He–$He^+$ system. The numerical results and analytical solution coincide as the distance between the donor and the acceptor. In order to compare with our pervious numerical algorithm with dielectric polarizable continuum model, self-exchange ET reactions between tetracyanoethylene, tetrathiafulvalene, and their corresponding ionic radicals in acetonitrile have been studied. Overall, the solvent reorganization energy calculated by IEF-PCM is more reasonable since IEF-PCM gives a better self-energy of surface element.

**Keywords** Electron transfer · Constrained density functional theory · Constrained equilibrium · Two-sphere model · Numerical solution

## 1 Introduction

Through thermal fluctuation [1] or light irradiation [2], an electron transfer (ET) from a donor chemical species to the acceptor is a fundamental step in all oxidation–reduction reactions that impacts a variety of chemical and biochemical processes. The studies about ET in photosynthesis, respiration, and various enzyme-catalyzed redox reactions have made many significant progresses.

ET reactions are also remarkable for their simple theoretical concept. The most widespread theory for ET was developed by Marcus and Hush [3, 4], which provides a helpful physical–chemical reference framework. With the harmonic approximation, two parabolas along with a reaction coordinate can be used to represent the energy curves of reaction and product states as showed in Fig. 1. In the diabatic representation, two curves intersect, and crossing point ($q_c$) corresponds to the transition state. With the assumption of both parabolas with same curvature, the activation energy $\Delta G^+$ is given by

$$\Delta G^+ = \frac{(\lambda + \Delta G^0)^2}{4\lambda} \tag{1}$$

where $\Delta G^0$ is the reaction heat, in other words, the driving force, and $\lambda$ is called the reorganization energy including contributions from both the solute and the solvents. An ET is the simplest chemical reaction because it does not involve any bond-breaking or bond-forming. For a self-exchange ET, the activation energy is only related to reorganization energy, i.e., $\Delta G^+ = \lambda/4$. $\lambda$ is usually separated into two

Dedicated to Professor Guosen Yan and published as part of the special collection of articles celebrating his 85th birthday.

T.-J. Bi · M.-J. Ming · H.-S. Ren · X.-Y. Li (✉)
College of Chemical Engineering, Sichuan University, Chengdu 610065, China
e-mail: xyli@scu.edu.cn

J.-Y. Ma
Institute of Atomic and Molecular Physics, Sichuan University, Chengdu 610065, Sichuan, China

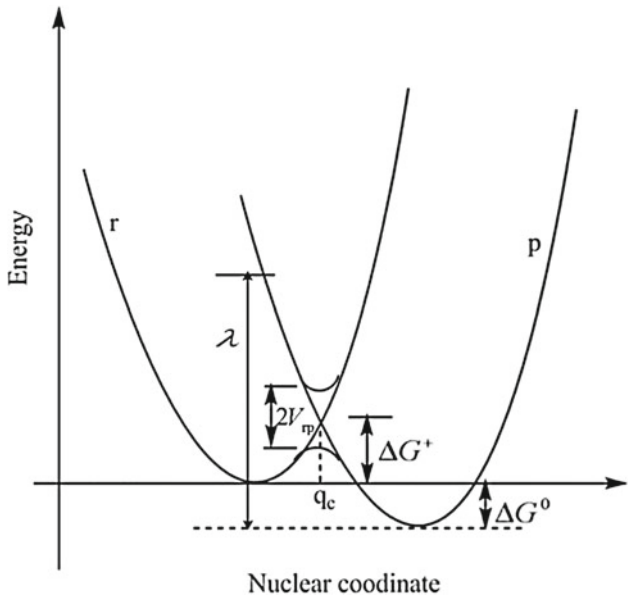


**Fig. 1** Potential energy curves of ET reaction

parts: the inner reorganization energy $\lambda_m$ corresponding to the energy needed to distort the bonds and angles in the reactant, while the solvent reorganization energy $\lambda_s$ arising from the polarization of surrounding solvent. For $\lambda_m$, many theoretical computational methods, such as the most common Nelsen's four-point methods [5] and its correction forms [6], have been established. Another widely used method is based on the diabatic state through constrained density functional theory (CDFT) [7]. For evaluation of $\lambda_s$, the key problem is to correctly deal with the scheme of nonequilibrium solute–solvent interaction. Therefore, how to set up a rational expression of nonequilibrium solvation energy is a big challenge in theory [8, 9].

By introducing the constrained equilibrium approach in continuum model, our group proposed a new way to the nonequilibrium solvation model and obtained the expression for electrostatic solvation energy in the nonequilibrium polarization case [10–12]. This expression has been successfully applied to the evaluation of vertical ionization energy of hydrated electron making use of approximation of spherical cavity and point charge [10], solvatochromic shift of absorption spectra with solvation model of sphere cavity and point dipole moment [11], and $\lambda_s$ of ET reactions by two-sphere model [12] and numerical solution [13]. In present work, we re-derive a matrix expression of $\lambda_s$ for the gain of the popularization potential and the self-energy of surface element. IEF-PCM has been applied for the implementation of numerical solution of $\lambda_s$.

## 2 Theory

As shown in Scheme 1, for an ET, or a photo absorption/emission process in the solvent, the system firstly establishes an initial equilibrium state 1 $[\rho_1, \varphi_1^{eq}]$, where $\rho_1$ and $\varphi_1^{eq}$ stand for solute charge distribution and solvent polarization potential (total electric potential excluding the vacuum potential due to solute charge), respectively. After a fast change of solute charge from $\rho_1$ to $\rho_2$, the dynamic polarization of the solvents adjusts itself quickly to equilibrate with $\rho_2$, while the inertial polarization keeps fixed. The system reaches the nonequilibrium polarization state 2 $[\rho_2, \varphi_2^{non}]$, where $\varphi_2^{non}$ is the nonequilibrium polarization potential. After enough long time, the inertial polarization finally reaches to the one which equilibrates to the solute charge $\rho_2$, and the system relaxes to the equilibrium state 2 $[\rho_2, \varphi_2^{eq}]$, with $\varphi_2^{eq}$ being the equilibrium polarization potential corresponding to $\rho_2$.

The rational description of $\lambda_s$ requires a proper account of thermodynamical nonequilibrium effect, and how to obtain the energy for nonequilibrium state theoretically is in general a difficult task [9–14]. Usually, classical thermodynamics cannot be directly adopted to handle the nonequilibrium polarization of dielectric media, but the constrained equilibrium approach proposed by Leontovich [15] provides in some cases a way to the gain of the free energy of a thermodynamically nonequilibrium state. This approach is based on the following three assumptions [10, 11, 16–18]. Firstly, by imposing suitable external conservative forces, a nonequilibrium state of an isothermal system without flow can be mapped to a constrained equilibrium state, which has the same internal variables as those in the nonequilibrium state. Secondly, the differences in state function between the constrained equilibrium and any other equilibrium state can be calculated simply by means of classical thermodynamics. Thirdly, the external forces can be removed suddenly without friction from the constrained equilibrium system so as to recover the true nonequilibrium situation. Recently, our group applied this thermodynamical principle to construct the constrained equilibrium states $[\rho_2 + \rho_{ex}, \varphi_2^{non}]$ where $\rho_{ex}$ represents the external electric charge. In this way, $\lambda_s$ can be obtained as below [10–12]:

$$\lambda_s = -\frac{1}{2}\int_V \rho_{ex}\left(\varphi_2^{non} - \varphi_2^{eq}\right)\mathrm{d}V \tag{2}$$

The detailed derivation for Eq. (2) can be found in the pervious papers [16–18]. An alternative form of Eq. (2) can be derived by means of Gauss formula,

**Scheme 1** .

$$\left[\rho_1, \varphi_1^{eq}\right] \xrightarrow{\text{fast}} \left[\rho_2, \varphi_2^{non}\right] \xrightarrow{-\lambda} \left[\rho_2, \varphi_2^{eq}\right] \xrightarrow{+\rho_{ex},\text{quasistatic}} \left[\rho_2 + \rho_{ex}, \varphi_2^{non}\right]$$

$$\lambda_s = -\frac{1}{2}\oint_S V_{ex}(\sigma_2^{non} - \sigma_2^{eq})dS$$
$$= -\frac{1}{2}\oint_S (\Delta\sigma^{dyn} - \Delta\sigma^{eq})V_{ex}dS \quad (3)$$

where $V_{ex}$ is electric potential arising from $\rho_{ex}$, $\sigma_2^{non}$and $\sigma_2^{eq}$ are the nonequilibrium and equilibrium polarization distributions on the surface, respectively. $\Delta\sigma^{dyn}$ is surface polarization charge density generated by the change of the solute charge $\Delta\rho$ ($\Delta\rho = \rho_2 - \rho_1$) in the medium with a dielectric constant of $\varepsilon_{op}$, while $\Delta\sigma^{eq}$ is that in the medium with a dielectric constant of $\varepsilon_s$. Equation (3) can be easily changed into matrix form, i.e.,

$$\lambda_s = -\frac{1}{2}V_{ex}^T(\Delta q^{dyn} - \Delta q^{eq}) \quad (4)$$

here, $V_{ex}^T$ is transposed matrix of the column matrix $V_{ex}$ for electrostatic potentials produced by $\rho_{ex}$. $\Delta q^{dyn}$ and $\Delta q^{eq}$ are the matrix forms of $\Delta\sigma^{dyn}$and $\Delta\sigma^{eq}$, respectively. In order to obtain the elements of $\Delta q^{dyn}$, $\Delta q^{eq}$, and $V_{ex}$, we can solve the linear matrix equation of IEF-PCM [19, 20], i.e.,

$$D_q = -V \quad (5)$$

where D is the interaction square matrix collecting elements related to geometry of the cavity and the dielectric constants $\varepsilon(\varepsilon_s$ or $\varepsilon_{op})$. The column vector $q$ collects the polarization surface charges [21]. According to the equilibrium polarization, we have

$$D_{\varepsilon_s}q_2^{eq} = -V_{2c} \quad (6)$$

$$D_{\varepsilon_s}\Delta q^{eq} = -\Delta V_c \quad (7)$$

$$D_{\varepsilon_{op}}\Delta q^{dyn} = -\Delta V_c \quad (8)$$

$$D_{\varepsilon_s}(\Delta q^{dyn} - \Delta q^{eq}) = \Delta V_{ex} \quad (9)$$

Then, a new matrix form for the solvent reorganization energy is given by

$$\lambda_s = \frac{1}{2}\left[(D_{\varepsilon_s}^{-1} - D_{\varepsilon_{op}}^{-1}) \times \Delta V_c\right]^T \times D_{\varepsilon_s} \times \left[(D_{\varepsilon_s}^{-1} - D_{\varepsilon_{op}}^{-1}) \times \Delta V_c\right] \quad (10)$$

Equation (10) tells that the solvent reorganization energy from our new theory depends on the interaction matrix D and the solute potential change $\Delta V_c$. The detailed derivation of Eq. (10) can be found in our recently submitted paper [22]. This equation can easily be obtained by IEF-PCM. More interestingly, differing from D-PCM, the self-energy of a given surface element is not involved in the above expressions. It means that IEF-PCM is more suitable for our new model. In this work, we have developed a subroutine coupled with the Q-Chem package [23] to numerically calculate the values of $\lambda_s$.

## 3 Results and discussion

The self-exchange ET reaction in helium and its cation radical (He–$He^+$) system is here taken as a simple test example. The motivation of choosing this system is to check our numerical algorithm by comparing the numerical values with the results of analytical two-sphere model. It is well known that the diatomic system is an ideal system for us to apply two-sphere model; thus, we can take this ET as a benchmark example. In our previous work [18], we obtained the expression of analytic solution for $\lambda_s$ with two-sphere model as follow:

$$\lambda_s = \frac{\Delta q^2}{2}\left(\frac{1}{r_D} + \frac{1}{r_A} - \frac{2}{d}\right)\frac{(\varepsilon_{op}^{-1} - \varepsilon_s^{-1})^2}{(1 - \varepsilon_s^{-1})} \quad (11)$$

where $\Delta q$ is defined as the amount of point charge transferred from sphere D to A as showed in Fig. 2. $r_A$ and $r_D$ are radii of the acceptor and donor sphere, respectively, while $d$ is the distance between the two spherical centers. $\varepsilon_{op}$ and $\varepsilon_s$ are the optical and static dielectric constants. According to our pervious study [12], this equation gives a satisfying estimation of $\lambda_s$ for pyrene-fumaronitrile and ferrous-ferric systems compared with available experimental values. Here, we use Eq. (11) to calculate $\lambda_s$ of He–$He^+$. When the two helium atoms are far from each other, the cavity consists of two separated spheres. When $d$ is large enough, the values of $\lambda_s$ by numerical solution ought to approach to the results by two-sphere model. So, this example can be considered as the criteria to detect whether the numerical program is correct or not.

For the numerical algorism, the well-known Generating Polyhedra (GEPOL) procedure [24] has been applies, with the Waals radii being scaled by a factor of 1.2 in the construction of the cavity. The van der Waals radius of helium

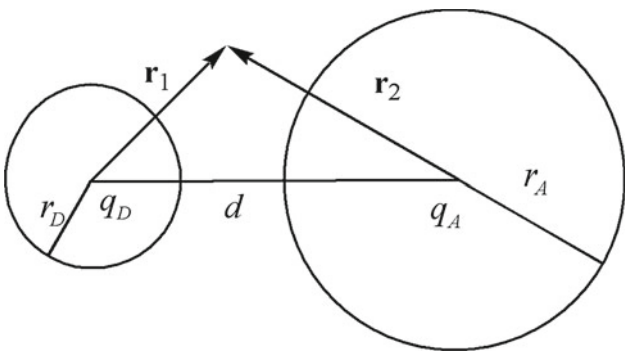


**Fig. 2** Two-sphere model

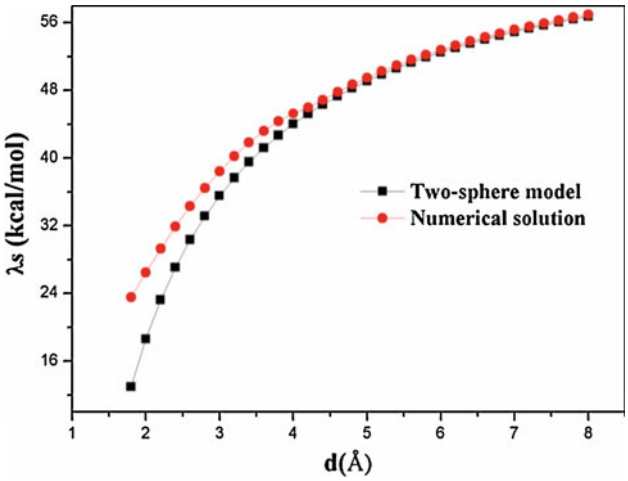


**Fig. 3** Distance dependency of the solvent reorganization energy

is 1.2 Å. Thus, the cavity radius equals to 1.44 Å. Each sphere is divided into 960 tesserae in order to guarantee the computation precision. We take water as solvent, for which the static and the optical dielectric constants are 78.5 and 1.778, respectively. When the distance of two helium atoms is less than 2.88 Å, the solvent cavity consists of two intersected spheres. Increasing the distance to 4.0 Å, the cavity is divided into two independent spheres, and each has 960 tesserae.

The values of $\lambda_s$ with the increasing of the separation distance by both two-sphere model and numerical solution are depicted in Fig. 3. It can be seen that the numerical solution and two-sphere model give consistent results when the distance is larger than about 4.5 Å. At the critical value of 2.88 Å of separation distance, i.e., $d = r_A + r_D$, where the two cavities just contact with each other, the value of $\lambda_s$ is 33.12 kcal/mol by two-sphere model and 36.47 kcal/mol by the numerical solution. If we take the numerical solution as accurate, it will be found that two-sphere model underestimates $\lambda_s$ by about 10 %. This indicates that two-sphere approximation behaves very well when the two spheres are far from each other. However, the results of two-sphere model become worse when the two spheres intersect ($d < 2.88$ Å). Therefore, we should pay attention to the limitation of two-sphere model in applying it to calculate $\lambda_s$ of ET reactions.

Recently, CDFT was used to construct the diabatic states of ET [7, 20, 21, 23]. We studied the self-exchange ET reactions between TCNE, TTF, and their corresponding ionic radicals in acetonitrile. The structures TCNE and TTF are given in Fig. 4. We use the same method of CDFT as pervious paper [13] to optimize the geometries of the species and construct the diabetic states of those two ET systems. The values of the inner reorganization energy $\lambda_m$ were reported in Ref. [13] where one can find the detailed description of the geometry optimization and the calculation of $\lambda_m$. Here, we recalculate $\lambda_s$ for those two systems by means of the above IEF-PCM-based matrix expression of numerical algorithm. With explicitly constraining one moiety in the complex to have one charge more than the other moiety, the geometries have been optimized by changing the separation distance ($R_{AD}$) from 2.5 to 4.0 Å by CDFT with B3LYP/6-31 + g(d) method. The minimum energy structures are located at $R_{AD} = 3.35$ Å for TCNE/TCNE$^-$ and $R_{AD} = 3.42$ Å for TTF/TTF$^+$.

At the fixed donor–acceptor distances, CDFT method has been adopted to perform the calculation. The charge densities for the complex systems before and after the ET have been obtained [13]. With these charge distributions, the solvent reorganization energy has been calculated with Q-Chem according to Eq. (10), by introducing the Q-Chem output files to a separated subroutine that carries out the cavity construction and the calculation of polarized charges in the framework of IEFPCM. The obtained results for $\lambda_s$,with the experimental values available [25–27], are listed in Table 1. Besides, other theoretical data from the smoothed multisphere model (SMSM) [26] have been listed as well.

A quick glance at the SMSM results given in Table 1 leads us to a wrong impression that the traditional theory gives the rational reorganization energy. However, if we revisit the theoretical treatments by other authors, we will find there are some inconsistent treatments in selecting the cavity sizes comparing with the well-established

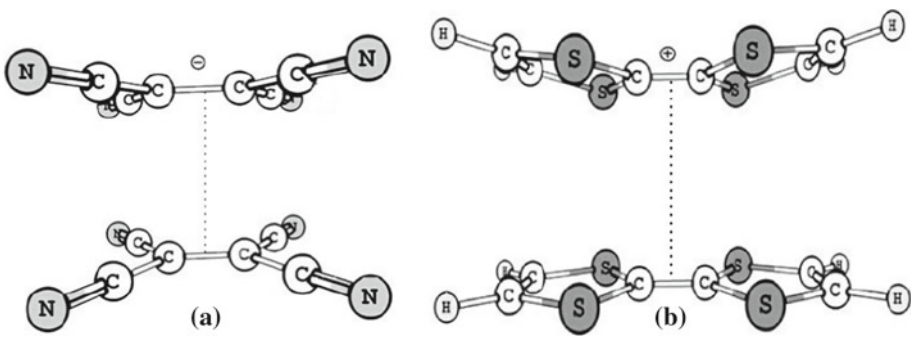


**Fig. 4** Structures of **a** TCNE/TCNE$^-$ and **b** TTF/TTF$^+$ complexes

**Table 1** Comparison of the theoretically calculated reorganization energies ($cm^{-1}$) with the experiment values in acetonitrile for ET systems $TCNE/TCNE^-$ and $TTF/TTF^+$

| System | $\lambda_s$ | $\lambda_m$ | $\lambda$ |
|---|---|---|---|
| $TCNE/TCNE^-$ | 5008[a] 5350[b] | 2265[a] 2300[b] | 7273[a] 7620[b] 7250[c] |
| $TTF/TTF^+$ | 3623[a] 4520[b] | 2274[a] 2270[b] | 5897[a] 6820[b] 5810[c] |

[a] This work. $\lambda_m$ is from our previous work based on D-PCM [13]

[b] Values based on the SMSM [26]

[c] Experiment data obtained from the intervalence absorption, Refs. [25–27]

equilibrium solvation. It is well-known that in the treatment of DPCM for equilibrium solvation, the solute cavity is constructed by taking the atomic sphere with van der Waals radii being scaled by a factor of 1.2. Such a cavity size usually exhibits reasonable equilibrium solvation energies. However, in the calculation of nonequilibrium solvation energy, authors in general need to use much larger solute cavities so as to obtain the solvent reorganization energy comparable to the experimental measurements, since the same cavity size as that used for equilibrium solvation energy calculation definitely leads to a much larger $\lambda_s$ by the previous theory. Here, we take the following examples for our arguments. As for experimental values, the energy of the diagnostic NIR band in the Class II mixed-valence $TCNE/TCNE^-$ and $TTF/TTF^+$ complex provides the direct measurement of the reorganization energy for ET as $\lambda = \nu_{IV}$ with $\nu_{IV}$ being the energy of the NIR band maximum [26, 28]. In the theoretical aspect, Kochi et al. applied the SMSM for the calculation of solvent reorganization. In the construction of the cavity, a value of ~2 Å for $r_p$, the radius of an effective sphere was taken for the solvent acetonitrile, and hence, the sphere radius takes a value of van der Waals radius plus $r_p$ in constructing the solute cavity [26]. We see that the H atomic sphere will take a radius of 3.2 Å, while in DPCM treatment for equilibrium salvation, this value is only 1.44 Å. So, in the SMSM treatment for nonequilibrium solvation, a much larger solute cavity is spanned compared with DPCM cavity for equilibrium solvation calculation. In fact, if one uses the widely accepted cavity size spanned by the spheres with 1.2 times of atomic van der Waals radii, it is expected that the SMSM will produces the doubled solvent reorganization energies, rather than those as listed in Table 1 by means of SMSM.

Apparently, the calibration to the experimental results in solvent reorganization energy calculation by enlarging the solute cavity is illogical, and it covers up the original mistakes in the traditional theories of nonequilibrium solvation and will cause the confusions in the sphere radius choice in solvent effect evaluation by continuum model. Moreover, these confused treatments for solute cavity size are also harmful to the confidence for the applications of continuum model, since people sometimes incorrectly attribute the ill results of solvent reorganization energy by Marcus model to the inaccuracies of continuum model [29].

## 4 Conclusion

In this work, a numerical algorithm for $\lambda_s$ has been introduced. After the development of a subroutine coupled with the Q-Chem package based on IEF-PCM algorithm, the matrix form of the solvent reorganization energy has been calculated. In order to prove its rationality, the self-exchange ET in $He–He^+$ system was investigated using both numerical solution and two-sphere model. Actually, $He–He^+$ system is just a positively charged diatom system. The choice of He atom here is just for the purpose of the gain of the atomic radius. For the point charge approximation, the calculation in fact has nothing to do with other properties of the atom selected, except the atom radius. From Fig. 2, one can see that the numerical and analytical treatments give consistent results when the distance between two helium atoms is larger than 4.5 Å. However, when the two spheres intersect ($d < 2.88$ Å), the results of two-sphere model become worse. This fact reminds us to be careful with the limitation of two-sphere model in applying to calculate $\lambda_s$ of ET. Finally, self-exchange ET reactions between TCNE, TTF, and their corresponding ionic radicals in acetonitrile have been investigated. The obtained reorganization energies $\lambda$ of 7,273 $cm^{-1}$ for TCNE and 5,897 $cm^{-1}$ for TTF are in good agreement with available experimental results of 7,250 and 5,810 $cm^{-1}$, respectively.

## References


1. Skourtis SS, Waldeck DH, Beratan DN (2010) Annu Rev Phys Chem 61:461
2. Piotrowiak P (1991) Chem Soc Rev 28:143
3. Hush N (1968) Electrochim Acta 13:1005
4. Marcus RA (1993) Rev Mod Phys 65:599
5. Nelsen SF, Blackstock SC, Kim Y (1987) J Am Chem Soc 109:677
6. Rauhut G, Clark T (1993) J Am Chem Soc 115:9127
7. Wu Q, Van Voorhis T (2006) J Phys Chem A 110:9212
8. Cramer CJ, Truhlar DG (2008) Acc Chem Res 41:760
9. Tomasi J, Mennucci B, Cammi R (2005) Chem Rev 105:2999
10. Wang X-J, Zhu Q, Li YK, Cheng XM, Li XY, Fu KX, He FC (2010) J Phys Chem B 114:2189
11. Ren HS, Li YK, Zhu Q, Zhu J, Li X-Y (2012) Phys Chem Chem Phys 14:13284
12. Wu HY, Ren HS, Zhu Q, Li XY (2012) Phys Chem Chem Phys 14:5538
13. Ren HS, Ming MJ, Ma JY, Li XY (2013) J Phys Chem A 117:8017
14. Mennucci B Cammi R, Interscience W (2007) Continuum solvation models in chemical physics: from theory to applications; Wiley Online Library

15. Leontovich M (1983) Statistical physics, vol 28. Nauka, Moscow, p 99
16. Li XY, Zhu Q, He FC, Fu KX (2011) Extension of classical thermodynamics to nonequilibrium polarization. In: Tadashi M (ed) InTech, Vol 11, p 206
17. Li XY, Wang QD, Wang JB, Ma JY, Fu KX, He FC (2010) Phys Chem Chem Phys 12:1341
18. Li XY, He FC, Fu KX, Liu W (2010) J Chem Theory Comput 9(1):23–37
19. Scalmani G, Frisch MJ (2010) J Chem Phys 132:114110
20. Cances E, Mennucci B, Tomasi J (1997) J Chem Phys 107:3032
21. Cossi M, Barone V (2000) J Phys Chem A 104:10614
22. Ming MJ, Bi TJ, Ma JY, Wang F, Li XY (2014) submitted for publication
23. Shao Y, Molnar LF, Jung Y, Kussmann J, Ochsenfeld C, Brown ST, Gilbert AT, Slipchenko LV, Levchenko SV, O'Neill DP (2006) Phys Chem Chem Phys 8:3172
24. Farazdel A, Dupuis M, Clementi E, Aviram A (1990) J Am Chem Soc 112:4206
25. Improta R, Barone V, Newton MD (2006) Chem Phys Chem 7:1211
26. Rosokha SV, Kochi JK (2007) J Am Chem Soc 129:828
27. Rosokha SV, Kochi JK (2007) J Am Chem Soc 129:3683
28. Rosokha S, Newton M, Head-Gordon M, Kochi JK (2006) Chem Phys 324(1):117
29. Johnson MD, Miller JR, Green NS, Closs GL (1989) J Phys Chem 93:1173

Theor Chem Acc (2014) 133:1550
DOI 10.1007/s00214-014-1550-1

REGULAR ARTICLE

# Adsorption of water molecules on sodium chloride trimer

**Cheng-Wen Liu · Gao-Lei Hou · Wei-Jun Zheng · Yi Qin Gao**

Received: 31 May 2014 / Accepted: 16 July 2014 / Published online: 12 August 2014
© Springer-Verlag Berlin Heidelberg 2014

**Abstract** The hydration of NaCl has been widely studied and believed to be important for understanding the mechanisms of salt dissolution in water and the formation of ice nucleus, cloud, and atmospheric aerosols. However, understanding on the *poly*-NaCl ion pair interacting with water is very limited. Here, we investigated the adsorption of water molecules on $(NaCl)_3$, using both theoretical calculations and anion photoelectron spectroscopy measurements. The calculated vertical detachment energies and the experimental ones agree well with each other. Furthermore, we found that, for neutral $(NaCl)_3(H_2O)_n$ ($n$ = 2–7) clusters, the water-doped cuboid and structures formed by adding water molecules on the Na–Cl edges of the cuboid are energetically favored; water molecules preferentially bind to the Na–Cl edge if the NaCl ion pair has larger partial charges than others. We also found the anionic structures are more various compared with neutral ones, and the $Na^+$ and $Cl^-$ ions are hydrated more easily in the anionic clusters than in the corresponding neutrals.

**Keywords** NaCl–water cluster · Integrated tempering sampling · Water-doped sodium chloride · Water adsorption on NaCl

Dedicated to Professor Guosen Yan and published as part of the special collection of articles celebrating his 85th birthday.

**Electronic supplementary material** The online version of this article (doi:10.1007/s00214-014-1550-1) contains supplementary material, which is available to authorized users.

C.-W. Liu · Y. Q. Gao (✉)
Beijing National Laboratory for Molecular Sciences,
Institute of Theoretical and Computational Chemistry,
College of Chemistry and Molecular Engineering,
Peking University, Beijing 100871, China
e-mail: gaoyq@pku.edu.cn

G.-L. Hou · W.-J. Zheng (✉)
Beijing National Laboratory for Molecular Sciences,
State Key Laboratory of Molecular Reaction Dynamics,
Institute of Chemistry, Chinese Academy of Sciences,
Beijing 100190, China
e-mail: zhengwj@iccas.ac.cn

Y. Q. Gao
Biodynamic Optical Imaging Center (BIOPIC),
Peking University, Beijing 100871, China

## 1 Introduction

Salt ions can strongly affect the water/air surface tension and the solubility of proteins [1–5]. They are also related to the formation and reactivity of sea salt aerosols [6–8]. Thus, one challenge is to understand the ion–water and water–water interactions at the molecular level and to obtain the detailed solvation mechanisms of ions and/or ion pairs in water [9–11]. Molecular clusters are considered to play important roles in providing the connection between the properties of isolated molecules/atoms and those of the condensed phase systems. In particular, due to their significance in many fields, small clusters of sodium chloride and water molecules $NaCl(H_2O)_n$ have called attention from both experimental [11–16] and theoretical [17–33] groups.

In contrast to the large number of studies on the clusters formed by a single sodium chloride ion pair and water molecules, i.e., $NaCl(H_2O)_n$, studies on $(NaCl)_x$ (with $x > 1$) are rare. There do exist several studies on sodium chloride clusters [34–37]. For example, Sunil and Jordan [34] performed theoretical calculations on negative $(NaCl)_{2–4}$ clusters and discussed the properties of the excess electron binding. This topic was revisited by Anusiewicz et al. [35] and they argued that there are two types of anions in this

system, dipole-bound anions and solvated-electron species based on their high-level calculations. Iwona et al. [36] reported results on $(NaCl)_{1-6}$ calculations in which various isomers with different bonding forms are presented. Ayuela et al. [37] also theoretically predicted the structures of $(NaCl)_n$ ($n \leq 19$) clusters, using the ab initio perturbed-ion model. It is noted that these two studies [36, 37] actually gave two similar minimal structures of $(NaCl)_3$. However, these studies do not include water molecules in the clusters, and thus, the detailed interactions of $(NaCl)_x$ with water remain unexplored. Motivated by the potential importance of $(NaCl)_3(H_2O)_n$ clusters in the formation of doped crystals [38], atmospheric processes at the ocean surface [39, 40], and salt dissolution processes [41], we herein investigated the initial hydration of $(NaCl)_3$ by using theoretical calculations and photoelectron spectroscopy experiments, for clusters $(NaCl)_3(H_2O)_n$ ($n = 0$–6). The calculations were performed for the clusters both in the anionic and neutral states.

Photoelectron spectroscopy in combination with quantum calculations is a very mature tool to study clusters [42]. However, computational studies on the clusters with relatively large size are hindered by the outstanding difficulty in covering the large configuration space of the clusters. There exist many local minima on the potential energy surfaces; thus, it is computationally challenging to locate all the stable isomers. In the current study, to overcome this difficulty, we used our well-established integrated tempering sampling (ITS) molecular dynamics [43] to generate structures of low configuration energies. ITS allows efficient search of structures by sampling over a broad energy range and thus permits fast identification of low-energy structures and transition states. The low-energy structures obtained from the ITS calculations are then optimized using both classical force field and DFT functional. This procedure was proven effective and efficient in structure search for $(H_2O)_n$, $LiI(H_2O)_n$, $CsI(H_2O)_n$ [44], and $NaCl(H_2O)_n$ [45] with $n$ being up to 20 in our previous studies. We note here that other global minimization methods besides ITS can be efficient and effective for searching the low-energy structures. However, through ITS simulation, one can readily obtain the various thermodynamic properties in addition to stable structures as well [44].

The rest of this account is organized as follows: In Sect. 2, we described the experimental details and theoretical methodologies; experimental spectra and computational results of both anions and neutrals and discussions are arranged in Sect. 3; and Sect. 4 is the concluding remarks.

## 2 Experimental details and theoretical methodologies

In this part, we will first describe the details of the anion photoelectron spectroscopy experiments. Then, a brief introduction of the basic principles of the integrated tempering sampling (ITS) method will be discussed. The theoretical details, including the classical MD (and ITS) simulations and the DFT calculations, are described in the last part.

### 2.1 Photoelectron spectroscopy

The experiments were conducted on a homebuilt apparatus consisting of a time-of-flight (TOF) mass spectrometer and a magnetic-bottle photoelectron spectrometer, which has been described previously [46]. Briefly, the $(NaCl)_3^-(H_2O)_n$ clusters were produced in a laser vaporization source, by laser ablating a rotating and translating NaCl disk target with the second harmonic (532 nm) light pulses from a Nd:YAG laser, while helium carrier gas with ~4 atm backing pressure seeded with water vapor was allowed to expand through a pulsed valve to generate and cool the hydrated $(NaCl)_3^-$ clusters. The cluster anions were mass-analyzed by the TOF mass spectrometer. The $(NaCl)_3^-(H_2O)_n$ ($n = 0$–6) clusters were each mass-selected and decelerated before being photodetached by the 532 nm (2.331 eV) photons from another Nd:YAG laser. The photodetached electrons were energy-analyzed by the magnetic-bottle photoelectron spectrometer. The instrumental resolution was approximately 40 meV for electrons with 1 eV kinetic energy.

### 2.2 Integrated tempering sampling (ITS) method

Briefly, in the ITS simulation, a modified potential energy function is obtained from the original potential by making use of an energy distribution function with the form of a summation of Boltzmann factors over a series of temperatures:

$$P(U) = \sum_{k=1}^{N} n_k e^{-\beta_k U} \tag{1}$$

where $\beta = 1/k_B T$, $k_B$ is the Boltzmann constant, $T$ the temperature, and $U$ the potential energy of the system.

The sampled potential energy range by such a method is largely expanded, to both low and high potential energies, when compared to standard MD simulations. In the current study, we used 300 discrete temperatures even spaced in the range of 100–250 K. In the ITS simulation, the system is governed with a biased potential function in the form of Eq. (1). An equilibrium simulation with ITS yields a biased distribution function as a function of the potential energy of the system,

$$\rho'(r) = \frac{e^{-\beta U'(r)}}{Q'} \tag{2}$$

where $Q' = \int e^{-\beta' U(r)} dr$. In ITS, since $U'(r)$ is a known function of $U(r)$, the distribution function $\rho(r)$ for the system with the unbiased potential can be recovered back from $\rho'(r)$ as:

$$\rho(r) = \frac{e^{-\beta U(r)}}{Q} = \rho'(r) \frac{e^{-\beta[U(r)-U'(r)]} Q'}{Q} \quad (3)$$

where $Q = \int e^{-\beta U(r)} dr$. More details can be found in our previous publications [43, 47].

### 2.3 Simulation details

We used SANDER module of AMBER 9.0 program package [48] to perform MD simulations of $(NaCl)_3(H_2O)_n$ ($n$ = 0–7), in which the ions 08 parameters [49] and single-point-charge/extended (SPC/E) water model [50] were utilized. The ion-water cross terms were calculated with the Lorentz Berthelot combination rules. These models are popular and well established in AMBER program package, and they give convincing bulk solution properties comparing to experimental data [49, 50]. One may expect more reliable thermodynamic properties in the classical simulations when more accurate models, such as polarizable force field, are utilized to these systems, but our earlier studies did show that the classical force field used in this study provides reasonable description of the cluster structures compared with the quantum calculations [44]. The initial configurations used for MD were generated randomly and followed by an energy minimization. To avoid the molecules to escape from the clusters to the vacuum, a spherical potential is applied to the center of mass of every atom. The restricting force of the added potential has the form of:

$$F(R) = \frac{\varepsilon}{1 + e^{-2\alpha\varepsilon|(r-r_0)|}} \quad (4)$$

where $r$ is the spatial vector of an atom, $\varepsilon$ is the maximal restrict force [here, we set = 5 kcal/(mol Å)], $r_0$ is the radius of sphere (here, we set $r_0$ = 7 Å), and is the flexibility constant of the sphere shell (we set = 5). In this way, the molecules are confined in a spherical space with a radius of 7 Å.

We collected a 100-ns-long ITS simulation trajectory for each system of $(NaCl)_3(H_2O)_n$. Hundreds of different low-energy configurations were chosen from simulated trajectory as the initial structures for structure optimization using classical force field. These structures then converged to several dozens of local minimal structures, and then, re-optimizations by DFT calculations were performed. The DFT calculations were performed using GAUSSIAN 09 program package [51]. The structures of $(NaCl)_3(H_2O)_n$ were fully optimized with DFT employing the dispersion-corrected hybrid functional ωB97XD [52]. The Pople's all-electron basis set 6-311++G(d,p) was used for all the atoms. The ωB97XD functional has been shown to perform extraordinarily well on describing dispersion interaction [53], which is the main consideration for such weak-interaction cluster systems. As the energetics and geometries of one electron-bound anion clusters will be evaluated, we add the diffuse functions to all atoms. After these structures were fully optimized, harmonic vibrational frequencies were calculated to confirm that they are indeed local minima and to obtain the zero-point energy corrections and the Gibbs free energies. Zero-point vibrational energy corrections were incorporated to the sum of the electron energies.

## 3 Results and discussions

### 3.1 The experimental and theoretical vertical detachment energies

The photoelectron spectra of $(NaCl)_3^-(H_2O)_n$ ($n$ = 0–6) clusters recorded at 532 nm are shown in Fig. 1. In general, all the spectral features of the clusters are broad, and their maxima are about 0.99, 1.04, 1.09, 1.11, 1.03, 1.05, and 1.07 eV for $n$ = 0–6, respectively. Specifically, for $(NaCl)_3^-(H_2O)$, there is an additional small feature centered at about 1.51 eV. Figures 2 and 3 present the typical low-energy structures for each cluster size along with their relative energies and calculated VDEs (the geometries and energetics are discussed below). The calculated VDEs of the lowest energy structures of $(NaCl)_3^-(H_2O)_n$ ($n$ = 0, 1, and 3–6) are in good accord with the experimental values. While for $(NaCl)_3^-(H_2O)_2$, the theoretical VDE of the lowest energy isomer, which is a distorted cuboid structure, is 0.54 eV and much lower than the experimental value of 1.09 eV. The VDE value is also 0.54 eV when calculated at the MP2/aug-cc-pvtz level of theory. These results at both ωB97XD and MP2 levels suggest that the structure $2A^-$ is unlikely the structure observed in the experiments. By examining the Gibbs free energies of these structures, it is found that structure $2C^-$ has the lowest Gibbs free energy and its theoretical VDE is 1.05 eV, consistent with the experimental measurement of 1.09 eV very well. For $(NaCl)_3^-(H_2O)_n$ ($n$ = 0, 1, and 3–6) clusters, we also checked their Gibbs free energies and found that the lowest electronic energy structures also have the lowest Gibbs free energies. These results suggest that the photoelectron spectra may relate to the structures of relative large stability in Gibbs free energies. The good performance of ωB97XD/6-311++G(d,p) on the $(NaCl)_3^-(H_2O)_n$ clusters shown above provides the credence of the following discussions on the corresponding neutral clusters.

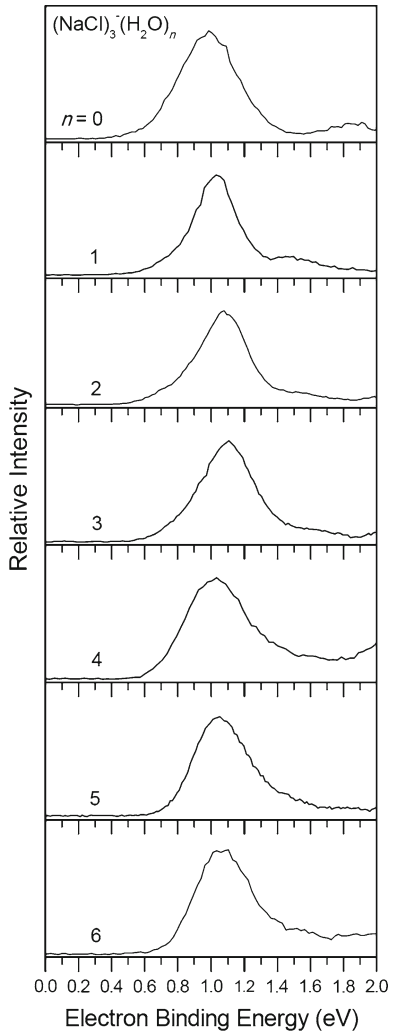


**Fig. 1** Photoelectron spectra of the $(NaCl)_3^-(H_2O)_n$ ($n$ = 0–6) clusters taken with 532 nm photons

## 3.2 Structures of $(NaCl)_3^-(H_2O)_n$

### *3.2.1 Typical minimal energy structures of $(NaCl)_3^-$*

The typical minimal energy structures of $(NaCl)_3^-$ are displayed in Fig. 2. As discussed later, the structures of salt–water molecules being adsorbed on $(NaCl)_3^-$ mostly evolve from these pure salt structures. The global minimum of the anion ($0A^-$ in Fig. 2) is a "Λ-shaped" structure, similar to that reported in the previous studies [34–37]. The VDE of this structure is calculated to be 1.045 eV, in good agreement with the experimental measured value of 0.99 eV. Structure $0B^-$ is higher in energy by only 0.001 eV than the structure $0A^-$. To the best of our knowledge, this "fish-shaped" $C_{2V}$-symmetric structure (structure $0B^-$) has not been reported so far for either anionic or neutral forms. The kite-shaped $0C^-$and a little distorted kite-shaped $0F^-$, which are optimized from the initial configuration of by changing the positions of $Na^+$ and $Cl^-$ of structure $0C^-$, are higher in energy than $0A^-$ by 0.170 and 0.519 eV, respectively. The linear $0D^-$ and Y-shaped $0E^-$ structures are much less stable than others identified here. In summary, most of the structures found in the current study are very similar to those reported previously. Therefore, we followed Anusiewicz et al. [35] for the naming of these structures. Besides, the current study also identifies a new low-energy "fish-shaped" structure ($0B^-$), which has not been reported before. Furthermore, the excess electron substantially increases the complexity of the potential energy surface, which will be shown by the richness of the anionic structures in comparison with the corresponding neutral ones.

### *3.2.2 Typical minimal energy structures of $(NaCl)_3^-(H_2O)_n$ ($n$ = 1–6)*

Figure 3 shows the typical minimal energy structures of $(NaCl)_3^-(H_2O)_n$ ($n$ = 1–6). For $n$ = 1, five of the six lowest energy structure are formed through adsorbing one water molecule to the "Λ-shaped" structure of $(NaCl)_3^-$ (see $0A^-$ in Fig. 2). In structure $1A^-$, the O atom of the water interacts with two Na atoms, and the two H atoms of the water are dangled. Due to the excess electron, it can be seen that the two dangling H atoms forming two O–H···$e^-$ bonds (see Fig. S1 in Supporting Information), which have been suggested to be strongly favored in the liquid phase of methanol [54].

For $n$ = 2, the global minimum structure $2A^-$ is a slightly distorted cuboid. As mentioned above, the calculated VDE of this configuration is 0.54 eV. Yang et al. [55] have previously found that the neutral $(NaCl)_4$ forms a particularly stable cuboid and should have relatively low electron affinity. The other "Λ-shaped"-based structures are formed by re-orientation of the water molecule to interact with Na or Cl ions in different ways for both $n$ = 1 and 2. In addition to these structures, the $1D^-$ and $2C^-$ structures are derived from the newly identified "fish-shaped" structure ($0B^-$ in Fig. 2).

For $(NaCl)_3^-(H_2O)_n$ ($n$ = 3–6) clusters, the excess electron causes a significant perturbation to the neutral structures. It can be seen that all the local minimal structures are derived from the distorted cuboid $(NaCl)_3^-(H_2O)_2$ ($4A^-$ and $6A^-$) or much more distorted structures ($3A^-$ and $5A^-$). For these clusters with larger number of water molecules, the cuboid-based structures no longer dominate. At the same time, the $Na^+$ and $Cl^-$ ions are much more hydrated in the anions (such as $3A^-$, $3C^-$, and $3D^-$) than in the corresponding neutrals, which can be seen later. It therefore appears that the excess electron causes enhanced hydration of Na and Cl ions. For the rest of the large number of

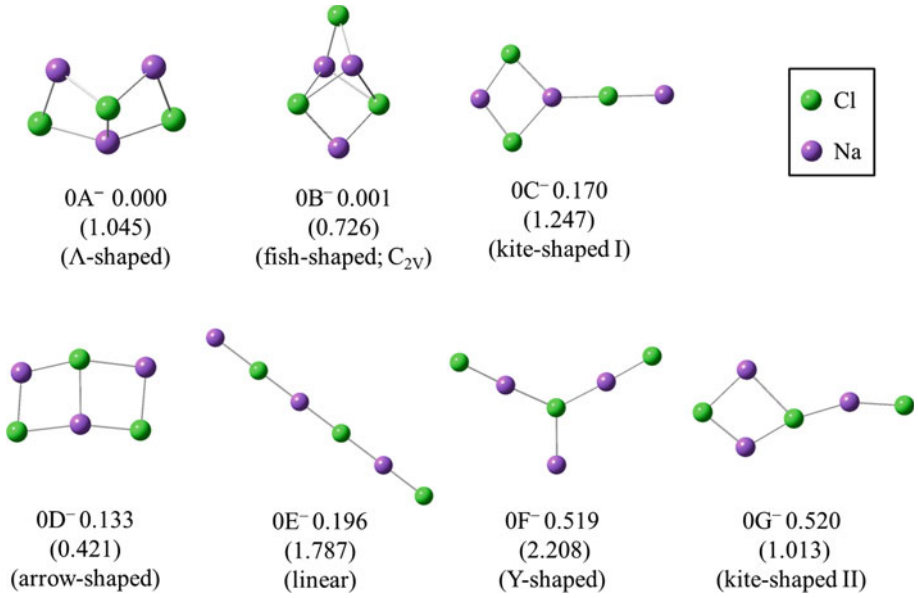


**Fig. 2** Typical minimal energy structures of $(NaCl)_3^-$. The relative energies to the corresponding smallest values (*first line*) and the theoretical VDEs (*second line*) are presented. All the energies are in eV

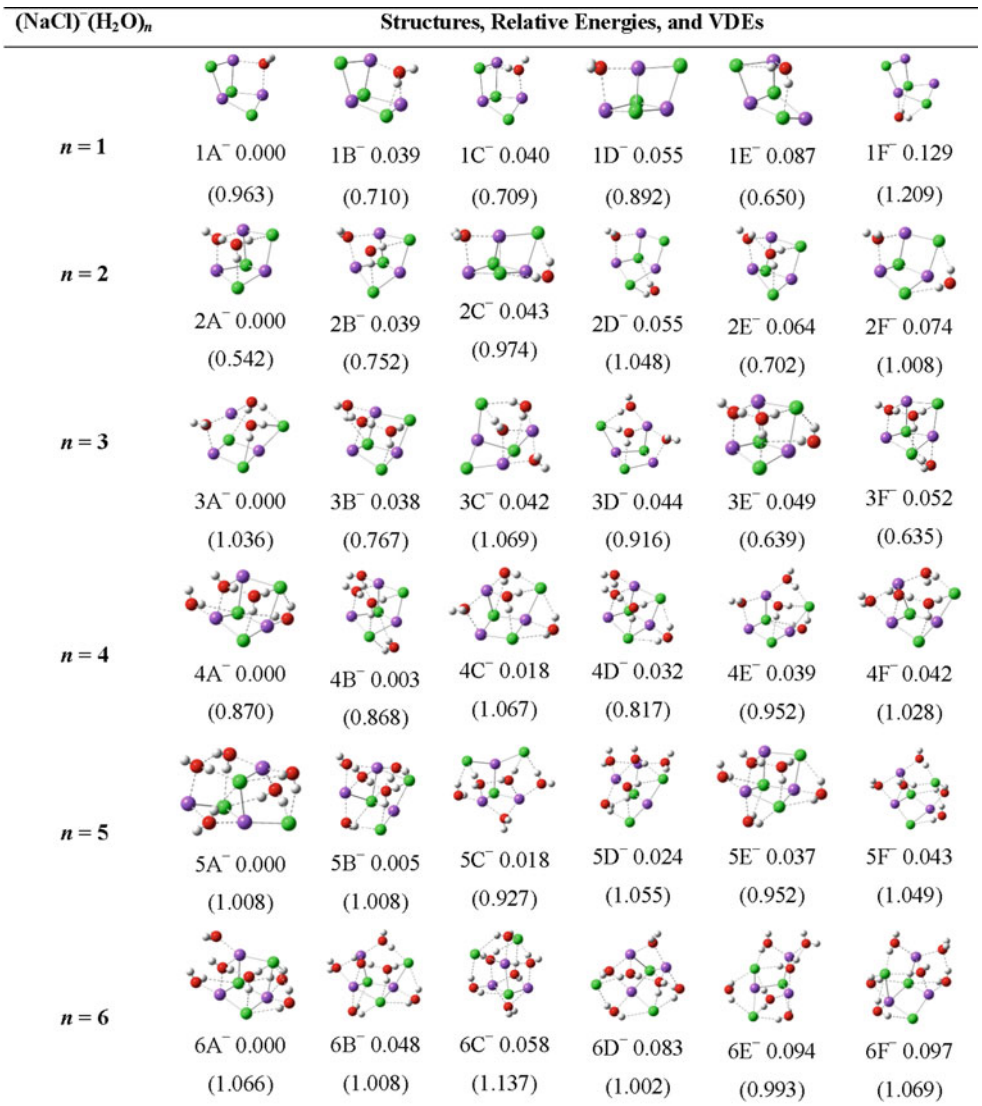


**Fig. 3** Typical minimal energy structures of $(NaCl)_3^-(H_2O)_n$ ($n = 1$–6). They are presented in the similar way as those in Fig. 2

anionic clusters not discussed in details here, we provided their Cartesian coordinates, corresponding relative energies, and theoretical VDEs in Supporting Information.

### 3.3 Structures of $(NaCl)_3(H_2O)_n$

#### *3.3.1 Typical minimal energy structures of $(NaCl)_3(H_2O)_n$ ($n = 0$–$2$)*

To understand salt–water interactions, it is certainly more interesting to study the neutral salt–water clusters. Figure 4 shows the typical minimal energy structures for $(NaCl)_3(H_2O)_n$ ($n = 0$–$2$) clusters. For $(NaCl)_3$, the previous studies [34–37] identified and discussed two minimal energy structures, i.e., the global minimum 0A, which is a 2-dimensional (2D) plane structure and the $D_{3h}$-symmetric 0B structure as shown in Fig. 4. In the current study, a third minimal energy structure ("fish-shaped" 0C in Fig. 4) was also identified though it is relatively high in energy (0.174 eV higher than 0A). It is also noted here that the $D_{3h}$-symmetric structure is not found to be stable in the anionic form. The optimization from 0B in the anionic state leads the structure into the arrow-shaped $0D^-$ structure. These findings are consistent with previous studies [35] and could be a result of the high symmetry of 0B, whose dipole moment is *zero*, and thus, its binding of an excess electron is too weak to form a stable anion.

Among the $(NaCl)_3(H_2O)$ structures, 1A is resulted from adsorbing the water molecule on the edge of Na–Cl of the structure 0A of $(NaCl)_3$. Adsorption of one water leads to a structure transition from planar $(NaCl)_3$ ("arrow-shaped" 0A) to structure 1B, which is higher in energy than 1A by 0.034 eV. In structure 1B, $(NaCl)_3$ is actually very similar to the "Λ-shaped" structure, which is the global minimum of the anionic state ($0A^-$ in Fig. 2). The other local minimum structures with much higher energies than the global minimum structure can be seen to arise from the cyclic (1C and 1D), "fish-shaped" (1E), or "arrow-shaped" (1F) $(NaCl)_3$ structures.

It is well known that the lowest energy structure of the $(NaCl)_4$ cluster is a $T_d$-symmetric cuboid [36, 37]. This study finds that the global minimum structure of $(NaCl)_3(H_2O)_2$ cluster is a distorted cuboid (2A in Fig. 4). In structure 2A, two water molecules occupy the sites of $Na^+$ and $Cl^-$ of $(NaCl)_4$, respectively, with one water molecule interacting with the other two $Na^+$ through its O atom, and another one connecting to two $Cl^-$ via hydrogen bonds. One hydrogen bond also forms between the two water molecules, and one hydrogen atom of the Na-coordinated water is dangling. Other structures such as 2B, 2C, 2D, 2E, and 2F can all be regarded as the distorted forms of the 2A structure. In these structures, the positions and orientations of the two water molecules deviate from the cuboid 2A structure. 2G is a derivative of the planar arrow-shaped structure 0A and is much higher in energy than others. Different from $(NaCl)_3(H_2O)$, most of the seven low-energy structures of the $(NaCl)_3(H_2O)_2$ cluster are non-planar. From the above analyses, we can see that the adsorption of one/two water molecule(s) or one electron causes a $(NaCl)_3$ structure transition from planar to non-planar.

#### *3.3.2 Typical minimal energy structures of $(NaCl)_3(H_2O)_n$ ($n = 3$–$7$)*

We show the typical low-energy structures of $(NaCl)_3(H_2O)_n$ ($n = 3$–$7$) clusters in Fig. 5. Interestingly,

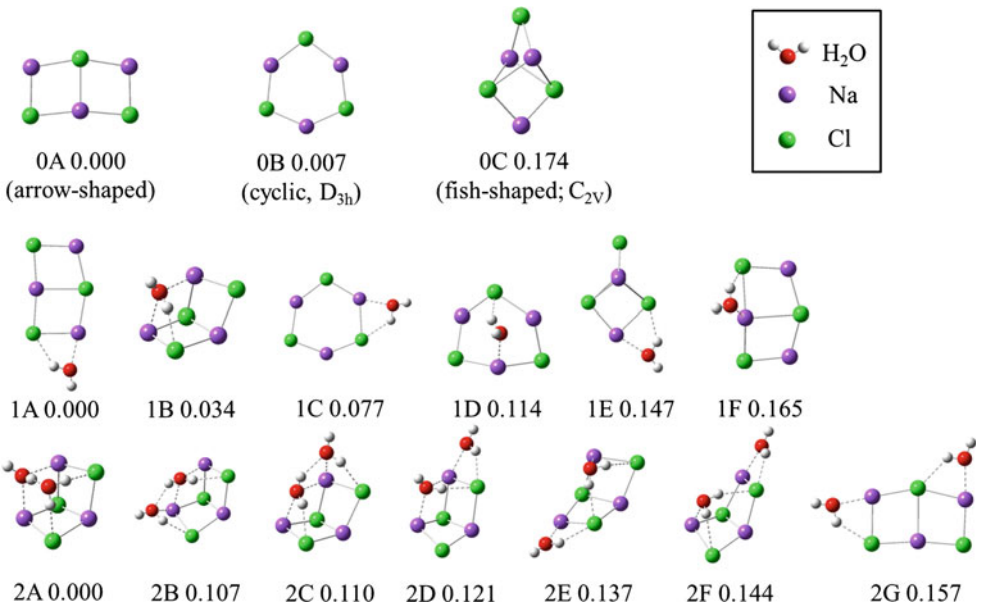


**Fig. 4** Typical minimal energy structures of $(NaCl)_3(H_2O)_n$ ($n = 0$–$2$). The relative energies to the corresponding smallest values are presented. All the energies are in eV

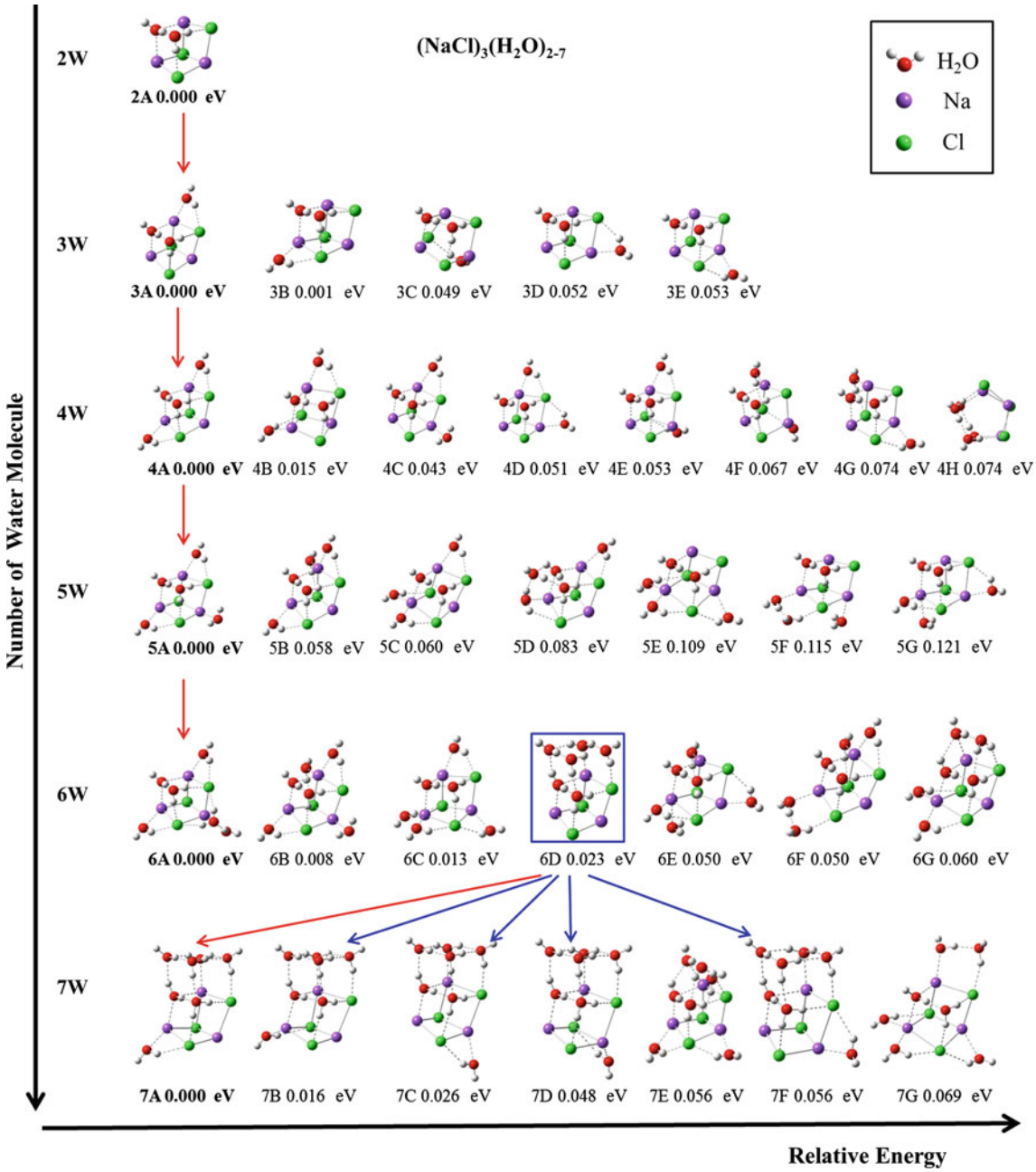


**Fig. 5** Cuboid structure evolution in the clusters of $(NaCl)_3(H_2O)_n$ ($n = 2$–7). The relative energies to the corresponding smallest values are presented. All the energies are in eV

the cuboid formed by $(NaCl)_3(H_2O)_2$ is maintained in many low-energy structures. A chart of possible structure evolution is given in Fig. 5.

For $(NaCl)_3(H_2O)_3$, 3A and 3B are almost degenerate in energy with the latter being higher by only 0.001 eV. The water molecule that does not belong to the cuboid, as mentioned above, binds to the Na–Cl edges. By examining the Mülliken charge of the atoms in structure 2A, it is found that water molecules prefer to bind to the Na–Cl edges, for which the Na and Cl atoms have the largest sum of partial charges (SPCs) (see the Supporting Information for the Mülliken charges in Table S1). Interestingly, when the SPC values of the two atoms are both small, binding of the water molecule to a Na–Cl edge causes the separation of $Na^+$ and $Cl^-$ (see 3C in Fig. 5 and the Na–Cl distance in Table S2 in Supporting Information). Adsorption on the Na–Cl edge of medium SPC values results in two structures much higher in energy (3D and 3E in Fig. 5). In these two structures, $Na^+$ and $Cl^-$ remain in contact.

The lowest energy structure of $(NaCl)_3(H_2O)_4$ cluster 4A is resulted from adsorbing the other two water molecules on the two Na–Cl edges, and it is noted that the SPCs of these two edges are the highest and second highest values in structure 3A. When adsorption of water is on the other Na–Cl edges (4B to 4G), the resulted structures are of higher energies. A penta-prism structure 4H, higher in energy than 4A by 0.074 eV, was also found for the $(NaCl)_3(H_2O)_4$ cluster. In this structure, the four water molecules form a four-member ring, and this ring further connects to the Λ-shaped-like $(NaCl)_3$ structure.

The lowest energy structure of $(NaCl)_3(H_2O)_5$ cluster 5A can be constructed from 4A with the newly added water molecule interacting with two $Cl^-$ and one $Na^+$ ions. The dipole of the water molecule is almost parallel to the plane composed of Cl–Na–Cl. The binding pattern of the water molecule in this cluster is similar to that on NaCl(001) surface [56]. The adsorbed water molecules, as mentioned above, preferentially interact with Na and Cl ions rather than other water molecules. In the latter case, less stable structures form, such as structures 5D and 5F in Fig. 5.

The low-energy structures of $(NaCl)_3(H_2O)_6$ also remain the basic cuboid form. The adsorbed water molecules on the NaCl ions can be seen in 6A, 6B, and 6C. Interestingly, a fused cuboidal structure 6D, which can be seen as two cuboid units sharing a face formed by $(NaCl)(H_2O)_2$ fragment, is also obtained. Although the water molecules form more water–water hydrogen bonds in 6D than in 6A, 6B, and 6C, it is still less stable than 6A by 0.023 eV.

Different from $(NaCl)_3(H_2O)_n$ ($n$ = 2–6), the low-energy structures of $(NaCl)_3(H_2O)_7$ are derivatives of the fused face-sharing cuboid 6D. The seventh water molecule can be adsorbed on the different Na–Cl edges (7A, 7B, 7C, 7D, and 7F). As can be predicted from the partial charge analysis of structure 6D, the most stable structure of $(NaCl)_3(H_2O)_7$ is formed by adding water molecule on the Na–Cl edge of the largest SPC value, which is the edge composed of "1Cl" and "5Na" (see the label in Table S1 in Supporting Information). Two structures 7E and 7G, maintaining only one cuboid consisting of $(NaCl)_3(H_2O)_2$ fragment, also appear as local minimal structures on the energy surface, and they are higher in energy than 7A by 0.056 and 0.069 eV, respectively.

By using enhanced sampling simulations followed by optimization using ωB97XD density functional, we also obtained a larger number of structures of the non-cuboid nature, including the structures formed by adsorbing water molecule(s) on the several basic structures of $(NaCl)_3$ and other structures with $Na^+$ and $Cl^-$ being hydrated. These structures are not shown or discussed here, and the Cartesian coordinates and energetics of all the fully optimized cluster structures are provided in Supporting Information.

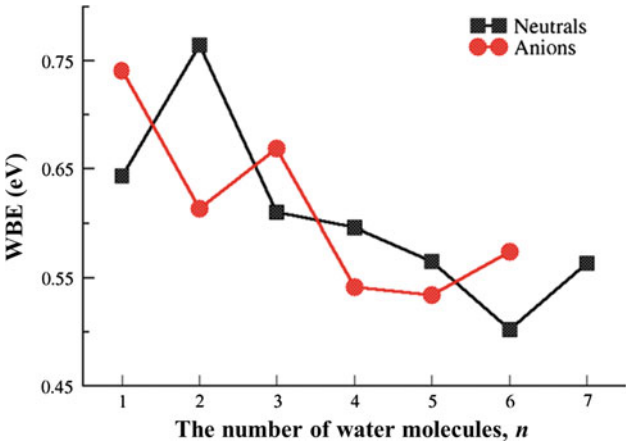


**Fig. 6** The change of water binding energies (WBEs) versus the number of water molecules $n$ for the most stable isomers of $(NaCl)_3(H_2O)_n$

## 3.4 Water binding energies of the lowest energy structures

To examine the stability of the cluster as a function of cluster size, we define the water binding energy (WBE) using Eq. (5):

$$\mathbf{E}\left[(NaCl)_3(H_2O)_n\right] = \mathbf{E}\left[(NaCl)_3(H_2O)_{n-1}\right] + \mathbf{E}(H_2O) - \mathrm{WBE} \quad (5)$$

In the above equation, $\mathbf{E}[(NaCl)_3(H_2O)_n]$ and $\mathbf{E}[(NaCl)_3(H_2O)_{n-1}]$ are the energy of the clusters with the number of water molecules being $n$ and $n-1$, respectively; $\mathbf{E}(H_2O)$ is the energy of water monomer (zero-point energy correction is included) and the value is −76.410660 atomic unit. WBE characterizes the absolute value of the energy decrease when a water molecule binds on the cluster. Figure 6 shows the WBEs as a function of the number of water molecules $n$ in the lowest energy structures for both neutrals and anions. The binding energies for $(NaCl)_3(H_2O)_n$ ($n$ = 1–7) are 0.644, 0.765, 0.610, 0.597, 0.565, 0.502, and 0.563 eV, respectively. The largest WBE of 0.765 eV is responsible for the second water molecule binding to structure 1A to form structure 2A. When $n$ changes from 3 to 6, the WBE slightly decreases, which means that the further binding of water molecules to the clusters stabilizes the cluster less than the second water molecule does. When $n$ changes from 6 to 7, a small increase of the WBE can also be found, which, as reflected from the structures changes, is due to that the fused face-sharing cuboid structure (7A) becomes the lowest energy structure in $(NaCl)_3(H_2O)_7$. The two maxima of the WBE in Fig. 6 are in accord with the first and second cuboid structures being the lowest energy ones when $n$ = 2 and 7.

For the anions, the maximum WBE is 0.741 eV when $n = 1$, corresponding to the energy difference when the structure changes from $0A^-$ to $1A^-$. As can be seen in Figs. 2 and S1 and as mentioned earlier, the two dangling O–H···$e^-$ bonds likely stabilize the cluster; the binding of the second water molecule results in the cuboidal $2A^-$ structure, but the WBE of 0.613 eV is smaller than when the first water is added. For $n = 2$ to 6, the WBEs are all smaller than the corresponding value for $n = 1$. A maximum of WBE occurs at $n = 3$ and a slight increase exists when $n$ changes from 5 to 6. However, these sudden increases in WBE cannot be apparently indicated by the structural changes because, as mentioned in Sect. 3.2, the anionic structures are largely perturbed and $Na^+$ and $Cl^-$ are more hydrated than the corresponding neutral ones.

## 4 Concluding remarks

Water adsorption on $(NaCl)_3$ in both anionic and neutral states is investigated in this study by photoelectron spectroscopy experiments and DFT calculations. The possible observed structures in experiments are assigned according to the DFT results. The calculated vertical detachment energies (VDEs) and the experimental ones agree well with each other. The enhanced sampling method, ITS, was employed to ensure that the low-energy structures of the clusters are fully sampled. The efficiency of this approach has been shown in finding new minimal energy structures of $(H_2O)_{12}$ and $(H_2O)_{20}$ clusters [44], which were missed by other methods. The effectiveness of this method was again demonstrated in the present study. For instance, we identified a new "fish-shaped" $C_{2V}$-symmetric structure in both anionic and neutral states, which has not been reported before [35–37, 57]. The anionic one is very competitive to (higher in energy by only 0.001 eV) the previously regarded global minimum structure in terms of our DFT calculations. In addition, by using dispersion-corrected ωB97XD functional and diffusive basis set, a more convincing ranking of these structures (by energy) was obtained.

For neutral $(NaCl)_3(H_2O)_n$ clusters, the water-doped cuboid and the structures derived from adding water molecules on the Na–Cl edges of the cuboid are energetically favored. We found that the most stable structure of $(NaCl)_3(H_2O)_2$ is a water-doped cuboid (2A in Fig. 5). This finding expands the class of dopant sodium chloride clusters: This study shows not only the metals [58] and hydroxide [59], but also water molecules can be the proper candidate for the doped NaCl clusters (crystals). The cuboid is so stable that the low-energy structures of $(NaCl)_3(H_2O)_n$ ($n = 3$–6) are those that all maintain the cuboid. The fused face-sharing cuboid structure appears when $n$ is up to 6 though its energy is slightly higher than the water-doped cuboid structure. Finally, the derivative structures from the fused face-sharing cuboid become dominant for the low-energy structures of $(NaCl)_3(H_2O)_7$. The lowest energy structures change from $n = 1$ to 2 and 6 to 7 are well reflected on the two maxima, which can be seen from the plot of the water binding energy (WBE) versus the cluster size (Fig. 6). Through this study, the pattern of water binding on $(NaCl)_3$ is established. From the structure evolution of the cuboid (Fig. 5), we can clearly find that the water molecule preferentially binds to the Na–Cl edge if the NaCl ion pair has larger partial charges than others. The fused face-sharing cuboid (6D) is the first structure in which the salt is fully covered by one layer of water molecules. The seventh water molecule again binds to the Na–Cl edge instead of other water molecules in the low-energy structures of $(NaCl)_3(H_2O)_7$. Thus, water molecules will preferentially bind to the Na–Cl edges than interact with other water molecules.

Finally, we want to note that the anionic clusters are more distorted and have higher configuration diversity than the corresponding neutral ones. For example, for the water-free $(NaCl)_3$ cluster, only three local minima were found for neutral form with relatively low energies, but for anionic clusters, seven low-energy stable structures were identified. For $(NaCl)_3^-(H_2O)_n$ ($n = 1$–6) clusters, although the majority of structures are similar to the corresponding neutral ones, the $Na^+$ and $Cl^-$ ions are much more hydrated in the former.

**Acknowledgments** Y.Q.G. acknowledges the NSFC (91027044, 21233002, and 21125311) and National Key Basic Research Foundation of China (2012CB917304) for financial support. W.-J.Z. acknowledges the Natural Science Foundation of China (Grant No. 21273246) and the Knowledge Innovation Program of the Chinese Academy of Sciences (Grant No. KJCX2-EW-H01) for finanical support. The calculations were performed on the supercomputers of the Shanghai Supercomputer Center (SSC).

## References

1. Collins KD, Neilson GW, Enderby JE (2007) Biophys Chem 128:95
2. Tobias DJ, Hemminger JC (2008) Science 319:1197
3. Gao YQ (2011) J Phys Chem B 115:12466
4. Gao YQ (2012) J Phys Chem B 116:9934
5. Yang LJ, Fan YB, Gao YQ (2011) J Phys Chem B 115:2456
6. Oum KW, Lakin MJ, DeHaan DO et al (1998) Science 279:74
7. Knipping EM, Lakin MJ, Foster KL et al (2000) Science 288:301
8. Finlayson-Pitts BJ (2003) Chem Rev 103:4801
9. Ohtaki H, Radnai T (1993) Chem Rev 93:1157
10. Dedonder-Lardeux C, Gre´goire G, Jouvet C et al (2000) Chem Rev 100:4023
11. Blandamer MJ, Fox MF (1970) Chem Rev 70:59
12. Ohtaki H, Fukushima N (1992) J Solu Chem 21:23
13. Ault BS (1978) J Am Chem Soc 100:2426
14. Mizoguchi A, Ohshima Y, Endo Y (2003) J Am Chem Soc 125:1716

15. Mizoguchi A, Ohshima Y, Endo Y (2011) J Chem Phys 135:064307
16. Partanen L, Mikkelä M-H, Huttula M et al (2013) J Chem Phys 138:044301
17. Belch AC, Berkowitz M, McCammon JA (1986) J Am Chem Soc 108:1755
18. Karim OA, McCammon JA (1986) J Am Chem Soc 108:1762
19. Ohtaki H, Fukushima N (1988) Pure Appl Chem 61:179
20. Ohtaki H, Fukushima N, Hayakawat E et al (1988) Pure Appl Chem 61:1321
21. Makov G, Nitzan A (1992) J Phys Chem 96:2965
22. Woon DE, Thom H, Dunning J (1995) J Am Chem Soc 117:1090
23. Petersen CP, Gordon MS (1999) J Phys Chem A 103:4162
24. Jungwirth P (1999) J Phys Chem A 104:145
25. Yamabe S, Kouno H, Matsumura K (2000) J Phys Chem B 104:10242
26. Godinho SSMC, do Couto PC, Cabral BJC (2004) Chem Phys Lett 399:200
27. Olleta AC, Lee HM, Kim KS (2006) J Chem Phys 124:024321
28. Asada T, Nishimoto K (1995) Chem Phys Lett 232:518
29. Laria D, Fernández-Prini R (1995) J Chem Phys 102:7664
30. Smith DE, Dang LX (1994) J Chem Phys 100:3757
31. Siu C-K, Fox-Beyer BS, Beyer MK et al (2006) Chem Eur J 12:6382
32. Joung IS, Luchko T, Case DA (2013) J Chem Phys 138:044103
33. Ghosh MK, Re S, Feig M et al (2013) J Phys Chem B 117:289
34. Sunil KK, Jordan KD (1987) J Chem Phys 91:1710
35. Anusiewicz I, Skurski P (2003) J Phys Chem A 107:2356
36. Malliavin M-J, Coudray C (1997) J Chem Phys 106:2323
37. Ayuela A, López JM, Alonso JA et al (1993) Z Phys D: At, Mol Clusters 26:213
38. Hooton IE, Jacobs PWM (1988) Can J Chem 66:830
39. Tsyro S, Aas W, Soares J et al (2011) Atmos Chem Phys 11:10367
40. Ming Y, Russell LM (2001) J Geophys Res D: Atmos 106:28
41. Wick CD (2009) J Phys Chem C 113:2497
42. Li RZ, Liu CW, Gao YQ et al (2013) J Am Chem Soc 135:5190
43. Gao YQ (2008) J Chem Phys 128:134111
44. Liu C-W, Wang F, Yang L et al (2014) J Phys Chem B 118:743
45. Hou G-L, Liu C-W, Gao YQ et al Unpublished Results
46. Xu H-G, Zhang Z-G, Feng Y et al (2010) Chem Phys Lett 487:204
47. Yang L, Shao Q, Gao YQ (2008) J Phys Chem B 113:803
48. Case DA, Darden TA, Cheatham ITE et al (2006) Amber 9. University of California, San Francisco
49. Joung IS, Cheatham TE (2008) J Phys Chem B 112:9020
50. Berendsen HJC, Grigera JR, Straatsma TP (1987) J Chem Phys 91:6269
51. Frisch MJ, Trucks GW, Schlegel HB et al (2009) Gaussian 09 Revision A.02. Gaussian Inc, Wallingford
52. Chai J, Head-Gordon M (2008) Phys Chem Chem Phys 10:6615
53. Grimme S (2011) Wiley Interdiscip Rev Comput Mol Sci 1:211
54. Turi L (1999) J Chem Phys 110:10364
55. Yang YA, Conover CWS, Bloomfield LA (1989) Chem Phys Lett 158:279
56. Pramanik A, Kalagi RP, Barge VJ et al (2005) Theor Chem Acc 114:129
57. Phillips NG, Conover CWS, Bloomfield LA (1991) J Chem Phys 94:4980
58. Watterich A (1978) Phys Status Solidi B 88:K51
59. Barnett RN, Landman U (1996) J Phys Chem 100:13950

Theor Chem Acc (2014) 133:1567
DOI 10.1007/s00214-014-1567-5

REGULAR ARTICLE

# Thermal decomposition of FOX-7 studied by ab initio molecular dynamics simulations

**Yang Liu · Feng Li · Huai Sun**

Received: 1 June 2014 / Accepted: 13 August 2014 / Published online: 3 September 2014
© Springer-Verlag Berlin Heidelberg 2014

**Abstract** Ab initio molecular dynamics simulations were conducted to study the thermal decomposition mechanisms of solid FOX-7. We found that the initial decomposition of FOX-7 has three main reaction routes. The C–$NO_2$ bond fission as reported previously is indeed the most common route. However, the inter- and intramolecular hydrogen transfers are also found to be valid, which is contradictory to previous energy minimization calculation results. The simulations agree well with known experimental data in terms of activation energy and reaction side products. A complete reaction network that describes how the main products, $H_2O$, $CO_2$ and $N_2$ form in FOX-7 decomposition, is constructed from the simulation trajectories.

**Keywords** FOX-7 · Ab initio simulation · Reaction mechanism · Activation energy

## 1 Introduction

FOX-7 (1,1-diamino-2,2-dinitroethene) is a new energetic molecule superior to well-known RDX (1,3,5-trinitro-2-oxo-1,3,5-triazacyclo-hexane) and HMX (1,3,5,7-tetranitro-1,3,5,7-tetraazacyclo-octane) due to low sensitivity and easy synthesis procedure [1]. Although all of these molecules have similar molecular stoichiometry, their decomposition mechanisms are expected to be different because of the differences in detonation performances. Understanding the decomposition mechanisms of FOX-7 is of great importance to design appropriate usage, transport and storage methods for this new energetic material [2, 3].

Considerable amount of experimental and theoretical work has been conducted with FOX-7 to study its reaction mechanisms [4–8]. A recent investigation using laser and mass spectroscopy techniques has been carried out to detect reaction products and transient intermediates [4]. Combining the measured data with quantum mechanical calculations, a reaction network was proposed [4]. Several calculations [5–8] were performed to study the decomposition mechanisms for FOX-7. The C–$NO_2$ and C–$NH_2$ bond dissociation energies were compared, and the former (293 kJ/mol) was found to be more favorable than the later (466 kJ/mol) [5]. The nitro-to-nitrite rearrangement was investigated, and an energy barrier of 247 kJ/mol was obtained [6]. The effects of charged and excited states on the decomposition mechanism of FOX-7 were studied [7]. The intramolecular and intermolecular hydrogen transfers were also investigated [8]. All of these calculations were based on characterizations of potential energy surfaces for proposed reaction pathways using a series of energy minimizations. We refer this type of calculations as *energy minimizations* in this manuscript.

Decompositions of energetic materials are usually characterized by complex reaction networks consisting of a large number of unit reactions and intermediates, which are correlated with the thermodynamic conditions such as temperature, pressure and concentration [9, 10]. Unlike reactions occurring in low-pressure gas phase or low-concentration solution, which can be usually described by a few unit reactions, reactions in high pressure or high concentration cannot be treated well by energy minimizations on preset reaction pathways because the *real* reaction pathways

Dedicated to Professor Guosen Yan and published as part of the special collection of articles celebrating his 85th birthday.

Y. Liu · F. Li · H. Sun (✉)
School of Chemistry and Chemical Engineering and Ministry of Education Key Lab of Scientific and Engineering Computing, Shanghai Jiao Tong University, Shanghai 200240, China
e-mail: huaisun@sjtu.edu.cn

are too complicated to be postulated based on chemical intuitions. Although the energy minimizations can be used to accurately predict energies and structures of the reactants, products, intermediates and transition states, the calculations are not suitable for predicting new (unknown) reaction pathways, especially for those strongly depend on thermodynamic conditions. Generally speaking, it is highly challenging to obtain complete decomposition mechanisms of energetic materials.

Reactive molecular dynamics (RMD) simulation offers a promising way to study the complex chemical reactions without prior knowledge of reaction pathways and to include thermodynamic conditions into consideration. In RMD simulations, atoms are treated as classical particles moving on potential energy surfaces that represent the multi-atom interactions. The time trajectories of atoms are determined by numerical integration of the Newton's equation of motion. From the trajectories, chemical species including reactants, products and intermediates, as well as chemical reaction types that connect the species can be obtained. If the trajectories are ergodic, complex reaction mechanisms can be uncovered by the simulation. Two types of representation of the potential energy surfaces are used for RMD. One is to use empirical functional forms to describe the atom–atom interactions (called reactive force field or RFF); the other is to solve Schrödinger equation or Kohn–Sham equation instantly for each configuration generated in the simulation (ab initio molecular dynamics or AIMD). The empirical RFF method can be applied to systems containing up to millions of atoms and lasting up to microsecond time length, but it requires tedious and difficult parameterization. The AIMD method is computationally expensive so that it can only be applied to small systems and a short period of simulation time, but it is ab initio, unbiased by empirical inputs and suitable for discovering complex reaction pathways. The AIMD method has been used in studies of various chemical reactions, including the initial reactions of energetic materials such as CL-20 and nitromethane [3, 11, 12].

In this work, we carried out AIMD simulations using the Car–Parrinello scheme [13] to study the thermal decomposition of solid FOX-7. The purpose of these simulations was to discover unknown reaction pathways. By analyzing the simulation trajectories obtained at different temperatures thoroughly, we found important species and reaction types that have not been reported in previous theoretical and experimental studies. In addition, the reaction network that connects the major species by reaction types from the initial reactant (FOX-7) to the main end products is obtained. Due to exceptionally high expenses, the AIMD simulations were conducted with fairly small time and length scales, and consequently the statistical data reported in this manuscript are associated with large uncertainties. Given the uncertainties, the data are still very valuable for us to describe the reactions mechanisms in a qualitative manner. The reaction pathways identified in this work provide a basis for further potential energy calculations, from which RFF can be developed to simulate decomposition reactions in much larger time and length scales.

## 2 Computational details

The constant number, volume and temperature (NVT) MD simulations were conducted using the Kohn–Sham DFT method with the plane wave and pseudopotential formulation as implemented in CPMD software [14]. The BLYP exchange–correlation functional and Troullier–Martins norm-conserving pseudopotentials [15] for core electrons were applied. A plane wave cutoff of 85 Ry was utilized. The mass for orbitals was set to 400 au. The Nosé–Hoover thermostats [16] were applied to control the temperature. A 0.05 fs time step was used for the integration of motion equations.

FOX-7 solid was represented by a super-cell with the periodic boundary condition. The super-cell consists of two unit cells, and the unit cell structure was taken from the Cambridge Structural Database (α-FOX-7 at 298 K) [17]. The initial configuration was equilibrated for 1 ps using NVT MD simulation at room temperature (298 K) to release any tensions between the reported structures and DFT predicted structures. No chemical reaction was observed by the end of the equilibration period. The relaxed structure was then used for four parallel simulations conducted at different simulations: 2,500, 3,000, 3,500 and 4,000 K, which are in the range of rapid laser detonation (2,500–5,000 K) [11]. The temperatures were assigned to the simulations with the same initial configuration so that the decomposition rates at different temperatures can be evaluated.

For each frame of the trajectories, chemical species were identified based on atom–atom distances. If the distance between two atoms is shorter than a threshold value, which is the sum of the covalent radius of two atoms plus a buffer size of 0.2 Å, the atoms are considered to be connected with a chemical bond. The covalent bond radii for C, H, O and N atoms are 0.77, 0.32, 0.73 and 0.75 Å, respectively. The species were uniquely labeled using the standard IUPAC International Chemical Identifier (InChI) code, version 1 [18]. By tracking the evolution of the identified species in the trajectories, chemical reaction types that connect species were tabulated. The analysis requires large amount of data processing, so we implemented a computer program based on relational database concept to facilitate data searching and sorting.

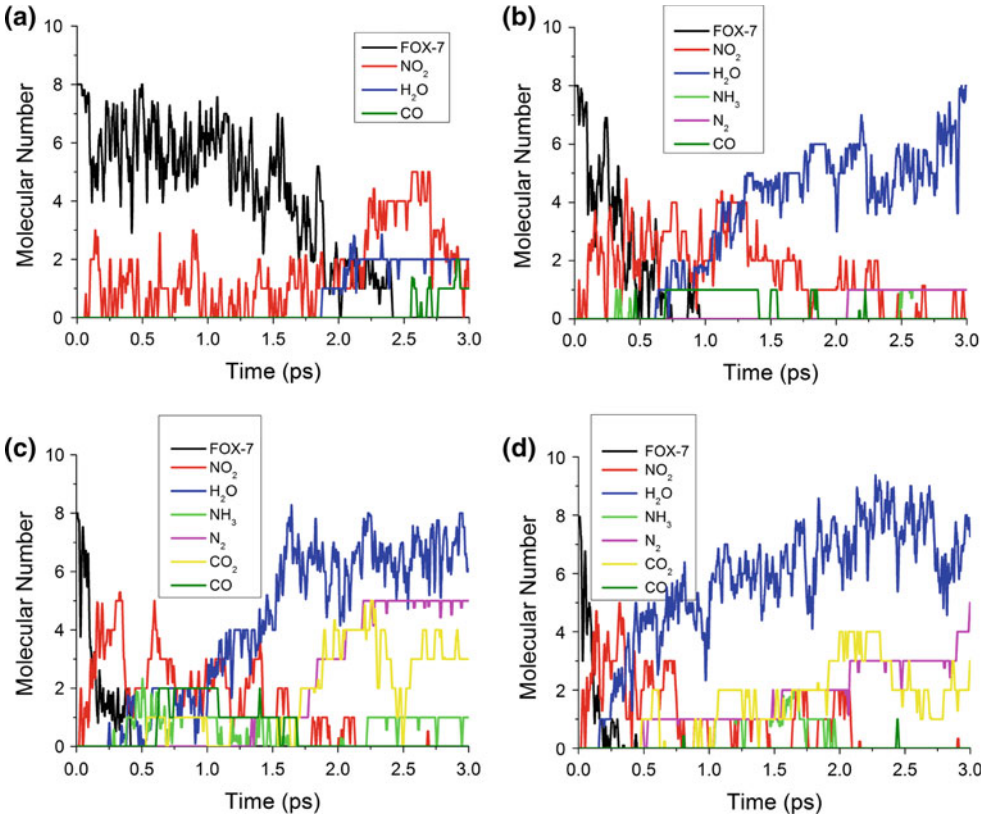


**Fig. 1** Population distributions of reactant FOX-7 (*black*); intermediates $NO_2$ (*red*), $NH_3$ (*lawn green*), CO (*forest green*); and products $H_2O$ (*blue*), $N_2$ (*magenta*), $CO_2$ (*yellow*) for simulation time, at (**a**) 2,500 K, (**b**) 3,000 K, (**c**) 3,500 K and (**d**) 4,000 K

## 3 Results and discussion

### 3.1 Overview of the reactions

The numbers of seven stable molecules (FOX-7, $NH_3$, $NO_2$, CO, $N_2$, $H_2O$ and $CO_2$) with simulation time at different temperatures are plotted in Fig. 1. Due to the small size of these simulations, the fluctuations in the population curves are large, but general trends can be seen. The reactant FOX-7 population declines from initial value of eight, and the decline rate increases as the temperature increases. FOX-7 molecules decomposed completely near 2.5 ps at 2,500 K, 1.0 ps at 3,000 K, 0.5 ps at 3,500 K and less than 0.5 ps at 4,000 K. As soon as FOX-7 decomposition starts, $NO_2$ appears in the trajectory, as shown in Fig. 1a (2,500 K). $NO_2$ is an intermediate as its population reaches a maximum value of 5 and then decreases. The second compound appears in the trajectory is water ($H_2O$) which is one of the main products. The population of water fluctuates largely, indicating water acts as catalyst in part as well. Almost at the same time of water generation, two more intermediates, CO and $NH_3$, and another main product $CO_2$ are formed. The populations of intermediates CO and $NH_3$ are relatively low and their maximum values are about two. The $CO_2$ is not very stable as shown by the large fluctuations in its population curve. The last main product formed in the simulation is $N_2$, which is a very inert compound with triple nitrogen–nitrogen bonds and its fluctuation in population curve is very small. Due to the small simulation length and time scales, the reactions are not completely finished at any temperature. However, the evolutions of species at 3,500 and 4,000 K as shown in Fig. 1 are similar. At the end of simulation, FOX-7 decomposition is finished and intermediates including $NO_2$, CO and $NH_3$ are converted to more stable products. In addition, main products $N_2$, $H_2O$ and $CO_2$ are formed in the simulation system. In other words, the reaction processes at 3,500 and 4,000 K is close to completion.

The initial decomposition rates of FOX-7 are estimated from the population curves in Fig. 1. Assuming the initial decomposition of FOX-7 is a first-order reaction, we estimated the rate constants by fitting the population data of FOX-7 to:

$$A(t) = A(0)\exp(-kt)$$

where $A(0)$ is the initial number density and $A(t)$ is the number density at certain time. The fitting curves with the simulation data are shown in Fig. 2. The fitting is not quite accurate for the low-temperature (2,500 K) data, but fairly good for other temperatures. The rate constants in logarithm at different temperatures are depicted in Fig. 3. Apparently the rate constants cannot be fit by a straight line using the Arrhenius law:

$$\ln(k) = \ln(A) - \left[\frac{E_a}{R}\right]\frac{1}{T}$$

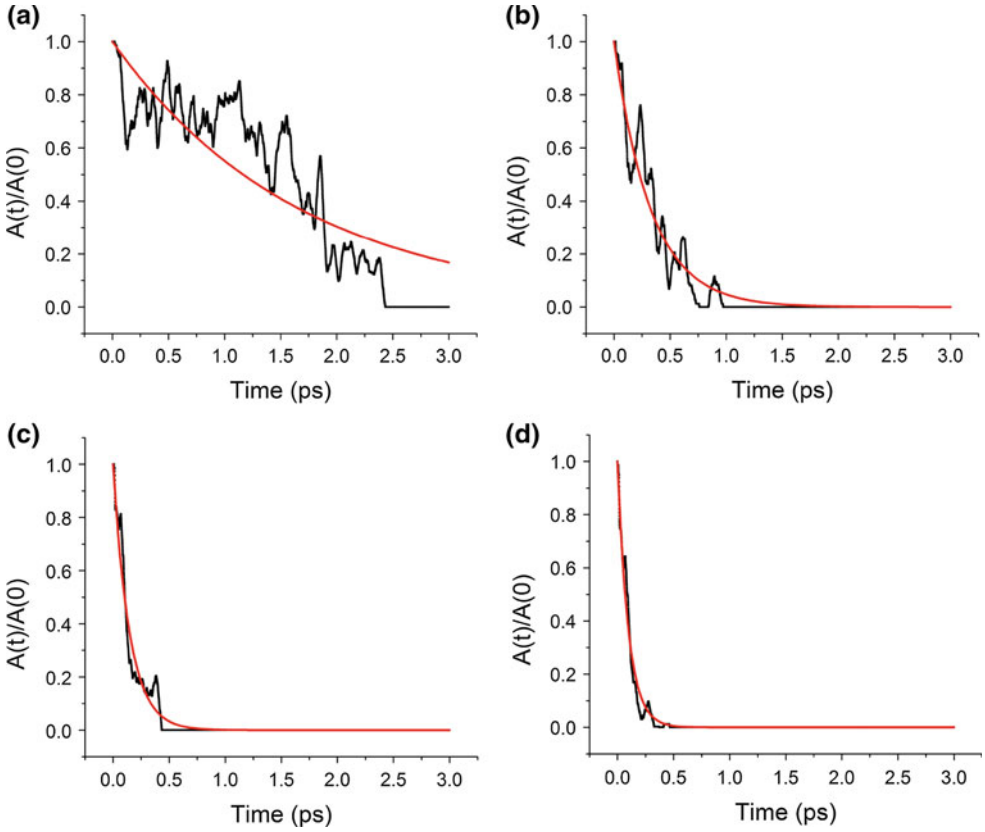


**Fig. 2** Exponential fits of reaction rates at different temperatures, **a** 2,500 K, **b** 3,000 K, **c** 3,500 K, **d** 4,000 K. $A(0)$ is the initial number and $A(t)$ is the instant number of FOX-7. The *black line* is measured from the simulation trajectory, and the *red line* is exponential fit curve

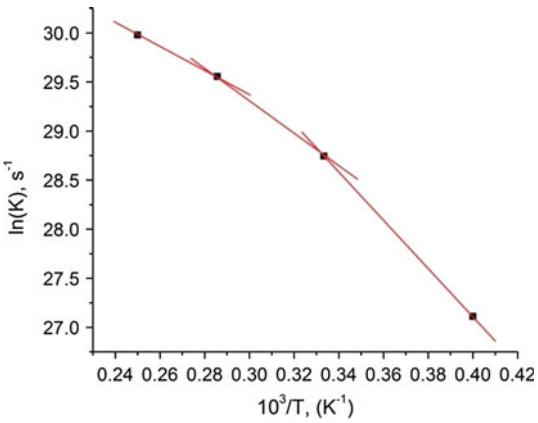


**Fig. 3** The decomposition rate constant versus reciprocal temperature. The *dots* are calculated rate constants. The *lines connecting two dots* are used to derive activation energies using the Arrhenius equation

**Table 1** Molecular weight (MW) distribution of chemical species generated in the simulations at different temperatures

| MW | 2,500 K | 3,000 K | 3,500 K | 4,000 K |
|---|---|---|---|---|
| 1–10 | 1 | 1 | 1 | 1 |
| 11–20 | 5 | 7 | 11 | 10 |
| 21–50 | 22 | 51 | 65 | 59 |
| 100–199 | 42 | 155 | 300 | 327 |
| 101–200 | 148 | 219 | 300 | 359 |
| 201–300 | 56 | 43 | 42 | 88 |
| 301–400 | 8 | 8 | 6 | 7 |
| 401–500 | 2 | 0 | 0 | 0 |
| Total | 284 | 484 | 725 | 851 |

The nonlinearity is presumably due to the large temperature spans (1,500 K) in which the frequency factor $A$ is temperature dependent. Using two adjacent data to estimate the activation energies in different temperature ranges, we obtained 98 kJ/mol from 3,500 to 4,000 K, 142 kJ/mol from 3,000 to 3,500 K and 204 kJ/mol from 2,500 to 3,000 K. These values are in reasonable agreement with the experimental value of 242 kJ/mol, which was measured at the temperature range between 483 and 523 K [19].

### 3.2 Generated molecular species

A large number of molecular species were found in the trajectories of different temperatures. The numbers of molecular species found at different temperatures, grouped by molecular weight (MW), are listed in Table 1. The only species with MW less than 10 is hydrogen atom (either in

radical or proton form), and most species are in the range of 100–200 MWs. The total number of species appears to be dependent on temperature. The species number is 284 at 2,500 K, 484 at 3,000 K, 725 at 3,500 K and 851 at 4,000 K, respectively. Two factors contribute to this trend: The extents of reaction are different (see Fig. 1) and the entropy effect that favors smaller fragments. The first factor can be seen from the fact that the species numbers are similar for results at 3,500 and 4,000 K, since reactions are close to completion at these two temperatures. The second factor is evident from the MW distributions at different temperatures—the distribution shifts slightly to smaller species and the total number of species increases as the temperature increases.

The numbers of reaction types that connect the species are about twice larger than the numbers of species. Table 2 lists the number of reaction types at different temperatures, grouped by the number of occurrence. The numbers of reaction types are 571 at 2,500 K, 923 at 3,000 K, 1,360 at 3,500 K and 1,480 at 4,000 K. Again we see that the reaction type number at 3,500 K is close to that at 4,000 K. The majority of reaction types (~78 %) occurred only once and only a couple of them (<0.1 %) occurred more than 100 times. In addition, ~19 % of reaction types occurred from 2 to 10 times and a few (~3 %) occurred from 11 to 100 times. Many reactions are conjugated (paired) forward and backward reactions. If we count the conjugated reaction types only, the total numbers are reduced by less than a half to 318, 494, 784 and 925, respectively. Furthermore, we examined the reaction types and found that about a half of these reaction types are unimolecular decompositions, while the other half are bimolecular collisions. This ratio is about the same at different temperatures.

Tables 1 and 2 show the reactions are very complicated, and the number of species and reactions are much greater than that in typical energy minimization calculations. The large numbers of species and reaction types were caused by the non-equilibrium process in which new species were generated and eliminated constantly. For a complete trajectory, the numbers of species and reactions should be close to constant at a given temperature. For analysis of reaction mechanism, we need a complete trajectory from initial reactant to final products. Since the reactions are close to finish at 3,500 and 4,000 K, we take the data of 3,500 K for following analysis.

The reactant, transient intermediates and products can be identified by counting activity of each species in the trajectory. For each species, its activity is defined by two parameters: the number of reactions acting as reactant (R) and the number of reactions acting as product (P). If R > P, there is net gain of this species and it is a product. If R < P, there is a net loss and it is a reactant. If R = P, the species is an intermediate. There are much more intermediates than products and reactant in the system. Table 3 lists the activity of products and reactant at 3,500 K. There was only one reactant ($C_2H_4N_4O_4$) FOX-7, which acted as a reactant for 66 times and as a product for 58 times in the simulation time, leading to the net loss of 8, as expected. The data also indicate that the initial decomposition of FOX-7 was a reversible reaction; it reversed for 58 times in the simulation time period. As shown in the table, all of the species were participants in reversible reactions and the difference is how active they were. Some were involved in reactions more frequently than others, indicating some molecules are easier to be activated.

**Table 2** Numbers of reaction types found in the simulations at different temperatures, grouped by the numbers of occurrence

| Count | 2,500 K | 3,000 K | 3,500 K | 4,000 K |
|---|---|---|---|---|
| 1 | 415 | 716 | 1,059 | 1,196 |
| 2–10 | 137 | 181 | 267 | 258 |
| 11–100 | 17 | 25 | 32 | 24 |
| >100 | 2 | 1 | 2 | 2 |
| Total | 571 (318) | 923 (494) | 1,360 (784) | 1,480 (925) |

Most of the reaction types are conjugated (forward and backward) reactions. The total numbers of conjugated reaction types are in the parenthesis

**Table 3** The occurrence numbers of reactant and product molecules in the 3,500 K simulation

| Formula | Molecular name | R | P | Net |
|---|---|---|---|---|
| $C_2H_4N_4O_4$ | 2,2-dinitro-1,1-ethenediamine | 66 | 58 | −8 |
| $C_2H_2N_4O_2$ | (See InChi code a) | 1 | 2 | 1 |
| $C_5H_3N_5O_3$ | (See InChI code b) | 1 | 2 | 1 |
| HO | Hydroxyl radical | 252 | 253 | 1 |
| $H_3N$ | Ammonia | 60 | 61 | 1 |
| CHNO | Isocyanic acid | 50 | 51 | 1 |
| $HNO_2$ | Nitrous acid | 39 | 40 | 1 |
| $C_2N_2O$ | Cyanic isocyanate | 23 | 24 | 1 |
| CHN | Hydrocyanic acid | 13 | 14 | 1 |
| $CH_2O_3$ | Carbonic acid | 11 | 12 | 1 |
| $N_2O$ | Dinitrogen monoxide | 6 | 7 | 1 |
| $CH_2NO$ | Imidoformate | 6 | 7 | 1 |
| H | Hydrogen radical | 921 | 923 | 2 |
| $CO_2$ | Carbon dioxide | 32 | 35 | 3 |
| NO | Nitric oxide | 89 | 93 | 4 |
| $N_2$ | Nitrogen | 10 | 15 | 5 |
| $H_2O$ | Water | 307 | 314 | 7 |

The occurrence numbers are listed for the species acting as reactant (R) and product (P) in reactions found in the simulation trajectory. The net number of gain or loss, calculated as the difference between R and P, indicates the species is a reactant (loss) or product (gain)

(a) InChI = 1S/$C_2H_2N_4O_2$/c3-1-2-4-6(8)5-7/h2,4H, (b) InChI = 1S/$C_5H_3N_5O_3$/c6-2-9-4(11)10-3(7)1-8-5(12)13/h1,10,12H

**Table 4** The occurrence number (Occur.) distribution of transient intermediates acting as reactants (R), products (P) and net gain (Net) in 3,500 K simulation

| R | P | Net | Occur. |
|---|---|---|---|
| 1 | 1 | 0 | 406 |
| 2 | 2 | 0 | 117 |
| 3 | 3 | 0 | 56 |
| 4 | 4 | 0 | 27 |
| 5 | 5 | 0 | 20 |
| 6 | 6 | 0 | 12 |
| 7 | 7 | 0 | 8 |
| 8 | 8 | 0 | 7 |
| 9 | 9 | 0 | 8 |
| 10 | 10 | 0 | 3 |
| >10 | >10 | 0 | 44 |
| Total | | | 708 |

**Table 5** Average life time (ALT) of products and reactant in 3,500 K simulation

| Formula | Molecular species | R | P | Net | ALT (fs) |
|---|---|---|---|---|---|
| $C_2H_4N_4O_4$ | 2,2-dinitro-1,1-ethenediamine | 66 | 58 | −8 | 106 |
| $N_2$ | Nitrogen | 10 | 15 | 5 | 1,151 |
| NO | Nitric oxide | 89 | 93 | 4 | 912 |
| $N_2O$ | Dinitrogen monoxide | 6 | 7 | 1 | 560 |
| $CO_2$ | Carbon dioxide | 32 | 35 | 3 | 542 |
| $C_2N_2O$ | Cyanic isocyanate | 23 | 24 | 1 | 297 |
| $H_2O$ | Water | 307 | 314 | 7 | 240 |
| CHN | Hydrocyanic acid | 13 | 14 | 1 | 208 |
| $H_3N$ | Ammonia | 60 | 61 | 1 | 122 |
| CHNO | Isocyanic acid | 50 | 51 | 1 | 115 |
| $CH_2O_3$ | Carboxylic acid | 11 | 12 | 1 | 21 |
| $CH_2NO$ | Imidoformate | 6 | 7 | 1 | 10 |
| $HNO_2$ | Nitrous acid | 39 | 40 | 1 | 29 |
| $C_2H_2N_4O_2$ | (See InChI code a) | 1 | 2 | 1 | 7 |
| $C_5H_3N_5O_3$ | (See InChI code b) | 1 | 2 | 1 | 7 |
| H | Hydrogen radical | 921 | 923 | 2 | 111 |
| OH | Hydroxyl radical | 252 | 253 | 1 | 57 |

(a) InChI = 1S/$C_2H_2N_4O_2$/c3-1-2-4-6(8)5-7/h2,4H; (b) InChI = 1S/$C_5H_3N_5O_3$/c6-2-9-4(11)10-3(7)1-8-5(12)13/h1,10,12H

There was a total of 16 products at the end of 3,500 K simulation trajectory, ranked differently by the net populations in the last column. In addition to the main products $H_2O$(7), $N_2$(5) and $CO_2$(3) (number in parenthesis denotes the population, and the same as follows), which can be derived from stoichiometry with assumption of complete reaction, we also obtained side products: NO(4), H(2), $CH_2NO$(1), $N_2O$(1), $CH_2O_3$(1), HCN(1), $C_2N_2O$(1), HONO(1), CHNO(1), $NH_3$(1), HO(1), $C_2H_2N_4O_2$(1) and $C_5H_3N_5O_3$(1). These side products overlap with those reported by laser and mass spectroscopic measurements [4], but cannot be predicted by energy minimization calculations [6].

The existence of H by the end of the reaction is not surprising because of the very high temperature (3,500 K). As shown in Table 3, H was very active; it acted 921 times as reactant and 923 times as product. Therefore, there is a good chance to see a couple of H left by the end of the simulation. The reaction types and products were also determined by the high pressure in the simulation system. Due to the fixed volume, the pressure in the simulation box was estimated to be in the order of $10^3$–$10^4$ atm. The existence of two relatively large products, O=N–N(O)=N–$CH_2$–CN and HO–C(O)–N=CH–C(N)–NH–C(O)–N=C=N, in the list is due to the high pressure. Relevant to real explosion, the simulation condition represents a small region of the material and a very short time in which the reaction has started but the expansion has not yet. Once the expansion is allowed, the temperature and pressure will decrease, and the products will be different since the large fragments will decompose into smaller ones.

Subtracting one reactant and 16 products (Table 3) from the total number of 725 (Table 1), we obtained 708 transient intermediates. Table 4 shows the activity distribution of these intermediates. Most (57 %) intermediates acted as reactant and product only once. The number of intermediates with higher activity parameters is smaller. Only 44 (6.7 %) acted more than 10 times. However, it should be pointed out that the intermediate activity does not necessarily reflect its importance. In fact, some critical intermediates appeared only a couple of times in the reaction trajectories.

The average life time (ALT) of a species indicates its stability. For each species, its life time was calculated by subtracting its appearing time from its disappearing time and the ALT was calculated by averaging over multiple existences. Table 5 lists the ALT for products and reactant in femtosecond (fs). It is interesting to note that the ALT of the reactant FOX-7 is only 106 fs, which is similar to that of the hydrogen atom (ion) 111 fs, indicating FOX-7 is highly unstable at 3,500 K. The most stable one is $N_2$ (1,151 fs), as expected, other stable compounds are nitrogen oxides and carbon dioxide. An interesting point to make is that water ($H_2O$, 240 fs), hydrogen cyanide (HCN 208 fs) and ammonia ($NH_3$, 122 fs) are fairly active molecules at high temperature like 3,500 K.

In Table 6, we list the most stable intermediates with ALT longer than 102 fs. Many of these intermediates exhibit ALT longer than the products listed in Table 5. Similar to the discussion of activity parameters, the

**Table 6** Average life time (ALT) of intermediates in 3,500 K simulation

| Formula | Molecular species | R | P | Net | ALT (fs) |
|---|---|---|---|---|---|
| $NO_3$ | Nitric acid | 14 | 14 | 0 | 613 |
| CO | Carbon monoxide | 5 | 5 | 0 | 369 |
| $H_4N$ | Ammonium | 34 | 34 | 0 | 349 |
| $CH_2N_2$ | Cyanamide | 45 | 45 | 0 | 300 |
| $C_3HN_4O$ | (a) | 6 | 6 | 0 | 256 |
| $C_3N_3O$ | (b) | 14 | 14 | 0 | 197 |
| $NO_2$ | Nitrogen dioxide | 68 | 68 | 0 | 191 |
| $C_2N_2$ | Oxalonitrile | 2 | 2 | 0 | 186 |
| $C_2HNO_2$ | (Hydroxyimino)ethenone | 2 | 2 | 0 | 158 |
| $C_2HN_2O$ | Cyano(nitroso)methanide | 3 | 3 | 0 | 143 |
| $CH_4N$ | Aminomethyl | 9 | 9 | 0 | 137 |
| CN | Cyanide | 33 | 33 | 0 | 136 |
| $CH_3N_3$ (c) | (c) | 9 | 9 | 0 | 133 |
| $CH_4N_2O$ (d) | (d) | 24 | 24 | 0 | 133 |
| $CH_3N_2O_3$ (e) | (e) | 11 | 11 | 0 | 129 |
| $CH_3N_3O_2$ (f) | (f) | 5 | 5 | 0 | 129 |
| $CH_2NO_2$ (g) | (g) | 36 | 36 | 0 | 125 |
| $CH_3NO_2$ (h) | (h) | 42 | 42 | 0 | 124 |
| $CN_2O$ | Oxocyanamide | 12 | 12 | 0 | 123 |
| $C_2H_3N_2O_2$ (i) | (i) | 4 | 4 | 0 | 121 |
| $C_2H_3N_2$ (j) | (j) | 12 | 12 | 0 | 116 |
| $C_3H_2N_2O_2$ (k) | (k) | 3 | 3 | 0 | 115 |
| CHN | Nitriliomethanide | 8 | 8 | 0 | 111 |
| HNO | Nitroxyl | 27 | 27 | 0 | 110 |
| $C_3H_3N_3O_2$ | (l) | 7 | 7 | 0 | 109 |
| $C_2HO$ | Ethynyloxidanyl | 10 | 10 | 0 | 106 |
| $C_2H_4N_2O$ | Diaminoethenone | 6 | 6 | 0 | 102 |

(a) InChI = 1S/$C_3HN_4O$/c4-1-6-3(8)7-2-5/h6H, (b) InChI = 1S/$C_3N_3O$/c4-1-3(7)6-2-5, (c) InChI = 1S/$CH_3N_3$/c2-1-4-3/h2-4H, (d) InChI = 1S/$CH_4N_2O$/c2-1(3)4/h2-3$H_2$, (e) InChI = 1S/$CH_3N_2O_3$/c4-2-1-3(5)6/h1,5-6H, (f) InChI = 1S/$CH_3N_3O_2$/c2-1(5)3-4-6/h3H,2$H_2$, (g) InChI = 1S/$CH_2NO_2$/c2-1(3)4/h2-3H, (h) InChI = 1S/$C_2H_3N_2O_2$/c3-1(4)2(5)6/h3H,4$H_2$, (i) InChI = 1S/$C_2H_3N_2$/c3-1-2-4/h3H,1$H_2$, (j) InChI = 1S/$C_3H_2N_2O_2$/c4-1-2-5-3(6)7/h2,6H, (k) InChI = 1S/$C_3H_3N_3O_2$/c4-2-5-3(7)1-6-8/h5H,4H2, (l) InChI = 1S/$C_3H_3N_3O_2$/c4-2-5-3(7)1-6-8/h5H,4$H_2$

higher ALT does not equal to more importance; in fact, some critically important intermediates exhibit very short time. We list the intermediates with long ALT for the purpose that these species may be detected using experimental techniques. The transient intermediate species H, CN, OH, NO, C and N were detected before [4], but species like $NO_3$, $NH_4^+$ and $CH_2N_2$ which are fairly stable based on our simulation data have not been reported by experimental work yet. We should make a note that one of the intermediates, $NO_2$, was treated as a product by the measurement [4].

### 3.3 Reaction network and mechanisms

The large amount of data generated in the simulation is very valuable for understanding the FOX-7 reaction mechanisms at extreme condition. However, in order to draw a clear picture on the reaction network, we should focus on specific purposes. We used a reverse mapping strategy to identify the reaction pathways from initial reactant, FOX-7 to the most common products $N_2$, $CO_2$ and $H_2O$. Starting from the products, we used the atom sequence numbers (a unique number assigned to each atom) to find out all species that contain the same atoms in the trajectory. Then, we looked up the reaction list in a backward manner and found out reactions that connect those species. By doing so, we built up a simplified reaction network that describes how the most common products are formed, as shown in Fig. 4.

Reaction networks have been proposed previously based on experimental and quantum chemistry data [4, 6]. In those published papers, water is considered to be formed between OH and H, and $CO_2$ is formed by carbon oxidization step by step with reaction intermediates such as C=CO($NO_2$), C=C=O, C–CH=O and $CO_2$. The network reported in this work is more comprehensive and unbiased; it gives a complete description of the formation of the three common products. We obtained the formations of $H_2O$ and $CO_2$ in similar routes as previously suggested. However, the formation of $N_2$ has not been described before because it occurred in later stage and is much more complicated than those of $H_2O$ and $CO_2$.

With the reaction network established, we outline the pathways as follows. In the following schemes (1–11), each species is labeled with a code and ALT for convenience in discussion. First of all, we identified three types of initial decompositions for reactant FOX-7. They are (1) C–$NO_2$ bond fission, (2) intermolecular hydrogen transfer and (3) intramolecular hydrogen transfer.

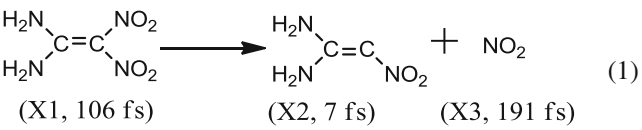


(X1, 106 fs) (X2, 7 fs) (X3, 191 fs) (1)

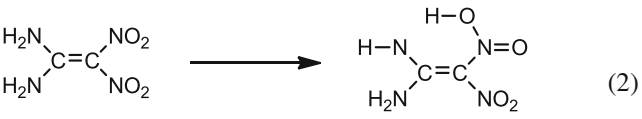


(X1, 106 fs) (X4, 22 fs) (2)

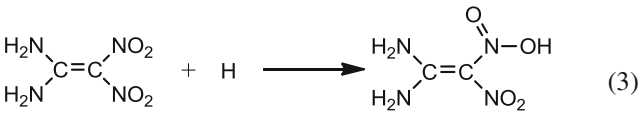


(X1, 106fs) (X5, 111 fs) (X6, 14 fs) (3)

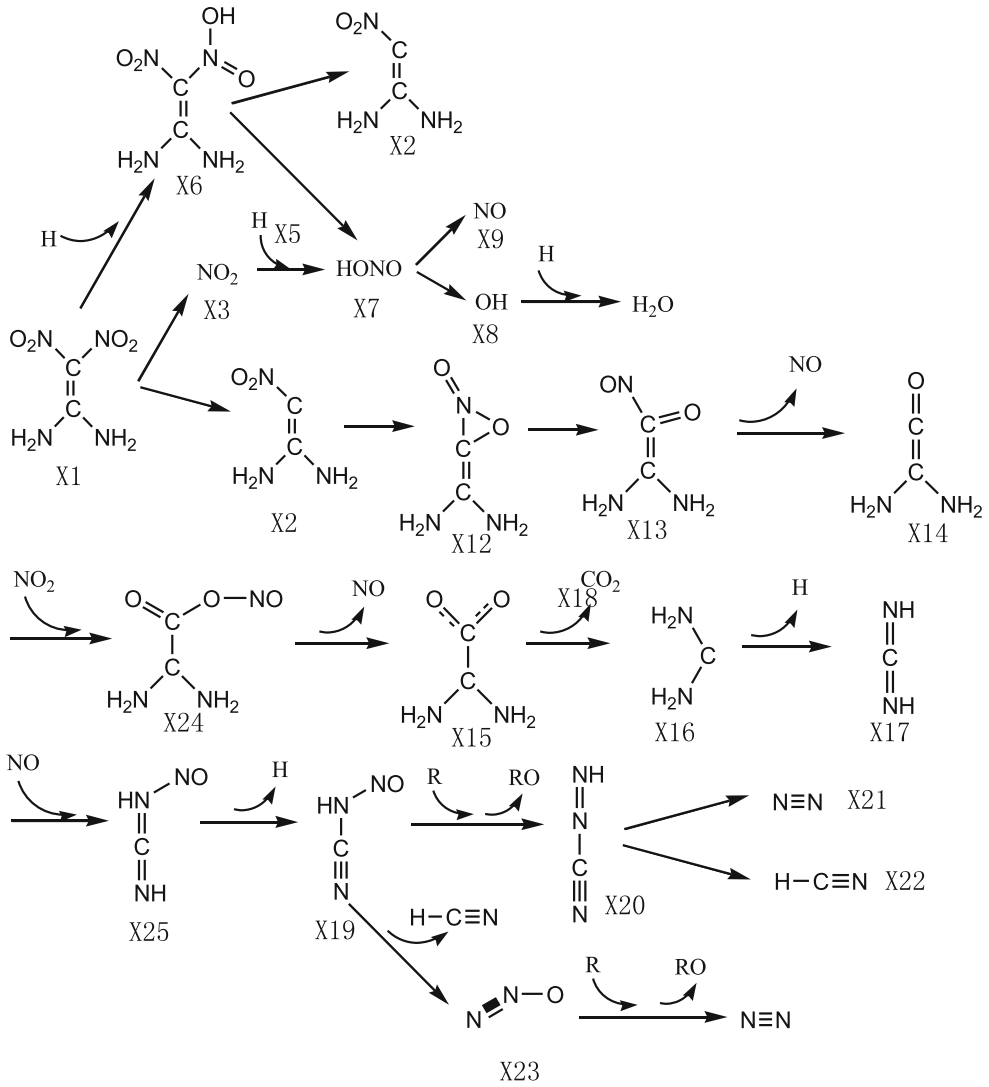


**Fig. 4** Reaction map from reactant FOX-7 to main products $H_2O$, $CO_2$ and $N_2$

The occurrence times of the three initial decomposition types are 4, 3 and 1, respectively (for 8 FOX-7 molecules). Due to small sizes and short simulation times, the occurrence times are associated with large uncertainties. However, analysis shows that all of the three types of initial reactions were observed in simulations at different temperatures. The occurrence percentage of the three initial decomposition types are 45, 33 and 22 % at 2,500 K, 33, 50 and 17 % at 3,000 K, 50, 13 and 17 % at 3,500 K, and 50, 33 and 17 % at 4,000 K. The most popular route is through the C–$NO_2$ bond fission, as indicated in previous energy minimization calculations [5]. This reaction generates an intermediate, 2-nitroethene-1,1-diamine (X2, 7 fs) and $NO_2$ (X3, 191 fs), which explains why $NO_2$ is the first intermediate generated in the reactions as we discussed above (Fig. 1). We did not observe nitro-to-nitrite rearrangement as initial reaction in the trajectory. The important finding here is that both intramolecular hydrogen transfer (Scheme 2) and intermolecular hydrogen transfer (Scheme 3) were found to be feasible, contradictory to the previous energy minimization calculation results [8]. This shows that the significant differences between energy minimization calculations and dynamic simulations. With many atoms, the thermal fluctuation is a driving force for the reactions, but it is not feasible by energy minimization calculations. It should be noted that this study is aimed to discover unknown reaction pathways that are beyond what can be postulated based on chemical intuition and to prepare reaction information for developing reactive force field, which can be used to get quantitative prediction of reaction mechanisms, kinetics with enhanced sampling techniques, large simulation size and time scale.

As a matter of fact, the hydrogen transfer reactions (1) and (2) are very important as they produced two highly active intermediates (X4, 22 fs) and (X6, 14 fs), in which the C–N bonds are activated and will be broken rapidly to generate nitrosyl hydroxide (X7, 29 fs) and another intermediate. From (X6, 14 fs), it produces:

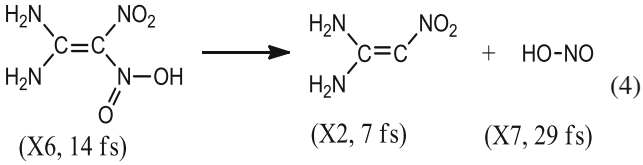


(4)

In addition, nitrous acid, HONO (X7, 29 fs), can be generated from $NO_2$ (X3, 191 fs) by accepting a proton from other intermediate. Nitrous acid is reactive (29 fs), and it rapidly decomposes to NO and OH radicals:

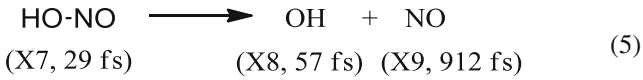


(5)

OH radical reacts with proton to produce one of the final products, $H_2O$. NO is relative stable, but it can react with other species as shown in scheme (9) below.

The intermediate 2-nitroethene-1,1-diamine (X2, 7 fs) is very reactive and may react with a proton to form $NH_3$ and intermediate (X10, 42 fs):

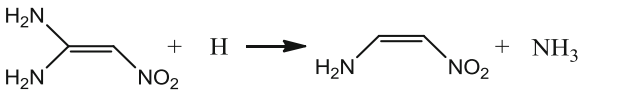


(6)

In addition, (X2, 7 fs) undergoes C–$NO_2$ isomerization through a three-member-ring transition state (X12, 8 fs), in which the first C–O bond starts to form. (X12, 8 fs) is then converted to the intermediate (X13, 5 fs), in which a carbonyl (C=O) bond is formed. Afterward, (X13, 5 fs) loses a NO group to generate a relatively stable intermediate (X14, 99 fs).

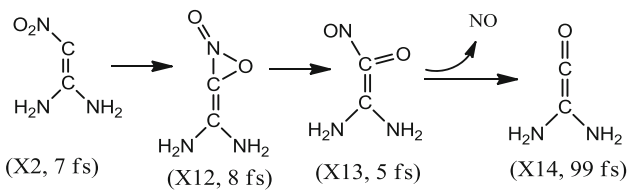


(7)

(X14, 99 fs) is oxidized by $NO_2$ to form the intermediate (X15, 69 fs), which undergoes the C–C bond fission to produce the intermediate (X16, 6 fs) and another final product ($CO_2$, 541 fs). (X16, 6 fs) is very reactive and quickly releases two hydrogen atoms to form carbodiimide (X17, 68 fs).

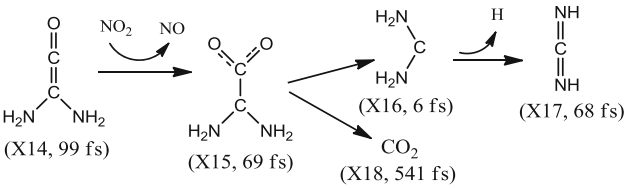


(8)

Carbodiimide (X17, 68 fs) is a reactive molecule widely used in the direct conjugation of carboxylic acid to primary amine for organic synthesis. In the simulated trajectory, carbodiimide (X17) reacts with NO to generate the first N–N bond:

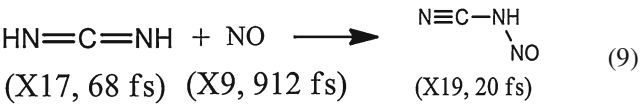


(9)

The intermediate (X19, 20 fs) reacts with a reducing agent denoted by R to form the intermediate (X20, 25 fs), which generates the final products $N_2$ (X21, 1,150 fs) and HCN (X22, 207 fs) by internal hydrogen transfer and C–N bond fission.

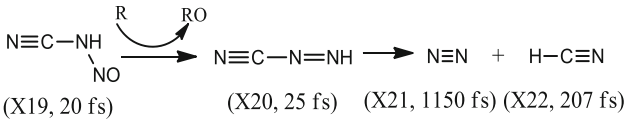


(10)

(X19, 20 fs) has another route in which the C–N bond fission occurs before the reduction. The C–N bond fission and internal hydrogen transfer generates HCN (X22, 207 fs) and $N_2O$ (X23, 560 fs), which is then reduced to form $N_2$ (X21, 1,150 fs).

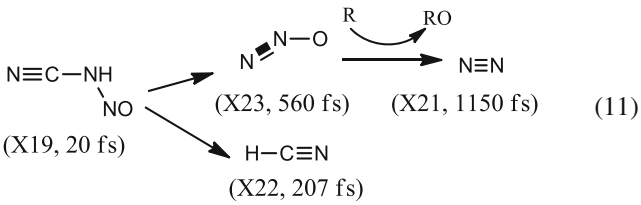


(11)

## 4 Conclusion

In order to obtain the thermal decomposition mechanism of solid FOX-7 at high temperature, we carried out NVT ensemble AIMD simulations at 2,500, 3,000, 3,500 and 4,000 K. The simulated reactions progress in different extents as the reaction rate is directly related with temperature. The simulation results show that reactions at the end of 3 ps simulation are close to completion at 3,500 and 4,000 K while they are still in the middle way at 2,500 and 3,000 K. Taking data obtained at different temperatures, we obtained a whole picture of the decomposition process for FOX-7 under extreme condition.

The simulation data demonstrates that the reactions in high-pressure gas phase are very complex. There are

hundreds of unit reactions and about the same number of transient intermediates. Unlike reactions in dilute solution or low-pressure gas phase in which reaction pathways consist few unit reactions, the complex reaction pathways in high-pressure gas phase are too complicated to be made solely based on chemical intuitions. It is necessary to use molecular dynamics method to study this type of reactions. Similar problems exist for reactions in high-concentration solutions, such as the condensation reactions in polymers and zeolite syntheses.

One of the main findings of this work is about the initial decomposition of FOX-7. The C–$NO_2$ bond fission mechanism [5] is found to be the most common route. However, the inter- and intramolecular hydrogen transfers which have been excluded by previous energy minimization calculations [8] are found to be plausible. The most popular initial decomposition is the C–$NO_2$ bond fission process, followed by the intramolecular hydrogen transfer, and the least popular one is the intermolecular hydrogen transfer. The nitro-to-nitrite rearrangement suggested by previous energy minimization calculation [6] is not observed in the simulated data. These findings demonstrate that the reactions in ideal gases are dramatically different from those in highly condensed phases.

The simulation results agree well with known experimental data [4]. Using the multiple temperature data, the activation energy of initial decomposition was estimated and the result is in agreement with the experimental value [19]. The molecules identified in the simulation process agree with experimental observation. It is important to note that, in addition to the main products, which can be deduced from stoichiometry, we found more than a dozen of side products. Among those side products, HCN, NO, $NH_3$, $H_2O$, HCN, HONO, $NO_2$ are identified in the experiment [4], which is pretty encouraging result. The quantitative agreement has not been achieved because the simulations condition is still different from the real experimental considering the system size and reaction time scale.

In order to capture reaction details, we collected trajectory at an interval of 0.5 fs, which is short enough to catch very fast reactions. The data set was too large to be analyzed by hand. With computer software, we carried out statistical analysis of the data and tracked out how the main products are generated. For the first time, we were able to map out a complete reaction network for $H_2O$, $CO_2$ and $N_2$ formations in the thermal decomposition of FOX-7. Although the network may not be the same for all products, the investigation method is generally applicable. One can use this method to track back any product to find out how it is produced, and then possibly how to promote or demote its production. This would be very useful for targeted synthesize or for environment protection.

There is still large room for future improvement. The small simulation size, short simulation time and high simulation temperature are obviously problems to be addressed in future work. One of the possibilities is to develop RFF based on AIMD simulation result obtained from this study. If RFF represents the reaction potential energy surface well, MD simulations with RFF can be carried out with much larger (in 2–3 orders of magnitude higher) size and time scales than what can be done using AIMD. The quantitative results with smaller fluctuation can be anticipated from large-scale MD simulation with RFF and high-performance supercomputer.

**Acknowledgments** This work was funded in part by the National Science Foundation of China (#21073119, #21173146) and National Basic Research Program (#2014CB239702).

## References

1. Bellamy AJ (2007) High energy density materials. Springer, Berlin
2. Badgujar DM, Talawar MB, Asthana SN, Mahulikar PP (2008) Advances in science and technology of modern energetic materials: an overview. J Hazard Mater 151:289–305
3. Isayev O, Gorb L, Qasim M, Leszczynski J (2008) Ab initio molecular dynamics study on the initial chemical events in nitramines: thermal decomposition of CL-20. J Phys Chem B 112:11005–11013
4. Civis M, Civis S, Sovova K, Dryahina K, Spanel P, Kyncl M (2011) Laser ablation of FOX-7: proposed mechanism of decomposition. Anal Chem 83:1069–1077
5. Politzer P, Concha MC, Grice ME, Murray JS, Lane P, Habibollazadeh D (1998) Computational investigation of the structures and relative stabilities of amino/nitro derivatives of ethylene. Theochem-J Mol Struct 452:75–83
6. Gindulyte A, Massa L, Huang LL, Karle J (1999) Proposed mechanism of 1,1-diamino-dinitroethylene decomposition: a density functional theory study. J Phys Chem A 103:11045–11051
7. Kimmel AV, Sushko PV, Shluger AL, Kuklja MM (2007) Effect of charged and excited states on the decomposition of 1,1-diamino-2,2-dinitroethylene molecules. J Chem Phys 126:234711
8. Kimmel AV, Sushko PV, Shluger AL, Kuklja MM (2008) Effect of molecular and lattice structure on hydrogen transfer in molecular crystals of diamino-dinitroethylene and triamino-trinitrobenzene. J Phys Chem A 112:4496–4500
9. Reed EJ, Rodriguez AW, Manaa MR, Fried LE, Tarver CM (2012) Ultrafast detonation of hydrazoic acid ($HN_3$). Phys Rev Lett 109:038301
10. Nomura KI, Kalia RK, Nakano A, Vashishta P, van Duin ACT, Goddard WA (2007) Dynamic transition in the structure of an energetic crystal during chemical reactions at shock front prior to detonation. Phys Rev Lett 99:148303
11. Manaa MR, Reed EJ, Fried LE, Galli G, Gygi F (2004) Early chemistry in hot and dense nitromethane: molecular dynamics simulations. J Chem Phys 120:10146–10153
12. Chang J, Lian P, Wei DQ, Chen XR, Zhang QM, Gong ZZ (2010) Thermal decomposition of the solid phase of nitromethane: ab initio molecular dynamics simulations. Phys Rev Lett 105:188302
13. Car R, Parrinello M (1985) Unified approach for molecular-dynamics and density-functional theory. Phys Rev Lett 55:2471–2474
14. CPMD 3.13. Copyright IBM Corp. 1990–2006, Copyright MPI fuer Festokoerperforschung Stuttgart 1997–2001. See also http://www.cpmd.org

15. Troullier N, Martins JL (1991) Efficient pseudopotentials for plane-wave calculations. Phys Rev B 43:8861–8869
16. Martyna GJ, Tuckerman ME (1999) A reciprocal space based method for treating long range interactions in ab initio and force-field-based calculations in clusters. J Chem Phys 110:2810–2821
17. Evers J, Klapotke TM, Mayer P, Oehlinger G, Welch J (2006) Alpha- and beta-FOX-7, polymorphs of a high energy density material, studied by X-ray single crystal and powder investigations in the temperature range from 200 to 423 K. Inorg Chem 45:4996–5007
18. IUPAC International Chemical Identifier Project Page (2012) IUPAC. http://www.iupac.org
19. Anniyappan M, Talawar MB, Gore GM, Venugopalan S, Gandhe BR (2006) Synthesis, characterization and thermolysis of 1,1-diamino-2,2-dinitroethylene (FOX-7) and its salts. J Hazard Mater 137:812–819

Theor Chem Acc (2014) 133:1540
DOI 10.1007/s00214-014-1540-3

REGULAR ARTICLE

# Hemibond complexes between $H_2S$ and free radicals (F, Cl, Br, and OH)

**Benjamin Alday · Ryan Johnson · Jun Li · Hua Guo**

Received: 2 June 2014 / Accepted: 10 July 2014 / Published online: 12 August 2014
© Springer-Verlag Berlin Heidelberg 2014

**Abstract** The interaction of hydrogen sulfide ($H_2S$) with F, Cl, Br, and OH is investigated using ab initio methods to identify the two-center three-electron hemibond responsible for their complexation. The binding energies are found to be stronger than those in the analogous water complexes, but follow the same trend of increasing strength: F > Cl > Br > OH. The radicals are located nearly perpendicular to the $H_2S$ plane forming an angle of about 90°. Analysis of molecular orbitals and natural bond orbitals are carried out to understand the energetics, structures, and bonding characteristics of these hemibonded complexes.

**Keywords** Hemibond · Radical · Ab initio

## 1 Introduction

Hydrogen sulfide ($H_2S$) is present in many atmospheric, interstellar, and industrial environments. In Earth's atmosphere, for example, $H_2S$ released from biota, volcanoes, and industrial processes may contribute to climate changes [1]. This molecule is also known to react with free radicals such as OH in atmosphere [2] and in combustion [3]. Such reactions typically result in the abstraction of a hydrogen from $H_2S$ by the radical, and these processes are activated with a barrier. Very recently, we have systematically studied similar reactions involving $H_2O$ and free radicals such as F [4–8] and Cl [9] and found that there often exists a pre-reaction complex between the two reactants. The existence of such complexes has also been reported in other ab initio studies [10–13]. Interestingly, the $F\cdots H_2O$ complex has been shown to aid the $F + H_2O$ reaction by guiding the trajectories to the transition state, resulting in a significant enhancement of the reactivity, particularly at low collision energies [14]. More interestingly, it was demonstrated that such complexes are not van der Waals or electrostatic in nature, but due to covalent interactions based on a two-center three-electron bond [15].

Such a two-center three-electron bond was first discussed by Pauling [16]. Due to the fact that one electron is in the antibonding orbital, such a covalent bond is usually quite weak with a relatively long bond length and hence called a hemibond [17]. Hemibond bonding has been found in many branches of chemistry [18], particularly between molecules with lone pairs of electrons and a free radical with an unpaired electron [19–31]. As mentioned above, such hemibond complexes are not only of a fundamental interest, but might also play an important role in molecule–radical reactions. Like oxygen-containing molecules, sulfur compounds may also provide lone electron pairs on S, thus allowing the formation of hemibonds with free radicals. In the literature, however, most such complexes investigated before are charged [17, 19, 21, 22, 24–26], which complicates the bonding with electrostatic interactions. To further understand the sulfur-containing hemibond complexes, we report here an extensive high-level ab initio and density functional theory (DFT) study of the complexes formed by $H_2S$ and several free radicals. The major aim is to understand the similarities and differences between the $H_2O\cdots X$ and $H_2S\cdots X$ complexes with X = F, Cl, Br, and OH by examining the structural, energetic, and electronic aspects of these interesting systems.

Dedicated to Professor Guosen Yan and published as part of the special collection of articles celebrating his 85th birthday.

B. Alday · R. Johnson · J. Li · H. Guo (✉)
Department of Chemistry and Chemical Biology, University of New Mexico, Albuquerque, NM 87131, USA
e-mail: hguo@unm.edu

For the $H_2S\cdots OH$ complex, we also investigate the competing hydrogen bond complex.

## 2 Theory

Most of the calculations were carried out at an F12 version of the unrestricted coupled cluster method with singles, doubles, and perturbative triples based on restricted open-shell Hartree–Fock reference wave functions (ROHF-UCCSD(T)-F12a) [32, 33]. The 1*s*, 2*s,* and 2*p* core electrons in S were frozen, similar to the work done in the analogous water systems [15]. The F12a method converges well to the complete basis set (CBS) limit with relatively small basis sets; so, the augmented correlation-consistent polarized valence triple zeta (aug-cc-pVTZ or AVTZ) basis set [34] was used. The minimum energy structures of both the complex and monomers were obtained by optimization at the UCCSD(T)-F12a level. The binding energy ($E_b$) of the complexes was computed directly from the difference of the complex and separated monomers. This direct approach is justified as the basis set superposition error (BSSE) was examined for the $F\cdots H_2S$ complex and was found to be quite small (less than 0.02 $cm^{-1}$). The calculations were performed using MOLPRO 2010.1 [35].

Additional calculations have been carried out using the spin-restricted open-shell density functional theory (RO-DFT) with the modified Perdew–Wang 1-parameter functional for kinetics (MPW1K) suggested by Truhlar and coworkers [36], which has been shown to yield comparable energetics for the $F\cdots H_2O$ complex with the UCCSD(T)/cc-pV5Z level of theory [11]. The same AVTZ basis set was used. The DFT calculations are used as a diagnostic tool to understand the bonding nature. Molecular orbitals within the DFT treatment were also used in the natural bond orbital (NBO) analysis [37], which allows the description of the bonding and lone pair orbitals within the intuitive Lewis structure framework. These molecular orbital calculations were carried out using Gaussian 09 [38].

| | θ (deg) | R (Å) | ϕ (deg) |
|---|---|---|---|
| F | 87.3 | 1.95 | |
| Cl | 87.8 | 2.58 | |
| Br | 87.9 | 2.80 | |
| OH | 68.0 | 2.62 | 87.6 |

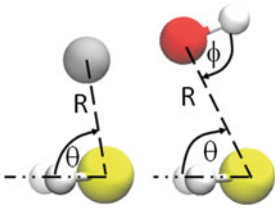


**Fig. 1** Geometries and binding energies for the $H_2S\cdots X$ (X = F, Cl, Br, and OH) complexes obtained at the UCCSD(T)-F12a/AVTZ level of theory

## 3 Results and discussion

All $H_2S\cdots X$ complexes were found to have the $C_s$ symmetry, with the mirror plane bisecting the H–S–H bond. The relative position of the two moieties is defined by $\theta$ (the angle between the X–S line and $H_2S$ plane) and R (the distance between X (O in the case of OH) and S) as indicated in Fig. 1. For the $H_2S\cdots OH$ complex, an additional bond length for the OH and the S–O–H angle are needed. A summary of the geometries of the complexes formed between $H_2S$ and X = F, Cl, Br, and OH is given in Table 1. For comparison, the equilibrium geometries of the isolated $H_2S$ and OH are also included for comparison. In addition, the optimized DFT geometries are also given for comparison. Interestingly, the intramolecular H–S and O–H bonds are only slightly elongated in the complex, and the bonding angle remains roughly same as the $H_2S$ and OH monomers. This observation suggests that the complexation has an insignificant effect on the $H_2S$ monomer as well as OH in the $H_2S\cdots OH$ complex.

It is interesting to note that the X–S bond lengths are quite long, suggesting a relatively weak interaction characterizing the hemibonds. The long bond lengths are consistent with previous theoretical results for hemibond complexes involving sulfur [17, 19, 21, 22, 24–26]. For example, the S–O distance in the $H_2S\cdots OH$ complex is 2.62 Å, which can be

**Table 1** Geometric parameters of $H_2S$ and its complexes with various free radicals obtained at the UCCSD(T)-F12a/AVTZ level and at the MPW1K/AVTZ level (in parentheses)

| | $R_{SH1}$ | $R_{SH2}$ | $R$ | $R_{OH3}$ | $\theta_{H1SH2}$ | $\theta$ | $\phi$ |
|---|---|---|---|---|---|---|---|
| $H_2S$ (Expt.) [40] | 1.3356 | 1.3356 | | | 92.12 | | |
| $H_2S$ | 1.325 (1.336) | 1.325 (1.336) | | | 92.9 (92.7) | | |
| OH | | | | 0.970 (0.963) | | | |
| $H_2S\cdots F$ | 1.338 (1.335) | 1.338 (1.335) | 1.948 (1.993) | | 94.4 (94.1) | 87.3 (87.3) | |
| $H_2S\cdots Cl$ | 1.340 (1.336) | 1.340 (1.336) | 2.580 (2.591) | | 92.8 (93.1) | 87.8 (87.8) | |
| $H_2S\cdots Br$ | 1.340 (1.336) | 1.340 (1.336) | 2.802 (2.788) | | 92.6 (93.0) | 87.9 (87.9) | |
| $H_2S\cdots OH$ | 1.339 (1.335) | 1.339 (1.335) | 2.621 (2.825) | 0.969 (0.961) | 92.6 (92.8) | 68.0 (72.3) | 87.6 (81.6) |
| $H_2S\cdots HO$ | (1.343) | (1.343) | (3.569) | (0.979) | (92.7) | (158.8) | (16.6) |

The intermolecular geometric parameters are defined in Fig. 1. Bond length in angstroms and angle in degrees

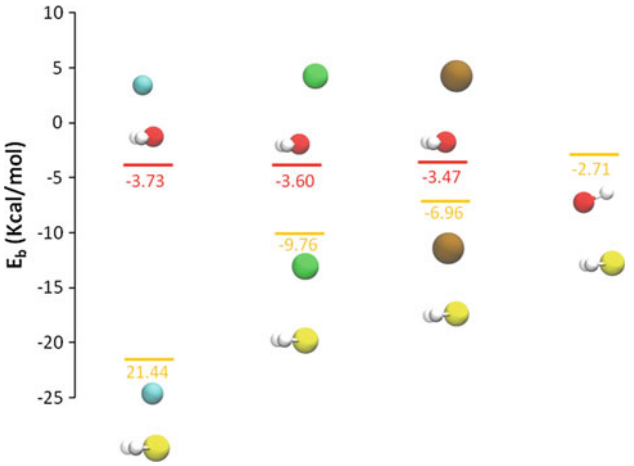


**Fig. 2** Comparison of the binding energies and structures $H_2S\cdots X$ and $H_2O\cdots X$ (X = F, Cl, Br, and OH) complexes obtained at the UCCSD(T)-F12a/AVTZ level of theory

**Table 2** Comparison of binding energies obtained at the UCCSD(T)-F12a/AVTZ level and at the MPW1K/AVTZ level (in parentheses)

| Complex | $E_b$ (kcal/mol) hemibond | $E_b$ (kcal/mol) hydrogen bond |
|---|---|---|
| $H_2S\cdots F$ | −21.44 (−16.87) | – |
| $H_2S\cdots Cl$ | −9.76 (−11.59) | – |
| $H_2S\cdots Br$ | −6.96 (−8.82) | – |
| $H_2S\cdots OH$ | −2.71 (−2.07) | −2.66* (−1.11) |

* Single point CCSD(T)-F12a result from DFT geometry

compared with that in the $NCS^-\cdots OH$ complex (2.179 Å) [26]. (The shorter distance in the latter complex is presumably due to the additional charge–dipole interaction.) In addition, the free radical typically bonds above (or equivalently below) the molecular plane of $H_2S$, which is analogous to the hemibond complexes involving $H_2O$ [15]. However, the angle $\theta$ is somewhat different for the two types of complexes. While the angle $\theta$ is larger than 90° in the $H_2O\cdots X$ (X = Cl, Br) complexes, the corresponding angle in the $H_2S\cdots X$ complexes is near 90°. Similar right-angled hemibond complexes have been reported before between sulfur-containing molecules and free radicals [17, 19, 21, 22, 24–26].

As shown in Fig. 2 and Table 2, binding energies of the complexes are in general much stronger than that in the corresponding water complexes. Among them, the $H_2S\cdots F$ complex is the strongest, with a large binding energy of 21.44 kcal/mol. The binding energy decreases in the order F ≫ Cl > Br > OH. These binding energies are consistent with those found previously for hemibond complexes involving sulfur [19, 22, 24–26].

In Table 3, the harmonic vibrational frequencies of these complexes are listed along with those of the monomers.

**Table 3** Harmonic vibrational frequencies ($cm^{-1}$) for monomers and complexes at the UCCSD(T)-F12a/AVTZ level and at the MPW1K/AVTZ level (in parentheses)

| | HSH bend | S–H symmtrical. stretch | S–H asymmtrical. stretch | S–X stretch | $H_2S$–X wagging | $H_2S$–X bending | S–O twisting | OH wagging | O–H stretch |
|---|---|---|---|---|---|---|---|---|---|
| OH expt. [40] | | | | | | | | | 3,737.76 |
| $H_2S$ expt. [40] | 1,183 | 2,626 | 2,615 | | | | | | |
| $H_2S$ | 1,212.3 (1,231.3) | 2,719.4 (2,782.5) | 2,735.3 (2,796.3) | | | | | | |
| $H_2S\cdots F$ | 1,181.1 (1,208.6) | 2,715.0 (2,787.4) | 2,740.6 (2,804.0) | 435.9 (347.4) | 552.8 (461.6) | 609.7 (539.3) | | | |
| $H_2S\cdots Cl$ | 1,205.1 (1,229.9) | 2,714.31 (2,756.5) | 2,730.8 (2,769.3) | 237.6 (242.0) | 366.0 (384.9) | 396.6 (426.8) | | | |
| $H_2S\cdots Br$ | 1,205.5 (1,227.4) | 2,711.08 (2,783.1) | 2,726.1 (2,797.1) | 164.7 (175.0) | 306.4 (321.1) | 332.5 (346.8) | | | |
| $H_2S\cdots OH$ | 1,206.2 (1,232.0) | 2,739.9 (2,765.5) | 2,756.9 (2,777.8) | 78.0 (132.5) | 149.0 (257.8) | 251.8 (316.9) | 284.6 (397.2) | 504.9 (606.1) | 3,765.6 (3,787.6) |

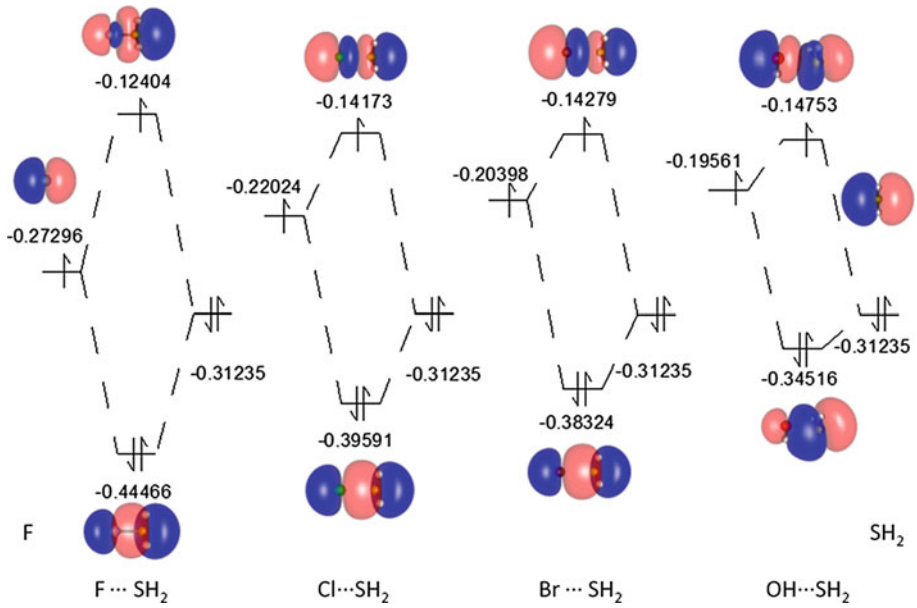


**Fig. 3** Molecular orbital energy level diagram for $H_2S\cdots X$ (X = F, Cl, Br, OH) complexes with corresponding MO wavefunctions obtained at the MPW1K/aug-cc-pVTZ level of theory

Again, the complexation changes the monomer frequencies very little. The vibrational frequencies between the monomers in the complex are typically low, consistent with the weak interactions in the hemibonded complexes. Similar conclusions can be formed from the DFT frequencies also listed in the Table 3.

To understand these structural and energetic trends, we resort to the molecular orbital (MO) analysis using the DFT method. In Fig. 3, MO energy level diagrams for the $H_2S\cdots X$ complexes are displayed. The two major monomer MO wavefunctions that contribute to the hemibond MO wavefunctions in the complexes are displayed with isosurface plots. The resulting electronic structures clearly indicate the formation of a two-center three-electron hemibond. It is also clear that the magnitude of the binding energy can be attributed to the energy difference between the highest occupied molecular orbital (HOMO) of S (i.e., a lone pair orbital) and the singly occupied molecular orbital (SOMO) of the radical. Since the hemibond strength is controlled by the stabilization energy of the bonding orbital between the two, the smaller this HOMO-SOMO gap, the greater the stabilization of the resulting bonding MO, the stronger the bond. The energy difference is the smallest for the $H_2S\cdots F$ complex, resulting in the strongest binding energy. The energy gap increases in the order F < Cl < Br < OH. The larger binding energies in the $H_2S\cdots X$ complexes than those in the $H_2O\cdots X$ complexes can be largely attributed to the higher energy of the $H_2S$ HOMO (−0.312 au) than that of $H_2O$ (−0.384 au) [15].

The geometry of the complex can also be understood in terms of the hemibond as well. For the $H_2O\cdots X$ complexes, it was demonstrated [15] that the geometry of the complexes is largely dictated by the overlap between the radical SOMO and molecular HOMO. In $H_2S$, there are two lone pair nonbonding MOs in S. One is perpendicular to the molecular plane while the other is within the molecular plane, as shown in Fig. 4 by both the MO and NBO wavefunctions. They are the HOMO ($E$ = −0.312 a.u.) and HOMO-1 ($E$ = −0.419 a.u.), respectively. As discussed above, the radical SOMO interacts primarily with the $H_2S$ HOMO, which is perpendicular to the $H_2S$ plane. As a result, the complexes are all formed with an angle $\theta$ close to 90°.

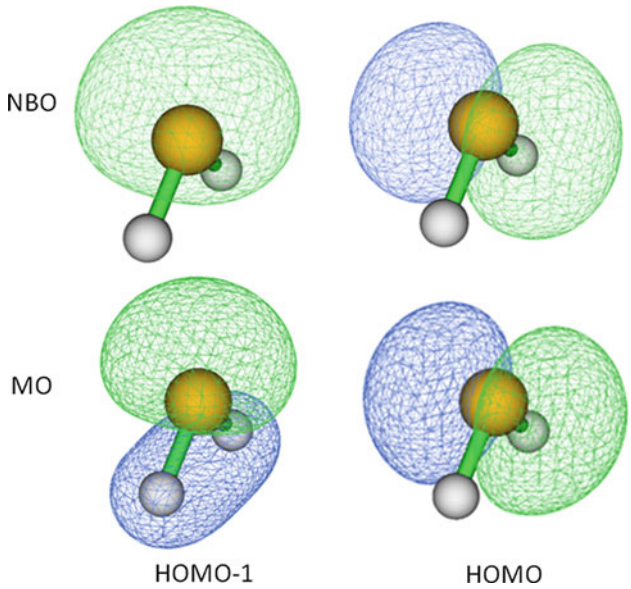


**Fig. 4** Images of the lone pair orbitals from NBO and corresponding MOs of $H_2S$

For the $H_2S\cdots OH$ complex, there is another configuration in which the H of the OH moiety points toward S.

This isomer of the complex is apparently due to the dipole–dipole or hydrogen bond interaction. Although this hydrogen-bonded complex was identified by DFT optimization, we were unable to converge the CCSD(T)-F12 calculation for this complex, presumably due to flatness of the potential energy surface near the minimum. The DFT geometric parameters of this complex are also included in Table 1. Its binding energy is −1.11 kcal/mol at the DFT level. The single point CCSD(T)-F12 calculation at the DFT geometry gives a binding energy of −2.66 kcal/mol. These results suggest that the hemibond complex is slightly more stable than the hydrogen bond complex. There have been extensive discussions in the literature on the relative stability of the similar isomers in the complexes formed between $H_2O$ and OH, which also have comparable binding energies [29, 31].

Finally, we note in Tables 1 and 2 that DFT values are qualitatively similar to those obtained at the UCCSD(T)-F12/AVTZ level, although there are quantitative differences. This is in further support of the covalent nature of these complexes as DFT is considered incapable of handling dispersion and other weak interactions. This observation is consistent with the recent work that DFT is capable of describing hemibonds [31, 39], although such a description is not expected to be quantitative. This is important as it lends credence to DFT based simulations in hemibond systems.

## 4 Conclusions

In summary, our high-level ab initio calculations predict that $H_2S$ forms a strong hemibond with a free radical such as F, Cl, Br, and OH. These hemibond complexes have much stronger binding energies than those involving $H_2O$, thanks to good energy match between the SOMO of the radical and lone pair HOMO of $H_2S$, which is perpendicular to the $H_2S$ molecular plane. The complexes formed between $H_2S$ and the radicals assume a $C_s$ geometry where the radical is above (or below) the molecular plane immediately above the S atom, which can again be attributed to the SOMO–HOMO interaction. These interesting properties of the hemibond complexes will have an important impact on our future investigations of the reactions between $H_2S$ and free radicals.

**Acknowledgments** This work was supported by the Department of Energy (DE-FG02-05ER15694). The computations were performed at the National Energy Research Scientific Computing (NERSC) Center.

## References

1. Charlson RJ, Lovelock JE, Andreae MO, Warren SG (1987) Nature 326:655
2. Warneck P (2000) Chemistry of the natural atmosphere. Academic Press, San Diego
3. Glassman I (1996) Combustion, 3rd edn. Academic Press, San Diego
4. Li J, Dawes R, Guo H (2012) J Chem Phys 137:094304
5. Li J, Jiang B, Guo H (2013) J Chem Phys 138:074309
6. Li J, Jiang B, Guo H (2013) J Am Chem Soc 135:982
7. Nguyen TL, Li J, Dawes R, Stanton JF, Guo H (2013) J Phys Chem A 117:8864
8. Li J, Guo H (2013) Chin J Chem Phys 26:627
9. Li J, Dawes R, Guo H (2013) J Chem Phys 139:074302
10. Deskevich MP, Nesbitt DJ, Werner H-J (2004) J Chem Phys 120:7281
11. Li G, Zhou L, Li Q-S, Xie Y, Schaefer HF III (2012) Phys Chem Chem Phys 14:10891
12. Guo Y, Zhang M, Xie Y, Schaefer HF III (2013) J Chem Phys 139:041101
13. de Oliveira-Filho AGS, Ornellas FR, Bowman JM (2014) J Phys Chem Lett 5:706
14. Li J, Jiang B, Guo H (2013) Chem Sci 4:629
15. Li J, Li Y, Guo H (2013) J Chem Phys 138:141102
16. Pauling L (1931) J Am Chem Soc 53:3225
17. Gill PMW, Radom L (1988) J Am Chem Soc 110:4931
18. Fourré I, Silvi B (2007) Heteroatom Chem 18:135
19. Deng Y, Illies AJ, James MA, McKee ML, Peschke M (1995) J Am Chem Soc 117:420
20. McKee ML, Nicolaides A, Radom L (1996) J Am Chem Soc 118:10571
21. Nichols LS, Illies AJ (1999) J Am Chem Soc 121:9176
22. Braïda B, Hazebroucq S, Hiberty PC (2002) J Am Chem Soc 124:2371
23. Gao Y, Alecu IM, Hsieh P-C, Morgan BP, Marshall P, Krasnoperov LN (2006) J Phys Chem A 110:6844
24. Aloisio S (2006) Chem Phys 326:335
25. Joshi R, Ghanty TK, Naumov S, Mukherjee T (2007) J Phys Chem A 111:2362
26. Pathak AK, Mukherjee T, Maity DK (2008) J Mol Struct Theochem 851:158
27. Fourré I, Bergès J, Houée-Levin C (2010) J Phys Chem A 114:7359
28. Monge-Palacios M, Espinosa-Garcia J (2010) J Phys Chem A 114:4418
29. Chipman DM (2011) J Phys Chem A 115:1161
30. Yamaguchi M (2011) J Phys Chem A 115:14620
31. Codorniu-Hernandez E, Boese AD, Kusalik PG (2013) Can J Chem 91:544
32. Adler TB, Knizia G, Werner H-J (2007) J Chem Phys 127:221106
33. Knizia G, Adler TB, Werner H-J (2009) J Chem Phys 130:054104
34. Kendall RA, Dunning TH, Harrison RJ (1992) J Chem Phys 96:6796
35. Werner H-J, Knowles PJ, Knizia G, Manby FR, Schütz M et al (2012) MOLPRO, version 2012.1, a package of ab initio programs. http://www.molpro.net
36. Lynch BJ, Fast PL, Harris M, Truhlar DG (2000) J Phys Chem A 104:4811
37. Weinhold F, Landis CR (2005) Valency and bonding. A natural bond orbital donor–acceptor perspective. Cambridge University Press, Cambridge
38. Frisch MJ, Trucks GW, Schlegel HB, Scuseria GE, Robb MA, Cheeseman JR, Scalmani G, Barone V, Mennucci B, Petersson GA, Nakatsuji H, Caricato M, Li X, Hratchian HP, Izmaylov AF, Bloino J, Zheng G, Sonnenberg JL, Hada M, Ehara M, Toyota K, Fukuda R, Hasegawa J, Ishida M, Nakajima T, Honda Y, Kitao O, Nakai H, Vreven T, Montgomery J, J. A., Peralta JE, Ogliaro F, Bearpark M, Heyd JJ, Brothers E, Kudin KN, Staroverov VN, Kobayashi R, Normand J, Raghavachari K, Rendell A, Burant JC,

Iyengar SS, Tomasi J, Cossi M, Rega N, Millam NJ, Klene M, Knox JE, Cross JB, Bakken V, Adamo C, Jaramillo J, Gomperts R, Stratmann RE, Yazyev O, Austin AJ, Cammi R, Pomelli C, Ochterski JW, Martin RL, Morokuma K, Zakrzewski VG, Voth GA, Salvador P, Dannenberg JJ, Dapprich S, Daniels AD, Farkas Ö, Foresman JB, Ortiz JV, Cioslowski J, Fox DJ (2009) Gaussian Inc., Vol. A.01, Wallingford CT

39. Tentscher PR, Arey JS (2013) J Chem Theo Comput 9:1568
40. Hayes WM (2014) CRC handbook of chemistry and physics. Taylor and Francis, Boca Raton

Theor Chem Acc (2014) 133:1531
DOI 10.1007/s00214-014-1531-4

REGULAR ARTICLE

# DFT and TD-DFT studies on osmacycle dyes with tunable photoelectronic properties for solar cells

**Mingjun Sun · Zexing Cao**

Received: 3 June 2014 / Accepted: 26 June 2014 / Published online: 5 July 2014
© Springer-Verlag Berlin Heidelberg 2014

**Abstract** B3LYP and CAM-B3LYP functionals have been used to determine structures, electronic and optical properties of osmium-bridged tricyclic aromatic compounds. Calculations show that the optical properties and charge separation features of these osmacycle derivatives can be well modified by incorporating different π-bridge groups. In particular, the newly designed osmacycle dyes **5** and **6** by embedding thiophene and thienothiophene bridge units to osmium polycyclic aromatic system show very strong and broad adsorptions in the whole visible region and excellent charge separation in the first excited state of $^1(\pi\pi^*)$ from the hightest occupied molecular orbital to the lowest unoccupied molecular orbital excitation. Furthermore, the predicted relatively high light harvesting efficiency and large driving force for electron injection suggest that they are quite promising for design of high-performance dye-sensitized solar cells.

**Keywords** Metal-bridged tricyclic aromatic systems · Density functional calculations · Osmacycle dyes · Structural modification · Absorption spectra · Electron injection

Dedicated to Professor Guosen Yan and published as part of the special collection of articles celebrating his 85th birthday.

**Electronic supplementary material** The online version of this article (doi:10.1007/s00214-014-1531-4) contains supplementary material, which is available to authorized users.

M. Sun · Z. Cao (✉)
State Key Laboratory of Physical Chemistry of Solid Surfaces and Fujian Provincial Key Laboratory of Theoretical and Computational Chemistry, College of Chemistry and Chemical Engineering, Xiamen University, Xiamen 361005, China
e-mail: zxcao@xmu.edu.cn

## 1 Introduction

Solar power plays an important role in turning energy systems toward sustainability. Among the photovoltaic devices, the dye-sensitized solar cell (DSSC) is the only solar device that mimics the photosynthesis process in a green leaf. Owing to its simplicity of manufacturing process, low cost, and relatively high energy conversion efficiency, DSSCs become the promising one of renewable energy devices [1, 2]. In general, DSSC is composed of five components, including conductive mechanical support, semiconductor film, sensitizer, electrolyte containing $I^-/I_3^-$ redox couple and counter electrode with a trioxide reduction catalyst [3–6]. As one of the crucial parts in DSSCs, the photosensitizer to harvest sunlight has been viewed as a breakthrough for performance improvement of DSSCs.

Since O'Regan and Grätzel reported the first successful DSSC based on the mechanism of a fast regenerative photoelectrochemical process in 1991, the design of high-performance sensitizers has attracted considerable attention, both experimentally and theoretically [3–20, 29, 41, 46–48], in order to enhance the power conversion efficiency (PCE) of DCCSs. High-efficient dyes commonly should fulfill some essential requirements, including the broad absorption ranging from the whole visible region to the near-infrared part, the novel anchoring groups with strong adsorption on the semiconductor surface, the adaptation of corresponding energy levels among the conduction edge of semiconductor, the excited-state and oxidized-state levels of dyes, and the redox potential of electrolyte, as well as high electrochemical and thermal stability.

At present, among widely used metal–organic and metal-free organic sensitizers for DSSCs [7], the metal-free organic dyes such as coumarin, indoline, cyanine, triphenylamine, and porphyrin have attracted considerable

interest for renewable energy devices because of their significant advantages in terms of synthesis procedures, diversiform structures, and low costs [8–12]. However, the PCE for the metal–organic dyes has been recently climbed to 12.3 % [13, 14]. Among the numerous metal–organic dyes, ruthenium dyes, such as Ru bipyridine complex (red dye) [15] and Ru terpyridine complex (black dye) [16], have been extensively investigated [17, 18], and at the same time, the Os terpyridine complex was also examined for comparison. As a consequence, the osmium compounds exhibit extremely broad UV–Vis absorption, perfectly reversible electrochemistry, and prominent photochemical stability, although they suffer from lower $V_{oc}$ or $J_{sc}$ values under different conditions [19, 20].

Very recently, a series of novel metal-bridged polycyclic aromatic compounds have been successfully synthesized, and they show outstanding stability and unusual optical property [21–23]. To have an insight into their photoelectronic properties and possible applications in DSSCs, herein extensive density functional calculations have been performed. Based on calculations, electronic and structural properties, as well as structural modification effects on charge separation and light harvesting ability of the osmium metallacycle dyes, have been discussed.

## 2 Computational details

### 2.1 Theoretical background

It is well known that the performance of DSSCs can be characterized by the overall power conversion efficiency ($\eta$) and the monochromatic incident photo-to-electron power conversion efficiency (IPCE). The power conversion efficiency is generally defined as the ratio of the maximum solar power, $P_{max}$, and the incident solar power on the cell, $P_{inc}$, and it can be obtained by the following equation [5, 24]:

$$\eta = \frac{P_{max}}{P_{inc}} = \frac{I_{max} \cdot V_{max}}{P_{inc}} = \frac{J_{max} \cdot V_{max} \cdot S}{P_{inc}} = \frac{FF \cdot J_{sc} \cdot V_{oc} \cdot S}{P_{inc}} = \frac{FF \cdot J_{sc} \cdot V_{oc}}{I_s} \quad (1)$$

where $J_{sc}$ is the short-circuit current density, $V_{oc}$ is the open-circuit photovoltage, FF is the fill factor of the cell, $I_s$ is the intensity of the incident light, and $J_{max}$ and $V_{max}$, respectively, are the photocurrent density and photovoltage under the maximum solar power. The fill factor ranging from 0 to 1 is the ration of the maximum power ($P_{max}$) and the product of the open-circuit voltage ($V_{oc}$) and the short-circuit current ($I_{sc}$), exhibiting the extent to which the power is lost due to ohmic resistance and overpotential. According to Eq. 1, manipulation of $J_{sc}$ and $V_{oc}$ is an effective way to enhancement of $\eta$.

The photocurrent density, $J_{sc}$, is defined by integrating IPCE($\lambda$) over the solar spectral density, $I_s(\lambda)$:

$$J_{sc} = e \int \mathrm{IPCE}(\lambda) I_s(\lambda) \mathrm{d}\lambda \quad (2)$$

$$\mathrm{IPCE}(\lambda) = \frac{n_e}{n_p} = \mathrm{LHE}(\lambda) \times \Phi_{inject} \times \eta_{collect} \times \eta_{reg} \quad (3)$$

where LHE($\lambda$) is the light harvesting efficiency at a given wavelength, $\Phi_{inject}$ is the electron injection efficiency, $\eta_{collect}$ is the charge collection efficiency at the conducting glass substrate, and $\eta_{reg}$ is the dye regeneration efficiency, and therein LHE($\lambda$) and $\Phi_{inject}$ affect prominently on IPCE($\lambda$). LHE($\lambda$) can be expressed as:

$$\mathrm{LHE}(\lambda) = 1 - 10^{-f} \quad (4)$$

where $A(f)$ is the absorption (oscillator strength) of the dye at the maximum wavelength [25], and the oscillator strength associated with the $\lambda_{max}^{ICT}$ can be written as:

$$f = \frac{2}{3} \lambda_{max}^{ICT} |\vec{\mu}_0 - \mathrm{ICT}|^2 \quad (5)$$

Hence, $f$ is determined by the maximum wavelength $\lambda_{max}^{ICT}$ (ICT: intramolecular charge transfer) and the dipolar transition moment $|\vec{\mu}_0 - \mathrm{ICT}|$ associated with the electronic excitation [26, 27].

The electron injection efficiency $\Phi_{inject}$ is in direct proportion to the driving force ($\Delta G_{inject}$) of the electron injection from the photoinduced excited states of sensitizer to semiconductor surface, and it can be expressed as (in eV) [28]:

$$\Delta G_{inject} = E_{ox}^{dye*} - E_{CB}^{TiO_2} \quad (6)$$

where $E_{ox}^{dye*}$ is the oxidation potential of the dye in the excited state, and $E_{CB}^{TiO_2}$ is the bottom of conduction band of titanium dioxide whose experimental value is considered as −4.0 eV [29]. As for $E_{ox}^{dye*}$, it was assumed that the electron injection occurs from the unrelaxed excited state because the primary electron transfer event in DSSCs is much faster than the vibrational relaxation of the photoexcited dyes [28], and $E_{ox}^{dye*}$ can be computed as:

$$E_{ox}^{dye*} = E_{ox}^{dye} - \lambda_{max} \quad (7)$$

$\lambda_{max}$ is the vertical transition energy which is the approximation of the 0–0 transition energy $E_{0-0}$ [28, 30], and $E_{ox}^{dye}$ is the redox potential of the ground state of the dye which can be estimated by the Nernst equation and can also be written in the energy scale as Eq. 8.

$$E_{ox}^{dye} = \Delta G_{(aq)} / nF \quad (8)$$

The value of $\Delta G_{(aq)}$ is Gibbs free energy change due to the oxidation of the dye in solution, and it can be

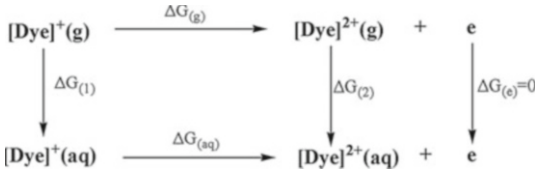


**Scheme 1** Thermodynamic cycle for calculation of redox potentials

calculated according to the Born–Haber cycle, as shown in Scheme 1, where $F$ represents the Faraday constant of 96,485.3 C $mol^{-1}$, and $n$ is the number of electrons involved in the redox couple $[dye]^{2+}/[dye]^{+}$ (here $n = 1$) [31, 32].

### 2.2 Computational methods

Here, theoretical calculations of geometries, frequencies, electronic structures, as well as electronic absorption spectra for the osmapentalyne derivatives have been performed by the B3LYP functional [33, 34] with the basis sets of LANL2DZ for Os and P atoms and the 6-31G(d) basis set for other atoms implemented in Gaussian09 package [35]. Polarization functions of P ($\zeta(d) = 0.340$), S($\zeta(d) = 0.421$), and Os ($\zeta(d) = 0.886$) [36] are also added to the LANL2DZ basis set. The solvent effects of dichloromethane used in experiment have been considered using the SMD continuum solvation model [37]. Previous time-dependent density functional theory (TD-DFT) assessment suggested that the hybrid functionals of B3LYP, CAM-B3LYP, M06-2X, and PBE0 are suitable for the optical 0–0 transition of dyes in solution [30]. The coulomb-attenuating method CAM-B3LYP functional taking long-range correction into account has been proved to be appropriate for electronic excitations with character of charge transfer (CT), but the conventional exchange–correlation functional such as B3LYP is also practicable for some complexes [38–42]. Herein TD-DFT calculations with both CAM-B3LYP and B3LYP functionals were used for determination of the vertical excitation energies and corresponding oscillator strengths. In order to reduce computational costs, the triphenylphosphine ligand in the experimental complex is replaced by the phosphine ($PH_3$), and test calculations indicate that such simplification of ligands has only negligible influences on the structural and electronic properties of the relatively large metallacycles.

## 3 Results and discussion

### 3.1 Structural and optical properties of osmium polycyclic aromatic complexes

The geometry and absorption spectrum of the osmium-bridged tricyclic aromatic compound **1** were determined by B3LYP calculations. The optimized structure and selected bond lengths are shown in Fig. S1 and Table S1 in Supporting Information). As shown in Table S1, the B3LYP-predicted bond lengths of complex **1** with the 6-31G(d) basis set are similar with those obtained with the relatively large 6-311++G(d,p) basis set, and they are all consistent with the experimental values. Furthermore, the B3LYP/6-31G(d)-predicted strong absorptions at 350, 378, 421, and 549 nm can reasonably match the experimental bands at 353, 367, 407, and 557 nm, respectively, as shown in Fig. S2. Accordingly, the B3LYP functional with the 6-31G(d) basis set is practicable for this kind of osmium polycyclic aromatic systems.

Among the most recently synthesized osmium polycyclic aromatic systems [23], the complex with an oxygen heterocycle (**2′** in Fig. 1) was found to have strong and broad adsorptions in almost whole visible region, suggesting that it may be of high potential for the photosensitizer in solar cells, and this osmium tricyclic aromatics **2′** served as a parent was considered for subsequently computational design of osmacycle dyes.

Here, DFT calculations show that the osmacycle complex **2** from substitution of $PH_3$ for $PPh_3$ groups in **2′** has the singlet ground state, like **2′**. As shown in Fig. 1 and Table 1, both complexes **2** and **2′** have quite similar geometries, lending support to simplification of $PPh_3$ ligands in calculation. In particular, all predicted Os–C bond lengths in **2** (2.062–2.190 Å) as well as **2′** (2.062–2.208 Å) are within the range of Os–C single- and double-bond lengths, in which Os1–C27 (2.190 Å), Os1–C7 (2.098 Å), and Os1–C12 (2.135 Å) bear more single-bond character, while Os1–C16 (2.062 Å) has partial character of double bond [43]. Their corresponding Wiberg bond indices of **2** are 0.761, 0.894, 0.779, and 0.912, respectively. The natural charge populations at atoms Os1, C7, C12, C16, and C27 are −1.337, −0.180, −0.115, 0.432, and −0.118, respectively. Therein the relatively large natural positive charges at C16 may stem from the adjoining oxygen with large electronegativity. The dihedral angles of C27–C16–C7–C10, C22–Os1–C13–C9 are 177.6° and 178.2°, respectively, and thus complex **2** has an approximately planar conformation.

The canonical molecular orbital nucleus-independent chemical shift (CMO-NICS) analyses [44] indicate that NICS(1) values at the center of A, B, and C rings (see Scheme S1 and Table S2) are −4.3, −6.1, and −9.0 ppm, respectively. Such negative NICS values reveal the presence of notable aromaticity in this metallacycle from extending π conjugation interaction, which may play an important role in stabilizing metal-bridged tricyclic aromatic complexes.

The hightest occupied molecular orbital (HOMO) and the lowest unoccupied molecular orbital (LUMO) are generally responsible for the strong electronic transition

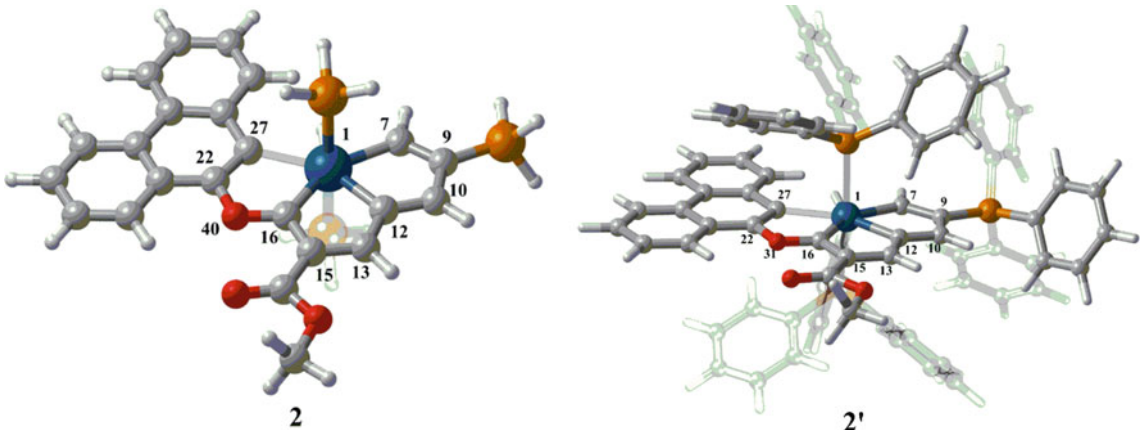


**Fig. 1** Optimized structures of osmium-bridged tricyclic aromatic compounds **2** and **2′** in dichloromethane solution

**Table 1** Selected predicted bond lengths (Å), bond angles (°), dihedral angels (°), charge populations, and Wiberg bond indexes (WBI) of **2** and **2′** (in parenthesis)

| Bonds | | Angles/dihedral angles | | Charge | | WBI | |
|---|---|---|---|---|---|---|---|
| Os1–C7 | 2.098 (2.107) | C7–Os1–C12 | 74.3 (73.3) | Os1 | −1.337 (−1.160) | Os1–C7 | 0.8942 (0.9006) |
| Os1–C12 | 2.135 (2.126) | C12–Os1–C16 | 73.7 (73.5) | C7 | −0.180 (−0.199) | Os1–C12 | 0.7791 (0.7740) |
| Os1–C16 | 2.062 (2.062) | C16–Os1–C27 | 74.1 (73.9) | C12 | −0.115 (−0.131) | Os1–C16 | 0.9122 (0.9176) |
| Os1–C27 | 2.190 (2.208) | C27–C16–C7–C10 | 177.6 (179.7) | C16 | 0.432 (0.423) | Os1–C27 | 0.7614 (0.7427) |
| | | C22–Os1–C13–C9 | 178.2 (178.0) | C27 | −0.118 (−0.132) | | |

from the ground state to the first excited state. To understand the nature of absorption spectra, the electron density differences between the first excited state and the ground state and distribution of related molecular orbitals were discussed. The electron density diagrams and energies of selected frontier molecular orbitals of the complex **2** in dichloromethane solution are displayed in Fig. 2. As Fig. 2 shows, the energy levels of HOMO and LUMO are −5.20 and −2.32 eV, respectively, indicating that the HOMO–LUMO excitation may occur in the visible region.

The orbital composition analysis shows that HOMO is mainly localized over the phenanthrene moiety, while LUMO is contributed by the metal-bridged blended five membered rings in **2**. As shown in Fig. 3b, the electron densities are significantly depleted at the phenanthrene group, whereas there are increases at the metal-bridged tricyclic moiety, resulting in partial charge transfers as the electronic transition occurs from the ground state to the first excited state.

Absorption spectra of complexes **2** and **2′** in dichloromethane solution were investigated by both TD-B3LYP and TD-CAM-B3LYP calculations with the SMD solvation model, and experimental and theoretical absorption spectra are displayed in Fig. 3a. Experimentally, the dominant absorptions appear at 397 and 541 nm for

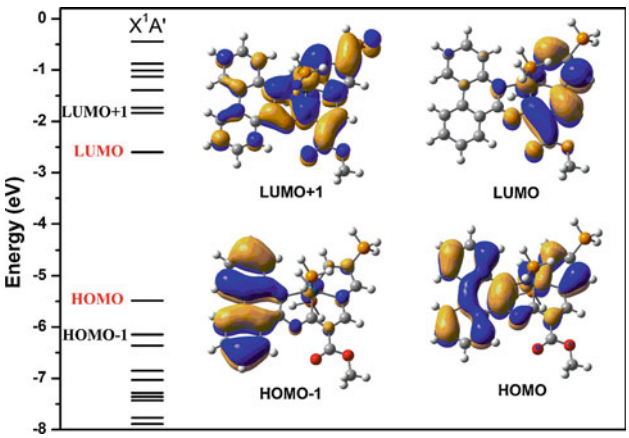


**Fig. 2** Selected key frontier molecular orbitals and energy levels in the complex **2**

complex **2′** [21–23], respectively. TD-B3LYP calculations indicate that the electronic absorptions at 396 and 529 nm have relatively large oscillator strengths of 0.11 and 0.13, respectively, showing good agreement with the experimental observations. We note that here TD-CAM-B3LYP calculations systematically overestimate the transition energies, as shown in previous studies [26]. However,

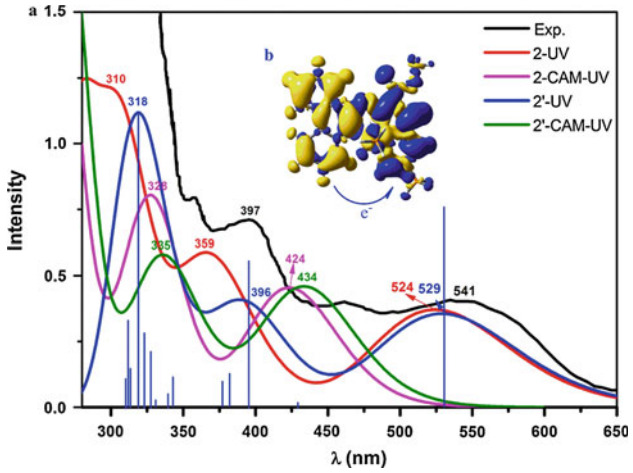


**Fig. 3** **a** Electronic absorption spectra of **2** and **2′** predicted by TD-B3LYP and TD-CAM-B3LYP in dichloromethane solution; **b** Electron density differences between the first excited state and the ground state of the osmacycle **2** (*Yellow* and *blue* refer to a decrease and an increase in electron density, respectively; isovalue: 0.0004 au.)

the TD-CAM-B3LYP-predicted spectra nicely match the experimental bands both in peak positions and relative intensities if a redshift of 0.57 eV is introduced to the TD-CAM-B3LYP spectrum (refer to Fig. S3). Hence, both B3LYP and CAM-B3LYP approaches have been applied to simulation of UV/Vis spectra in following calculations. As Fig. 3a shows, the absorption spectra of complexes **2** and **2′** are similar and they all have broad absorptions in the visible region. Accordingly, the ligand-simplified complex **2** is also promising for design of high-performance dyes through introduction of various π-bridge-conjugated groups and anchoring groups.

### 3.2 Effects of structural modification on electronic and optical properties

To have an insight into effects of structural modification on charge separation and light harvesting ability, here four metal-bridged tricyclic aromatic derivatives in Scheme 2 have been considered, which are derived from the embedding of various π-bridge-conjugated groups to the complex **2**, based on previous studies [41, 45–47]. Considering the direction of charge transfer, the steric effect of triphenylphosphine groups, and the features of frontier orbitals, the C10 site in **2** was served as the π-bridge junction. Predicted electronic and light harvesting properties related to the dye performance are collected in Table 2. The electron density differences between the first excited state and the ground state calculated by Multiwfn [48], and distributions of HOMO and LUMO orbitals in dyes **3**–**6** are presented in Fig. 4 and Fig. S4, respectively.

We note that the donor (D) moiety has dominant contribution to HOMO orbitals, while the π-bridge (**B**) and the acceptor (A) groups dominate the LUMO orbitals in dyes **3**–**6** here. The predicted electron density differences in Fig. 4 show that the electronic densities in the donor moiety decrease remarkably, while sharp increases appear in the bridge and acceptor moieties in the low-lying states from the $S_0 \rightarrow S_1$ transition in **3**–**6**. This suggests that introduction of the electron-deficient pyrimidine and electron-rich thiophene bridges can further facilitate charge separation during the electronic transition in the dyes **3**–**6**, compared to **2**.

As Fig. 5 shows, the osmacycle **3**–**6** have much stronger and broad absorptions in the visible region, compared to the complex **2**. In particular, the newly designed dyes **5** and **6** containing thiophene and thienothiophene units exhibit very strong absorptions in the whole visible region. These novel spectroscopic features are highly required for enhancement of the light harvesting ability of dyes and improvement of the performance of DSSCs.

The predicted transition energies, corresponding oscillator strengths, the light harvesting efficiency LHE(λ), and the driving force $\Delta G_{\text{inject}}$ are compiled into Table 2. The CAM-B3LYP functional is proved to be appropriate for the charge-transfer (CT) excitations, and it has been used to determine the vertical energies and the oscillator strengths within the TD-DFT framework. In Table 2, all strongest $S_0 \rightarrow S_1$ transitions are generally mainly contributed by the HOMO–LUMO excitation, and the first excited state is characterized by $^1(\pi\pi^*)$.

Here, all LUMO energy levels of these dyes are more positive than the bottom of conduction band of $TiO_2$

**Scheme 2** Molecular structures of osmacycle dyes **3**–**6**

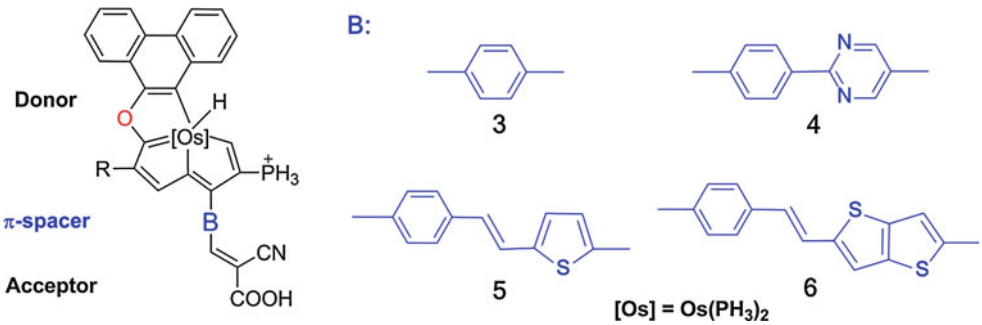

**Table 2** HOMO and LUMO energies (eV), transition energies (λ in nm), corresponding oscillator strengths (*f*), the light harvesting efficiency (LHE), redox potentials ($\Delta E^{dye}$ in eV), and the driving force ($\Delta G_{inject}$ in eV) for osmacycle dyes by B3LYP and CAM-B3LYP

| Dye | HOMO/LUMO | $\lambda_{max}$ | Main configurations | *f* | LHE | $\Delta E^{dye}$ | $\Delta G_{inject}$ |
|---|---|---|---|---|---|---|---|
| *B3LYP* | | | | | | | |
| 1 | −5.15/−2.49 | 549 | H → L(0.70) | 0.33 | 0.53 | 4.96 | −1.30 |
| 2 | −5.20/−2.32 | 529 | H → L(0.69) | 0.13 | 0.26 | 5.23 | −1.11 |
| 2′ | −5.48/−2.60 | 524 | H → L(0.69) | 0.14 | 0.28 | 4.98 | −1.39 |
| 3 | −5.51/−3.02 | 595 | H → L(0.69) H-1 → L(0.12) | 0.37 | 0.57 | 5.31 | −0.77 |
| 4 | −5.48/−3.11 | 603 | H → L(0.68) H → L + 1(0.19) | 0.38 | 0.58 | 5.24 | −0.81 |
| 5 | −5.44/−2.99 | 590 | H → L(0.66) H → L + 1(0.24) | 0.77 | 0.83 | 5.29 | −0.81 |
| 6 | −5.43/−2.99 | 591 | H → L(0.65) H → L + 1(0.26) | 1.03 | 0.91 | 5.27 | −0.82 |
| *CAM-B3LYP* | | | | | | | |
| 1 | −6.31/−1.32 | 431 | H → L(0.58) H-1 → L(0.32) | 0.53 | 0.70 | 5.11 | −1.76 |
| 2 | −6.44/−1.17 | 434 | H → L(0.63) H-1 → L(0.14) | 0.17 | 0.32 | 5.32 | −1.54 |
| 2′ | −6.70/−1.41 | 424 | H → L(0.62) H → L + 1(0.15) | 0.17 | 0.32 | 5.16 | −1.76 |
| 3 | −6.71/−1.83 | 448 | H → L(0.55) H → L + 1(0.32) | 0.45 | 0.65 | 5.68 | −1.08 |
| 4 | −6.68/−1.91 | 445 | H → L + 1(0.50) H → L(0.38) | 0.49 | 0.68 | 5.39 | −1.40 |
| 5 | −6.64/−1.83 | 451 | H → L(0.43) H → L + 1(0.44) | 1.00 | 0.90 | 5.38 | −1.37 |
| 6 | −6.62/−1.84 | 452 | H → L + 1(0.44) H → L(0.41) | 1.22 | 0.94 | 5.68 | −1.06 |

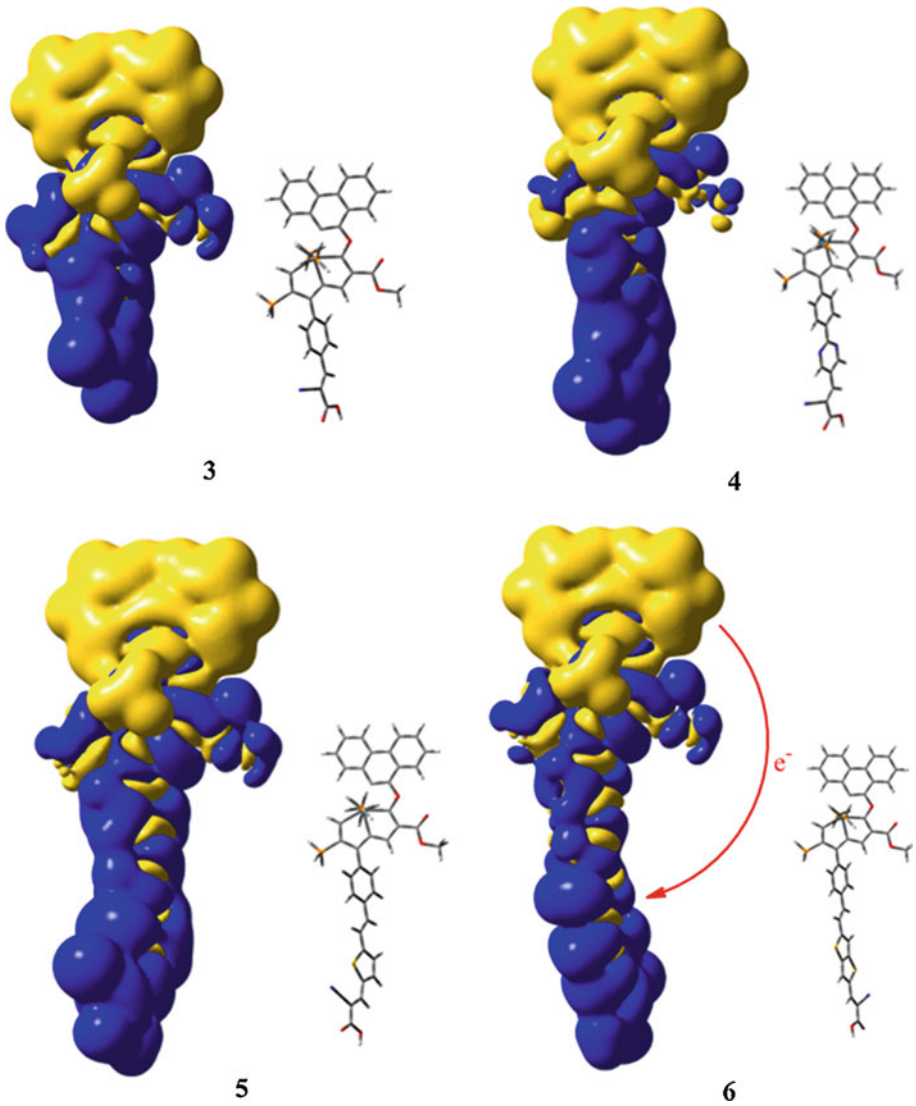


**Fig. 4** Electron density differences between the first excited state and the ground state of dyes **3**–**6** (*yellow* and *blue* refer to a decrease and an increase in electron density, respectively; isovalue: 0.00002 au)

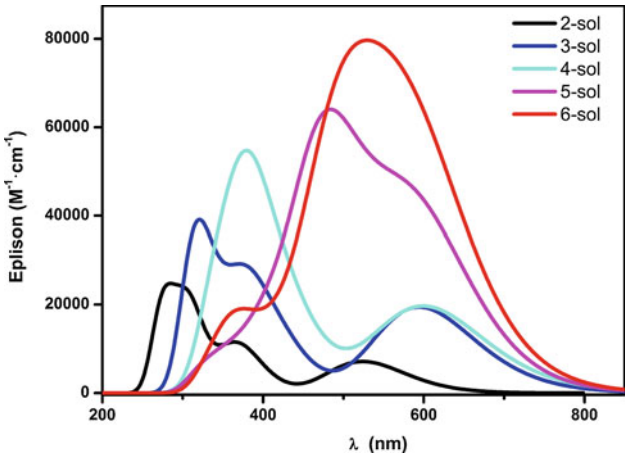


**Fig. 5** Predicted absorption spectra of the new designed osmacycle dyes **2**–**6** in the dichloromethane solution by B3LYP

(−4.0 eV vs. vacuum) and HOMO energies are more negative than the potential of $I^-/I_3^-$ redox couple (−4.8 eV vs. vacuum) [29]. Such nice adaptation among corresponding energy levels could ensure effective electron injection of the excited-state dyes and fast regeneration of the oxidized dyes. The dyes **5** and **6** have relatively larger LHE values among them, indicating that the introduction of thiophene and thienothiophene units can enhance the light absorption to a great extent. We note that there is a balance between $\lambda_{max}$ and $\mathbf{\Delta}G_{inject}$ under this circumstance which $\Delta E^{dye}$ keeps certain values. Hence, the value of $\mathbf{\Delta}G_{inject}$ can maintain around −1.2 eV with a red-shifted absorption as expected [49]. These results suggest that the dyes **5** and **6** among this series of osmacycles are the most promising candidates for the high-performance photosensitizers.

## 4 Conclusion

Both B3LYP and CAM-B3LYP calculations on electronic and optical properties of the recently synthesized osmium-bridged tricyclic aromatic complex **2′** show good agreement with the experimental observation, and the calculated CMO-NICS values reveal the strong aromaticity for its relatively high stability. Several new osmacycle dyes, derived from introduction of various π-bridge-conjugated groups based on the complex **2′**, have been designed and characterized theoretically. Calculations show that their electronic and optical properties can well be modulated by incorporating thiophene or thienothiophene bridge unit. The electron density differences between the first excited state and the ground state show much remarkable charge transfer features in the first excited states of dyes **3**–**6**, compared to **2**. In particular, the newly designed osmacycles **5** and **6** were predicted to have excellent charge separation and strong light harvesting ability, as well as large driving forces for electron injection, and they may be potential photosensitizers for high-performance DSSCs.

**Acknowledgments** This work was supported by the National Science Foundation of China (NSFC) (Grant Nos. 21133007 and 21373164) and the Ministry of Science and Technology (Grant Nos. 2011CB808504 and 2012CB214900). Authors thank Prof. HP Xia and CQ Zhu for useful discussions and dedicated to Professor Guosen Yan on the occasion of his 85th birthday.

## References

1. Li B, Wang LD, Kang BN, Wang P, Qiu Y (2006) Sol Energy Mater Sol Cells 90:549–573
2. Hagfeldt A, Boschloo G, Sun L, Kloo L, Pettersson H (2010) Chem Rev 110:6595–6663
3. O'Regan B, Grätzel M (1991) Nature 353:737–740
4. Grätzel M (2001) Nature 414:338–344
5. Grätzel M (2003) J Photochem Photobiol C 4:145–153
6. Nazeeruddin MK, Grätzel M (2007) Struct Bond 123:113–175
7. Ahmad S, Guillen E, Kavan L, Grätzel M, Nazeeruddin MK (2013) Energy Environ Sci 6:3439–3466
8. Hara K, Sayama K, Ohga Y, Shinpo A, Suga S, Arakawa H (2001) Chem Commun 569–570
9. Ito S, Zakeeruddin SM, Humphry-Baker R, Liska P, Charvet R, Comte P, Nazeeruddin MK, Péchy P, Takata M, Miura H, Uchida S, Grätzel M (2006) Adv Mater 18:1202–1205
10. Sayama K, Tsukagoshi S, Mori T, Hara K, Ohga Y, Shinpou A, Abe Y, Suga S, Arakawa H (2003) Sol Energy Mater Sol Cells 80:47–71
11. Tsao HN, Burschka J, Yi C, Kessler F, Nazeeruddin MK, Grätzel M (2011) Energy Environ Sci 4:4921–4924
12. Xu W, Peng B, Chen J, Liang M, Cai F (2008) J Phys Chem B 112:874–880
13. Yella A, Lee HW, Tsao HN, Yi C, Chandiran AK, Nazeeruddin MK, Diau EWG, Yeh CY, Zakeeruddin SM, Grätzel M (2011) Science 334:629–634
14. Kinoshita T, Dy JT, Uchida S, Kubo T, Segawa H (2013) Nat Photonics 7:535–539
15. Nazeeruddin MK, Kay A, Rodicio I, Baker RH, Mueller E, Liska P, Vlachopoulos N, Grätzel M (1993) J Am Chem Soc 115:6382–6390
16. Nazeeruddin MK, Péchy P, Renouard T, Zakeeruddin SM, Baker RH, Comte P, Liska P, Cevey L, Costa E, Shklover V, Spiccia L, Deacon GB, Bignozzi CA, Grätzel M (2001) J Am Chem Soc 123:1613–1624
17. Han L, Islam A, Chen H, Malapaka C, Chiranjeevi B, Zhang S, Yang X, Yanagida M (2012) Energy Environ Sci 5:6057–6060
18. Kandada ARS, Fantacci S, Guarnera S, Polli D, Lanzani G, Angelis FD, Petrozza A (2013) ACS Appl Mater Interfaces 5:4334–4339
19. Altobello S, Argazzi R, Caramori S, Contado C, Fré SD, Rubino P, Choné C, Larramona G, Bignozzi CA (2005) J Am Chem Soc 127:15342–15343
20. Argazzia R, Larramona G, Contado C, Bignozzi CA (2004) J Photoch Photobio A 164:15–21
21. Zhu C, Li S, Luo M, Zhou X, Niu Y, Lin M, Zhu J, Cao Z, Lu X, Wen T, Xie Z, Schleyer PvR, Xia H (2013) Nat Chem 5:698–703
22. Zhu C, Luo M, Zhu Q, Zhu J, Schleyer PVR, Wu J, Lu X, Xia H (2014) Nat Commun 5:3265
23. Zhu C, Zhu Q, Fan J, Zhu J, He X, Cao X, Xia H (2014) Angew Chem Int Ed 53:6232–6236

24. Akimov AV, Neukirch AJ, Prezhdo OV (2013) Chem Rev 113:4496–4565
25. Wang ZS, Yamaguchi T, Sugihara H, Arakawa H (2005) Langmuir 21:4272–4276
26. Al-Sehemi AG, Irfan A, Asiri AM (2012) Theor Chem Acc 131:1199
27. Harris DC, Bertolucci MD (1998) Symmetry and spectroscopy. Dover, New York
28. Katoh R, Furube A, Yoshihara T, Hara K, Fujihashi G, Takano S, Murata S, Arakawa H, Tachiya M (2004) J Phys Chem B 108:4818–4822
29. Asbury J, Wang YQ, Hao E, Ghosh H, Lian T (2001) Res Chem Intermed 27:393–406
30. Jacquemin D, Planchat A, Adamo C, Mennucci B (2012) J Chem Theory Comput 8:2359–2372
31. Fu Y, Liu L, Yu HZ, Wang YM, Guo QX (2005) J Am Chem Soc 127:7227–7234
32. Wang J, Bai FQ, Xia BH, Feng L, Zhang HX, Pan Q (2011) Phys Chem Chem Phys 13:2206–2213
33. Lee C, Yang W, Parr RG (1988) Phys Rev B 37:785–789
34. Becke AD (1993) J Chem Phys 98:5648–5652
35. Frisch MJ, Trucks GW, Schlegel HB, Scuseria GE, Robb MA, Cheeseman JR, Barone GV, Mennucci B, Petersson GA et al (2009) Gaussian 09, revision B.01. Gaussian, Inc, Wallingford
36. Ehlers AW, Böhme M, Dapprich S, Gobbi A, Höllwarth A, Jonas V, Köhler KF, Stegmann R, Veldkamp A, Frenking G (1993) Chem Phys Lett 208:111–114
37. Marenich AV, Cramer CJ, Truhlar DG (2009) J Phys Chem B 113:6378–6396
38. Yanaia T, Tew DP, Handy NC (2004) Chem Phys Lett 393:51–57
39. Dreuw A, Head-Gordon M (2005) Chem Rev 105:4009–4037
40. Autschbach J (2009) Chem Phys Chem 10:1757–1760
41. Zhu C, Liang JX, Cao ZX (2013) J Phys Chem B 117:13388–13395
42. Xu LC, Li J, Shi S, Zheng KC, Ji LN (2008) J Mol Struct Theochem 855:77–81
43. Based on a search of the Cambridge Structural Database, CSD version 5.34 (May 2013)
44. Chen Z, Wannere CS, Corminboeuf C, Puchta R, Schleyer PVR (2005) Chem Rev 105:3842–3888
45. Pelado B, Cruz P, Pedro VG, Barea EM, Langa F (2012) Tetrahedron Lett 53:6665–6669
46. Zhang CR, Liu ZJ, Chen YH, Chen HS, Wu YZ, Yuan LH (2009) J Phys Chem B 899:86–93
47. Guo MY, He RX, Dai Y, Shen W, Li M (2012) J Phys Chem C 116:9166–9179
48. Lu T, "Multiwfn: Multifunctional wavefunction analyzer", Version 3.2.1. http://Multiwfn.codeplex.com
49. Zhang J, Li HB, Sun SL, Geng Y, Wu Y, Su ZM (2012) J Mater Chem 22:568–576

Theor Chem Acc (2014) 133:1551
DOI 10.1007/s00214-014-1551-0

REGULAR ARTICLE

# First-principles investigations on the anisotropic charge transport in 4,4′-bis((*E*)-2-(naphthalen-2-yl)vinyl)-1,1′-biphenyl single crystal

**Lili Lin · Xin Li · Guangjun Tian · Hua Geng · Zhigang Shuai · Yi Luo**

Received: 30 June 2014 / Accepted: 19 July 2014 / Published online: 6 August 2014
© Springer-Verlag Berlin Heidelberg 2014

**Abstract** We applied the master equation method to investigate the anisotropic transport property of the 4,4′-bis((*E*)-2-(naphthalen-2-yl)vinyl)-1,1′-biphenyl molecular crystal based on first-principles calculation. It is found that the hole mobility has the largest value along the [100] direction, while electrons have the best transport property along the [010] direction. The anisotropic transport property was found to have close relationship with the charge transfer integral which is determined by the molecular stacking network in the crystals as well as the intermolecular frontier orbital overlap. In addition, the effect of the charge carrier density and the electronic field on the charge transport was also studied, and little effect was found except that the density is larger than 0.01 and the electronic field is increased to $1.0 \times 10^6$ V/cm. The kinetic Monte Carlo simulation method has also been used to study the anisotropic charge transport property, and consistent results were obtained as with the master equation method.

**Keywords** Organic electronics · Carrier mobility · Charge transfer · Master equation · Crystal anisotropy

## 1 Introduction

Organic molecular crystals, as one of the most important components in organic solar cells, organic field-effect transistors, and organic light-emitting diodes, have attracted much attention of both theoretical and experimental researchers, and many excellent molecular crystals have been designed and integrated into functional devices [1–3]. Since the charge transport is an essential process in all these devices, its mechanism has become an enthusiastically controversial topic regarding both electrical and optical measurements [4–6] and some general rules have been proposed [7, 8]. To better understand the transport mechanism, it is desirable to gain knowledge of the anisotropic transport property of organic molecular crystals which is closely related to the stacking configurations and the molecular structures. To date, the anisotropy of transport property has been investigated only in a few molecular crystals, such as rubrene (5,6,11,12-tetraphenyltetracene), CH4T(dicyclohexyl-α-quaterthiophene), pentacene, and tetracene, all of which are studied on the two-dimensional (2-D) charge transport [9–14]. Recently, Tao group for the first time performed the measurement of the three-dimensional (3-D) charge transport in the 4,4′-bis((*E*)-2-(naphthalen-2-yl)vinyl)-1,1′-biphenyl (BNVBP) molecular

Dedicated to Professor Guosen Yan and published as part of the special collection of articles celebrating his 85th birthday.

L. Lin
College of Physics and Electronics, Shandong Normal University, Jinan 250014, China

L. Lin · X. Li · G. Tian · Y. Luo
Department of Theoretical Chemistry and Biology, School of Biotechnology, Royal Institute of Technology, 10691 Stockholm, Sweden

H. Geng
Key Laboratory of Organic Solids, Beijing National Laboratory for Molecular Sciences (BNLMS), Institute of Chemistry, Chinese Academy of Sciences, Beijing 100190, China

Z. Shuai (✉)
Department of Chemistry, Tsinghua University, Beijing 100084, China
e-mail: zgshuai@tsinghua.edu.cn

Y. Luo
Hefei National Laboratory for Physical Sciences at the Microscale, University of Science and Technology of China, Hefei 230026, Anhui, China

crystal with two kinds of morphology and orientation and the highest hole mobility was found along the *a*-axis direction [15]. In this work, we apply the master equation (ME) method to investigate the anisotropic property of the charge carrier mobility based on the first-principles calculations. The calculated results are found in good agreement with the experiment. The influence of the electric field and the carrier density on mobility has also been studied. The 3-D transport property of the intrinsic diffusion mobility was also investigated based on the kinetic Monte Carlo (MC) simulations, and the similar anisotropic property was found. The theoretical investigation helps for better understanding of the transport mechanism and intrinsic property of the BNVBP molecular crystal.

## 2 Methodology

In this paper, both the drift mobility and the diffusion mobility are investigated. For the drift mobility, the incoherent motion of the carriers is described by the Pauli Master equation [16]:

$$\frac{\partial \rho_i}{\partial t} = -\sum_{j\neq i}\left[W_{ji}\rho_i\left(1-\rho_j\right) - W_{ij}\rho_j(1-\rho_i)\right] \tag{1}$$

Here, $\rho_i$ is the charge carries population density of site $i$ and the $(1-\rho_j)$ represents the Coulomb penalty of site $j$ due to the occupation of charge carriers. $W_{ji}$ is defined as the charge carrier transition rate from site $i$ to site $j$, and it can be calculated using the Marcus–Hush electron transfer theory at the high-temperature limit [17, 18]:

$$W_{ji} = \frac{V_{ji}^2}{\hbar}\sqrt{\frac{\pi}{K_B T\lambda}}\cdot\exp\left[-\frac{\left(\mp\Delta G_{ji}+\lambda\right)^2}{4\lambda K_B T}\right] \tag{2}$$

Here, $V_{ji}$ is the transfer integral between site $i$ and site $j$, and λ is the reorganization energy. $\Delta G_{ji}$ is the site energy difference between the site $i$ and site $j$, and it is defined as

$$\Delta G_{ji} = E_j - E_i \tag{3}$$

where $E_i$ is the free energy of site $i$. The sign of minus before the site energy difference in Eq. (2) is adopted for holes, and the positive sign is used for the electrons. When an electric field is applied, the site energy is modulated as

$$\Delta G_{ji} = E_j - E_i + |e|\vec{F}\cdot\vec{R}_{ji} \tag{4}$$

where $\vec{F}$ is the electronic field and $\vec{R}_{ji}$ is the displacement between site $i$ and site $j$:

$$\vec{R}_{ji} = \vec{R}_j - \vec{R}_i. \tag{5}$$

As the measurement is performed at the steady state, the charge carrier population is assumed to be constant. The steady master equation is expressed as follows:

$$0 = -\sum_{j\neq i}\left[W_{ji}\rho_i\left(1-\rho_j\right) - W_{ij}\rho_j(1-\rho_i)\right] \tag{6}$$

The charge carrier population at the steady state can be calculated by the iterative procedure:

$$\rho_i = \frac{\sum_j W_{ij}\rho_j}{\sum_j W_{ji} + \sum_j\left(W_{ij}-W_{ji}\right)\rho_j} \tag{7}$$

Then, the charge carrier mobility can be calculated:

$$\mu = \frac{\sum_{i,j} W_{ji}\rho_i\left(1-\rho_j\right)\widehat{F}\cdot\vec{R}_{ji}}{\rho_{\text{tot}}|F|} \tag{8}$$

Here, $\widehat{F}$ is the unit vector of the electric field, and $\rho_{\text{tot}}$ is the total charge carrier population in the investigated supercell. In this paper, the $5\times5\times5$ supercell is large enough to give the consistent result and periodic boundary condition has also been applied. Based on these equations, we can also investigate the influence of the charge carrier density and the electric field.

When there is no electric field, the charge carriers can also diffuse in the molecular crystals, and the intrinsic charge mobility can be calculated using the Einstein equation

$$\mu = \frac{eD}{K_B T} \tag{9}$$

where $D$ is the diffusion coefficient, and it can obtained by performing the kinetic Monte Carlo simulation. In the simulation, the crystal structure is used and one charge is only allowed to transport to neighbor molecules with the probability as $P_{ki} = \frac{W_{ki}}{\sum_j W_{kj}}$. The sum runs over all the possible paths when one charge is located at site $k$. At each step, one random number $r$ is generated. If the number $r$ satisfies $\sum_{i=1}^{\alpha-1}P_{ki} < r \leq \sum_{i=1}^{\alpha}P_{ki}$, then the charge will transport through the $\alpha$ path. For the detailed simulation method, one can refer to the Ref. [19]. By repeating the process for thousands times, the averaged value with respect to the time follows a linear relationship. The ratio is the diffusion coefficient according to

$$D = \lim_{t\to\infty}\frac{r^2}{2nt} \tag{10}$$

where $r$ and $t$ are the averaged displacement and total time span. Here, $n$ represents the dimension of the charge transport in the crystal. In our calculation, the $10\times10\times3$ supercell is adopted. The time limit for each simulation was set as 0.01 ns and 2,000 trajectories were chosen to get the average value of the diffusion coefficient $D$.

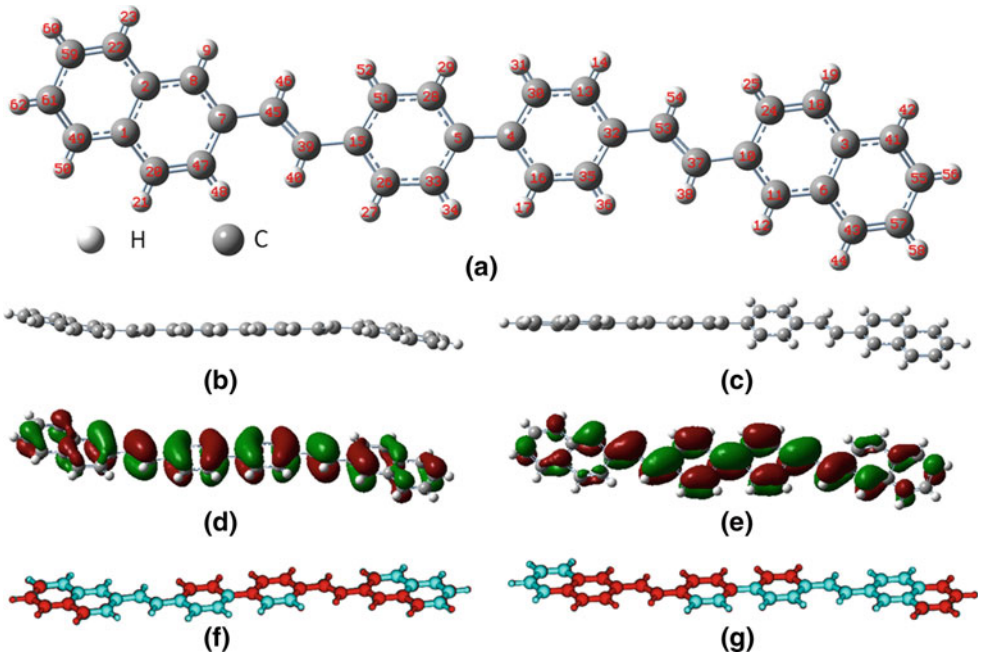


**Fig. 1** **a** The structure and atom labels of the BNVBP molecule, **b** and **c** are the structure of the BNVBP molecule in the crystal and the gas phase separately, **d** and **e** show the electron distribution of the HOMO and LUMO, respectively, **f** shows the overlayer structure of the optimized neutral (*cyan*) and cation (*red*) molecule, and **g** is the overlayer structure of the neutral (*cyan*) and anion (*red*) molecule

In this work, the charge carrier transition rate is calculated using the Marcus rate equation where the transfer integral and the reorganization energy are two important parameters. Lots of methods have been developed to calculate the transfer integral [20–26], and here, the site energy correction method is adopted [23–25]. The reorganization energy is calculated using the adiabatic potential energy surface method (AP) [23]. The normal mode analysis method (NM) [27] has also been used for validation [28]. The calculation of the transfer integral is based on the electronic structure calculation using the PW91PW91/6-31g* method. To calculate the reorganization energy, the geometry of the molecule is first optimized and then, the frequency and electronic structure calculation are performed using the B3LYP/6-31g* method. All the quantum chemistry calculation is realized in the Gaussian 09 program [29].

**Table 1** Structure parameters of the BNVBP molecule in the crystal and gas phase. The numbers shown in the first column are the atom numbers shown in Fig. 1a (unit: degree)

| Angles | Crystal | Gas | Difference |
|---|---|---|---|
| 47-7-45-39 | −9.337 | 1.087 | 10.424 |
| 53-37-10-24 | 11.295 | 0.189 | 11.106 |
| 45-39-15-51 | 4.039 | 1.637 | 2.402 |
| 13-32-53-37 | 175.110 | 179.860 | 4.750 |
| 28-5-4-30 | 0.051 | 34.682 | 34.631 |
| 47-7-45 | 121.647 | 123.043 | 1.396 |
| 45-39-15 | 128.324 | 127.111 | 1.213 |
| 39-15-51 | 124.696 | 123.968 | 0.728 |
| 28-5-4 | 121.935 | 121.287 | 0.648 |
| 13-32-53 | 118.421 | 118.969 | 0.548 |
| 53-37-10 | 125.405 | 127.120 | 1.715 |
| 37-10-11 | 119.293 | 119.049 | 0.244 |

## 3 Results and discussion

### 3.1 Geometric comparison

To calculate the reorganization energy, the BNVBP molecule (see Fig. 1a) was first optimized in the gas phase. Compared with the structure in the crystal, the most significant difference lies in the dihedral angle between the two phenyls at the center of the molecule (see Fig. 1b, c). In the crystal structure, the two phenyl rings in the center are at the same surface, so are the C=C double bonds. However, significant dihedral angle (about 34.68°) can be found between the two phenyl rings in the center of the molecule in gas phase. From Fig. 1b, c, we can also see that the dihedral angles between the end naphthalene groups and the central part also differ with each other. In the crystal structure, the naphthalene groups at two ends outstand the central surface and the angles are as large as 10.42° and 11.10°, respectively; however, they keep the same surface with the phenyl rings connected by the C=C double bond at each side in gas phase. Other significant differences between the structures in crystal and gas phase are listed in Table 1. We can see that the differences mainly arise from the dihedral angles and the angles between bonds. The bond length involved in this molecule has little difference (no more than 0.1 Å) between the crystal and gas structures which is therefore not listed here.

**Table 2** Reorganization energy of electrons and holes calculated using the AP method and NM method (unit: meV)

| Method | Electron | Hole |
|---|---|---|
| AP | 215 | 175 |
| NM | 215 | 175 |

### 3.2 Electronic structure

Based on the electronic structure calculations of the BNVBP molecule in crystal structure, the highest occupied molecular orbital (HOMO) and the lowest unoccupied molecular orbital (LUMO) are shown in Fig. 1d, e. Clearly, both the HOMO and LUMO are delocalized orbitals; thus, similar transfer integrals are expected both for holes and electrons. The calculated energy for HOMO is −5.14 eV which is close to the work function of gold (5.1 eV). The energy for LUMO is −1.81 eV which does not match with the metal electrode and is easy to be ionized in the air. Consequently, BNVBP should be used as a p-type semiconductor material.

### 3.3 Reorganization energy

To simulate the property of BNVBP molecules in crystals, the dihedral angle 28-5-4-30 is frozen during the calculation of the reorganization energy. Two kinds of methods have been employed to calculate the reorganization energy, namely the AP method and NM method. It is shown in Table 2 that the reorganization energy calculated with the NM method is fully consistent with the AP method. As illustrated in this table, holes have smaller reorganization energy than electrons and larger mobility is expected for holes. The comparison between the structures of the cation and the neutral state is shown in Fig. 1f. These two structures have very good overlap, and no significant difference can be found, which reflects small reorganization energy induced when one electron is withdrawn from the molecule. The similar phenomenon can also be found for the anion and neutral states (see Fig. 1g).

The reorganization energy of holes contributed by every vibration modes can also be obtained with the NM method, as illustrated in Fig. 2. It is found that the profiles for the neutral state and the cation state are quite similar. Most of the vibration modes have little contribution to the reorganization energy. The main contribution comes from the C=C stretching vibration modes in the biphenyl of the molecule and the C=C bonds. The stretching mode of the two naphthalene groups in the molecule and the C–H in-plane bending modes have also significant contributions. The reorganization energy for anions contributed by vibration modes has also been calculated, and similar profile is obtained as that for holes.

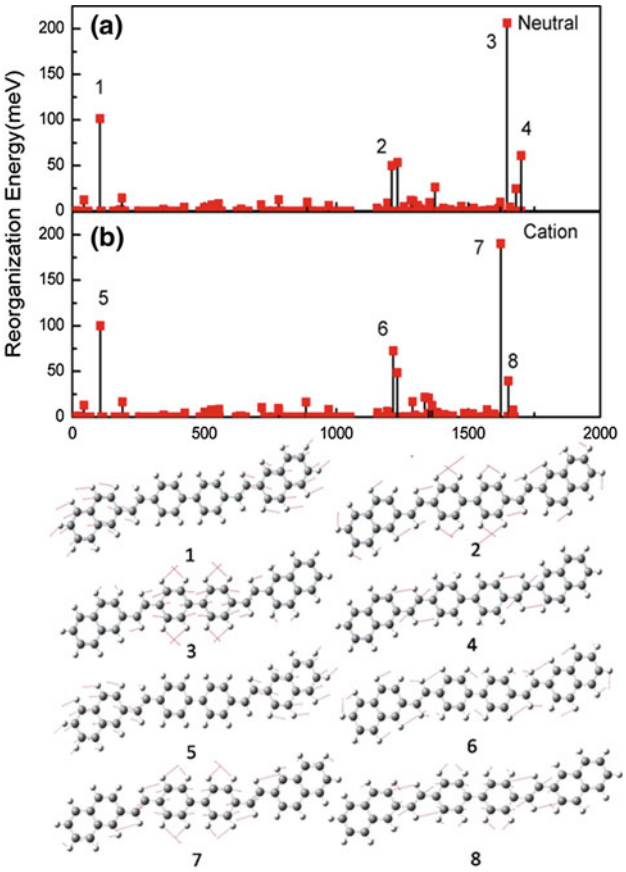


**Fig. 2** Reorganization energy contributed by vibration modes of neutral state (**a**) and cation state (**b**). The vibration profiles of vibration modes with significant contribution to the reorganization energy are shown at the *bottom* of the figure

### 3.4 Transfer integral

Another important factor that determines the charge carrier mobility is the intermolecular transfer integral which depends on both the molecule geometry and the stacking structure. The unit cell of the BNVBP molecular crystal is shown in Fig. 3a, where the crystal structure comes from Ref. [12]. One can see that molecule arranged in a herringbone pattern. The main transfer paths on the (001) and (010) surface are illustrated in Fig. 3b, c. The transfer integral of holes and the intermolecular distances are listed in Table 3. It can be seen that the transfer integrals along the six different paths on the (001) surface are much larger than those on the (010) surface. The large separation between the molecules along the paths on (010) surface makes the transfer integral very small. It has been widely accepted that larger transfer integral can be generated along $\pi$ stacking directions. In this study, the intermolecular distance along the $\pi$ stacking direction is larger than the other directions on the (001) surface; thus, smaller transfer integral is obtained. Correspondingly, the transfer integral of electrons is also shown in Table 3. One can see that

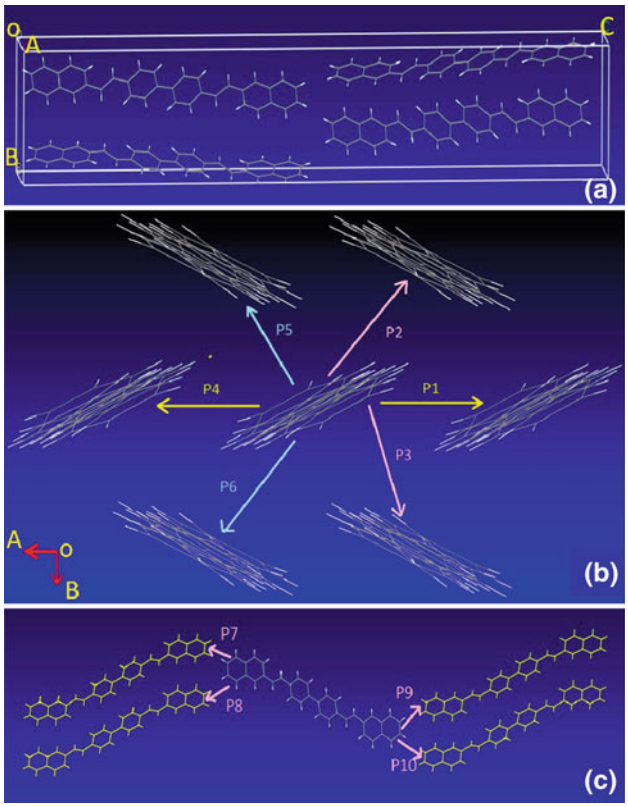


**Fig. 3** **a** The unit cell of the BNVBP molecular crystal detected in experiment, **b** and **c** present the transfer paths on the (001) surface and the (010) surface

the transfer integrals along the paths on the (010) surface are quite small as well. The transfer integrals along the $\pi$ stacking direction become much smaller than those along the other four paths on the (001) surface, which implies lower electron mobility along the $\pi$ stacking direction.

### 3.5 Electric field and charge carrier density dependences of drift mobility

Based on the above calculations, one can find that the transfer integral is much smaller than the reorganization energy for both holes and electrons, which implies that charge carriers transport by hopping between molecules. The hopping rate can be calculated according to the Marcus rate equation; consequently, the drift mobility can be obtained by solving the master equations. In the calculations of the drift mobility, two parameters need to be determined. One is the charge carrier density; the other is the magnitude of the electronic field. In the experiment, the applied voltage is 80 V and the length of the OFET is about 7.3 μm [15]. The electric field is about $F = V/L = 1.0 \times 10^5$ V/cm. The charge carrier density is determined by gate voltage, difficult to be measured in experiment. Nevertheless, the influence of the charge carrier density on the drift mobility can be simulated in our theoretical method (see Fig. 4a). Here, the electric field is assumed to be $1.0 \times 10^5$ V/cm, and the voltage is applied along the [100] direction. It is illustrated that there is no significant influence on the mobility when the charge carrier density is small. When the carrier density is larger than 0.01, the mobility decreases significantly with the increase in the carrier density. This is due to less available sites left for charge to transport in the molecular crystal; consequently, charge transport will be hindered.

The influence of the electric field on the drift mobility is quite complicated (see Fig. 4b). When the electronic field is in the range of $10^2$–$10^6$ V/cm, the drift mobility has no significant change. When the electric field is larger than $1.0 \times 10^6$ V/cm, the drift mobility increases at first and then decreases. This happens when the inverted regime of Marcus theory is approached (i.e., at the semiclassical level, when $\Delta G_{ji} > \lambda$). In that regime, the increase in driving force will lead to a reduction in transfer rate and hence in mobility. It should be noted that the charge carrier density of 0.001 is adopted. Similar properties can be found for electrons. It is found that the drift mobility for electrons is about half of the values of holes. In addition, one can find that the turning point of the electronic field for electrons is at $5.04 \times 10^6$ V/cm, but at $2.01 \times 10^6$ V/cm for holes. From Eqs. (2) and (4), one can conclude that the difference

**Table 3** Transfer integrals of holes and electrons along different paths in molecular crystals

| Transfer paths | Central distances (Å) | Transfer integral of holes (meV) | Transfer integral of electrons (meV) |
|---|---|---|---|
| P1 | 5.97 | −17.41 | 9.26 |
| P2 | 4.80 | 22.24 | −30.87 |
| P3 | 4.80 | 22.24 | −30.87 |
| P4 | 5.97 | −17.41 | 9.26 |
| P5 | 4.80 | 19.91 | −29.67 |
| P6 | 4.80 | 19.91 | −29.67 |
| P7 | 26.95 | 0.012 | 0.014 |
| P8 | 26.90 | 0.347 | −0.427 |
| P9 | 26.95 | 0.015 | 0.038 |
| P10 | 26.90 | 0.350 | −0.421 |

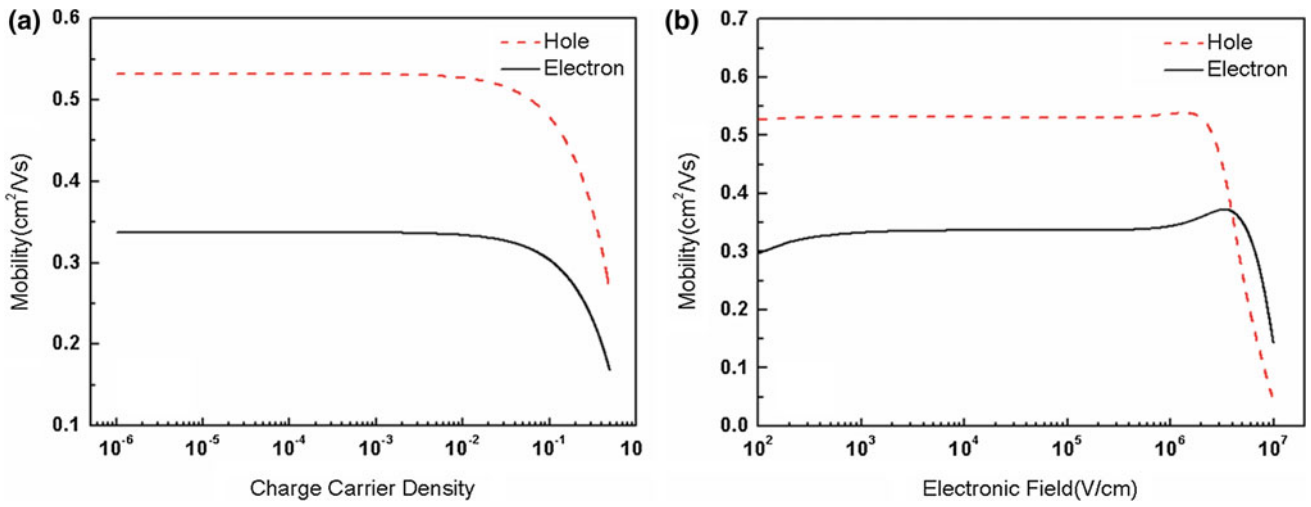


**Fig. 4** **a** Charge carrier density dependence of the hole mobility (*dashed line*) and electron mobility (*solid line*), **b** electronic field dependence of hole mobility and electron mobility

mainly arises from the deviation of the reorganization energy of electrons and holes.

### 3.6 Anisotropic property

In the study of the anisotropic property of the drift mobility, the electric field is fixed as $1.0 \times 10^5$ V/cm and the charge carrier density of 0.001 is adopted. The anisotropic properties of the holes as well as the electrons calculated with both ME and MC methods are shown in Fig. 5. The angles on the (001), (100), and (010) surface in Fig. 5 are defined as the angles between the electric field and the OA ([100]), OB ([010]), and OC ([001]) directions, respectively. It is clear that the mobility calculated with ME method has the same anisotropic property as the diffusion mobility calculated with the MC method for both holes and electrons. Considering the computational errors, the mobility calculated with both methods is in good agreement with each other. As illustrated in Fig. 5a, the holes have larger mobility along the [100] direction than that along the [010] direction. The hole mobility along the [001] direction is much smaller than that along the [010] direction (see Fig. 5b) and the [100] direction (see Fig. 5c). It is concluded that holes have the largest mobility along the [100] direction. This is understandable if we analyze the result of the transfer integrals. From Table 3 and Fig. 3b, we can see that not only the transfer integrals of holes along P1 and P4, but also that along P2, P3, and P4 and P5 will have large contribution to the charge transport along the [100] direction, although the transfer integral along P1 and P4 is smaller than that along the other four paths. However, charge transport along [010] direction is only determined by the transfer integral along P3, P4, P5, and P6. From Fig. 5d, we find that the electrons have the largest mobility along the [010] direction, which is different from that of holes. Similarly, the reason mainly arises from the difference of the transfer integral. One can see that the transfer integral of electrons along the $\pi$ stacking direction ([100]) is much smaller compared with that of holes, while the transfer integrals along other paths are relatively large which will induce large electron mobility on the [010] direction. The electron mobility on the [001] direction is also the smaller than that along [100] direction (see Fig. 5f), which is in consistent with that of holes. Our theoretical investigation shows the close relationship between the anisotropic property of the mobility and the transfer integrals.

The mobility of holes and electrons calculated with both ME and MC methods along [100], [010], and [001] directions is listed in Table 4. The anisotropic property of the hole mobility is [100] > [010] > [001]; however, for electrons, it is [010] > [100] > [001]. It is clear that the electron mobility along [100] direction is about one half of the hole mobility, while the electron mobility along the [010] direction is almost the same as the hole mobility. It can also be seen that the hole mobility along the [100] direction is 0.532 $cm^2$/Vs, which is a little smaller than the experimental value ($2.3 \pm 0.2$ $cm^2$/Vs) measured on the plate-shaped single-crystal OFETs but almost the same as the value ($0.40 \pm 0.25$ $cm^2$/Vs) measured on the rod-shaped single-crystal OFETs [15]. The calculated hole mobility along [100] direction is about one and half times as large as that along the [010] direction, which is in consistent with the experimental result. From the anisotropic property on the (001) surface, we can deduce that the hole mobility along [110] direction should be in the middle of the value along [100] direction and [010] direction. However,

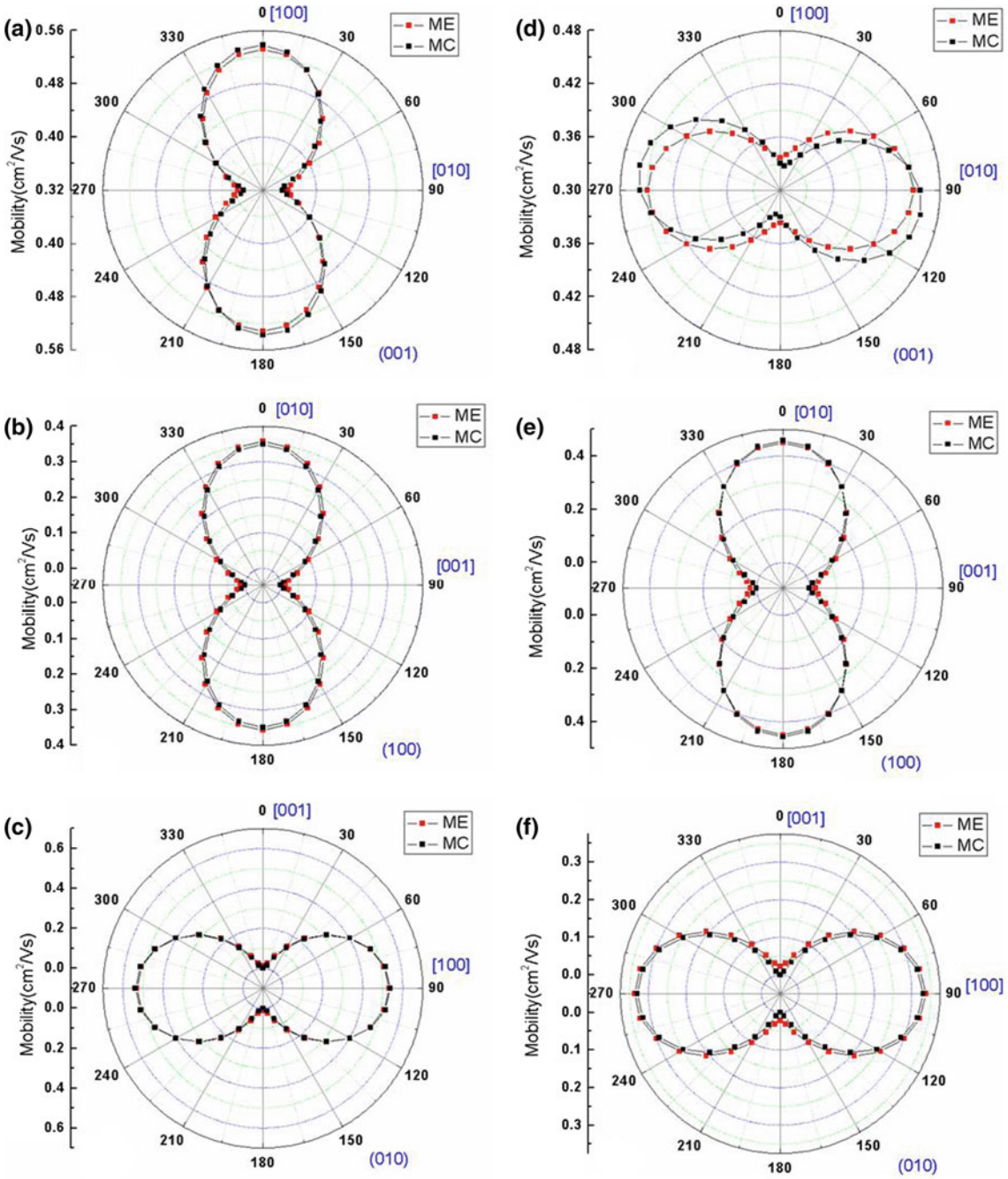


**Fig. 5** **a–c** Hole mobility on the (001), (100), and (010) surface, **d–f** electron mobility on the (001), (100), and the (010) surface

**Table 4** Mobility of holes and electrons along different directions calculated with both ME and MC methods and the averaged diffusion mobility (unit: $cm^2/Vs$)

| Methods | ME | | | MC | | | |
|---|---|---|---|---|---|---|---|
| Direction | [100] | [010] | [001] | [100] | [010] | [001] | Average |
| Hole | 0.532 | 0.358 | 0.013 | 0.538 | 0.349 | 0.000 | 0.444 |
| Electron | 0.337 | 0.450 | 0.020 | 0.330 | 0.458 | 0.000 | 0.394 |

the experimental measurement shows that the hole mobility along [110] direction is smaller than that along the [010] direction. This discrepancy may be induced by many factors, such as the defect, traps, grain boundaries, and so on.

## 4 Conclusion

In summary, the anisotropic property of the hole mobility and electron mobility of the BNVBP molecular crystal were investigated with both ME and MC methods. The charge carrier mobility values calculated with two methods are consistent with each other. The anisotropic property of electron mobility on the (001) surface is different from that of hole mobility, due to difference in intermolecular frontier orbital overlap: HOMO for hole and LUMO for electron. The BNVBP molecular crystal has the largest hole mobility on the [100] direction, while the best transport direction for electrons is along the [010] direction. The relationship between the anisotropic property of mobility and transfer integral has been established. Our calculation confirms that the BNVBP molecular crystal has better transport property as p-type materials than the n-type materials. The study indicates that the charge carrier density and the electronic field have little effect on the drift mobility except that the density is larger than 0.01 and the electronic field is increased to $1.0 \times 10^6$ V/cm. It should be noted that the basic assumption here is the localized charge hopping model, which is in qualitative agreement with the experiment. More general considerations should include charge delocalization effect, quantum nuclear tunneling, as well as non-perturbative charge dynamics, which deserve further investigations [30].

**Acknowledgments** This work is supported by the National Natural Science Foundation of China (Grant Nos. 21290191, 11247307, 11304172, and 91333202) and the Ministry of Science and Technology through 973 program (Grant Nos. 2010CB923300, 2011CB932304, 2011CB808405, 2013CB933503), and the Göran Gustafsson Foundation for Research in Natural Sciences and Medicine. The Swedish National Infrastructure for Computing (SNIC) is acknowledged for computational time. Great thanks to Professor Shiwei Yin, Dr Weijie Hua, and Dr. Sai Duan for helpful discussion.

## References

1. Lin Y, Li Y, Zhan X (2012) Small molecule semiconductors for high-efficiency organic photovoltaics. Chem Soc Rev 41(11):4245
2. Meng Q, Hu W (2012) Recent progress of n-type organic semiconducting small molecules for organic field-effect transistors. Phys Chem Chem Phys 14(41):14152
3. Wang C, Dong H, Hu W, Liu Y, Zhu D (2012) Semiconducting π-conjugated systems in field-effect transistors: a material odyssey of organic electronics. Chem Rev 112(4):2208–2267
4. Sakanoue T, Sirringhaus H (2010) Band-like temperature dependence of mobility in a solution-processed organic semiconductors. Nat Mater 9:736–740
5. Geng H, Peng Q, Wang LJ, Li HJ, Liao Y, Ma ZY, Shuai Z (2012) Toward quantitative prediction of charge mobility in organic semiconductors: tunneling enabled hopping model. Adv Mater 24:3568–3572
6. Jiang YQ, Xu HH, Zhao N, Peng Q, Shuai Z (2014) Spectral signature of intrachain and interchain polarons in donor-acceptor copolymers. Acta Chim Sinica 72(2):201–207
7. Shuai Z, Wang L, Li Q (2011) Evaluation of charge mobility in organic materials: from localized to delocalized descriptions at a first-principles level. Adv Mater 23(9):1145–1153
8. Troisi A (2011) Charge transport in high mobility molecular semiconductors: classical models and new theories. Chem Soc Rev 40(5):2347–2358
9. Sundar VC, Zaumseil J, Podzorov V, Menard E, Willett RL, Someya T, Gershenson ME, Rogers JA (2004) Elastomeric transistor stamps: reversible probing of charge transport in organic crystals. Science 303(5664):1644–1646
10. Zeis R, Besnard C, Siegrist T, Schlockermann C, Chi X, Kloc C (2006) Field effect studies on rubrene and impurities of rubrene. Chem Mater 18(2):244–248
11. Lee JY, Roth S, Park YW (2006) Anisotropic field effect mobility in single crystal pentacene. Appl Phys Lett 88(25):252106–252106–3
12. Mannsfeld SCB, Locklin J, Reese C, Roberts ME, Lovinger AJ, Bao Z (2007) Probing the anisotropic field-effect mobility of solution-deposited dicyclohexyl-α-quaterthiophene single crystals. Adv Funct Mater 17(10):1617–1622
13. Reese C, Bao Z (2007) High-resolution measurement of the anisotropy of charge transport in single crystals. Adv Mater 19(24):4535–4538
14. Xia Y, Kalihari V, Frisbie CD, Oh NK, Rogers JA (2007) Tetracene air-gap single-crystal field-effect transistors. Appl Phys Lett 90(16):162106–162106
15. He T, Zhang X, Jia J, Li Y, Tao X (2012) Three-dimensional charge transport in organic semiconductor single crystals. Adv Mater 24(16):2171–2175
16. Pasveer WF, Cottaar J, Tanase C, Coehoorn R, Bobbert PA, Blom PWM, de Leeuw DM, Michels MAJ (2005) Unified description of charge-carrier mobilities in disordered semiconducting polymers. Phys Rev Lett 94(20):206601
17. Hush NS (1968) Homogeneous and heterogeneous optical and thermal electron transfer. Electrochim Acta 13(5):1005–1023
18. Marcus RA (1993) Electron transfer reactions in chemistry. Theory and experiment. Rev Mod Phys 65(3):599–610
19. Wang L, Nan G, Yang X, Peng Q, Li Q, Shuai Z (2010) Computational methods for design of organic materials with high charge mobility. Chem Soc Rev 39(2):423–434
20. Paulson BP, Curtiss LA, Bal B, Closs GL, Miller JR (1996) Investigation of through-bond coupling dependence on spacer structure. J Am Chem Soc 118(2):378–387
21. Grozema FC, van Duijnen PT, Berlin YA, Ratner MA, Siebbeles LDA (2002) Intramolecular charge transport along isolated chains of conjugated polymers: effect of torsional disorder and polymerization defects. J Phys Chem B 106(32):7791–7795
22. Senthilkumar K, Grozema FC, Bickelhaupt FM, Siebbeles LDA (2003) Charge transport in columnar stacked triphenylenes: effects of conformational fluctuations on charge transfer integrals and site energies. J Chem Phys 119(18):9809–9817
23. Lemaur V, da Silva Filho DA, Coropceanu V, Lehmann M, Geerts Y, Piris J, Debije MG, van de Craats AM, Senthilkumar K, Siebbeles LDA, Warman JM, Brédas J-L, Cornil J (2004) Charge transport properties in discotic liquid crystals: a

quantum-chemical insight into structure−property relationships. J Am Chem Soc 126(10):3271–3279
24. Brédas J-L, Beljonne D, Coropceanu V, Cornil J (2004) Charge-transfer and energy-transfer processes in π-conjugated oligomers and polymers: a molecular picture. Chem Rev 104(11):4971–5004
25. Valeev EF, Coropceanu V, da Silva Filho DA, Salman S, Brédas J-L (2006) Effect of electronic polarization on charge-transport parameters in molecular organic semiconductors. J Am Chem Soc 128(30):9882–9886
26. Shuai Z, Geng H, Xu W, Liao Y, André JM (2014) From charge transport parameters to charge mobility in organic semiconductors through multiscale simulation. Chem Soc Rev 43:2662–2679
27. Kwon O, Coropceanu V, Gruhn NE, Durivage JC, Laquindanum JG, Katz HE, Cornil J, Brédas JL (2004) Characterization of the molecular parameters determining charge transport in anthradithiophene. J Chem Phys 120(17):8186–8194
28. Tian GJ, Duan S, Hua WJ, Luo Y (2012) DynaVib Version 1.0. Royal Institute of Technology, Sweden
29. Frisch M, Trucks G, Schlegel H, Scuseria G, Robb M, Cheeseman J, Scalmani G, Barone V, Mennucci B, Petersson G, et al Gaussian 09, revision a. 02. Gaussian, Inc., Wallingford, CT
30. Shuai Z, Xu W, Peng Q, Geng H (2013) From electronic excited state theory to the property predictions of the organic optoelectronic materials. Sci China Chem 56(9):1227–1284

Theor Chem Acc (2014) 133:1585
DOI 10.1007/s00214-014-1585-3

REGULAR ARTICLE

# Iron carbonyl thioboronyls: effect of substitution of sulfur for oxygen in the viability of binuclear complexes toward dissociation reactions

**Xiaoli Gong · Liyao Zhu · Jing Yang · Xiumin Gao · Yaoming Xie · R. Bruce King**

Received: 19 August 2014 / Accepted: 25 September 2014 / Published online: 14 October 2014
© Springer-Verlag Berlin Heidelberg 2014

**Abstract** The recent discovery of boronyl complexes of the type $(R_3P)_2Pt(BO)X$ (R = cyclohexyl; X = halogen) makes of interest the chemistry of complexes of the related thioboronyl (BS) ligand. In this connection, the binuclear iron carbonyl complex $Fe_2(BS)_2(CO)_8$ is predicted by density functional theory to have a symmetrical unbridged structure similar to the valence isoelectronic $Mn_2(CO)_{10}$. Higher-energy unsymmetrical $(OC)_5Fe \rightarrow Fe(BS)_2(CO)_3$ structures are also found as well as a doubly bridged $Fe_2(BS)_2(CO)_6(\mu\text{-}CO)_2$ structure. The complex $Fe_2(BS)_2(CO)_8$ is predicted to be viable toward symmetrical dissociation into $Fe(BS)(CO)_4$ fragments. However, the unsymmetrical dissociation of $Fe_2(BS)_2(CO)_8$ into $Fe(CO)_5 + Fe(BS)_2(CO)_3$ is predicted to be exothermic by ~9 kcal $mol^{-1}$. The low-energy structures of the mononuclear $Fe(BS)_2(CO)_3$ include structures in which the two BS ligands have coupled to form a $B_2S_2$ ligand through B–B bond formation.

**Keywords** Iron · Boron sulfides · Metal–metal bonding · Metal carbonyls · Density functional theory

## 1 Introduction

Metal carbonyl chemistry has evolved since the discovery of nickel carbonyl in 1890 into one of the most important and substantial subareas of coordination and organometallic chemistry [1]. However, coordination chemistry of the diatomic boron ligands BF, BO, and BS related to CO has only very recently begun to emerge to an extremely limited extent. Syntheses of metal complexes of these diatomic boron ligands have proven to be challenging because of the instability of the free ligands. Thus, the first well-characterized fluoroborylene (BF) metal complex $Cp_2Ru_2(CO)_4(\mu\text{-}BF)$ was synthesized only in 2009 by Vidović and Aldridge [2] and characterized structurally by X-ray crystallography. Similarly, the first boronyl (BO) metal complex $(Cy_3P)_2Pt(BO)Br$ (Cy = cyclohexyl) was synthesized and structurally characterized only in 2010 by Braunschweig et al. [3, 4]. Metal thioboronyl (BS) complexes remain unknown. Free BS is unstable under ambient conditions but can be detected spectroscopically in the gaseous mixture obtained by passing a microwave discharge through $B_2S_3$ vapor [5, 6].

The instability of the free BX (X = F, O, S) ligands under ambient conditions restricts the scope of viable methods for the syntheses of their metal complexes as compared with syntheses of similar metal carbonyls, which can use the very stable free CO gas as a chemical reagent, sometimes even at elevated pressures. For this

Dedicated to Professor Guosen Yan and published as part of the special collection of articles celebrating his 85th birthday.

**Electronic supplementary material** The online version of this article (doi:10.1007/s00214-014-1585-3) contains supplementary material, which is available to authorized users.

X. Gong (✉) · L. Zhu · X. Gao
College of Electronic Information, Hangzhou Dianzi University, Hangzhou 310018, Zhejiang, People's Republic of China
e-mail: gxl@hdu.edu.cn

J. Yang
Department of Chemistry, Tangshan Normal College, Tangshan 063000, People's Republic of China

Y. Xie · R. B. King (✉)
Department of Chemistry and Center for Computational Quantum Chemistry, University of Georgia, Athens, GA 30602, USA
e-mail: rbking@chem.uga.edu

reason, theoretical studies on metal BS complexes are important for predicting the potentially most productive areas of their coordination chemistry to explore by indirect synthetic methods using viable boron–sulfur compounds as sources of the BS ligand. In this connection, we have used density functional theory (DFT) to study mononuclear and binuclear metal carbonyl fluoroborylene (BF) and boronyl (BO) derivatives of manganese [7], iron [8, 9], and cobalt [10]. The theoretical work on the iron carbonyl boronyl $Fe_2(BO)_2(CO)_8$ led to the discovery of unbridged dimeric $(OB)(OC)_4Fe–Fe(CO)_4(BO)$ structures analogous to the well-known unbridged experimental $(OC)_5Mn–Mn(CO)_5$ structure [11, 12]. Such $Fe_2(BO)_2(CO)_8$ structures are predicted to be viable with respect to unsymmetrical dissociation into $Fe(CO)_5 + Fe(BO)_2(CO)_3$. We now report similar theoretical studies on the analogous $Fe_2(BS)_2(CO)_8$ system. Again, unbridged $(SB)(OC)_4Fe–Fe(CO)_4(BS)$ structures are predicted analogous to the $Mn_2(CO)_{10}$. However, such $Fe_2(BS)_2(CO)_8$ species are predicted to differ from their oxygen analogs by being disfavored energetically relative to unsymmetrical dissociation into $Fe(CO)_5 + Fe(BS)_2(CO)_3$.

## 2 Theoretical methods

Electron correlation effects were considered by employing DFT, which has evolved as a practical and effective computational tool, especially for organometallic compounds [13–19]. Two DFT methods were used in this study, namely the B3LYP and BP86 methods. The popular B3LYP method combines the Becke three-parameter functional (B3) [20] with the Lee–Yang–Parr (LYP) generalized gradient correlation functional [21]. The BP86 method combines Becke's 1988 exchange functional (B) with Perdew's 1986 gradient-corrected correlation functional (P86) [22, 23]. In general, these two methods predict geometries and relative energies in reasonable agreement. However, the BP86 method has been found to predict vibrational frequencies closer to experimental results.

For consistency with our previous research, double-ζ plus polarization (DZP) basis sets were adopted in the present study. Thus, one set of pure spherical harmonic *d* functions with orbital exponents $\alpha_d(B) = 0.7$, $\alpha_d(C) = 0.75$, $\alpha_d(O) = 0.85$, and $\alpha_d(S) = 0.7$ for boron, carbon, oxygen, and sulfur, respectively, was added to the standard Huzinaga–Dunning contracted DZ sets, designated as (9*s*5*p*1*d*/4*s*2*p*1*d*) for boron, carbon, and oxygen and (11*s*7*p*1*d*/6*s*4*p*1*d*) for sulfur [24, 25]. The loosely contracted DZP basis set for iron is the Wachters primitive set augmented by two sets of p functions and one set of d functions, contracted following Hood et al. [26], designated as (14*s*11*p*6*d*/10*s*8*p*3*d*).

The geometries of all structures were fully optimized using the two DFT methods. Harmonic vibrational frequencies and the corresponding infrared intensities were evaluated analytically. All computations were performed with the Gaussian 03 program package [27]. The fine grid (75, 302) was the default for evaluating integrals numerically. The finer grid (120, 974) was used for more precise resolution of the imaginary vibrational frequencies [28]. The tight ($10^{-8}$ hartree) designation was the default for the self-consistent field (SCF) convergence. All of the predicted triplet structures in the present study were found to have negligible spin contamination, with $S(S + 1)$ values close to the ideal value of 2.0. The energies reported in the text and figures are those obtained after zero-point vibrational correction.

A given $Fe_a(BS)_a(CO)_b$ structure is designated as **abA-c** where **a** and **b** are the number of BS and CO groups, **c** orders the structures according to their relative energies, and **A** indicates whether the structure is a singlet (**S**), doublet (D), triplet (**T**), or quartet (Q). Thus, the lowest energy singlet structure of $Fe_2(BS)_2(CO)_8$ is designated **28S-1**.

## 3 Results and discussion

### 3.1 Binuclear $Fe_2(BS)_2(CO)_8$ structures

Eleven optimized singlet structures were found for $Fe_2(BS)_2(CO)_8$ (Figs. 1, 2; Table 1) within 25 kcal $mol^{-1}$ of the global minimum **28S-1**. The lowest energy triplet $Fe_2(BS)_2(CO)_8$ structures were found to lie more than 25 kcal $mol^{-1}$ in energy above the global minimum **28S-1**. Therefore, triplet $Fe_2(BS)_2(CO)_8$ structures are not considered in this paper. The singlet $Fe_2(BS)_2(CO)_8$ structures include nine unbridged structures, one singly bridged structure, and one doubly bridged structure.

#### *3.1.1 Unbridged $Fe_2(BS)_2(CO)_8$ structures*

Among the nine unbridged $Fe_2(BS)_2(CO)_8$ structures (Fig. 1; Table 1), five structures, namely **28S-1**, **28S-2, 28S-3**, **28S-4**, and **28S-5**, all consist of two $Fe(BS)(CO)_4$ units linked by an iron–iron bond with no bridging CO or BS groups. Structures **28S-1**, **28S-2**, and **28S-3** have staggered configurations of the CO and BS groups, whereas **28S-4** and **28S-5** have eclipsed arrangements of the CO and BS groups. The other four unbridged $Fe_2(BS)_2(CO)_8$ structures **28S-6**, **28S-7**, **28S-8**, and **28S-11** all consist of one $Fe(BS)_2(CO)_3$ and one $Fe(CO)_5$ unit linked by an iron–iron bond (Fig. 1; Table 1). Structures **28S-6**, **28S-7**, and **28S-8** have staggered arrangements of the CO and BS groups, whereas **28S-11** has an eclipsed arrangement of the CO and BS groups. Their structural differences mainly lie in the

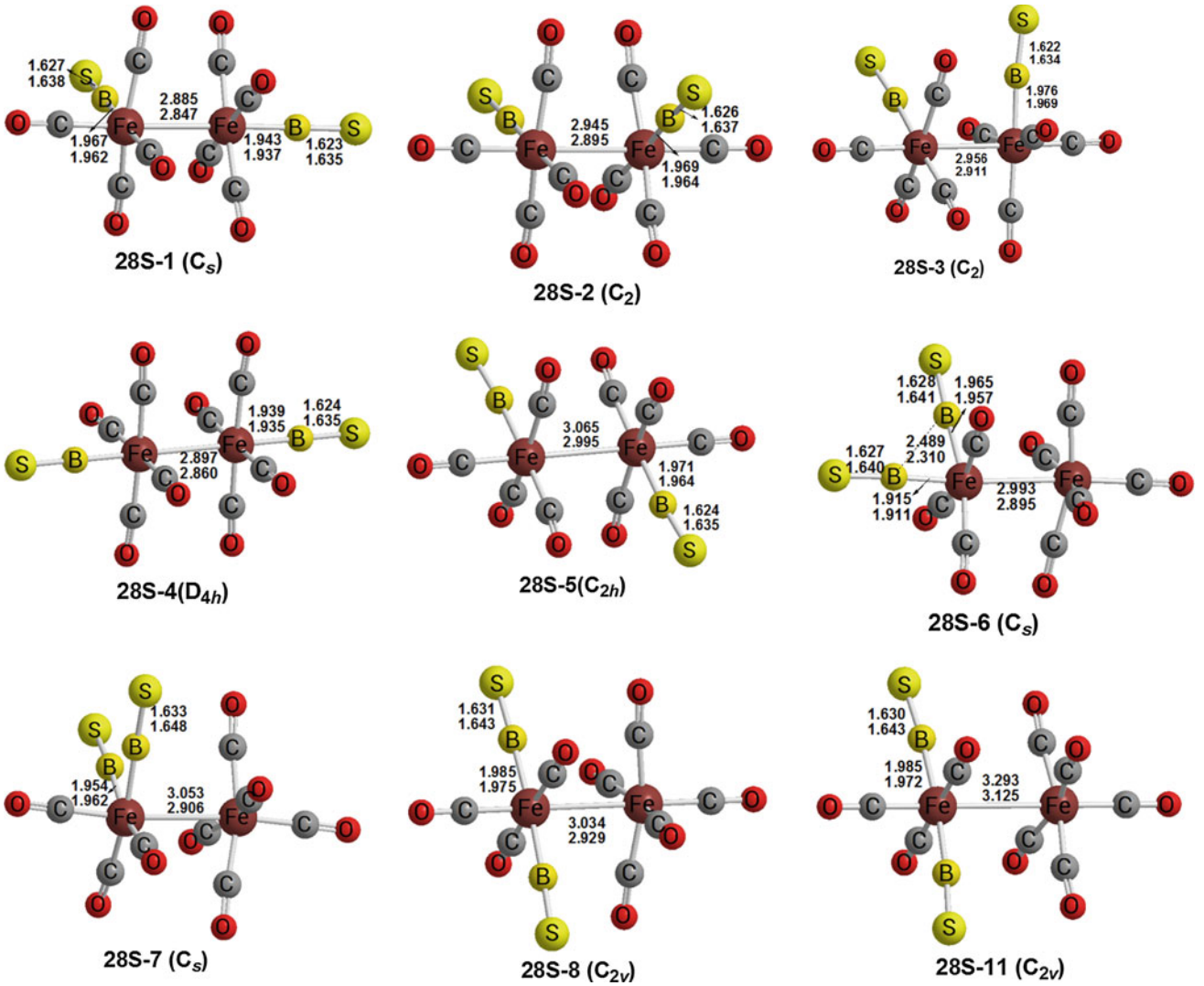


**Fig. 1** Nine unbridged $Fe_2(BS)_2(CO)_8$ structures. In these figures, the *upper numbers* refer to distances (in Å) obtained by B3LYP and the *lower numbers* to those obtained by BP86

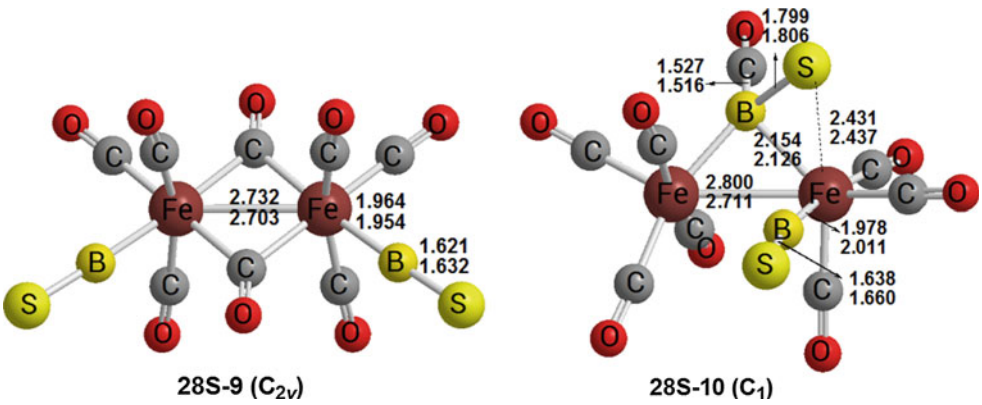


**Fig. 2** Two optimized bridged $Fe_2(BS)_2(CO)_8$ structures. The *upper numbers* refer to distances (in Å) obtained by B3LYP and the *lower numbers* to those obtained by BP86

relative positions of the two terminal BS groups. Structures **28S-5** and **28S-11** are predicted by both the B3LYP and BP86 methods to have imaginary vibrational frequencies. Following the corresponding normal modes leads from the eclipsed structures to the staggered structures, namely **28S-2** and **28S-8**, respectively.

**Table 1** Zero-point energies ($E$, in hartrees), relative energies ($\Delta E$, in kcal mol$^{-1}$), and the numbers of imaginary vibrational frequencies (Nimag) for the optimized $Fe_2(BS)_2(CO)_8$ structures

| Species | B3LYP | | | BP86 | | |
|---|---|---|---|---|---|---|
| | $-E_{ZPVE}$ | $\Delta E_{ZPVE}$ | Nimag | $-E_{ZPVE}$ | $\Delta E_{ZPVE}$ | Nimag |
| **28S-1** ($C_s$) | 4,280.499435 | 0.0 | None | 4,281.046436 | 0.0 | None |
| **28S-2** ($C_2$) | 4,280.498604 | 0.5 | None | 4,281.048253 | −1.1 | None |
| **28S-3** ($C_2$) | 4,280.495127 | 2.7 | None | 4,281.046199 | 0.2 | None |
| **28S-4** ($D_{4h}$) | 4,280.493995 | 3.4 | None | 4,281.037744 | 5.5 | 1 (37$i$) |
| **28S-5** ($C_{2h}$) | 4,280.490659 | 5.5 | 1 (27$i$) | 4,281.041927 | 2.8 | 1 (21$i$) |
| **28S-6** ($C_s$) | 4,280.488789 | 6.7 | None | 4,281.036497 | 6.2 | None |
| **28S-7** ($C_s$) | 4,280.483466 | 10.0 | None | 4,281.032484 | 8.8 | None |
| **28S-8** ($C_{2v}$) | 4,280.476025 | 14.7 | None | 4,281.019173 | 17.1 | 1 (19$i$) |
| **28S-9** ($C_{2v}$) | 4,280.473249 | 16.4 | 1 (78$i$) | 4,281.032683 | 8.6 | None |
| **28S-10** ($C_1$) | 4,280.472733 | 16.8 | None | 4,281.037039 | 5.9 | None |
| **28S-11** ($C_{2v}$) | 4,280.467981 | 19.7 | 1 (25$i$) | 4,281.010348 | 22.7 | 2 (30$i$, 24$i$) |

The $Fe_2(BS)_2(CO)_8$ structures **28S-1**, **28S-2**, and **28S-3** have staggered arrangements of the CO and BS ligands very similar to that of the isoelectronic $Mn_2(CO)_{10}$ (Fig. 1; Table 1). The energies of these three structures lie within 2.7 kcal mol$^{-1}$, suggesting a fluxional system. Structure **28S-1** is composed of two $Fe(BS)(CO)_4$ units linked by an iron–iron single bond of length 2.885 Å (B3LYP) or 2.847 Å (BP86). This iron–iron bond distance is very close to the experimental Mn–Mn distances in $Mn_2(CO)_{10}$ of 2.92 Å [29] and 2.895 Å determined by X-ray crystallography [30]. Structure **28S-1** is a genuine minimum by both the B3LYP and BP86 methods. The axial Fe–B distance of 1.943 Å (B3LYP) or 1.937 Å (BP86) in **28S-1** is slightly shorter than the equatorial Fe–B distance of 1.967 Å (B3LYP) or 1.962 Å (BP86). This implies stronger Fe → B back-bonding in the axial positions than in the equatorial position. This may be a consequence of the stronger *trans* effect of a strongly back-bonding CO group than that of an iron–iron bond.

The $Fe_2(BS)_2(CO)_8$ structures **28S-2** and **28S-1** differ only in the position of one of the terminal BS groups: equatorial for **28S-2** and axial for **28S-1**. The iron–iron bond distance of length 2.945 Å (B3LYP) or 2.895 Å (BP86) in **28S-2** is slightly longer than that in **28S-1** but still corresponds to a formal single bond. The B3LYP and the BP86 methods differ in the relative energy ordering of these structures. Thus, the B3LYP method predicts **28S-1** to lie 0.5 kcal mol$^{-1}$ in energy below **28S-2** (Fig. 1; Table 1). However, the BP86 method predicts **28S-2** to lie 1.1 kcal mol$^{-1}$ in energy below **28S-1**. Since these energy differences are small, these two structures may be considered to be nearly degenerate in energy.

The $Fe_2(BS)_2(CO)_8$ structure **28S-3** lies only 2.7 kcal mol$^{-1}$ (B3LYP) or 0.2 kcal mol$^{-1}$ (BP86) above **28S-1** (Fig. 1; Table 1). The iron–iron bond distance in **28S-3** of length 2.956 Å (B3LYP) or 2.911 Å (BP86) is slightly longer than those in **28S-1** and **28S-2**, but still implies a formal single bond.

The two eclipsed $Fe_2(BS)_2(CO)_8$ structures **28S-4** and **28S-5** consist of two completely equivalent $Fe(BS)(CO)_4$ units linked by an iron–iron bond, but differing in only the location of the two terminal BS groups. Thus, the terminal BS groups are located in axial positions for **28S-4** and in equatorial positions for **28S-5** (Fig. 1; Table 1). Structure **28S-4** lying 3.4 kcal mol$^{-1}$ (B3LYP) or 5.5 kcal mol$^{-1}$ (BP86) above **28S-1** has a small imaginary vibrational frequency of 37$i$ cm$^{-1}$ (BP86). The iron–iron bond distance of 2.897 Å (B3LYP) or 2.860 Å (BP86) in **28S-4** implies a formal single bond. The other eclipsed $Fe_2(BS)_2(CO)_8$ structure **28S-5**, lying 5.5 kcal mol$^{-1}$ (B3LYP) or 2.8 kcal mol$^{-1}$ (BP86) in energy above **28S-1**, has a small imaginary vibrational frequency of 27$i$ cm$^{-1}$ (B3LYP) or 21$i$ cm$^{-1}$ (BP86). The iron–iron bond distance in **28S-5** of 3.065 Å (B3LYP) or 2.995 Å (BP86) is significantly longer than that in **28S-4**, but still implies a formal single bond. The axial Fe–B distance of 1.939 Å (B3LYP) or 1.935 Å (BP86) in **28S-4** is somewhat shorter than that in **28S-1**.

The $Fe_2(BS)_2(CO)_8$ structures **28S-6**, **28S-7**, **28S-8**, and **28S-11** are different types of unbridged structures in which an $Fe(BS)_2(CO)_3$ unit is linked to an $Fe(CO)_5$ unit by an iron–iron bond (Fig. 1; Table 1). These unsymmetrical unbridged $Fe_2(BS)_2(CO)_8$ structures are significantly higher-energy structures than the symmetrical unbridged $Fe_2(BS)_2(CO)_8$ structures discussed above. Structures **28S-6**, **28S-7**, and **28S-8** have staggered arrangements of the ligands very similar to that of the isoelectronic $Mn_2(CO)_{10}$. These three structures have Fe–Fe distances of ~2.9–3.0 Å similar to $Mn_2(CO)_{10}$ implying formal single bonds. Their structural differences mainly lie in the relative positions of the two terminal BS groups.

The eclipsed $Fe_2(BS)_2(CO)_8$ structure **28S-11** is the highest energy of the eleven structures, lying 19.7 kcal mol$^{-1}$

(B3LYP) or 22.7 kcal mol$^{-1}$ (BP86) above **28S-1** (Fig. 1; Table 1). The Fe–Fe distance in **28S-11** of 3.293 Å (B3LYP) or 3.125 Å (BP86) is also the longest iron–iron distance in all eleven $Fe_2(BS)_2(CO)_8$ structures but implies a formal single bond. Structure **28S-11** has small imaginary vibrational frequencies of 25*i* cm$^{-1}$ (B3LYP) or 30*i* and 24*i* cm$^{-1}$ (BP86). The longer Fe–Fe distances in **28S-6**, **28S-7**, **28S-8**, and **28S-11** relative to **28S-5** can be considered as a donor–acceptor single bonds with the $Fe(CO)_5$ unit being the donor and the $Fe(BS)_2(CO)_3$ unit being the acceptor, i.e., $(OC)_5Fe \rightarrow Fe(BS)_2(CO)_3$.

### 3.1.2 *Bridged $Fe_2(BS)_2(CO)_8$ structures*

The $Fe_2(BS)_2(CO)_8$ structure **28S-9**, lying 16.4 kcal mol$^{-1}$ (B3LYP) or 8.6 kcal mol$^{-1}$ (BP86) in energy above **28S-1**, is predicted to have two bridging CO groups (Fig. 2; Table 1). Structure **28S-9** is a genuine minimum by BP86 but has a small imaginary vibrational frequency of 78*i* cm$^{-1}$ by B3LYP. An analogous doubly bridged $Mn_2(CO)_{10}$ structure is predicted in a previous theoretical study [31] to lie 21.0 kcal mol$^{-1}$ (B3LYP) or 14.8 kcal mol$^{-1}$ (BP86) in energy above the corresponding unbridged global minimum. The $Fe_2(BS)_2(CO)_8$ structure **28S-10**, lying 16.8 kcal mol$^{-1}$ (B3LYP) or 5.9 kcal mol$^{-1}$ (BP86) in energy above **28S-1**, has an unusual bridging μ-SBCO ligand formed by coupling the BS group with one of the CO groups and bridging the $Fe_2$ unit through the boron atom. Structure **28S-10** is a genuine minimum by both the B3LYP and BP86 methods. The Fe–Fe distances in both **28S-9** and **28S-10** of 2.732 Å and 2.800 Å (B3LYP) or 2.703 Å and 2.711 Å (BP86) are about 0.1 Å shorter than those in the unbridged structures, indicating the shortening of a formal iron–iron single bond by increasing the number of bridging groups.

## 3.2 Mononuclear $Fe(BS)(CO)_4$ and $Fe(BS)_2(CO)_3$ structures

### 3.2.1 *The tetracarbonyl $Fe(BS)(CO)_4$*

Both DFT methods (B3LYP and BP86) predict two doublet structures for $Fe(BS)(CO)_4$ with a 17-electron configuration for the central iron atom (Fig. 3; Table 2). These two structures are genuine minima without any imaginary vibrational frequencies by both B3LYP and BP86 methods. All of the quartet $Fe(BS)(CO)_4$ structures are predicted to have higher energies and thus are not discussed in this paper.

The global minimum $Fe(BS)(CO)_4$ structure **14D-1** is a $C_s$ symmetry doublet trigonal bipyramidal structure with a linear BS group in an axial position (Fig. 3; Table 2). The other $Fe(BS)(CO)_4$ structure **14D-2**, lying 7.7 kcal mol$^{-1}$ (B3LYP) or 6.6 kcal mol$^{-1}$ (BP86) in energy above **14D-1**, is a doublet $C_{2v}$ square pyramid with a linear BS group in the apical position. Structure **14D-2** has a shorter Fe–B distance than that in **14D-1** by both methods. In previous related theoretical studies, the singlet $Fe(CS)(CO)_4$ [32] and $Fe(BF)(CO)_4$ [33] structures with trigonal bipyramidal rather square pyramid geometry and linear CS and BF groups in the axial positions are found to have lower energies than those with the CS and BF groups, respectively, in the equatorial positions. However, the lowest energy $Fe(BO)(CO)_4$ structure has the BO group located in a basal position of the $FeC_4B$ square pyramid.

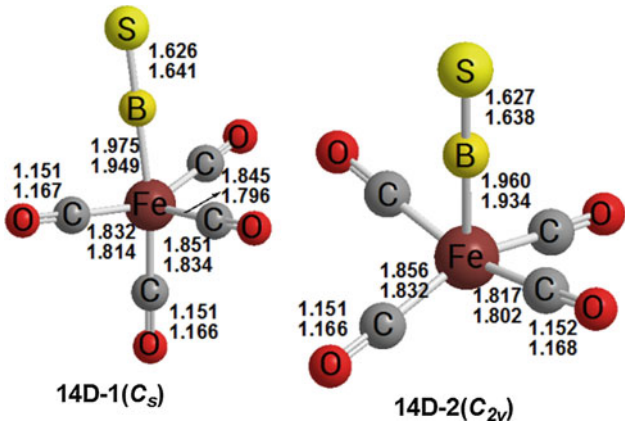


**Fig. 3** Two optimized $Fe(BS)(CO)_4$ structures

**Table 2** Zero-point energies (*E*, in hartrees) and relative energies ($\Delta E$, in kcal mol$^{-1}$) for the optimized $Fe(BS)(CO)_4$ structures

| Species | B3LYP | | BP86 | |
|---|---|---|---|---|
| | $-E_{ZPVE}$ | $\Delta E_{ZPVE}$ | $-E_{ZPVE}$ | $\Delta E_{ZPVE}$ |
| **14D-1** ($C_s$) | 2,140.241313 | 0.0 | 2,140.507374 | 0.0 |
| **14D-2** ($C_{2v}$) | 2,140.229054 | 7.7 | 2,140.496890 | 6.6 |

Neither structure has any imaginary vibrational frequencies

### 3.2.2 *The tricarbonyl $Fe(BS)_2(CO)_3$*

Both DFT methods (B3LYP and BP86) predict three singlet structures and three triplet structures for $Fe(BS)_2(CO)_3$ (Fig. 4; Table 3). The five structures **23S-1**, **23S-2**, **23T-1**, **23T-2**, and **23T-3** are genuine minima without any imaginary frequencies by both the B3LYP and the BP86 methods. Structures **23S-1**, **23S-2**, **23S-3**, and **23T-3** have square pyramidal geometry. In **23T-1** and **23T-2**, the two BS ligands have coupled to form a coordinated $B_2S_2$ unit. This $B_2S_2$ unit can be considered to be a two-electron donor to the iron atom, through either the BS bond in **23T-1** or the BB bond in **23T-2**. The two BS ligands in the singlet structure **23S-2** are also weakly coupled with B–B distances of 2.206 Å (B3LYP) or 2.063 Å (BP86).

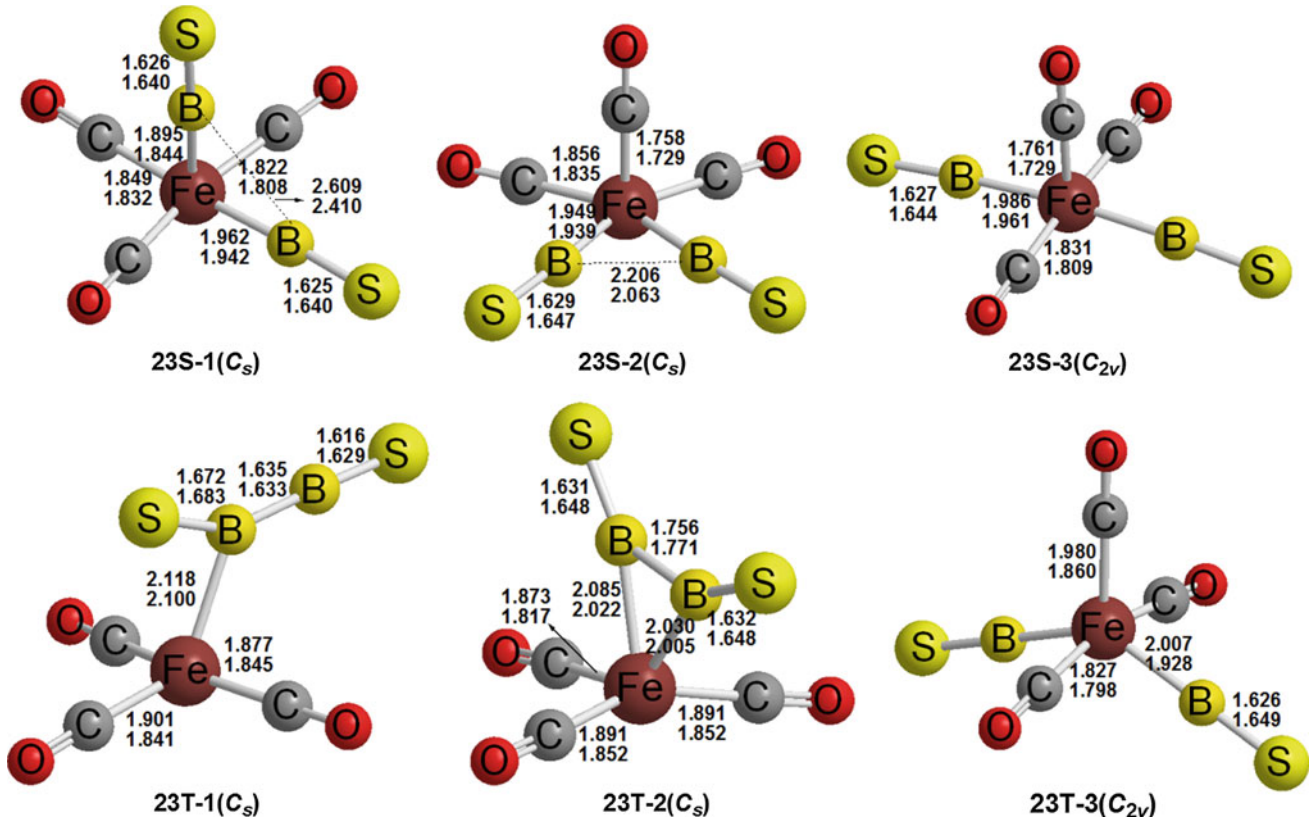


**Fig. 4** Six optimized $Fe(BS)_2(CO)_3$ structures

**Table 3** Zero-point energies ($E$, in hartrees), relative energies ($\Delta E$, in kcal mol$^{-1}$), and numbers of imaginary vibrational frequencies (Nimag) for the optimized $Fe(BS)_2(CO)_3$ structures

| Species | B3LYP | | | BP86 | | |
|---|---|---|---|---|---|---|
| | $-E_{ZPVE}$ | $\Delta E_{ZPVE}$ | Nimag | $-E_{ZPVE}$ | $\Delta E_{ZPVE}$ | Nimag |
| **23S-1** ($C_s$) | 2,449.934503 | 0.0 | None | 2,450.221965 | 0.0 | None |
| **23T-1** ($C_s$) | 2,449.940103 | −3.5 | None | 2,450.206853 | 9.5 | None |
| **23T-2** ($C_s$) | 2,449.934439 | 0.0 | None | 2,450.210802 | 7.0 | None |
| **23S-2** ($C_s$) | 2,449.930616 | 2.4 | None | 2,450.218032 | 2.5 | None |
| **23S-3** ($C_{2v}$) | 2,449.921136 | 8.4 | None | 2,450.203551 | 11.6 | 1 (63*i*) |
| **23T-3** ($C_{2v}$) | 2,449.913590 | 13.1 | None | 2,450.191690 | 19.0 | None |

The global minimum of $Fe(BS)_2(CO)_3$ is either a singlet or a triplet spin state structure, depending upon the theoretical method. The B3LYP method favors the high spin state, while the BP86 favors the low spin state in accord with observations by Reiher et al. [34, 35]. The global minimum predicted by B3LYP is a $C_s$ triplet structure **23T-1**, lying 3.5 kcal mol$^{-1}$ below the singlet structure **23S-1**. However, the BP86 method predicts a $C_s$ singlet structure **23S-1** to be the global minimum, lying 9.5 kcal mol$^{-1}$ below **23T-1**.

### 3.3 Vibrational frequencies

The $\nu$(CO) and $\nu$(BS) frequencies for the optimized $Fe(BS)(CO)_n$ structures ($n$ = 4, 3, 2, 1), $Fe(BS)_2(CO)_3$, and $Fe_2(BS)_2(CO)_8$ (Tables 4, 5) were predicted by the BP86 method, which has been shown to be more reliable for $\nu$(CO) frequencies than the B3LYP method when comparison with experimental data is available [36, 37]. The predicted terminal $\nu$(CO) frequencies for the $Fe(BS)(CO)_n$ ($n$ = 4, 3, 2, 1), $Fe(BS)_2(CO)_3$, and $Fe_2(BS)_2(CO)_8$ structures range from 1,950 to 2,108 cm$^{-1}$, which is typical for terminal CO groups. Table 4 also compares the terminal $\nu$(CO) frequencies of the $Fe(BS)(CO)_4$ global minimum **14D-1** (Fig. 3) with those of the corresponding $Co(BO)(CO)_4$, $Fe(BF)(CO)_4$, $Fe(CS)(CO)_4$, and $Fe(BO)(CO)_4$ structures predicted by using the same BP86 method. Our predicted $\nu$(CO) frequencies for the $Fe(BS)(CO)_4$ structure lie within 25 cm$^{-1}$ of the corresponding $\nu$(CO)

**Table 4** $\nu$(CO) and $\nu$(BS) frequencies (in $cm^{-1}$) of the mononuclear $Fe(BS)(CO)_n$ ($n = 4, 3, 2, 1$) structures (BP86 method)

| Structures | $\nu$(CO) | $\nu$(BS) |
|---|---|---|
| **14D-1** ($C_s$) | 1,999 (1,189), 2,006 (719), 2,012 (525), 2,063 (281) | 1,191 (112) |
| **14D-2** ($C_{2v}$) | 1,993 (1,291), 2,001 (1,163), 2,011 (169), 2,070 (83) | 1,216 (239) |
| $Co(BO)(CO)_4$ ($C_{3v}$) | 2,026 (893), 2,026 (893), 2,039 (471), 2,095 (90) | – |
| $Fe(BF)(CO)_4$ ($C_{2v}$) | 1,984 (1,310), 1,993 (1,011), 2,000 (293), 2,060 (113) | – |
| $Fe(CS)(CO)_4$ ($C_{2v}$) | 1,990 (1,047), 2,008 (331), 2,008 (1,239), 2,070 (191) | – |
| $Fe(BO)(CO)_4$ ($C_s$) | 2,006 (1,216), 2,010 (708), 2,018 (516), 2,075 (96) | – |
| **13D-1** ($C_{2v}$) | 1,985 (1,420), 1,998 (833), 2,059 (168) | 1,206 (199) |
| **13D-2** ($C_s$) | 1,967 (1,006), 1,985 (713), 2,035 (557) | 1,192 (129) |
| **13Q-1** ($C_s$) | 1,979 (1,049), 1,979 (1,049), 2,024 (453) | 1,141 (7) |
| **12Q-1** ($C_{2v}$) | 1,964 (1,651), 2,026 (163) | 1,162 (11) |
| **12Q-2** ($C_s$) | 1,964 (1,196), 2,021 (655) | 1,170 (52) |
| **12D-1** ($C_{2v}$) | 1,957 (1,568), 2,035 (30) | 1,202 (164) |
| **12D-2** ($C_s$) | 1,959 (815), 2,011 (759) | 1,194 (167) |
| **11Q-1** ($C_{\infty v}$) | 2,000 (902) | 1,200 (124) |
| **11D-1** ($C_s$) | 1,950 (526) | 1,195 (163) |
| **23S-1** ($C_s$) | 2,009 (1,121), 2,020 (679), 2,071 (199) | 1,197 (172), 1,226 (175) |
| **23T-1** ($C_s$) | 2,006 (649), 2,009 (801), 2,054 (613) | 1,151 (80), 1,191 (65) |
| **23T-2** ($C_s$) | 2,016 (523), 2,017 (1,059), 2,071 (29) | 1,168 (95), 1,189 (19) |
| **23S-2** ($C_s$) | 1,971 (1,506), 1,995 (651), 2,037 (345) | 1,076 (90), 1,422 (88) |
| **23S-3** ($C_{2v}$) | 1,994 (1,290), 1,995 (572), 2,038 (431) | 1,121 (179), 1,230 (70) |
| **23T-3** ($C_{2v}$) | 1,996 (1,156), 2,009 (620), 2,049 (181) | 1,124 (1), 1,129 (4) |

Infrared intensities in parentheses are in km $mol^{-1}$

**Table 5** $\nu$(CO) and $\nu$(BS) frequencies (in $cm^{-1}$) of the $Fe_2(BS)_2(CO)_8$ structures (BP86 method)

| Structures | $\nu$(CO) | $\nu$(BS) |
|---|---|---|
| $Mn_2(CO)_{10}$ | 1,992, 2,025, 2,053 (gas phase) | – |
| $Mn_2(CO)_{10}$ | 1,983, 2,014, 2,045 (*n*-hexane solution) | – |
| **28S-1** ($C_s$) | 1,989 (306), 2,004 (68), 2,009 (60), 2,028 (1,286), 2,028 (1,168), 2,049 (132), 2,049 (1,068), 2,099 (26) | 1,218 (277), 1,232 (303) |
| **28S-2** ($C_2$) | 1,997 (92), 2,011 (582), 2,015 (434), 2,024 (67), 2,033 (645), 2,035 (889), 2,055 (1,409), 2,090 (26) | 1,219 (439), 1,221 (67) |
| **28S-3** ($C_2$) | 1,996 (28), 2,002 (118), 2,017 (615), 2,022 (437), 2,022 (1,016), 2,028 (539), 2,052 (1,288), 2,087 (225) | 1,221 (108), 1,229 (325) |
| **28S-4** ($D_{4h}$) | 1,998 (0), 1,998 (0), 2,023 (0), 2,027 (1,788), 2,027 (1,788), 2,043 (0), 2,043 (463), 2,102 (0) | 1,229 (708), 1,232 (0) |
| **28S-5** ($C_{2h}$) | 1,989 (0), 2,006 (100), 2,018 (1,683), 2,023 (0), 2,026 (816), 2,026 (0), 2,052 (1,526), 2,084 (0) | 1,221 (503), 1,223 (0) |
| **28S-6** ($C_s$) | 1,985 (379), 1,998 (178), 2,024 (437), 2,027 (1,033), 2,034 (825), 2,040 (662), 2,048 (298), 2,103 (231) | 1,198 (210), 1,226 (292) |
| **28S-7** ($C_s$) | 1,981 (421), 1,990 (141), 2,021 (463), 2,034 (713), 2,040 (877), 2,040 (992), 2,060 (308), 2,104 (232) | 1,161 (198), 1,201 (196) |
| **28S-8** ($C_{2v}$) | 1,986 (525), 2,008 (194), 2,036 (305), 2,041 (734), 2,045 (1,159), 2,047 (768), 2,057 (0), 2,108 (184) | 1,186 (485), 1,213 (13) |
| **28S-9** ($C_{2v}$) | **1,864 (704), 1,890 (2),** 1,998 (0), 2,019 (1,754), 2,024 (34), 2,034 (564), 2,053 (726), 2,082 (186) | 1,231 (395), 1,235 (229) |
| **28S-10** ($C_1$) | 1,986 (148), 1,993 (193), 2,008 (360), 2,011 (798), 2,031 (572), 2,042 (1,221), 2,055 (1,300), 2,084 (377) | **780 (70),** 1,123 (160) |
| **28S-11** ($C_{2v}$) | 1,987 (355), 2,008 (148), 2,035 (203), 2,036 (1,366), 2,045 (759), 2,046 (720), 2,059 (123), 2,106 (250) | 1,181 (418), 1,207 (19) |

Infrared intensities in parentheses are in km $mol^{-1}$

The bridging (CO) and (BS) frequencies are in bold face

**Table 6** Dissociation energies (kcal mol$^{-1}$) for the symmetrical and unsymmetrical dissociations of $Fe_2(BS)_2(CO)_8$

| | B3LYP | BP86 |
|---|---|---|
| $Fe_2(BS)_2(CO)_8$ (**28S-1**) → 2 $Fe(BS)(CO)_4$ (**14D-1**) | 10.6 | 19.9 |
| $Fe_2(BS)_2(CO)_8$ (**28S-1**) → $Fe(BS)_2(CO)_3$ (**23S-1**) + Fe $(CO)_5$ | −10.3 | −8.2 |
| $Fe_2(BO)_2(CO)_8$ → $Fe(BO)_2(CO)_3$ + $Fe(CO)_5$ | 25.6 | 21.7 |

All results reported here refer to the global minima of reactant and products

frequencies of $Co(BO)(CO)_4$, $Fe(BF)(CO)_4$, $Fe(CS)(CO)_4$, and $Fe(BO)(CO)_4$. The terminal $\nu$(CO) frequencies (1,981–2,108 cm$^{-1}$) for the staggered $Fe_2(BS)_2(CO)_8$ structures are also agree well with the experimental infrared $\nu$(CO) frequencies in the isoelectronic $Mn_2(CO)_{10}$, namely 1,983, 2,014, and 2,045 cm$^{-1}$ in *n*-hexane solution and 1,992, 2,025, and 2,053 cm$^{-1}$ in the gas phase (Table 5).

The $\nu$(CO) frequencies for the bridging carbonyl groups in the binuclear $Fe_2(BS)_2(CO)_8$ derivatives are predicted to range from 1,864 to 1,890 cm$^{-1}$. They are typically 100–200 cm$^{-1}$ lower than the terminal $\nu$(CO) frequencies in similar compounds relating to the lower C=O bond orders in carbonyl groups bonded to two metal atoms rather than a single metal atom.

The terminal $\nu$(BS) frequencies for the $Fe(BS)(CO)_n$ ($n$ = 4, 3, 2, 1), $Fe(BS)_2(CO)_3$, and $Fe_2(BS)_2(CO)_8$ structures with uncoupled BS ligands are predicted to range from 1,121 to 1,235 cm$^{-1}$. The weak coupling of the terminal BS ligands in the $Fe(BS)_2(CO)_3$ structure **23S-2** leads to an abnormally low terminal $\nu$(BS) frequency of 1,076 cm$^{-1}$ and an abnormally high $\nu$(BS) frequency of 1,422 cm$^{-1}$. The $\nu$(BS) frequency of 780 cm$^{-1}$ for the bridging BS group in **28S-10** is much lower than those for the terminal BS groups. This suggests a lower effective B–S bond order in a BS group bonded to two metal atoms relative to a BS group bonded to a single metal atom.

### 3.4 Symmetrical and unsymmetrical dissociation of $Fe_2(BS)_2(CO)_8$ into mononuclear fragments

The only possible dissociation pathway of the homoleptic $Mn_2(CO)_{10}$ into mononuclear fragments involves symmetrical dissociation into ·$Mn(CO)_5$ radicals. This is an endothermic process with calculated and experimental dissociation energies around 40 kcal mol$^{-1}$ [38]. The analogous symmetrical dissociation of the isoelectronic binuclear thioboronyl $Fe_2(BS)_2(CO)_8$, like that of $Mn_2(CO)_{10}$, is also an endothermic process, but significantly less endothermic, requiring 10.6 kcal mol$^{-1}$ (B3LYP) or 19.9 kcal mol$^{-1}$ (BP86) (Table 6). However, the predicted dissociation energy for the unsymmetrical dissociation of $Fe_2(BS)_2(CO)_8$ into the stable $Fe(CO)_5$ plus the 16-electron species $Fe(BS)_2(CO)_3$ is exothermic by −10.3 kcal mol$^{-1}$ (B3LYP) or −8.2 kcal mol$^{-1}$ (BP86) suggesting that $Fe_2(BS)_2(CO)_8$ is thermochemically disfavored. This contrasts with the oxygen analog $Fe_2(BO)_2(CO)_8$ for which the unsymmetrical dissociation into the stable $Fe(CO)_5$ and the 16-electron complex $Fe(BO)_2(CO)_3$ is highly endothermic at ~23 kcal mol$^{-1}$. If the kinetic barrier for the unsymmetrical dissociation of $Fe_2(BS)_2(CO)_8$ into $Fe(CO)_5$ + $Fe(BS)_2(CO)_3$ is sufficiently high, it might still be possible to synthesize $Fe_2(BS)_2(CO)_8$ by dimerization of $Fe(BS)(CO)_4$, since that is an exothermic process.

## 4 Summary

The lowest energy structures for the thioboronyl $Fe_2(BS)_2(CO)_8$ are symmetrical unbridged structures having two $Fe(BS)(CO)_4$ units linked solely by an Fe–Fe bond. Such structures are analogous to the well-known unbridged structure of the valence isoelectronic $Mn_2(CO)_{10}$. Unsymmetrical unbridged structures consisting of an $Fe(CO)_5$ unit bonded to an $Fe(BS)_2(CO)_3$ unit by an Fe → Fe dative bond lie at least ~6 kcal mol$^{-1}$ in energy above the symmetrical unbridged structures. The lowest energy bridged $Fe_2(BS)_2(CO)_6(\mu\text{-}CO)_2$ structure lies ~12.5 kcal mol$^{-1}$ in energy above the lowest energy isomeric unbridged structure. A higher-energy isomeric $Fe_2(BS)(CO)_7(\mu\text{-}SBCO)$ structure is also found in which a BS and CO ligand have coupled to form a bridging SBCO ligand.

The structures of the mononuclear derivatives $Fe(BS)(CO)_n$ ($n$ = 4, 3, 2, 1) and $Fe(BS)_2(CO)_3$ were also investigated in order to evaluate the thermochemistry of the dissociation of $Fe_2(BS)_2(CO)_8$ into mononuclear fragments. The low-energy $Fe(BS)_2(CO)_3$ structures include triplet structures in which the two BS ligands have coupled through B–B bond formation to form a $B_2S_2$ ligand. The binuclear derivative $Fe_2(BS)_2(CO)_8$ is found to be viable with respect to symmetrical dissociation into two $Fe(BS)(CO)_4$ units. However, unsymmetrical dissociation of $Fe_2(BS)_2(CO)_8$ into the stable $Fe(CO)_5$ and $Fe(BS)_2(CO)_3$ is an exothermic process by ~9 kcal mol$^{-1}$, suggesting that $Fe_2(BS)_2(CO)_8$ is thermochemically unstable.

## 5 Supporting information

Tables S1 to S30: theoretical Cartesian coordinates (in Å) for the $Fe(BS)(CO)_n$ ($n$ = 4, 3, 2, 1), $Fe(BS)_2(CO)_3$, and $Fe_2(BS)_2(CO)_8$ structures using the B3LYP/DZP and BP86/DZP methods; Tables S31 to S60: Theoretical harmonic vibrational frequencies (in cm$^{-1}$) for the $Fe(BS)(CO)_n$ ($n$ = 4, 3, 2, 1), $Fe(BS)_2(CO)_3$, and $Fe_2(BS)_2(CO)_8$

structures using the B3LYP/DZP and BP86/DZP methods; Figure S1 and Table S61: $Fe(BS)(CO)_3$ structures; Figure S2 and Table S62: $Fe(BS)(CO)_2$ structures; Figure S3 and Table S63: Fe(BS)(CO) structures; Complete Gaussian reference (Ref. [27]).

**Acknowledgments** This work was partly supported by Special-funded Program on National Key Scientific Instruments and Equipment Development (2012YQ17000408), Zhejiang Province Public Technology Research Industrial Projects (2013C31073), National Nature Science Foundation of China (61378035), Science and Technology Major Project of Zhejiang Province (2012C12017-5), and 151 Talent Project of Zhejiang Province (12-2-008). We are also indebted to the US National Science Foundation (Grant CHE-1057466) for support of this work.

## References

1. Cotton FA (1976) Prog Inorg Chem 21:1
2. Vidović D, Aldridge S (2009) Angew Chem Int Ed 48:3669
3. Braunschweig H, Radacki K, Schneider A (2010) Science 328:345
4. Braunschweig H, Radacki K, Schneider A, Angew A (2010) Chem Int Ed 49:5993
5. McDonald JK, Innes KK (1969) J Mol Spect 29:251
6. Bell S, McLean MML (1976) J Mol Spect 63:521
7. Chang Y, Li Q-S, Xie Y, King RB (2013) J Phys Chem A 117:2260
8. Chang Y, Li Q-S, Xie Y, King RB, Schaefer HF (2012) New J Chem 36:1022
9. Chang Y, Li Q-S, Xie Y, King RB (2012) Inorg Chem 51:8904
10. Gong X, Li Q-S, Xie Y, King RB, Schaefer HF (2010) Inorg Chem 49:10820
11. Dahl LF, Rundle RE (1963) Acta Cryst 16:419
12. Martin M, Rees B, Mitschler A (1981) Acta Cryst B 38:6
13. Ziegler T, Autschbach J (2005) Chem Rev 105:2695
14. Bühl M, Kabrede H (2006) J Chem Theory Comput 2:1282
15. Brynda M, Gagliardi L, Widmark PO, Power PP, Roos BO (2006) Angew Chem Int Ed 45:3804
16. Sieffert N, Bühl M (2010) J Am Chem Soc 132:8056
17. Schyman P, Lai W, Chen H, Wang Y, Shaik S (2011) J Am Chem Soc 133:7977
18. Adams RD, Pearl WC, Wong YO, Zhang Q, Hall MB, Walensky JR (2011) J Am Chem Soc 133:12994
19. Lonsdale R, Olah J, Mulholland AJ, Harvey JA (2011) J Am Chem Soc 133:15464
20. Becke AD (1993) J Chem Phys 98:5648
21. Lee C, Yang W, Parr RG (1988) Phys Rev B 37:785
22. Becke AD (1988) Phys Rev A 38:3098
23. Perdew JP (1986) Phys Rev B 33:8822
24. Dunning TH (1970) J Chem Phys 53:2823
25. Huzinaga S (1965) J Chem Phys 42:1293
26. Hood DM, Pitzer RM, Schaefer HF (1979) J Chem Phys 71:705
27. Frisch MJ et al (2004) Gaussian 03, revision D 01. Gaussian, Wallingford (see Supporting Information for details)
28. Papas BN, Schaefer HF (2006) J Mol Struct 768:275
29. Dahl LF, Rundle RE (1963) Acta Cryst 16:419
30. Martin M, Rees B, Mitschler A (1981) Acta Cryst B 38:6
31. Xie Y, Jang JH, King RB, Schaefer HF (2003) Inorg Chem 42:5219
32. Zhang Z, Li Q-S, Xie Y, King RB, Schaefer HF (2009) Inorg Chem 48:1974
33. Xu L, Li Q-S, Xie Y, King RB, Schaefer HF (2010) Inorg Chem 49:1046
34. Reiher M, Salomon O, Hess BA (2001) Theor Chem Acc 107:48
35. Salomon O, Reiher M, Hess BA (2002) J Chem Phys 117:4729
36. See especially Furche F, Perdew JP (2006) J Chem Phys 124:044103
37. Wang HY, Xie Y, King RB, Schaefer HF (2005) J Am Chem Soc 127:11646
38. Barckholtz TA, Bursten BE (2000) J Organomet Chem 596:212